Centre for Research in Computational and Applied Mechanics
University of Cape Town
Rondebosch, Cape Town, South Africa

A COMPUTATIONAL NEUROMUSCULAR MODEL OF THE HUMAN UPPER AIRWAY

WITH APPLICATION TO THE STUDY OF OBSTRUCTIVE SLEEP APNOEA

Author: Jean-Paul Pelteret
Supervisor: Prof. B. Daya Reddy

Thesis presented for the degree of
Doctor of Philosophy
in the department of Mechanical Engineering
University of Cape Town
November 2013

cercecam

ABSTRACT

Numerous challenges are faced in investigations aimed at developing a better understanding of the pathophysiology of obstructive sleep apnoea. The anatomy of the tongue and other upper airway tissues, and the ability to model their behaviour, is central to such investigations.

In this thesis, details of the construction and development of a three-dimensional finite element model of soft tissues of the human upper airway, as well as a simplified fluid model of the airway, are provided. The anatomical data was obtained from the Visible Human Project, and its underlying micro-histological data describing tongue musculature were also extracted from the same source and incorporated into the model. An overview of the mathematical models used to describe tissue behaviour, both at a macro- and microscopic level, is given. Hyperelastic constitutive models were used to describe the material behaviour, and material incompressibility was accounted for. An active Hill three-element muscle model was used to represent the muscular tissue of the tongue. The neural stimulus for each muscle group to *a priori* unknown external forces was determined through the use of a genetic algorithm-based neural control model.

The fundamental behaviour of the tongue under gravitational and breathing-induced loading is investigated. The response of the various muscles of the tongue to the complex loading developed during breathing is determined, with a particular focus being placed to that of the genioglossus. It is demonstrated that, when a time-dependent loading is applied to the tongue, the neural model is able to control the position of the tongue and produce a physiologically realistic response for the genioglossus. A comparison is then made to the response determined under quasi-static conditions using the pressure distribution extracted from computational fluid-dynamics results. An analytical model describing the time-dependent response of the components of the tongue musculature most active during oral breathing is developed and validated. It is then modified to simulate the activity of the tongue during sleep and under conditions relating to various possible neural and physiological pathologies. The retroglossal movement of the tongue resulting from the pathologies is quantified and their role in the potential to induce airway collapse is discussed.

ACKNOWLEDGEMENTS

I would like to start by offering my deepest thanks to my supervisor, Prof. B. Daya Reddy. It has been a privilege and an inspiration working with you. Thank you for the knowledge that you have imparted to me, as well as the support you have provided and for the patience that you have had while I have conducted this work. I also appreciate the opportunities you have provided for me to showcase our work, as well as the financial support during my time at CERECAM.

Dr. Andrew McBride deserves a special mention for the many patient hours that he has spent with me discussing a wide variety of topics related to this work. He first introduced me to *deal.II* and has provided me much tutelage, guidance and mentorship. I have enjoyed our collaborations on several side projects. Furthermore, I wish to thank him for taking the time to proof-read portions of this document.

This topic was originally suggested by Dr. Yougan Saman through Dr. Indresan Govender. I thank you both for your insights and discussions on the problem of obstructive sleep apnoea and your encouragement to go forward with this work.

Thanks to my friends and colleagues at CERECAM and BISRU (both research groups at the University of Cape Town), with whom I spent many hours at work and at play. In particular, I wish to thank Dr. Harish Appa (my quiet partner in crime with whom I have shared a workspace for 3 theses and at least 7 full years), Yaseen Kajee (who worked with me on this topic for his MSc.), Beverley Grieshaber, Richard Curry, Dr. Reuben Govender, Ernesto Ismail, Marlan Perumal, Evan Smuts and Jonathan Bergh for their many years of friendship, support, and fruitful work discussions and debate. I offer further thanks to the individuals in our *deal.II* workgroup, and in particular Michael Rapson for his time, thoughts and help on the many problems we discussed. The support staff of CERECAM has done so much to make the work environment a focused and productive one and for this I thank them. This includes Olivia Goodhind in taking care of all of the exhausting administrative work, and to Graham Inggs for his time, patience and genius at fixing the myriad of computer-related issues that one faced.

I wish to also acknowledge my new friends and colleagues at the LTM (chair of applied mechanics at the Friedrich-Alexander Univesität Erlangen-Nürnberg) who have offered their support while I finished writing this document. I would like to express my gratitude to Prof. Paul Steinmann for the support and extra latitude that he has provided me while I have served two masters. I also appreciate the input that Dr. Denis Davydof has provided, as well as the proof-reading that he performed.

This work has seen much indirect input from several individuals that deserve mention. Dr. Reiner Wilhelms-Tricarico has provided a freely-available dataset and model of the tongue. A portion of this dataset was used

as a proof-of-concept for the first stage of the model developed in this work, and facilitated development of the constitutive model for the tongue while the geometric and histological data was being developed in parallel. A short tea-time conversation with Dr. Schalk Kok lead to a great improvement in the work-optimisation algorithm. The anonymous reviewers of our publications provided valuable feedback that contributed to the improvement of the model.

My final thanks goes to my family who have had infinite patience with me and have shown me nothing but love and support throughout my studies. My success is your success. My parents, Robin and Denise, have been unwavering in their belief in me. I am so very grateful for all that you both have done for me over the years. I must offer a special thanks to my father for the many hours that he has spent meticulously poring over my work and for the indispensable advice that he has provided. My brothers Marc and Eugene, sister-in-law Tammy, and my uncle David have consistently provided encouragement for me to work towards my goals and offered me guidance when I've asked for it. I have also appreciated Marc's assistance in critiquing the layout of this document. And lastly I would like to thank my wife, Kerryn, who not only spent many nights sleeping in my office to keep me company while I worked, but also methodically sifted through my bibliography and corrected it. You have done so much for me and I look forward to making it all up to you over the many free weekends to come!

Software

It is stated with complete honesty that this thesis could not have been accomplished without the work and dedication of various groups of people who openly share their projects with the world. Simulations were performed exclusively on the *Gnu/Linux* operating system and programs were built using the *GCC* compilers and toolchain. In particular, I am is extremely grateful to the authors and contributors of the following open-source scientific software packages that were directly used in the development of this work:

***deal.II*:** A high-performance finite element library [13, 14]

***GAlib*:** A genetic algorithm package [295]

***Trilinos*:** A framework and toolbox for large scale scientific computation [100]

***Metis*:** A graph partitioning toolbox [136]

***UMFPACK*:** A direct solver for unsymmetric sparse linear systems [55]

***GSL*:** A library of numerical routines and algorithms [81]

***OpenMPI*:** A high performance message passing library for multi-CPU communication [79]

Financial

Funding for this work was provided by the National Research Foundation through the South African Research Chair for Computational Mechanics, and the University of Cape Town.

PEER-REVIEWED CONTRIBUTIONS AND AWARDS

Papers

J-P. V. Pelteret and B. D. Reddy. Computational model of soft tissues in the human upper airway. *International Journal for Numerical Methods in Biomedical Engineering*, 28:111–132, 2012. doi: 10.1002/cnm.1487

Y. Kajee, J-P. V. Pelteret, and B. D. Reddy. The biomechanics of the human tongue. *International Journal for Numerical Methods in Biomedical Engineering*, 29:492–514, 2013. doi: 10.1002/cnm.2531

J-P. V. Pelteret and B. D. Reddy. Development of a computational biomechanical model of the human upper–airway soft–tissues towards simulating obstructive sleep apnea. *Clinical Anatomy*, 2013. doi: 10.1002/ca.22313. Accepted

Software

J-P. V. Pelteret and A. McBride. `deal.II` step-44 tutorial: Three-field formulation for non-linear solid mechanics, 2010. URL `http://www.dealii.org/developer/doxygen/deal.II/step_44.html`. Accessed July 2013

Awards

Best poster: J-P. V. Pelteret and B. D. Reddy. Computation model of tissues in the human upper airway, August 2010. Poster presented in Respiratory Mechanics Track, 6th World Congress of Biomechanics (WCB 2010), Singapore

TABLE OF CONTENTS

List of Figures

List of Tables

LIST OF ALGORITHMS

ABBREVIATIONS AND ACRONYMS

AOI	Angle of insertion
BC	Boundary condition
CAD	Computer-aided design
CE	Contractile element
CFD	Computational fluid dynamics
CG	Conjugate gradient
CSA	Cross-sectional area
DOF	Degree-of-freedom
EPH	Equilibrium point hypothesis
FE	Finite element
FEA	Finite element analysis
FEM	Finite element method
FSI	Fluid-structure interaction
FVM	Finite volume method
GA	Genetic algorithm
HUA	Human upper airway
PE	Parallel element
SE	Series element
SEF	Strain-energy function
SSOR	Symmetric successive over-relaxation
VHP	Visible Human Project
VWA	Volume-weighted average

Muscle abbreviations

DG	Digastric
GG	Genioglossus
GGa	Genioglossus, anterior component
GGm	Genioglossus, medial component
GGp	Genioglossus, posterior component
GH	Geniohyoid
HG	Hyoglossus
IL	Inferior longitudinal
LVP	Levator veli palatini
MH	Mylohyoid
PG	Palatoglossus
PP	Palatopharyneus
SG	Styloglossus
SH	Stylohyoid
SL	Superior longitudinal
TV	Transversus
TVP	Tensor veli palatini
UV	Musculus uvulae (uvula)
VT	Verticalis

GLOSSARY

General terminology

a priori	Pertaining to something that is known in advance.
Coanda effect	A flow effect describing the tendency of a moving stream of fluid in the near vicinity of a surface to deviate towards that surface.
FFMR	Abbreviation for fraction of full muscle response. Related to the muscle activation, this quantity describes how close to a state of tetany a muscle is.
mask	A collection of pixels or voxels defined using manual or automatic processes.
Re	Abbreviation for Reynold's number. A dimensionless number describing the ratio of inertial to viscous forces in a fluid. It can be used to infer the state of fluid flow, namely whether it is laminar, transitional or fully turbulent.
SMP	Abbreviation for shared memory processor. A computer architecture that utilises a single, common memory structure between multiple processors or processor cores.
voxel	The three-dimensional equivalent of a pixel.

Medical terminology

in vivo	Within in a living organism.

anterior An anatomical orientation implying "forwards" or towards the frontal profile. In official anatomical nomenclature it is used with reference to the ventral or belly surface of the body.

atonia Deficient muscle tonicity.

ATP Abbreviation for adenosine triphosphate. An important chemical compound which forms the basis of the metabolic process by providing energy to cells.

axial Of, or pertaining to, the long axis of a structure or part.

BMI Abbreviation for body mass index. A standard measure of risks associated with overweight in adults. A first-approximation of a subject's weight status made by dividing their weight (in kg) by the square of their height (in m).

CNS Abbreviation for central nervous system. The component of the nervous system responsible for co-ordination of bodily activities and processing and integration of sensory information.

coronal An anatomical plane parallel to the long axis of the body and perpendicular to the axial plane. Also known as the frontal plane.

CPAP Abbreviation for continuous positive airway pressure. A non-invasive medical technique used to treat sleep-disordered breathing by actively increasing the oropharyngeal pressure during inspiration thereby increasing airflow to the lungs; also jargon for the medical apparatus used to accomplish this process..

CT Abbreviation for computerised tomography (also CAT – computed axial tomography – scan). A medical imaging technique which uses multiple X-ray images to produce a three-dimensional view of a region of tissue.

distal An anatomical orientation describing an object further from a specified point.

DTI Abbreviation for diffusion tensor imaging. A medical imaging technique that tracks the movement of water molecules within tissues.

EMG Abbreviation for electromyogram. A medical device used to monitor skeletal muscle activity by measuring electrical potential within the tissue.

hypercapnia Excess of the carbon-dioxide content of the blood.

hypoxia A reduction of the oxygen content of the blood reaching the tissues.

incline The act or measurement taken from a supine to an upright orientation.

inferior An anatomical orientation implying "below" or towards the foot end.

isometric A term describing muscle contraction during which the length of the contracting muscle remains constant.

isotonic A term describing muscle contraction during which the force of contraction remains constant.

lateral An anatomical orientation implying "outside" or away from the median plane or anteroposterior line of the body; it also refers to the orientation coinciding with lying on the side.

MAD Abbreviation for mandibular advancement device. A medical device used to increase airway patency by physically repositioning the mandible, and therefore the tongue, forward.

medial An anatomical orientation implying "the middle" or closer to the median plane of the midline of the body or structure.

midsagittal An anatomical plane parallel to the long axis of the body.

MRI Abbreviation for magnetic resonance imaging. A medical imaging technique used to produce a three-dimensional view of a region of tissue by measuring magnetic fields generated by magnetisation of atomic nuclei.

NREM Abbreviation for non-rapid eye movement. A sleep-state in which brain activity is reduced and muscle atonia occurs. The later, regenerative stages of the sleep cycle are in NREM stages.

OSA Abbreviation for obstructive sleep apnoea (syndrome). A multi-causal sleep disorder resulting from the loss of patency in the oropharynx.

patency A description of the airway related to its dilation and the ease of movement of air within it. A loss of patency implies constriction or closure of a portion the airway.

pennation Having a structure like that of a feather; the angle between the direction of the muscle fibres and the line of action of the muscle.

PEPT Abbreviation for positron emission particle tracking. An industrial and medical imaging device, adapted from positron emission tomography, used to track the position of a radioactive marker undergoing beta decay.

posterior An official anatomical nomenclature used to imply "backwards" or towards the rear or dorsal profile.

prone The orientation that coincides with lying on the stomach or ventral surface.

proprioception A sense that provides spatial awareness of the position and orientation of the body's parts relative to one another.

proximal An anatomical orientation describing an object closer to a specified point.

recline The activity or measurement taken from an upright to a supine orientation.

REM Abbreviation for rapid eye movement. A sleep-state near arousal in which dreaming occurs.

sagittal Any anteroposterior plane parallel to the midsagittal plane.

SDB Abbreviation for sleep-disordered breathing. A broad classification of breathing-related disorders and syndromes that occur primarily during sleep.

superior An anatomical orientation implying "above" or towards the head end.

supine The orientation that coincides with lying on the back or dorsal surface.

tetany A physiological state with activation and subsequent contraction of muscular tissue; a term most commonly associated with pathophysiology.

transverse Situated at right angles to the long axis of the body or a part.

upright The orientation that coincides with the normal vertical positioning or posture.

Mathematical terminology

deterministic Given an identical set of starting parameters, the result of an operation or algorithm will be entirely repeatable.

major symmetry For a fourth-order tensor that possesses major symmetry, the following can be said of its components: $\mathbb{A}_{ABCD} = \mathbb{A}_{CDAB}$.

metaheuristic A category of typically non-deterministic algorithms that explore a given search-space to find a near-optimal solution to a given problem.

minor symmetry For a fourth-order tensor that possesses minor symmetries, the following can be said of its components: $\mathbb{A}_{ABCD} = \mathbb{A}_{BACD} = \mathbb{A}_{ABDC}$.

PDS Abbreviation for positive-definite symmetric; a symmetric tensor that has all positive eigenvalues.

RMSE Abbreviation for root mean squared error; defined as $\text{RMSE} = \sqrt{\frac{1}{n}\sum^{n}(x-\bar{x})^2}$.

NOMENCLATURE

Greek

α	Activation level
θ	Angle of incline, measured from the horizontal
γ	Orientation angle cosine
$\bar{\bar{\lambda}}$	Volume-weighted average stretch
$\boldsymbol{\sigma}$	Cauchy stress tensor
$\boldsymbol{\tau}$	Kirchhoff stress tensor
δ	Kronecker delta
ρ	Density
Π	Energy functional
γ	Shear strain
κ	Bulk modulus
Λ	Lagrange multiplier
$\boldsymbol{\varphi}$	Motion
ψ	Strain-energy per unit volume
λ	Stretch
τ_F	Activation level fall time
θ	Dilatation
τ_R	Activation level rise time
ε	True strain
ϕ	Volume fraction
ν	Poisson's ratio

Latin

a	Current area
A	Reference area
$\boldsymbol{a}$	Current area vector
$\boldsymbol{A}$	Reference area vector
$\boldsymbol{b}$	Left Cauchy-Green deformation tensor
$\boldsymbol{B}$	Material shape function gradient
$\overset{\star}{\boldsymbol{B}}$	Spatial shape function gradient
$\boldsymbol{b}$	Body force vector
$\boldsymbol{C}$	Right Cauchy-Green deformation tensor
$\boldsymbol{C}$	Second-order elastic tangent
$\boldsymbol{d}$	Rate-of-strain tensor
$\boldsymbol{E}$	Green-Lagrange strain tensor
$\boldsymbol{e}$	Local basis vector
$\boldsymbol{F}$	Deformation gradient

$\boldsymbol{f}$	Force vector
$\boldsymbol{g}$	Gravitational vector
$\boldsymbol{I}$	Second-order identity tensor
$\boldsymbol{l}$	Velocity gradient
$\boldsymbol{N}$	Reference normal vector
$\boldsymbol{n}$	Current normal vector
$\boldsymbol{P}$	First Piola-Kirchhoff stress tensor
$\boldsymbol{P}$	Point; coordinate position
$\boldsymbol{R}$	Rotation tensor
$\boldsymbol{S}$	Second Piola-Kirchhoff stress tensor
$\boldsymbol{t}$	Traction vector
$\boldsymbol{U}$	Material stretch tensor
$\boldsymbol{u}$	Displacement vector
$\boldsymbol{V}$	Spatial stretch tensor
$\boldsymbol{v}$	Velocity vector
$\boldsymbol{X}$	Material point
$\boldsymbol{x}$	Spatial point
c_L	Muscle stretch cut-off parameter
f_{c}^{L}	Contractile element length relationship
$f_{\mathrm{c}}^{\mathrm{V}}$	Contractile element velocity relationship
f_{p}	Parallel element length relationship
f_{s}	Series element length relationship
J	Volumetric Jacobian
L	Length
m	Mass
M	Muscle (global quantity)
u	Neural excitation
p	Pressure
$\overset{\star}{\boldsymbol{x}}$	Goal position
t	Time
t^*	Non-dimensional time
$T_0^{\max}$	Peak nominal isometric muscle stress
T_0^s	Peak muscle stress scaling factor
v	Current volume
V	Reference volume
w	Optimisation algorithm weight
W	Work
E	Small strain Young's modulus
G	Small strain shear modulus
K	Tangent stiffness
R	Residual
T	Nominal stress
N	Shape function

Operators, calligraphic and blackboard symbols

A	Assembly operator
$\mathbb{C}$	Spatial fourth-order elasticity tensor
$\mathbb{H}$	Material fourth-order elasticity tensor
$\mathbb{I}$	Fourth-order identity tensor
$\mathbb{P}$	Spatial deviator tensor
$\boldsymbol{\chi}$	Configuration transformation map
$\mathcal{B}$	Body
$\bar{\otimes}$	Non-standard dyadic tensor product
Γ	Boundary
Ω	Domain or configuration
$\nabla \times (\bullet)$	Curl of a quantity
$\det(\bullet)$	Determinant of a tensor
$\nabla \cdot (\bullet)$	Divergence of a quantity
$(\bullet)$	Generic quantity (typically a vector or tensor)

$(\bullet)^{\dot{}}$	Rate of a quantity	$\otimes$	Dyadic tensor product
$\nabla(\bullet)$	Gradient of a quantity	$\prime$	Derivative of scalar function
$\hat{(\bullet)}$	Vector normalisation	$\lambda_i^{(\bullet)}$	i^{th} principal value of a tensor
d	Infinitesimal increment	$(\bullet)^{\mathrm{S}}$	Symmetric part of a tensor
Δ	Linear increment	$\mathrm{tr}\,(\bullet)$	Trace of a tensor
δ	Virtual increment	$\overline{(\bullet)}$	Isochoric component of a tensor
$I_i^{(\bullet)}$	i^{th} tensor invariant	$\widehat{(\bullet)}$	Volumetric component of a tensor
$\mathbf{O}$	Objective function	D	Frechét derivative

Superscripts

-1	Inverse	S_α	Shear component
h	Discretisation	t	Traction
φ	Displacement	u	u^{th} Uzawa iteration
e	Element	CI	Initial to current
ext	External	CR	Reference to current
N	Normal component	RI	Initial to reference
n	n^{th} Newton-Raphson iteration	T	Transpose

Subscripts

c	Contractile	max	Maximum
ext	External	min	Minimum
f	Fibre (local quantity)	nom	Nominal (Reference value)
geo	Geometric	p	Parallel
I	Initial	0	Reference
int	Internal	s	Series
iso	Isochoric	t	Tissue
mat	Material	vol	Volumetric
M	Matrix	p	Point

1. INTRODUCTION

Sleep is an important part of our daily routine and plays a vital role in human's ability to perform effectively. From inception to awakening, the brain and muscle activity undergoes various changes as one moves between different states of sleep. In addition to the many critical cellular metabolic activities that occur during sleep, the reversal of fatigue and general physical and mental revitalisation may only occur when a state of deep-sleep is attained. Disruptions in sleep patterns lead to less time being spent in a state of deep-sleep, and thus a degradation in the quality of sleep.

A multitude of causes may result in interruptions to healthy sleep patterns. Excluding the obvious external environmental influences, short- and long-term physiological and anatomical changes may have an increasing role to play in this regard. During non-rapid eye movement (NREM) sleep, brain activity is reduced and a decrease in general muscle tone, atonia, occurs [308, 294]. The rapid eye movement (REM) state is, amongst other things, characterised by a temporary muscle paralysis initiated to prevent involuntary movement. Due to the process of aging, changing levels of fitness and general well-being, the human anatomy and physiology undergo numerous changes. Such changes include the modification of chemical and hormonal levels, general muscle tone, and quantity and distribution of adipose tissue. All of these influence bodily functions on both a conscious and unconscious level during the various stages of sleep.

Of the many sleep-related disorders, the understanding of those associated with breathing has become more important. Obstructive sleep apnoea (OSA) in particular is a syndrome of increasing prevalence in modern society, with the affliction presenting in approximately $4-9\%$ of the adult male population of the United States of America[1] [164, 238, 73], for example. Characterised by a partial or complete reduction in airway patency, the collapse of the upper airway leads to brief or, in the case of severe OSA, extended periods of hypoxia. During the process of restoring airway patency, the individual often performs violent movements. Collectively, these lead to a reduction in the quality of sleep. Although it severely reduces the quality of life of the individual, it is not necessarily life-threatening in itself[2]. However, associated with this disorder are many secondary effects which may have more severe direct consequences.

Many treatments have been evaluated and used to correct the syndrome but the success of these treatments, measured as an extended removal of symptoms associated with the disorder, is mixed. However, such treatments can only be utilised after a clinical diagnosis of the disorder is made. This requires a degree of intervention on the individual's behalf as the main presentation is non-restorative sleep and snoring of which the

[1] Up to 40% of all men suffer from a sleep-related disorder [294, 53]. It has been estimated that nearly a quarter of all American men experience some type of sleep-related breathing disorder which negatively impacts on quality of life [164].

[2] In rare instances, such as the occasion documented by Pearce and Saunders [209], it has been listed as the primary cause of death.

sufferer is unaware. A secondary person would have to draw attention to the problem and an individualised sleep study needs to be performed [53]. During a nocturnal polysomnogram, the number of apnoeic events and their effect on the body are measured. Due to the lack of public knowledge of the disorder and of the likely cause of their daytime tiredness, many live with the affliction undiagnosed and untreated. The need for complete understanding the disorder, its risk factors and the development a comprehensive and effective treatment has never been more relevant.

1.1 A description of OSA

OSA is a general category of disorders related to upper airway occlusion of varying location, cause and nature [168]. A simple description given by Avrahami et al. [7] for the cause of OSA is the narrowing of the oropharynx, which may occur in the region of the soft palate and uvula, or the base of the tongue. This region, that being the primary site of collapse, is highlighted in figure 1.1.

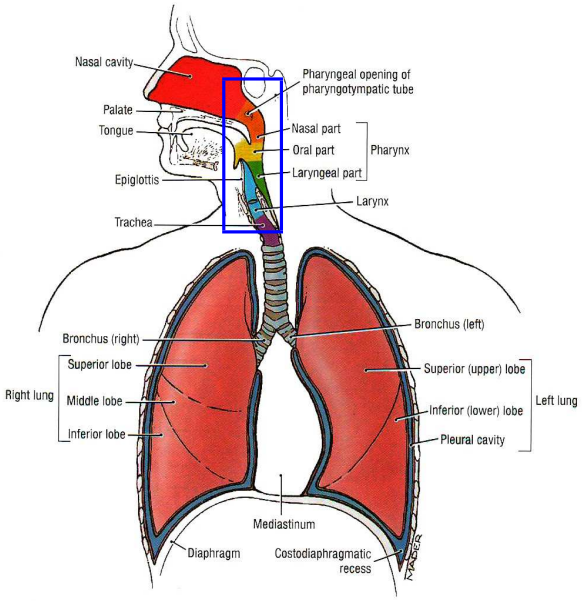

Figure 1.1: The respiratory system and area of focus for OSA research. Image sourced from Agur and Dalley [2, p. 28].

However, the underlying aetiology and pathophysiology, that is the root cause of the disorder, is complex and differs significantly between individuals. The dynamics of both neuromuscular control of the upper airway and airflow are not fully understood, and are currently the focus of significant research. Supplementing the basic information presented below are detailed reviews and discussions of the pathogenesis of OSA provided by Malhotra and White [164], Ryan and Bradley [238], White [308], Davidson [53], Waite [294], Fogel et al. [73], Ayappa and Rapoport [8].

Two main variations of sleep apnoea are considered by clinicians, namely obstructive and *central / complex* apnoea. While OSA is a result of the presence of an airway obstruction alone, complex apnoea has an additional component related to the dysfunction of the respiratory control system [276]. The primary result of an apnoeic spell is a reduction in the delivery of oxygen to the lungs, leading to hypoxia and hypercapnia. Successive episodes of apnoea cause the blood chemistry to change, with further oxygen desaturation and

an increase in carbon dioxide levels. This in turn leads to temporary sleep arousal as a corrective mechanism to the event. Increased respiratory effort and hyperventilation which may occur during arousal may lead to further destabilisation of the airway and the promotion of further apnoeas. [308]

Sleep-disordered breathing (SDB) is commonly a result of both neuromuscular and anatomical abnormalities in the human upper airway (HUA) [227]. The central respiratory system controls the dilators, but they react to multiple stimuli including the intrapharyngeal pressure, mechanoreceptors, blood chemistry and lung volume [238]. In healthy individuals, the airway muscles respond by a reflexive mechanism in the order of milliseconds to changing airway conditions during wakefulness [164, 238, 73]. OSA in particular is associated with a reduction in motor control of the oropharyngeal dilators, leading to sub-optimal muscle responsiveness to changing airway conditions [308, 164]. Due to the lack of anatomical support of the muscles in the upper airway[3], it is particularly vulnerable to negative effects of diminishing muscle activity [164, 73]. The loss of patency thus primarily occurs at the end of expiration or beginning of inspiration [238]. In most patients, the collapse of the airway generally begins at the retropalatal and oropharyngeal regions, followed by the base of the tongue and then hypopharynx [238]; these three sites provide classification to the form of OSA [294]. However, the overall characteristics of the presentation of the disorder differ between individuals [308]. A summary of the speculated sequence of events leading to one form of upper airway occlusion in obese patients is provided by Remmers et al. [231]:

1. The narrowing of the pharynx, aided by the compromise of upper airway muscle control, leads to a decrease in pharyngeal pressure below a critical value and subsequent pharyngeal collapse (loss of patency).

2. Reduction in airflow initiates involuntary chemical stimulation of the dilator muscles. Activity in the airway dilators, as well as other inspiratory muscles, increases but their action remains insufficient to overcome the low airway pressures.

3. Voluntary stimulation of the airway dilators results in the removal of the source of the occlusion and airway patency is restored.

Alternative hypotheses for the cause of OSA include timing irregularities between the oropharyngeal dilators and the diaphragm [164, 308] and the associated ventilatory instability [73], fatigue or injury of the dilators [164], fluid surface tension effects related to the airway mucosa [238] and chemistry related to neurotransmitters [238]. From a physiological perspective, the conclusion from a study conducted by BuSha et al. [31] was that the fundamental physiological behaviour of the muscles in OSA sufferers changes.

Further, the muscles respond differently during sleep and wakeful states. Experiments have determined that those inflicted with OSA require greater muscle activity during wakeful inspiration to overcome the lower pressures associated with narrower airways. The adaptive mechanisms of the neural system during periods of consciousness are able to accommodate these requirements, even for those that exhibit the worst characteristics associated with OSA. However, specifically during sleep, tonic activation of the dilators is not maintained. [164, 238, 73]

[3] The evolutionary cause for this is speculated to be related to the development of the capability of speech and the associated dual-use of the pharynx during respiration and eating, thus requiring a balance of flexibility and compliance for swallowing with rigidity to resist low airway pressures developed during inspiration.

Cause, effect and correction

It is well understood that the ultimate cause of pharyngeal collapse is the development of low airway pressures that the airway is not able to resist. However, there are a multitude of factors that directly and indirectly influence the susceptibility to the loss of airway patency. One environmental factor is the posture of the head and neck [205, 122, 269, 15, 8, 18, 268]. Studies have demonstrated that sleeping in the supine position leads to a more collapsible airway, mainly due to the change in muscle response as the posture is altered.

It is important at this point to consider that, even though the gross anatomical features of the human body remain largely the same between people, each person has their own individual physical characteristics that may contribute to the likelihood of them presenting with OSA. Many cephalometric studies have been performed to determine what these characteristics are and the degree to which they increase the chances of having SDB. There exists a strong correlation between length of the airway [249, 206, 166], neck circumference [294] and OSA. The orofacial skeletal structure [238, 308, 73, 125] also plays a role in this regard, and it has been observed that people with narrower upper airways and/or posteriorly-positioned maxillae and mandibles [76] are predisposed to the condition. These general features have been linked to genetics and the inheritance of anatomical traits [308, 294]. The general morphology of the oropharynx has also been studied [76, 270], and correlation between the occurrence of OSA and tongue size [73, 294, 248], the positioning of the hyoid bone [294] and the distribution of adipose tissue [164, 238, 73, 248] has been found. Linked to the latter is the subject's body mass index (BMI) [125, 173] and general obesity[4] [33, 8]. The presence of nasal obstructions [238, 294, 227, 236, 75] and increased nasal resistance [250] has been correlated to lower airway pressures or may possibly lead to the use of oral inspiration during sleep [174].

Linked to the issues of the gross anatomy are those of a physiological nature. Age [291, 173, 270], gender (which can be linked to airway length) and ethnicity [164, 238, 8] all have a role to play in this regard. Each is related to anatomical structure, hormones [8] and distribution of adipose tissue. Furthermore, studies show that muscle strength reduces with age [219]. In terms of blood chemistry, hypoxia leads to hypercapnia and other chemical changes, affecting the response of the muscles [261, 3, 8]. Neuromuscular abnormalities [227], including loss of coordination between upper airway dilators and diaphragm [308, 164] and a decrease in muscle tone [111, 3, 231, 8], may contribute to airway collapse. However, there is also is evidence that plasticity in the dilator muscles' functioning exists and that this may be altered due to OSA [31]. Muscular compensation has been viewed in patients with a strong disposition for airway collapse [138]. Fatigue and muscle recovery are also thought to contribute to the syndrome [25]. Furthermore, the response of the genioglossus (GG) changes measurably between wakeful and sleep states. It has been observed in OSA patients that the GG remains functional during wakefulness to prevent airway collapse [18], thus linking neuromuscular dysfunction to the sleep state as well.

The consequences of the disorder extend far beyond the direct effects airway collapse, namely to the development of hypoxia and hypercapnia. The most common association with the syndrome is snoring[5] [49], an affliction which affects almost all those having OSA. Narcolepsy and daytime sleepiness [294, 53] are prevalent, the direct result of which is an increase in occupational and vehicular accidents [294, 164, 53]. More serious medical conditions including hypertension, increased cardiac risk [30, 32, 294, 53] and strokes [164], all due to the increased stress on the body, have been linked to the condition.

Many forms of treatment have been tested for OSA and SDB in general. Surgical intervention [294, 181, 134,

[4] However, 30% of patients with OSA are not obese [164], but do present with narrower airways [238].
[5] It has been estimated that 10% of the population of snorers have one form of OSA [110].

162] is a common, and offers options that include tonsillectomy and adenoidectomy (which does not have a high rate of success in adults) [53], uvulopalatopharyngoplasty (also not particularly successful) [294] and maxillomandibular advancement [294]. Orthodontic devices [43, 200, 181, 239], which temporarily simulate the effect of maxillomandibular advancement through clamping and advancing the tongue, have been shown to increase the cross-sectional area (CSA) of the velopharynx. Manual electrical stimulation of the tongue [109, 126], used to initiate contraction of the airway dilators, has been used with mixed success. Devices, such as continuous positive airway pressure (CPAP) machines [294, 53, 30, 73, 137], have been developed to actively react to the occurrence of apnoeic spells by increasing the pressure of the airway. They have been shown to be extremely good at preventing the onset of OSA, but issues of compliance [164] render these machines only moderately successful overall.

1.2 Challenges involved in research of sleep disorders

One of the greatest challenges in both experimental and computational research of the oropharynx and the tongue is its multiple levels of complexity. The geometry of the oropharynx and tongue is highly complex, and the surrounding anatomy is intricate and greatly influences its movement. Some of the macroscopic features of the anatomy are very fine and difficult to incorporate into models. Furthermore, the histology of the tongue musculature is incredibly complex and difficult to describe. The correct functioning of the tongue relies heavily on this histology, and so it is important to have a good basis of understanding of its functioning and the interplay between muscles. It is the coordination of several muscle groups that maintains control of the movement of the tongue; this is an incredibly challenging aspect of tongue functioning to quantify.

The issue of complexity of muscle coordination has been succinctly addressed in an editorial penned by Sokoloff [256]. Though studies have focused on the action of a number of the extrinsic muscles, few have been performed to determine the activity of the intrinsic ones, and even less the co-activity of several muscles in unison. It has been hypothesised that both intrinsic and extrinsic muscles in the tongue must be co-active to facilitate its movement and functioning, and that they do not necessarily act discretely. The action of multiple muscles is required to support and control the tongue motion, and these controlling units change during inspiration and expiration. Movement also influences muscle fibre orientation and its underlying physiological construction, thereby changing the mechanical effect. The effect of an individual muscle unit is thus affected by that of all of the other units. With all of this complexity, the basis for the selection of active tongue motor units by the neurological system remains unknown. One possibility is that multiple muscle units (subsets of the muscles themselves) are recruited simultaneously in order to perform movements; another is that properties of the muscle units (such as location) are the basis for selection. The reason is simply unknown at this time.

Apart from that of the tongue's neurological control, a number of open questions remain to be addressed. From a clinical perspective, it is strongly believed that diminishing activity in the airway dilators during sleep is the primary cause of OSA [308]. It is noted that very little work has been done to understand the influence of the central nervous system (CNS) in this regard [308] and how this may be altered under changing blood chemistry [168]. Furthermore, the exact nature of the role of obesity in the onset of OSA is unclear [66, 227]. This plays out as subtleties in the treatment of the disorder, ergo that CPAP machines require reconfiguration after weight loss [168]. Overall, it remains to be seen whether the upper airway can be stabilised without an unstable ventilation control mechanism, such as that which may be yielded by treatment with CPAP [168].

Advanced experimental methods used to understand tongue functioning

The gross anatomy of the tongue is well understood and documented. However, some details regarding the structure and movement of this organ are only now being realised with the advent of modern technologies. Both experimental and computational methods are vital to the future of upper airway research.

Being as highly mobile as it is, large deformation and therefore strains are present in the tissues of the tongue. Dynamic magnetic resonance imaging (MRI) provides researchers with the ability to observe *in vivo* in-plane tongue movements. The strain attained during dynamic motion is able to be experimentally quantified using tagged MRI and can form a basis for experimental validation of finite element analysis (FEA) models such as the one presented in this work. On a histological note, diffusion tensor imaging (DTI) provides a method for mapping the distribution and direction of muscles fibres in the tongue *in vivo*, which can also provide data for the construction of computational models. A sample of results of each technique is shown in figure 1.2. Positron emission particle tracking (PEPT) is an emerging tool that allows for the tracking of individual radio-active tracer particles in space, which may be useful for visualising airflow in airway and conceptually tracking surface motion and deformations.

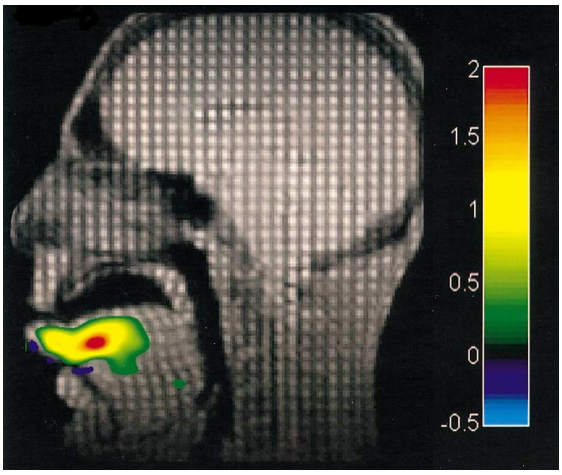

(a) Tagged MRI of human tongue depicting strain in the anterior-posterior direction. Image sourced from Napadow et al. [190].

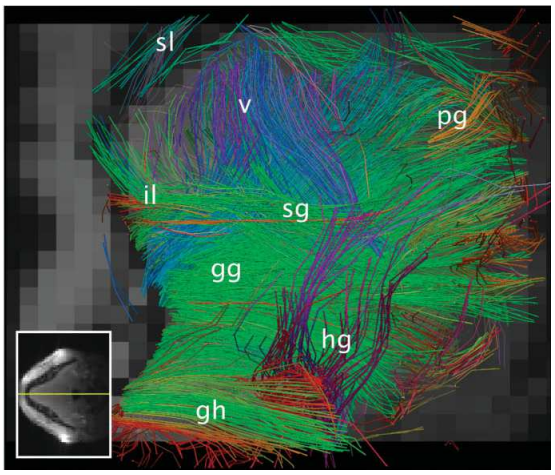

(b) Visualisation of constituent muscle groups using DTI. Image sourced from Gaige et al. [80].

Figure 1.2: Examples of modern technologies used to study tongue mechanics and histology

Understanding the active tissue response and behaviour is also crucial to the development of computer models. Above the standard indentation tests used to understand passive tissue behaviour (see appendix D.3.1), magnetic resonance elastography [39] can provide *in vivo* data of the viscoelastic properties of the tongue. Furthermore, electromyogram (EMG) (discussed further in section 2.6), which provides a recording of electrical signals sent to the muscles, gives insight into the active behaviour of muscles.

1.3 Goals of this work

In this work, we consider OSA restricted to the region of the upper oropharynx, and therefore primarily a consequence of movement of the tongue. A complete experimental dataset of muscle activation patterns

during breathing has not yet been described. Under very controlled environments, EMG data has been experimentally obtained for a principle few muscles, while the influences (if any) of the remaining muscles have been left unexplored. This is unsurprising considering the complex physiology and micro-histology of the upper airway. Furthermore, there are numerous physical and environmental factors that heavily influence this data. Although we understand that the GG long since has been experimentally identified as the main airway dilator in the tongue, it has not yet been fully described or quantified which factors influence its functioning. Furthermore, the roles of the other tongue muscles during breathing have not been extensively discussed.

The primary purpose of this work is to determine the outcome of reduced muscle activity in the main airway dilators, thereby simulating neural depression and the loss of reflexive mechanisms that both occur during sleep. In this way, it is desirable that one qualitatively describe the effect of diminished tongue muscle responsiveness and comment on its likely contribution to the reduction in airway patency.

In order to achieve this goal, several broader steps are to be taken. A physiologically accurate model of the tissues of the human upper airway should first be created. Such a model needs to incorporate accurate macro- and micro-scale models of the airway physiology. Representative models for both the passive and neurologically active muscle tissue response are to be developed, along with sufficiently representative models of other tissues also relevant to the problem geometry. The model is to be validated in terms of its ability to reproduce the physiologically correct motions of the tongue. A mechanism to determine muscle responses to resist complex or *a priori* unknown load distributions on the tongue needs to be developed. Using this, an examination of the effect of environmental factors on both the passive tissues and the active muscle response is to be conducted. Simultaneously, an investigation of the roles of the different muscles in the tongue, with an emphasis on the GG, in response to breathing is required to be performed. Once there is an understanding of the response of the tongue to the various external influences, some methodology for translating these relationships to one that is representative of its sleep-state response is to be formulated.

Towards accomplishing the primary goals of this work, several secondary tasks are to be considered. The loading distributions assumed to be present on the tongue should be validated. To this end, it is desirable to compare the results obtained from pressure distributions extracted from steady computational fluid dynamics (CFD) results to idealised descriptions of airway pressure fields. At the same time, it will be possible to quantify the difference between static and dynamic models of the tongue and the response of its muscles under these temporal assumptions. Furthermore, comparing the case of nasal to oral respiration is likely to provide insights into why oral respiration, particularly inspiration, during sleep plays a large role in the onset of apnoeic events. Insights towards producing simpler and more computationally efficient models to understand the OSA condition are to be presented and discussed.

1.4 Outline of this document

This thesis is decomposed into two main parts. In part I, a presentation of the underlying theory and development of the model is given. Part II is devoted to the presentation and discussion of the computational geometry and simulation results. Finally, further information on topics discussed in the previous two parts is provided in the Appendices.

The document addresses the concepts and theory relevant to the construction of a computational model of the human upper airway in the following order:

In chapter 2, the anatomy of the upper airway and the physiology of skeletal muscles are presented with a particular focus on the tongue. Mathematical details related to the field of continuum mechanics are subsequently discussed in chapter 3. Chapter 4 details the specific finite element (FE) implementation of nonlinear elastic media and some numerical algorithms used in this work. The description of energy functions that may be used to model general nonlinear, transversely isotropic materials are shown in chapter 5. Chapter 6 then provides specific information regarding the mathematical description and numerical implementation of active skeletal muscle. A novel mechanism to introduce active, dynamic control to the tongue is then outlined in chapter 7.

Now that the underlying theory and implementation has been detailed, the construction of the geometry for the solid model of the tongue and surrounding soft tissues is presented in chapter 8, alongside a preliminary fluid model that is used in validation studies. Numerous studies are then performed using the tongue model and an assumed pressure distribution. Firstly, the passive response of the tongue to gravitational and pressure loading is conducted in chapter 9. Its active response and the effect of the contraction of individual muscles on the underlying histology is examined in chapter 10. These two studies are followed by an optimisation study and evaluation of the performance of the neural control model under dynamic loading conditions, which is presented in chapter 11. Basic, steady state fluid-flow studies using a matching geometry to the solid model are presented in chapter 12. Finally, the results of the dynamic studies and static results obtained from pressure-data extracted from the fluid-flow study are compared in chapter 13. Further work is presented in order to translate these sets of information into an analytical model that is subsequently used to analyse the movement of the tongue in conditions of sub-optimal muscle functioning.

PART I

THEORY AND DEVELOPMENT OF THE MATHEMATICAL MODELS

2. ANATOMY AND PHYSIOLOGY

In this chapter, the gross anatomy of the HUA relevant to the OSA condition is presented. Details of the histology of soft and hard tissue components are given and the basic functioning of the muscles groups is described.

2.1 Overview of the upper airway

The human airway consists of a number of distinct anatomical regions, namely the oral cavity and oropharynx (which itself is divided into the velopharynx, hypopharynx, retroglossus), the nasal passages and nasopharynx, larynx, upper and lower trachea, the bronchial tree, and the lung parenchyma. Each region of the airway is surrounded by a complex arrangement of tissues with distinct properties and functions, all of which greatly influences the dynamics of air passing through the airway. This study focuses on the upper airway, outlined in figure 1.1. For more detailed reference of the general anatomy of the upper airway, figures 2.1 to 2.4 are provided and are referred to in the following text in which a very brief summary of the upper airway construction is presented.

2.1.1 Oral cavity

The oral cavity describes that cavernous region of the mouth that houses the tongue. A general orientation of its anatomy can be view in figures 2.1 and 2.2, and a detailed view of the anatomy its presented in figure 2.3. The tongue, whose volume occupies the greater part of the oral cavity, is an agile muscular organ that plays a vital role in speech and swallowing. Its complex physiology is detailed in section 2.2. The tongue has a number of bony attachments, most important of which are the mandible (inferior) and the hyoid bone (distal), and as such its movement within the closed oral cavity is restricted.

The other bony structure of the oral cavity is the maxilla. This forms the foundation of the anterior facial profile and the cheeks, and the hard palate that provides the floor to the nasal passages and the roof to the oral cavity. The hard palate is the point of attachment of the soft palate (distal) from which arises the uvula. The oropharynx, situated posterior to the oral cavity, is a soft anatomical structure constituted largely of muscle.

Externally, the soft tissue components of the cheeks are skin, adipose tissue and muscle (the buccinator). Internally, sublingual and submandibular glands that generate saliva lie inferior, anterior and lateral to the

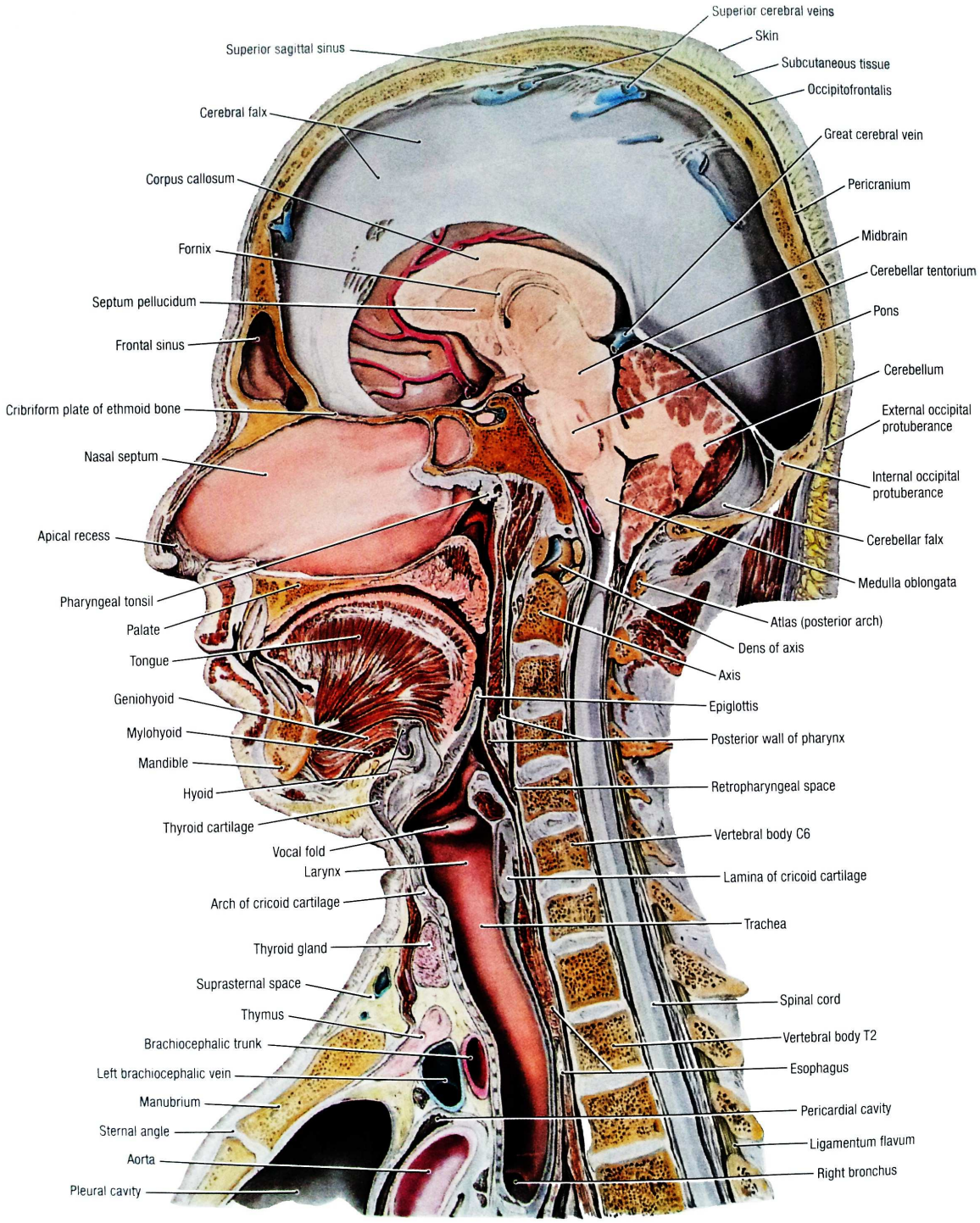

Figure 2.1: Midsagittal section through the upper airway. Image sourced from Agur and Dalley [2, p788].

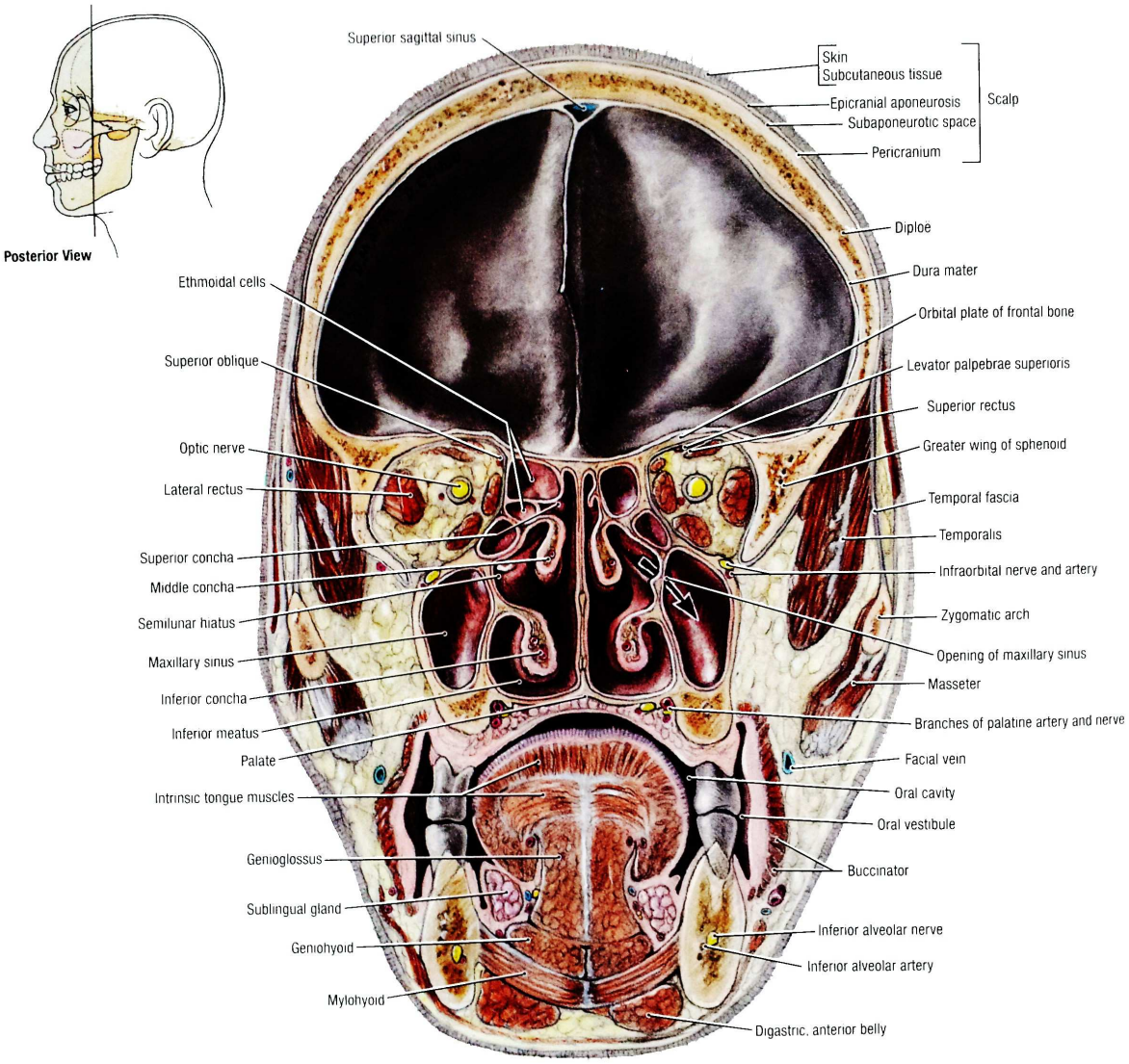

Figure 2.2: Coronal section through the oral cavity and nasal cavity (posterior view). Image sourced from Agur and Dalley [2, p. 694].

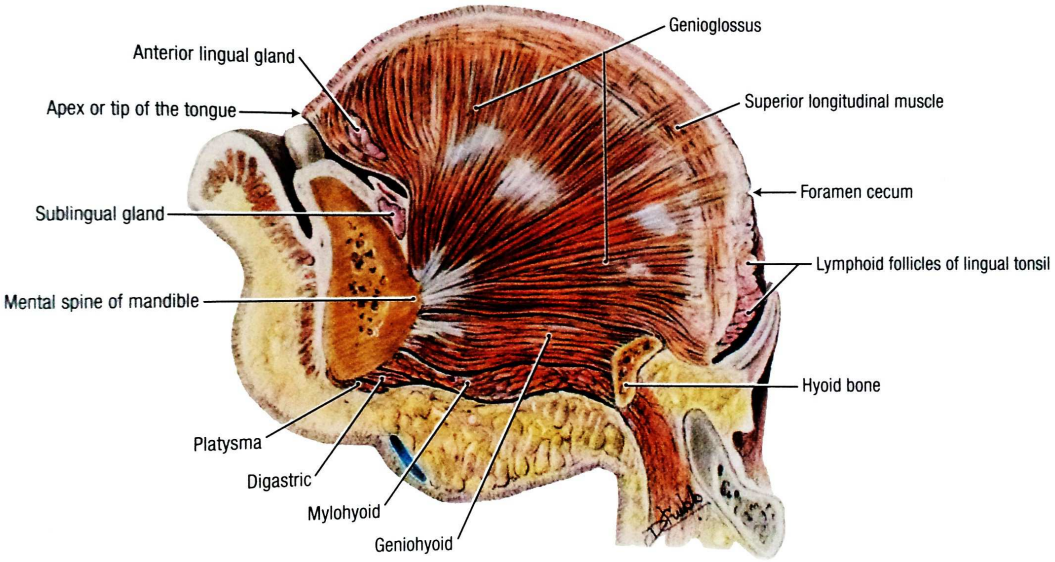

(a) Medial section of tongue

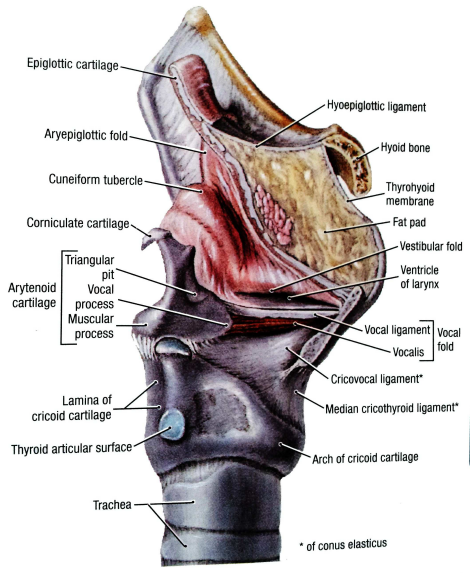

(b) Medial section of epiglottis

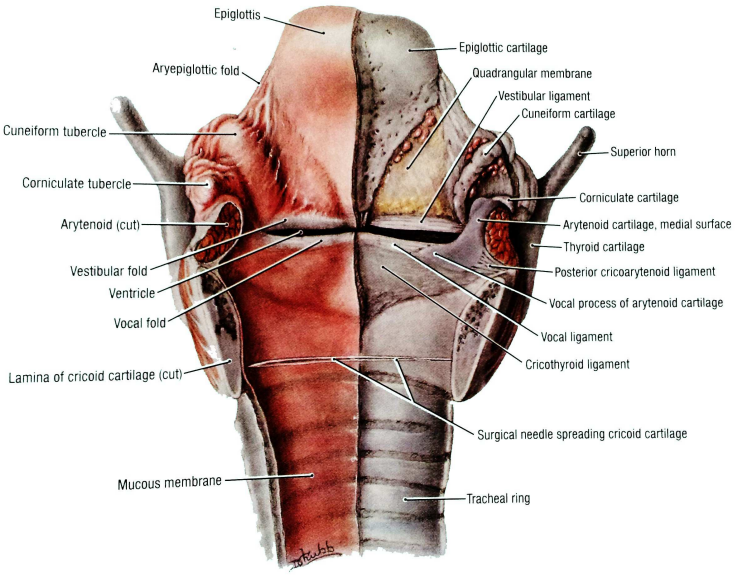

(c) Coronal section of epiglottis (posterior view)

Figure 2.3: Detailed sections of the anatomy of the oral cavity. Image sourced from Agur and Dalley [2, pp. 669,781,783].

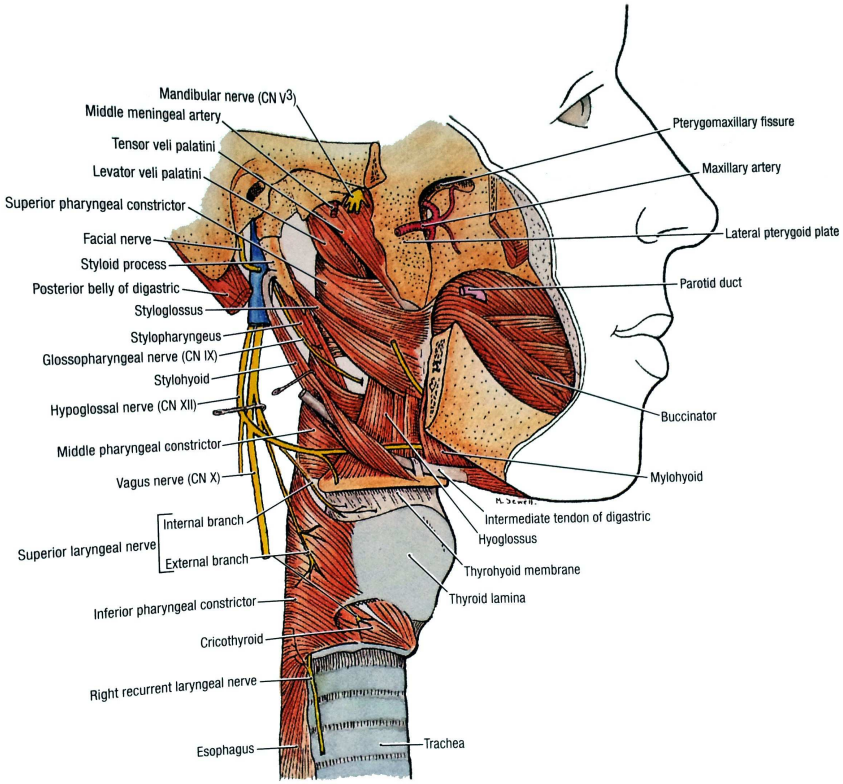

(a) Muscles of the neck. Visible are some of the muscles of the tongue and hyoid that have origin outside the tongue body.

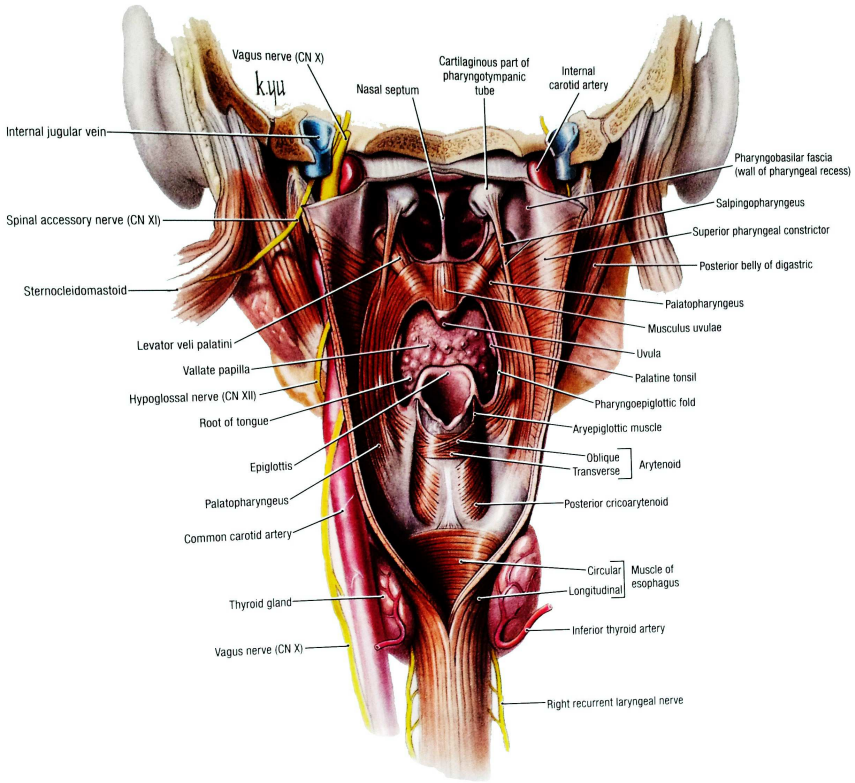

(b) Coronal section of the oropharynx (posterior view). The anatomy of the soft palate, as well as the arrangement of the oropharyngeal constrictors is visible, as are some of the extrinsic muscles of the tongue and soft palate.

Figure 2.4: Detailed sections of the anatomy of the neck and pharynx. Image sourced from Agur and Dalley [2, pp. 767,771].

tongue and buccal glands adjacent to the medial surface of the mandible. Numerous muscles, anatomically separate from the tongue body, comprise the floor of the oral cavity. The hyoid is a fragile, floating bone located posterior to the tongue in the floor of the mouth, and vital in speech formation. From the main body of this bone protrude the greater and lesser processes, giving the hyoid a U-shape. There are a number of muscles both superior and inferior that are inserted into it and control its position. The epiglottis, a tissue-covered thin cartilaginous flap, is located at the root of the tongue and posterior to the hyoid. It covers the entrance to the larynx, functions to prevent the entrance of foreign material into the trachea and plays a crucial role in swallowing. Located in the anterior region of the fat pad on which the epiglottis is bedded, posterior to the thyroid membrane, is a bursa.

The throat is a broad colloquial term used to describe that part of the neck that lies in front of the vertebra and houses these structures plus the trachea, oesophagus and vascular, neurological, lymphatic and muscular complexes.

2.1.2 Nasal cavity and nasopharynx

There are two nasal passages or canals, each with a meatus, the nostril, opening to the exterior and separated from each other by a cartilaginous nasal septum. The nasal canals are asymmetrically arranged around the midsagittal axis. The nostrils lead to the vestibule, posterior to which the canals are divided into a complex network of channels by mucosa-covered turbinates supported by conchae (the superior, middle and inferior), underlying bony structures of the skull. These structures which project into the nasal space create in turn three structures or meatuses (the superior, middle and inferior). The general structure of the nasal canals is illustrated in figure 2.2, although their longitudinal construction is not visible from any of the images previously presented. A number of important anatomical structures lie in close proximity to the nasal passages; these include large air-filled cavities (the maxillary and ethmoid sinuses), the orbits and critical vascular and neurological entities.

2.1.3 Oropharynx

The oropharynx is the region of the airway posterior to the base of the tongue and oral cavity, inferior to the soft palate and uvula and superior to the epiglottis and larynx. Figure 2.1 illustrates the cross-section of the region (a transverse view can be seen in Agur and Dalley [2, fig. 7-53]). The pharynx is enclosed by muscular and glandular tissues of which the tonsils and tonsillar pillars are preeminent. A retropharyngeal space lies posterior to the pharyngeal constrictor muscles and anterior to vertebrae. Figure 2.4b shows a posterior view of through the oropharynx, depicting the complex arrangement of the muscles of the palate and the oropharyngeal constrictors. Lateral to the pharyngeal muscles are a collection of muscles, arteries, veins and adipose tissue.

The constrictor muscles that line the pharynx are divisible into upper, middle and lower parts and overlap each other. The inside layer of muscles is longitudinally aligned while the external layer has a circumferential orientation. As is visible in figure 2.4a, the regions of partition between the pharyngeal constrictors serve as entry points for other muscles into buccal region the floor of the mouth. Penetrating through the raphae are muscles of the tongue, such as the stylohyoid (SH) which inserts into the floor of the mouth, and the soft palate, for example levator veli palatini (LVP) which inserts into its superior surface.

2.1.4 Laryngopharynx and trachea

The larynx, or glottis, is that region of the airway between the pharynx and trachea in which the vocal apparatus responsible for sound production is located. It is a complex, hollow, mixed cartilaginous and muscular organ through which air passes with a two-piece cartilage structure; the superior portion is known as the thyroid cartilage and inferior part of the inferior structure the cricoid cartilage. The cricoid cartilage is connected to the first tracheal ring on its posterior surface.

The trachea is the last anatomical entity in the airway before the bronchial tree. It has a number of mucosal layers under which muscle and cartilage are present. Critical are the U-shaped cartilages that maintain airway patency in this region. These are connected one to the other by ligaments. The opening to the oesophagus, thence the stomach, is located at the level of the inferior part of the epiglottis, posterior to glottis.

2.2 Physiology and histology of the tongue

As with most parts of the human anatomy, the histology of the tongue is quite complex, with important physiological features prevalent at all scales of magnification. In this section, the most important details regarding the composition of the tongue are surveyed from both a macroscopic and a microscopic perspective.

2.2.1 Macro-histology

Although it may appear to be a single organ and simple in structure, the tongue is a complex, composite organ comprised of numerous intrinsic and extrinsic interwoven muscle groups supported by intramuscular tissues and glands. Each muscle plays a specific role in controlling the motion of the tongue, and this confers on it a propensity for high manoeuvrability. The lack of actual physical restriction of the tongue is remarkable. Its apex, most of each lateral side, and the superior and posterior surfaces, remain free to move.

The root of the tongue is inhibited however by certain muscles in the floor of the mouth, through attachments to the mandible and hyoid bone (which itself is free-floating), and groups of muscles that originate from a point exterior to the oral cavity (in some cases from locations lateral to the nasopharynx). The floor of the mouth, known as the submandibular triangle, is made up of the mylohyoid (MH), the anterior part of the digastric (DG), the geniohyoid (GH) and SH. The left and right halves of the MH originate from the mandible and meet one another near the midsagittal plane and insert into the hyoid. The GH, aligned in the sagittal plane, extends from the mandible to the body of the hyoid bone. Additionally, there is a small tag of tissue on the underside of the anterior portion of the tongue blade, the frenulum, that provides an anatomical anchor. Table 2.1 and figure 2.5 describe the configuration of the component muscles of the tongue and their action.

Each muscle relating to the tongue is able to perform a specific action due to its location in the tongue, points of origin and insertion and fibre directionality. The muscles are largely placed symmetrically about the midsagittal line and those that are not on the centreline have an antagonist, allowing lateral movements to be performed.

For some movements, such as protrusion of the tongue, multiple muscle groups are contracted simultaneously to perform the motion that no single muscle could achieve. Figure 2.5 depicts sections of the tongue

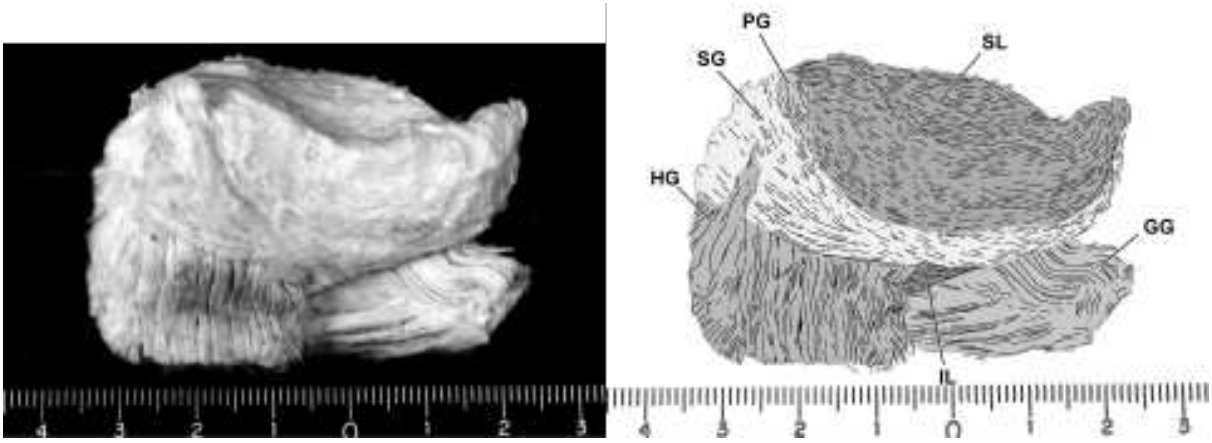

(a) External anatomy of tongue and its extrinsic muscles. Image sourced from Takemoto [271].

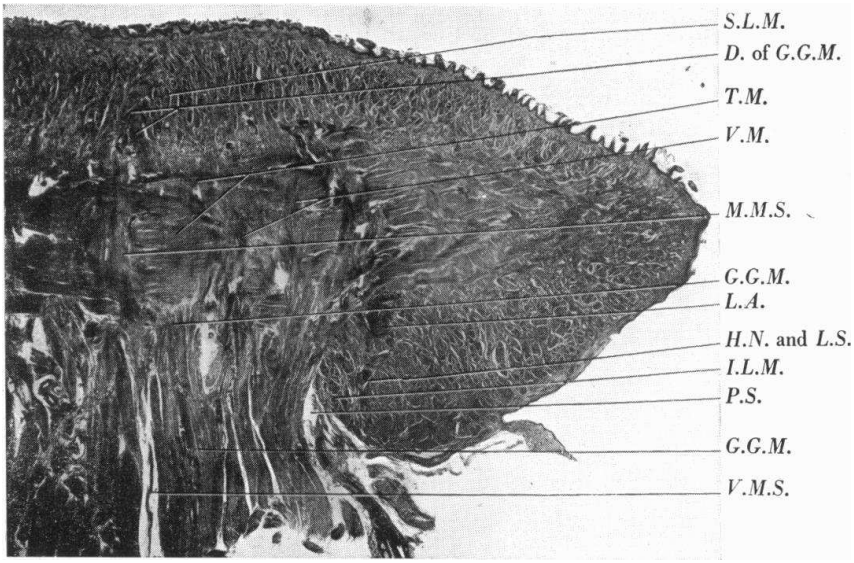

(b) Photograph of internal tongue histology. Image sourced from Abd-el Malek [1].

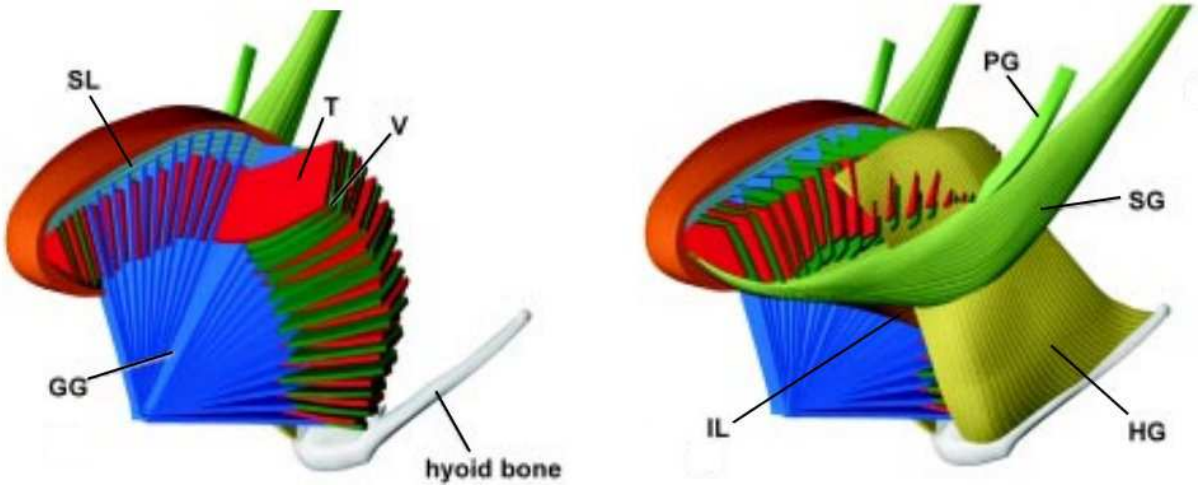

(c) Details of muscle arrangement within the tongue body. Image sourced from Takemoto [271].

Figure 2.5: The macro-histology of the tongue

Table 2.1: Muscles of the human tongue and the surrounding tissue

(a) Extrinsic muscles [2, 185]

Muscle	Origin	Insertion	Main action
Genioglossus (GG)[a]	Superior part of mental spine of mandible	Dorsum of tongue and body of hyoid bone	Depresses tongue; Its posterior part pulls tongue anteriorly for protrusion
Hyoglossus (HG)	Body and greater horn of hyoid bone	Side and inferior aspect of tongue	Draws down sides of tongue; Depresses and retracts tongue
Styloglossus (SG)[b]	Styloid process and stylohyoid ligament	Side and inferior aspect of tongue	Retracts tongue and draws it up to create a trough for swallowing
Palatoglossus (PG)[b]	Palatine aponeurosis of soft palate	Side of tongue	Elevates posterior part of tongue

[a] Act simultaneously to protrude tongue
[b] Offset from midsagittal line; has a left- and right-hand-side component

(b) Intrinsic muscles: Tongue body [2]

Muscle	Origin	Insertion	Main action
Superior longitudinal (SL)	Submucous fibrous layer and median fibrous septum	Margins of tongue and mucous membrane	Curls tip and sides of tongue superiorly and shortens tongue
Inferior longitudinal (IL)[b]	Root of tongue and body of hyoid bone	Apex of tongue	Curls tip of tongue inferiorly and shortens tongue
Transversus (TV)[a]	Median fibrous septum	Fibrous tissue at margins of tongue	Narrows and elongates the tongue
Verticalis (VT)[a]	Superior surface of borders of tongue	Inferior surface of boarders of tongue	Flattens and broadens the tongue

(c) Intrinsic muscles: Mouth floor; suprahyoid [185, 54, 2]

Muscle	Origin	Insertion	Main action
Digastric (DG)[b]	Mastoid notch of temporal bone	Digastric fossa on base of mandible	Raises the hyoid bone and the floor of the mouth
Geniohyoid (GH)	Back of symphysis menti	Anterior surface of body of hyoid bone	Raises hyoid and floor of mouth, widens pharynx
Stylohyoid (SH)[b]	Posterior surface of styloid process	Body of hyoid bone	Raises hyoid and elongates floor of mouth
Mylohyoid (MH)	Mylohyoid line of mandible	Median fibrous tissue (Anterior, medial fibres); Front of the body of the hyoid bone (posterior fibres)	Forms floor of mouth; Contraction raises floor of mouth, hyoid bone and base of tongue

and illustrates the geometrically complex description of the tongue and its constituent muscle groups. Figure 2.5a depicts a tongue specimen with some of the muscles present on the exterior of the tongue body indicated for clarity. The stylised illustration presented by Takemoto [271] in figure 2.5c is consistent with anatomical references Agur and Dalley [2], Davies [54] and demonstrates clearly the complex arrangement of the muscle of the tongue that cannot be easily discerned from photographs and slides. Although they may appear distinct, it can be seen in figure 2.5b that the muscles in the body of the tongue interweave and that, even at a macroscopic level, some non-muscular tissue is evident in the tongue. Muscle fibres that constitute each muscle group are distributed in a non-uniform manner and have directionality that change depending its location in the tongue.

The genioglossus (GG), which is the focus of much of this work, is a fan-shaped extrinsic muscle of large volume lying on either side of the median plane. It has its origin on the two superior mental spines of the mandible and inserts throughout the body of the tongue as far back as the hyoid bone.

2.2.2 Micro-histology

At the length scale of individual muscle fibres, the histology of muscle appears very different to that observed at the macroscopic level. Depending on where the anatomical section is taken, fibres from different muscle families with differing densities and orientations are present.

Studies performed by Nashi et al. [191] demonstrate that the local fat fraction varies considerably throughout the tongue. Figure 2.6 depicts a measured example from the study, which highlights that closer inspection of the histology is required in order to quantify the proportion of the tongue volume that is made of muscle fibres.

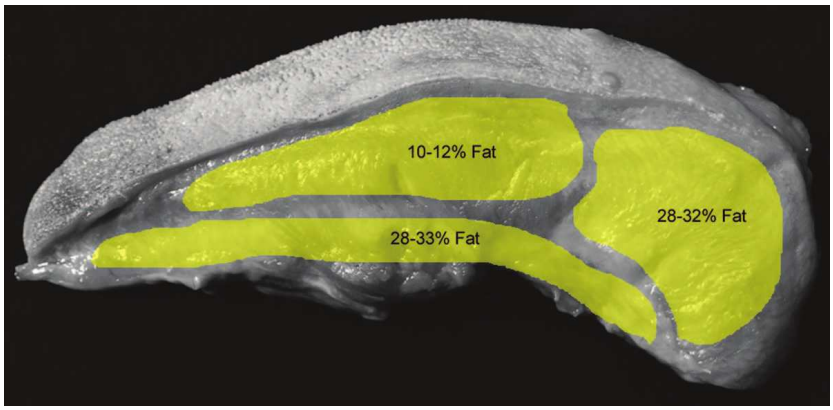

Figure 2.6: Quantified adipose tissue concentrations at various regions in the tongue. Image sourced from Nashi et al. [191].

Figure 2.7 shows tissue sections taken of some of the intrinsic muscles of the tongue. The slides demonstrate that muscle groups that occupy the same region of the anatomy (and which in these examples appear largely orthogonal to one another) are not segregated, but rather interweave with one another.

Muscle fibres of varying diameter are packed into fascicles around which interstitial connective tissue, adipose and vascular tissue together with collagen, are present. It is reported that throughout the entire body of the tongue some form of connective or glandular tissue is present in close proximity to muscular tissue [259].

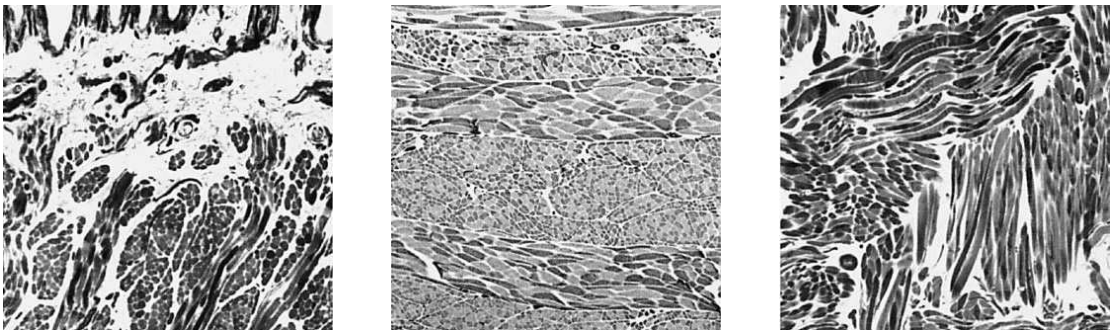

(a) SL (mostly unidirectional fibres) **(b)** VT (fibres visible in two planes) **(c)** TV (fibres visible in three planes)

Figure 2.7: Cross-sections of muscles in middle anterior region of the tongue demonstrating fibre orientations and difference in interstitial tissue concentrations. All images sourced from Stål et al. [259].

(a) Anterior **(b)** Medial **(c)** Posterior

Figure 2.8: Variations in fibre organisation and connective and adipose tissue concentrations at various regions in the tongue. All images sourced from Miller et al. [179].

The cross-sectional slides shown in figure 2.8 indicate that the quantity of adipose and other non-muscular tissue varies considerably with the site of the sample. Although not quantified in these slides, a visual inspection suggests that the ratio of muscular tissue (shown in red) versus other soft tissues (stained blue and white) is not consistent throughout the tongue.

In the axial sections of the tongue shown in figure 2.9 it appears that the distribution of interstitial tissue is locally regular, although the concentration of adipose tissue is irregular at the macroscopic level. These sections through the uni-directionally orientated muscle in the tongue also reveal that packing and distribution of the muscle fascicles is non-uniform.

2.3 Physiology of the palate

The human palate consists of two parts with distinctly different properties, namely the hard palate and the soft palate. Their location, form and proximity relative to the tongue and retroglossus can be seen in both figures 2.1 and 2.4b. The hard palate is a bony structure covered by a thin soft tissue layer. The soft palate, or velum, extends distally from the hard palate and terminates in the free-hanging uvula. Both are mostly comprised of glandular tissue, but also includes muscular tissue component. Both palates serve to divide

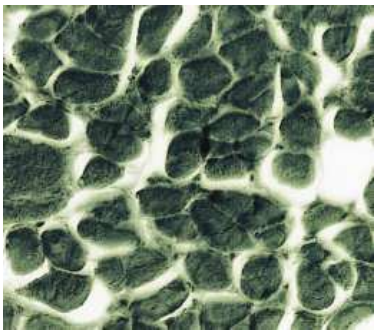

(a) Light-micrograph of transverse (posterior). Image sourced from Saigusa et al. [241].

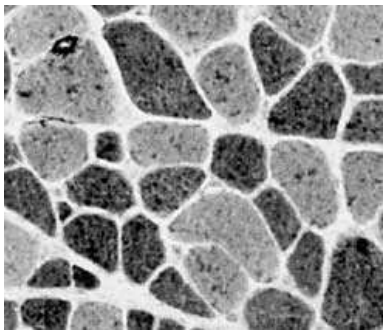

(b) Stained section of superior longitudinal. Image sourced from Stål et al. [259].

Figure 2.9: Axial sections of muscles of the tongue.

the oral and nasal cavities and are critical in the processes of swallowing and speech formation. It should be noted that some of the muscles of the soft palate directly contribute to the functioning and movement of the tongue. In particular, the palatoglossus (PG) inserts into the side of the tongue and is used to assist in lifting the posterior region of the tongue.

2.4 Composition and function of non-muscular tissues

The upper airway anatomy is comprised of a multitude of tissues, including bone, cartilage, fatty tissues, ligaments and tendons. A brief description of the composition of the first three is given here.

Cartilage is a composite material, consisting of fluid-filled cells, intercellular matrix and network of collagen fibres. The consistency of the cartilage, in terms of the volume comprised by matrix and fibres, depends on its location within the body. The movement of fluid within the tissue bestows it with viscoelastic qualities. Cartilage acts as a shock-absorption material, provides lubrication for joints and can also be of structural significance. The main structural component of the body, bones, are a form of calcified cartilage. At the macroscopic level, they are a histologically complex structure composed of the dense cortical outer layer with a porous interior made of trabecular bone. They are brittle, only functioning in the small strain regime but have an anisotropic and viscoelastic response. [78]

Adipose or fatty tissue is comprised of cells that contain lipids, interspersed with other connective tissues [163]. The exact nature of the composition of the tissue depends on its site. The resulting collection of tissues is elastic in nature and serves as a cushioning material, insulator and energy deposit.

2.5 Composition and functioning of skeletal muscle

Skeletal muscle is a striated voluntary muscle that is able to be controlled through somatic motor innervation. In general, it is made up of three main components, namely the tendon, collagen connective tissue and striated muscle fibres. Each component is comprised of increasingly complex sub-units, the arrangement of which has a great effect on the mechanical properties of the muscle unit. The total force that a muscle can

generate is dependent on a number of factors such as the cross-sectional area of the muscle, the number of muscle fibres implicated in the contraction, the length and contraction rate of the muscle and the manner in which the muscle is stimulated. In order to better understand the the physiology of skeletal muscle, the composition of muscle and its basic sub-units are first discussed.

2.5.1 Composition of skeletal muscle

The basic structure of skeletal muscle is depicted in figure 2.10.

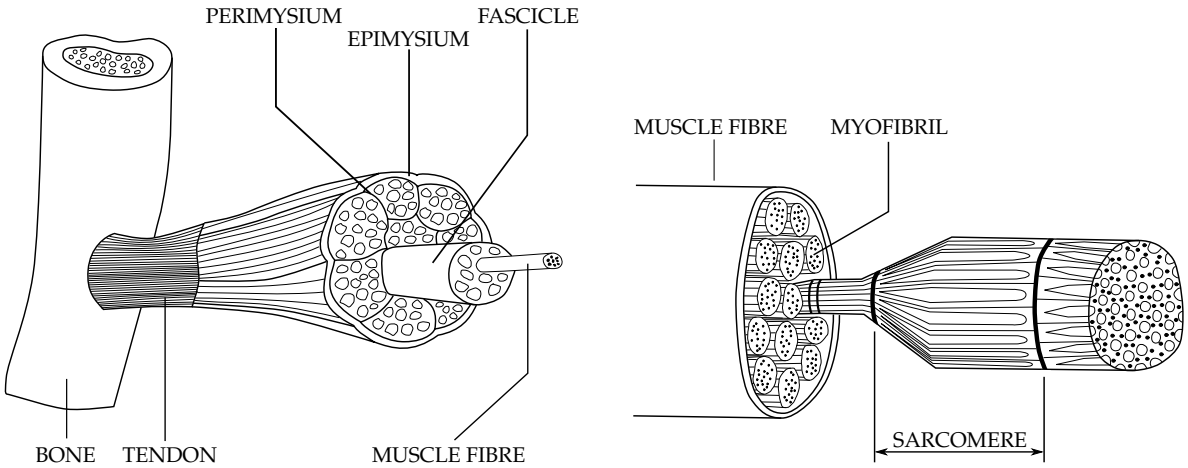

(a) Muscle components **(b)** Muscle fibre components

Figure 2.10: Structure of skeletal muscle

Skeletal muscle is attached to its bony origin by means of a tendon. The muscle is divided into several sub-units, the largest of which is a fascicle. Each fascicle, which is composed of a parallel collection of muscle fibres, is surrounded by a layer of connective tissue known as the perimysium. The collection of fascicles that compose each muscle are encapsulated by the epimysium. Pennation, which describes the angle of attachment of the fascicles to the tendon, varies depending on the muscle. In a muscle such as the rectus femoralis the pennation angle is significant; however, the muscles of the tongue and the upper airway have no pennation [54].

The fibres that make up skeletal muscle are not uniform in their properties. Type I fibres are known as slow-twitch fibres, taking of the order of tenths of a second to reach a state of maximum contraction, while type II fibres are fast-twitch taking milliseconds to produce maximum tension. These fibre types also have different contractile strengths, fatigue and metabolic rates. Both of these fibre types are present in the tongue, as observed in figure 2.11. [74]

Each muscle fibre, as shown in figure 2.10b, contains several myofibrils with a diameter of approximately 1μm that run the length of the muscle fibre, and the remaining space is filled by sarcoplasm. It is the arrangement of the myofibrils and muscle fibres that give the muscle its striated appearance. The myofibrils are subdivided into myofilaments, which contain a specific arrangement of sarcomeres. Each myofilament is 2.5μm long, dependant on the force in- and excitation state of- the muscle. Sarcomeres are arranged both serially and in parallel to make up each myofibril. The is the action of the myofilaments that cause active contraction of the muscle unit. [78, 74]

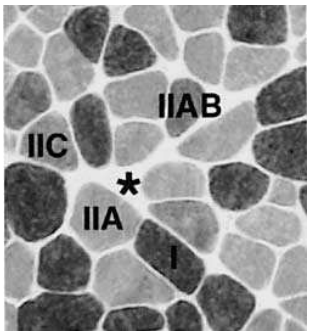

Figure 2.11: Fast and slow action muscle fibres depicted in a stained tongue section from undeclared region. Each fascicle in this image is of the order of $20 - 80\mu$m in diameter. Image sourced from Stål et al. [259].

2.5.1.1 Composition of the sarcomere

Figure 2.12 illustrates the arrangement of sarcomeres in a muscle and provides a representative drawing of the structure of a single sarcomere. At the end of each sarcomere is a Z-disc. Three protein filaments make up the composition of the myofilaments. Titin filaments serve to anchor myosin filaments to the Z-disc. Titin filaments are elastic, and are considered to contribute to the elastic recoil of the muscle during relaxation. Protruding from each end of the myosin are numerous 19nm long cross-bridges. Parallel to the titin and myosin filaments are actin filaments which serve as attachment points for the cross-bridges. Actin and myosin have diameters of approximately 5nm and 12nm respectively. The arrangement of actin and myosin filaments appears as a hexagonal pattern if viewed in cross-section through the myofibre. [78, 74]

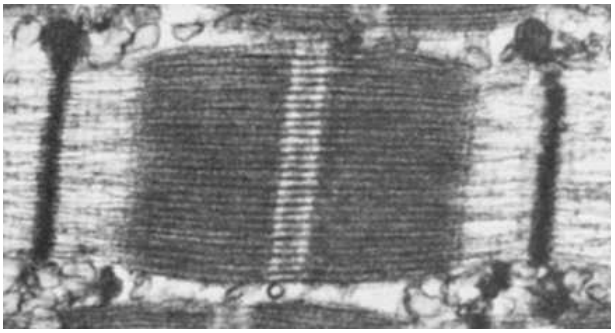

(a) Electron microscope image of glycerinated chick pectoral muscle. Multiple sarcomeres are visible, with the Z-discs. Image sourced from Hagopian [95].

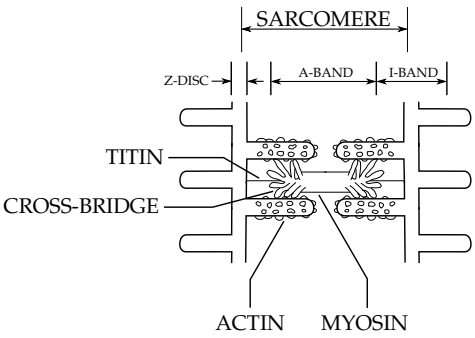

(b) Sarcomere components

Figure 2.12: Electron micrograph of skeletal muscle sarcomeres. In figure 2.12a, the approximate lengths of the I- and A-bands are 1μm and 1.5μm respectively and the overall length of the sarcomere is approximately 2.2μm.

In figure 2.12a, a number of distinct histological features of the horizontally aligned collection of sarcomeres are visible. The dark bands on either side of the image are Z-discs. The large grey band in the centre of the image, known as the A-band, is the region where the actin and myosin filaments overlap and interact by the action of the cross-bridges. Central to the figure is a narrow white band, the H-band, indicating the extents of the actin filaments that extend from either Z-disc. The white bands that extrude from either side of the Z-disc are the I-band, and indicate the region that has actin filaments but no myosin.

2.5.2 Functioning of skeletal muscle

When at rest, skeletal muscle displays viscoelastic properties. This is not an entirely passive state for in this resting state the muscle maintains its tone as a consequence of continued stimulation by motor neurones (anterior horn cells). The resting stress determines the resting length of a muscle, and does not affect the muscle mechanics in any other way. The total contractile force of the activated muscle is dependent on the arrangement of the muscle fibres with respect to the overall line of action of the muscle. [78]

2.5.2.1 Histological process of muscle contraction

Muscle contraction, from the viewpoint of the changes occurring within each sarcomere, is presently best described by the *sliding filament* theory of contraction. During contraction, neither the actin nor myosin filaments change in length. The myosin slides over the actin into the I-band, an open region of space [74]. Contraction therefore results in the reduction in length of the I- and H- bands, while muscle relaxation will result in their elongation. Contraction can occur as long as there is free space in the I-band to permit this - at this point, there is a slight overlap of actin filaments. When the sarcomere is in a state of extension (due to the influence of an external entity), the I-band may open up to the point where there is no A-band present. Since this indicates that there is no overlap of the actin and myosin filaments, no cross-bridges between these proteins can be made and active contraction is not possible. Ultimately, the shortening of the sarcomeres results in the shortening of the myofibrils and therefore the myofibres that constitute a particular region of the muscle.

Contraction occurs through the action of the cross-bridges, described in the *cross-bridge* theory. A cross-bridge is the collective unit produced when a myosin head attaches to a binding site on an actin filament. The sliding action of the actin filament over the myosin filament is produced through the action of the cross-bridges, and the intensity of the contraction is proportional to the number of active cross-bridges. During a single contraction cycle of the cross-bridges, the muscle is shortened by approximately 1% of its resting length. Many cycles occur to produce an eventual shortening of up to 60% of the muscle's original length. [74]

A number of complex chemical processes are involved in the functioning of the cross-bridges, causing the eventual conversion of chemical energy into mechanical energy. Chemical energy in the form of adenosine triphosphate (ATP) is required to control the creation and breakage of cross-bridges. Once a cross-bridge has been created and a chemical transformation taken place, the power-stroke of the myosin-complex is produced, resulting in the mechanical deformation of the myosin and the displacement of the myosin filament relative to the actin.

2.5.2.2 Sarcomere force-length relationship

The force-length relationship of a sarcomere has been experimentally determined to take the form shown in figure 2.13. At the ideal resting length for sarcomeres, the actin and myosin filaments are aligned such that there are a maximum number of cross-bridges exposed to potential binding sites. This means that, upon activation, an optimal number of cross-bridges can be formed to produce the maximal contractile force. This ideal resting length is maintained during passive stretching by reflex contractions. [74]

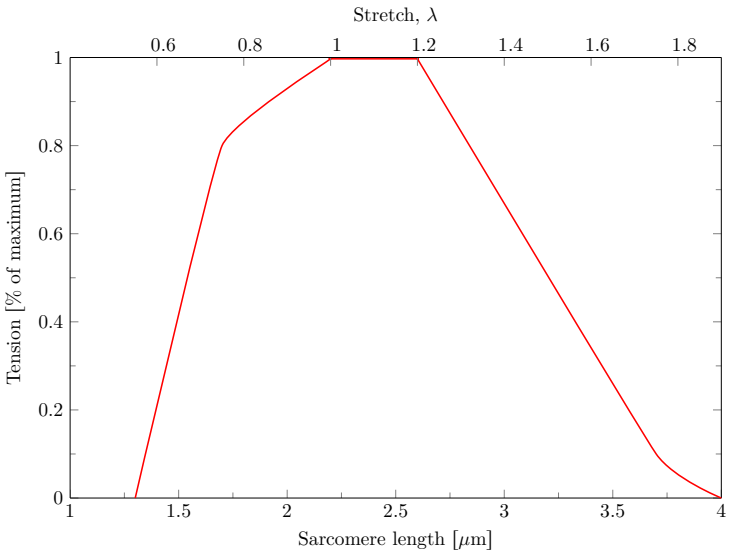

Figure 2.13: Sarcomere force-length relationship [78]

It is also shown that the maximal performance of the muscle deteriorates as the length of the sarcomere deviates from the ideal length. The mechanism governing the performance reduction differs for elongation and contraction. As the distance between the Z-discs of the sarcomere increases, the overlap between the actin and myosin filaments is reduced and the number of myosin-heads exposed to binding sites on the actin filament decreases. Under conditions of extreme elongation, the myosin will no longer be adjacent to the actin and no cross-bridges can be formed. The hypothesis offered for explaining the loss of a capability for contractile force generation during shortening is that, as the muscle becomes shorter and the cross-sectional area increases, the distance between the actin and myosin filaments increases. This in turn decreases the likelihood of a successful cross-bridge formation. Additionally, it is speculated that the pressure of fluid in the muscle increases, generating a force opposed to contraction. Furthermore, when the contraction is large enough for the H-band to disappear, the actin filaments overlap causing and interference with normal function and a resultant reduced performance. [74]

2.5.2.3 Muscle force-length and force-velocity relationships

Skeletal muscle is sensitive to both its length in relation to the resting length and the rate at which its length it is changing. Figure 2.14 depicts the experimental results used to gain an understanding of the relationship between the force present in a muscle and its length and rate of change of length.

Figure 2.14a shows the typical force-stretch response for active skeletal muscle tested at a macroscopic level. This data is produced from isometric (and thus iso-velocity) stretches of a stimulated muscle. It is observed that the activated muscle responds to the elongation in two distinct stages. The initial response shows the short-range stiffness of the muscle. This has been attributed to the deformation of the passive series-elastic components, with little action of the cross-bridges. As the muscle continues to stretch, the tautness of the muscle decreases as the cross-bridges start to break and reform. In this region, the stiffness of the muscle is related to the rate at which cross-bridges detach from and reattach to the actin molecules. [45]

Isotonic experiments performed by Hill [103] to demonstrate the force-velocity relationship of fully tetanised skeletal muscle, are illustrated in figure 2.14b. Under conditions of a constant preload force, the clamped

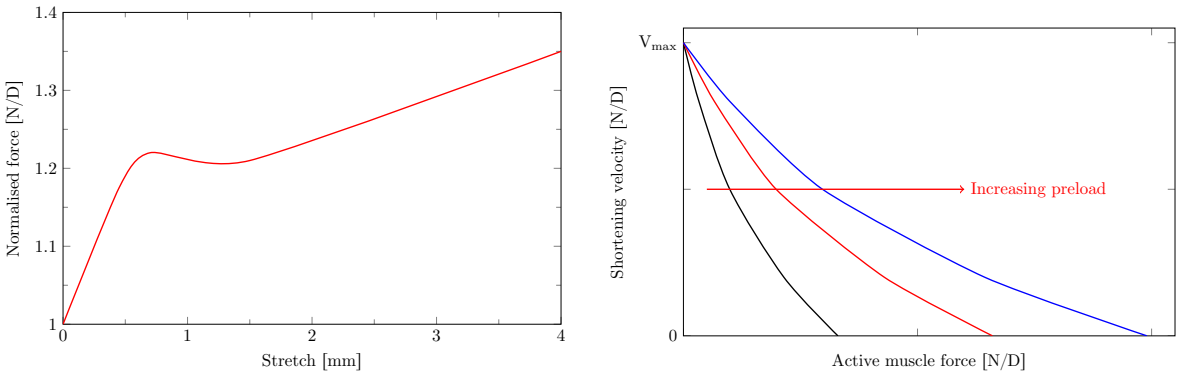

(a) Force-stretch [45]

(b) Force-velocity [78]

Figure 2.14: Typical experimental responses for bulk skeletal muscle.

muscle is maximally stimulated and released against a variable load. There is an inverse relationship between the generated contractile force and the velocity of contraction. The contractile velocity was also observed to increase as the preload increased. One physiological factor dictating this relationship is the rate at which cross-bridges can attach to the opposing moving filament.

2.5.3 The nervous system and muscle contraction

Muscle contraction occurs through a complex electro-chemical and mechanical event facilitated by the delivery of specific chemical substances at nerve endings. The activation of a varying number of neurones causes the recruitment of a varying number of muscle fibres and therefore a gradual and controlled contraction event.

The impulse controlling contraction and relaxation is delivered to each myofibre by a somatic motor nerve, a subset of the central nervous system. The motor nerve can end in several neuromuscular junctions, collectively known as a motor unit, each of which stimulates a single muscle fibre. The activation of a somatic nerve can therefore lead to the simultaneous activation of a number of muscle fibres. Through the asynchronous stimulation of several motor units, the contraction of the entire muscle can be accurately controlled. The strength of muscle contraction is determined by the number of motor units recruited (and therefore the number of muscle fibres involved in active contraction), as well as rate at which a stimulus or impulse is delivered to the muscle. The larger the group of myofibres recruited for contraction, the greater the overall contractile strength but the less the degree of fine motor control available. [74]

Temporary stimulation of a muscle fibre results in a contraction that is not sustained. The contraction is sustained as long as the signal is delivered and when a signal ceases the muscle relaxes. This cycle of contraction and relaxation is known as a twitch. Each individual stimulus causes the muscle to twitch. The process whereby successive twitches build up contractile strength, a phenomenon known as the summation of twitches, is described with the aid of figure 2.15.

At a low stimulation frequency, the muscle contracts and then undergoes a period of relaxation and the tone reduces. Before the muscle can completely relax, it may be stimulated once more and thus reach a peak contractile force greater than in the previous twitch. Continued stimulation at a low frequency will only result in the force developing to a level less than the maximum that the muscle is physiologically capable

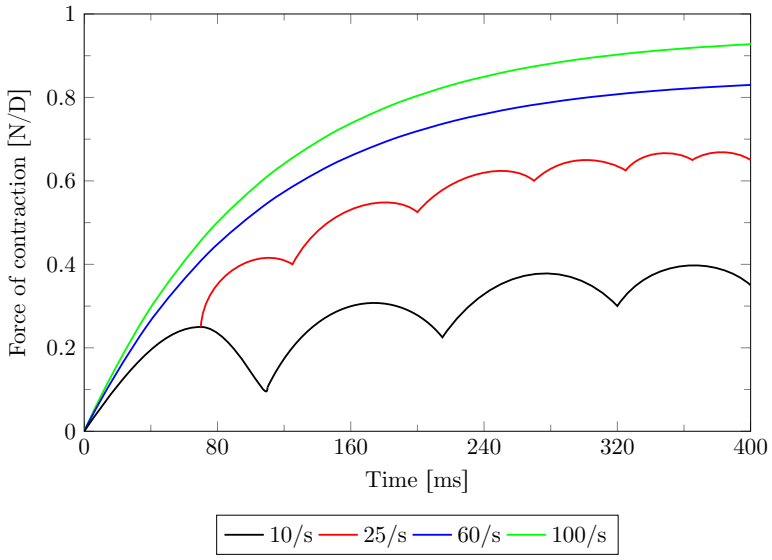

Figure 2.15: Tetanisation and the summation of twitches [78, 74]. Increased stimulation frequency of muscle results in the generation of greater contractile forces. Each curve represents the force history resulting from a differing period between impulses.

of producing. Increasing the frequency of stimulation causes the muscle to twitch more rapidly until each individual twitch is indistinguishable from another. In this state, a critical stimulation frequency has been reached or exceeded, and the muscle is said to be fully tetanised or in a state of complete tetany. In this state, the muscle is able to produce its maximum contractile force. Above any critical frequency, the increase in contraction force is slight. [74]

2.6 Measured neurological response of the tongue

Due to its primary role in maintaining airway patency, the activity of the GG is commonly probed in research involving human sleep disorders. The early experimental work of Sauerland and Harper [247], EMG monitoring of the tongue muscles (by wire-electrodes) lead to the conclusion that the tonic loss of GG activity during REM sleep may lead to upper airway obstruction. Later in the important work of Remmers et al. [231], it was demonstrated that the GG response, measured with the use of EMG, is very different in patients experiencing upper airway occlusion compared to healthy subjects. In the OSA patients, is a marked decline in reflexive response of the GG to airway pressure, with lower levels of activity recorded in these cases across a range of airway pressures.

Figure 2.16 illustrates typical post-processed EMG data demonstrating the response of the GG to the changing airway pressure. Similar results under differing experimental conditions can be seen in Malhotra et al. [165], Stanchina et al. [261]. This particular dataset highlight indicates four potential apnoea events, where upon inspiration the airway pressure has lowered considerably without any additional activity being recorded in the GG response. More complex electrical studies, such as those involving manual electrical stimulation of the GG, have been performed by Oliven et al. [199], Isono et al. [126, 127] to determine the relationship between GG contraction and airway CSA.

Akahoshi et al. [3] designed experiments where the ventilation of the airway in healthy, awake subjects (in the

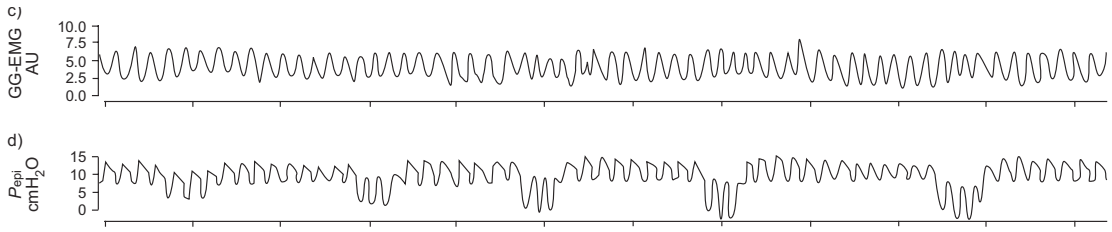

Figure 2.16: Typical raw EMG results indicating four events of decreased epiglottal pressure without a corresponding additional recruitment of the GG. Image sourced from Pierce et al. [221].

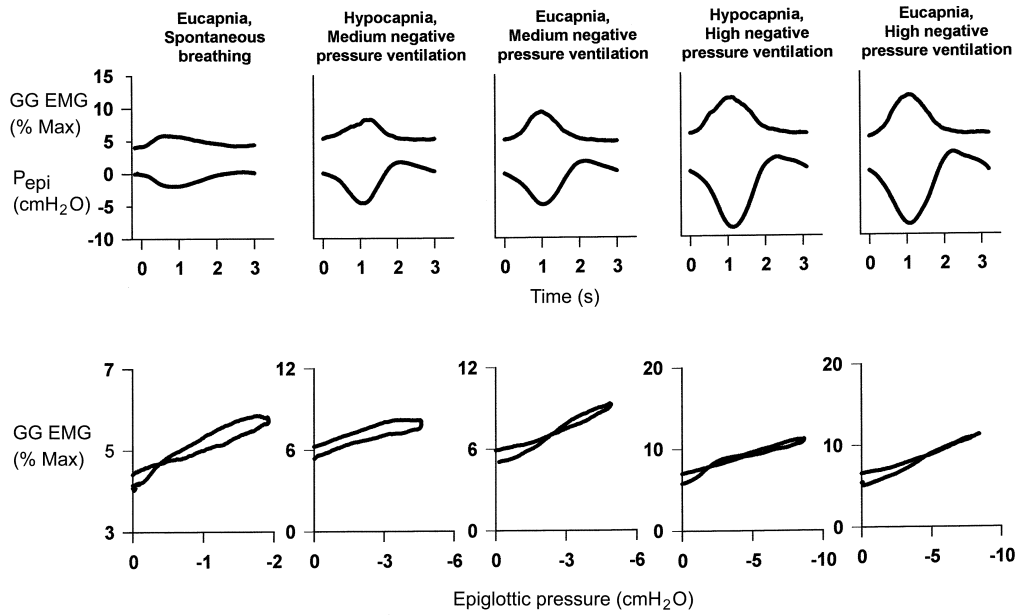

Figure 2.17: Results of a passive ventilation experiment demonstrating the relationship between the negative airway pressure and GG activity. Image sourced from Akahoshi et al. [3].

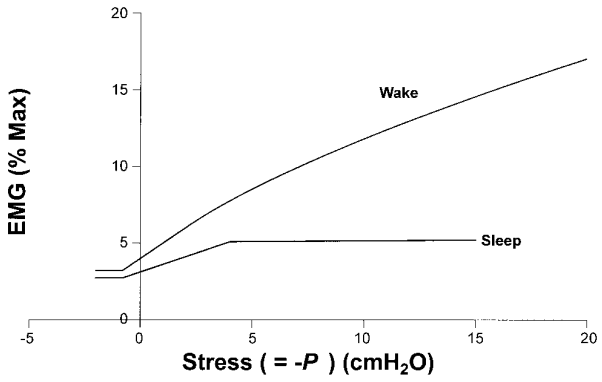

Figure 2.18: Approximation of GG activity during sleep and wake states for use in computational simulations of the tongue. Sleep state transition occurs at approximately 450Pa, and a general reduction in muscle tone is visible. Image sourced from Huang et al. [111].

supine position) was controlled in order to determine the relationship between the GG activity and airway pressure. These results, indicating a direct link between the airway pressure and GG activity, are presented in figure 2.17. The authors noted that the loss of this reflexive response by the GG could lead to OSA. Similar trends indicating a linear response of the GG to inspirational airway pressure [164], and hysteresis in different stages of breathing, have been presented by Remmers et al. [231], Malhotra et al. [167], White [308], Fogel et al. [73]. This proportional response during the wakeful condition, as well a stagnation of the response during sleep (that is, that the GG response peaks at a threshold pressure during sleep and has no increasing response as the pressure continues to drop), is also indicated by Malhotra et al. [165].

Huang et al. [111] used the above information to estimate the activity of the GG during sleep. In figure 2.18, their approximation for the response of the GG in wakeful and sleep conditions is shown. The authors, based on information in the literature, assumed that the slow and fast (tonic and phasic) muscle reactions during sleep would be reduced by 15% for normal breathing. Furthermore, the critical pressure threshold at which there is a loss of reflexive mechanisms in the GG [231], resulting in the practically negligible change in contractile state of dilator muscles, was set at approximately -450Pa. Using this model, the airway collapse pressure was estimated by the authors to be -490Pa and -687Pa for male and female subjects respectively.

3. CONTINUUM MECHANICS

Continuum mechanics provides a basis for formulating the mathematical descriptions of materials that demonstrate complex behaviours. In this chapter, the fundamental notation, finite-strain kinematics, kinetics and balance laws governing homogenised continuous solid media are presented.

Following the description of motion and deformation, strain measures and their invariants are presented. A redefinition of the basic kinematic terms to account for the prestressing of biological materials follows. Various stress measures are defined in the context of large-deformation mechanics. Thereafter, the development of the theory of elasticity for both isotropic and transversely isotropic hyperelastic materials is summarised; and, as the modelling of biological materials involves incompressible media, the procedure to decouple the volumetric and isochoric material behaviour is described. Lastly, the kinematics of two motion-dependent boundary conditions used to approximate complex physiological conditions is developed.

3.1 Kinematics

The basic kinematic configuration is presented in figure 3.1. The position of material points in $\mathcal{B}_0 \in \mathbb{R}^3$, defined in a stationary reference configuration Ω_0, are denoted by $\boldsymbol{X}$. The boundary of $\mathcal{B}_0$ is denoted as Γ_0. Upon deformation, the body $\mathcal{B}_0$ is transformed to $\mathcal{B}$ defined in the spatial configuration Ω, with points denoted by $\boldsymbol{X}$ displacing to $\boldsymbol{x}$ and the surface to Γ.

The motion $\boldsymbol{\varphi}$, a nonlinear map transforming points in $\mathcal{B}_0$ to points in $\mathcal{B}$, is defined by

$$\boldsymbol{x} = \boldsymbol{\varphi}\left(\boldsymbol{X}, t\right) \quad . \tag{3.1}$$

The displacement and velocity fields respectively are given by

$$\boldsymbol{u}\left(\boldsymbol{X}, t\right) = \boldsymbol{x} - \boldsymbol{X} \quad , \quad \boldsymbol{v} = \dot{\boldsymbol{u}} \quad . \tag{3.2}$$

The deformation gradient associated with the motion is given by

$$\boldsymbol{F} = \frac{\partial \boldsymbol{\varphi}}{\partial \boldsymbol{X}} = \nabla_0 \boldsymbol{\varphi} = \boldsymbol{I} + \nabla_0 \boldsymbol{u} \tag{3.3}$$

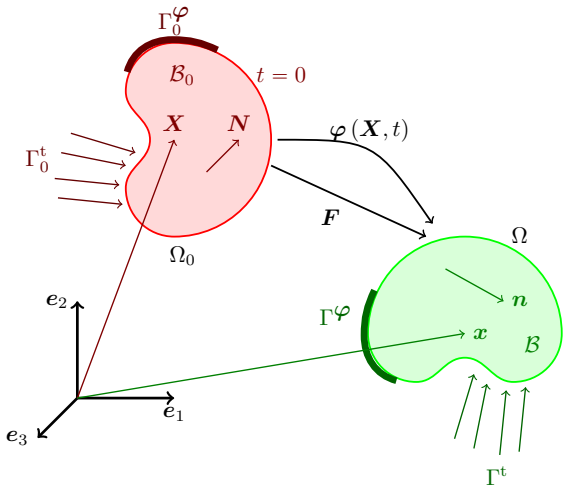

Figure 3.1: Kinematics described by deformation of a general body. Illustrated are the bodies in the reference and current configurations, the transformation maps and operators, and the definition of boundary conditions.

where the gradient is taken with respect to the material coordinate system. The deformation gradient describes the transformation a line element in Ω_0, denoted as $\mathrm{d}\boldsymbol{X}$, to Ω by

$$\mathrm{d}\boldsymbol{x} = \boldsymbol{F}\mathrm{d}\boldsymbol{X} \quad . \tag{3.4}$$

For consistency in the index notation used in this text, quantities defined in the Ω_0 will be capitalised while quantities in Ω will be presented in lowercase. The requirement that equation 3.1 remains single valued and produces a compatible strain field implies that

$$\nabla_{_0} \times \boldsymbol{F} = \boldsymbol{0} \quad . \tag{3.5}$$

Furthermore, the requirement of the invertibility of $\boldsymbol{\varphi}$ implies that the inverse map

$$\boldsymbol{X} = \boldsymbol{\varphi}^{-1}(\boldsymbol{x}, t) \tag{3.6}$$

exists. The inverse of the deformation gradient is given by

$$\boldsymbol{F}^{-1} = \frac{\partial \boldsymbol{\varphi}^{-1}}{\partial \boldsymbol{x}} = \nabla \boldsymbol{\varphi}^{-1} \tag{3.7}$$

and the volumetric Jacobian by

$$J := \det \boldsymbol{F} = \lambda_1 \lambda_2 \lambda_3 > 0 \tag{3.8}$$

where λ_i are the eigenvalues of $\boldsymbol{F}$. Note that the spatial gradient of the motion can be represented in terms of the material quantities

$$\nabla \boldsymbol{\varphi} = \frac{\partial \boldsymbol{\varphi}}{\partial \boldsymbol{x}} = \frac{\partial \boldsymbol{\varphi}}{\partial \boldsymbol{X}} \frac{\partial \boldsymbol{X}}{\partial \boldsymbol{x}} = \nabla_{_0} \boldsymbol{\varphi} \boldsymbol{F}^{-1} \quad . \tag{3.9}$$

The velocity gradient, defined with respect to the spatial configuration, is given by

$$\boldsymbol{l} := \nabla \boldsymbol{v} = \frac{\partial \boldsymbol{v}}{\partial \boldsymbol{x}} = \frac{\partial \boldsymbol{v}}{\partial \boldsymbol{X}} \frac{\partial \boldsymbol{X}}{\partial \boldsymbol{x}} = \nabla_{_0} \boldsymbol{v} \boldsymbol{F}^{-1} = \dot{\boldsymbol{F}} \boldsymbol{F}^{-1} \tag{3.10}$$

and the rate-of-strain tensor

$$\boldsymbol{d} = \boldsymbol{l}^{\mathrm{S}} = \frac{1}{2}\left(\boldsymbol{l} + \boldsymbol{l}^{T}\right) \tag{3.11}$$

where the deformation rate $\dot{\boldsymbol{F}} := \nabla_{0}\,\dot{\boldsymbol{\varphi}}$ and $(\bullet)^{\mathrm{S}} := \frac{1}{2}\left[(\bullet) + (\bullet)^{T}\right]$ denotes an operation that produces the symmetric part of the tensor $(\bullet)$.

At any position in the domain $\mathcal{B}_0$, the change in volume of an infinitesimal volume element is related to the motion by

$$\mathrm{dv} = J\mathrm{dV} \quad . \tag{3.12}$$

To define the transformation of surface normals between configurations, consider an area vector $\mathrm{d}\boldsymbol{A} = \boldsymbol{N}\mathrm{dA} = \mathrm{d}\boldsymbol{Y} \times \mathrm{d}\boldsymbol{Z}$ defined in the reference configuration, where $\boldsymbol{N}$ is the normal to the surface and $\mathrm{d}\boldsymbol{Y}, \mathrm{d}\boldsymbol{Z}$ are orthogonal vectors tangent to Γ_0 at the material point $\boldsymbol{X}$. Nanson's formula describes the transformation of an area element to the current configuration by

$$\boldsymbol{n}\mathrm{da} = \mathrm{d}\boldsymbol{y} \times \mathrm{d}\boldsymbol{z} = \boldsymbol{F}\mathrm{d}\boldsymbol{Y} \times \boldsymbol{F}\mathrm{d}\boldsymbol{Z} = J\boldsymbol{F}^{-T}\boldsymbol{N}\mathrm{dA} \tag{3.13}$$

where $\boldsymbol{n}$ is normal to the surface Γ at $\boldsymbol{x}$.

The right (material) and left (spatial) Cauchy-Green deformation tensors are defined by

$$\boldsymbol{C} := \boldsymbol{F}^{T}\boldsymbol{F} \tag{3.14a}$$

$$\boldsymbol{b} := \boldsymbol{F}\boldsymbol{F}^{T} \tag{3.14b}$$

respectively. Utilising the polar decomposition theorem, the deformation gradient can be decomposed into two discrete motions

$$\boldsymbol{F} = \boldsymbol{U}\boldsymbol{R} = \boldsymbol{R}\boldsymbol{V} \tag{3.15}$$

where $\boldsymbol{R}$ is a proper, orthogonal rotation tensor ($\boldsymbol{R}^{T} = \boldsymbol{R}^{-1}$, $\det \boldsymbol{R} = 1$) associated with the deformation, and $\boldsymbol{U}, \boldsymbol{V}$ are the positive-definite symmetric (PDS) material and spatial stretch tensors respectively. As the Cauchy-Green tensors are PDS, they have the spectral decomposition

$$\boldsymbol{C} = \boldsymbol{U}^{2} = \sum_{\alpha} \lambda_{\alpha}^{2}\boldsymbol{E}_{\alpha} \otimes \boldsymbol{E}_{\alpha} \tag{3.16a}$$

$$\boldsymbol{b} = \boldsymbol{V}^{2} = \sum_{\alpha} \lambda_{\alpha}^{2}\boldsymbol{e}_{\alpha} \otimes \boldsymbol{e}_{\alpha} \tag{3.16b}$$

where λ_i represents the principal stretch (or eigenvalue) corresponding to the principal direction (or eigenvector) $\boldsymbol{E}_i, \boldsymbol{e}_i$ respectively defined in the material and spatial reference frames. The associated deformation gradient is decomposed into

$$\boldsymbol{F} = \sum_{\alpha} \lambda_{\alpha}\boldsymbol{e}_{\alpha} \otimes \boldsymbol{E}_{\alpha} \quad . \tag{3.17}$$

The Green-Lagrange strain tensor is related to the right Cauchy-Green tensor, and therefore the displacement gradient, by

$$\boldsymbol{E} := \frac{1}{2}\left(\boldsymbol{C} - \boldsymbol{I}\right) = \frac{1}{2}\left(\nabla_{0}\,\boldsymbol{u} + \nabla_{0}\,\boldsymbol{u}^{T} + \nabla_{0}\,\boldsymbol{u}^{T}\,\nabla_{0}\,\boldsymbol{u}\right) \quad . \tag{3.18}$$

The true strain of a line element aligned in the principal direction is related to the stretch of a line element by

$$\varepsilon = \int_L \frac{\mathrm{d}L}{L_0} = \ln\left(\frac{L}{L_0}\right) = \ln\left(\lambda\right) \tag{3.19}$$

where λ is a principal stretch. An arbitrary unit line element originating at $\boldsymbol{X}$ with direction $\boldsymbol{N}$ is reorientated by equation 3.4 to the direction $\boldsymbol{n}$ and undergoes a stretch of magnitude $\lambda = |\boldsymbol{FN}|$ as described by

$$\lambda \boldsymbol{n} = \boldsymbol{FN} \quad . \tag{3.20}$$

The scalar invariants of a symmetric strain tensor provide measures of deformation that are reference frame-invariant. Given a symmetric deformation or strain quantity $\boldsymbol{A}$, the three commonly defined invariants of $\boldsymbol{A}$ are

$$I_1^A = \mathrm{tr}\,(\boldsymbol{A}) = \boldsymbol{A} : \boldsymbol{I} = \lambda_1^A + \lambda_2^A + \lambda_3^A \quad , \quad I_1^A = A_{ii} \tag{3.21a}$$

$$I_2^A = \frac{1}{2}\left(\mathrm{tr}\,(\boldsymbol{A})^2 - \mathrm{tr}\,\left(\boldsymbol{A}^2\right)\right) = \lambda_1^A\lambda_2^A + \lambda_2^A\lambda_3^A + \lambda_1^A\lambda_3^A \quad , \quad I_2^A = \frac{1}{2}\left(A_{ii}A_{jj} - A_{ij}A_{ji}\right) \tag{3.21b}$$

$$I_3^A = \det \boldsymbol{A} = \lambda_1^A\lambda_2^A\lambda_3^A \quad , \quad I_3^A = \epsilon_{ijk}A_{1i}A_{2j}A_{3k} \tag{3.21c}$$

where λ_i^A are the principal values of $\boldsymbol{A}$.

Note that the volumetric Jacobian and the third invariant of the right Cauchy-Green tensor are related by

$$I_3^C = J^2 \tag{3.22}$$

and that the first three invariants of $\boldsymbol{C}$ and $\boldsymbol{b}$ are equal. An additional invariant of the Cauchy-Green deformation tensors, often referred to as I_4, is one that describes a directional value and is defined in terms of the right Cauchy-Green tensor as

$$\lambda^2 = \boldsymbol{N}\cdot\boldsymbol{CN} = \boldsymbol{C} : (\boldsymbol{N}\otimes\boldsymbol{N}) \quad . \tag{3.23a}$$

Here $\boldsymbol{N}$ describes a direction vector defined on Ω_0. This relationship can be derived from equation 3.20 or inferred from the principal value decomposition given in equation 3.16a. If $\boldsymbol{N}_i$ is aligned with the principal directions of its counterpart deformation tensor, then the invariants described by equation 3.23a give the principal values λ_i^2.

3.1.1 Zero strain configuration

The presence of the gravitational body force acting on the pliable tissues of the HUA implies that the configuration from which the images are extracted is not stress- or strain-free. To account for the pre-strain and prestress, an additional configuration state, namely the zero strain configuration, is introduced. Figure 3.2 illustrates the three configurations and the relationship between them.

The initial configuration, not necessarily the same as the reference configuration, is denoted Ω_I. The total displacement and deformation gradient are redefined as

$$\boldsymbol{u}^{\mathrm{CI}} = \boldsymbol{x} - \boldsymbol{x}^{\mathrm{I}} = (\boldsymbol{x} - \boldsymbol{X}) + \left(\boldsymbol{X} - \boldsymbol{x}^{\mathrm{I}}\right) = \boldsymbol{u}^{\mathrm{CR}} + \boldsymbol{u}^{\mathrm{RI}} \tag{3.24}$$

$$\boldsymbol{F}^{\mathrm{CI}} := \boldsymbol{F} = \frac{d\boldsymbol{x}}{d\boldsymbol{x}^{\mathrm{I}}} = \boldsymbol{F}^{\mathrm{CR}}\boldsymbol{F}^{\mathrm{RI}} \tag{3.25}$$

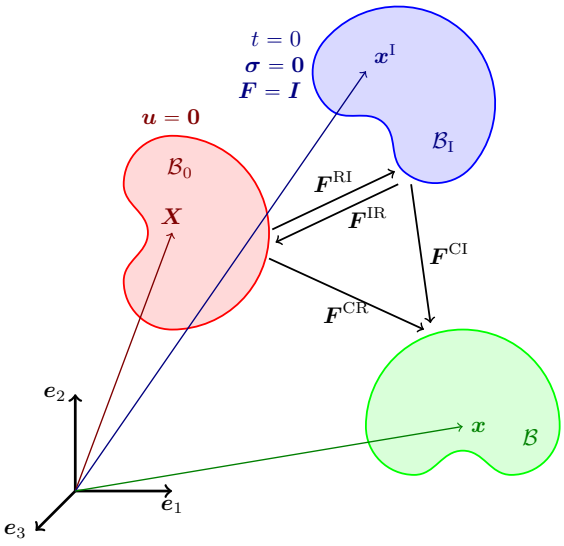

Figure 3.2: Deformation of a general body with a non-trivial zero strain configuration. The kinematic configurations illustrate the initial Ω_{I}, undeformed Ω_0 and current Ω configurations and the relationship between the deformation gradients.

such that

$$\mathrm{d}\boldsymbol{x} = \boldsymbol{F}^{\mathrm{CI}}\mathrm{d}\boldsymbol{x}^{\mathrm{I}} \tag{3.26}$$

with $\boldsymbol{x}^{\mathrm{I}} = \boldsymbol{\varphi}\left(\boldsymbol{X}\right)\Big|_{\Omega_{\mathrm{I}}=\Omega, t=0}$ and $\mathrm{d}\boldsymbol{x}^{\mathrm{I}}$ representing specifically a point and line-element in the initial configuration respectively. The subscript notation C, R, I is used to denote the current, reference and initial configurations respectively. The definitions of the deformation gradients between the various states are

$$\boldsymbol{F}^{\mathrm{CR}} := \nabla_{_0}\,\boldsymbol{\varphi} = \frac{d\boldsymbol{x}}{d\boldsymbol{X}} \quad \text{and} \quad \boldsymbol{F}^{\mathrm{IR}} := \frac{d\boldsymbol{x}^{\mathrm{I}}}{d\boldsymbol{X}} \quad , \quad \boldsymbol{F}^{\mathrm{RI}} = \left(\boldsymbol{F}^{\mathrm{IR}}\right)^{-1} \quad . \tag{3.27}$$

The total deformation gradient is multiplicatively decomposed into two parts with $\boldsymbol{F}^{\mathrm{RI}}$ and $\boldsymbol{F}^{\mathrm{CR}}$ respectively mapping line segments from the initial to the reference configuration and the reference to the current configuration.

The total stretch of any line element in therefore

$$\lambda^{\mathrm{CI}} := \lambda = \lambda^{\mathrm{CR}}\,\lambda^{\mathrm{RI}} \equiv |\boldsymbol{F}\boldsymbol{n}^{\mathrm{I}}| \tag{3.28}$$

with the stretch of the line element from the reference to the initial and current configurations calculated by

$$\lambda^{\mathrm{CR}} = |\boldsymbol{F}^{\mathrm{CR}}\boldsymbol{N}| \quad \text{and} \quad \lambda^{\mathrm{IR}} = |\boldsymbol{F}^{\mathrm{IR}}\boldsymbol{N}| \quad , \quad \lambda^{\mathrm{RI}} = \left(\lambda^{\mathrm{IR}}\right)^{-1} \tag{3.29}$$

respectively. The updated direction of the line element in the current configuration is calculated directly from the reference direction with

$$\boldsymbol{n} = \left(\lambda^{\mathrm{CR}}\right)^{-1}\boldsymbol{F}^{\mathrm{CR}}\boldsymbol{N} \quad . \tag{3.30}$$

A brief proof of the validity of the decomposition is provided in appendix A.1.

3.2 Kinetics

The description of forces acting on bodies and stress quantities relevant to large-strain mechanics are now discussed. Work conjugacy, a key component to the development of constitutive relations between kinematic and kinetic quantities, is then presented.

3.2.1 Stress measures

The definition of stress can be produced by considering a force acting on the (internal) surface of a body to produce deformation. Figure 3.3 illustrates the forces and traction vectors acting on a body in the spatial configuration and their equivalent counterparts in the material setting. The Cauchy stress theorem states that

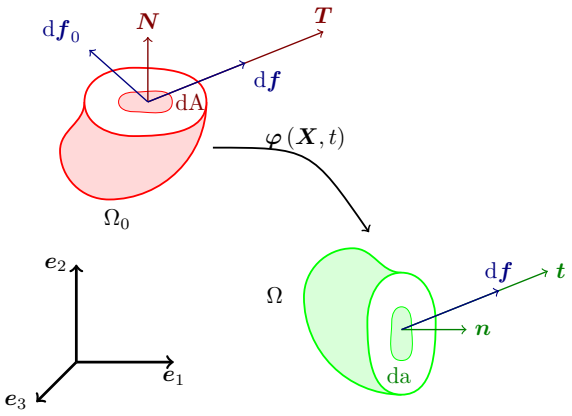

Figure 3.3: The relationship between material and spatial normal, force and traction vectors visualised on the internal surface of a body.

force acting on a surface area da is related to the Cauchy stress through the traction vector

$$\mathrm{d}\boldsymbol{f} = \boldsymbol{t}\mathrm{da} := \boldsymbol{\sigma}\boldsymbol{n}\mathrm{da} \tag{3.31}$$

where the traction $\boldsymbol{t}$ is the force per unit current surface area and the Cauchy stress $\boldsymbol{\sigma}$ is a symmetric second-order tensor that acts on a surface normal to produce the traction.

The Cauchy postulate,

$$\boldsymbol{t}\mathrm{da} = \boldsymbol{t}_0\mathrm{dA} \quad , \tag{3.32}$$

links the traction vectors defined in the two configurations. Through the application of Nanson's formula (equation 3.13) to equation 3.32, the traction defined on the spatial domain in equation 3.31 can be expressed in terms of quantities in the reference domain by

$$\boldsymbol{t}\mathrm{da} = \left(J\boldsymbol{\sigma}\boldsymbol{F}^{-T}\right)\boldsymbol{N}\mathrm{dA} \tag{3.33}$$

with the first Piola-Kirchhoff stress, which has mixed bases, defined as

$$\boldsymbol{P} := J\boldsymbol{\sigma}\boldsymbol{F}^{-T} \quad . \tag{3.34}$$

To facilitate the description of the relationship between force and stress measures in the different configurations, the push-forward and pull-backward operations are introduced. For vectors, the respective operations are

$$\boldsymbol{\chi}(\bullet) := \boldsymbol{F}(\bullet) \tag{3.35}$$

$$\boldsymbol{\chi}^{-1}(\bullet) := \boldsymbol{F}^{-1}(\bullet) \tag{3.36}$$

and second-order tensors they are defined as

$$\boldsymbol{\chi}(\bullet) := \boldsymbol{F}(\bullet)\boldsymbol{F}^{T} \tag{3.37}$$

$$\boldsymbol{\chi}^{-1}(\bullet) := \boldsymbol{F}^{-1}(\bullet)\boldsymbol{F}^{-T} \quad . \tag{3.38}$$

Using equation 3.36 on the boundary force $\mathrm{d}\boldsymbol{f}$, a fictitious force describing an equivalent force acting on the reference configuration can be produced. The result of this is

$$\mathrm{d}\boldsymbol{f}_0 = \boldsymbol{\chi}^{-1}(\mathrm{d}\boldsymbol{f}) = \left(J\boldsymbol{F}^{-1}\boldsymbol{\sigma}\boldsymbol{F}^{-T}\right)\boldsymbol{N}\mathrm{dA} \tag{3.39}$$

where the second Piola-Kirchhoff stress tensor is related to the Cauchy and first Piola-Kirchhoff stresses by

$$\boldsymbol{S} := J\boldsymbol{F}^{-1}\boldsymbol{\sigma}\boldsymbol{F}^{-T} = \boldsymbol{F}^{-1}\boldsymbol{P} \quad . \tag{3.40}$$

An additional symmetric stress quantity is the Kirchhoff stress tensor, defined as

$$\boldsymbol{\tau} := J\boldsymbol{\sigma} = \chi(\boldsymbol{S}) \tag{3.41}$$

and describes the current traction per unit reference area.

3.2.2 Work conjugacy

The requirement for a body in equilibrium is that there is a balance of forces acting on the body, or more precisely that the sources of momentum acting on the surface of a body and those acting on its interior are in equilibrium. This can be described mathematically by

$$\int_{\Omega} \boldsymbol{b}\,\mathrm{d}\Omega + \int_{\Gamma} \boldsymbol{t}\,\mathrm{d}\Gamma - \frac{\partial}{\partial t}\int_{\Omega} \rho\boldsymbol{v}\,\mathrm{d}\Omega = \boldsymbol{0} \quad . \tag{3.42}$$

Assuming that the inertial forces $\rho\dot{\boldsymbol{v}}$ are negligible, equation 3.42 reduces to

$$\int_{\Omega} \boldsymbol{b}\,\mathrm{d}\Omega + \int_{\Gamma} \boldsymbol{t}\,\mathrm{d}\Gamma = \boldsymbol{0} \quad . \tag{3.43}$$

The divergence (or Gauss) theorem,

$$\int_{\Gamma} \boldsymbol{a}\cdot\boldsymbol{n}\,\mathrm{d}\Gamma = \int_{\Omega} \nabla\cdot\boldsymbol{a}\,\mathrm{d}\Omega \quad , \quad \int_{\Gamma} a_i n_i\,\mathrm{d}\Gamma = \int_{\Omega} \frac{\partial a_i}{\partial x_i}\,\mathrm{d}\Omega \quad , \tag{3.44}$$

provides a relationship between the flux of a vector field $\boldsymbol{a}$ through the surface of a body and the vector field within the body itself.

Testing equation 3.43 with an arbitrary velocity $\boldsymbol{v}$, restructuring the boundary term using equation 3.31 and utilising equation 3.44 in conjunction with the chain rule results in the description of mechanical power due to volume and surfaces forces

$$\dot{W} = \int_{\Omega} \boldsymbol{v} \cdot (\boldsymbol{b} + \nabla \cdot \boldsymbol{\sigma}) \ \mathrm{d}\Omega + \int_{\Omega} \boldsymbol{\sigma} : \boldsymbol{d} \ \mathrm{d}\Omega \quad . \tag{3.45}$$

The terms collected in the first integral are the weak form of the equilibrium equation (equation 3.43) and are consequently equal to zero. The Cauchy stress $\boldsymbol{\sigma}$ and symmetric rate-of-strain tensor $\boldsymbol{d}$ are power conjugate pairs and the domain integral of the their inner-product is a measure of the work rate of internal stresses.

The domain of integration in equation 3.43 can be changed using equation 3.12 such that

$$\int_{\Omega} \mathrm{d}\Omega = \int_{\Omega_0} J \ \mathrm{d}\Omega_0 \quad . \tag{3.46}$$

Manipulation of equation 3.45 using equations 3.34, 3.40 and 3.46 identifies the power conjugate pairs for the first and second Piola-Kirchhoff stresses,

$$\begin{aligned}
\int_{\Omega} \boldsymbol{\sigma} : \boldsymbol{d} \ \mathrm{d}\Omega &= \int_{\Omega_0} \boldsymbol{\tau} : \boldsymbol{d} \ \mathrm{d}\Omega_0 && \text{(3.47a)} \\
&= \int_{\Omega_0} \boldsymbol{P} : \dot{\boldsymbol{F}} \ \mathrm{d}\Omega_0 && \text{(3.47b)} \\
&= \int_{\Omega_0} \boldsymbol{S} : \dot{\boldsymbol{E}} \ \mathrm{d}\Omega_0 && \text{(3.47c)} \\
&= \int_{\Omega_0} \boldsymbol{S} : \frac{1}{2}\dot{\boldsymbol{C}} \ \mathrm{d}\Omega_0 \quad \text{with} \quad \dot{\boldsymbol{E}} = \frac{1}{2}\dot{\boldsymbol{C}} \text{ from equation 3.18.}
\end{aligned}$$

The strain-rate conjugates for $\boldsymbol{P}$ and $\boldsymbol{S}$ are the deformation rate and time-rate of the Lagrangian strain tensors respectively.

3.3 Hyperelasticity

Hyperelastic materials are idealised elastic materials for which a constitutive model can be derived from a strain-energy function (SEF). Assuming that the scalar SEF ψ describes the stored energy per unit reference volume of a single material, it can equivalently expressed using various strain variables through application of the principle of frame-indifference

$$\psi = \hat{\psi}(\boldsymbol{F}) = \bar{\psi}(\boldsymbol{C}) = \breve{\psi}(\boldsymbol{E}) = \tilde{\psi}(\boldsymbol{b}) \quad . \tag{3.48}$$

Utilising the chain rule, the time-rate of the SEF is

$$\dot{\psi} = \frac{\partial \hat{\psi}}{\partial t} = \frac{\partial \hat{\psi}}{\partial \boldsymbol{F}} : \frac{\partial \boldsymbol{F}}{\partial t} = \frac{\partial \hat{\psi}}{\partial \boldsymbol{F}} : \dot{\boldsymbol{F}} \quad . \tag{3.49}$$

Comparing equation 3.49 to equation 3.34, it is observed that the first Piola-Kirchhoff stress can be expressed in terms of the SEF by

$$\boldsymbol{P} = \frac{\partial \hat{\psi}(\boldsymbol{F})}{\partial \boldsymbol{F}} \quad . \tag{3.50}$$

Similarly, using equations 3.18 and 3.40, it can be demonstrated that the SEF and the second Piola-Kirchhoff stress are related by

$$\boldsymbol{S} = \frac{\partial \breve{\psi}(\boldsymbol{E})}{\partial \boldsymbol{E}} = 2\frac{\partial \bar{\psi}(\boldsymbol{C})}{\partial \boldsymbol{C}} \quad . \tag{3.51}$$

Starting with $\widetilde{\psi}(\boldsymbol{b})$, taking the time derivative, applying the chain rule and comparing to equation 3.47a, it is deduced that

$$\boldsymbol{\tau} = 2\frac{\partial\widetilde{\psi}(\boldsymbol{b})}{\partial\boldsymbol{b}}\boldsymbol{b} = 2\boldsymbol{b}\frac{\partial\widetilde{\psi}(\boldsymbol{b})}{\partial\boldsymbol{b}} \quad . \tag{3.52}$$

Furthermore, the application of equation 3.41 to equation 3.51 shows that the following identity holds

$$\boldsymbol{\tau} = \boldsymbol{\chi}\left(2\frac{\partial\bar{\psi}(\boldsymbol{C})}{\partial\boldsymbol{C}}\right) \quad . \tag{3.53}$$

This demonstrates that equation 3.53 can be derived from equation 3.51 using equation 3.37 and noting that the invariants of $\boldsymbol{C}$ and $\boldsymbol{b}$ are the same.

3.3.1 Elasticity tensor

A first-order expansion of the second Piola-Kirchhoff stress for a general material

$$\dot{\boldsymbol{S}} = \frac{\partial\boldsymbol{S}(\boldsymbol{E})}{\partial\boldsymbol{E}} : \dot{\boldsymbol{E}} = \mathbb{H} : \dot{\boldsymbol{E}} \tag{3.54}$$

is derived from equation 3.51 using the chain rule. The referential elasticity tensor has been defined as $\mathbb{H} = \frac{\partial\boldsymbol{S}(\boldsymbol{E})}{\partial\boldsymbol{E}} = 2\frac{\partial\boldsymbol{S}(\boldsymbol{C})}{\partial\boldsymbol{C}}$. Due to the symmetries exhibited by the stress and strain tensors in equation 3.54, $\mathbb{H}$ exhibits minor symmetries.

As $\boldsymbol{S}$ is derived from a scalar SEF, then following from equation 3.51, the referential elasticity tensor is of the form

$$\mathbb{H} = \frac{\partial\boldsymbol{S}(\boldsymbol{E})}{\partial\boldsymbol{E}} = \frac{\partial^2\psi(\boldsymbol{E})}{\partial\boldsymbol{E}\partial\boldsymbol{E}} = 4\frac{\partial^2\psi(\boldsymbol{C})}{\partial\boldsymbol{C}\partial\boldsymbol{C}} \tag{3.55}$$

which demonstrates that $\mathbb{H}$ also exhibits major symmetry as the order in which the differential operation occurs is arbitrary.

The spatial elasticity tensor $J\mathbb{C} = \chi(\mathbb{H})$ can be developed from equation 3.55 using the push-forward operation

$$\boldsymbol{\chi}(\bullet) := \boldsymbol{F}\bar{\otimes}\boldsymbol{F} : (\bullet) : \boldsymbol{F}^T\bar{\otimes}\boldsymbol{F}^T \quad , \tag{3.56}$$

where the non-standard tensor product is defined as

$$(\boldsymbol{A}\bar{\otimes}\boldsymbol{B})_{ijkl} := A_{ik}B_{jl} \quad , \tag{3.57}$$

with the result that

$$J\mathbb{C} = 4\boldsymbol{b}\frac{\partial^2\psi(\boldsymbol{b})}{\partial\boldsymbol{b}\partial\boldsymbol{b}}\boldsymbol{b} \quad . \tag{3.58}$$

The elasticity tensors discussed here are required for the linearisation of the weak form of the governing equations discussed in chapter 4.

3.4 Material behaviour

Following the description of general hyperelastic materials, the general form for SEFs that describe isotropic and transversely isotropic materials is presented.

3.4.1 Isotropy

An elastic material is considered isotropic if the constitutive equation for the material is independent of the orientation of the body. As they are direction independent, the SEF governing the material behaviour must similarly objective (that is, independent of the reference frame of measurement). Thus, the SEF must be a function of the strain invariants or the principle stretches

$$\psi = \bar{\psi}\left(I_1, I_2, I_3\right) \tag{3.59a}$$

$$= \widetilde{\psi}\left(\lambda_1, \lambda_2, \lambda_3\right) \quad . \tag{3.59b}$$

Additionally, the SEF description in terms of the principal stretches $\lambda_1, \lambda_2, \lambda_3$ must be independent of the order of the function parameters, that is

$$\psi = \widetilde{\psi}\left(\lambda_i, \lambda_j, \lambda_k\right) \quad \forall \quad i \neq j \neq k \quad . \tag{3.60}$$

Using the relationships presented in equations 3.51, 3.52 and 3.59a, the stresses can derived from the relevant SEF by application of the chain rule, with the result that

$$\boldsymbol{S} = 2\left(\frac{\partial \psi}{\partial I_1^C}\frac{\partial I_1^C}{\partial \boldsymbol{C}} + \frac{\partial \psi}{\partial I_2^C}\frac{\partial I_2^C}{\partial \boldsymbol{C}} + \frac{\partial \psi}{\partial I_3^C}\frac{\partial I_3^C}{\partial \boldsymbol{C}}\right) \tag{3.61}$$

$$\boldsymbol{\tau} = 2\boldsymbol{b}\left(\frac{\partial \psi}{\partial I_1^b}\frac{\partial I_1^b}{\partial \boldsymbol{b}} + \frac{\partial \psi}{\partial I_2^b}\frac{\partial I_2^b}{\partial \boldsymbol{b}} + \frac{\partial \psi}{\partial I_3^b}\frac{\partial I_3^b}{\partial \boldsymbol{b}}\right) \tag{3.62}$$

where I_i^C and I_i^b are invariants of the right and left Cauchy-Green tensors given by equations 3.21a to 3.21c. The derivation of the elasticity tensors from equations 3.55 and 3.58 can be arrived at in a similar manner. The components of these stress and elasticity tensors are derived for a general fibrous material in appendix C.1,

3.4.2 Transverse isotropy

Transversely isotropic materials, for example those with fibre-reinforcement, have a preferred directionality. The material properties in the plane orthogonal to the preferred direction are isotropic, as shown in figure 3.4. The unit line element $\boldsymbol{N}_{\mathrm{f}} = \boldsymbol{N}_{\mathrm{f}}\left(\boldsymbol{X}\right)$, which describes the directionality of the material, is transformed to $\boldsymbol{n}_{\mathrm{f}} = \boldsymbol{n}_{\mathrm{f}}\left(\boldsymbol{X}, t\right)$ under deformation by equation 3.20.

The desire to describe the behaviour of such a material using a SEF which must be reference frame indifferent, requires that the description given in equation 3.59a and therefore equation 3.48 be modified to include additional invariants that are direction dependent. The additional directional contribution to the SEF in equation 3.59a is

$$\psi_{\mathrm{f}} = \psi_{\mathrm{f}}\left(\lambda_{\mathrm{f}}\right) \tag{3.63}$$

with the directional stretch λ_{f}, dependent on a predefined referential direction vector $\boldsymbol{N}_{\mathrm{f}}$, calculable from equation 3.23a. The direction-dependent stretch is related to the traditional description of the fourth invariant by

$$I_4^C = {\lambda_{\mathrm{f}}}^2 \tag{3.64}$$

but due to the generality of the materials to be described, the notation presented in equation 3.63 is retained.

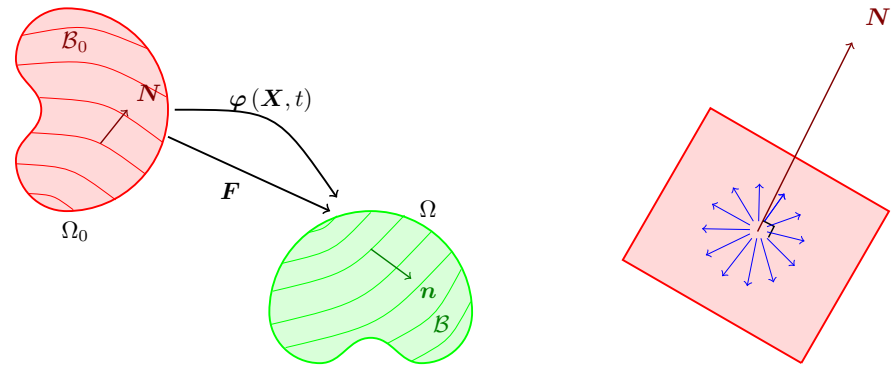

(a) The normal to the contours identifies the direction of material reinforcement. Material properties in the direction of the normal and tangential to the contour are dissimilar.

(b) Material properties on the plane of isotropy are identical.

Figure 3.4: Depiction of a general transversely isotropic material.

The second Piola-Kirchhoff stress associated the directionally dependent component of the SEF given in equation 3.63 is

$$\boldsymbol{S}_{\mathrm{f}} = 2\frac{\partial \psi_{\mathrm{f}}(\lambda_{\mathrm{f}})}{\partial \boldsymbol{C}} = 2\frac{\partial \psi_{\mathrm{f}}(\lambda_{\mathrm{f}})}{\partial \lambda_{\mathrm{f}}}\frac{\partial \lambda_{\mathrm{f}}}{\partial \boldsymbol{C}} = 2\psi_{\mathrm{f}}'\frac{\partial \lambda_{\mathrm{f}}}{\partial \boldsymbol{C}} \tag{3.65}$$

where, as shown in equation A.11, the quantity $\dfrac{\partial \lambda_{\mathrm{f}}}{\partial \boldsymbol{C}}$ can be calculated from equation 3.23a by specifying the direction vector $\boldsymbol{N} = \boldsymbol{N}_{\mathrm{f}}$.

3.5 Balance laws

The relevant classical balance laws for Newtonian systems, namely the conservation of mass and linear momentum, are summarised in this section.

3.5.1 Conservation of mass

The principle of mass conservation states that the total mass in a system remains constant, which implies that

$$\dot{m} = 0 \quad . \tag{3.66}$$

An infinitesimal mass element in the reference configuration therefore retains its mass under deformation and, using equation 3.12, it follows that

$$\begin{aligned} \mathrm{d}m = \rho_0 \mathrm{dV} = \rho \mathrm{dv} = \rho J \mathrm{dV} \\ \Rightarrow \quad \rho_0 = J\rho \end{aligned} \tag{3.67}$$

where ρ_0, ρ are the density of the infinitesimal volume as described in the material and spatial configurations respectively.

3.5.2 Balance of linear momentum

The conservation of linear momentum, which can be derived from the first law of thermodynamics, is presented in the strong form in terms of the spatial setting. It describes the balance of forces due to inertial, internal and body forces. Variational principles are applied to the linear momentum equation to produce the weak form of the equilibrium equation governing quasi-static, elastic solids.

3.5.3 Strong form

The conservation of linear momentum under the assumption of quasi-static conditions reads

$$\nabla \cdot \boldsymbol{\sigma} + \boldsymbol{b} = \boldsymbol{0} \quad \text{on} \quad \Omega \tag{3.68}$$

where the $\boldsymbol{b}$ denotes the body force. The quasi-static conditions are relevant for this problem due to the assumption of slow movement of the anatomy. The conservation of angular momentum dictates that the Cauchy stress is symmetric, that is $\boldsymbol{\sigma} = \boldsymbol{\sigma}^T$.

3.5.4 Weak form

Multiplying equation 3.68 from the left by an arbitrary test function $\delta \boldsymbol{v}$ and integrating over the current domain, the weak form of the linear momentum equation reads

$$\int_\Omega \delta \boldsymbol{v} \cdot (\nabla \cdot \boldsymbol{\sigma}) \; \mathrm{d}\Omega + \int_\Omega \delta \boldsymbol{v} \cdot \boldsymbol{b} \; \mathrm{d}\Omega = 0 \quad . \tag{3.69}$$

Application of the product rule and divergence theorem, namely

$$\nabla \cdot (\boldsymbol{A}\boldsymbol{b}) = (\nabla \cdot \boldsymbol{A}) \cdot \boldsymbol{b} + \boldsymbol{A} : \nabla \boldsymbol{b} \quad \text{and} \tag{3.70a}$$

$$\int_\Omega \nabla \cdot \boldsymbol{c} \; \mathrm{d}\Omega = \int_\Gamma \boldsymbol{c} \cdot \boldsymbol{n} \; \mathrm{d}\Gamma \quad \Rightarrow \quad \int_\Omega \nabla \cdot (\boldsymbol{A}\boldsymbol{b}) \; \mathrm{d}\Omega = \int_\Gamma \boldsymbol{A}\boldsymbol{n} \cdot \boldsymbol{b} \; \mathrm{d}\Gamma \quad , \tag{3.70b}$$

for the arbitrary tensor $\boldsymbol{A}$ and vectors $\boldsymbol{b}, \boldsymbol{c}$, to the first term of equation 3.69 transfers the derivative from the stress-term to the test function, with the result that

$$-\int_\Omega \nabla \delta \boldsymbol{v} : \boldsymbol{\sigma} \; \mathrm{d}\Omega + \int_{\Gamma^\mathrm{t}} \delta \boldsymbol{v} \cdot \boldsymbol{\sigma}\boldsymbol{n} \; \mathrm{d}\Gamma^\mathrm{t} + \int_\Omega \delta \boldsymbol{v} \cdot \boldsymbol{b} \; \mathrm{d}\Omega = \boldsymbol{0} \quad . \tag{3.71}$$

The test function is defined such that $\delta \boldsymbol{v} := 0$ on the Dirichlet boundary $\Gamma^{\boldsymbol{\varphi}}$.

Recognising that the second term of equation 3.71, namely the boundary integral, involves the surface traction, we can write the final weak form of the equilibrium equation as

$$\int_\Omega \nabla \delta \boldsymbol{v} : \boldsymbol{\sigma} \; \mathrm{d}\Omega = \int_{\Gamma^\mathrm{t}} \delta \boldsymbol{v} \cdot \boldsymbol{t} \; \mathrm{d}\Gamma^\mathrm{t} + \int_\Omega \delta \boldsymbol{v} \cdot \boldsymbol{b} \; \mathrm{d}\Omega \quad . \tag{3.72}$$

The left-hand side of equation 3.72 is the rate of internal work, previously derived in equation 3.45.

3.6 Decoupling of the volumetric and isochoric contributions

In this section, the concept of separating the description of the motion into volume-preserving and dilatational components is presented. This is necessary to describe an equivalent pressure for incompressible media, for which the bulk modulus is infinite, through the use of Lagrange multipliers. Rubber-like materials and many other physical media, be they compressible or incompressible, exhibit greatly different behaviour under hydrostatic pressure versus shear stress. This methodology assists in providing a mechanism for the accurate representation of this behaviour.

3.6.1 Decomposition of deformation gradient

Assuming a multiplicative split of the motion into a volume preserving- and a dilatational part [254], the deformation gradient can be decomposed into

$$\boldsymbol{F} = \widehat{\boldsymbol{F}}\bar{\boldsymbol{F}} \quad , \tag{3.73}$$

with

$$\widehat{\boldsymbol{F}} := J^{\frac{1}{3}}\boldsymbol{I} \qquad (\text{ volumetric }) \quad \text{and} \tag{3.74a}$$

$$\bar{\boldsymbol{F}} := J^{-\frac{1}{3}}\boldsymbol{F} \qquad (\text{ isochoric }) \quad . \tag{3.74b}$$

The isochoric deformation gradient $\bar{\boldsymbol{F}}$ has a determinant $\det \bar{\boldsymbol{F}} = 1$. The right and left Cauchy-Green deformation tensor have isochoric counterparts, calculated using equation 3.74b and expressed as

$$\bar{\boldsymbol{C}} = J^{-\frac{2}{3}}\boldsymbol{C} = \bar{\boldsymbol{F}}^T\bar{\boldsymbol{F}} \quad , \tag{3.75}$$

$$\bar{\boldsymbol{b}} = J^{-\frac{2}{3}}\boldsymbol{b} = \bar{\boldsymbol{F}}\bar{\boldsymbol{F}}^T \quad . \tag{3.76}$$

The invariant isochoric directional stretch derived from equation 3.23a is

$$\bar{\lambda}_{\mathrm{f}}^{\,2} = \bar{\boldsymbol{C}} : (\boldsymbol{N}_{\mathrm{f}} \otimes \boldsymbol{N}_{\mathrm{f}}) \quad . \tag{3.77}$$

3.6.2 Decomposition of strain-energy function

Under the assumption that the volumetric response of the material is independent of the isochoric response [254, 176, 314], the transversely isotropic SEF can be additively decomposed as

$$\psi = \psi_{\mathrm{vol}}\left(J\right) + \psi_{\mathrm{iso}}\left(\bar{\boldsymbol{b}}, \bar{\lambda}_{\mathrm{f}}\right) \tag{3.78}$$

where ψ_{vol} describes the total energy due to volumetric deformation and ψ_{iso} describes the total energy due to the component of deformation that is volume-preserving. Note that the relationship described in equation 3.22 has been used to introduce the volumetric Jacobian in place of the third invariant used in equation 3.59a.

Using the relationship given in equation 3.52, the Kirchhoff stress for the decoupled SEF can be developed from equation 3.78, which results in

$$\boldsymbol{\tau} = \boldsymbol{\tau}_{\mathrm{vol}}\left(J\right) + \boldsymbol{\tau}_{\mathrm{iso}}\left(\bar{\boldsymbol{b}}, \bar{\lambda}_{\mathrm{f}}\right) \tag{3.79}$$

where

$$\boldsymbol{\tau}_{\text{vol}}\left(J\right) = 2\boldsymbol{b}\left[\frac{\partial \psi_{\text{vol}}}{\partial J}\frac{\partial J}{\partial \boldsymbol{b}}\right] \tag{3.80}$$

and

$$\boldsymbol{\tau}_{\text{iso}}\left(\bar{\boldsymbol{b}}, \bar{\lambda}_{\text{f}}\right) = 2\boldsymbol{b}\left[\frac{\partial \psi_{\text{iso}}}{\partial \bar{\boldsymbol{b}}} : \frac{\partial \bar{\boldsymbol{b}}}{\partial \boldsymbol{b}}\right] = 2\boldsymbol{b}\left[\left(\frac{\partial \psi_{\text{iso}}}{\partial \bar{\boldsymbol{b}}}\bigg|_{\bar{\lambda}_{\text{f}}} + \frac{\partial \psi_{\text{iso}}}{\partial \bar{\lambda}_{\text{f}}}\bigg|_{\bar{\boldsymbol{b}}}\frac{\partial \bar{\lambda}_{\text{f}}}{\partial \bar{\boldsymbol{b}}}\right) : \frac{\partial \bar{\boldsymbol{b}}}{\partial \boldsymbol{b}}\right] \quad . \tag{3.81}$$

The result of this derivation is listed in equations 3.82a to 3.82c in table 3.1.

Table 3.1: Continuum mechanics relationships for volumetric-isochoric decomposition.

Kirchhoff stresses		**Spatial elasticity tensors**	
$\boldsymbol{\tau}_{\text{vol}} = pJ\boldsymbol{I}$	(3.82a)	$J\mathbb{C}_{\text{vol}} = J\left(\tilde{p}\boldsymbol{I}\otimes\boldsymbol{I} - 2p\mathbb{I}\right) \quad , \quad \tilde{p} = p + J\dfrac{\partial p}{\partial J}$	(3.83a)
$\boldsymbol{\tau}_{\text{iso}} = \mathbb{P} : \bar{\boldsymbol{\tau}}$	(3.82b)	$J\mathbb{C}_{\text{iso}} = \dfrac{2}{3}\,\text{tr}\,\bar{\boldsymbol{\tau}}\,\mathbb{P} + \mathbb{P} : J\bar{\mathbb{C}} : \mathbb{P} - \dfrac{2}{3}\left(\boldsymbol{\tau}_{\text{iso}}\otimes\boldsymbol{I} + \boldsymbol{I}\otimes\boldsymbol{\tau}_{\text{iso}}\right)$	(3.83b)
$\bar{\boldsymbol{\tau}} = 2\dfrac{\partial \psi_{\text{iso}}\left(\boldsymbol{b}\right)}{\partial \boldsymbol{b}}\boldsymbol{b}\Big\|_{\boldsymbol{b}=\bar{\boldsymbol{b}}} = \hat{\boldsymbol{\tau}}_{\text{iso}}\left(\boldsymbol{b}, \lambda_{\text{f}}\right)\Big\|_{\boldsymbol{b}=\bar{\boldsymbol{b}}}$	(3.82c)	$J\bar{\mathbb{C}} = J\hat{\mathbb{C}}_{\text{iso}}\left(\boldsymbol{b}, \lambda_{\text{f}}\right)\Big\|_{\boldsymbol{b}=\bar{\boldsymbol{b}}}$	(3.83c)

In equation 3.82a, $p = \dfrac{\partial \psi_{\text{vol}}}{\partial J}$ denotes the pressure response[1] and $\boldsymbol{I}$ is the identity tensor. The tensor $\hat{\boldsymbol{\tau}}_{\text{iso}}$ in equation 3.82c is the Kirchhoff stress derived from the isochoric parts of the material constitutive equations outlined later in table 5.1. The deviatoric projection tensor $\mathbb{P}$ is defined as

$$\mathbb{P} = \mathbb{I} - \frac{1}{3}\boldsymbol{I}\otimes\boldsymbol{I} \tag{3.84}$$

where the symmetric fourth-order identity tensor is given by

$$\mathbb{I}_{ijkl} = \frac{1}{2}\left(\delta_{ik}\delta_{jl} + \delta_{il}\delta_{jk}\right) \quad . \tag{3.85}$$

The relationship between the elastic modulii in the current configuration and the decomposed SEF, provided in equation 3.58, results in the following definition of the elastic modulus

$$J\mathbb{C} = J\mathbb{C}_{\text{vol}}\left(J\right) + J\mathbb{C}_{\text{iso}}\left(\bar{\boldsymbol{b}}, \bar{\lambda}_{\text{f}}\right) \tag{3.86}$$

which are tabulated in table 3.1. The material tangent tensor $\hat{\mathbb{C}}_{\text{iso}}$ is determined from the isochoric parts of the constitutive equations listed later in table 5.1. The spatial elasticity tensors for the decoupled problem retain the major symmetry and minor symmetries that exist in the coupled form. A full derivation of the uncoupled model for hyperelastic materials is presented in appendix A.3.

3.7 Motion-dependent boundary conditions

The geometry of the HUA is complex and capturing the dynamics of all of the components of the anatomy is an extremely challenging task. However, the challenges lie not only in geometric reconstruction, but also

[1] The pressure response is simply the negative value of the hydrostatic pressure.

in representing the physical interaction between mobile and fixed parts due to muscle contraction and constrained motion by contact interaction.

The tongue uses both extrinsic and intrinsic muscles to perform a broad spectrum of movements. The extrinsic muscles have a bony attachment outside the tongue and terminate inside the body of the tongue. For example, the styloglossus (SG) originates at the base of the skull and inserts into the posterior surface of the tongue after traversing tissues in the neck. Direct inclusion of some of these extrinsic muscles into a computational model is difficult as the geometry of the extrinsic muscles and the tissues that surround them is challenging to define.

This section details two physically representative boundary-related models that remove the difficulties associated with incorporating these anatomical features. They necessitate the formulation of boundary conditions that provide a balance between geometric complexity, physical accuracy and computational effort. As these boundary terms are motion-dependent, their consistent linearisation is also detailed.

With reference to figure 3.1, the boundary of the reference domain is decomposed into regions with prescribed displacements and tractions such that $\Gamma_0 = \Gamma_0^{\varphi} \bigcup \Gamma_0^{\mathrm{t}}$. The region with prescribed traction is further decomposed into position dependent and displacement dependent portions $\Gamma_0^{\mathrm{t}} = \Gamma_0^{\mathrm{t}(X)} \bigcup \Gamma_0^{\mathrm{t}(u)}$. The motion dependent contribution is further decomposed such that

$$\boldsymbol{t} = \boldsymbol{t}\left(\boldsymbol{u}\right) \quad \text{on} \quad \Gamma_0^{\mathrm{t}(u)} = \Gamma_0^{\mathrm{t_t}} \bigcup \Gamma_0^{\mathrm{t_f}} \quad \text{and} \quad \Gamma_0^{\mathrm{t_t}} \bigcap \Gamma_0^{\mathrm{t_f}} \neq \varnothing \quad . \tag{3.87}$$

The former component of the displacement dependent traction boundary, $\Gamma_0^{\mathrm{t_t}}$, is discussed in section 3.7.1 while the latter is presented in section 3.7.2.

3.7.1 Fictitious material layer

This boundary model describes a fictitious layer of tissue of prescribed composition and thickness that surrounds a region of the boundary $\Gamma_0^{\mathrm{t_t}}$. The motivation for the development of this model lies in the necessity for a weak motion constraint on some of the extrinsic muscles of the tongue. *In vivo*, these muscles are attached to a complex arrangement of tissues that extend through the full thickness of the throat. All the tissues (muscle, adipose tissue and others) are flexible and none are fully constrained. However, although *in vivo* they collectively act to support these structures, and their presence therefore is required to provide a stress condition on the tissues of interest, their complex geometric nature makes their inclusion in this study undesirable.

This boundary contribution therefore, in a simple but consistent manner, approximates the normal and shear stresses at the interface between the parts of the anatomy that have been excluded from the model and those that are directly captured in the computational domain. Appendix D.2 provides an example of the model, while a fully-detailed derivation of the model is given in appendix A.4.1.

3.7.1.1 Kinematics of the material layer

By definition, the thickness of the material layer is measured with respect to the normal $\boldsymbol{N}$, that is the outward-normal at $\boldsymbol{X}$ on $\Gamma_0^{\mathrm{t_t}}$. The opposite side of the boundary is considered to be completely fixed in space. Figure 3.5 depicts the description of the terms defined to describe the boundary traction.

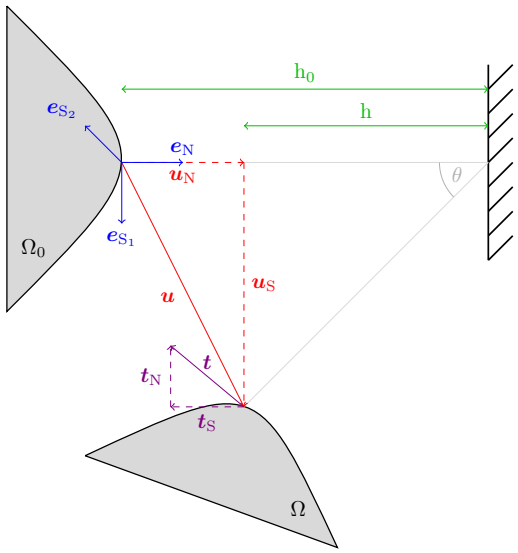

Figure 3.5: Visual description of the fictitious material layer boundary condition.

An orthonormal basis at $\boldsymbol{X}$ is defined such that

$$\text{Normal:} \quad \boldsymbol{e}_{\mathrm{N}} := \boldsymbol{N}(\boldsymbol{X}) \tag{3.88}$$

$$\text{Tangential:} \quad \boldsymbol{e}_{\mathrm{S}_\alpha} := \xi_\alpha(\boldsymbol{X}) \quad , \quad \alpha \in \{1,2\} \quad . \tag{3.89}$$

The tangential basis vectors are arbitrarily chosen on the surface $\Gamma_0^{\mathrm{t_t}}$ at $\boldsymbol{X}$. Note that the bases for the calculations are defined on the reference configuration, and are therefore constant with changing displacement. The component of the displacement normal to the boundary is

$$\boldsymbol{u}_{\mathrm{N}} = (\boldsymbol{u} \cdot \boldsymbol{N})\, \boldsymbol{e}_{\mathrm{N}} \quad , \tag{3.90}$$

while the tangential displacement is given by

$$\boldsymbol{u}_{\mathrm{S}_\alpha} = (\boldsymbol{u} \cdot \boldsymbol{e}_{\mathrm{S}_\alpha})\, \boldsymbol{e}_{\mathrm{S}_\alpha} \quad . \tag{3.91}$$

Note that when $\boldsymbol{u} \cdot \boldsymbol{N} > 0$, material compression occurs. Given the prescribed thickness of surface material layer h_0, the current thickness of surface material layer under deformation is

$$\mathrm{h} = \mathrm{h}_0 - \boldsymbol{u} \cdot \boldsymbol{N} \quad . \tag{3.92}$$

Consistent with equation 3.90, from equation 3.92 it is observed that $\mathrm{h} < \mathrm{h}_0$ if $\boldsymbol{u} \cdot \boldsymbol{N} > 0$, which implies that compression occurs.

From the definitions of displacement, strain measures can be formulated. The 1-d true strain in the direction of the normal is

$$\varepsilon = \varepsilon(\boldsymbol{u}) = \ln\left(\frac{\mathrm{h}(\boldsymbol{u})}{\mathrm{h}_0}\right) \tag{3.93}$$

and the 1-d shear strain, aligned with the corresponding tangential basis, is given by

$$\gamma = \gamma(\boldsymbol{u}) = \tan\theta = \frac{u_{\mathrm{S}}}{\mathrm{h}} = \frac{\boldsymbol{u} \cdot \boldsymbol{e}_{\mathrm{S}_\alpha}}{\mathrm{h}} \quad . \tag{3.94}$$

It should be noted that the sign changes in ε and γ can be used to orientate the traction with respect to the normal and tangential basis vectors. Ultimately it is expected that the traction opposes the motion.

3.7.1.2 Kinetics of the material layer

The traction vector acting on the boundary can be resolved into normal and tangential components

$$\boldsymbol{t}_{\mathrm{t}}^{\mathrm{ext}} = \boldsymbol{t}_{\mathrm{N}} + \boldsymbol{t}_{\mathrm{S}} \tag{3.95}$$

with each component decomposed into a scalar value and direction vector

$$\boldsymbol{t}_{\mathrm{t}}^{\mathrm{N}} := t_{\mathrm{N}} \boldsymbol{N} \tag{3.96a}$$

$$\boldsymbol{t}_{\mathrm{t}}^{\mathrm{S}_\alpha} := \sum_{\alpha} t_{\mathrm{S}_\alpha} \boldsymbol{e}_{\mathrm{S}_\alpha} \quad , \quad \alpha \in \{1, 2\} \quad . \tag{3.96b}$$

The 1-d normal stress is

$$t_{\mathrm{N}} = \sigma_{\mathrm{N}}(\varepsilon) \approx \frac{\partial \sigma}{\partial \varepsilon} \varepsilon = E(\varepsilon)\, \varepsilon \tag{3.97}$$

while the 1-d shear stresses are given by

$$t_{\mathrm{S}_\alpha} = \sigma_{\mathrm{S}_\alpha}(\gamma_\alpha) \approx -G(|\gamma_\alpha|)\, \gamma_\alpha = -\frac{E(|\gamma_\alpha|)}{2(1+\nu)} \gamma_\alpha \quad . \tag{3.98}$$

Here E and G represent the small strain Young and shear modulus respectively, and ν is the material Poisson's ratio. Another observation concerning the signs in equations 3.97 and 3.98 must be made. For the normal component, $\sigma_{\mathrm{N}} > 0$ if $\varepsilon > 0$ (that is, tension occurs as the normal displacement is anti-parallel to normal basis) and $\sigma_{\mathrm{N}} < 0$ if $\varepsilon < 0$ (implying that compression occurs). In the shear direction, $\sigma_{\mathrm{S}_\alpha} > 0$ if $\gamma < 0$ (tangential displacement is anti-parallel to tangential basis). Given the current formulation, the material is considered isotropic in shear and therefore exhibits a transversely isotropic behaviour overall.

3.7.1.3 Linearisation of the material layer traction contributions

The linearisation of the traction vector given in equation 3.95 with respect to the displacement yields the stiffness contribution

$$\boldsymbol{C}_{\mathrm{t}}^{\mathrm{ext}} = \frac{\partial \boldsymbol{t}_{\mathrm{t}}^{\mathrm{ext}}}{\partial \boldsymbol{u}} = \frac{\partial \boldsymbol{t}_{\mathrm{t}}^{\mathrm{N}}}{\partial \boldsymbol{u}} + \sum_{\alpha} \frac{\partial \boldsymbol{t}_{\mathrm{t}}^{\mathrm{S}_\alpha}}{\partial \boldsymbol{u}} \tag{3.99}$$

where the tangent[2] for the normal part of the traction vector

$$\boldsymbol{C}_{\mathrm{t}}^{\mathrm{N}} = \frac{\partial \boldsymbol{t}_{\mathrm{t}}^{\mathrm{N}}}{\partial \boldsymbol{u}} = -\left(\frac{\partial E}{\partial \varepsilon} \varepsilon + E \right) \mathrm{h}^{-1} \boldsymbol{N} \otimes \boldsymbol{N} \tag{3.100}$$

and that of the tangential part of the traction vector is

$$\boldsymbol{C}_{\mathrm{t}}^{\mathrm{S}_\alpha} = \frac{\partial \boldsymbol{t}_{\mathrm{t}}^{\mathrm{S}_\alpha}}{\partial \boldsymbol{u}} = -\left(\frac{\partial G}{\partial |\gamma_\alpha|} |\gamma_\alpha| + G \right) \mathrm{h}^{-1} \boldsymbol{e}_{\mathrm{S}_\alpha} \otimes (\boldsymbol{e}_{\mathrm{S}_\alpha} + \gamma \boldsymbol{N}) \tag{3.101a}$$

$$\approx -\left(\frac{\partial G}{\partial |\gamma_\alpha|} |\gamma_\alpha| + G \right) \mathrm{h}^{-1} \boldsymbol{e}_{\mathrm{S}_\alpha} \otimes \boldsymbol{e}_{\mathrm{S}_\alpha} \quad \text{for} \quad \gamma_\alpha \ll 1 \quad . \tag{3.101b}$$

The term in equation 3.101a involving the shear strain does not have a symmetric counterpart so it is removed with a small shear strain assumption[3] resulting in equation 3.101b.

[2] Although the local tangent contribution is negative definite, its contribution to the global tangent matrix will be a positive definite one due to a sign change in the global contribution. This can be observed in table 4.1.

[3] Alternatively, this term could be symmeterised, leading to an alternative tangent approximation that suits the symmetric formulation utilised in this work.

3.7.2 External fibres

The external fibre model developed in this section provides a simplified representation of the region of the muscles that extends beyond the computational domain. This allows the force-generating effect of an excluded volume of muscle tissue to be captured while reducing the complexity of the model geometry. Although applied specifically to muscle fibres in this work, the model is derived for fibrous structures in general. A full derivation of the model is presented in appendix A.4.2, and an example demonstrating its use is presented in section 7.2.1.1.

3.7.2.1 Kinematics of external fibres

A schematic of the kinematics for a single fibre is shown in figure 3.6. The origin or permanent fixture point for the fibre is represented by $\boldsymbol{X}^{\mathrm{O}}$, and the insertion point $\boldsymbol{X}^{\mathrm{I}}$ on $\Gamma_0^{\mathrm{t_f}}$ that, under deformation, is displaced to $\boldsymbol{x}^{\mathrm{I}} = \boldsymbol{\varphi}\left(\boldsymbol{X}^{\mathrm{I}}\right)$.

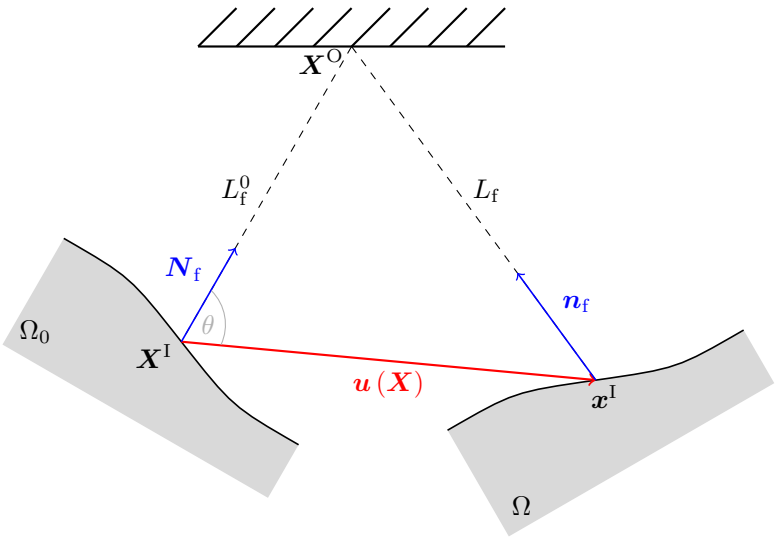

Figure 3.6: Representation of external fibres attached at the model boundaries. Note that the fibres are not necessarily orthogonal to the surface, but by definition $\boldsymbol{N} \cdot \boldsymbol{N}_{\mathrm{f}} > 0$. Additionally, due to the physical scenario being represented, it should be ensured at the condition $\boldsymbol{n} \cdot \boldsymbol{n}_{\mathrm{f}} > 0$ is always met.

The fibre direction is defined to be in the direction of the surface outwards normal. The original and current fibre length vector is given by

$$\boldsymbol{L}_{\mathrm{f}}^0 = L_{\mathrm{f}}^0 \boldsymbol{N}_{\mathrm{f}} := \boldsymbol{X}^{\mathrm{O}} - \boldsymbol{X}^{\mathrm{I}} \tag{3.102a}$$

$$\boldsymbol{L}_{\mathrm{f}} = L_{\mathrm{f}} \boldsymbol{n}_{\mathrm{f}} = \boldsymbol{X}^{\mathrm{O}} - \boldsymbol{x}^{\mathrm{I}} \tag{3.102b}$$

with $\boldsymbol{N}_{\mathrm{f}}, \boldsymbol{n}_{\mathrm{f}}$ unit vectors in the direction of the material and spatial fibre directions. Using the relationship between the displacement and current position given in equation 3.2, the current configuration vector quan-

tities can be redefined in terms of the displacement, namely that

$$\boldsymbol{L}_{\mathrm{f}} := \boldsymbol{L}_{\mathrm{f}}^{0} - \boldsymbol{u} \tag{3.103}$$

$$\boldsymbol{n}_{\mathrm{f}} = \boldsymbol{n}_{\mathrm{f}}(\boldsymbol{u}) := \frac{1}{L_{\mathrm{f}}}\left(\boldsymbol{L}_{\mathrm{f}}^{0} - \boldsymbol{u}\right) \quad . \tag{3.104}$$

Using the defined length measures, the motion-dependent fibre stretch is therefore

$$\lambda_{\mathrm{f}} = \lambda_{\mathrm{f}}(\boldsymbol{u}) := \frac{L_{\mathrm{f}}}{L_{\mathrm{f}}^{0}} \quad . \tag{3.105}$$

3.7.2.2 Kinetics of external fibres

It is expected that the line of action of the force generated by the fibre be aligned with the fibre direction. To this end, the external fibre traction vector is defined as

$$\boldsymbol{t}_{\mathrm{f}}^{\mathrm{ext}} := \phi_{\mathrm{f}}\lambda_{\mathrm{f}}T_{\mathrm{f}}\boldsymbol{n}_{\mathrm{f}} = \boldsymbol{\sigma}_{\mathrm{f}}\boldsymbol{n} \tag{3.106}$$

as motivated by equation 5.4c. The magnitude of the traction, $t_{\mathrm{f}}^{\mathrm{ext}} = \phi_{\mathrm{f}}\lambda_{\mathrm{f}}T_{\mathrm{f}}$, results naturally from the description of direction-dependent hyperelastic materials. The nominal fibre stress $T_{\mathrm{f}} = T_{\mathrm{f}}(\lambda_{\mathrm{f}})$ is governed by the fibre constitutive model.

3.7.2.3 Linearisation of external fibre traction contributions

The linearisation of the current traction equation 3.106 results in the material stiffness contribution

$$\boldsymbol{C}_{\mathrm{f}}^{\mathrm{ext}} = \frac{d\boldsymbol{t}_{\mathrm{f}}^{\mathrm{ext}}}{d\boldsymbol{u}} = -\frac{\phi_{\mathrm{f}}}{L_{\mathrm{f}}^{0}}\left[\lambda_{\mathrm{f}}\frac{dT_{\mathrm{f}}}{d\lambda_{\mathrm{f}}}\boldsymbol{n}_{\mathrm{f}}\otimes\boldsymbol{n}_{\mathrm{f}} + T_{\mathrm{f}}\boldsymbol{I}\right] \quad . \tag{3.107}$$

This second-order tensor is symmetric and contains stiffness contributions in the fibre direction as well as the directions orthogonal to the fibre direction. A comment on the validity of the negative definite nature of the tangent is made in footnote 2 on page 47.

4. FINITE ELEMENT METHOD

As many biological materials are incompressible, it is necessary to utilise a FE formulation that does not exhibit the locking behaviour that standard low-order formulations exhibit in the incompressible limit. Motivated by these considerations, a robust, stable and computationally efficient three-field formulation for incompressible media is presented in section 4.1. The finite element method (FEM) implementation of the mixed problem is described in section 4.2. The resulting mean-dilatation Q1-P0-P0 element, proposed by Nagtegaal et al. [189] and developed by Simo et al. [254], has all of the required characteristics. It alleviates the issues of volumetric locking in incompressible materials and shear-locking in bending dominated problems experienced by standard low-order elements [176]. Coupled with an augmented Lagrangian method, it has been successfully used to model incompressible biological soft tissues [306, 82].

4.1 Variational functional: A mixed formulation for incompressibility

The equation describing the incompressibility condition is

$$J - 1 = 0 \quad \text{on} \quad \Omega \quad . \tag{4.1}$$

Satisfaction of the incompressibility condition naturally ensures that conservation of mass (equation 3.67) occurs. An extra variable θ, namely the dilatation describing the volume change due to hydrostatic loading, is introduced to prevent ill-conditioning of the tangent matrices [176]. Equation 4.1 is replaced with the amended equations

$$J - \theta = 0 \quad \text{on} \quad \Omega \tag{4.2a}$$

$$\theta - 1 = 0 \quad \text{on} \quad \Omega \tag{4.2b}$$

where equation 4.2a describes the equivalence of the volumetric Jacobian and the dilatation in the incompressible limit, and equation 4.2b is used to enforce incompressibility.

A three-field functional that describes total stored energy in the system and incorporates equations 4.2a and 4.2b was developed [253, 176]. This functional, which exploits the additive split of the SEF, is given by

$$\Pi = \Pi\left(\boldsymbol{\varphi}, \theta, \Lambda, p\right) := \Pi_{\text{int}}\left(\boldsymbol{\varphi}, \theta, \Lambda, p\right) + \Pi_{\text{ext}}\left(\boldsymbol{\varphi}\right) \Rightarrow \text{stationary} \quad , \tag{4.3a}$$

$$\Pi_{\text{int}}\left(\boldsymbol{\varphi}, \theta, \Lambda, p\right) := \int_{\Omega_0} \left\{ \left[\psi_{\text{vol}}\left(\theta\right) + \psi_{\text{iso}}\left(\bar{\boldsymbol{b}}\left(\boldsymbol{\varphi}\right), \bar{\lambda}_{\text{f}}\left(\boldsymbol{\varphi}\right)\right)\right] + p\left(J\left(\boldsymbol{\varphi}\right) - \theta\right) + \Lambda\left(\theta - 1\right) \right\} \mathrm{d}\Omega_0 \quad , \tag{4.3b}$$

$$\Pi_{\text{ext}}\left(\boldsymbol{\varphi}\right) := -\int_{\Omega_0} \boldsymbol{\varphi} \cdot \boldsymbol{b}_0 \, \mathrm{d}\Omega_0 - \int_{\Gamma_0^{\text{t}}} \boldsymbol{\varphi} \cdot \boldsymbol{t}_0\left(\boldsymbol{\varphi}\right) \, \mathrm{d}\Gamma_0^{\text{t}} \tag{4.3c}$$

where the leading terms in the square bracket describe the elastic potential, p is a Lagrange multiplier interpreted as the pressure response[1], Λ is a Lagrange multiplier enforcing the incompressibility constraint, and $\boldsymbol{b}_0, \boldsymbol{t}_0$ are the referential body and traction forces. It should be noted that ψ_{vol} is now a function of the dilatation.

4.1.1 Weak form of equilibrium equation

The stationary point of equation 4.3a is the equilibrium solution to the problem. Minimisation of the energy functional leads to the weak form of the equilibrium equation, which satisfies the strong form of the governing equations.

The Frechét derivative (or, more generally, the Gâteaux derivative), defined for vector and scalar quantities by

$$D_{\boldsymbol{x}}\Pi\left(\boldsymbol{x},\boldsymbol{y},z\right)\cdot\delta\boldsymbol{x}=\left.\frac{d}{d\varepsilon}\right|_{\varepsilon=0}\Pi\left(\boldsymbol{x}+\varepsilon\delta\boldsymbol{x},\boldsymbol{y},z\right)\quad,\quad D_{z}\Pi\left(\boldsymbol{x},\boldsymbol{y},z\right)\cdot\delta z=\left.\frac{d}{d\gamma}\right|_{\gamma=0}\Pi\left(\boldsymbol{x},\boldsymbol{y},z+\gamma\delta z\right)\quad, \tag{4.4}$$

gives the directional derivative of a potential function Π with respect to a dependent variable. The stationary point of the problem is the solution where the total derivative of the potential function is zero. The variation of equation 4.3a using the Frechét derivative leads to the weak form of three-field formulation, namely

$$\mathrm{R}_{\text{int}}^{\delta\boldsymbol{\varphi}}=D_{\boldsymbol{\varphi}}\Pi_{\text{int}}\cdot\delta\boldsymbol{\varphi}=\int_{\Omega_0}\left(\nabla\,\delta\boldsymbol{\varphi}\right):\left[\boldsymbol{\tau}_{\text{iso}}+pJ\boldsymbol{I}\right]\,\mathrm{d}\Omega_0 \tag{4.5a}$$

$$\mathrm{R}_{\text{ext}}^{\delta\boldsymbol{\varphi}}=D_{\boldsymbol{\varphi}}\Pi_{\text{ext}}\cdot\delta\boldsymbol{\varphi}=-\int_{\Omega_0}\delta\boldsymbol{\varphi}\cdot\boldsymbol{b}_0\,\mathrm{d}\Omega_0-\int_{\Gamma_0^{\text{t}}}\delta\boldsymbol{\varphi}\cdot\boldsymbol{t}_0\left(\boldsymbol{\varphi}\right)\,\mathrm{d}\Gamma_0^{\text{t}} \tag{4.5b}$$

$$\mathrm{R}_{\text{int}}^{\delta p}=D_{p}\Pi_{\text{int}}\cdot\delta p=\int_{\Omega_0}\delta p\left(J-\theta\right)\,\mathrm{d}\Omega_0 \tag{4.5c}$$

$$\mathrm{R}_{\text{int}}^{\delta\theta}=D_{\theta}\Pi_{\text{int}}\cdot\delta\theta=\int_{\Omega_0}\delta\theta\left(\psi_{\text{vol}}'\left(\theta\right)+\Lambda-p\right)\,\mathrm{d}\Omega_0\quad. \tag{4.5d}$$

Equations 4.5a and 4.5b collectively give the weak form of the balance of linear momentum, identical to equation 3.72, while the addition of equations 4.5c and 4.5d ensures that a configuration satisfying material incompressibility is attained. The procedure of deriving equations 4.5a to 4.5d is detailed in appendix B.2.1.

As these equations have a nonlinear nature, the stationary point cannot be determined directly. An iterative nonlinear solution algorithm was employed to linearise the governing equations and solve them. The procedure of linearisation and a nonlinear solution algorithm is presented in section 4.2.

4.2 Linearisation

To illustrate the linearisation process, consider the one vector-field functional $\widetilde{\Pi}\left(\boldsymbol{\varphi}\right)$. The stationary point of $\widetilde{\Pi}$ is found at

$$\frac{\partial\widetilde{\Pi}\left(\boldsymbol{\varphi}\right)}{\partial\boldsymbol{\varphi}}=\boldsymbol{0}\quad, \tag{4.6}$$

[1] This quantity is related to the hydrostatic pressure in that the one is the negative of the other. Written in terms of the hydrostatic pressure, equation 4.3b would take the form of a saddle point problem.

which can be solved for using an iterative method. The first-order Taylor expansion of equation 4.6 is

$$\frac{\partial \widetilde{\Pi}(\boldsymbol{\varphi})}{\partial \boldsymbol{\varphi}} + \frac{\partial^2 \widetilde{\Pi}(\boldsymbol{\varphi})}{\partial \boldsymbol{\varphi}^2} \Delta\boldsymbol{\varphi} + \mathrm{O}\left(\Delta\boldsymbol{\varphi}^2\right) = \mathbf{0} \quad . \tag{4.7}$$

Ignoring the higher-order terms, the resulting linearisation of $\widetilde{\Pi}$ provides the incremental update for the Newton-Raphson method, namely

$$\frac{\partial^2 \widetilde{\Pi}(\boldsymbol{\varphi})^{\mathrm{n}}}{\partial \boldsymbol{\varphi}^2} \Delta\boldsymbol{\varphi}^{\mathrm{n}} = -\frac{\partial \widetilde{\Pi}(\boldsymbol{\varphi})^{\mathrm{n}}}{\partial \boldsymbol{\varphi}} \quad \Rightarrow \quad \Delta\boldsymbol{\varphi}^{\mathrm{n}} = \left[\frac{\partial^2 \widetilde{\Pi}(\boldsymbol{\varphi})^{\mathrm{n}}}{\partial \boldsymbol{\varphi}^2}\right]^{-1} \left(-\frac{\partial \widetilde{\Pi}(\boldsymbol{\varphi})^{\mathrm{n}}}{\partial \boldsymbol{\varphi}}\right) \tag{4.8}$$

where the Newton increments n occur at a chosen and constant time t. The vector $\Delta\boldsymbol{\varphi}^{\mathrm{n}}$ is a predicted approximation for the solution update from the configuration $\boldsymbol{\varphi}^{\mathrm{n}}\big|_t$. The updated configuration for the next Newton step is therefore

$$\boldsymbol{\varphi}^{\mathrm{n}+1} = \boldsymbol{\varphi}^{\mathrm{n}} + \Delta\boldsymbol{\varphi}^{\mathrm{n}} \quad . \tag{4.9}$$

The quantities $\frac{\partial \widetilde{\Pi}(\boldsymbol{\varphi})^{\mathrm{n}}}{\partial \boldsymbol{\varphi}}$ and $\frac{\partial^2 \widetilde{\Pi}(\boldsymbol{\varphi})^{\mathrm{n}}}{\partial \boldsymbol{\varphi}^2}$ are the residual and tangent respectively, both of which are evaluated at the n^{th} Newton increment.

From the three-field functional (equation 4.3a), a full variation results in a residual equation that can be further linearised for implementation in a Newton-Raphson solution algorithm, as demonstrated by Simo et al. [254]. The procedure and result of linearising equations 4.5a to 4.5d using the Frechét derivative (equation 4.4) is described in appendix B.2.2. As the implementation will be carried out solely for Q1-P0-P0 elements, a simplification of the resulting equations can be performed. The dilatation and pressure field are considered piecewise constant on each finite element and can therefore be condensed out of the formulation at the element level. Simo and Taylor [253] show that substitution of the known dilatation and pressure variables into the full residual and tangent equations leads to a reduced formulation given in equations 4.16a and 4.17a. The steps taken to attain this result are shown in appendix B.3.

The result of the linearisation of the free-energy functional given in equation 4.3a and subsequent static-condensation procedure is summarised in table 4.1. The dilatation and pressure variables are determined for the displacement configuration using equations 4.12 to 4.15. The dilatation is first calculated as the ratio of the current to reference cell volume, and the calculation of the pressure follows using the value of the dilatation and the volumetric SEF defined by equation 5.7. As the pressure response is no longer a field variable, the volumetric Kirchhoff stress term and its associated tangent are defined as

$$\boldsymbol{\tau}_{\mathrm{vol}} := p^{\mathrm{e}} J \boldsymbol{I} \quad , \quad J\mathbb{C}_{\mathrm{vol}} := p^{\mathrm{e}} J \left(\boldsymbol{I} \otimes \boldsymbol{I} - 2\mathbb{I}\right) \quad . \tag{4.10}$$

4.2.1 Enforcement of incompressibility condition

The field variable Λ is treated as an augmented Lagrange multiplier in order to effectively enforce incompressibility without creating an overly stiff system that is computationally expensive to solve. Use of the Uzawa update scheme [253] allows the field to be treated as constant within a Newton-Raphson loop and then updated for the next Uzawa iteration as

$$\Lambda^{\mathrm{u}+1} = \Lambda^{\mathrm{u}} + \kappa^{\mathrm{u}} \left(\theta^{\mathrm{u}} - 1\right) \quad . \tag{4.11}$$

Table 4.1: Linearisation of three-field functional and static-condensation of piecewise constant pressure and dilatation fields.

Element reference and current volumes

$$\mathrm{V}^{\mathrm{e}} = \int_{\Omega_0^{\mathrm{e}}} \mathrm{d}\Omega_0^{\mathrm{e}} \tag{4.12}$$

$$\mathrm{v}^{\mathrm{e}} = \int_{\Omega_0^{\mathrm{e}}} J \, \mathrm{d}\Omega_0^{\mathrm{e}} \tag{4.13}$$

Element dilatation and pressure

$$\theta^{\mathrm{e}} = \frac{\mathrm{v}^{\mathrm{e}}}{\mathrm{V}^{\mathrm{e}}} \tag{4.14}$$

$$p^{\mathrm{e}} = \psi'_{\mathrm{vol}}\left(\theta^{\mathrm{e}}\right) + \Lambda^{\mathrm{e}} \tag{4.15}$$

Residual

$$\mathrm{R}\left(\delta\boldsymbol{\varphi}, \boldsymbol{\varphi}\right) = \mathrm{R}_{\mathrm{int}}\left(\delta\boldsymbol{\varphi}, \boldsymbol{\varphi}\right) + \mathrm{R}_{\mathrm{ext}}\left(\delta\boldsymbol{\varphi}, \boldsymbol{\varphi}\right) \tag{4.16a}$$

$$\mathrm{R}_{\mathrm{int}}\left(\delta\boldsymbol{\varphi}, \boldsymbol{\varphi}\right) = \int_{\Omega_0} \nabla\left(\delta\boldsymbol{\varphi}\right) : \left[\boldsymbol{\tau}_{\mathrm{vol}} + \boldsymbol{\tau}_{\mathrm{iso}}\right] \, \mathrm{d}\Omega_0 \tag{4.16b}$$

$$\mathrm{R}_{\mathrm{ext}}\left(\delta\boldsymbol{\varphi}, \boldsymbol{\varphi}\right) = -\int_{\Omega_0} \left(\delta\boldsymbol{\varphi}\right) \cdot \rho_0 \boldsymbol{g} \, \mathrm{d}\Omega_0 - \int_{\Gamma_0^{\mathrm{t}(X)}} \left(\delta\boldsymbol{\varphi}\right) \cdot \boldsymbol{t}_0\left(\boldsymbol{X}\right) \, \mathrm{d}\Gamma_0^{\mathrm{t}(X)} - \int_{\Gamma_0^{\mathrm{t}(u)}} \left(\delta\boldsymbol{\varphi}\right) \cdot \boldsymbol{t}_0{}^{\mathrm{ext}}\left(\boldsymbol{\varphi}\right) \, \mathrm{d}\Gamma_0^{\mathrm{t}(u)} \tag{4.16c}$$

Linearisation of residual

$$\mathrm{K}\left(\delta\boldsymbol{\varphi}, \Delta\boldsymbol{\varphi}, \boldsymbol{\varphi}\right) = \mathrm{K}_{\mathrm{mat}} + \mathrm{K}_{\mathrm{geo}} + \mathrm{K}_{\mathrm{vol}} + \mathrm{K}_{\mathrm{t}(u)} \tag{4.17a}$$

$$\mathrm{K}_{\mathrm{mat}} = \int_{\Omega_0} \nabla\left(\delta\boldsymbol{\varphi}\right) : \left[J\mathbb{C}_{\mathrm{vol}} + J\mathbb{C}_{\mathrm{iso}}\right] : \nabla\left(\Delta\boldsymbol{\varphi}\right) \, \mathrm{d}\Omega_0 \tag{4.17b}$$

$$\mathrm{K}_{\mathrm{geo}} = \int_{\Omega_0} \nabla\left(\delta\boldsymbol{\varphi}\right) : \left(\nabla\left(\Delta\boldsymbol{\varphi}\right)\left[\boldsymbol{\tau}_{\mathrm{vol}} + \boldsymbol{\tau}_{\mathrm{iso}}\right]\right) \, \mathrm{d}\Omega_0 \tag{4.17c}$$

$$\mathrm{K}_{\mathrm{vol}} = \sum_{\mathrm{e}=1}^{\mathrm{n_{el}}} \left[\frac{1}{\mathrm{V}^{\mathrm{e}}} \int_{\Omega_0^{\mathrm{e}}} \nabla\left(\delta\boldsymbol{\varphi}\right) : J\boldsymbol{I} \, \mathrm{d}\Omega_0^{\mathrm{e}}\right] \left[\psi''_{\mathrm{vol}}\left(\theta^{\mathrm{e}}\right) \mathrm{V}^{\mathrm{e}}\right] \left[\frac{1}{\mathrm{V}^{\mathrm{e}}} \int_{\Omega_0^{\mathrm{e}}} J\boldsymbol{I} : \nabla\left(\Delta\boldsymbol{\varphi}\right) \, \mathrm{d}\Omega_0^{\mathrm{e}}\right] \tag{4.17d}$$

$$\mathrm{K}_{\mathrm{t}(u)} = -\int_{\Gamma_0^{\mathrm{t}(u)}} \left(\delta\boldsymbol{\varphi}\right) \cdot \boldsymbol{C}_{\mathrm{t}}^{\mathrm{ext}} \cdot \left(\Delta\boldsymbol{\varphi}\right) \, \mathrm{d}\Gamma_0^{\mathrm{t}(u)} \tag{4.17e}$$

For incompressible materials, the effective bulk modulus at each Uzawa iteration is calculated by

$$\kappa^{\mathrm{u}} = \kappa \times 1.5^{\mathrm{u}} \tag{4.18}$$

where $\kappa = \dfrac{E}{3\left(1-2\nu\right)}$ represents an initial approximation material bulk modulus that, in the incompressible limit, tends to ∞. This function increases exponentially with each iteration to accelerate the enforcement of the condition. Incompressibility is considered to be attained when the overall dilatation error is less than 0.1%.

4.2.2 Boundary conditions

The boundary $\Gamma := \partial\Omega$ is decomposed into non-overlapping Dirichlet and Neumann parts $\Gamma^{\boldsymbol{\varphi}}$ and Γ^{t} such that

$$\Gamma = \Gamma^{\boldsymbol{\varphi}} \bigcup \Gamma^{\mathrm{t}} \quad \text{with} \quad \Gamma^{\boldsymbol{\varphi}} \bigcap \Gamma^{\mathrm{t}} = 0 \quad . \tag{4.19}$$

The essential boundary condition

$$\boldsymbol{\varphi} = \bar{\boldsymbol{\varphi}} \quad \text{on} \quad \Gamma^{\boldsymbol{\varphi}} \tag{4.20}$$

is imposed on degrees-of-freedom for which a prescribed displacement exists.

The natural boundary condition, imposed on all other surfaces, is

$$\boldsymbol{t} = \begin{cases} \bar{\boldsymbol{t}} = \boldsymbol{\sigma}\boldsymbol{n} & \text{on} \quad \Gamma^{\mathrm{t}(X)} \\ \boldsymbol{t}^{\mathrm{ext}} & \text{on} \quad \Gamma^{\mathrm{t}(u)} \end{cases} \tag{4.21a}$$

where $\boldsymbol{\sigma}$ represents external stresses acting on the body, $\boldsymbol{n}$ is the outward normal at the surface of the body in the spatial configuration. Nanson's formula (equation 3.13) is used to transform the traction description given above to the referential form used in equation 4.16c. For surfaces that experience the influence of fluid pressure, $\boldsymbol{\sigma} = -p\boldsymbol{I}$ and free boundaries have no traction, i.e. $\boldsymbol{t} = \boldsymbol{0}$. The external traction conditions that $\boldsymbol{t}^{\mathrm{ext}}$ encompasses are described in sections 3.7.1.2 and 3.7.2.2.

4.3 Finite element implementation

In solid mechanics, a Lagrangian framework is commonly used. The natural description of the governing equations is one in which the coordinate system remains stationary. In particular, this work uses the total Lagrangian formulation where all calculations are performed on a permanent and unchanging reference domain.

Setting the body configuration to the current configuration, the motion $\boldsymbol{\varphi} = \boldsymbol{x}$ is related to the material points by equation 3.2 and the variation and increments of the motion are

$$\delta\boldsymbol{\varphi} = \delta\boldsymbol{x} = \delta\left(\boldsymbol{X} + \boldsymbol{u}\left(\boldsymbol{\varphi}\right)\right) = \delta\boldsymbol{u} \quad , \quad \Delta\boldsymbol{\varphi} = \Delta\boldsymbol{u} \quad . \tag{4.22}$$

The gradients of the motion are therefore

$$\nabla\left(\delta\boldsymbol{\varphi}\right) = \nabla\left(\delta\boldsymbol{u}\right) \quad , \quad \nabla\left(\Delta\boldsymbol{\varphi}\right) = \nabla\left(\Delta\boldsymbol{u}\right) \quad . \tag{4.23}$$

The motion can be approximated in terms of the FE shape functions. The FE approximation/interpolation for the displacement field $\boldsymbol{u}$ is given by [114]

$$\boldsymbol{\varphi}\left(\boldsymbol{X}, t\right) \approx \boldsymbol{\varphi}^{\mathrm{h}}\left(\boldsymbol{X}, t\right) = \sum_{\mathrm{I}=1}^{\mathrm{n_{node}}} N^{\mathrm{I}}\left(\boldsymbol{X}\right)\ \boldsymbol{u}^{\mathrm{I}}\left(t\right) \tag{4.24}$$

where $N^{\mathrm{I}}\left(\boldsymbol{X}\right)$ represents the standard continuous scalar piecewise-linear finite element shape functions defined on Ω^{h} and the vector $\boldsymbol{u}^{\mathrm{I}}\left(t\right)$ gives the nodal values of the unknown displacement field at a given time t. That continuous shape functions are used for the displacement field, the compatibility condition (equation 3.5) is naturally satisfied. Figure 4.1 illustrates the form of the linear shape functions associated with the central node of a domain discretised into 4 regular elements. Similarly, the virtual and incremental nodal displacements can be represented as

$$\delta\boldsymbol{\varphi}^{\mathrm{h}} = \sum_{\mathrm{I}=1}^{\mathrm{n_{node}}} N^{\mathrm{I}}\,\delta\boldsymbol{u}^{\mathrm{I}} \quad , \quad \Delta\boldsymbol{\varphi}^{\mathrm{h}} = \sum_{\mathrm{I}=1}^{\mathrm{n_{node}}} N^{\mathrm{I}}\,\Delta\boldsymbol{u}^{\mathrm{I}} \tag{4.25}$$

respectively. Given the identity

$$\nabla\left(c\boldsymbol{a}\right) = c\,\nabla\,\boldsymbol{a} + \boldsymbol{a}\otimes\nabla\,c \quad , \tag{4.26}$$

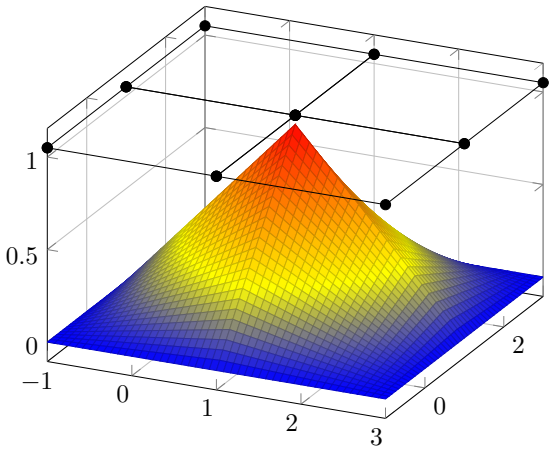

Figure 4.1: Piecewise-bilinear shape function on a regular two-dimensional domain of 4 elements.

for the scalar quantity c and vector $\boldsymbol{a}$, the discretised gradient of the motion with respect to the reference configuration becomes

$$\nabla_0 \boldsymbol{\varphi} \approx \sum_{\mathrm{I}=1}^{\mathrm{n_{node}}} \boldsymbol{u}^{\mathrm{I}} \otimes \nabla_0 N^{\mathrm{I}} = \sum_{\mathrm{I}=1}^{\mathrm{n_{node}}} \boldsymbol{u}^{\mathrm{I}} \otimes \boldsymbol{B}^{\mathrm{I}} \tag{4.27}$$

due to the independence of $\boldsymbol{u}^{\mathrm{I}}(t)$ on position. The material shape function gradient vector is

$$\nabla_0 N^{\mathrm{I}} = \boldsymbol{B}^{\mathrm{I}} = \left\{ \frac{\partial N^{\mathrm{I}}}{\partial X_1} \; \frac{\partial N^{\mathrm{I}}}{\partial X_2} \; \frac{\partial N^{\mathrm{I}}}{\partial X_3} \right\}^T \quad . \tag{4.28}$$

Similarly, the discretised gradient of the motion with respect to the current configuration is

$$\nabla \boldsymbol{\varphi} = \frac{\partial}{\partial \boldsymbol{x}} (\boldsymbol{\varphi}) \approx \sum_{\mathrm{I}=1}^{\mathrm{n_{node}}} \boldsymbol{u}^{\mathrm{I}} \otimes \overset{\star}{\boldsymbol{B}}{}^{\mathrm{I}} \tag{4.29}$$

where $\overset{\star}{\boldsymbol{B}}{}^{\mathrm{I}} = \nabla N^{\mathrm{I}}$.

However, as the total Lagrangian formulation is utilised, the spatial gradient shape functions used in equations 4.16b, 4.17b and 4.17c are not directly available during computation. On the other hand, the reference gradient shape functions can be pushed forward into the current configuration by

$$\nabla \boldsymbol{\varphi} = \frac{\partial \boldsymbol{\varphi}}{\partial \boldsymbol{X}} \frac{\partial \boldsymbol{X}}{\partial \boldsymbol{x}} = \nabla_0 \boldsymbol{\varphi} \boldsymbol{F}^{-1} \approx \sum_{\mathrm{I}=1}^{\mathrm{n_{node}}} \boldsymbol{u}^{\mathrm{I}} \otimes \boldsymbol{B}^{\mathrm{I}} \boldsymbol{F}^{-1} \quad \text{with} \quad \boldsymbol{F}^{-1} \equiv \left(\boldsymbol{F}^{\mathrm{CR}} \right)^{-1} \quad , \tag{4.30}$$

thereby keeping the shape function gradient evaluations on the reference domain. The virtual and incremental nodal gradients can thus be represented as

$$\nabla \left(\delta \boldsymbol{\varphi}^{\mathrm{h}} \right) = \sum_{\mathrm{I}=1}^{\mathrm{n_{node}}} \delta \boldsymbol{u}^{\mathrm{I}} \otimes \overset{\star}{\boldsymbol{B}}{}^{\mathrm{I}} \quad , \quad \nabla \left(\Delta \boldsymbol{\varphi}^{\mathrm{h}} \right) = \sum_{\mathrm{I}=1}^{\mathrm{n_{node}}} \Delta \boldsymbol{u}^{\mathrm{I}} \otimes \overset{\star}{\boldsymbol{B}}{}^{\mathrm{I}} \quad \text{with} \quad \overset{\star}{\boldsymbol{B}}{}^{\mathrm{I}} = \boldsymbol{B}^{\mathrm{I}} \boldsymbol{F}^{-1} \tag{4.31}$$

respectively.

Applying the finite element decomposition, the finite element approximation of the residual and linearised stiffness are

$$\mathrm{R}(\delta \boldsymbol{u}, \boldsymbol{u}) = \sum_{\mathrm{I}=1}^{\mathrm{n_{node}}} \delta \boldsymbol{u}^{\mathrm{I}} \cdot \mathbf{R}^{\mathrm{I}} \quad , \tag{4.32a}$$

$$\mathrm{K}(\delta \boldsymbol{u}, \Delta \boldsymbol{u}, \boldsymbol{u}) = \sum_{\mathrm{I,J}=1}^{\mathrm{n_{node}}} \delta \boldsymbol{u}^{\mathrm{I}} \cdot \mathbf{K}^{\mathrm{IJ}} \cdot \Delta \boldsymbol{u}^{\mathrm{J}} \tag{4.32b}$$

respectively.

Since equations 4.32a and 4.32b should hold for arbitrary $\delta\boldsymbol{u}^{\mathrm{h}}$, it follows that equation 4.8 can be rewritten in matrix form as

$$\mathbf{K}\,\Delta\boldsymbol{u} = -\mathbf{R} \tag{4.33}$$

where $\mathbf{R}$, $\mathbf{K}$ are the global residual vector and tangent stiffness matrix respectively.

Table 4.2 presents the discrete form of the linear problem. The symmetry of the Kirchhoff stress tensor and the elasticity tensors have been exploited and the tangent matrix described by equations 4.35b to 4.35d is PDS. Though equation 4.35e appears negative, the local tangent contribution $\boldsymbol{C}_{\mathrm{t}}^{\mathrm{ext}}$ is negative definite, resulting in the overall positive definite contribution from the term.

Table 4.2: FE description of the linearised problem at time t and Newton step n.

Residual

$$\mathbf{R}^{\mathrm{I}}\left(\delta\boldsymbol{\varphi},\boldsymbol{\varphi}\right) = \mathbf{R}^{\mathrm{I}}_{\mathrm{int}}\left(\delta\boldsymbol{\varphi},\boldsymbol{\varphi}\right) + \mathbf{R}^{\mathrm{I}}_{\mathrm{ext}}\left(\delta\boldsymbol{\varphi},\boldsymbol{\varphi}\right) \tag{4.34a}$$

$$\mathbf{R}^{\mathrm{I}}_{\mathrm{int}}\left(\delta\boldsymbol{\varphi},\boldsymbol{\varphi}\right) = \mathop{\mathsf{A}}_{\mathrm{e}=1}^{\mathrm{n_{el}}} \int_{\Omega_0^{\mathrm{e}}} \overset{\star}{\boldsymbol{B}}{}^{\mathrm{I}} \cdot \left[\boldsymbol{\tau}_{\mathrm{vol}} + \boldsymbol{\tau}_{\mathrm{iso}}\right]\, \mathrm{d}\Omega_0^{\mathrm{e}} \tag{4.34b}$$

$$\begin{aligned}\mathbf{R}^{\mathrm{I}}_{\mathrm{ext}}\left(\delta\boldsymbol{\varphi},\boldsymbol{\varphi}\right) = \mathop{\mathsf{A}}_{\mathrm{e}=1}^{\mathrm{n_{el}}} \Bigg[&- \int_{\Omega_0^{\mathrm{e}}} N^{\mathrm{I}}\, \rho_0 \boldsymbol{g}\, \mathrm{d}\Omega_0^{\mathrm{e}} - \int_{\Gamma_0^{\mathrm{e,t}(X)}} N^{\mathrm{I}}\, \boldsymbol{t}_0\left(\boldsymbol{X}\right)\, \mathrm{d}\Gamma_0^{\mathrm{e,t}(X)} \\ &- \int_{\Gamma_0^{\mathrm{e,t}(u)}} N^{\mathrm{I}}\, \boldsymbol{t}_0{}^{\mathrm{ext}}\left(\boldsymbol{\varphi}\right)\, \mathrm{d}\Gamma_0^{\mathrm{e,t}(u)} \Bigg]\end{aligned} \tag{4.34c}$$

Tangent stiffness matrix

$$\mathbf{K}^{\mathrm{IJ}}\left(\delta\boldsymbol{\varphi},\Delta\boldsymbol{\varphi},\boldsymbol{\varphi}\right) = \mathbf{K}^{\mathrm{IJ}}_{\mathrm{mat}} + \mathbf{K}^{\mathrm{IJ}}_{\mathrm{geo}} + \mathbf{K}^{\mathrm{IJ}}_{\mathrm{vol}} + \mathbf{K}^{\mathrm{IJ}}_{\mathrm{t}(u)} \tag{4.35a}$$

$$\mathbf{K}^{\mathrm{IJ}}_{\mathrm{mat}} = \mathop{\mathsf{A}}_{\mathrm{e}=1}^{\mathrm{n_{el}}} \int_{\Omega_0^{\mathrm{e}}} \overset{\star}{\boldsymbol{B}}{}^{\mathrm{I}} \cdot \left[J\mathbb{C}_{\mathrm{vol}} + J\mathbb{C}_{\mathrm{iso}}\right] \cdot \overset{\star}{\boldsymbol{B}}{}^{\mathrm{J}}\, \mathrm{d}\Omega_0^{\mathrm{e}} \tag{4.35b}$$

$$\mathbf{K}^{\mathrm{IJ}}_{\mathrm{geo}} = \mathop{\mathsf{A}}_{\mathrm{e}=1}^{\mathrm{n_{el}}} \int_{\Omega_0^{\mathrm{e}}} \overset{\star}{\boldsymbol{B}}{}^{\mathrm{I}} \cdot \left[\boldsymbol{\tau}_{\mathrm{vol}} + \boldsymbol{\tau}_{\mathrm{iso}}\right] \cdot \overset{\star}{\boldsymbol{B}}{}^{\mathrm{J}} \delta^{IJ}\, \mathrm{d}\Omega_0^{\mathrm{e}} \tag{4.35c}$$

$$\mathbf{K}^{\mathrm{IJ}}_{\mathrm{vol}} = \mathop{\mathsf{A}}_{\mathrm{e}=1}^{\mathrm{n_{el}}} \left[\frac{1}{\mathrm{V}^{\mathrm{e}}} \int_{\Omega_0^{\mathrm{e}}} \overset{\star}{\boldsymbol{B}}{}^{\mathrm{I}} \cdot J\boldsymbol{I}\, \mathrm{d}\Omega_0^{\mathrm{e}}\right] \left[\psi''_{\mathrm{vol}}\left(\theta^{\mathrm{e}}\right) \mathrm{V}^{\mathrm{e}}\right] \left[\frac{1}{\mathrm{V}^{\mathrm{e}}} \int_{\Omega_0^{\mathrm{e}}} J\boldsymbol{I} \cdot \overset{\star}{\boldsymbol{B}}{}^{\mathrm{I}}\, \mathrm{d}\Omega_0^{\mathrm{e}}\right] \tag{4.35d}$$

$$\mathbf{K}^{\mathrm{IJ}}_{\mathrm{t}(u)} = \mathop{\mathsf{A}}_{\mathrm{e}=1}^{\mathrm{n_{el}}} \left[- \int_{\Gamma_0^{\mathrm{e,t}(u)}} N^{\mathrm{I}}\, \boldsymbol{C}_{\mathrm{t}}^{\mathrm{ext}}\, N^{\mathrm{J}}\, \mathrm{d}\Gamma_0^{\mathrm{e,t}(u)}\right] \tag{4.35e}$$

4.4 Implementation of the finite element problem

The finite element method, in conjunction with a Newton-Raphson algorithm, was used to solve for the displacement field. The FEM problem was solved using the open-source finite-element library *deal.II* [13, 14]. The most computationally costly portions of the algorithms were the assembly and solving of the linear system, as well as the update of discontinuous local variables performed by solving complex nonlinear equations. In this section, a brief description of some of the practical aspects of the implementation of the FE

problem is given. A study was also performed to validate the implementation of quasi-incompressible finite-strain elasticity using the Q1-P0-P0 element. This is presented in appendix D.1.

The following points pertaining to the assembly and information update operations are relevant:

Multithreading: Modern technologies provide frameworks with which to perform computational tasks while utilising multiple CPU cores simultaneously. The threaded building blocks [123, 142] framework was used here to share discrete and computationally expensive tasks between cores on a large shared memory processor (SMP) machine. In particular, this was applied for the assembly process and to update information at computational points. Implementing this framework saved much time as the local problem solved at computational (quadrature) points is expensive[2], performed regularly[3] and problem dependent[4].

Precomputation and optimisation: Minimising the number of redundant calculations at the expense of memory results in faster algorithms being produced[5]. The *valgrind* [193] toolbox in conjunction with *KCachegrind* [303] were used to optimise the workflow and minimise computation as much as possible.

Symmetry: The numerous symmetries in the global system, and various stress and elasticity tensors, were exploited as often as possible. Data was stored in a symmetric form frequently as the algorithms integrated into *deal.II* utilise the nature of symmetric tensors to perform computations more rapidly. A significant reduction in the computational expense of system assembly was attained by exploiting the symmetry of the global problem[6].

The linear system resulting from the incompressible solid problem is symmetric and may under certain circumstances be stiff. With regards to solving the linearised system of equations, the following details are pertinent:

Solver: For small problems (usually those being test cases) the direct solver UMFPACK [55] was utilised. For mid-size problems, the conjugate gradient (CG) solver (valid for symmetric systems) provided by *deal.II* was used. To minimise the linear solver time for large problems or those that were anticipated to take extended periods of time to solve, the *Trilinos* [100] CG solver [99] in conjunction with multi-core communication framework *OpenMPI* [79] and the domain decomposition toolbox *Metis* [136] was used.

Preconditioner: The use of a preconditioner assisted with attaining convergence and reducing the amount of computational effort required for convergence (i.e. minimise iterations in linear solver). The symmetric successive over-relaxation (SSOR) solver was used in conjunction with the CG solver as it was found

[2] At each computational point in muscle tissue, there may exist a number of fibres that have a discrete equilibrium problem to be solved. In finding this solution, there are many nested computations in the muscle model which make it an expensive operation to perform.

[3] The nonlinearly varying fibre variables are not solved as field variables, but rather using a staggered approach. At each state change, Newton and linesearch iterations, it is required that the equilibrium solution for fibres at all computational points be recomputed. As the stability of the problem relies heavily on the use of a damping procedure, the linesearch operation becomes an expensive procedure.

[4] The domain is composed of numerous materials which make effective domain decomposition difficult for CPU load balancing difficult. It is desirable that the time spent performing local updates involving the complex muscle problem be minimised. This implies that the CPU usage should maximised.

[5] During assembly operations, stress and elasticity tensors were precomputed at each calculation point. The spatial shape function gradients were precomputed values for each cell using equation 4.30.

[6] The global stiffness matrix was produced by assembling its diagonal contributions and lower half. The latter was subsequently copied into the upper half upon the completion of the assembly process.

that the simple Jacobi preconditioner was not suitable for the biological problem at the core of this work. An algebraic multigrid (AMG) preconditioner [83] was used to reduce linear iterations when using the *Trilinos* CG solver. Since the inertial terms are ignored, the problem is elliptic, and the AMG preconditioner was optimised for this property.

Step control: It was observed that step-size control was critical in order to attain reasonable convergence rates for the highly nonlinear problems being solved. This point is discussed in section 4.4.1.

4.4.1 Damped Newton method

Due to the highly nonlinear nature of the governing and constitutive equations, there is a need for some form of step optimisation. This is to ensure optimal convergence in the Newton-Raphson algorithm, as well as prevent possible divergence. However, using the full-step, or an arbitrary choice of damping parameter, may result in solution instability or sub-optimal convergence rates. The backtracking linesearch algorithm was implemented to determine the optimal step size at each Newton increment.

The updated displacement solution can be written in terms of the previous solution and the damped Newton update

$$\boldsymbol{u}^{\mathrm{n}+1} = \boldsymbol{u}^{\mathrm{n}} + \beta \Delta \boldsymbol{u}^{\mathrm{n}} \tag{4.36}$$

for the damping parameter bounds

$$0 < \beta_{\min} \leqslant \beta \leqslant \beta_{\max} \quad . \tag{4.37}$$

where the choice $\beta_{\max} \leqslant 1$ is appropriate for the Newton-Raphson algorithm. Here $\Delta \boldsymbol{u}^n$ is guaranteed to be the direction of steepest descent to minimise the residual $\mathbf{R}(\boldsymbol{u}^n)$ as the exact tangent is evaluated for each displacement configuration.

It is desired that the optimum step-size β is determined as to ensure that the residual at each Newton iteration n is less than that of the previously evaluated step. That is,

$$\|\mathbf{R}(\boldsymbol{u}^{\mathrm{n}} + \beta \Delta \boldsymbol{u}^n)\| < \|\mathbf{R}(\boldsymbol{u}^{\mathrm{n}})\| \quad . \tag{4.38}$$

This is achieved by minimising the total system energy with respect to the step size [314]

$$\frac{\partial \Pi(\boldsymbol{\varphi})}{\partial \beta} = \frac{\partial \Pi(\boldsymbol{\varphi})}{\partial \boldsymbol{\varphi}} \frac{\partial \boldsymbol{\varphi}}{\partial \beta} = \mathbf{R}(\boldsymbol{u}^{\mathrm{n}} + \beta \Delta \boldsymbol{u}^{\mathrm{n}}) \cdot \Delta \boldsymbol{u}^n = 0 \quad . \tag{4.39}$$

This implies that the step-size should be chosen such that the displacement update and new residual vectors are orthogonal. Solving this problem is the same as minimising the energy function

$$g(\beta) = -\mathbf{R}^0 \cdot \mathbf{R}^{\mathrm{i}} = 0 \tag{4.40}$$

with

$$\mathbf{R}^0 = \mathbf{R}(\boldsymbol{u}^{\mathrm{n}}) \quad , \quad \mathbf{R}^{\mathrm{i}} = \mathbf{R}\left(\boldsymbol{u}^{\mathrm{n}} + \beta^{\mathrm{i}} \Delta \boldsymbol{u}^{\mathrm{n}}\right) \quad . \tag{4.41}$$

A new value of the step-size $\beta^{\mathrm{i}+1}$ must be iteratively selected within each Newton step n until the optimum step-size is determined. There are a number of methods to solve for the appropriate value of β. For example, Bonet and Wood [26] approximate $g(\beta)$ as quadratic, Press et al. [224] assume the function is cubic, and

both solve for the roots and update the approximation iteratively. Since the functions involved in this work are highly nonlinear, these methods exhibit poor convergence characteristics, and we find that the linear approximation suggested by Wriggers [314] works better in practise for this particular problem. The updating for the step-size parameter was calculated using the secant method [314]

$$\beta^{\mathrm{i}+1} = \beta^{\mathrm{i}} - g^{\mathrm{i}} \frac{\beta^{\mathrm{i}} - \beta^{i-1}}{g^{\mathrm{i}} - g^{\mathrm{i}-1}} \tag{4.42}$$

was found to work best in practise. If $g(0) \cdot g(1) \leqslant 0$, then, assuming that $g(\beta)$ is continuous, by the intermediate value theorem there must be a value of β such that $g(\beta) = 0$. If $g(0) \cdot g(1) > 0$, then extrapolation occurs to find a minimum value for $g(\beta)$ within the bounds set by equation 4.37. The initialisation values for the algorithm are

$$g^{\mathrm{i}-1} = g(0) = -\mathbf{R}^0 \cdot \mathbf{R}^0 \quad \text{with} \quad \beta^0 = 0 \tag{4.43}$$

$$g^{\mathrm{i}} = g(1) = -\mathbf{R}^0 \cdot \mathbf{R}^1 \quad \text{with} \quad \beta^1 = 1 \quad . \tag{4.44}$$

In order to minimise the number of linesearch iterations i, we define a termination tolerance with an acceptable value for β being one that satisfies the strong Wolfe conditions. The two conditions that compose the Wolfe conditions are the Armijo rule [184]

$$g^{\mathrm{i}} \leqslant g^0 + c_1 \beta^{\mathrm{i}} \Delta \boldsymbol{u}^{\mathrm{n}} \cdot \mathbf{R}^0 \tag{4.45}$$

that checks whether a sufficient decrease in residual is attained and the modified curvature condition [184]

$$|\Delta \boldsymbol{u}^{\mathrm{n}} \cdot \mathbf{R}^i| \leqslant c_2 |\Delta \boldsymbol{u}^{\mathrm{n}} \cdot \mathbf{R}^0| \tag{4.46}$$

which prevents too short a step from being taken. The parameters for the Wolfe conditions were chosen to be $c_1 = 1 \times 10^{-4}, c_2 = 0.9$.

5. MATERIAL MODELS

Now that the continuum framework has been discussed, the constitutive models that govern material behaviour are presented. The general constitutive equation for a decoupled fibrous hyperelastic material is developed, followed by the constitutive models of biological tissues. The constitutive model for muscular tissue is defined separately in chapter 6.

5.1 Constitutive equations for fibrous hyperelastic materials

A SEF that governs the behaviour of a general fibrous hyperelastic material, described in terms of the invariants of the left Cauchy-Green tensor and the fibre stretch, is given by

$$\psi = \psi\left(J, \bar{b}, \bar{\lambda}_{\mathrm{f}}\right) = \psi_J\left(J\right) + \phi_{\mathrm{M}}\psi_{\mathrm{M}}\left(\bar{I}_1^b, \bar{I}_2^b\right) + \sum_{\mathrm{f}} \phi_{\mathrm{f}}\psi_{\mathrm{f}}\left(\bar{\lambda}_{\mathrm{f}}\right) \tag{5.1a}$$

$$= \psi_J\left(J\right) + \psi_{\mathrm{M}}\left(\bar{I}_1^b, \bar{I}_2^b\right) + \sum_{\mathrm{f}} \phi_{\mathrm{f}}\left(\psi_{\mathrm{f}}\left(\bar{\lambda}_{\mathrm{f}}\right) - \psi_{\mathrm{M}}\left(\bar{I}_1^b, \bar{I}_2^b\right)\right) \tag{5.1b}$$

where ψ describes the strain-energy per unit volume. This description is an altered form of that presented by Humphrey and Yin [116], Martins et al. [170], Holzapfel et al. [107] that was modified to include an arbitrary collection of fibre families and the volumetric contribution of fibres as presented by Baaijens et al. [9], Planas et al. [222], van Oijen [290].

The rule of mixtures [9, 222], valid for incompressible materials, is applied to describe the volume fractions of the constituent components

$$\phi_{\mathrm{M}} + \sum_{\mathrm{f}} \phi_{\mathrm{f}} = 1 \quad . \tag{5.2}$$

The first term of equation 5.1b describes the volumetric response of the material, while the second term describes the isochoric response of a general bulk material. The third term introduces isochoric anisotropic contributions from any fibres that may be embedded in the bulk material[1].

Note that this allows for the presence of multiple interweaving fibre families at any point in the domain [107]. The bulk material can therefore be one that is isotropic, uniaxially orthotropic, transversely isotropic or

[1] Sansour [246] has demonstrated that enforcing the fibre contribution to exhibit isochoric behaviour leads to a material response that is not necessarily consistent with the assumptions used in the development of one-dimensional fibre models. However the description used here is not only commonly used to introduce fibre contributions in models of this nature (see [116, 107]), but also required by the mixing theory to satisfy the compatibility condition [290].

Table 5.1: Continuum mechanics relationships for general fibrous hyperelastic materials.

Tensor invariants		**Kirchhoff stresses**	
$I_1^b = \mathrm{tr}\ (\boldsymbol{b})$	(5.3a)	$\boldsymbol{\tau}_J = \psi'_J J \boldsymbol{I}$	(5.4a)
$I_2^b = \frac{1}{2}\left(\mathrm{tr}\ (\boldsymbol{b})^2 - \mathrm{tr}\ (\boldsymbol{b}^2)\right)$	(5.3b)	$\boldsymbol{\tau}_M = 2\left[\left(\frac{\partial \psi_{\mathrm{M}}}{\partial I_1^b} + I_1^b \frac{\partial \psi_{\mathrm{M}}}{\partial I_2^b}\right)\boldsymbol{b} - \frac{\partial \psi_{\mathrm{M}}}{\partial I_2^b}\boldsymbol{b}^2\right]$	(5.4b)
$I_3^b = J^2 = \det\left(\boldsymbol{F}\right)^2$	(5.3c)	$\boldsymbol{\tau}_{\mathrm{f}} = \sum_{\mathrm{f}} \phi_{\mathrm{f}} \psi'_{\mathrm{f}} \lambda_{\mathrm{f}} \boldsymbol{n}_{\mathrm{f}} \otimes \boldsymbol{n}_{\mathrm{f}}$	(5.4c)
${\lambda_{\mathrm{f}}}^2 = \boldsymbol{C} : (\boldsymbol{N}_{\mathrm{f}} \otimes \boldsymbol{N}_{\mathrm{f}})$	(5.3d)		
Spatial elasticity tensors			
$J\mathbb{C}_J = J\left[\left(\psi'_J + J\psi''_J\right)\boldsymbol{I} \otimes \boldsymbol{I} - \left(2\psi'_J\right)\mathbb{I}\right]$	(5.5a)		
$J\mathbb{C}_M = 4\left[\left(\frac{\partial^2 \psi_{\mathrm{M}}}{\partial {I_1^b}^2} + 2I_1^b \frac{\partial^2 \psi_{\mathrm{M}}}{\partial I_1^b \partial I_2^b} + {I_1^b}^2 \frac{\partial^2 \psi_{\mathrm{M}}}{\partial {I_2^b}^2} + \frac{\partial \psi_{\mathrm{M}}}{\partial I_2^b}\right)\boldsymbol{b} \otimes \boldsymbol{b} - \left(\frac{\partial^2 \psi_{\mathrm{M}}}{\partial I_1^b \partial I_2^b} + I_1^b \frac{\partial^2 \psi_{\mathrm{M}}}{\partial {I_2^b}^2}\right)\left(\boldsymbol{b}^2 \otimes \boldsymbol{b} + \boldsymbol{b} \otimes \boldsymbol{b}^2\right) + \left(\frac{\partial^2 \psi_{\mathrm{M}}}{\partial {I_2^b}^2}\right)\boldsymbol{b}^2 \otimes \boldsymbol{b}^2 - \left(\frac{\partial \psi_{\mathrm{M}}}{\partial I_2^b}\right)\boldsymbol{b} \bar{\otimes} \boldsymbol{b}\right]$	(5.5b)		
$J\mathbb{C}_F = \sum_{\mathrm{f}} \phi_{\mathrm{f}}\left(\psi''_{\mathrm{f}} - \psi'_{\mathrm{f}} {\lambda_{\mathrm{f}}}^{-1}\right){\lambda_{\mathrm{f}}}^2 \boldsymbol{n}_{\mathrm{f}} \otimes \boldsymbol{n}_{\mathrm{f}} \otimes \boldsymbol{n}_{\mathrm{f}} \otimes \boldsymbol{n}_{\mathrm{f}}$	(5.5c)		

completely anisotropic. Fibre families are assumed not to interact with one another through friction or any other direct mechanism. The overall response is, however, coupled.

Table 5.1 provides the definitions[2] of the Kirchhoff stresses and tangent matrices for general fibrous hyperelastic materials given in equation 5.1b in terms of the governing SEF. These relationships are defined for the appropriate parts of equations 3.79 and 3.86. It should be noted that the elasticity contributions presented in equations 5.5a to 5.5c display both major and minor symmetries.

5.2 Volume-averaged stress

As observed in those micro-histological specimens illustrated in section 2.2.2, a major portion of muscle tissue consists of muscle fibres as opposed to interstitial tissue. The infinitesimal fibre volume models used by Humphrey and Yin [116], Martins et al. [170], Holzapfel et al. [107] are not appropriate when representing materials with large fractions of embedded fibres. Because the fibres now have a finite volume, they are required to sustain transverse and shear loads. However, the material model for the muscle fibres, presented in chapter 6, describes only the axial loading response of the one-dimensional fibres which can hold no load in compression or shear. It is assumed that the transverse and shear loading response of a fibre bundle is the same as that of the underlying matrix. However, they are still presumed to have no compressive load bearing

[2] These equations, the development of which is shown in appendix C.1, are consistent with the definitions provided by Weiss et al. [306], Martins et al. [170], Düster et al. [59]

capabilities.

The overall Kirchhoff stress at any point in the domain is given by [290, 9]

$$\boldsymbol{\tau} = \boldsymbol{\tau}_J\left(J\right) + \phi_{\mathrm{M}}\boldsymbol{\tau}_M\left(\bar{I}_1^b, \bar{I}_2^b\right) + \sum_{\mathrm{f}} \phi_{\mathrm{f}}\boldsymbol{\tau}_{\mathrm{f}}\left(\bar{\lambda}_{\mathrm{f}}\right) \tag{5.6a}$$

$$= \boldsymbol{\tau}_J + \boldsymbol{\tau}_M + \sum_{\mathrm{f}} \phi_{\mathrm{f}}\left(\lambda_{\mathrm{f}}\psi'_{\mathrm{f}} - \sum_{\mathrm{f}} \phi_{\mathrm{f}}\left(\boldsymbol{\tau}_M : \boldsymbol{n}_{\mathrm{f}} \otimes \boldsymbol{n}_{\mathrm{f}}\right)\right)\boldsymbol{n}_{\mathrm{f}} \otimes \boldsymbol{n}_{\mathrm{f}} \tag{5.6b}$$

$$\approx \boldsymbol{\tau}_J + \boldsymbol{\tau}_M + \sum_{\mathrm{f}} \phi_{\mathrm{f}}\lambda_{\mathrm{f}}\psi'_{\mathrm{f}}\boldsymbol{n}_{\mathrm{f}} \otimes \boldsymbol{n}_{\mathrm{f}} \quad . \tag{5.6c}$$

Equation 5.6a gives the stress with a fibre description that can hold transverse and shear loads, and equation 5.6b has the transverse and shear loading processed out as described by Baaijens et al. [9] for multiple fibre families.

This model does not easily describe behaviour representative of the experimentally obtained relationships for passive muscular tissue (e.g. Van Ee et al. [282]). This is because the fibre volume fraction is high and the passive component of muscle fibre is very compliant at small strains and only resists tensile deformation [286]. These difficulties are mentioned by van Oijen [290] in their discussion on their application of the rule-of-mixtures. The matrix stress component in the fibre direction was therefore retained, resulting in equation 5.6c, which better reproduces the stress-strain relationships observed in the experimental data but introduces an extra stiffness component in the fibre direction under tensile deformation[3].

5.3 General constitutive models

The following section outlines the hyperelastic constitutive models used to describe the biological materials applied in the computational model and provides material parameters for each material. The bulk material models used in the main body of this work and the validation studies performed for the work were derived from three general material types. They are all described in terms of deformation tensor invariants and therefore fit into the framework listed in table 5.1. In addition to those models described below, the Yeoh and two parameter Mooney-Rivlin models were also implemented for the purpose of evaluating material data presented in the literature.

5.3.1 Volumetric function

The polyconvex volumetric SEF used in this work, which satisfies the criteria outlined in [253], is defined by

$$\psi_J\left(\theta\right) = \frac{1}{4}\left(\theta^2 - 1 - 2\ln\left(\theta\right)\right) \quad , \tag{5.7}$$

and is valid for both compressible and quasi-incompressible materials. This is a specialisation of the general function proposed by Ogden [106], namely

$$\psi_J\left(\theta\right) = \beta^{-2}\left(\theta^{-\beta} - 1 + \beta\ln\left(\theta\right)\right) \tag{5.8}$$

with $\beta = -2$. Such a function satisfies the conditions that $\psi_J\left(\theta\right)\big|_{\theta\to 0^+} = \infty$, $\psi_J\left(\theta\right)\big|_{\theta\to\infty} = \infty$ and $\psi'_J\left(1\right) = 0$.

[3] It has been noted that further consideration should be given to the matrix-fibre model. Effects, such as the stiffness ratio between the fibres and matrix, have been shown by Lu et al. [160] to play a prominent role in the overall response of the constitutive model. Sharafi and Blemker [251] also demonstrate that the model used to represent the underlying histology affects the material response.

5.3.2 Neo-Hookean model

The Neo-Hookean model is a specialised form of the Mooney-Rivlin model. Having only a single parameter, it makes it easy to characterise materials that the model fits. The small strain behaviour of the Neo-Hookean material is nearly linear, so this model can be used to represent stiff materials that experience low magnitude strains under load. The single material constant is given by

$$c_0 = \frac{\mu}{2} \tag{5.9}$$

where the shear modulus is related to the Young's modulus by

$$\mu = \frac{E}{2\left(1+\nu\right)} \quad . \tag{5.10}$$

5.3.3 Fung model

The Fung material model [78, 240], in this instance presented as a two-parameter model, can be used to represent materials that exhibit exponentially increased stiffening at large strains, such as the isotropic bed matrix for muscular tissue [116, 170, 107].

According to Humphrey and Yin [116], a SEF that describes the Fung model is

$$\psi_{\text{Fung}} = A_1 \left(e^{B_1\left(I_1^b - 3\right)} - 1 \right) \quad . \tag{5.11}$$

Note that the material nominally has a hydrostatic prestress $p = -A_1 B_1$ as the first derivative of equation 5.11 is non-zero when $I_1^b = 1$, i.e. for $\boldsymbol{F} = \boldsymbol{I}$. However, the decoupling of the volumetric and isochoric stresses and specifically the isochoric projection equation 3.82b removes this prestressing.

5.3.3.1 1-d model for representation of external tissues

The materials that are used in the model outlined in section 3.7.1 are all of the Fung-type. Uniaxial tests give Young's modulus for adipose and muscle (which is presented in the next chapter). Due to the difference in stiffness in compression and tension, the uniaxial stiffness of these materials can be approximated by

$$E_{\text{Fung}} = \begin{cases} E_0 e^{b_0 |\varepsilon|^{a_0}} & \text{if} \quad \varepsilon \geqslant 0 \\ E_0 e^{b_1 |\varepsilon|^{a_1}} & \text{otherwise} \end{cases} \quad , \tag{5.12}$$

where E_0 is the zero strain Young's modulus.

5.4 Tissue models

A brief description of the choice of material models and the properties of various tissues represented in this work is given below.

5.4.1 Bone

For the loading conditions considered, the hard tissues are expected to undergo significantly less deformation than soft tissues. Both bone and cartilage are considerably stiffer materials in comparison to muscle and adipose tissue. For this reason, a simple Neo-Hookean model give in section 5.3.2 is adopted as it is able to capture the small strain nature of their deformation adequately.

Bone is assumed to have a zero strain Young's modulus of 15GPa [219] (with a range of $0.76 - 42.1$GPa based on bone location, species and test conditions [219, 230]), Poisson's ratio of 0.4 [230] (with a tested range of between $0.08 - 0.482$ depending on species, bone type, specimen location and test conditions as bone is strain-rate dependent [230]) and density of 1900kg/m^3 (with a range of $1100 - 3217$kg/m^3 dependent on bone type and specimen location [124]).

5.4.2 Cartilage

For the cartilage of the epiglottis, the zero strain elastic modulus was assumed to be 3MPa for the slow load changes exerted on the tissue [219] and a Poisson's ratio of 0.42 [152], although documented values range between 0.31 [233] and 0.47 [34] depending on the location of the specimen tested. The density of the cartilage was assumed to be 1000kg/m^3 as it is comprised mainly of water.

The Neo-Hookean material model has been chosen to best represent cartilage due to the expectation that these tissues will experience a low degree of deformation.

5.4.3 Adipose tissue

A Fung free-energy function, presented in section 5.3.3, was used to describe the behaviour of the adipose tissue. Although it exhibits viscoelastic effects [180], for the sake of simplicity these have been ignored.

The parameters $A_1 = 2.5$kPa and $B_1 = 2.75$, were chosen to fit[4] uniaxial compression test data for the plantar region of the foot [65]. A density of 920kg/m^3 [69] was assumed. Figure 5.1 provides a comparison between the experimental data presented by Erdemir et al. [65] and the model parameters chosen to describe fatty tissue[5]. Parameters were chosen to fit the average stress-strain data provided in the literature.

5.4.3.1 1-d material model to represent external tissue

An equivalent 1-d material model for adipose tissue must be developed for use in the boundary model presented in section 3.7.1. For this purpose, the model given in section 5.3.3.1 was appropriate. The uniaxial test data presented in figure 5.1 was used to develop a nonlinear model of the strain-dependent stiffness modulus. Assuming a Poisson's ratio of $\nu = 0.5$ for incompressible tissue, the parameters presented in

[4] In the uniaxial tests, displacement control is provided in the axial direction $\boldsymbol{E}_1$, while the surfaces in orthogonal $\boldsymbol{E}_2 - \boldsymbol{E}_3$ plane remain traction-free such that $\sigma_{2i} = \sigma_{3i} = 0$. This provides one with a direct relationship between σ_{11} and ε_{11} and can therefore be used to determine Young's modulus $E = \frac{\partial \sigma_{11}}{\partial \varepsilon_{11}}$. Here, the the true strain $\varepsilon_{11} = \ln \sqrt{\boldsymbol{E}_1 \cdot \boldsymbol{C}\boldsymbol{E}_1}$.

[5] Additional literature, such as [146, 47, 180], provided further insights into the nature of adipose tissue behaviour. However, the data presented in these texts was not suitable for the determination of model parameters as they do not specify which stress and strain measures have been used.

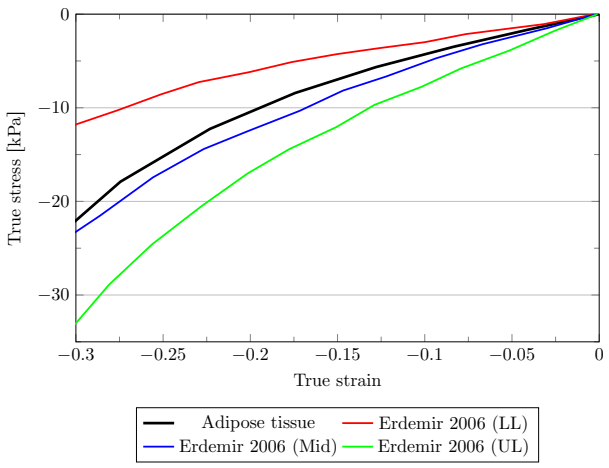

(a) Stress-strain curve

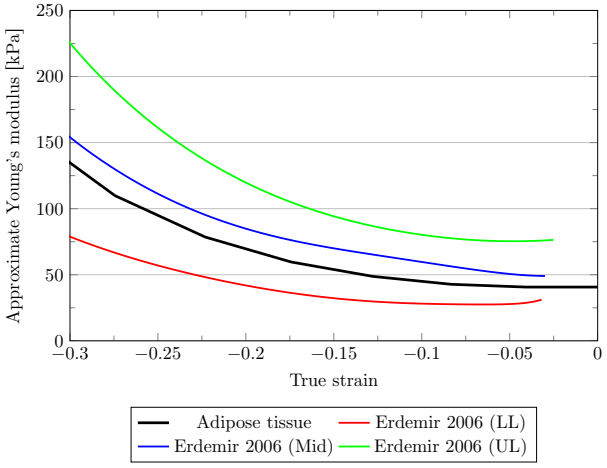

(b) Young's modulus-strain curve

Figure 5.1: Comparison of adipose tissue model against compression test data given in Erdemir et al. [65]. Model results were obtained using a uniaxial FEM test.

table 5.2 were determined to best represent the uniaxial behaviour of fatty tissue. Figure 5.2 reflects the uniaxial stiffness of adipose tissue as represented by a full constitutive model and the 1-d material model. It is demonstrated that the chosen parameters provide an accurate estimate for the uniaxial stiffness of the adipose tissue model. A practical demonstration of its functioning is provided in appendix D.2.

Table 5.2: Parameters for 1-d model of adipose tissue.

True strain	E_0	a	b
$\varepsilon \geqslant 0$	10kPa	1.6	14.6
$\varepsilon < 0$		1.6	9.6

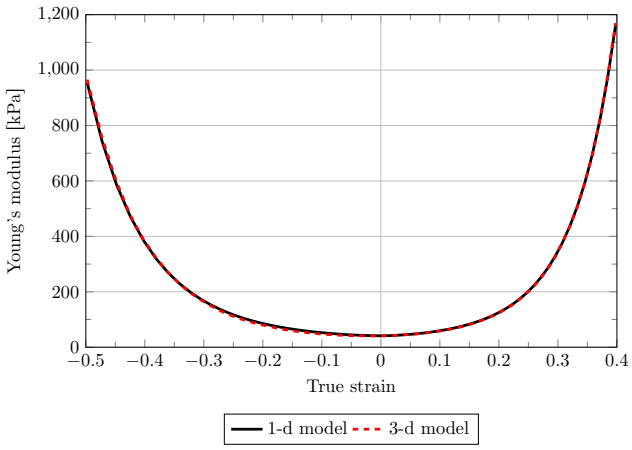

Figure 5.2: Young's modulus for 1-d adipose tissue model. Data plotted against measured results from uniaxial FEM test.

6. MUSCLE MODEL

There are two facets to modelling muscles that need careful consideration. These are the constitutive relationships governing the fundamental behaviour of muscular tissue, and the signals to the muscle that influences its contractile behaviour. Chapter 7 deals with the latter, while this section focuses on the former issue.

Key to the development of constitutive models is the concept of homogenisation, where the non-uniform multi-scale effects are smoothed out to produce descriptions that approximate the average properties of the material in the locale. Figures 2.10 and 2.12b depict the macro- and microscopic anatomical components of general skeletal muscle. Using this as a point of departure, it becomes apparent that the following anatomical structures are likely to affect the physiological functioning of muscle and need to be considered when developing a material model for muscle[1]:

Tendon: Collagenous structures that connect muscle to bone must be pulled taut before muscle movement can occur.

Connective tissue: The epimysium and perimysium prevent overextension and offer additional passive resistance to movement.

Actin-Myosin complex: The foundation of muscle contraction here represented in a manner that is consistent with experimental analysis of the function of the sarcomere.

Titin filament: Fine structures that hold the myosin filament in place contribute and to the elastic response of muscle whilst offering passive resistance to muscle extension.

Z-disc: Like the titin filament these have passive elastic effect during tensile loading but also may provide compressive resistance.

Firstly, we provide a brief introduction into the experimental research in the field of muscle mechanics. It is this work that has formed the basis for development of theories of muscle contraction and the mathematical models that describe these theories.

[1] Experimental analysis of the behaviour of muscle during cyclic loading indicates that some secondary considerations must be made. These include hysteresis, creep, relaxation and fatigue [78]. The first three phenomena are categorised as viscoelastic and viscoplastic effects as they result in a difference in stress response during loading and unloading conditions.

6.1 History of muscle models

6.1.1 Experimental research

Seminal work on understanding the basic functioning of muscular tissue was conducted by Hill [103] through isometric and isotonic tests on a frog sartorius. It was demonstrated that the force generated by a tetanised muscle during contraction and the velocity of contraction have a hyperbolic relation. It was also determined that the tension depended on the resting length of the muscle and the number of active cross-bridges. From this, it became clear that the response of a muscle in active contraction is vastly different to the passive muscle, which displays a viscoelastic behaviour. Hill [104] later went on to further document the fundamentals of active muscle mechanics and the length-tension relationship. In this work, a description of the passive and active contributions to the total muscle force is provided.

Huxley proposed the sliding filament theory, describing the configuration of the functional active unit of muscular tissue, the actin-myosin complex, based on research conducted in 1954 [78]. Detailed experiments were conducted by Gordon et al. [90, 91] to accurately measure the length-tension relationship in striated muscle and determine the state of the actin-myosin complex in terms of the sliding filament theory. Corroborating results were obtained by ter Keurs et al. [274]. Huxley [118] provides a detailed summary of experimental findings and their links to the sliding filament theory.

As seen in these landmark studies, with evolving research tools comes an evolution in our understanding of the functioning of muscles from a number of viewpoints. At the most fundamental level, the biochemistry involved in the actin-myosin complex is now well understood; this is detailed by Herzog and Ait-Haddou [101] in their summary of Huxley's models. Accurate rate-control in experimental analysis of active and passive tissue, such as those performed by Grover et al. [94], have further developed the macroscopic viscoelastic properties of the tissue.

6.1.2 Fundamental models for the representation of muscle contraction

6.1.2.1 Cross-bridge theory

Cross-bridge theory, a mathematical representation of the sliding-filament theory proposed by Huxley [78, 218, 324, 312], describes the interaction of actin and myosin filaments. The underlying hypothesis of the model is that the tensile stress in the contractile element can be expressed in terms of a probability frequency function that that is dependent on the activation, the number of active cross-bridge sites and several physical parameters. Kinetic theory is used to predict the response of the contractile element. It describes the probability of a cross-bridge having been bonded to its activation site on the myosin filament, facilitating contraction in the element.

Although this model makes several assumptions about the functioning of the cross-bridges [78, 324], it provides a good mathematical correlation between microscopic modelling and the macroscopic functioning of the muscle and is widely considered to provide the most accurate description of the muscular contraction process [45, 280]. However, other elastic muscle structures are ignored and the transmission of forces between muscle fibres is not accounted for. The cumulative effect of deformation of one part of the muscle on another is also neglected and its ability to model fast activation has been questioned [48, 316].

Additions to the model were provided by Mijailovich et al. [178], wherein they accounted for the extensibility of the actin and myosin filaments measured during isometric contraction. The mechanics of individual sarcomeres have also been explained by Cooke et al. [48] using cross-bridge theory. Both classical and modified forms of the Huxley model have been used to explain mechanics and characteristics present at the level of a single muscle fibre by Wu and Herzog [316], Rassier et al. [228].

6.1.2.2 Distribution moment model

The distribution moment model (DMM) was originally proposed by Zahalak in 1981 as an enhancement of cross-bridge theory. The enhancements, which account for the effects of calcium activation on the cross-bridges, are presented by Zahalak and Ma [324] (and also in [78]). Each cross-bridge can bond to its nearest actin site provided that it has been activated by a calcium ion. The kinetic model of the Huxley model is reinterpreted as the probability of finding an active cross-bridge at a binding site at any given time, and is coupled to equations governing the concentration of calcium ions in the vicinity of cross-bridges.

Based on the Huxley-model, the distribution moment retains its benefits (and limitations [315]) and, in addition, can potentially describe the change in muscle properties during a rapid stretch in the muscle. However, much experimental work is required to determine model parameters and, due to its derivation, requires that the contractile tissue is considered incompressible.

Work performed by Zahalak and Ma [324] validated the accuracy of the model against cross-bridge theory and experimental results, and demonstrated its application in modelling isometric contraction. Zahalak [323] extended the application to the evaluation of muscle fibres, placed in the presence of solutes, in compressive and tensile states.

6.1.2.3 Hill's model

Hill [103] provided a simple, accurate representation of tetanised muscle. However, the application of this model was limited due to the conditions under which it was produced. The model was unable to describe a single twitch, wave-summation, the mechanical behaviour of unstimulated muscle or the force-velocity relation when the tetanised muscle is released slowly or when strain varies with time.

The Hill three-element model, a phenomenological model which is an evolution of Hill's model, was developed to correct some of its fundamental limitations. Fung [78] presented a version of the Hill three-element model, shown in figure 6.1, which is consistent with the 1-d model as described by Hill and is widely adopted. The arrangement of the elements used to describe the model are not unique as they can be used to represent different parts of muscle physiology at different length scales. The configuration shown here has three separate components which together describe the motion of a single sarcomere. The representation of muscle-tendon systems, for which it appears to be the most common model used in musculoskeletal modelling applications [45], requires an alternate arrangement.

The equations that govern the motion of each element is derived from isometric and isotonic contractions of muscle. The contractile component provides the active shortening of the muscle and is governed by force-length and force-velocity relationships. Additionally, the dynamics of active state of the element can be modelled using differential equations [280]. This model has been described as a "black-box model", since the equations for the contractile element, although at a high-level consistent with sliding-filament theory, provide

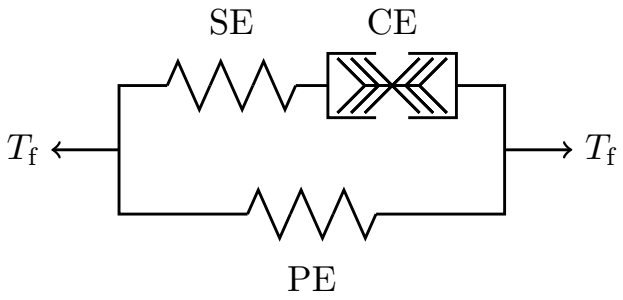

Figure 6.1: Schematic of the Hill three-element model for the sarcomere, showing the arrangement of the elements that represent components sarcomere physiology.

a relationship between input parameters and output results without directly representing the mechanism of muscle force production [280].

The three-element model has been used to successfully predict the movement of muscle under various scenarios. However, some of the fundamental assumptions leading to the construction of the model are flawed and it remains valid for only tetanised muscle. It must be modified further in order to describe single twitches and wave-summation, and is unable to simulate yielding in muscles that are stimulated by low frequencies during stretch [45]. The methods used for experimental evaluation are dependant on chosen assumptions. Furthermore, the division of forces between contractile and parallel elements, as well as that of the strain between contractile and series elements, is arbitrary. It has also been noted that the complex interaction of force-length, force-velocity and activation dynamics may cause the Hill-model to be unreliable in complex contractile conditions [280].

6.1.2.4 Comparative studies of micro-physiological models for muscle

Cole et al. [45] evaluated the transient force response of a Hill-based muscle-tendon model and a DMM during stretches at different velocities. The results were compared to experimental data taken from a cat soleus during iso-velocity stretches at maximal activation. The authors were able to accurately reproduce the force-time and force-length response of the muscle at the set velocities using the Hill-model with a single set of parameters. They did not succeed in doing similar using the DMM and it was determined that a single set of parameters were not sufficient to describe the kinetic behaviour of muscle beyond the short-range stiffness region at different velocities of stretch.

van den Bogert et al. [280] reviewed the methods for developing mathematical models to represent human anatomy. They used both mechanistic (DMM) and phenomenological (Hill-based) models to describe the iso-velocity dependence of muscle-tendon system of a maximally activated cat soleus. It was concluded that the Hill-model was superior in its ability to predict muscle forces under different conditions using the same model parameters. The Hill model was able to successfully simulate both slow and fast stretches with a single set of input parameters, whereas the DMM was greatly inaccurate for fast stretches. However, Hill-models were unable to reproduce the observed effect of muscle force decreasing below the isometric force when lengthening occurs at submaximal activation. Overall, it was decided that the Hill-model is able to reproduce experimental results, and is the better option to simulate accurate muscle behaviour.

Wu and Herzog [315] demonstrated that in some cases discrepancies arise in results produced by the DMM when compared to the exact solution Huxley-model. The authors contend that, with respect to describing the

fundamental characteristics of muscle contraction observed in experimental analysis, the cross-bridge model remains unrivalled.

Further enlightenment on the differences between the Hill- and Huxley-models, from the perspective of cardiac modelling, is provided by Peskin [218].

Direct modelling of the underlying histology of muscle samples allowed Sharafi and Blemker [251] to explore the ability of muscle models to accurately describe passive tissue in shear. A representative cell unit, describing either a collection of fibre or fascicle bundles, was deformed in shear. It was found that the behaviour of the models in terms of the overall shear stiffness of the modelled sample could differ considerably. Transversely isotropic behaviour was exhibit by the fibre-level model, while models aimed at the fascicle-level displayed transversely anisotropic behaviour.

6.2 Constitutive formulations of fibrous materials

Due to the presence of some similarities in the physiology of cardiac tissue (striated muscle) and skeletal muscle, approaches and principles used from a continuum-mechanics and muscle-mechanics view-point are often similar. Due to this and that some skeletal models are derivative works of cardiac models, a brief survey of the cardiac models was conducted. The various descriptions for skeletal muscle in the literature were also surveyed. This literature, along with that which makes critical analysis of these approaches, is appraised.

6.2.1 Cardiac, arterial and collegenous fibrous models

The seminal work on which many fibrous constitutive models are derived is that performed by Spencer in 1984. This model was developed further by Humphrey and Yin [116] and combined the features of phenomenological and microstructural modelling to provide a unified continuum description of incompressible pseudo-elastic tissues[2] in which embedded fibres exist. The authors describe their aim as being to develop a pseudo-SEF for fibrous materials from which the form is inspired by experimental data. These fibres are considered to be non-interacting, with a fibre family having the same directionality and material description, and contribute stiffness only when in a state of tension. This SEF was assumed to be additively decomposed into homogeneous matrix and fibre components, with the fibre component representing the total strain energy of all fibre families and only the matrix having a hydrostatic contribution. The matrix was considered to be a function of the first and second invariants of the right Cauchy-Green tensor, and the fibres were assumed to be dependent on the deformation only through the definition of their stretch, also an invariant quantity. The fibres only contributed to the material stiffness in their current direction. Formulation of a biaxial test for a thin-sheet of material with two perpendicular fibre families lead to the formulation of three plausible constitutive models for fibres, with one chosen on the basis of experimental data. The resulting framework was used to describe the pleura, consisting of collagen and elastin fibres. The SEF for the matrix was chosen to have an exponential dependence on the first invariant, while that of the collagen had an exponential dependence on the fibre stretch. Similar material models were also used to represent myocardial tissue, with the resulting constitutive model accurately reproducing experimental data.

[2] These are viscoelastic materials that can be represented by a single material model using two different sets of material parameters to describe the loading and unloading characteristics.

The basic decomposition of the SEF and the form of the constitutive models for incompressible, anisotropic fibrous materials developed by Humphrey and Yin [116] are regularly used in the literature. The exponential form of the fibre SEF was used by Holzapfel et al. [107][3], Gasser and Holzapfel [82], van Oijen [290], Stålhand et al. [260], Driessen et al. [58] in the development of arterial models, Driessen et al. [58], Baaijens et al. [9] in describing collagen in vascular leaflets and Weiss et al. [306] in their model of the human medial collateral ligament. Zulliger et al. [329] used a SEF, linear in engineering strain, to model fibres in arteries under the influence of active vascular smooth muscle. Federico and Gasser [70], modelling articular cartilage, expressed the fibre SEF in terms of a Taylor-series of the fibre stretch. Further development by Humphrey et al. [117] has lead to a more complex description of the response of passive myocardial tissue which did not take the form of any of their previously presented models. A SEF which couples the fibre and matrix contributions was utilised by Weinberg and Kaazempur-Mofrad [304] to model mitral valve leaflets.

More advanced concepts of fibre modelling include the addition of cross-fibre terms, which is discussed by Holzapfel et al. [107]. Consideration for multiple fibre families is made in [107, 290]. Gasser and Holzapfel [82] included a strain-rate independent plasticity model to incorporate the effects of relative slip between fibres under deformation and plastic hysteresis. Holzapfel et al. [107] also discusses the inclusion of residual stresses or prestressing, important in the simulation of arteries, which was subsequently used by Driessen et al. [58]. Fibres may be considered to be of finite volume if they form a large component of the overall material volume. A framework for the inclusion of the concept of the fibre volume-fraction was presented by van Oijen [290], and later used and discussed in [58, 9]. An alternate description of the volume-fraction concept is provided by Federico and Gasser [70]. Zulliger et al. [329] weighted the components of the additively decomposed SEF by their cross-sectional area. Active muscle mechanics, accounting for muscle tone and response to the deformation, and the length-tension relationship of individual contractile elements were also introduced in [329]. In their development of a heart valve model, Li et al. [151] utilised a nonlinear, anisotropic stiffness modulus where the elastic modulii were expressed by independent nonlinear functions of the strain and the shear modulii calculated from these.

6.2.2 Skeletal muscle models

In the area of skeletal muscle modelling, Hill-based models have proved to be most popular in terms of providing a mathematical description of muscle functioning [286]. Examples of their use in the development of musculoskeletal models include the works of Pandy et al. [208], Pandy [207], Lloyd and Besier [158].

Hyperelastic continuum models based are regularly developed using the concept of additive strain-energies for matrix and fibre contributions as described by Humphrey and Yin [116]. Martins et al. [170] demonstrated how the definition of the muscle fibre contribution in [116] could be modified such that it fitted with the physical definitions described by the Hill-model. This permits the inclusion of the force-length, force-velocity relationships[4] as well as the effects of activation in the constitutive relations for muscular tissue. This concept, leading to the additive decomposition of the total stress tensor derived from a SEF, has since been used to model the human biceps brachii [170], the pelvic floor [52, 171] and squid tentacles [272].

Spyrou and Aravas [258] forgo the use of a phenomenological model to represent muscle and tendonous tissue of squid tentacles and a portion of the human hamstring, but do however include the force-length

[3] Holzapfel et al. [107] also provides a comprehensive review of- and description of a framework for- fibrous hyperelastic materials.

[4] It should be noted that the description of these relationships and numerical implementation of the Hill-model varies considerably in the literature.

and force-velocity relationships. A similar procedure was followed by Johansson et al. [133] in their model of squid tentacles and simple pennate muscles. Alternate methods for the inclusion of active muscle contributions, which do not rely specifically on Hill-elements, are provided described by Lemos et al. [149] in the modelling a cat medial gastrocnemius, as well as in [24, 235]. In the above papers, the total stress tensor is decomposed without any specific link between the fibre constitutive model and a SEF being described. Röhrle [234], although utilising a free-energy function for both active and passive contributions, also did not utilise phenomenological models in their work. More recently, complete SEF descriptions of muscle mechanics which forgo some of the assumptions made in [116] as well as phenomenological models have been developed by Odegard et al. [197], Ehret et al. [62].

The literature does contain numerous examples of models created on the bases of completely different descriptions of muscle tissue. The Huxley model, in combination with the DMM, has been utilised by Oomens et al. [201] to simulate contraction of the rat tibialis anterior. A less conventional linked fibre-matrix mesh model, which uses two separate meshes to represent the extracellular matrix and muscle fibres, has been developed by Yucesoy et al. [322] to more accurately represent the interaction between constituents of the myofibres and the surrounding matrix. Following from the work of Li et al. [151], Van Loocke et al. [286] describe a nonlinear transversely isotropic constitutive model of passive skeletal muscle using strain-dependent Young's modulii (SYM) thus negating the use of a phenomenological model. This model has since been improved by incorporating the effects of viscoelasticity [288, 289].

Pertaining specifically to modelling of muscles in the HUA, Wilhelms-Tricarico [311] included the force-length and force-velocity relationship in their continuum model of muscle contraction. As no phenomenological model was used, the fibre constitutive model was based on the stretch of the representative fibres. An isotropic exponential SEF was used to represent the passive elastic components of tissue. Mention was made of inclusion of fibre density, but no details were provided. A similar representation of the muscle force-length relationships has been used by Wu et al. [317], however an additional passive contribution from the muscle fibres was included. Baker [11] describe a force-length relationship based on the length-change of sarcomeres.

A Hill-model, representative of muscle sarcomeres, was also used by Huang et al. [111, 112, 113] to model the GG of the tongue. Specifically, the GG was modelled using a nonlinear relation in the axial direction of its constituent fibres. Further use of the Hill-model is made in by Kojic et al. [143] in a model of the uvula. Notable in this work is that Kojic et al. also scaled the stress generated in the muscles by their volume fraction.

Another representation of muscles is that of the *force effectors* [263]. With this technique, muscles are represented as line segments connecting nodes, and forces are applied directly to the nodes of a FE model. In some instances, muscles are modelled using a macro-scale representation of fibres that were positioned on the edges of the FEM elements. Prescribed muscle forces, under the assumption of spatial uniformity, was used by Fujita et al. [77], Vogt et al. [293], Vogt [292], Gérard et al. [85, 87], Perrier et al. [215]. Leading from the description of motor-control mechanisms (discussed in some depth in section 7.1), an exponential force-activation relationship, which is stated to describe the effects of the Hill-model series element (SE) and contractile element (CE) [244], was used by Perrier et al. [214], Sanguineti et al. [244, 245] to produce active muscle forces. Buchaillard et al. [29] made additions to this model to take into account the changing CSA of the muscles and the force-velocity relationship. Phenomenological models can also be represented by force effectors. The Artisynth project incorporates a Hill-model in their muscle model [263, 159]. Both active and viscoelastic passive components of muscles were modelled by Dang and Honda [50, 51], Fang et al. [68] using a complex rheological model that incorporated a Hill-model. Perrier et al. [215] included active local stiffening of the tissue surrounding contracting myofibres.

6.2.3 Comparative studies of continuum-based implementations of muscle models

Van Loocke et al. [287, 286] provide a valuable discussion on the topics of the available experimental data for passive skeletal muscle and the literature relevant to modelling it, both in terms of microstructural and continuum models. Experimental data was obtained under quasi-static conditions, from which two material models were developed and evaluated. A multi-parameter hyperelastic transversely isotropic model, dependant on the stretch ratio in the fibre direction and the first invariant of the right Cauchy-Green tensor, was derived from the work of Humphrey et al. [117]. This model was compared to a SYM model based on the work of Li et al. [151].

It was determined that the Humphrey et al. SEF accurately fitted the experimental data in the fibre direction up to 20% strain and in the non-fibre direction up to strains of 40%. The model was unsuccessful in predicting muscle behaviour at 45° from the fibre direction. In contrast, the SYM model provided a good correlation to the experimental data at strains of up to 40%, as well as in the direction 45° from the fibre orientation.

6.2.4 Discussion on the methods of modelling skeletal muscle

A review of the literature has determined that the use of a continuum approach in conjunction with SEFs (be they active or only passive) is an overwhelmingly popular approach to modelling large deformations of muscular tissue. This method allows for the incorporation of phenomenological models and can be used to describe an arbitrary geometries with an arbitrary arrangement of muscle histology. However, the accuracy of material response in cross-fibre direction remains questionable. Furthermore, for models such as that of Humphrey et al. [117], there exist difficulties in the estimation of input parameters, although this could be partially accounted for by the breadth of the experimental results obtained to date [286].

The direct application of nodal forces through force effectors provides an alternative method to modelling active tissue to the continuum approach. The resulting material model appears to be simple to implement and computationally inexpensive. However, they are strongly linked to the geometry of the FE mesh, which provides further difficulties in the development of a geometric model. There also exists a disconnect between response of the muscle model and the underlying physiology of muscle tissue in terms of its local deformation. The SYM method, the third alternative approach, uses model constants that have a physical interpretation and are directly correlated to experimental data [287]. However, it has only been demonstrated for transversely isotropic (1-fibre family) passive tissue. As the histology of the tongue is complex, there exists the need for a completely anisotropic material model. Furthermore, the inclusion of muscle activation within a SYM model not yet been demonstrated.

Regarding the simulation of the mechanism of force-production in the tongue, the Huxley and DMM are not particularly popular for this purpose due to their complexity and level of detail. The Hill model, which models muscle on a functional level and incorporates all of the major features of passive and active muscle response, provides a good balance between model detail and complexity of implementation.

6.3 Muscle as a composite

Muscle tissue is composed of a largely homogeneous and isotropic bed matrix consisting of adipose and interstitial tissue in which muscle fibres are embedded. Each group of muscle fibres is made up of several

sub-units, of which the smallest functional unit is the sarcomere. Figure 6.2 depicts the arrangements of the sarcomeres in a muscle fibre. By assuming that in a small control volume all sarcomeres belonging to a fibre family behave identically, one can describe the local motion of the fibre by describing the motion of a single sarcomere.

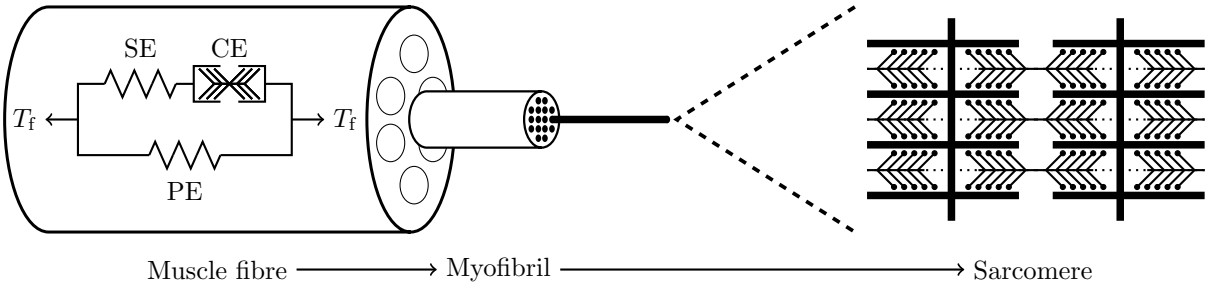

Figure 6.2: Physiology of a skeletal muscle fibre: Macro-scale (muscle fibre) to micro-scale (sarcomere). The Hill three-element model, overlaid on a muscle fibre, represents the behaviour of a collection of sarcomeres. The PE and SE are passive and the CE is responsible for the active reduction of muscle length.

In producing a mechanical model for muscle, individual fibres are considered to have a negligible cross-sectional area in comparison to their length. No restriction is placed on the number of muscle fibre families present at each point in the muscle. This allows for the notion of crossing and interweaving muscle groups, a histological feature found in the tongue. Adjacent fibre families are assumed to slide over each other, so no cross-terms and direct interaction are modelled in the constitutive equations.

6.3.1 The Hill three-element muscle model

In section 2.5.1.1 it was mentioned that the sarcomere is the smallest physiological unit of muscle tissue. The Hill three-element model, illustrated within the muscle fibre in figure 6.2 and described by Fung [78], is a representation of muscle at a sarcomere level. Each of the elements represent a collection of different physical components of the sarcomere.

It is assumed that, locally, all sarcomeres belonging to a muscle group behave identically. More particularly, it is assumed that these sarcomeres undergo identical deformation, receive the same neurological input and have the same force-generation capabilities as one another. Since the serial and parallel arrangement of sarcomeres that comprise a muscle fibre behave identically, through homogenisation the net action of the numerous components of varying physiological scales within the muscle fibre can be represented locally by a single Hill element.

The Hill element used to model the composition of skeletal muscle, as adopted by Fung [78], Martins et al. [170], comprises of three individual units with an arrangement and constitutive relation that characterises the underlying physiology that it represents. Two of the elements, the SE and CE are in series with one another and collectively in parallel with the parallel element (PE). Both the PE and SE are passive components of the model and respond to the deformation of the surrounding tissue. The components of the Hill model represent the following aspects of skeletal muscle tissue [78, 170]:

PE: Connective tissue and collegenous sheaths such as the perimysium and epimysium.

SE: Z-bands, titin-filaments, connective tissues and passive components of the actin-myosin complex.

CE: Active components of the actin-myosin complex.

The PE accounts for the resting elasticity of tissue. A further contribution to the PE may be necessary, dependant on the contraction or stress-strain history of the muscle due to residual coupling of the actin-myosin complex. The difference between the properties of the whole muscle and the parallel component characterises the properties of the contractile and series elements. It should be noted that the effect of the collegenous tendons have been ignored. Muscles of the tongue (although catagorised as skeletal muscle) do not have tendon components of any significance.

The SE captures the intrinsic nonlinear elastic characteristics of the sarcomere. Contributions to the elasticity of this component may also include the non-uniform activation of myofibril filaments and non-uniformity of the sarcomeres themselves. This element is known to have an exponential length-tension relationship [78].

The contractile force, which results in the active shortening of muscle, is generated by the CE in response to a neural stimulus. It has zero tension at rest, and is capable of shortening when activated due to the sliding action of the actin-myosin complex. An increase in tension in this component is developed by increasing the number of active cross-bridges. It is required that the relationships that govern the response of the CE capture the length and velocity relationships presented in section 2.5.2.3.

A detailed comparison between the model chosen for this work, which is presented in the following paragraphs, and that in the literature is provided in appendices D.3 and D.4. Some initial observations concerning the reinforcing properties of the passive muscle fibres, as well as the proportion of the tissue volume that they occupy, are also included therein. Representative mathematical models for the components of the Hill three-element model are presented in section 6.5.2. A discussion of the active components of the model is presented in section 7.2.1, that is subsequent to the presentation of the model that governs neural input to the muscle groups.

6.4 Muscle matrix

There are numerous models (e.g. [293, 111, 244, 86, 28]) that have been used to describe the isotropic skeletal muscle matrix of the tongue, each with significantly different characteristics.

Martins et al. [170, 171] consider the muscle matrix to be a Fung-type hyperelastic material. This model is also used in [116, 311]. The parameters for the muscle matrix, given in table 6.1, were chosen such that Young's modulus at zero strain and high strain, as approximated under uniaxial tension conditions, would be within the range of values described in the literature.

Table 6.1: Material parameters for muscle and muscle matrix.

	Muscle	**Matrix**	
Parameter	ρ_0	B_1	A_1
Units	$\mathrm{kg/m^3}$	–	$\mathrm{kN/m^2}$
Value	1060	0.625	1.652

The hyperelastic model used does not account for significant features of viscoelastic and high strain-rate effects [288, 289] nor directly the increased stiffness observed during compression tests of muscle with transverse-

orientated fibres [286]. However, these simplifications can be justified as low strain-rates are expected in the scenarios being modelled and the contraction of muscle increases its stiffness by a substantially greater margin than the mentioned effects. The scenarios being modelled in this work have a limited number of contraction cycles. Therefore, the viscoelastic and hysteresis effects will not have sufficient time to reduce to the steady state which would be present in a real-world scenario of cyclic loading and contraction[5].

6.4.1 1-d material model to represent external tissue

As with adipose tissue, simplified models of regions of the HUA require that the bedding tissue of skeletal muscles be represented as a one-dimensional model. Since the Fung model was used to as the constitutive model for muscle matrix, equation 5.12 was applicable to this material. The model parameters, shown in table 6.2, were set such that the material stiffness matched that obtained from uniaxial tests for the parent material. The Poisson's ratio set to 0.5 as the tissue is incompressible. Figure 6.3 demonstrates that the 1-d material model and the uniaxial stiffness of muscle matrix determined by a full constitutive model match with sufficient accuracy.

Table 6.2: Parameters for 1-d model of muscle matrix.

True strain	E_0	a	b
$\varepsilon \geqslant 0$	6.2kPa	1.5	5.3
$\varepsilon < 0$		2.4	4.35

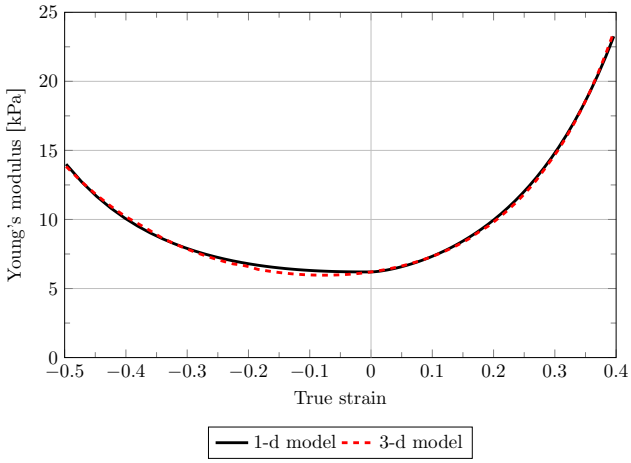

Figure 6.3: Young's modulus for 1-d muscle matrix model. Data plotted against measured results from uniaxial FEM test.

6.5 Muscle fibres

The presentation of the constitutive model for active muscle fibres is decomposed into two parts. In the first, section 6.5.1, the method of quantifying the volume of fibres occupying a control volume in muscle tissue is presented. Section 6.5.2 details the mathematical description applied to each of the Hill elements used to represent active skeletal muscle fibres.

[5] Rodrigues et al. [232] noted that in their simulations of laryngoscopy, the limited experimental data they acquired was better matched by a hyperelastic material model than a viscoelastic material for simulations of the order of 10s in duration.

6.5.1 Volume fraction

The concept of fibres occupying finite space within a control volume in muscular tissue was introduced in section 5.2. This representation requires the quantification of the fibre volume fraction within each region of the muscular tissue. Histological samples of tongue, such as those shown in figures 2.7 to 2.9, suggest that the volume fraction of fat and interstitial space is relatively large and varies in quantity throughout the muscle tissue. Furthermore, as noted in Nashi et al. [191], the quantity of adipose tissue present in the tongue increases considerably with BMI. A brief survey of the estimated fibre volume fraction for the tongue, extracted from various studies, is presented in table 6.3.

Table 6.3: Literature survey of skeletal muscle total fibre volume fraction $\sum_{\mathrm{f}} \phi_{\mathrm{f}}$ for the tongue. In studies where ϕ_{Adipose} is listed, the total fibre volume fraction is estimated as $\sum_{\mathrm{f}} \phi_{\mathrm{f}} = 1 - \phi_{\mathrm{Adipose}}$.

Miller et al. [179]	**Humbert et al.** [115]	**Liang** [153]	**Lieber et al.** [155]
$0.44 - 0.64$ [a]	0.74 [b]	0.9 [c]	$0.87 - 1$ [d]
Nashi et al. [191]			

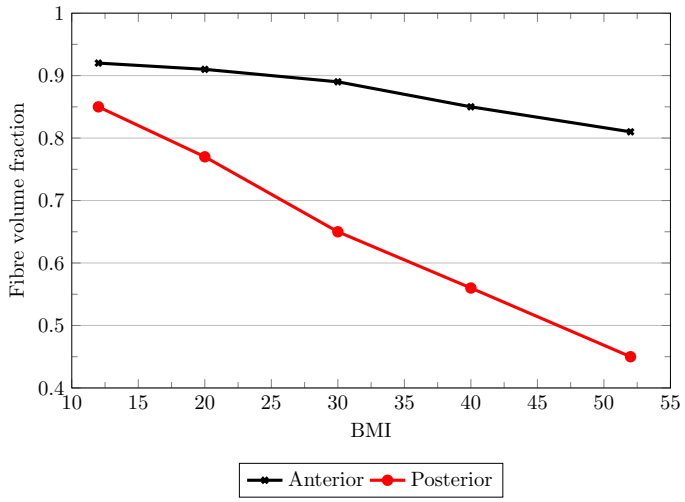

[a] Tongue; muscle fibres + connective tissue; High statistical variation
[b] Tongue; value derived from fat volume fraction measured
[c] Tongue FEM model; uncited source
[d] Various muscles; healthy tissue

Based on the data described in the literature, the chosen parameter for the total fibre volume fraction for the tongue model is $\sum_{\mathrm{f}} \phi_{\mathrm{f}} = 0.7$. This value appears suitable for the average adult with a healthy BMI. The spatial variation of the adipose tissue concentration in the tongue is not accounted for.

6.5.1.1 Local fibre volume fraction

Throughout the tongue and the other muscular anatomy presented in section 2.1, numerous muscle groups weave and interact at a micro-histological level. As multiple fibre families occupy the same control volume, the total fibre fraction has to be divided amongst the locally present muscle groups. Due to the lack of spatial

data, the local volume fraction of each fibre family that occupies a position in space is equally split such that

$$\phi_f = \sum_f \phi_f / f \tag{6.1}$$

where the denominator f represents the total number fibre families (different to M, the total number of muscles represented in the geometry) present at each point. The packing of fibres at a micro-scale varies throughout the anatomy and equation 6.1 provides a first-estimate in lieu of better data to build a more comprehensive model. Figure 6.4 provides a visual description of the idealised packing that is assumed at the micro-scale of muscular tissue.

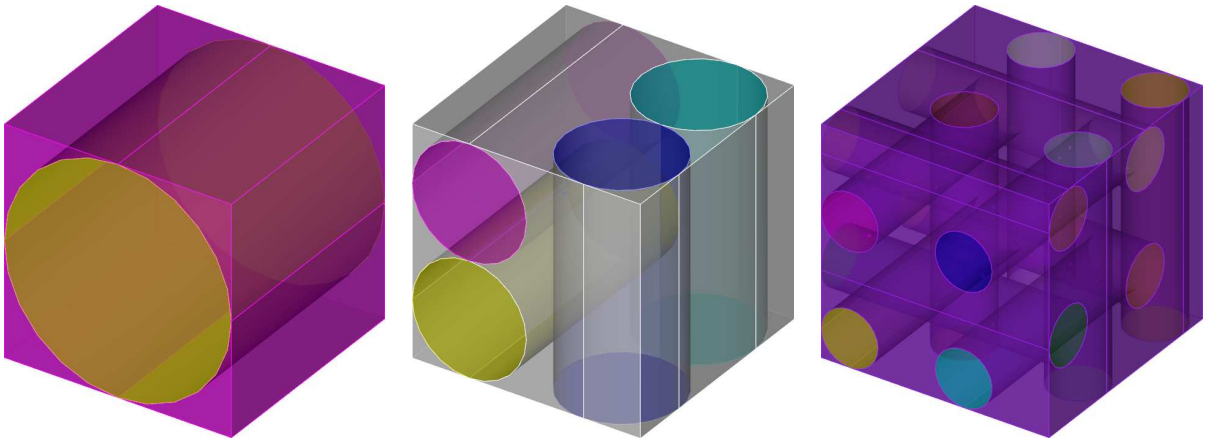

(a) One fibre family **(b)** Two orthogonal fibre families **(c)** Three orthogonal fibre families

Figure 6.4: Idealised fibre packing scenario for multiple non-intersecting cylindrical fibre families within a representative volume. Each of the muscle fibres are assumed to be of the same functional-diameter.

The consequence of this representation is that the contractile force generated in regions where a large quantity of fibre families are present will be less than those where few muscles intersect. For fibre families that are parallel to one another this is a reasonable outcome as, in a control volume under ideal packing situation, the CSA of each muscle must be reduced. Off-axis rotation of any fibre family depicted in figure 6.4 results in a similar but shifted packing arrangement with the same total volume fraction of each fibre group in the control volume. This indicates that, for fibres of the same size, there is no requirement of orthogonality for the model to be valid. However, the simplified model is invalid when different size fibres are present or upon the introduction of a fourth fibre family to the scenario represented by figure 6.4c where clearly the fibres aligned in one direction would have to be divided between the two muscle groups. Histological sections shown in figures 2.7 and 2.8, as well as [251], indicate that the muscle fibres must have a more complex packing arrangement than is represented here, due to their bundling and non-uniformity.

6.5.2 Constitutive model of active skeletal muscle fibres

The material behaviour of muscle fibres is described in terms of a general, but undefined, SEF ψ_f that is dependent on the stretch in the fibre direction. The resulting equation for stress, equation 5.4c, involves the derivative of the SEF with respect to the fibre stretch; this term is interpreted as the one-dimensional tensile force in the muscle fibre [171] as described in equation 6.3.

As the Hill three-element model assumes identical behaviour of sarcomeres in a near vicinity to one another, we use the terms *sarcomere*, *myofibre* and *muscle fibre* interchangeably as, locally, they all behave identically. In this instance, *locally* is defined as at each independent representative computational point.

Using this phenomenological model, the total force in the muscle fibre can be additively decomposed into the sum of the tension in the parallel and series element: that is to say that[6]

$$\psi'_{\mathrm{f}}\left(\lambda_{\mathrm{f}}\right) := T_{\mathrm{f}} = T_{\mathrm{f}}^{\mathrm{p}}\left(\lambda_{\mathrm{f}}\right) + T_{\mathrm{f}}^{\mathrm{s}}\left(\lambda_{\mathrm{f}}, \lambda_{\mathrm{c}}\right) \quad , \tag{6.3}$$

where T_{f} is the nominal stress generated in the Hill element, with the additional relationship that the series and contractile tension are equal

$$T_{\mathrm{f}}^{\mathrm{s}}\left(\lambda_{\mathrm{f}}, \lambda_{\mathrm{c}}\right) = T_{\mathrm{f}}^{\mathrm{c}}\left(\lambda_{\mathrm{c}}, \dot{\lambda}_{\mathrm{c}}, \alpha\right) \quad . \tag{6.4}$$

As the skeletal muscle to be modelled has no pennation, the fibre force vector (the magnitude of which is given by equation 6.3) is completely aligned with the line of action of the muscle. However, given that λ_{f} is a function of the deformation gradient, the generated stress in the Hill-element, and thus the local contractile force generated by the muscle fibres, is in general spatially non-uniform. From equation 6.3, the SEF governing the muscle model can be defined by [116, 170]

$$\psi_{\mathrm{f}} := \int_{1}^{\lambda_{\mathrm{f}}} \left(T_{\mathrm{f}}^{\mathrm{p}}\left(\lambda_{\mathrm{f}}\right) + T_{\mathrm{f}}^{\mathrm{s}}\left(\lambda_{\mathrm{f}}, \lambda_{\mathrm{c}}\right)\right) \mathrm{d}\lambda_{\mathrm{f}} \tag{6.5}$$

and the fibre contribution to the Kirchhoff stress by

$$\boldsymbol{\tau}_{\mathrm{f}} = \lambda_{\mathrm{f}} T_{\mathrm{f}} \boldsymbol{n}_{\mathrm{f}} \otimes \boldsymbol{n}_{\mathrm{f}} \tag{6.6}$$

with the form of the structure tensor $\boldsymbol{n}_{\mathrm{f}} \otimes \boldsymbol{n}_{\mathrm{f}}$ indicating that zero dispersion of the fibres is present.

In [171], a multiplicative split of the contractile and series strain is assumed; that is, the total fibre stretch in the two-element branch can be described as a composition of the stretch of the series element superimposed on that of the contractile element:

$$\lambda_{\mathrm{f}} = \lambda_{\mathrm{p}} \quad , \tag{6.7a}$$

$$\lambda_{\mathrm{f}} := \lambda_{\mathrm{s}} \lambda_{\mathrm{c}} \quad . \tag{6.7b}$$

The split considered here is the one-dimensional equivalent of the deformation gradient decompositions presented in equations 3.25 and 3.73. Using the implicit relationship given in equation 6.7b, the SE stress equation $T_{\mathrm{f}}^{\mathrm{s}}\left(\lambda_{\mathrm{s}}\right) = T_{\mathrm{f}}^{\mathrm{s}}\left(\lambda_{\mathrm{f}}, \lambda_{\mathrm{c}}\right)$ presented in equations 6.3 and 6.4 has been posed in terms of the fibre and contractile element stretches by removing the second unknown stretch variable λ_{s}. Section 6.5.3 presents a method of solving for the internal fibre variable λ_{c} using equations 6.4 and 6.7b.

[6] Because the muscle tissue consists of a conglomeration of fast and slow twitch fibres (shown in figure 2.11), the total fibre stress due to the recruitment of each fibre type is

$$\phi_{\mathrm{f}} T_{\mathrm{f}}\left(\lambda_{\mathrm{f}}, \lambda_{\mathrm{c}}, \dot{\lambda}_{\mathrm{c}}, \alpha\right) = \phi_{\mathrm{f}}{}^{\mathrm{fast}} T_{\mathrm{f}}{}^{\mathrm{fast}}\left(\lambda_{\mathrm{f}}{}^{\mathrm{fast}}, \lambda_{\mathrm{c}}{}^{\mathrm{fast}}, \dot{\lambda}_{\mathrm{c}}{}^{\mathrm{fast}}, \alpha^{\mathrm{fast}}\right) + \phi_{\mathrm{f}}{}^{\mathrm{slow}} T_{\mathrm{f}}{}^{\mathrm{slow}}\left(\lambda_{\mathrm{f}}{}^{\mathrm{slow}}, \lambda_{\mathrm{c}}{}^{\mathrm{slow}}, \dot{\lambda}_{\mathrm{c}}{}^{\mathrm{slow}}, \alpha^{\mathrm{slow}}\right) \tag{6.2a}$$

where the total fibre volume fraction is decomposed into the contributions from either fibre type

$$\phi_{\mathrm{f}} = \phi_{\mathrm{f}}{}^{\mathrm{fast}} + \phi_{\mathrm{f}}{}^{\mathrm{slow}} \quad . \tag{6.2b}$$

However, it is assumed that the LHS of equation 6.2a provides a sufficiently accurate representation of its decomposition, and thus the actual decomposition does not need to be modelled directly. It represents the homogenisation of the properties of the different fibre types. Knowledge of the recruitment strategy of each fibre type under different dynamic scenarios is therefore not necessary.

The aforementioned relationships are presented in detail in equations 6.8a to 6.8c. Martins et al. [171] describe the force in each element in terms of $T_0^{\max}$, the maximum tensile force that can be attained in the element, and experimentally determined scaling functions by

$$T_{\mathrm{f}}^{\mathrm{p}}\left(\lambda_{\mathrm{f}}\right) = T_0^{\max}\, f_{\mathrm{p}}\left(\lambda_{\mathrm{f}}\right) \quad , \tag{6.8a}$$

$$T_{\mathrm{f}}^{\mathrm{s}}\left(\lambda_{\mathrm{f}}, \lambda_{\mathrm{c}}\right) = T_0^{\max}\, f_{\mathrm{s}}\left(\lambda_{\mathrm{f}}, \lambda_{\mathrm{c}}\right) \quad , \tag{6.8b}$$

$$T_{\mathrm{f}}^{\mathrm{c}}\left(\lambda_{\mathrm{c}}, \dot{\lambda}_{\mathrm{c}}, \alpha\right) = T_0^{\max} T_0^{s}\, f_{\mathrm{c}}\left(\lambda_{\mathrm{c}}, \dot{\lambda}_{\mathrm{c}}, \alpha\right) \quad . \tag{6.8c}$$

Here, $T_0^{\max} = \dfrac{F_0^{\max}}{A_0}$ represents the peak nominal isometric stress that can be attained in the muscle at resting length [171]. The scalar value $T_0^{\max} T_0^{s} := T_0^{\mathrm{c}}$, motivated and described in chapter 7, gives the maximum contractile stress that can be developed.

The parallel element representing the connective tissue and collagenous sheaths surrounding the fibre have an exponential constitutive law[7] [104, 171]

$$f_{\mathrm{p}}\left(\lambda_{\mathrm{f}}\right) = \begin{cases} 2aA\left(\lambda_{\mathrm{f}} - 1\right) e^{a\left(\lambda_{\mathrm{f}}-1\right)^2} & \text{if} \quad \lambda_{\mathrm{f}} > 1 \\ 0 & \text{otherwise} \end{cases} \quad . \tag{6.9}$$

The intrinsic elastic properties internal to the sarcomere are represented by the series element. It also has an exponential stretch-tension relationship[7] [104] described by [171]

$$f_{\mathrm{s}}\left(\lambda_{\mathrm{f}}, \lambda_{\mathrm{c}}\right) = \begin{cases} c_1\left(e^{c_2\left(\lambda_{\mathrm{f}}-\lambda_{\mathrm{c}}\right)} - 1\right) & \text{if} \quad \lambda_{\mathrm{s}} > 1 \\ 0 & \text{otherwise} \end{cases} \quad . \tag{6.10}$$

It should be noted that both the parallel and series elements function only when under tension and therefore provide no reinforcement under compression. The parameters used in the relationships governing the passive components of muscle fibres are listed in table 6.4.

Table 6.4: Material parameters for muscle fibres, and the Hill model PE and SE.

	Fibre	**PE f_{p}**		**SE f_{s}**	
Parameter	$T_0^{\max}$	a	A	c_1	c_2
Units	$\mathrm{kN/m^2}$	–	–	–	–
Value	668.8 [a]	8.568×10^{-4}	12.43	0.1	100

[a] The estimation of muscle properties is a difficult task [280]. A value of 220 $\mathrm{kN/m^2}$ is suggested by Wilhelms-Tricarico [311] for the GH muscle. Fung [78] also documents the tensile strength of the actin filament to be at least 2.2MPa. van den Bogert et al. [280] note that values of between 20 and 100 $\mathrm{N/cm^2}$ have been used in literature, while Martins et al. [170] quotes that the figure ranges from $0.16 - 1$MPa. Kojic et al. [143] used a figure of 2.2×10^5 $\mathrm{N/m^2}$ in their model of the soft palate. Röhrle and Pullan [235] utilised a value of 0.3MPa in their human mastication model.

The contractile element has a dependence on its stretch, rate of stretch and the level of activation (tetany) of the muscle. The force-length and force-velocity relationships are well defined in the literature (see [103,

[7] Currently modelled as an elastic component, an alternative constitutive model might include the effects of viscoelasticity.

91, 78, 133, 101, 154]) but exhibit discontinuous behaviour. In order to overcome this, Gaussian-type mollifier functions are proposed. These match the experimental data closely while being infinitely differentiable functions and easier to use in algorithms. The governing equation for the contractile element is [171]

$$f_{\mathrm{c}}\left(\lambda_{\mathrm{c}}, \dot{\lambda}_{\mathrm{c}}, \alpha\right) = f_{\mathrm{c}}^{L}\left(\lambda_{\mathrm{c}}\right) f_{\mathrm{c}}^{\mathrm{V}}\left(\dot{\lambda}_{\mathrm{c}}\right) \alpha\left(\mathrm{u}\left(t\right)\right) \tag{6.11}$$

where the length and velocity[8] dependent functions are described by

$$f_{\mathrm{c}}^{L}\left(\lambda_{\mathrm{c}}\right) = \begin{cases} \sum_{n_L} g_{n_L}\left(\lambda_{\mathrm{c}}\right) & \text{if} \quad \lambda_{\mathrm{c}}^{\min} < \lambda_{\mathrm{c}} < \lambda_{\mathrm{c}}^{\max} \\ 0 & \text{otherwise} \end{cases} \tag{6.12}$$

$$f_{\mathrm{c}}^{\mathrm{V}}\left(\dot{\lambda}_{\mathrm{c}}\right) = \begin{cases} 0 & \text{if} \quad \dot{\lambda}_{\mathrm{c}} \leqslant \dot{\lambda}_{\mathrm{c}}^{\min} \\ \sum_{n_{\mathrm{V}}} g_{n_{\mathrm{V}}}\left(\dot{\lambda}_{\mathrm{c}}\right) & \text{if} \quad \dot{\lambda}_{\mathrm{c}}^{\min} < \dot{\lambda}_{\mathrm{c}} < \dot{\lambda}_{\mathrm{c}}^{\max} \\ 1.5 & \text{otherwise} \end{cases}, \tag{6.13}$$

or $f_{\mathrm{c}}^{\mathrm{V}} = 1$ in the completely quasi-static (non-dynamic) case.

A backward Euler time discretisation for the rate of stretch of the contractile element was assumed, giving

$$\dot{\lambda}_{\mathrm{c}} := \frac{{\lambda_{\mathrm{c}}}^{t} - {\lambda_{\mathrm{c}}}^{t-1}}{\Delta t} = \frac{\Delta \lambda_{\mathrm{c}}}{\Delta t} \quad . \tag{6.14}$$

The Gaussian-mollifier function is defined as

$$g_n\left(\lambda\right) = \begin{cases} \left(A_n e^{-B_n\left(\lambda - \mu_n\right)^{p_n}}\right)\left(\left[\lambda - \mu_n\right]^{q_n} - R_n^{q_n}\right)^{s_n} & \text{if} \quad |R_n| - |\lambda - \mu_n| > 0 \\ 0 & \text{otherwise} \end{cases}. \tag{6.15}$$

In equation 6.15 the terms in the first bracket define the shape of the curve in most of the region of interest, while the terms in the second bracket forces the function towards zero at a selected radius from a chosen epicentre so that the function is closed. The condition prescribed in equation 6.15 is crucial as the function has a zero-tangent at the cut-off radius but is non-zero beyond its extents.

Table 6.5 lists the parameter values used in the above equations. These parameters were tuned according to data and functions described in literature.

Figure 6.5a illustrates the correlation of equation 6.12 to the force-length data described in Herzog and Ait-Haddou [101] (which is identical to that shown in Gordon et al. [91]), while figure 6.6a shows the degree to which equation 6.13 matches data from Lieber [154]. Some newer models, such as those used by Ehret et al. [62], provide more accurate approximations to the experimental data than those to which comparison of this model was first drawn.

6.5.3 Internal equilibrium: Solving for fibre element stretches

In sections 4.2 and 4.3, the solution methodology of the global equilibrium equation was presented. As only equation 6.3 is considered, the satisfaction of global equilibrium does not ensure that the each local Hill three-element system that is coupled to, but discontinuous from, the global problem is in equilibrium. There

[8] Regardless of the constitutive model used for the muscle matrix, active muscle tissue is often classified as a viscoelastic media due to the temporal dependence of this term.

Table 6.5: Material parameters for muscle fibres, and the Hill model CE.

Parameter	CE f_c^L			CE f_c^V			
n	1	2	3	1	2	3	4
μ	0.8	1.3	1.325	-0.75	0.4	2.3	0.45
p	2	2	1	2	4	0	4
A	0.475	0.1	4830.635	3×10^{-5}	2.5×10^{-4}	5×10^{-4}	1662.25
B	90	10	3	0.01	0.01	0.5	2
R	1	1	0.75	10	6	4	0.5
q	4	2	4	2	2	2	6
s	8	8	8	2	2	2	2
λ_c^{min}		0.5		$\dot{\lambda}_c^{min}$		-10	
λ_c^{max}		2		$\dot{\lambda}_c^{max}$		0.5	

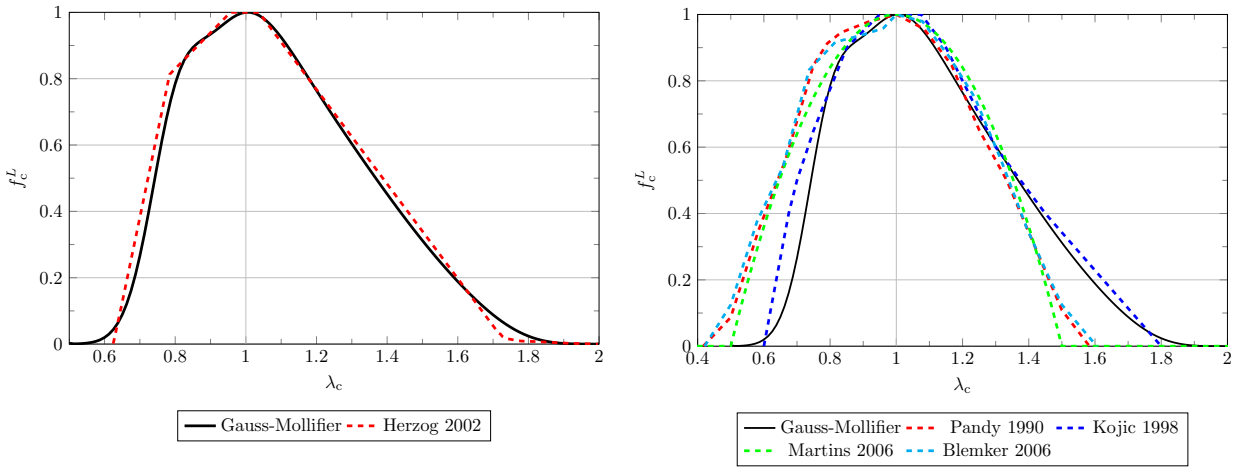

(a) Comparison with experimentally obtained relationship [101] **(b)** Comparison with computational models used in literature [208, 143, 171, 23]

Figure 6.5: CE length relationship.

remains the need to ensure that the fibre stress equilibrium condition given in equation 6.4 is satisfied at each global equilibrium state. The achieve this total equilibrium state, a staggered method is employed to solve the set of local $\{\lambda_c\}$ for a prescribed field variable $\boldsymbol{u}$ and resulting local variable $\{\lambda_f\}$.

As λ_f is derived directly from the field variables, the remaining unknown to be solved for in each decoupled local problem is λ_c. The algorithm used to solve for local equilibrium in the active Hill element branch is a bracketed safe-search Newton/bisection method derived from that described by Press et al. [224]. It has proved to be a robust technique that is well-suited to solving the highly nonlinear local residual equation. It provides a measure of algorithmic stability as the relationships describing the contractile element are, under certain circumstances, highly sensitive to perturbations.

Assuming a fixed value of λ_f as determined from equilibrium of macro-problem, the scalar function that is derived from equation 6.4 and minimised using the hybrid method is given as

$$\mathrm{R}^{\mathrm{f}}\left(\lambda_{\mathrm{c}},\dot{\lambda}_{\mathrm{c}}\right)\Big|_{\lambda_{\mathrm{f}},\alpha} = f_{\mathrm{s}}\left(\lambda_{\mathrm{f}},\lambda_{\mathrm{c}}\right) - T_0^s f_{\mathrm{c}}^L\left(\lambda_{\mathrm{c}}\right) f_{\mathrm{c}}^{\mathrm{V}}\left(\dot{\lambda}_{\mathrm{c}}\right)\alpha\left(\mathrm{u}\left(t\right)\right) \to 0 \tag{6.16}$$

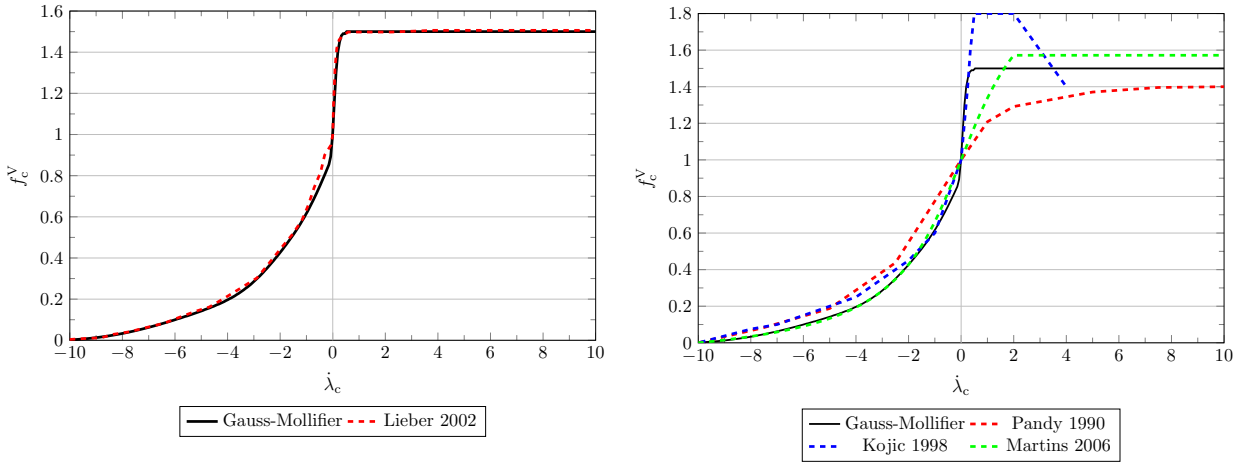

(a) Comparison with experimentally obtained relationship [154] **(b)** Comparison with computational models used in literature [208, 143, 171]

Figure 6.6: CE velocity relationship.

and with a Jacobian defined by

$$\frac{\partial \mathrm{R}^{\mathrm{f}}}{\partial \lambda_{\mathrm{c}}} = \frac{\partial f_{\mathrm{s}}}{\partial \lambda_{\mathrm{c}}} - T_0^s \left(\frac{\partial f_{\mathrm{c}}^L}{\partial \lambda_{\mathrm{c}}} f_{\mathrm{c}}^{\mathrm{V}} + f_{\mathrm{c}}^L \frac{\partial f_{\mathrm{c}}^{\mathrm{V}}}{\partial \dot{\lambda}_{\mathrm{c}}} \frac{\partial \dot{\lambda}_{\mathrm{c}}}{\partial \lambda_{\mathrm{c}}} \right) \alpha \quad . \tag{6.17}$$

The first term can be evaluated using the definition given by equation 6.10,

$$\frac{\partial f_{\mathrm{s}}}{\partial \lambda_{\mathrm{c}}} = \begin{cases} -c_1 c_2 e^{c_2(\lambda_{\mathrm{f}} - \lambda_{\mathrm{c}})} & \text{if} \quad \lambda_{\mathrm{s}} > 1 \\ 0 & \text{otherwise} \end{cases} \tag{6.18}$$

while the derivative of the CE length and velocity functions can be calculated using

$$\frac{\partial f_{\mathrm{c}}^L}{\partial \lambda_{\mathrm{c}}} = \sum_{n_L} \frac{\partial g_{n_L}(\lambda_{\mathrm{c}})}{\partial \lambda_{\mathrm{c}}} \quad , \quad \frac{\partial f_{\mathrm{c}}^{\mathrm{V}}}{\partial \dot{\lambda}_{\mathrm{c}}} = \sum_{n_{\mathrm{V}}} \frac{\partial g_{n_{\mathrm{V}}}\left(\dot{\lambda}_{\mathrm{c}}\right)}{\partial \dot{\lambda}_{\mathrm{c}}} \tag{6.19}$$

where seen appropriate from the fundamental description of the functions presented in equations 6.12 and 6.13. The first derivative of the Gaussian-mollifier function is

$$\frac{\partial g_n(\lambda)}{\partial \lambda} = \begin{cases} \left(A_n e^{-B_n(\lambda-\mu_n)^{p_n}}\right)\left(-p_n B_n (\lambda-\mu_n)^{p_n-1}\right) & \text{if} \quad s=0, |R_n| - |\lambda-\mu_n| > 0 \\ \left(A_n e^{-B_n(\lambda-\mu_n)^{p_n}}\right)\left((\lambda-\mu_n)^{q_n} - R_n^{q_n}\right)^{s_n-1} & \\ \quad \times \left(p_n B_n R_n^{q_n} (\lambda-\mu_n)^{p_n-1} - p_n B_n (\lambda-\mu_n)^{p_n+q_n-1}\right. & \text{if} \quad s \neq 0, |R_n| - |\lambda-\mu_n| > 0 \\ \qquad \left. + q_n s_n (\lambda-\mu_n)^{q_n-1}\right) & \\ 0 & \text{otherwise} \quad . \end{cases} \tag{6.20}$$

Figure 6.7 shows the first derivative of the length and velocity functions. Although the derivative of the force-length function is smooth in the usual region of operation for the models used in this work, the force-velocity function has a highly nonlinear first-derivative in the positive portion of the range with a large gradient change near the y-intercept. This could result in poor convergence properties of equation 6.16, but in practise this has not occurred when using the hybrid Newton/bisection method.

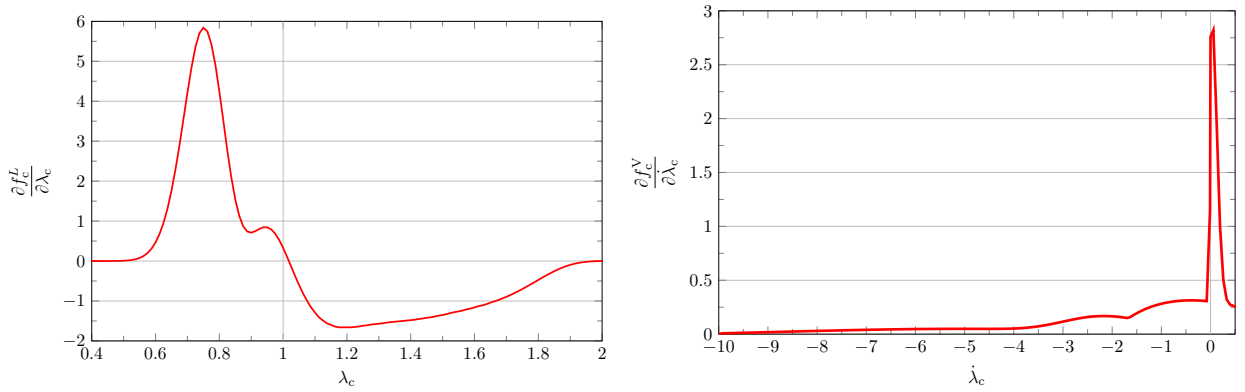

(a) Force-length relationship

(b) Force-velocity relationship

Figure 6.7: First derivatives of functions describing CE length and velocity relationships.

From equation 6.14, the derivative of the contractile velocity with respect to the contractile stretch at the current time is simply

$$\frac{\partial \dot{\lambda}_c}{\partial \lambda_c} = \frac{1}{\Delta t} \quad . \tag{6.21}$$

For muscles that are inactive or have become deactivated due to over-extension or over-contraction, by definition

$$\lambda_c\big|_{\alpha=0} := \lambda_c\big|_{\lambda_c > \lambda_c^{\max}} := \lambda_c\big|_{\lambda_c < \lambda_c^{\min}} := \lambda_f \quad \ni \quad \lambda_s = 1 \quad . \tag{6.22}$$

The history for the contractile element length is critical for the correct calculation of $\dot{\lambda}_c$ and so the evolution of the CE stretch must be tracked even when the muscle is not active or the local fibre bundle deactivates.

Rewriting equation 6.16 in terms of an update increment, the residual for a given $\widehat{\lambda}_c = {\lambda_c}^{t-1} + \Delta\widehat{\lambda}_c{}^{t}$ where ${\lambda_c}^{t-1}$ is the CE stretch at the previous equilibrium solution is given by

$$\mathrm{R}^{\mathrm{f}}\left(\widehat{\lambda}_c\right) = f_s\left(\lambda_f^t, \widehat{\lambda}_c\right) - T_0^s f_c^L\left(\widehat{\lambda}_c\right)\ f_c^V\left(\Delta\widehat{\lambda}_c, \Delta t\right)\ \alpha\left(\mathrm{u}\right) \quad . \tag{6.23}$$

Using algorithm 1, it is possible to solve for the CE stretch update $\Delta\widehat{\lambda}_c{}^{t}$ to attain local equilibrium between the SE and CE. Figure 6.8 illustrates the procedure of bracketing the root of the equation and decreasing the distance between the brackets as trial solutions closer to the root are found. An event of solution divergence in the preferred Newton-method is depicted in the diagram. In this scenario, the algorithm switches to a bisection method that moves one of the brackets and recommends a restart position for the Newton algorithm on the next iteration of the inner solver loop.

Although the hybrid algorithm is robust, it is possible that the solution may be so highly nonlinear that the bracketing process may falsely skip over the position of a root and may present a case where no root is found. Such a case should be dealt with using an even more robust, and likely more costly algorithm. A further potential complication which is not accounted for in this algorithm is the existence of multiple roots. However, for the purposes of this work, algorithm 1 worked as expected as long as control over the global displacement solution step was maintained through the use of load and step limiting methods.

Algorithm 1 Calculate $\lambda_c = \lambda_c^{t-1} + \Delta\lambda_c$ for internal stress equilibrium at time t using safe-search hybrid Newton/bisection method derived from Press et al. [224].

Require: ${\lambda_f}^{t-1}, {\lambda_c}^{t-1}, {\Delta\lambda_c}^{t-1}, \alpha^{t-1}$ ▷ Values from previous time-step

Require: ${u}^t, \Delta t, {\lambda_f}^t$ ▷ Values from the current time-step global solution and neural algorithm

Calculate: $\alpha^t = \alpha^t\left(\alpha^{t-1}, u^t, \Delta t\right)$ ▷ Determine muscle activation levels

Choose: $\Delta\widehat{\lambda}_c^{\,*}$ ▷ Uncertainty of initial value of $\Delta\widehat{\lambda}_c$ [a]

$\Delta\widehat{\lambda}_c^{\,1} = \Delta\widehat{\lambda}_c^{\,t-1} - \Delta\widehat{\lambda}_c^{\,*}, \Delta\widehat{\lambda}_c^{\,2} = \Delta\widehat{\lambda}_c^{\,t-1} + \Delta\widehat{\lambda}_c^{\,*}$ ▷ Calculate initial brackets

$\mathrm{R}_1^{\mathrm{f}} = \mathrm{R}^{\mathrm{f}}\left(\Delta\widehat{\lambda}_c^{\,1}\right), \mathrm{R}_2^{\mathrm{f}} = \mathrm{R}^{\mathrm{f}}\left(\Delta\widehat{\lambda}_c^{\,2}\right)$ ▷ Calculate function values at brackets using equation 6.23

while $\mathrm{R}_1^{\mathrm{f}} \cdot \mathrm{R}_2^{\mathrm{f}} > 0$ **do** ▷ No root between brackets

Update initial bracket positions according to table 6.6 ▷ Increase bracket size until root is enclosed

end while

if $\mathrm{R}_1^{\mathrm{f}} < \mathrm{tol}$ **then** $\Delta\lambda_c^t = \Delta\widehat{\lambda}_c^{\,1}$ ▷ Bracket is located on the root

else if $\mathrm{R}_2^{\mathrm{f}} < \mathrm{tol}$ **then** $\Delta\lambda_c^t = \Delta\widehat{\lambda}_c^{\,2}$ ▷ Bracket is located on the root

else ▷ Brackets enclose root. Use Newton / bisection method to solve for root.

Set up bracketing conditions and initial guess

$\Delta\widehat{\lambda}_c^{\,\mathrm{h}} = \max\left(\Delta\widehat{\lambda}_c^{\,1}, \Delta\widehat{\lambda}_c^{\,2}\right), \Delta\widehat{\lambda}_c^{\,\mathrm{l}} = \min\left(\Delta\widehat{\lambda}_c^{\,1}, \Delta\widehat{\lambda}_c^{\,2}\right)$ ▷ Record high and low bracket values

$\mathrm{R}_2^{\mathrm{f}} = \max\left(\mathrm{R}_1^{\mathrm{f}}, \mathrm{R}_2^{\mathrm{f}}\right), \mathrm{R}_1^{\mathrm{f}} = \min\left(\mathrm{R}_1^{\mathrm{f}}, \mathrm{R}_2^{\mathrm{f}}\right)$ ▷ Orient search such that $\mathrm{R}_1^{\mathrm{f}} < 0$

$\Delta\lambda_c^{\,t} = \frac{1}{2}\left(\Delta\widehat{\lambda}_c^{\,\mathrm{l}} + \Delta\widehat{\lambda}_c^{\,\mathrm{h}}\right)$ ▷ Choose initial values for the root search

Perform search for root while residual is unacceptable

while $\mathrm{R}^{\mathrm{f}} = \mathrm{R}^{\mathrm{f}}\left({\lambda_c}^{t-1} + {\Delta\lambda_c}^t\right) > \mathrm{tol}$ **do** ▷ Not converged on root. Calculate residual using equation 6.23

$\mathrm{R}'^{\mathrm{f}} = \mathrm{R}'^{\mathrm{f}}\left({\lambda_c}^{t-1} + {\Delta\lambda_c}^t\right)$ ▷ Calculate Jacobian using equation 6.17

if $\left(\left({\Delta\lambda_c}^t - \Delta\widehat{\lambda}_c^{\,\mathrm{h}}\right) \cdot \mathrm{R}'^{\mathrm{f}} - \mathrm{R}^{\mathrm{f}}\right) \times \left(\left({\Delta\lambda_c}^t - \Delta\widehat{\lambda}_c^{\,\mathrm{l}}\right) \cdot \mathrm{R}'^{\mathrm{f}} - \mathrm{R}^{\mathrm{f}}\right) > 0$ **then** ▷ Newton method overshoots brackets

${\Delta\lambda_c}^t \leftarrow \Delta\widehat{\lambda}_c^{\,\mathrm{l}} + \frac{1}{2}\left(\Delta\widehat{\lambda}_c^{\,\mathrm{h}} - \Delta\widehat{\lambda}_c^{\,\mathrm{l}}\right)$ ▷ Use bisection method for this inner iteration

else

$\Delta\lambda_c^t \leftarrow \Delta\lambda_c^t - \dfrac{\mathrm{R}^{\mathrm{f}}\left(\Delta\lambda_c^t\right)}{\mathrm{R}'^{\mathrm{f}}\left(\Delta\lambda_c^t\right)}$ ▷ Use Newton method for this inner iteration

end if

Tighten brackets around solution

if $f < 0$ **then** $\Delta\widehat{\lambda}_c^{\,\mathrm{l}} = \Delta\lambda_c^t$ ▷ Shift lower bracket

else $\Delta\widehat{\lambda}_c^{\,\mathrm{h}} = \Delta\lambda_c^t$ ▷ Shift upper bracket

end if

end while

Check for element stretch violations (equation 6.22) and consequent muscle deactivation

if $\lambda_c^{t-1} + \Delta\lambda_c^t > \lambda_c^{\max}$ **then** ▷ Over-extension of CE

$\Delta\lambda_c^t = \lambda_f^t - \lambda_c^{t-1}$ ▷ CE deactivation: $f_c = 0$

else if $\lambda_c^{t-1} + \Delta\lambda_c^t < \lambda_c^{\min}$ **then** ▷ Over-compaction of CE

$\Delta\lambda_c^t = \lambda_f^t - \lambda_c^{t-1}$ ▷ CE deactivation: $f_c = 0$

else if $\dfrac{\lambda_f^t}{\lambda_c^{t-1} + \Delta\lambda_c^t} < 1$ **then** ▷ Over-compaction of SE

$\Delta\lambda_c^t = \lambda_f^t - \lambda_c^{t-1}$ ▷ SE deactivation: $f_s = 0$

end if

Update values for current time-step

$\lambda_c^t = \lambda_c^{t-1} + \Delta\lambda_c^t$

end if

[a] The degree to which λ_c is expected to change relies on too many variables to accurately and reliably predict whether the CE will extend or contract, even when muscle contraction ($\alpha^t > \alpha^{t-1} \geqslant 0$) is specified.

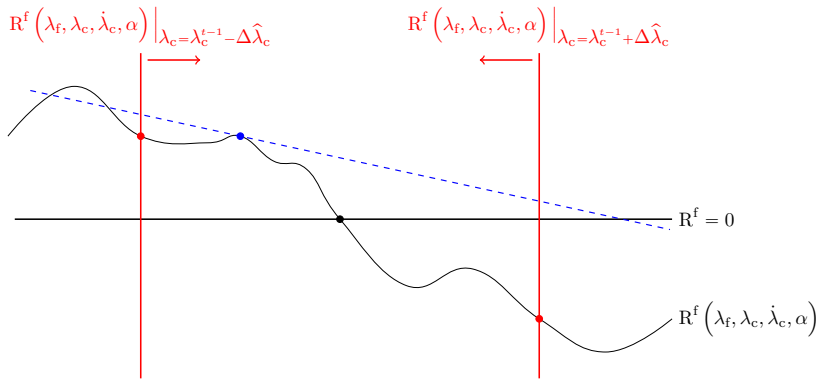

Figure 6.8: The safe-search Newton/bisection method.

Table 6.6: Initial hybrid-method bracket updates using a search acceleration factor A.

Case					Update	
$\mathrm{R}_1^{\mathrm{f}}>0$ $\mathrm{R}_1^{\mathrm{f}}<0$	and and	$\mathrm{R}_2^{\mathrm{f}}>\mathrm{R}_1^{\mathrm{f}}$ $\mathrm{R}_2^{\mathrm{f}}<\mathrm{R}_1^{\mathrm{f}}$	and and	$\Delta\hat{\lambda}_{\mathrm{c}}{}^{1}>\Delta\hat{\lambda}_{\mathrm{c}}{}^{2}$ $\Delta\hat{\lambda}_{\mathrm{c}}{}^{1}>\Delta\hat{\lambda}_{\mathrm{c}}{}^{2}$	$\Delta\hat{\lambda}_{\mathrm{c}}{}^{2}=\Delta\hat{\lambda}_{\mathrm{c}}{}^{1}+A\Delta\hat{\lambda}_{\mathrm{c}}{}^{*}$	$\mathrm{R}_2^{\mathrm{f}}=\mathrm{R}^{\mathrm{f}}\left(\lambda_{\mathrm{c}}{}^{t-1}+\Delta\hat{\lambda}_{\mathrm{c}}{}^{2}\right)$
$\mathrm{R}_1^{\mathrm{f}}>0$ $\mathrm{R}_1^{\mathrm{f}}<0$	and and	$\mathrm{R}_2^{\mathrm{f}}>\mathrm{R}_1^{\mathrm{f}}$ $\mathrm{R}_2^{\mathrm{f}}<\mathrm{R}_1^{\mathrm{f}}$	and and	$\Delta\hat{\lambda}_{\mathrm{c}}{}^{2}>\Delta\hat{\lambda}_{\mathrm{c}}{}^{1}$ $\Delta\hat{\lambda}_{\mathrm{c}}{}^{2}>\Delta\hat{\lambda}_{\mathrm{c}}{}^{1}$	$\Delta\hat{\lambda}_{\mathrm{c}}{}^{2}=\Delta\hat{\lambda}_{\mathrm{c}}{}^{1}-A\Delta\hat{\lambda}_{\mathrm{c}}{}^{*}$	$\mathrm{R}_2^{\mathrm{f}}=\mathrm{R}^{\mathrm{f}}\left(\lambda_{\mathrm{c}}{}^{t-1}+\Delta\hat{\lambda}_{\mathrm{c}}{}^{2}\right)$
$\mathrm{R}_2^{\mathrm{f}}>0$ $\mathrm{R}_2^{\mathrm{f}}<0$	and and	$\mathrm{R}_1^{\mathrm{f}}>\mathrm{R}_2^{\mathrm{f}}$ $\mathrm{R}_1^{\mathrm{f}}<\mathrm{R}_2^{\mathrm{f}}$	and and	$\Delta\hat{\lambda}_{\mathrm{c}}{}^{1}>\Delta\hat{\lambda}_{\mathrm{c}}{}^{2}$ $\Delta\hat{\lambda}_{\mathrm{c}}{}^{1}>\Delta\hat{\lambda}_{\mathrm{c}}{}^{2}$	$\Delta\hat{\lambda}_{\mathrm{c}}{}^{1}=\Delta\hat{\lambda}_{\mathrm{c}}{}^{2}-A\Delta\hat{\lambda}_{\mathrm{c}}{}^{*}$	$\mathrm{R}_1^{\mathrm{f}}=\mathrm{R}^{\mathrm{f}}\left(\lambda_{\mathrm{c}}{}^{t-1}+\Delta\hat{\lambda}_{\mathrm{c}}{}^{1}\right)$
$\mathrm{R}_2^{\mathrm{f}}>0$ $\mathrm{R}_2^{\mathrm{f}}<0$	and and	$\mathrm{R}_1^{\mathrm{f}}>\mathrm{R}_2^{\mathrm{f}}$ $\mathrm{R}_1^{\mathrm{f}}<\mathrm{R}_2^{\mathrm{f}}$	and and	$\Delta\hat{\lambda}_{\mathrm{c}}{}^{2}>\Delta\hat{\lambda}_{\mathrm{c}}{}^{1}$ $\Delta\hat{\lambda}_{\mathrm{c}}{}^{2}>\Delta\hat{\lambda}_{\mathrm{c}}{}^{1}$	$\Delta\hat{\lambda}_{\mathrm{c}}{}^{1}=\Delta\hat{\lambda}_{\mathrm{c}}{}^{2}+A\Delta\hat{\lambda}_{\mathrm{c}}{}^{*}$	$\mathrm{R}_1^{\mathrm{f}}=\mathrm{R}^{\mathrm{f}}\left(\lambda_{\mathrm{c}}{}^{t-1}+\Delta\hat{\lambda}_{\mathrm{c}}{}^{1}\right)$

6.5.4 Linearisation of Hill three-element components

The material-dependent contribution to the stiffness modulus in equation 5.5c from the muscles is described by the scalar function

$$\psi_{\mathrm{f}}''\left(\lambda_{\mathrm{f}}\right)=\frac{\partial T_f}{\partial\lambda_{\mathrm{f}}}=\frac{\partial T_{\mathrm{f}}^{\mathrm{p}}\left(\lambda_{\mathrm{f}}\right)}{\partial\lambda_{\mathrm{f}}}+\frac{\partial T_{\mathrm{f}}^{\mathrm{s}}\left(\lambda_{\mathrm{f}},\lambda_{\mathrm{c}}\right)}{\partial\lambda_{\mathrm{f}}} \tag{6.24a}$$

$$=T_0^{\max}\left(\frac{\partial f_{\mathrm{p}}}{\partial\lambda_{\mathrm{f}}}+\frac{\partial f_{\mathrm{s}}}{\partial\lambda_{\mathrm{f}}}\right)\quad. \tag{6.24b}$$

Although equal, the SE nominal stress is preferentially utilised over the CE as the functions governing this element are less computationally intensive than that of the CE.

The slope of the parallel function with respect to fibre stretch is determined from equation 6.9 to be

$$\frac{\partial f_{\mathrm{p}}}{\partial\lambda_{\mathrm{f}}}=\begin{cases}2aA\left(1+2a\left(\lambda_{\mathrm{f}}-1\right)\right)e^{a\left(\lambda_{\mathrm{f}}-1\right)^2} & \text{if}\quad\lambda_{\mathrm{f}}>1\\ 0 & \text{otherwise}\end{cases} \tag{6.25}$$

while the implicit relationship of the series function derivative with respect to fibre stretch, derived from equation 6.10, is

$$\frac{\partial f_{\mathrm{s}}}{\partial\lambda_{\mathrm{f}}}=\begin{cases}c_1c_2\left(1-\dfrac{\partial\lambda_{\mathrm{c}}}{\partial\lambda_{\mathrm{f}}}\right)e^{c_2\left(\lambda_{\mathrm{f}}-\lambda_{\mathrm{c}}\right)} & \text{if}\quad\lambda_{\mathrm{s}}>1\\ 0 & \text{otherwise}\end{cases} \tag{6.26}$$

as from equation 6.7b, $\lambda_c = \lambda_c(\lambda_f, \alpha)$. To solve for the derivative of contractile element stretch with respect to fibre stretch, λ_c is determined at perturbed values of λ_f using the internal equilibrium equation 6.16 and a second-order central difference method[9]

$$\left.\frac{\partial \lambda_c}{\partial \lambda_f}\right|_{\lambda_f,\alpha} = \frac{f(\lambda_f + \delta\lambda_f) - f(\lambda_f - \delta\lambda_f)}{2\delta\lambda_f} \tag{6.27}$$

is used to determine the derivative. The perturbation was specified as $\delta\lambda_f = \dfrac{\lambda_f}{100}$.

6.6 External muscles

Since the DG, SH, SG muscles insert into the body of the tongue, the portion of the muscles that are within the tongue are treated as internal fibres whilst acknowledging that both the internal and external components collectively constitute the extrinsic muscle group. The action of external muscle regions are incorporated into the geometry through the traction boundary conditions described in section 3.7. The insertion region on the boundary, $\Gamma_0^{t_f}$, on which the muscles act define the interface where the external fibres transition to internal fibres. $\boldsymbol{X}^I$ in equation 3.102a defines the insertion points on this transition surface. The traction exerted by any external muscle is represented by equation 3.106 with the nominal stress in the fibre defined by equation 6.3. The values of $\boldsymbol{t}_t^{ext}, \boldsymbol{t}_f^{ext}$ are continuously updated as the displacement solution is updated, ensuring that the displacement-dependent load is consistently linearised.

6.7 Discussion of convergence and stability of the muscle model

The following observations were made with respect to the use of the muscle model for the simulation of test cases, as well as the muscles in the HUA:

Convergence: Quadratic convergence of the Newton-Raphson algorithm is attained if the geometric and material parameters are simple, such as activation of a single muscle embedded in a regular computational domain. However, complex scenarios may result in a superlinear convergence rate. An explanation for this behaviour is that the fibre model is very sensitive to the solution, as well as material and geometric parameters governing equilibrium. The local interaction of multiple fibre families is complex and the staggered global-local algorithm is not suited to these cases. It therefore takes a number of Newton iterations for a local equilibrium to be established between contracting muscle groups.

Stability: It is possible to produce a bifurcation problem where the solution is unstable. Any scenario where antagonistic muscle groups are simultaneously active and producing a force of the same order of magnitude may fit into this category. For example, two axially-aligned muscles of the same properties and cross-sectional area acting on opposite sides of a common interface should result in the interface not moving, but is very sensitive to perturbations in the generated solution. In these cases, the unstable equilibrium solution is the correct solution. A better load and solution limiting procedure, as well as more accurate computational and numerical algorithms, must be implemented to cope with such a scenario.

[9] A more computationally expensive fourth-order central difference method was also tested, but no significant gain in accuracy or convergence rate of the global or local solution was observed.

Computational expense: The muscle model described here can be very computationally expensive. The local or inner problem, namely that of equation 6.16, must be solved for each displacement update (and numerous times if a linesearch algorithm is employed). It must be solved several more times when calculating the tangent stiffness contributions in equation 6.27. Each of these involve the evaluation of numerous Gaussian-mollifier functions, although the incorporated cut-off radius does assist in reducing the number of their evaluations.

7. NEURAL MODEL

Achieving efficient task-based motor control in a system is a complex matter. The *motor equivalence problem*, first formally described by Bernshteĭn [16], maintains that there exists no one-to-one map between the motor coordination problem and the motor solution to a task. Simply stated, in a multiple degree-of-freedom system, there is more than one way to coordinate muscle movements in order to achieve a desired motor-driven goal. In a body of intricate construct, the problem complexity is increased as not only do physical DOFs representing locations catering for bending and rotation exist, but also kinematic DOFs that introduce flexibility in the velocity state. Although this is the case, during early childhood development we learn the *muscle synergies* required for lifelong coordinated movement and function. Muscle synergies, as defined by Ting and McKay [278], are the "pattern of relative levels of muscle activation". It has been suggested that movements are a result of a combination of muscle synergies invoked through muscles controlled by the central nervous system [278, 277].

In this chapter, we address the issue of neural control in two steps, in which the model describing the mechanism for muscle activation is presented alongside a neural control model. The neural model is decomposed into two parts, the first of which is the definition of neural stimulus in the context of the muscle activation model. The second part is a neural control model that governs the selection of active and inactive sets of muscles, that is the muscle synergies required to complete a desired task. This model is devised to overcome the difficulties arising from the need to produce a configuration for soft tissues in the presence of geometric and material complexities, as well as traction forces that are not known *a priori*.

7.1 Models and algorithms for muscle activation and control

As noted by Sanguineti et al. [245], the main issue in modelling the tongue musculature is that "no direct empirical evidence exists on which to identify the organization of control signals to spatially distributed muscles". That is to say that the activation patterns for the individual functional muscle groups in the tongue, and which are required in order to perform some task, have not yet been fully documented. Therefore, control algorithms have been developed to circumvent the lack of experimental data. Different fields of research classically use differing approaches to describing the excitation of muscle tissue. Here, an overview of the methods available for consideration are presented.

7.1.1 Electro-potential and state equations for activation

For the modelling of the heart physiology, a detailed description of the electrophysiology is required in order to accurately simulate the propagation of the electrical signal from the nerves to the tissue. This is important to capture as the basic pulsatile motion of the heart that is produced by the rhythmic excitation of cardiac muscle fibres propagating outwards from the source of innervation.

Clayton et al. [44] provide a detailed review of the methods routinely used to calculate the spatially variable potential difference (electrical voltage) that drive muscular contraction. The implementation of these models, namely the bidomain and monodomain equations, is not trivial and requires numerous physiological parameters as input. Recently Röhrle [234] developed an electro-potential description of skeletal muscle contraction using the bidomain equations to govern each motor-unit controlling numerous muscle fibres. An additional model was utilised to determine the ion concentrations in the muscle which were then correlated to the muscle activation level by describing the number of active cross-bridges during and after contraction cycle.

In contrast, activation models more aligned with the implementation in this work are those that use a discrete signal to directly drive a Hill-type model. These signals are assumed to instantaneously propagate through space and can therefore be used as a direct input to control the muscles without the need for an intermediate model. These models assume a multiplicative split in the functions governing the contractile force, with one term representing the activation level. Direct prescription of the activation was used in application by Stavness et al. [263] in a hybrid jaw-tongue-hyoid model, Röhrle and Pullan [235] to control the muscles of the masseter in a lower jaw model, Kojic et al. [143] in a model of the soft palate, d'Aulignac et al. [52] in a pelvic model, Blemker et al. [24] in a model of the biceps brachii and the tongue models of Wilhelms-Tricarico [311], Fujita et al. [77], Wu et al. [317], Baker [11]. Further constitutive models that make use of this decomposition include that of Odegard et al. [197] and Spyrou and Aravas [258].

To link the concepts of neural excitation and muscle activation, Pandy et al. [208], Pandy [207] describe a first order differential equation that governs the build-up of the muscle activation level. Such a model captures the delay between muscle excitation and activation, approximating the chemical (ionic) changes in the tissue. Detailed later, this model has been used to simulate jumping [208, 207], jumping and walking [207] in musculoskeletal models, as well as continuum models of the brachialis [170], the pelvis [171] and in this work.

As an alternative, cross-bridge modelling has been used by Williams [312] in their implementation of the Huxley-model of muscle contraction. Zahalak and Ma [324] included the rate-dynamics of calcium uptake and bonding in their activation model for the Huxley-model. Murtada et al. [187] also used the number of active cross-bridges as a scaling factor in their active constitutive model. Ehret et al. [62] utilised an activation parameter in their model, but assume a more complex relationship between the active portion of the constitutive model and the activation parameter. This method allows for a kinematic interpretation of this parameter.

7.1.2 EMG data as input to computational models

The experimental data attained from EMG studies provides insight into the activity of muscles used to perform a specified task. By defining some correlation between data extracted from these studies and the acti-

vation level, the EMG data can be used as a direct input into computational models. Lloyd and Besier [158] produced an EMG-driven musculoskeletal model to estimate muscle forces and knee joint moments *in vivo*. Filtered EMG data was used as input to a nonlinear activation function which, in conjunction with a Hill-type muscle model, was used to describe muscle forces.

Huang et al. [111, 112, 113] developed a constitutive model for the CE that describes the contractile stress as a linear function of the contractile strain. The contractile stress was also considered directly proportional to the stiffness and number of active cross-bridges, which in turn were inferred from the EMG level. This experimental data was further correlated to the epiglottal pressure, making the GG response proportional to the assumed airway pressure. It also accounted for the different response during the sleep and awake states of the subject. It was assumed that fully awake, the number of attached cross-bridges increases continuously as the pressure decreases in the airway, thus maintaining patency. During sleep the rate of cross-bridge binding decreases, reducing the reflex mechanism that maintains the airway open.

7.1.3 Forward and inverse simulation

Detailed multi-body musculoskeletal models have been developed on the basis of rigid-body dynamics. Anthropomorphic data is collected to recreate an anatomically accurate model of a system consisting of rigid elements, which represent bones, and active deformable elements representing muscles. There exist various methods to describe the dynamics of these systems, some general examples of which are provided in Murray-Smith [186], Otten [204]. The works of Delp et al. [57], Prilutsky and Zatsiorsky [225], Neptune et al. [192] demonstrate that this class of model has application in gait, surgical and athletic performance analysis [57].

In forward kinematic models, prescribed internal forces and torques are provided as an input from which to calculate the motion of the system. The converse occurs in inverse kinematics, where the internal forces and joint torques are calculated from experimentally measured displacement and angle data. This data consists of both forces applied to the system (reaction forces) and the joint angles. These internal forces can then be resolved into a plausible set of muscle activations that constitute the neurological impulses to the controlling muscles. Muscle contraction in the model of Delp et al. [57] is governed by first-order differential equation relating the muscle activity to the neural signal.

A major issue that must be resolved in the both approaches is that of muscle redundancy. Due to the biological complexity of the modelled system, the number of input variables (namely the muscles being controlled) is often larger than the number of unknowns (joint angles and forces), leading to an indeterminate system of equations. The addition of further constraints, in the form of metabolic cost minimisation (work and fatigue performance) [192, 225], assist in this regard.

Recently, inverse simulation using a forward-dynamics model was introduced by Stavness [264] (also documented in [159]) into a FEM model of the tongue. Recognising the muscle activations as unknown quantities, the potential function to be minimised included a term relating to the goal movement with constraints on the unknown muscle activations. This required that the internal forces be decomposed into passive and active components, and leveraged the linear relationship between the force generated in the CE of the Hill-model and the muscle activation level. The muscle redundancy problem was solved using an advanced optimisation algorithm [61]. Using this technique, very good spatial-tracking characteristics in the tongue model, constructed with many functional motor units, was achieved. Forward simulation with two optimal-

ity conditions has been used by Wang et al. [301] to deduce the activation of muscle groups corresponding to prescribed motions of the tongue.

7.1.4 The EPH and the λ-theory

The equilibrium point hypothesis (EPH), as described by Bizzi et al. [22], is a hypothesis developed by Feldsman in 1966 suggesting the way that the CNS generates movement in the body. In summary, it was hypothesised that, with specific reference to articulatory joints, posture is attained through the equilibrium of antagonistic muscle groups that have a spring-type nature and length-dependent characteristics. To initiate a change in posture, the CNS is assumed to change the relative activation levels that have maintained the current equilibrium position, thus leading to the development of a new equilibrium position. Although the ideas for the EPH were derived from behavioural experiments, it has since been in part confirmed by measured neurological data [22].

Two models of the control mechanism were proposed by Feldsman, one of which is the λ-theory that is popularly applied in the field of speech research. In this model, the feedback mechanism for muscle activation is described as a function of the difference between the muscle length and a control parameter, λ, which describes some threshold length. This control parameter can, in turn, be a function of the desired equilibrium position. In this way, the model describes reflexive contractions of the muscles due to a shift in the equilibrium configuration with respect to the desired configuration: the muscles act like "tunable springs". For each muscle group, the overall force developed is a described a family of length-tension curves, each of which is characterised by the threshold length [244]. Although the theory has undergone much scrutiny and debate [92, 129, 71], some doubts as to the validity of the λ-model and the applicability of it and the EPH exist [105, 215]. Further criticism of the λ-theory is given in [22] and all control models in general in [203].

In their model of the tongue, Sanguineti et al. [244] used the λ-theory as a control mechanism for the intrinsic and extrinsic muscles of the tongue. An activation function identical to that described in [22] was utilised and the norm of the muscle force vector was minimised to deal with muscle redundancy. The control parameters were defined in terms of a smaller set of control parameters, as well as the jaw and hyoid displacements. The model was later advanced by Sanguineti et al. [245], wherein a rate-dependent term was introduced into the activation model to account for delays in muscle reflexes and muscle damping. The control parameters were determined by correlating the movement of the tongue to data extracted from an imaging process. A muscle-control model of the same description had been used previously by Perrier et al. [214] to model jaw-articulation and Buchaillard et al. [29] to control the tongue for the purpose of speech formation. The tongue model of Perrier et al. [215] includes a control model consistent with that described in [244]. Other models that make use of the EPH include [28, 264].

7.1.5 The muscle control workspace and equilibrium point map

As an alternative to the EPH-based models, Dang and Honda [50] proposed the concept of muscle workspace. This concept is a follow-on from Honda [108] who describe the equilibrium position as the sum of EMG vectors and their mapping onto the muscle force space. In this method, the effect of activation of each individual muscle on the displacement of a single observation point from its current equilibrium position is probed. A set of displacement vectors are used to determine which muscles contribute positively towards the goal motion. From this map, a plausible set of muscle activations can be developed as a linear combination of the

individual contributions. Developing this set is an iterative procedure, with a revision of the displacement vectors required as the trajectory of the observation point is realised. A optimal activation combination is found by minimising a cost function, defined by the summation of the norm of the difference between the optimal trajectory of the displacement resulting from the activation of each individual muscle component. Although this methodology proved successful for their work, the authors conceded that zero contraction of agonist-antagonist muscle pairs was assumed and that the inclusion of multiple observation points was therefore not tested. Advancement of these ideas, including the co-contraction of muscle pairs, was discussed by Dang and Honda [51].

7.1.6 Learning algorithms

Neptune et al. [192] use simulated annealing as an optimisation algorithm in a forward kinematic model of the lower limbs, which solves for the muscle excitations to minimise the error corresponding to experimentally derived displacement data. A similar result was achieved by Ibrahim et al. [120], where a genetic algorithm (GA) was utilised to determine the active properties of the muscles controlling the angle of the knee joint. Ibrahim et al. [121] later used a multi-objective GA to optimise the number of constraints on the model thus reducing its complexity.

Baker [11] developed a neural network to learn the muscle activations required to attain a prescribed tongue posture. The model learned, under static conditions, the displacement due to contraction of individual and combinations of muscles. Special techniques involving the projection of parameter spaces were used to enable the reduction of the parameter search-space. The neural network, in association with statistical models, was then able to predict the combination and activation level of muscle groups to obtain the desired tongue posture.

7.1.7 Discussion on muscle control models

Active constitutive models such as that described by Huang et al. [111], are ideal for use in research of sleep disorders as they are simple to integrate into a model and directly correlate experimentally obtained information to the muscle response. However, the question of robustness of such a model exists:

1. Under which physical conditions does the model remain valid?
2. If the physical conditions are altered, can the model be adapted to account for the change in environment?
3. How does the activity of the other muscles, which may not be experimentally corroborated, relate to the same environmental factors?

It is these issues that drive the need for adaptive models such as the others that have been described. Ultimately, the neural model implemented in this work is of the forward-kinematic type, which has some issues of its own [203]. To ratify this choice, a brief commentary on some of the predicted issues with implementing the alternative approaches is presented.

Inverse dynamics: The driving force behind muscle activation is the airway pressure that is applied over the surface of the tongue. This same surface is one that we assume to remain stationary during the course of application of the load. This zero-constraint of the traction-surface would lead to a trivial solution in the equations of motion, and therefore similar in the predication for muscle activation. Infinite solutions exist to the state of isometric contraction as the stress-state depends on the muscle activation level.

EPH/λ-model: The primary issue with utilising the λ-model is that, in its current form, it and continuum based approaches to muscle modelling appear incompatible. The inconsistencies between the two models and implementation difficulties are summarised as follows: The view of the length-scale of the representative model for muscles does not match, in that the λ-model assumes that fibres are macro-scale elements. Although stated in [244] that it remains consistent with the Hill-model, the constitutive equation for the contractile force in the λ-model lacks a direct link to the rate-based dynamics (force-velocity relationship) inherent to muscular tissue. Values characterising the representative lengths of the muscle do not exist in the continuum-based approaches. A length scale is required for the activation function used for the λ-model employed by Sanguineti et al. [245], amongst others. Furthermore, a functional CSA is required to link the measured peak muscle stress and the force generated in the model's muscle elements. Due to the arbitrary arrangement of the collection of fibres that constitute a muscle, these values cannot be directly attained without further assumptions. Lastly, describing the control parameters is challenging. As stated by Dang and Honda [50], "the most commonly used version of this theory requires length parameters and firing information of the muscles, which are difficult to obtain empirically... observation of EMG signals is limited to only a few large muscles such as the extrinsic tongue muscles."

Muscle-workspace control strategy: The strategy adopted by Dang and Honda [50] as an alternative to the EPH models is appealing, but issues arise in its application to large, 3-d FEM models. Due to the various non-linearities incorporated in the model, epistasis is prevalent in the process of active tongue mechanics. Therefore small steps towards optimal activation pattern would be required. As each step requires re-evaluation of all individual muscle contributions, this remains computationally expensive. The introduction of multiple control points may require conflicting activation strategies, leading to additional evaluation as the effect of antagonistic muscle contraction is resolved. Furthermore, there appears no simple manner in which to introduce further optimisation arguments, such as those based on metabolic and energetic minimisation.

Quadratic modelling: The minimisation of a total energy functional, as achieved by Stavness [264], appears most viable and could be directly applied to this muscle model. Although not described in this work, a vector of nodal forces generated through muscle contraction could be expressed using a manipulation of equations 4.16b and 5.6c and the additive decomposition equation 6.3 and constitutive relation equation 6.4. Realisation of this method of solving the problem relies on the complex algorithm described by Edelsbrunner and Mücke [61]. Fang et al. [68] also employ a gradient method to minimise a cost function, based on the spatial orientation of the tongue, to determine the muscle activity required to attain the prescribed tongue configuration. The Jacobian of the cost function was computed using a perturbation procedure, which would be prohibitively expensive for a highly detailed geometry.

7.2 Muscle activation model

The CE is an active element, so the contractile stress developed by the element, as defined by equation 6.8c, is related to the level of activation α_{M} in each muscle group M. The activation level, a quantity directly proportional to the contractile force, is dependent on the electrical stimulus applied to the muscle.

The dynamics of the active state of the element can be modelled using differential equations [280]. Such a model represents the concentration of calcium ions that controls the extent of muscle contraction. Pandy et al. [208], Pandy [207] present a time-dependent ordinary differential equation, which approximates the activation function under simplified conditions. This is defined, for each muscle M, by

$$\dot{\alpha}\left(t\right) = \frac{1}{\tau_R}\left[1-\alpha\right]\mathrm{u} + \frac{1}{\tau_F}\left[\alpha_{\min}-\alpha\right]\left[1-\mathrm{u}\right] \tag{7.1}$$

where α is the muscle activation level, $\alpha_{\min}$ is the minimum muscle activation level and $\mathrm{u} = \mathrm{u}\left(t\right) = \{0,1\}$ is the net neural control signal to the muscle. This description of muscle activation does not account for the differing degrees of maximal muscle contraction determined by signal frequency. With the chosen material parameters, the zero strain stiffness of the matrix model accounts for the resting muscle tone [29], thus the appropriate value of $\alpha_{\min}$ is zero. Section 7.3 further discusses the excitation or neural input, u, to each muscle family.

Although it can be solved directly using the two possible values of u and the temporal evolution of its value for each muscle, in practise equation 7.1 is solved using a backward Euler method. The activation level at the current time is given by

$$\alpha_t = \frac{\alpha_{t-1} + q\left(\mathrm{u}\right)\Delta t}{1 + p\left(\mathrm{u}\right)\Delta t} \tag{7.2}$$

with the scalar functions

$$q\left(\mathrm{u}\right) = b\cdot\mathrm{u} + c \quad , \quad p\left(\mathrm{u}\right) = d\cdot\mathrm{u} + e$$

and values

$$b = \frac{1}{\tau_R} - c \quad , \quad c = \frac{1}{\tau_F} \quad , \quad d = \frac{1}{\tau_R} - e \quad , \quad e = \frac{\alpha_{\min}}{\tau_F} \quad .$$

The state of contraction of the muscle depends on the frequency of the electrical impulse transmitted to the muscle [78]; the concept is illustrated in figure 2.15. Maximal muscle activation, where the muscle becomes tetanised, requires a high impulse frequency, while a low impulse frequency results in a lower force of contraction. Regular motions of the tongue do not require extreme forces to be generated by its muscles; this statement is confirmed computationally in section 10.1.

Since the contraction model collectively described by Martins et al. [171] and Pandy et al. [208] does not cater for this concept, we decompose the peak contractile stress into two components, namely

$$T_0^{\mathrm{c}} = T_0^s\, T_0^{\max} \quad . \tag{7.3}$$

Now $T_0^{\max}$ is the absolute maximum isometric stress that can be produced by the muscle and $T_0^s \in [0,1]$ is a scaling factor specified for each muscle M that reduces the maximum contractile stress that can be developed. The product of this scaling factor and the muscle activation level describe the degree of contraction as a fraction of full muscle response (FFMR), namely

$$\mathrm{FFMR} := T_0^s\alpha \quad . \tag{7.4}$$

With this decomposition of the parameters, three noteworthy cases can arise:

1. $T_0^s = 1, \alpha = 1$: The muscle is producing the maximum contractile stress at the given deformation rate.

2. $T_0^s < 1, \alpha = 1$: The muscle is fully activated at a lower impulse frequency. This case describes the asymptotic values of figure 2.15 for the majority of the depicted stimulation frequencies.

3. $T_0^s \leqslant 1, \alpha < 1$: The muscle has not yet developed a maximum allowable state of contraction.

By altering the values of T_0^s, τ_R and τ_F, more precise control of movement is developed by the neural model.

7.2.1 Combination of orthogonal muscle contraction with incompressible matrix

Now that the activation model has been presented, the functioning of the active portions of the muscle model can be demonstrated. Comparison of the active model against examples presented in the literature is provided in appendix D.4. To further illustrate the functioning of internal muscle model, a simple experiment was devised. This problem configuration will be used later to demonstrate further functionality of the tissue and neural models.

A block of incompressible muscle tissue of size $1 \times 1 \times 1\text{mm}^3$, with one vertex at the origin, has a planar motion constraint on the coordinate planes. The other three sides are nominally traction-free, but a provision to impose a traction force on the $\boldsymbol{e}_1$ and $\boldsymbol{e}_3$ faces is made. Three orthogonal internal muscle families, each aligned with a coordinate direction, are embedded and a fourth external muscle[1] inserts into the +y surface of the block from an origin plane 2mm away from the surface. The origin of each external fibre is governed by a spacing rule

$$P_0^O = c_s\, P_0^I \;,\; P_1^O = h + P_1^I \;,\; P_2^O = c_s\, P_2^I \tag{7.5}$$

with $h = 2\text{mm}$ the height above the surface and c_s a spacing constant that controls the angle of insertion (AOI) of the fibre into the surface. The basic geometry is shown in figure 7.1a.

For all cases, the block was discretised into 8^3 equally sized cells. The time-step size was 5ms, with a cumulative time of 500ms, and the activation parameters $\tau_R = \tau_F = 150\text{ms}$ and $T_0^s = 0.1$ for all active muscle groups. Each scenario presented has no prescribed activation histories and nominally no applied traction.

Simultaneous activation of the transverse orthogonal muscle groups leads to motion in the their mutually orthogonal direction. The $\boldsymbol{e}_1$ and $\boldsymbol{e}_3$ aligned fibres are activated by setting $\text{u}_\text{M} = 1$, resulting in the y-displacement depicted in figure 7.1b. The incompressible nature of the material ensures that the displacement must be perpendicular to enforce the preservation of the material volume[2].

[1] In this example, the matrix contribution $\boldsymbol{t}_\text{t}^\text{ext}$ was not included.

[2] This point relates directly to the main topic of this thesis. The human tongue relies on this phenomenon to function correctly and achieve its full range of motion. This experiment demonstrates that the incompressibility of the material is enforced sufficiently well to capture this effect.

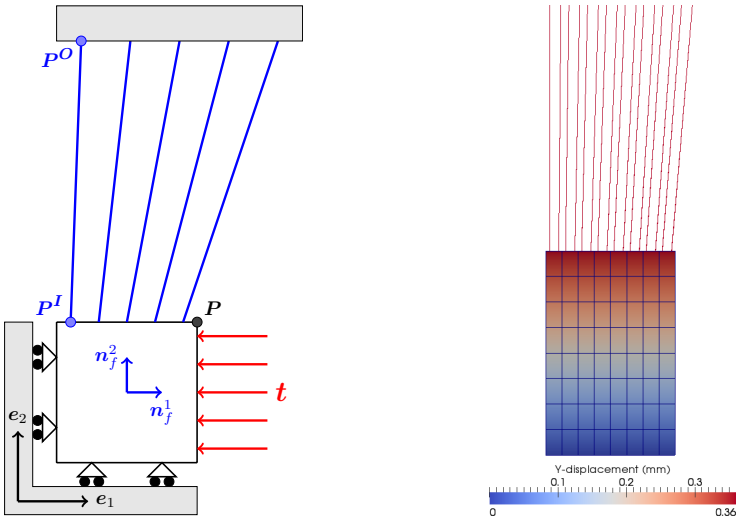

(a) Example problem description: A 1mm^3 block of muscle tissue with deformation controlled by manual activation of the specified muscle groups.

(b) Contraction of the internal muscles aligned in the e_1 and e_3 directions with no pressure-induced traction.

Figure 7.1: Example problem description and result of internal transverse fibre contraction.

7.2.1.1 External muscles

The model presented in figure 7.1a was used further to demonstrate the functioning of the external muscle model and the role of the AOI on the deformation of the surface tissue. In the first case, the incidence angle of the fibres to the surface is made very small by setting the spacing parameter $c_s = 1$, while in the second $c_s = 2$, resulting in a significant AOI.

The result of external muscle contraction in the two configurations is shown in figure 7.2. It demonstrates that a displacement field similar to that depicted in figure 7.1b can be achieved using an anatomically different configuration. The lateral displacement of the upper surface in the second case is substantially larger than the first due to the greater AOI and thus an increased tangential component of traction at the surface. It was observed that, due to the nonlinear muscle force-length relationship, the final contractile stress distribution in the external fibres is less uniform as the AOI increases. This results in a noticeable variation in vertical displacement of the surface, as the fibres closer to the axis planes are significantly shorter than those at the edge of the body. The central fibres thus achieve a lower value for λ_c than the peripheral fibres as the surface displaces vertically.

7.3 Control of neural input signals

During a cycle of inhalation and exhalation, pressure within the airway fluctuates and distorts the soft tissue of the oropharynx, thereby altering the airflow within the upper airway. In response to this, various muscle groups contract and relax in order to minimise movement of the soft tissues and a blockage of the airway as a consequence.

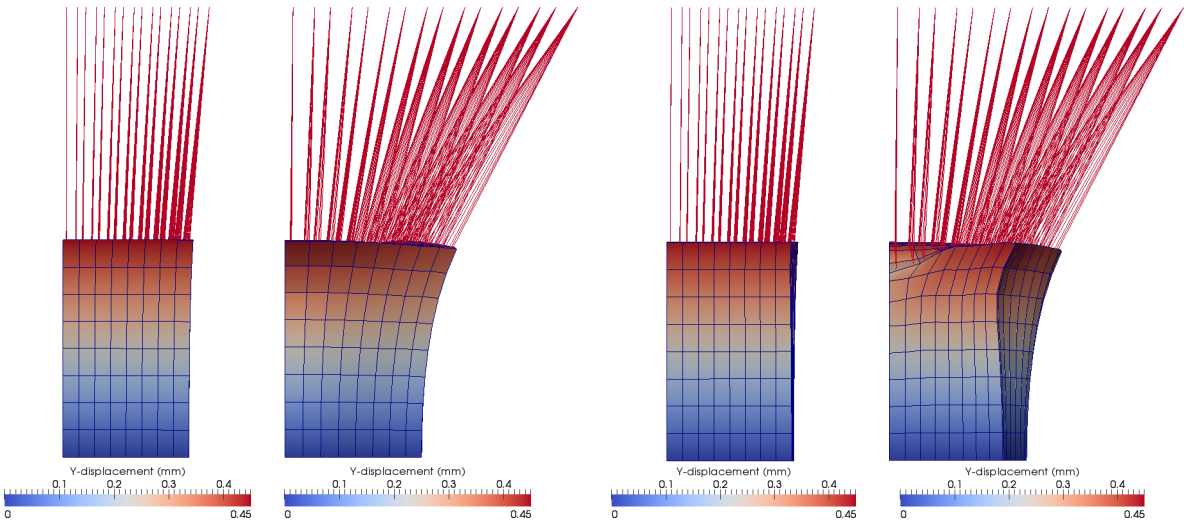

(a) $c_s = 1$: View of traction-free surface

(b) $c_s = 2$: View of traction-free surface

(c) $c_s = 1$: View of symmetry plane

(d) $c_s = 2$: View of symmetry plane

Figure 7.2: Contraction of external muscles at differing AOI to the insertion surface. Increase of insertion angle results in greater lateral displacement of insertion surface and prominent length-effects. Results are shown at $t = 500$ms.

In a healthy subject, the tongue is held forward and down in the mouth throughout the respiratory cycle. Cheng et al. [38] observed a posterior displacement of less than 2mm on the distal surface of the tongue during the respiratory cycle. A complex sequence of neural activation in both the GG and other muscles of the HUA is triggered in response to the changing forces acting on the tongue. This autonomic response with the muscular tissues is mediated primarily through the action of the GG; and a very distinct pattern of electrical activity can be observed in EMG readings of the GG during any respiratory cycle [3, 165, 261, 221, 10].

To accommodate changing forces acting on tissues due to posture, intra-airway pressures, muscular contraction and the spatial position of the tissues, muscle input and activation levels cannot be known *a priori*. In the case of OSA, it is considered that muscle activation, particularly for the tongue, depends on several factors:

Desired motion or configuration: Specific muscles contribute to specific motions of the tissues. To achieve this motion, a muscle or combination of muscles must be recruited to displace the tissues as necessary.

Current position and state of activation of the muscle: If the tissues are positioned unfavourably, conceivably it may be impossible for a muscle to produce active contraction (by virtue of the length of the CE), necessitating some other combination of muscles first moving the body into an optimal position. Additionally, and hypothetically, should an antagonistic muscle body be highly activated, then plausibly either this would need to be deactivated in order to prevent resistance to motion or the primary muscle would be required to have a greater contractile force than antagonistic muscle body.

Previous activation history: The rate of change of activation level is a function of the current activation level. There is a lag between the initial signal to a completely inactive muscle and the time at which it becomes tetanised. This may affect the ability of the tissue to respond in the desired manner with respect to the stimulus.

Sleep state: Muscles have been shown to respond differently when a patient is asleep compared to when

awake. This is demonstrated in data highlighted in section 2.6.

The section that follows details the mathematical descriptions of two points salient to the problem of the moving soft tissue bodies, and a method for determining the appropriate combination of active muscles to produce a prescribed motion during complex loading conditions.

7.3.1 Control of spatial orientation of soft tissues

Proprioception provides a physiological mechanism for an awareness of the spatial orientation of the body's tissues without processing visual data. Thus the body is aware of the configuration of the tongue at all times and is able to recruit the necessary muscles to perform a task. Coupled with this is the learned information regarding which muscles should be used to carry out the given task optimally in terms of speed and energy expenditure.

7.3.1.1 Spatial control function

An alternative to the methods described in the literature for continuum models is the minimisation of a spatially-dependent function similar to those used for forward kinematic models. This hinges on the idea that there exists a combination of muscles that, when activated simultaneously, move the tissues into an orientation close to that specified by a position-dependent function. Due to the complexities of the model, namely the highly nonlinear material models and the geometric complexity, no guarantee of such a solution is assured. However, it is hypothesised that a suitable combination of muscles could be activated to produce a spatial configuration close to the desired state.

The idea of mimicking the proprioceptive capabilities of the tongue was explored by capturing information regarding the current three-dimensional position of the surface of the tongue in relation to the desired position of those points. The resulting motion is dependent on the action of the muscles whose selection is variable, and seemingly a consequence of the current orientation of the tongue. Using this method, a simplified form of proprioception thus would assist in the tongue predicting the consequence of muscle activation before it is performed and thus precisely controlling the motion of the tongue through space.

In general, an objective function that defines this motion (or lack there-of) is

$$\mathbf{O}^{\varphi} = \min\left[f^{\varphi}\left(\boldsymbol{x}, \{\mathbf{u}\}, t\right)\right] \tag{7.6}$$

where the spatial function, influenced by the set of neural signals $\{\mathbf{u}\}$, is defined by

$$f^{\varphi}\left(\boldsymbol{x}, \{\mathbf{u}\}, t\right) := \sum_{p} \left\| w_p \left[\boldsymbol{x}_p\left(\boldsymbol{X}_p, \{\mathbf{u}\left(t\right)\}, t\right) - \overset{\star}{\boldsymbol{x}}_p\left(\boldsymbol{X}_p, t\right)\right] \right\| \quad . \tag{7.7}$$

This function provides a measure of the distance of a number of points $\boldsymbol{x}_p$ away from their respective goal positions, scaled by a weighting factor. The weighting factor introduces a method to place greater significance on the accuracy of some points over others. The standard choice $w_p = 1$ was made for all control points unless explicitly stated.

For the simulation of breathing in particular, equation 7.7 was specified such that a number of points on the surface of the soft tissues were to remain as close to their original position as possible; that is, we seek

position maintenance. The objective function was therefore chosen to be one that is to keep the tongue in its reference state, that is $\overset{\star}{\boldsymbol{x}}_p(\boldsymbol{X}_p, t) = \boldsymbol{X}_p$. However, the minimisation of such a function does not ensure that an energetically optimal solution is found. To account for this, we introduce a second objective function in section 7.3.2.

7.3.2 Minimisation of energy expenditure

The problem of energy minimisation has been considered in the context of one-dimensional skeletal models. Neglecting constraints not valid for this work, an energy minimisation parameter is presented by Epstein and Herzog [64], Herzog and Binding [102] as

$$\phi = \sum_{\mathrm{M}} \left(\frac{F_{\mathrm{M}}}{\mathrm{a}_{\mathrm{M}}} \right)^{a} = \sum_{\mathrm{M}} \sigma_{\mathrm{M}}^{a} \tag{7.8}$$

with the exponent $a \geqslant 1$ a value debated in the literature. Bhargava et al. [20] provide a phenomenological model describing the total energy expenditure rate during contraction by a decomposition into physically motivated components. Their description,

$$\dot{E} = \dot{A} + \dot{M} + \dot{S} + \dot{B} + \dot{W} \quad , \tag{7.9}$$

includes contributions from activation heat rate, maintenance heat rate, shortening heat rate, basal metabolic rate and work done during shortening. The contractile work done was defined as

$$\dot{W} = f^{\mathrm{c}}\left(L_{\mathrm{c}}, \dot{L}_{\mathrm{c}}, \alpha\right) \dot{L}_{\mathrm{c}} \tag{7.10}$$

where L_{c} is the length of the muscle and F^{c} is a contractile force function.

Inspired by the description given by Bhargava et al. [20], a continuum description of the muscle work rate was developed. It was assumed that, given a small enough time-step, the contribution from the work component of equation 7.9 dominates and the other terms could be neglected.

Minimisation of the total contractile work is the same as minimising the total contractile work done for a specified time-step for a problem discretised in time. So, for each muscle M

$$\min\left[W_{\mathrm{c}}\right] = \min\left[\int_t \dot{W}_{\mathrm{c}}\, \mathrm{d}t\right] \equiv \min\left[\textstyle\sum_t \dot{W}_{\mathrm{c}}^{t} \Delta t\right] = \displaystyle\sum_t \min\left[\dot{W}_{\mathrm{c}}^{t}\right] \Delta t \quad . \tag{7.11}$$

To achieve this, we define an objective function

$$\mathbf{O}^{\dot{W}_{\mathrm{c}}} = \min\left[f^{\dot{W}_{\mathrm{c}}}\left(\boldsymbol{x}, \dot{\boldsymbol{x}}, \mathrm{u}\right) \right] \tag{7.12}$$

in terms of a work rate function. The function to be minimised is presented below after a short digression, as a brief review of the source of energy required to institute motion is necessary to motivate its form.

Length change of the muscle and thus the sarcomere CE is always a mechanically based mechanism. However, chemical energy in the form of ATP is required to break and reattach cross-bridges (briefly discussed in section 2.5.2.1 and detailed in Chapman and Gibbs [36]). The state of the muscle at the time when CE length change occurs gives insight into the sources of energy that induce the motion:

1. $\alpha = 0$: No cross-bridges are active or attached, meaning that the CE is a free sliding element and λ_{c} can change freely with the change in λ_{f}. No chemical energy (from the muscle itself) is required to institute any length change.

2. $\alpha > 0$: Cross-bridges are active and chemical energy is required to break bonds between myosin heads and actin filaments before length change can occur. Chemical energy must be expended once more to reattach cross-bridges. In this state, the contractile element may be lengthening or shortening depending on the neural stimulus:

   (a) $\dot{\lambda}_c < 0$: Contraction of the CE occurs. Mechanical energy is expended by the muscle during the power stroke of the cross-bridge cycle.

   (b) $\dot{\lambda}_c > 0$: Elongation of the CE occurs. After the cross-bridges are broken, an external source (e.g. tissue elasticity or an active antagonistic muscle) expends energy causing a change in the relative position between the myosin and actin filaments.

Based on the above, from continuum principals, the mechanical work rate for any muscle group M can be derived. The full derivation, presented in appendix C.2, is summarised here. Starting from equation 3.45, the work rate for the muscle tissue can be decomposed into the volumetric, matrix and fibre contributions. The power due to fibre contributions,

$$\dot{W}_f = \int_{\Omega_0^f} \phi_f \boldsymbol{\tau}_f : \boldsymbol{l} \, d\Omega_0^f \tag{7.13}$$

can be reduced to the scalar computation

$$\dot{W}_f = \int_{\Omega_0^f} \phi_f T_f \dot{\lambda}_f \, d\Omega_0^f \tag{7.14}$$

using the definition of the fibre stress (equation 6.6), the transformation of fibre elements (equation 3.20) and the identities

$$(\boldsymbol{F}\boldsymbol{N}_f)^{\cdot} = \dot{\boldsymbol{F}}\boldsymbol{N}_f = \dot{\lambda}_f \boldsymbol{n}_f + \lambda_f \dot{\boldsymbol{n}}_f \tag{7.15}$$

$$1 = \boldsymbol{n}_f \cdot \boldsymbol{n}_f \quad \Rightarrow \quad 0 = \boldsymbol{n}_f \cdot \dot{\boldsymbol{n}}_f \quad . \tag{7.16}$$

The Hill stretch (equation 6.7b) and stress (equations 6.3 and 6.4) decompositions are used in conjunction with the time derivative of the fibre stretch with

$$\dot{\lambda}_f = (\lambda_s \lambda_c)^{\cdot} = \dot{\lambda}_s \lambda_c + \lambda_s \dot{\lambda}_c \tag{7.17}$$

to produce the final result that the contributions of the Hill three-element components to the fibre work rate are

$$\dot{W}_f = \underbrace{\int_{\Omega_0^f} \phi_f T_p \lambda_f \dot{\lambda}_f \lambda_f^{-1} \, d\Omega_0^f}_{\dot{W}_p} + \underbrace{\int_{\Omega_0^f} \phi_f T_s \lambda_f \dot{\lambda}_s \lambda_s^{-1} \, d\Omega_0^f}_{\dot{W}_s} + \underbrace{\int_{\Omega_0^f} \phi_f T_c \lambda_f \dot{\lambda}_c \lambda_c^{-1} \, d\Omega_0^f}_{\dot{W}_c} \quad . \tag{7.18}$$

Motivated by the argument in the paragraphs above the derivation of equation 7.18, a modification of the CE

work rate is made. The active mechanical contribution to contractile work is defined as[3]

$$\dot{W}_{\mathrm{c}}^{\mathrm{A}} := \int_{\Omega_0^{\mathrm{f}}} H\left(\dot{\lambda}_{\mathrm{c}}\right) \cdot \phi_{\mathrm{f}} T_{\mathrm{c}} \lambda_{\mathrm{f}} \dot{\lambda_{\mathrm{c}}} \lambda_{\mathrm{c}}{}^{-1} \, \mathrm{d}\Omega_0^{\mathrm{f}} \quad , \quad H\left(\dot{\lambda}_{\mathrm{c}}\right) = \begin{cases} 1 & \text{if} \quad \dot{\lambda}_{\mathrm{c}} < 0 \\ 0 & \text{if} \quad \dot{\lambda}_{\mathrm{c}} \geqslant 0 \end{cases} \tag{7.19}$$

where the function $H\left(\dot{\lambda}_{\mathrm{c}}\right)$ is similar to the discrete form of the heaviside function. Note that the contractile work rate is always negative as energy is expended by the muscle to produce a mechanical motion only if contraction occurs. Therefore, minimisation of the function

$$f^{\dot{W}_{\mathrm{c}}^{\mathrm{A}}}(\boldsymbol{x}, \mathrm{u}) := -\sum_{\mathrm{M}} \dot{W}_{\mathrm{c}}^{\mathrm{A}}\left(\lambda_{\mathrm{f}}, \lambda_{\mathrm{c}}, \dot{\lambda}_{\mathrm{c}}, \alpha, \mathrm{u}\right) \tag{7.20}$$

results in the least amount of mechanical energy being expended by the specified collection of muscles actively involved in the production of the desired displacement configuration.

7.4 Genetic algorithms with multi-objective optimisation

A number of alternative strategies exist that can be employed to simultaneously minimise equations 7.6 and 7.12. As both of these functions depend on $\alpha(\mathrm{u})$, direct minimisation of the problem, such as that implemented by Stavness [264] is possible. However, as noted by Fang et al. [68], it is challenging to describe an analytical relationship between these functions as the interplay between the tongue configuration and muscle activation is complex.

For this study, a customised GA [88, 89, 182, 309, 98] was implemented to optimise the active muscle set based on several conditions. This choice of solution method was made as it is relatively simple to describe and implement the problem and conditions in the framework of a GA. It has been shown to be a suitable choice for constrained and unconstrained uni- and multi-objective optimisation of nonlinear general [150, 194] biological [158, 35, 140, 37, 321] engineering problems.

Other metaheuristic methods, such as random hill-climbing, neural networks [11] or particle swarm optimisation could be utilised, and, like GAs, these require careful configuration in terms of evolution parameters and weighting factors. Swarm methods, however, rely on having a large number of sample points, which made them too computationally expensive to be utilised in this application. Less suitable are gradient methods, such as Newton and conjugate-gradient methods, Kuhn-Tucker theory and constrained optimisation [145, 19] as these rely on the calculation of derivatives with respect to the the functional parameters. Due to the multiple levels of nonlinearity of the given problem, this was considered too difficult a task to perform analytically and expensive to approximate by perturbation methods.

[3] It is noted that the potential sign change in the contractile work rate function as the difference between the muscle performing work on the system (negative work rate as the CE shortens) or the system expending energy to lengthen the CE (positive work rate). We need to remember that a positive work rate does not imply work being put back into the muscle resulting in a cumulative increase in muscle chemical energy - energy is required to make cross-bridges or break them, both of which occur during lengthening or shortening of the CE. For this reason, we must discard quantities involving a positive work rate in order to ensure that we keep track of the energy expended by the muscle during contraction to produce motion. A more complete model of the actin-myosin complex could be used to create a more accurate description of the energy expenditure of CE element length change. Such a model could be based on the statistical distribution moment model [324] which could be used to relate the number of broken and reattached cross-bridges to the quantity of chemical energy involved to alter the state of the cross-bridges, and/or the forementioned work of Bhargava et al. [20].

7.4.1 Background

Genetic algorithms mimic the evolutionary processes of selection and recombination to probe a search space for the optimum combination of input parameters to minimise a selected function [309]. Therefore, they fall into the category of metaheuristic evolutionary algorithms.

The fundamental formula of a Genetic algorithm, depicted in algorithm 2, is the following:

Algorithm 2 The genetic algorithm. The unique genome id's are indicated in yellow and their evaluated score in green. The genes, represented by the sequence of blocks, have a binary representation and represent traits that are either "on" (red) or "off" (blue).

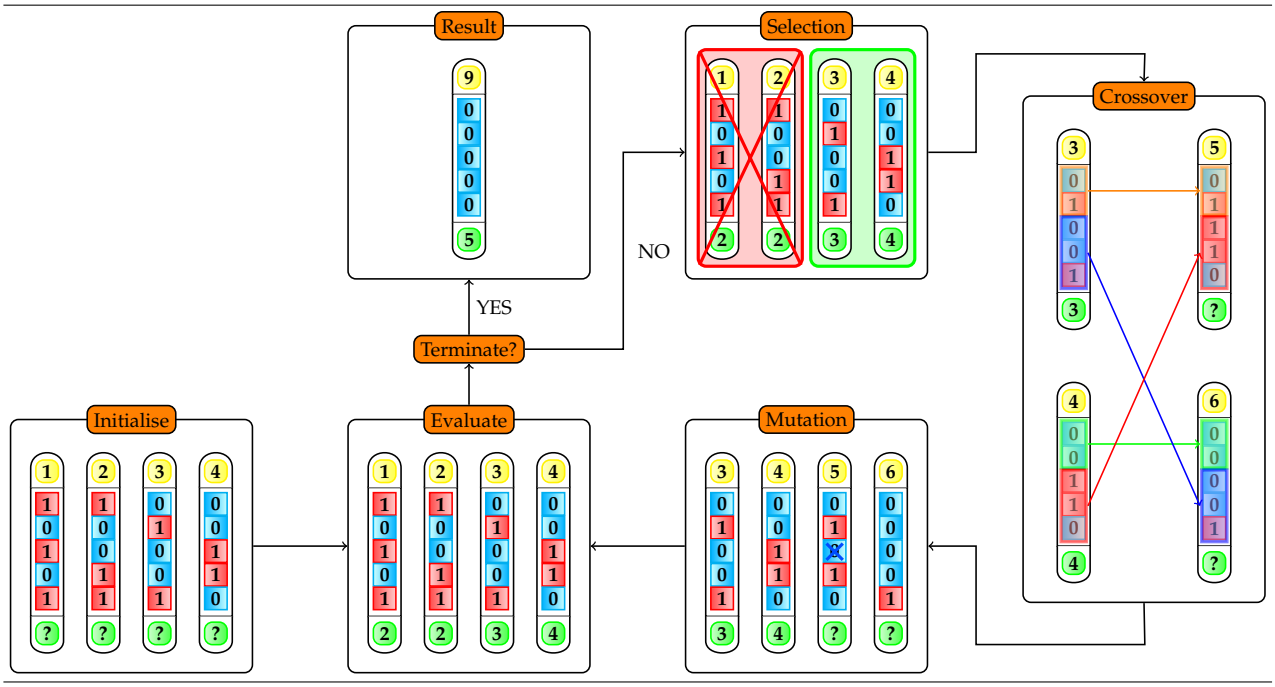

An initial population of candidate solutions, each known as a genome, is produced. The genome is decomposed into a number of genes, each of which is interpreted as a trait that is to be optimised. This first group of candidates, and each subsequent collection of genomes that are generated form part of a generation. Given a generation of candidate solutions, each solution is tested and evaluated according to a prescribed objective function. The candidates are ranked according to their fitness and the best solutions from the current generation are predominantly used to produce the next generation, which will contain a mixture of the best traits of the previous generation. However, some deviation away from the "ideal" hierarchical traits evolved from the initial population is allowed through the process of mutation and a random statistical chance that a poorer candidate may be involved in the breeding process. The description of the methods used to describe, solve and optimise the muscle selection problem is given in section 7.4.2.

7.4.1.1 Mathematical traits

The term *search space* is used to describe the total number of possible combinations of input parameters wherein an optimum solution lies. For a binary input set with M parameter parameters, the search space is a hypercube of the size 2^M, with each sampling point lying at a corner of the hypercube. Thus, for the example of 4 muscle families a total of 16 combinations exist, each defined at the corners of a four-dimensional cube

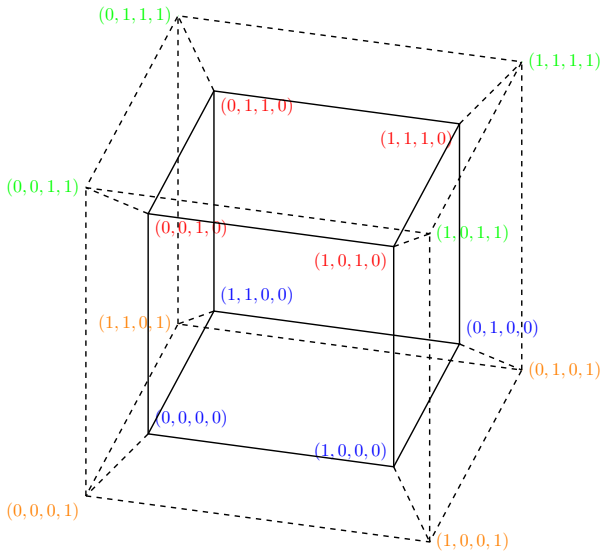

Figure 7.3: Possible solutions for a binary genome on a 4-dimensional hypercube. Increasing the complexity of the genome populates the boundary and interior of the hypercube with additional candidate solutions, exponentially growing the size of the search space.

as shown in figure 7.3. The search space expands exponentially with each additional parameter that is to be tested[4].

Evolutionary algorithms leverage the theory of *implicit parallelism* [309] to find the solution minima while probing a reduced sample of solution candidates. In the process of evaluating a population of candidate solutions, many hyperplanes are sampled when each genome is tested. Statistical data on the global effectiveness of each hyperplane in producing a fit genome is developed as the size of the tested population is increased. The recombination process ensures that these effective hyperplanes become and remain dominant in the process of evolution. Given a sufficiently adequate evolution time and the correct evolution properties, GAs have been proven to demonstrate convergence on the global solution [237, 97].

7.4.1.2 Evaluation, selection and recombination operators

Evaluation refers to the generation of a value representing the candidate solution's viability to be the function minimiser. This value, or score, is determined by inputting the candidate into the objective functions, and in the case of having multiple objectives, producing numerous scalar values that are combined to form a single value taken as the score. Typically the candidate in the final generation with the lowest score is considered to be the overall best solution.

The process of evolution relies on the two recombination operators, crossover and mutation, which permute and alter the characteristics of a selection of the previous populations to produce viable candidates that evolve as to be global minimisers of the objective function. The steps used to produce a new generation of candidates are detailed here.

The selection process determines which members of the previously evaluated generation are brought forward to form the basis of the next generation. Generally, there is a bias towards the fittest candidates being used,

[4] Baker [11] discusses the difficulty associated with this issue with regard to sampling the effect of muscle contractions within the tongue.

as especially after a number of generations, they demonstrate dominant traits that could produce optimal solution. However, the inclusion of a less-viable candidate may assist in preventing convergence on a local minima. Multiple selection methods exist, each with different properties suiting different applications.

Recombination occurs after selection, and the previous generation is discarded as it is assumed that the new generation will always produce a more viable candidate than the previous. In some cases, this may not be an ideal choice and *elitism* may be a preferred option. Elitism ensures that the overall best candidate that has been evaluated within the entire population is always brought forward as a member of the next generation. Should the global optimum be produced early on in the evolution process, elitism would ensure that this solution is preserved.

The *crossover* (or cross-breeding) procedure, where the traits from two parent genomes are combined to form children, is first applied. In one-point crossover (which is depicted in algorithm 2), a crossover point is randomly selected and the genes above the point from one parent is mixed with those below the point on the second parent to produce a new genome, and the remaining genes in the parents are combined to form a second candidate. However, one-point crossover cannot necessarily produce all solution combinations [182], and two-point crossover, where an internal segment of genes is swapped between parents, or other crossover schemes, may be appropriate. The parameterised uniform crossover procedure [182] performs an exchange of parental traits on a gene-by-gene basis, with the parent from which the trait will be inherited being chosen on the basis of statistical probability.

Mutation is a low-probability operator that modifies individual genes of the children produced as a consequence of crossover. Evaluated on a per-gene basis, it presents an opportunity for the value of a gene to be modified to produce some variation in the course of the solution evolution. For example, in a binary genome the value of the gene would be flipped. The rationale behind this procedure is to perturb the course of the solution evolution and prevent convergence on a local minimum as opposed to the global minimum.

7.4.2 Implementation and application to the selection of an active muscle set

It is desired that the solution of the class of nonlinear functions of the form

$$\mathbf{O} = \min\left[f\left(g\left(\mathrm{u}_1, \mathrm{u}_2, \ldots, \mathrm{u}_\mathrm{M}\right)\right)\right] \tag{7.21}$$

be found. Here, the nonlinear composite function $f \circ g$ describes some scalar measure of the performance of the input parameters u_M. In this work, the parameters u_M are interpreted as the binary neural input to each muscle fibre family[5]. The inner function g is one that has a highly nonlinear evolution in space and time. Evaluation of the objective function, $\mathbf{O}$, requires solving the global displacement problem, g, for the given neural input signals and subsequently evaluating f based on the result of g.

The prevalence of the phenomenon of *epistasis* [309], the interaction between parameters, ensures that the parameters cannot be evaluated independently. Given the nonlinearity of g, it is expected that epistasis may play a significant role in a muscle problem involving interweaving muscle fibre families, as the roles of several muscle groups may overlap given a certain configuration and desired motion of the tissues. Furthermore, given their interaction through tissue deformation and the nature of the governing equations of

[5] It would be ideal to solve for a physically appropriate spectrum of $\mathrm{u}, \tau_R, \tau_F$ (or simply α) as, through a variation of impulse frequency, the control mechanism of muscles is much finer that modelled here. However, given the framework presented here, this problem would be exceptionally expensive to evaluate, requiring computational power well beyond the capabilities of modern computers.

the Hill-elements, the performance of each spatially-independent fibre would be related indirectly to the configuration of the others.

7.4.2.1 Implementation

A binary GA, implemented using the open-source library *GAlib* [295], was used to predict a set of neural input signals $\{\mathbf{u}\}$ such that the objective function, described in its complete form in section 7.4.2.2, was minimised at all evaluation time-steps. The elitist and non-deterministic (stochastic) algorithm selected from *GAlib* for use in this work is based on the work of Goldberg [88]. The initial population size was determined based on the size of the active set to be evaluated.

One of the key choices made in the implementation was the maximisation of genetic variation between individuals of a particular generation. A uniform crossover procedure with high probability of crossover and mutation was therefore used to achieve this. The choice of constants used for the probability that crossover or mutation would occur were 0.5 and 0.1 respectively.

7.4.2.2 Multi-objective optimisation

It is desired that the functions presented in equations 7.6 and 7.12 (utilising equations 7.7 and 7.20) either be simultaneously minimised, or that a solution that is an adequate compromise between minimising both be found. Reformulating equation 7.21, the composite problem is described by

$$\mathbf{O} = \min \left[\sum_o w^o \cdot \overset{\star}{f}{}^o \left(g^o \left(\mathrm{u}_1, \mathrm{u}_2, \ldots, \mathrm{u}_\mathrm{M} \right) \right) \right] \quad , \tag{7.22}$$

with a linear scaling of weights[6] $\sum_o w^o = 1$ selected. The first component of the objective function, g^1, requires the determination of the actual displacement of the control points. Second objective function, g^2, requires the evaluation of local parameters stored at each calculation point containing active fibres.

A difficulty in utilising these two functions simultaneously is that their nature is very contrasting. Firstly, they have different units (length vs power) and the scale of the values returned by the two outer functions f^o may not be of the same order. Secondly, they play antagonistic roles in the promotion of muscle activation.

Ultimately, the solution to the problem is to non-dimensionalise the scores by transforming all $f^o \Rightarrow \overset{\star}{f}{}^o$ for all quantities to be considered. This leaves comparable scores since they now have the same units. A weighting factor w^o is then applied to the scores and the weighted scores cumulated to a final total that is interpreted as the solution fitness. To non-dimensionalise, a scaling factor for each function is required. Sensible factors include the $\mathcal{L}^2$-norm and ∞-norm. Choosing the infinity norm will ensure that all values lie in the range $[0, 1]$. However, it leaves an open range $(0, 1]$ for the minimum score. Additionally, there is no guarantee that the values are distributed in the range such that the choice of weighting factor is at all appropriate.

A further issue for consideration is that the norm cannot be known *a priori* but rather can only be developed as the search space is tested. To this end, a sliding scaling rule was developed where, for each objective

[6] A number of methods could be used in the process of multi-objective optimisation with a GA. Pareto optimisation [98], where the front providing the potential candidates for global minima is resolved, is a popular method and would be ideal for this purpose. However, resolving the front requires a large number of evaluations and therefore more judicious use of computational resources.

function o, the following rule is applied to each element i of the set of calculated scores f:

$$\overset{\star}{f}^{i} = \frac{f^{i} - \boldsymbol{f}_{-}}{\boldsymbol{f}^{+} - \boldsymbol{f}_{-}} \tag{7.23}$$

where $\boldsymbol{f}_{-}$ and $\boldsymbol{f}^{+} = \|\boldsymbol{f}\|_{\infty}$ describe the minimum and maximum elements in $\boldsymbol{f}$. This leaves all scores for each objective function in the range $[0, 1]$ with the best score always equal to zero and the worst with a value of unity. The distribution of values over the range is expected to be more regular, with an easier distinction between the optimal result and other contenders.

One point to consider when continuously re-evaluating the scores is how each relates to the selection of the best genome when elitism is considered. During elitist selection for the next GA population, the current genome with the best score is chosen. However, since the actual score is continuously re-evaluated with each new genome, a genome that has a non-constant score, but which may change at a later evaluation, is selected. This fact is irrelevant, as elitism chooses the best genome against the current population of genomes and these are all scaled by the same factors. Therefore, relative to one another, the ranking of each genome in a specific generation will remain constant and the final result will be the same as if the final scaling factors were predetermined for a given time-step and applied up-front. However, the rank of the elite genome relative to a new generation is not fixed as the members of the new population are evaluated.

7.4.2.3 Expectation of the results

Presenting the simple case where increasing muscle activation is required, it is shown that the activation parameters could be chosen such that the contractile force can be adequately predicted by this muscle model. The expected result for the muscle activation problem is shown in figure 7.4.

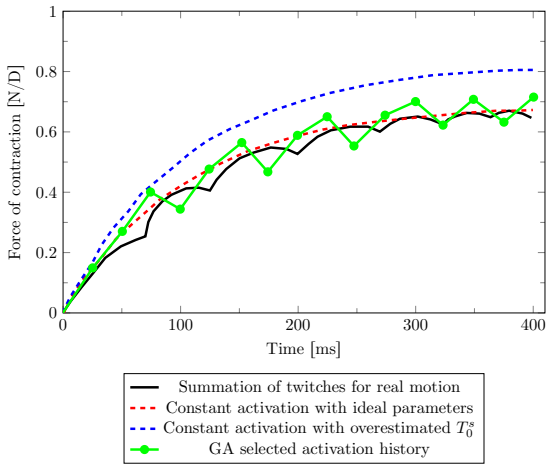

Figure 7.4: GA parameter selection for achievement of optimal activation pattern. Given an overestimated set of muscle characteristics, the GA behaves in a self-correcting manner leading to the evolution of the trend which follows the optimal activation history.

Should some optimisation scheme not be utilised, it is more likely that the over- or under-estimation of the optimum contractile history be deduced *a priori*. However, given an adequate, but not necessarily optimal, selection of parameters, it is assumed (and it will be demonstrated) that the solution provided by the GA will oscillate around these values. In fact, it is required that the parameters (i.e. T_0^s, τ_R, τ_F) provided to

the model reproduce the curve illustrating overestimation, which itself provides the GA with a buffer from which to select a reduced contractile force as the optimum solution. Due to the large number of parameters that would be required to be tuned to match the activation pattern, the probability of exactly reproducing the real activation history is minimal but a trend following the optimal solution is expected to be observed.

However, the selection of weights for the spatial error and work rate minimisation functions has a major role in the obtained result. As previously mentioned, the former function promotes muscle contraction while the latter restricts it, and therefore the accuracy of the trend observed depends on these factors. A balance between the two must thus be maintained: too much emphasis on the former may lead to over-stimulation of various muscle groups (e.g. co-contraction of antagonistic muscles when muscle relaxation would suffice), while increasing the effect of the latter would result in poor spacial maintenance due to sub-optimal muscle deactivation.

7.4.3 Reducing the computational cost

The evaluation process is a costly procedure, as a fully nonlinear, incompressible FEM problem is to be solved for each evaluated combination of muscle signals. Choices made to reduce the number of evaluations and the cost of each evaluation were as follows:

Utilise a binary GA: The leading choice of driving muscle activation with a binary signal constricts the search space to a finite size. Solving for the optimal muscle activation level directly, as opposed to using the neurally-controlled activation model given in equation 7.1, would require searching the bounded space $\alpha_{\mathrm{M}}(t) = [0, 1] \ \forall\, \mathrm{M}$, $\alpha_{\mathrm{M}} \in \mathbb{R}$ at each time-step and would be a prohibitively expensive task.

Simplify the nonlinear problem: Given that an augmented framework for dealing with incompressibility is utilised, only the compressible step is solved using the GA. The displacement solution produced by optimised active muscle set determined by the GA is subsequently refined using the incompressibility scheme. This is a practical solution if the dilatation error produced in the compressible phase of the augmented algorithm is not overly large. In practical cases involving the tongue, the solution produced appears adequate but it was noted that in some cases (such as that demonstrated in section 7.5) the fully incompressible problem must be solved in order to obtain sensible results.

Prevent GA evaluation at each time-step: Given that the GA can accurately predict muscle activation for current time-step due to the smoothness of the loading conditions, it was assumed that this result would be a sensible choice for the next number of time-steps. The GA can then correct the optimal active set at the next evaluation step which, in practise, was separated from the previous evaluation step by only a single time-step.

Prevent re-evaluation of data: The entire history of data and solutions produced by the GA is stored for each time-step. This allows the construction of a look-up table to which the data of each genome can be tested. Should the genome have already been evaluated in this time-step, the solution and scores can be immediately deduced from the history.

Limit the number of generations: A contentious decision was severely limiting the number of generations tested. A value of 5 (as opposed to the norm of > 100 [120]) was chosen for this parameter. It was assumed that the time-evolution of the active set would be continuously corrected by the GA. In practice, this appeared to be the case with the solution becoming viable after the first few time-steps.

Reduce the size of the search space: To reduce the size of the search space, certain muscle groups were excluded from evaluation based on whether the muscle is overall in a tensile or compressive state. It appeared reasonable to assume that muscles in an overall tensile state may assist in returning the tissue to its original position by contracting and returning to their original length, while muscles that are in a compressive state should likely undergo relaxation.

To gauge the state of the muscle, a measure of the average fibre stretch $\bar{\bar{\lambda}}_{\mathrm{f}}$ at the current time was compared to that calculated in the pre-strained reference configuration $\bar{\bar{\lambda}}_{\mathrm{f}}^{0}$. Given a cut-off parameter c_L which made provision for uncertainty in the approximation, it was specified that a muscle be considered to be in a tensile configuration if

$$\bar{\bar{\lambda}}_{\mathrm{f}} \geqslant c_L \bar{\bar{\lambda}}_{\mathrm{f}}^{0} \tag{7.24}$$

where c_L has been heuristically chosen as to minimise the active muscle set, thus reducing computational time, without compromising the result.

Analysing the outcomes of several simulations of the tongue, the heuristic definition of the muscle selection factor was chosen to be

$$c_L\left(\theta\right) := \frac{\theta}{90} c_L^{\min} + \left(1 - \frac{\theta}{90}\right) c_L^{\max} \quad , \tag{7.25}$$

where $c_L^{\min} = 0.98$, $c_L^{\max} = 0.995$ and θ is the angle of incline of the body in degrees (with 0 indicating the supine position and 90 the upright configuration). The volume-weighted average (VWA) stretch value[7] , defined as

$$\bar{\bar{\lambda}}_{\mathrm{f}} := \frac{\Omega^{\mathrm{f}} \int \phi_{\mathrm{f}} \lambda_{\mathrm{f}} L_{\mathrm{f}}^{0} \, \mathrm{d}\Omega^{\mathrm{f}}}{\Omega_0^{\mathrm{f}} \int \phi_{\mathrm{f}} L_{\mathrm{f}}^{0} \, \mathrm{d}\Omega_0^{\mathrm{f}}} \quad , \tag{7.26}$$

was chosen to provide the value of $\bar{\bar{\lambda}}_{\mathrm{f}}$. This calculation required an estimate of the embedded fibre's length as well as the effective volume occupied by the external muscles.

The volume of external muscles was approximated by representing each muscle fibre as a hexahedral entity. Since the length of the fibre was known, the effective cross-sectional area of the muscle was approximated as the area of the face into which it was inserted. The volume was therefore considered the region swept by the cross-section along the fibre length.

The reference local (internal) fibre length L_{f}^{0} was approximated from the computational cell geometry and the fibre orientation using a projection method illustrated in figure 7.5.

A value proportional to the "true" fibre length was determined by projecting the fibre unit vector, defined at each calculation point, from the cell barycentre to the faces of the cell. The geometry of the faces was approximated by four linear triangles, thereby approximating each region of the face as a plane. If the projection of a line emanating from the barycentre along the direction of the fibre intersected with the plane within the boundaries of the triangle, then this point was considered a valid projection point. Once the two face intersection points were found, the norm of their difference in

[7] Possible alternatives that were evaluated include a simple summation calculation point data $\bar{\bar{\lambda}}_{\mathrm{f}} = \frac{\sum_{\mathrm{f}} \lambda_{\mathrm{f}} L_{\mathrm{f}}^{0}}{\sum_{\mathrm{f}} L_{\mathrm{f}}^{0}}$ and the tracking of a set of points within the domain that are collectively representative of the configuration of muscle fibres that constitute a muscle group. Although all of the methods produced identical trends in the results, it was decided that the VWA would provide the most mathematically rigorous result (as it accounted for the volume of influence of the fibre) and was therefore most likely to be more accurate than the other methods.

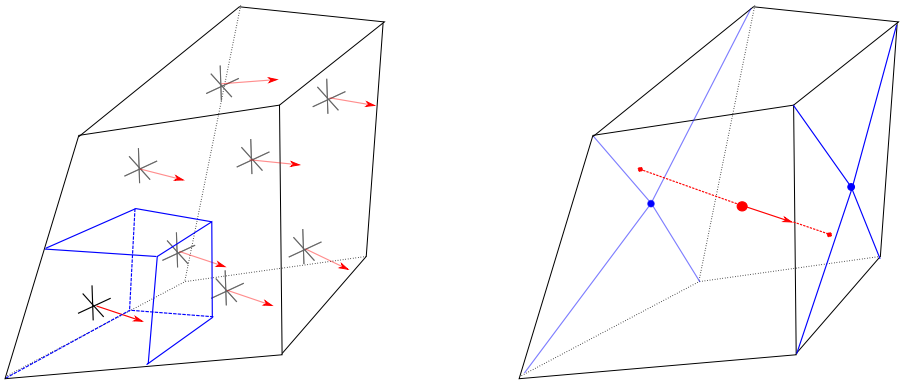

(a) Distribution of fibre data at calculation points for one muscle group. An octant in which the one can assume the fibre direction uniform is highlighted in blue.

(b) Triangulation and projection method used to approximate the fibre length

Figure 7.5: Estimation of local fibre length.

spatial position was considered, due to number and distribution of calculation points, to be twice the length of the fibre. The constant of proportion was chosen based on the assumed region of influence of the calculation point, as shown in figure 7.5a.

7.4.4 Assistance with solution convergence

Given that some of the steps used to reduce computational cost likely destroy the convergence properties of the GA, a number of methods were employed to ensure that a reasonable result was produced after the first few time-steps:

Population initialisation: It was expected that the previous "optimal" solution was a fair approximation to the solution at the current time-step. Such an assumption is appropriate given the smoothness of the material models and loading conditions. The initial generation was thus produced with the previous solution as a member, along with all singular options to evaluate the corners of the hypercube. The corners were evaluated as it was expected the action of certain muscles would be dominant in the solution and the solution thus similar to the previous one. This, in effect, mimics the initial analysis step of the muscle workspace strategy proposed by Dang and Honda [50].

Critical muscles: Experimental data suggested that the action of a few muscles should dominate the solution. Therefore, an *a priori* decision to enforce the evaluation of critical muscle groups, regardless of other filters used to limit the search space size, was made. For the model of the tongue, the components of the GG were tested regardless of the body's configuration.

Elitism: As the number of generations that were evaluated was low, it was ensured that each generation had at least one good reference point from which to produce alternative solutions using the recombination operations. This was to reduce the number of evaluations wasted on poor guesses due to suboptimal recombination.

7.5 Validation of neural model

To demonstrate the capabilities and shortcomings of the GA approach, two illustrative examples based on the problem demonstrated in section 7.2.1.1 are presented and discussed. In both instances, a compressive pressure load described by

$$p = -2500\left(\sin \pi t^*\right)^{1.75} \quad , \quad t^* = \frac{t \mod 2.5}{2.5} \quad , \tag{7.27}$$

resulting in a maximal pressure magnitude of 2500Pa with a period of 2.5s, is applied to the side faces of the block. We choose to monitor the point $\boldsymbol{P} = (1, 1, 1)$ mm on the corner of upper surface and the two specified-traction surfaces. All muscle groups are allowed to activate as necessary in order to prevent motion of the upper surface.

7.5.1 Position maintenance during temporally-dependent pressure load

In this first example only the displacement function is considered. The objective function, given singularly by equation 7.6, is that under the action of muscle contraction four control points located on the corners of the positive $\boldsymbol{e}_2$-face remain in their reference position.

Position control though the selection of neural stimulus was simulated and compared to a fully passive scenario. In figure 7.6a, the evolution of the distance that of corner $\boldsymbol{P}$ from the expected equilibrium position is depicted, along with a trace of the applied pressure.

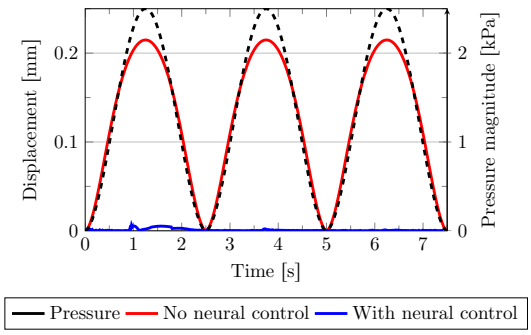

(a) Total displacement of corner $\boldsymbol{P}$

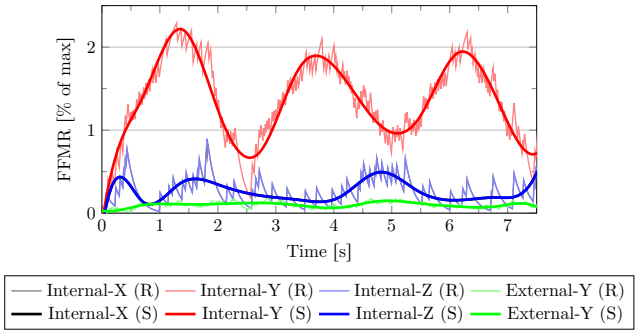

(b) Raw (R) and splined (S) neural response data for internal muscles

Figure 7.6: Active and passive behaviour of a block under a sinusoidal compressive pressure load applied to the $+\boldsymbol{e}_1$ and $+\boldsymbol{e}_3$ surfaces. The maximum compressive pressure magnitude was 2500Pa and $T_0^s = 0.025$ for all internal muscles and $T_0^s = 0.0025$ for the external muscle. Only a displacement objective function was considered.

In the passive case, where the loading causes an extension in direction $\boldsymbol{e}_2$ and compression in $\boldsymbol{e}_1$ and $\boldsymbol{e}_3$, only the matrix and PE of the $\boldsymbol{e}_2$ orientated fibres provide resistance to deformation. Comparison of the passive and active cases demonstrates that the GA was able to maintain $\boldsymbol{P}$ close to its goal position.

The muscle contraction history for the internal muscle groups is shown in figure figure 7.6b. A cyclic response, coinciding with the regularly changing traction load, is present in each muscle group. At the start of

each cycle, the e_2 fibre contracts to oppose the motion generated by the load. However, since control of the developed contractile stress is limited, the e_1 and e_3 muscles co-contract to oppose the excessive force generated in the e_2 fibres. Towards the middle of the cycle, where the load is at a maximum, the e_1 and e_3 muscles deactivate and the e_2 muscle attains a maximum activation level. As the load decreases, a similar activation pattern seen in the beginning of the cycle is present to provide fine position control. At the end of each cycle the activation levels of all muscles are non-zero, thereby locking the cube in its original configuration.

This example demonstrates that the neural model functions as expected. However, the model is reactive to its current state and not predictive in a way that truly mimics the motion control exhibited *in vivo*. It has been observed that, although the results are not repeatable due to the random nature of the GA, the trends in the results are repeatable, as demonstrated here and in chapter 11.

7.5.1.1 Optimising for work rate

In the second example, the problem configuration was the same as before but now both the displacement and work rate objective functions were considered. In order to demonstrate the effect of a bias towards energetic efficiency, a spectrum of weighting options were chosen and sequentially evaluated.

Driving the control model is the decision to contract or relax each muscle group. Figure 7.7 illustrates that signal for contraction of the primary muscle became more sparse as energy conservation is made a priority. In particular, the contractile duration was banded around the time of peak pressure, when displacement would otherwise be greatest.

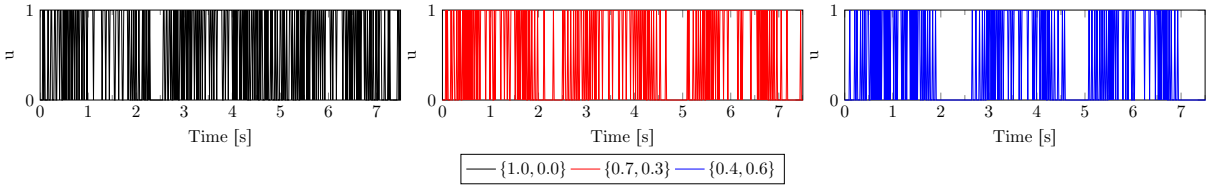

Figure 7.7: Neural activation pattern for the internal e_2 orientated muscle for various weightings of objective functions.

The effect of the weighting on the ability of the block to obtain the desired displacement configuration is illustrated in figure 7.8a. It was observed that shifting the bias from an optimal displacement result to an energetically optimal result produced increasing displacement of the block, of which the underlying cause can be extracted from figures 7.8b and 7.8c.

These figures demonstrate that the e_2 muscle that is primarily used to oppose motion produces less contractile force as the weights shift towards energetic efficiency. Furthermore, the amount of co-contraction of the e_1 and e_3 muscles required as the applied pressure was removed from the tissue was, in general, reduced. This was because, without actively contracting at a particular time-step, the force generated in the CE of the e_2 muscle remained sufficient to resist the applied pressure.

It was observed that there existed a band of weights that produced a similar result for both displacement of the measured point and the predicted optimal muscle contractile force. These weights remained energetically competitive. Utilising weights beyond that band produced nonsensical results as the need for energy conservation dominated and resistance to motion was almost completely ignored. Comparing figure 7.6a to

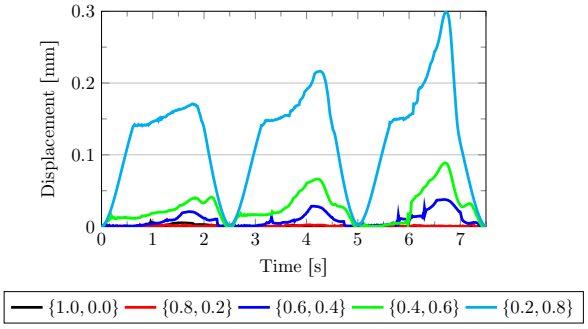

(a) Total displacement of $\boldsymbol{P}$

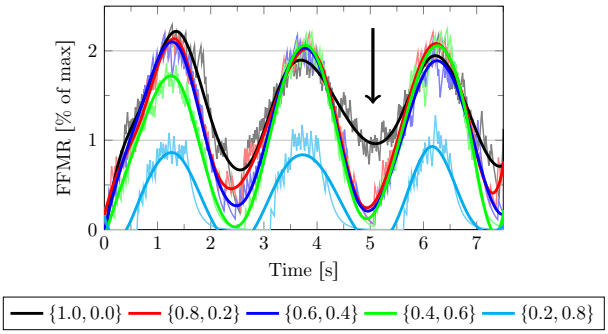

(b) Raw and splined neural response data for $\boldsymbol{e}_2$-aligned muscle

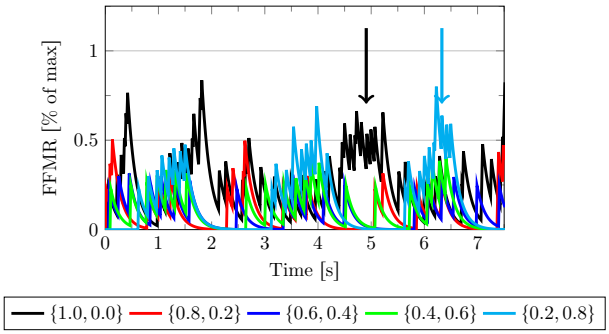

(c) Raw neural response data for $\boldsymbol{e}_1$-aligned muscle

Figure 7.8: Active behaviour of a block with sinusoidal compressive pressure load applied to the $+\boldsymbol{e}_1$ and $+\boldsymbol{e}_3$ surfaces. Both a displacement and an energetic objective function were considered, with the respective weights provided in the legend. With a higher work rate bias, displacement control is lost leading to large deformation of the block. An example of energetically sub-optimal co-contraction of antagonistic muscles is indicated by the black arrows. The blue arrows show an example of antagonist co-contraction contributing towards a poor displacement performance.

figure 7.8a for the weights $\{w^1, w^2\} = \{0.2, 0.8\}$, at the latter stages of the third pressure cycle the displacement of $\boldsymbol{P}$ exceeds that of the purely passive case. In this instance, co-contraction of the $\boldsymbol{e}_1$ and $\boldsymbol{e}_3$ was performed to reduce the rate at which the $\boldsymbol{e}_2$ length changed, thereby conserving energy but leading to inferior overall performance.

An analysis of the cumulative contractile work performed highlights additional characteristics of the control model. Figure 7.9a shows that concurrent with reduced contraction is reduced energy expenditure by the primary muscle. For the most part the same trends were observed for the total contractile work performed in the system, illustrated in figure 7.9b. However, for very low displacement-function weights, the overall energy consumption is far from optimal and may ultimately exceed that resulting from having a greater emphasis on position control. There exist periods of no muscle activation, but also durations of intense but unsustained activation of all muscle groups, resulting in great energy expenditure in these brief periods.

Taking all of the results into consideration, it can be concluded that a reasonable choice of candidate sets for weighting factors are in the range of $\{0.8, 0.2\}$-$\{0.6, 0.4\}$ for this problem. These weights provide a good balance between displacement control and energy expenditure, while maintaining the FFMR trends observed demonstrated by the optimal displacement solution.

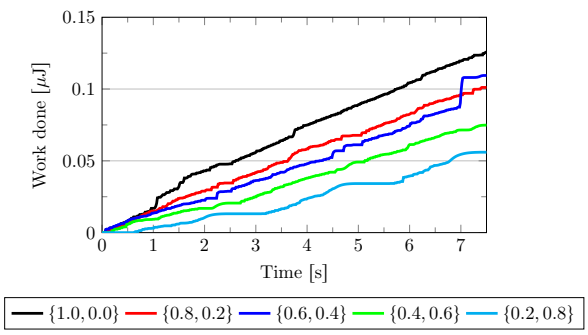

(a) Cumulative contractile work done by the internal e_2 orientated muscle.

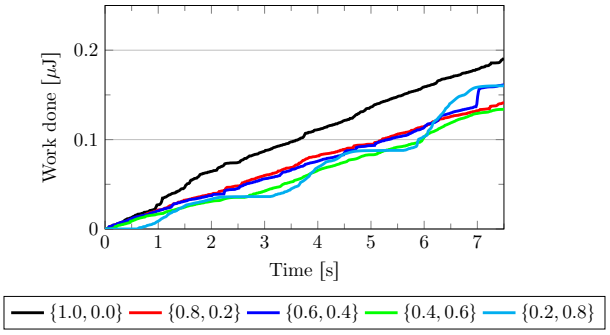

(b) Cumulative contractile work done by all muscle groups.

Figure 7.9: Comparison of energy use during test case for various weightings of objective functions. The integral value of work at time t is estimated as $W_c = \int_0^t \dot{W}_c dt = \sum_{ts=0}^{t} \dot{W}_c{}^{ts} \Delta t^{ts}$.

7.5.1.2 Evaluation of multi-objective optimisation function scaling scheme

A more detailed examination of the efficacy of the linear scaling scheme used for the multi-objective optimisation simulations presented above demonstrates how the optimal selection is made, as well as the nature of the optimal solution to the given problem. Two performance metrics, namely the entirely population scores collected over the course of a simulation and the corresponding best genomes, were examined.

The tested population score data for a non-trivial case was collected and the cumulative data for an entire simulated plotted in figure 7.10. On average, 11.27 of a possible 16 combinations of muscle groups were evaluated at each step, a reduction of 29.6%. It was observed that the scores for the active muscle sets were distributed towards the extremes, with a distinct collection of good and poor choices being evaluated. This established that, on average, a clear selection of potentially good candidates arises from the use of the GA. This said, one must keep in mind that the distribution is made relative to the best and worst selected genome in each population.

Further decomposition of the total scores into the contributions made from the individual objective functions was analysed. These results demonstrate that the displacement criterion generally produces an obvious choice in respect of a good candidate, as the dispersed distribution has very few candidates that fall into the middle-range of scores. However, the work rate objective also has a similar distribution, which is to be expected due to the symmetric arrangement of muscles and the geometry, as well as the uniform distribution and properties of the muscles.

Plotting the decomposition of the scores of the best genome selected at each time-step, it is possible to determine where within the average population the chosen best candidate typically resides. Figure 7.11 shows that, in general, the genome that was considered to be the best candidate exhibited excellent position control and energetic characteristics[8]. Only on rare occasions did the energy minimisation criterion lead to a solution with poor spatial governance traits being selected.

[8] Considering the nonlinearity of the scaling amongst the members of the population, optimality is difficult to define. For example, if no muscles are active, then the score for the work rate function is always zero, i.e. the most energetically efficient choice. However, activating a linearly increasing number of muscle groups does not necessarily result in a linear increase in the objective score, due to the nonlinear nature of the material, the evolution of the body configuration and muscle-muscle interactions.

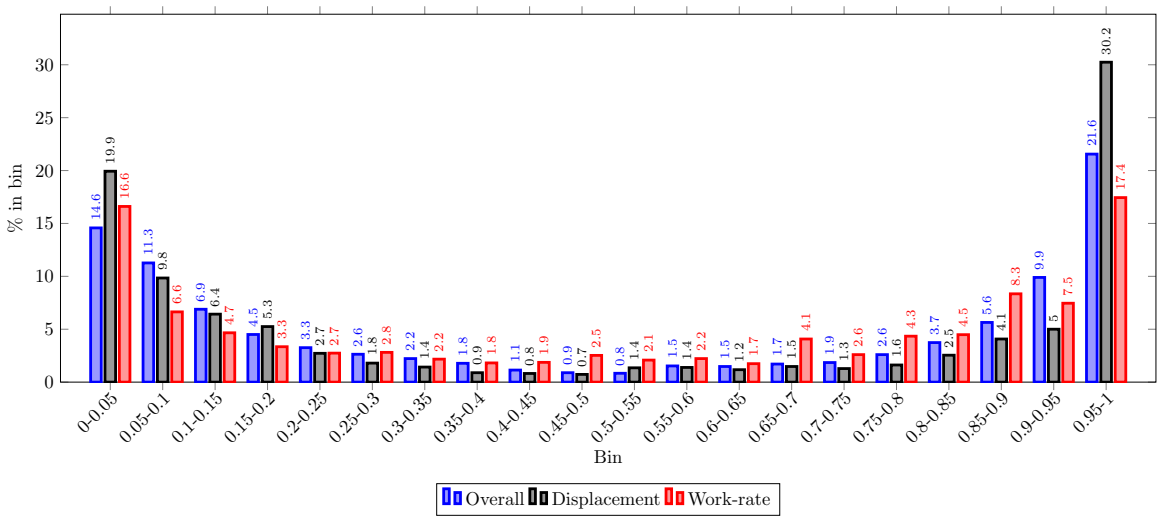

Figure 7.10: Histogram of scores of the evaluated population accumulated over the entire duration of a simulation of a test case. Weights for the displacement and work rate objective functions were 0.7 and 0.3 respectively. The overall score, a linear combination of the individual scores, is determined using equation 7.22.

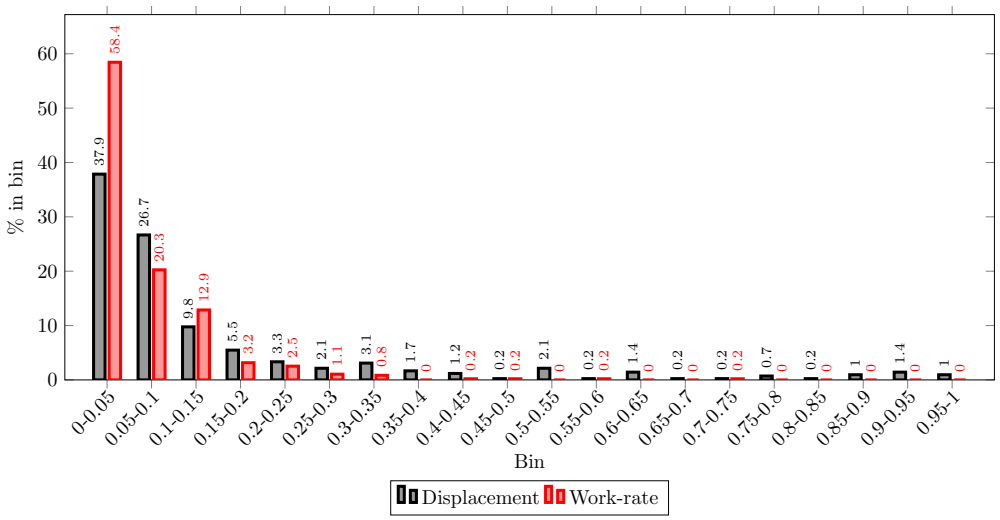

Figure 7.11: Histogram of scores of the best genome accumulated over the entire duration of a simulation of a test case. Weights for the displacement and work rate objective functions were 0.7 and 0.3 respectively. Many of the best candidates chosen with this weighting scheme exhibit excellent position control and energetic qualities compared the alternative candidates evaluated. The few chosen solutions with very sub-optimal displacement candidates were overly influenced by the need for energy minimisation.

PART II

COMPUTATIONAL GEOMETRY AND SIMULATION RESULTS

8. IMAGING, DATA EXTRACTION AND MODEL CONSTRUCTION

In order to create a representative model with which to carry out FEA studies, an anatomically accurate geometric dataset was required. The Visible Human Project (VHP) provided a repository from which data of a real specimen could be derived for geometric reconstruction. The process of data extraction and construction of the discretised FEA model are presented in this chapter.

8.1 The Visible Human Project

The VHP [279, 257] is a digital library that provides two anatomical datasets taken from human cadavers donated to the project. The data provided by the VHP has been used in numerous works, ranging from those involving reconstruction of only the tongue and surrounding anatomy [243, 310, 148, 11, 85], other regions of the anatomy [234] as well as the entire human muscular physiology [275].

The female dataset, a woman aged 59 who reportedly died of coronary heart disease [302], was produced in 1995 and consists of over 5000 axial photographs taken at a resolution of $\frac{1}{3}\text{mm}^3$. The photographs were created by cryosectioning, a technique that involves the freezing of the cadaver in a cryogenic gel, after which the body undergoes sectioning by a grinding method with a full-colour photograph of the exposed cross-section being taken after each pass. An example of the raw images from the dataset is shown in figure 8.1. The accompanying computerised tomography (CT) and MRI datasets were not used in this work due to the low resolution of the images.

8.1.1 Critique of VHP in the context of this work

There are several advantages and disadvantages to using the photographic dataset in the construction of a model of the HUA. The advantages include:

High resolution images: The quality and detail visible in the photographs assists in identifying anatomical features and tracking their shape through the serial image slices.

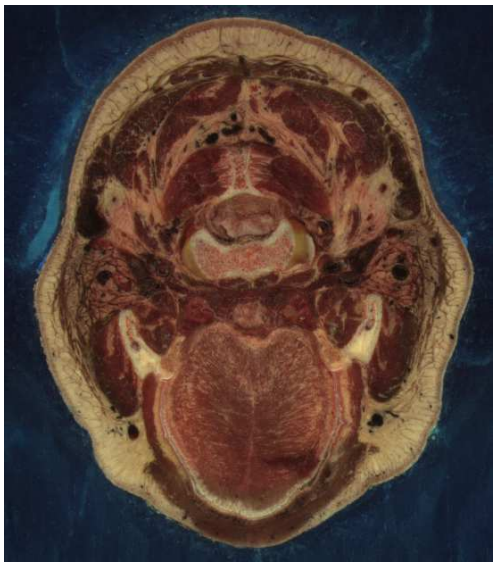

Figure 8.1: Axial slice of oral cavity and oropharynx from female VHP dataset.

Distinguishable soft tissue features: The most relevant soft tissue types are easily distinguishable in the photographic dataset.

Visible muscle macro-histology: The resolution of the photographs ensures that the striations of the skeletal muscle are easily visible, allowing for an accurate representation of these muscles to be made.

However, the following negative points are associated with this dataset:

Subject demographic: Although not documented, this subject most likely did not suffer OSA and would be an unlikely candidate for such a syndrome.

Anatomical positioning: Some structures of the oral cavity and oropharynx are not in the natural position adopted during breathing. Of most relevance is the tongue which has been raised and clamped down by the teeth on all sides.

Unsuitability of associated CT and MRI imaging: The nature of the CT technique makes it unsuitable for this purpose, while the same features cannot be observed in the MRI dataset due to its low resolution (38 times lower resolution per slice, with an interval of 4mm resulting in approximately 450 times less data per region of the anatomy).

Imaging technique: Some parts of the anatomy are not very well defined due to their colour and shade in relation to the surrounding anatomy.

Image artifacts: Cryogenic gel infiltrated parts of the internal anatomy. Although this shows up easily in the colour photographs, the distinction becomes less apparent when the images are viewed in black-and-white.

Image technique and associated artifacts: The axial slicing and photographing technique results in visual data appearing in the photograph that is not on the plane of the slice being processed. This is most apparent in cavernous regions and results in fictitious structures inferior to the slice plane infiltrating the image.

8.2 Existing upper airway tissue models

Numerous models of the tongue have been developed by the biomechanics community in order to study speech production, active muscle kinematics, respiratory mechanics, and the pathophysiology of anatomical defects and the effects of surgical interventions. These models have in common the ability to describe individual muscle activation that produce motion due to the contraction of particular muscle groups. However, the constitutive models describing muscle contraction, as well as the degree of accuracy to which they capture the complex underlying musculature histology, historically differ considerably.

A brief overview of relevant models of the tongue and upper airway tissues are presented.

8.2.1 Speech production and therapy

Purpose-built computational models have been developed to study the motion and shape of the tongue during speech and vowel formation. It is interesting to note that many of the models used in the field of speech research rely on the nodal coordinates of the computational grid to assist in the description of the location and directionality of muscle groups. Where this is not the case, notification of this will be provided.

Wilhelms-Tricarico [311] produced a partial model[1] comprised of only a directly-constrained tongue to study speech production. The active tongue, including the SG muscles, and eight constituent muscles were simulated using a FE model comprised of 42 trilinear elements. This model, which uses a fully continuum mechanics-based framework, has a description of the tongue histology at the computational points. An incompressible formulation that included the effects of viscoelasticity and inertia, as well as active muscle contraction, was produced. It was demonstrated that the model could be used to visualise the effect of gravity on the tongue, and contraction of specific muscle groups. It was shown that contraction of the SG caused the backwards movement of the tongue, simultaneous contraction of the genioglossus anterior (GGa) and hyoglossus (HG) resulted in lowering of the tongue and that protrusion of the tongue was performed by simultaneous contraction of the TV and VT. This model has since been described as ambitious, but too complex and limiting for use in the study of speech production [87].

As opposed to a using a FEM discretisation, Honda [108] constructed a mixed FE and mass-spring model of the tongue, hyoid, jaw and larynx to investigate articulation. The tongue musculature included both intrinsic and extrinsic muscle groups. EMG data was used to determine the activity of major muscle groups during the formation of vowels. Comparison was made between the experimental data and the results derived from a neurosensory model.

Dang and Honda [50] developed a model reconstructed from volumetric MRI data to study the dynamics of the speech organs during speech production. The midsagittal region of the tongue, hyoid, jaw and vocal tract were represented with a 2cm thick model and the palatal and pharyngeal walls were considered rigid. The epiglottis was not included in the model. The governing equations, which accounted for the incompressible, inertial and viscoelastic properties of the material, were approximated using the same technique as Honda [108]. An arrangement of the constituent muscle groups was made based on high-resolution MRI scans of the same subject. The GG was divided into three components, and numerous other muscles (11 in total), were

[1] Further information is provided in the unpublished text of Wilhelms-Tricarico [310].

included. The functional size of each muscle unit was taken into account. Bony structures were considered as viscoelastic materials with a very high stiffness.

Over time, Dang and Honda [51] refined this model. The spring-based model was replaced by a viscoelastic cylinder which properly accounted for the Poisson's ratio of the material. This model was later improved by Fang et al. [68] by creating a fully 3-d model and describing the complete musculature of the tongue. The model was used to analyse the muscle activations used during vowel formation and compared favourably to EMG data. These authors suggested that multiple functional divisions of the SG exist.

A planar 39 element FEM model of the midsagittal section of the human tongue was developed by Sanguineti et al. [244] to study tongue movements produced during speech. The domain discretisation was constructed from X-ray data and produced such that the element orientation reflected that of the modelled muscles. It was assumed that the position of the mandible and hyoid, both of which were not modelled but were represented through boundary conditions applied to the tongue, were unaffected by muscle forces and that they undergo only planar movement. A frictionless contact model was incorporated to account for interaction between the tongue and the palatal boundary.

Three intrinsic muscles, namely the inferior longitudinal (IL), SL and VT, and three extrinsic muscles, namely the GG, HG and SG, were represented in this model. Based on details in the published literature, different parts of the GG, and other muscle groups, were constructed such that they could be activated independently of other regions. The PG and the pharyngeal constrictor muscles were not incorporated into the model as the authors consider their effect on the movement of the tongue to be negligible. Importantly, the MH and GH were excluded on the basis that they are not anatomical constituents of the tongue itself.

From the solution to their neural control model, the activity of each muscle group required to produce the tongue configuration was inferred and compared to EMG data. It was demonstrated that co-contraction of muscles caused little change in tongue posture but resulted in an increase in internal muscle forces.

Sanguineti et al. [245] further developed the model described in [244]. The tongue was modelled using a linear viscoelastic material and the jaw was considered to be a rigid body with a rotational degree-of-freedom (DOF). The hyoid bone was modelled as a free rigid-body while the thyroid cartilage had only one DOF. Additional maxillofacial muscles were incorporated into the model. The static assumption of the previous work was removed, and a temporal formulation with time-dependent control parameters was introduced.

A study was performed to determine the independence of muscle units. It was concluded that larger groups of muscle fibre bundles did not act independently, but rather responded as a singly controlled unit. As before, a study was performed to detect the set of control parameters required to produce a configuration (jaw, tongue, hyoid and larynx) extracted from X-ray images. It was noted that horizontal tongue movements were more rapid than vertical movements. It was concluded that, for the muscle represented in the model, contraction commands to the tongue and jaw synergistic muscle groups resulted in similar displacement fields regardless of the initial configuration. This invariance of the commands effects lead the authors to suggest that additive models might be plausible for use.

Perrier et al. [215] used a 2-d plane-strain small strain FE model of the tongue and palate. Seven muscle groups were represented in the model and the local region stiffened by muscle contraction specified for each individual muscle. The model was used to simulate tongue posture and trajectory during the production of velar stop constants.

Collaboration between Institut National Polytechnique de Grenoble and Université Joseph Fourier

Gérard et al. [85] describe a 3-d dynamic, large-strain, hyperelastic FE model of the tongue. The discretisation of the mesh was such that adjacent elements could be used to represent eight of the main muscle groups used during speech. Various methods for coping with model instabilities were incorporated into the nonlinear solver. The model was used to demonstrate the role of the various components of the tongue musculature.

The model was refined further by Gérard et al. [87] to include an additional two muscles, as well as the jaw, hyoid-bone, palate and vocal tract walls. The tongue geometry was fitted to subject-specific geometry described from MRI data. It was demonstrated that synergistic activation of muscles could lead to realistic deformations of the tongue, as was required to understand the tongue's role during vowel formation.

Buchaillard et al. [29] improved the model of Gérard et al. in order to study tongue motion due to muscle activation and gravity, as well as aspects of vowel production[2]. The palate, and pharyngeal and laryngeal walls were included, as were additional muscles controlling the position of the hyoid. Due to the computational cost of the model, a fixed number of simulations (including some simplifications) were used to probe the relationships between motor commands, tongue posture and the acoustics of the airway. Using this model, the motor commands needed to produce prescribed tongue postures were resolved, thus highlighting the role of each muscle group in this regard. It was able to be discerned that certain reflexive muscle contractions occur during tongue movement.

The latest summary of this work, presented by Perrier et al. [216], describes the inclusion of an orofacial model, and reviews some general aspects of tongue modelling in the field of speech research.

Artisynth / OPAL

The Artisynth project[3] [159] revolves around the development of a toolkit to simulate anatomical structures. It provides an interface for developing coupled musculoskeletal and dynamic, nonlinear, viscoelastic FEM models with the inclusion of point-to-point (force-effector) description of muscles and the inclusion of frictional contact. Based on this toolkit, the OPAL project seeks to produce a comprehensive model of the upper airway musculature, inclusive of the surrounding soft and hard tissues.

Vogt [292] developed a model of the tongue-jaw complex based on the work of Gérard et al. [87]. A FEM technique known as lumped-mass FE, or stiffness-warping, was employed to significantly reduce computational cost. Validation of this model with respect to reference models further was presented in Vogt et al. [293]. A demonstration of matching the tongue posture to that seen in MRI images, through manually prescribed muscle activations, was also provided.

Stavness [264] further developed these models and produced a fully-coupled model of the jaw-tongue-hyoid complex and later an orofacial model that included the palate. Rigid-body dynamics coupled with a FEM model was utilised to describe the dynamics of the rigid and deformable tissues. Amongst other areas of application, predictive methods were utilised to understand the coordination of muscle activation required to produce predefined tongue postures. Stavness et al. [263] went on to describe the development of the tongue-jaw model.

[2] Further information provided in the unpublished text Buchaillard et al. [27].
[3] Further information is provided in the Fels et al. [72] and the unpublished text of van den Doel et al. [281].

8.2.2 Movement and mobility

Wu et al. [317] constructed a FE model of the tongue as part of the Physiome project. The muscle fibre data and tongue model, already available for the male specimen of the VHP, was refitted to conform to the female specimen on which this model was based. The mesh consisted of 10 cubic Hermetian FEs that enforced continuity of both the field variable and its first derivative. This was thought to offer the equivalent performance of standard element models using an larger number of elements. The muscle material was considered incompressible and fully nonlinear anisotropic. Demonstration of individual and combined muscle activation illustrated the movement of the tongue under the influence of the active muscles. Improvements to the model, including a more refined discretisation and the inclusion of fibre volume fraction, have since been presented by Wang et al. [301]. In this work its application is to optimisation of sensor location for tracking tongue motion. Kieser et al. [141] also utilised the model in the study of the tongue's mechanics during swallowing.

A continuum model of the tongue and its histology was developed by Baker [11]. The physiology and histology, including both intrinsic and extrinsic muscles, were identified and extracted from a photographic dataset; however sublingual physiology was not represented. A comprehensive mesh validation study determined that a large number of tetrahedral elements were required to attain convergence of tongue tip displacement and the internal stresses due to active contraction. Research was conducted to understand muscle functioning, the mechanism of swallowing, muscle activation during speech and to evaluate the effect of the loss of function in the tongue.

8.2.3 Surgery and medical procedures

A 3-d 280 element computational model of the mouth and tongue, developed from MRI and X-ray imaging, was produced by Rodrigues et al. [232] to simulate a laryngoscopic procedure. The geometry was restricted to a planer section near the midsagittal line. Simulations were performed to test the effect of material parameters on the force of contact between the tongue and the Machintosh blade required to sufficiently displace the tongue in order to view the larynx. The outcome of procedures involving surgical complications were also investigated.

Fujita et al. [77] investigated the range of motion of the tongue before and after the development of a tumour and the resulting glossectomy, a surgical procedure commonly used to treat oral cancer. A truss-based FE formulation, incorporating incompressibility effects, was used to simulate the tongue. The model was constructed from MRI data. Nine muscles, subdivided into 35 functional units, were described by the line-connection of mesh points, as was done in the articulation models. The mechanical properties of a region within the tongue were altered to simulate the presence of the tumour and its subsequent removal. The resulting model was experimentally validated and successfully demonstrated the conditions associated with the tumour pathology.

Buchaillard et al. [28] used the model designed by Gérard et al. to understand the outcomes of a hemiglossectomy and resection of the mouth floor. The bounding tissues of the oral cavity were represented by shell-elements and contact between the tongue and these accounted for. The regions affected by the surgeries had their mechanical properties altered. Muscle activation with differing passive tissue stiffness around the surgical region were assessed to determine the effect of these properties on the tongue mobility and the ability to articulate.

8.2.4 Breathing, sleep and OSA

Chouly et al. [42] constructed a 2-d geometry of the tongue (corresponding to the plane-strain condition) and retroglossal airway from pre- and post-maxillomandibular surgery radiographical data. A homogeneous, linear, isotropic material model was used to represent tongue tissue. Air moving within the airway was considered to be incompressible and within the laminar flow regime. The model was used to simulate pharyngeal collapse related to tongue position and its constriction of the airway, and to demonstrate the effect of mandibular advancement.

An anatomically correct, 2-d upper airway model was constructed by Huang et al. [111] to investigate OSA. It incorporated fluid-structure interaction (FSI) and a pressure- and state-dependant muscle contraction model for the GG . It was developed to establish a direct connection between measured EMG signals and the contractile forces generated in muscle fibres. Linear elastic constitutive equations were used to model fibre strain in the transverse direction. Here, soft tissues were considered incompressible and the fluid flow was considered laminar. The posterior pharyngeal wall was treated as being a rigid structure, while all other pharyngeal tissues or bones were modelled as linear elastic. It was acknowledged that other upper airway muscles which were neglected (namely dilator pharyngeal muscles), do contribute to upper airway patency during both the sleep and awake states, and that they should be considered during the later production of a full clinical model. They did state however that this provided a good approximation for the deformation of tissue along the midsagittal plane.

It was demonstrated that, in the wakeful state, the relative fibre stretch of the GG at epiglottal pressures of up to -1275Pa was comparable with that of passive tissue under -500Pa load. However, under the same loading conditions while in the sleep state the GG was stretched by nearly 100% compared to the -500Pa passive state. A parametric study was also conducted to determine the effects of variation in the material parameters on the results. Vibrations in the soft tissue due to fluid-interaction, indicative of snoring, were also detected under certain conditions.

Huang et al. [112] expanded on their work, studying the collapsibility of the airway, during sleep and whilst awake, after anatomical alterations were performed. Mandibular advancement of 1cm was found to significantly reduce the collapsibility of the airway by increasing the negative airway pressure required for pharyngeal closure by 780Pa. It was determined that uvulopalatopharyngoplasty (the removal of the uvula) increased upper airway patency by altering the fluid flow in the retroglossus. Palatal stiffening, the introduction of implants of varying stiffness into the palatal tissue, was also determined to decrease the pressure that induces airway collapse.

Huang et al. [113] later provided further information on their model when they extended it to the 3-d case. Multiple parasagittal MRI slices from representative OSA patients were used in addition to the midsagittal slice in order to recreate accurate geometry. The model was used to test the effect of several tongue stiffening mechanisms on the reduction of the negative airway pressure that induces sleep apnoea.

The soft palate, uvula, tongue and epiglottis were modelled as fully deformable and a sliding-contact model was included. The posterior pharyngeal wall was considered rigid and its geometry was modelled as anatomically symmetric about the mid-line. The passive tongue and all other pharyngeal tissues and bones were modelled as linear elastic because the strains in these regions were considered small.

Air in the pharyngeal airway was considered laminar and incompressible. The former property was applied

because estimates of the effects of turbulence indicated it to have only minor influence on the system. The pressure at the entrance and exit of the airway were specified. Simulation of the geometry was performed using commercial FEA software, wherein twenty-seven noded 3-d solid elements and four node 3-d fluid elements were used.

The impact of several surgical interventions were assessed. It was found that recession of the uvula significantly reduced the pressure of airway collapse. Tongue stiffening in the form of implants did not have as drastic an effect, however, increasing the stiffness of the muscle in the region of the medial GG did.

A full 3-d, 24349 element FE model of the human head was produced by Liu et al. [157] to study the source and intensity of snoring. The model, developed from a library database and anatomical literature, included several geometric simplifications. The tongue and soft palate were considered quasi-incompressible and viscoelastic. In subsequent tests, a sinusoidal pressure load simulating breathing was applied to the tissues at set frequencies to induce vibration. The resulting deformation in the tissues was consistent with the natural frequencies determined under no-load conditions.

Xu et al. [320] developed a 3-d FE model of the upper airway in rats from MRI data. The model, which represented the tongue and soft palate as deformable tissues and accounted for contact, was prescribed a negative airway pressure. The effect of tissue stiffening was evaluated by determining the sensitivity of collapse pressure to changes in material parameters. It was determined that altering the tongue stiffness greatly affected airway patency while a change in stiffness of the palate was less significant.

8.3 Defining the macroscopic anatomical dataset

A total of 1203 axial images from head and thorax datasets of the VHP were imported at their full resolution into the commercial software Mimics© [172] for the purpose of reconstructing the anatomy of the subject. Using this software, the set of two-dimensional colour images was transformed into a black-and-white voxel dataset, which essentially involves "stacking" the images onto one another thereby allowing for the traversal of the volumetric images in three dimensions. The dataset was cropped, with its extents reduced to the region between the nasal cavity and bronchial tree, and the lips to the vertebrae. However, the images were not rescaled due to the necessity for fibre data extraction.

The construction of the three-dimensional anatomical dataset involves a number of steps. In the first step of the segmentation process, each part of the anatomy must be masked. This is a process in which all voxels belonging to the described anatomical feature are differentiated from those belonging to other parts. Although the software has a number of automatic tools to assist with this, the transformation from colour to black-and-white images and the fact that the dataset originates from photographs make them unsuitable to this application. Therefore a strategy was adopted to manually segment the part involved, initially building a skeleton framework of the feature and then completing the details between each skeleton frame. Figure 8.2 illustrates the construction of the skeleton framework of the epiglottal cartilage.

Multiple passes for each anatomical component were made in the three planes (axial, coronal and sagittal) in order to reduce the segmentation of image artifacts and to hinder the erroneous incorporation of incorrect features into the part. Emphasis was placed on retaining the highest degree of anatomical accuracy possible, with constant reference being made to the anatomical literature [2, 185, 54].

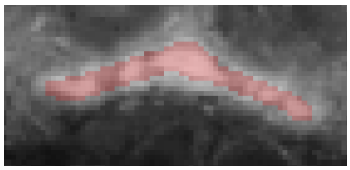

(a) Completely masked axial slice

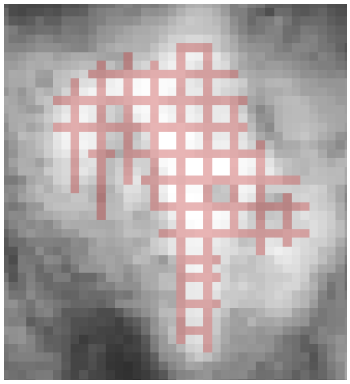

(b) Extents of the tissue are marked on the coronal slice, which are difficult to visualise, have become apparent through completion of masks on orthogonal planes

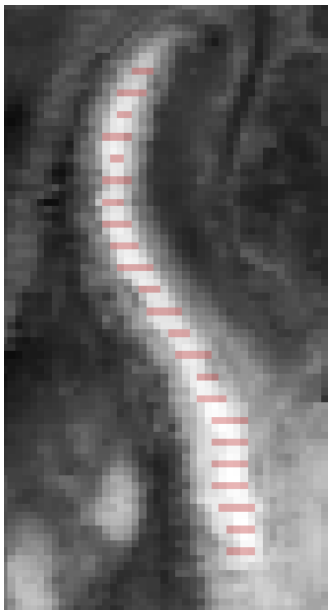

(c) Tissue boundaries for a mid-sagittal mask are highlighted by completed axial masks

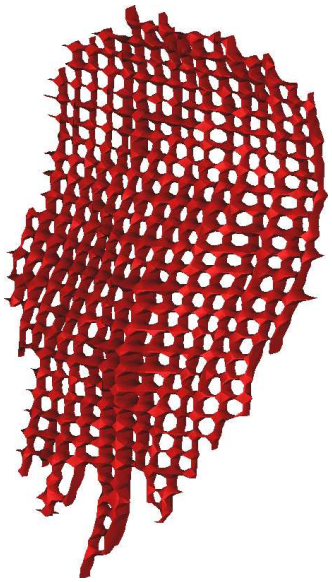

(d) Three-dimensional isometric view of the completed skeleton framework

Figure 8.2: Construction of a skeleton framework in Mimics©.

Where possible and advantageous, adjacent anatomical features that have complex geometries but similar material characteristics were joined to form a single body. Although the tongue consists of anatomically distinct extrinsic and intrinsic muscles, the muscles located in and near the tongue body were treated as a single continuum upon definition of the tongue body. Due to the close proximity of these muscles with one another, dividing the volume of the tongue to keep these muscles distinct would have resulted in a mesh of greater complexity and lower quality. An example of this is the tongue and mouth-floor complex shown in figure 8.3a. There is no evident variation in tissue type between the base of the tongue and floor of the mouth, and therefore no key reason to consider the two divided entities in the model. The same reasoning holds for combining the extrinsic and intrinsic tongue muscles into the tongue body.

Following the process of extraction, filters were applied to each mask in order to ensure that no overlap between the masks of adjacent parts was present. A three-dimensional representation of the raw masks, an example of which is depicted in figures 8.3b and 8.3c, was then generated. Contrary to the usual methodology of volumetric reconstruction, the unsmoothed volumetric masks were directly exported as a triangular tessellation so that the parts could be further manipulated in specialist computer-aided design (CAD) and meshing software. This ensured that the interfaces between parts remained as close to continuous as possible in order to assist in the reconstruction of the parts for the meshing process.

A satisfactorily comprehensive representation of the HUA, from which figure 8.4 depicts a portion of the oral anatomy, was extracted from the image data. This allowed for the construction of not only a model of the tissues in the HUA, but also a simplified CFD model from which to attain airway pressure data[4].

[4] Experimental analysis of the model is also to be performed, in a separate study, using PEPT. A solid representation of the airway is to be constructed using rapid prototyping and a study of the flow of air through the upper airway is to be conducted. Advances in PEPT technology also allow for the tracking of surfaces, conceptually facilitating the validation of models of passive tissue

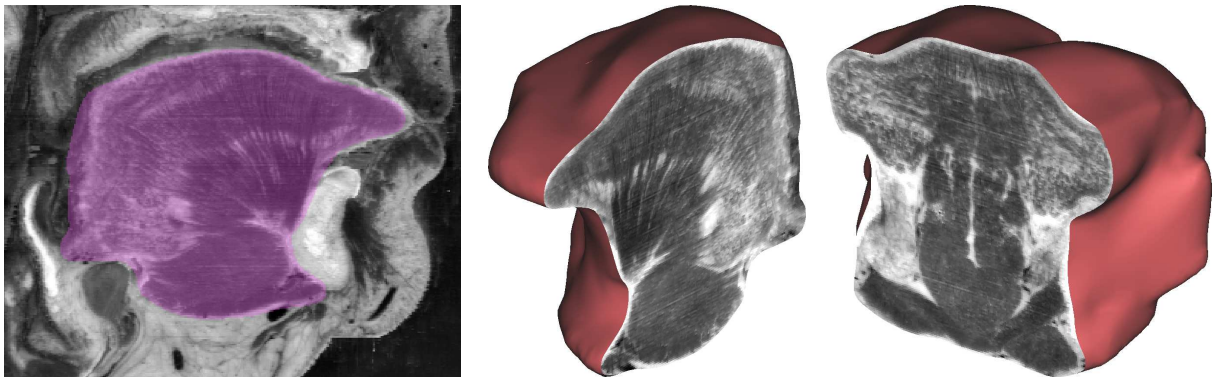

(a) Segmentation of tongue anatomy (midsagittal plane)

(b) Midsagittal view of reconstructed tongue

(c) Coronal view of reconstructed tongue

Figure 8.3: Extraction of anatomical data in Mimics©. Figure 8.3c demonstrates that glandular tissue regions on the lateral extents of the tongue have been included in the bulk region of the tongue.

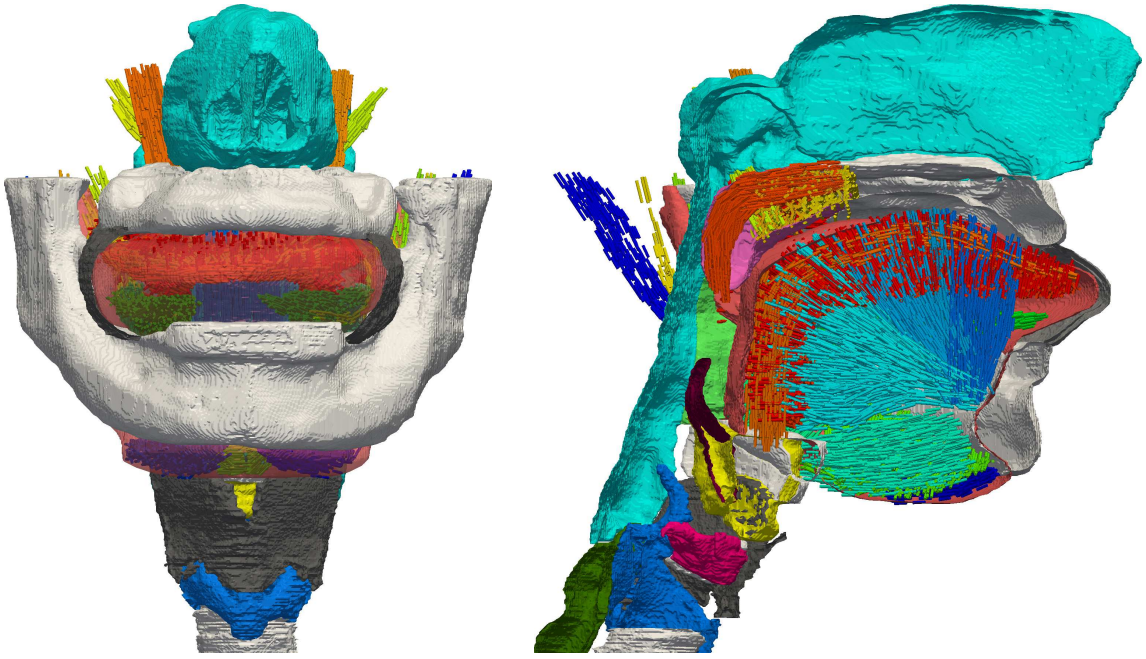

(a) Anterior view

(b) Sagittal view

Figure 8.4: The completed reconstruction of the imaging dataset showing the upper airway anatomy and micro-histology.

8.4 Defining the microscopic fibre dataset

The tongue is a histologically complex organ comprising, amongst other things, numerous interwoven muscle groups. Visible in the reconstructed high-resolution dataset was the gross directionality of the muscle groups that constitute the body of the tongue and mouth floor. Fibre data for each muscle group were defined in Mimics© by manually selecting sections of each muscle group that had a similar directionality. Muscle groups that were not highly visible in the photographs were extracted with consulting of the anatomical

displacement in the presence of a complex pressure distribution.

literature [54, 185, 2].

Figure 8.5a demonstrates the process in the orientation definition of fibre bundles for the medial portion of the fan-shaped GG. Here it was assumed that all fibres within each cylindrical bounding box have a similar orientation. Cylinders are made to overlap so as to ensure that all possible points that contain muscle fibres are enclosed by one or more cylinders. The overlap also assisted in artificially providing curvature to the dataset when it is interpolated onto the grid. This process is described in section 8.5.1.

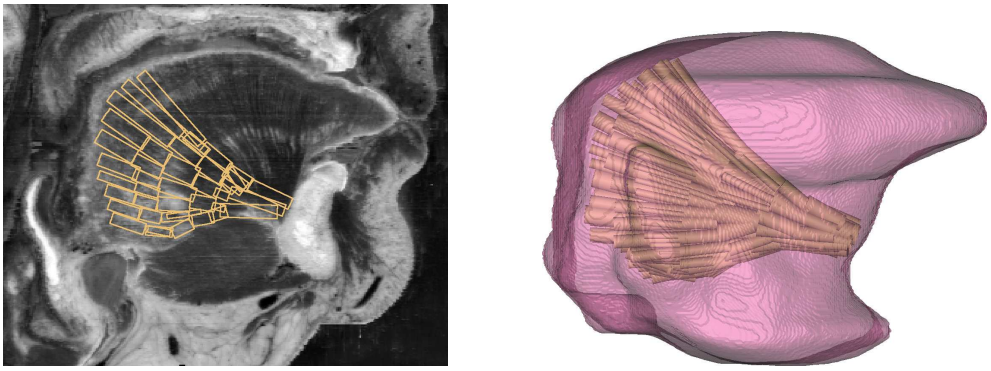

(a) Definition of GGp muscle fibre position and direction data (midsagittal plane)

(b) Three-dimensional representation of cylinders defining a muscle group

Figure 8.5: Extraction of fibre data in Mimics©.

In some parts of the muscle, the fibre alignment was such that large regions of the muscle could be approximated by a single cylinder having the same directionality. However, certain muscles such as the VT and TV have a very complex physiology and therefore required a more intricate description. Figure 8.6a illustrates the detail that was required in order to provide a sufficiently accurate account of the underlying histology of these muscles.

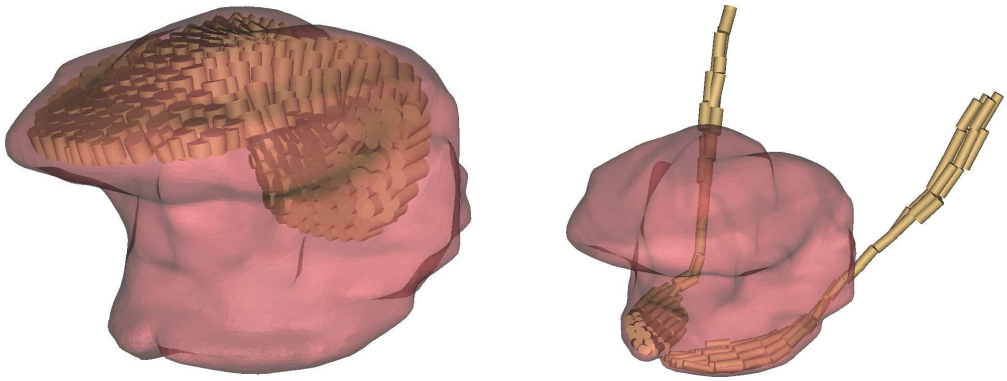

(a) The VT has a complex directionality

(b) The DG has an origin external to the bulk muscle body

Figure 8.6: Cylinder representation of muscles with complex histological descriptions.

Although the final solid model of the tongue was ultimately constructed so as to exclude certain external muscle groups, the directional description of these muscles was still captured in full. Figure 8.6b depicts the three-dimensional representation of the DG, with portions of the muscle inside and outside the main body of the tongue and mouth floor. In the muscle model used to describe the effect of these external models, the

point of origin of the muscle was chosen to be a point at which the cylinders terminated near the surface to which the muscle is attached at its origin.

Depicted later in section 8.6, a total of 18 unique muscle groups with differentiation between left- and right-side muscles were originally represented by 3377 individually orientated geometric primitives. Six of these muscle groups originate from a fixed anatomical structure that is external to the tongue body.

8.5 Construction of the discretised solid model

The tessellations of the anatomical data were subsequently imported into ICEMCFD© [4] for surface definition, assembly and meshing. Standard literature in human physiology [54, 185, 2] again was used to ensure that the integrity of the model was adequately preserved. Figure 8.7 highlights the extent of the model produced.

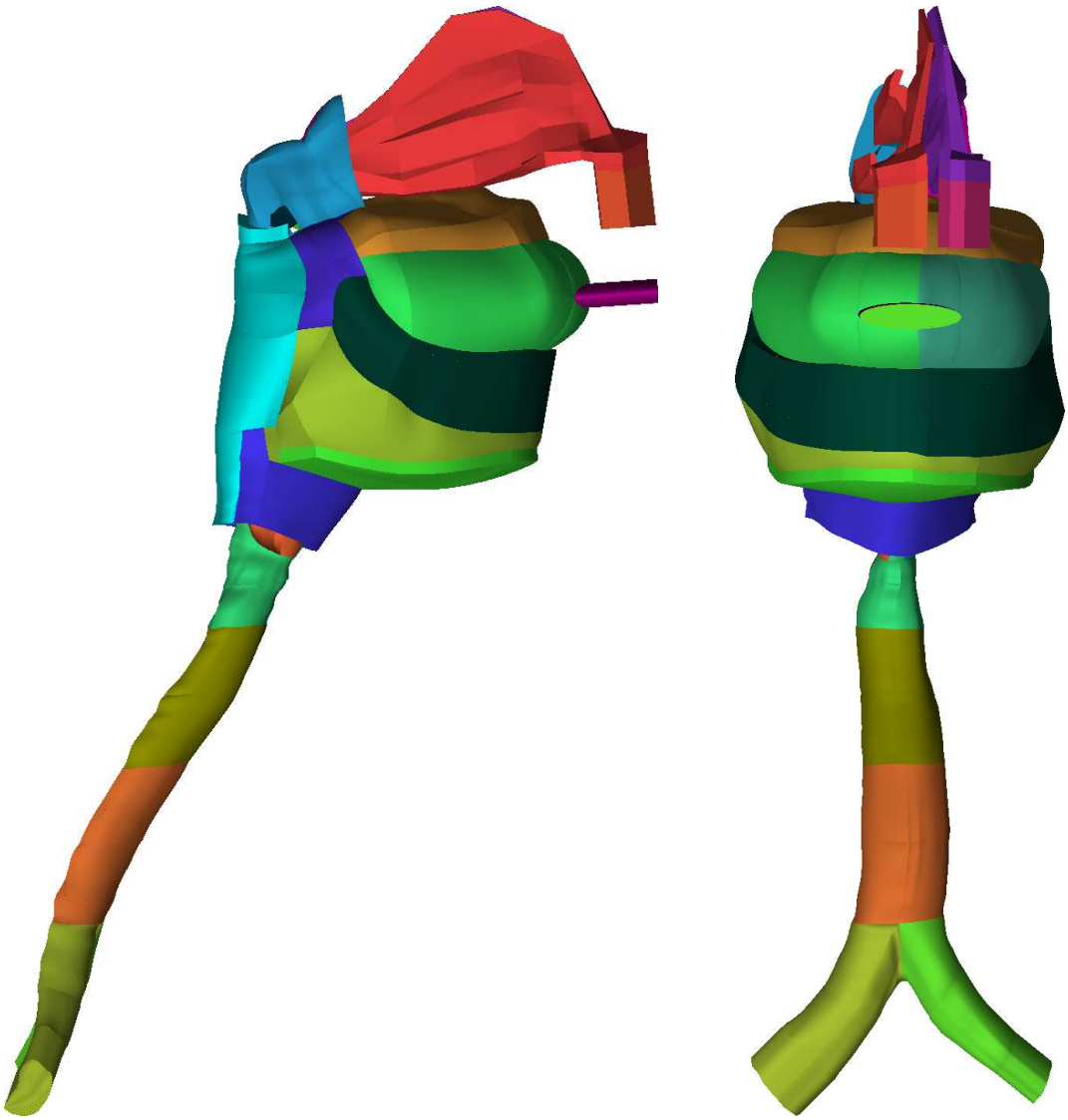

(a) Sagittal view **(b)** Coronal view

Figure 8.7: Representation of the completely reconstructed HUA by parametric surfaces in CAD software.

Before the tissue model was constructed, a number of potential complications had to be considered. A constraint of the FEA library used in the analysis process is that only hexahedral elements are supported. This limitation had to be considered at all steps of the reconstruction process. Additionally, the algorithm used to address the macro- and micro-morphology of muscles also had to be considered as it was likely to dictate how some portions of the geometry were created.

The surface geometry of the macro-scale anatomical parts was created manually by placing control points on selected surfaces of the tessellated parts. These control points were then joined by splined curves, which ultimately formed boundaries for closed parametric surfaces. An illustration of the reconstruction process is shown in figure 8.8. The surface definitions were iteratively modified to best fit the underlying tessellation while ultimately catering for the requirements of the meshing process that followed. Due to the orientation of the tongue and some of the abnormalities of the anatomy, some features required excessive simplification or modification. This is discussed in appendix E.2.

Discussed in section 3.7 were the complications involved with the incorporation of certain aspects of the HUA physiology in a simple model. The use of motion-dependent boundary conditions for muscular tissue allowed the volumes of some muscles to be discarded from the model. Figures 8.8b and 8.8c illustrate the removal of the SG, resulting in a simplified geometry of the tongue. Although the physical representation of the muscle is compromised, the action of the muscle external to the body of the tongue remains captured in the muscle model.

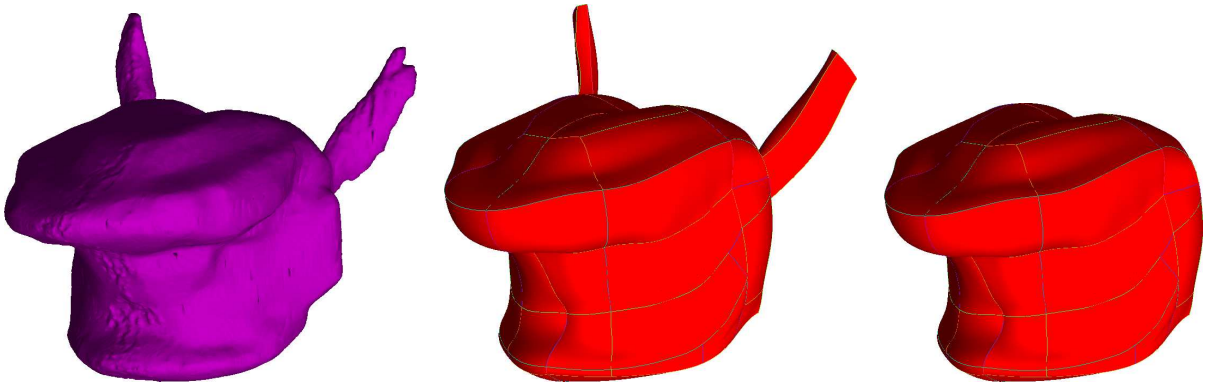

(a) Voxel description of the tongue from ICEMCFD©

(b) Parametric surface description of the tongue surface

(c) Tongue surface simplification by removal of the SG

Figure 8.8: Geometry reconstruction in ICEMCFD© of raw data extracted in Mimics©.

The fully-structured hexahedral mesh was created using a blocking technique, where connected master-blocks are positioned throughout each part in order to describe the coarse topology of the discretisation. An example of the underlying blocking strategy leading to the meshed components of the tissue model are shown in figure 8.9. Rules governing the point and line constraints for the mesh, as well as mesh size, were applied and a preliminary mesh produced. Upon discretisation, the master-blocks were subdivided and the mesh projected to the surface of each part in order to produce the discrete geometry. Smoothing operations were subsequently performed in order to increase the quality of the initial mesh.

It should be noted that, due to the nature of the muscle model used in this work, the mesh was able to be generated entirely independent of the underlying micro-scale physiology associated with the anatomy. This allowed the mesh to capture the details of the anatomy without any restriction on mesh directionality, thereby

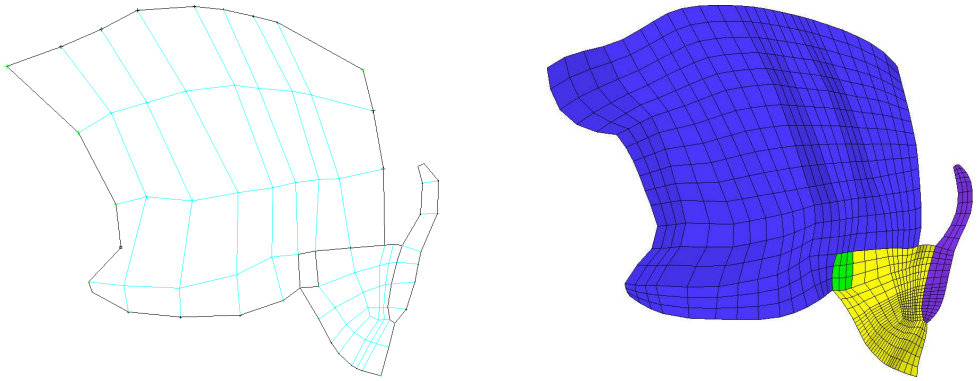

(a) Blocking in ICEMCFD©. Black lines indicate lines that will project mesh to a surface and blue lines produce internal mesh elements.

(b) Sagittal section of mesh resulting from the discretisation of blocks and projection of mesh onto surfaces

Figure 8.9: Part and volume discretisation during geometry reconstruction in ICEMCFD©.

avoiding a limitation imposed on some of the geometries described in the literature. The superposition of the micro-histological data on the discretised domain is discussed in section 8.5.1.

8.5.1 Importing the fibre data into the solid model

The dataset of the micro-scale fibre directionality was subsequently imported into the macro-scale geometry, providing a perfect match between them. Due to the general constitutive framework given in section 5.1, the description of the muscle model described in chapter 6, and the fact that the fibre and anatomical datasets correspond exactly, there was no requirement for the mesh to align with the direction of any of the underlying fibre groups. The underlying muscle histology data was interpolated directly onto the constructed mesh.

The data extracted from Mimics© consisted of the radius and end-points of each fibre-cylinder. A method expressed graphically in figure 8.10 was implemented to determine whether any point in the geometry was within the boundaries of a muscle group, as defined by the collection of relevant representative cylinders.

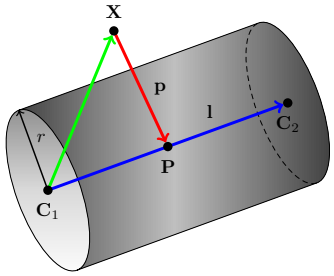

Figure 8.10: Geometric test for containment of point within a cylindrical volume

Given any point $\boldsymbol{X}$ and the fundamental information required to express the bounds of a cylinder that describes a portion of a muscle, namely the end-points $\boldsymbol{C}_1, \boldsymbol{C}_2$ and radius r, then the projection of $\boldsymbol{X}$ onto the cylinder axis is given by

$$\boldsymbol{P} = \boldsymbol{C}_1 + (\boldsymbol{X} - \boldsymbol{C}_1) \cdot \frac{\boldsymbol{l}}{\|\boldsymbol{l}\|} \tag{8.1}$$

where the cylinder length vector is defined by

$$\boldsymbol{l} = \boldsymbol{C}_2 - \boldsymbol{C}_1 \tag{8.2}$$

and the projection vector given by

$$\boldsymbol{p} = \boldsymbol{X} - \boldsymbol{P} \quad . \tag{8.3}$$

If the point $\boldsymbol{X}$ lies outside the bounds of the cylinder then the length of the projection is greater than the radius

$$\|\boldsymbol{p}\| > r \tag{8.4}$$

or the projection lies outside the cylinder end-points

$$(\boldsymbol{P} - \boldsymbol{C}_1) \cdot \boldsymbol{l} < 0 \quad \text{or} \quad (\boldsymbol{P} - \boldsymbol{C}_1) \cdot \boldsymbol{l} > \boldsymbol{l} \cdot \boldsymbol{l} \quad . \tag{8.5}$$

If the point was within the bounds of the muscle, the direction of the muscle fibre (as defined by the cylinder end points) was recorded. When the point was within a region of overlap where more than one cylinder contained the point, the average of the direction vectors was taken to be the fibre direction. This averaging process resulted in a smooth transition of the fibre direction in regions of curvature of the muscle group.

When the muscles traversed the boundary of a part of the anatomy, the fibre volumes output from Mimics© extended into the adjacent areas. During the discretisation process, an identification number was given to the various anatomical parts, and was subsequently used as a filter to ensure that the fibres were specified in the relevant muscular regions and did not erroneously continue into adjacent volumes.

When viewed from an *in vivo* perspective, the definition of the fibre direction is somewhat arbitrary for a one-dimensional force-generating element. This is to say that the action of a fibre with the alignment $\boldsymbol{n}$ is the equivalent to that of one with the opposite direction $-\boldsymbol{n}$. However, the geometric description required a preferred directionality to be described. Because of this requirement, care was taken during the direction interpolation procedure as vector addition (which is direction sensitive) was used to perform the operation. The alignment of the cylinders with respect to one another was inspected and it was ensured that the vectors used to express fibre-directionality did not conflict through misalignment, that is $\boldsymbol{n}_{\mathrm{f}_i} \cdot \boldsymbol{n}_{\mathrm{f}_j} > 0 \ \forall \ \mathrm{f}_i, \mathrm{f}_j \in \mathcal{B}_{\mathrm{M}}, i \neq j$. This was achieved in a preprocessing step, where all cylinders in each muscle group were checked and altered such that they satisfied either a dot or curl type constraint, depending on the muscle histology (radial/linear vs circumferential).

In section 8.5, the reason for the removal of muscles, such as the SG that had portions of their volume outside of the body on which they exert most influence, was presented. For these muscle groups, their point of origin was defined *a priori* and the point of insertion into the muscle body was marked as the region of the surface of the tongue that contained an adjacent internal muscle fibre of the same muscle type. In this manner, a continuous description from the interior to the exterior portion of the muscle was created.

8.6 Presentation of a representative model of the tongue and surrounding soft tissues

There is a great morphological variability between individuals *in vivo*. Embracing this variability with realistic boundary conditions is likely to be a challenge. There are numerous points of contact between parts of the

anatomy, and because tissues move past one another as well as support one another, these is no clear way to represent the boundaries in simplified models without imposing unrealistic constraints on the movement of the anatomy. Furthermore, some simplifications of the geometry itself require special considerations when it comes to the imposition of boundary forces on a particular part of the model. In the following paragraphs, the reduced model describing a sample of the HUA geometry are presented along with prescribed boundary conditions (BC) imposed on the model. The full tissue model from which this geometry was extracted is showcased in appendix I.1.

In figure 8.11, the model of the tongue, hyoid bone, epiglottis and the fat-pad on which it is bedded and the inner portion of the mandible are shown. It is assumed that the head remains still throughout the simulated period thus keeping the gravitational orientation and relative distances between fixture points constant. The inner part of the mandible (to which the tongue is affixed) as well as the interface between the epiglottal fat-pad and the thyroid cartilage, which represent fixture points, were therefore fully-constrained.

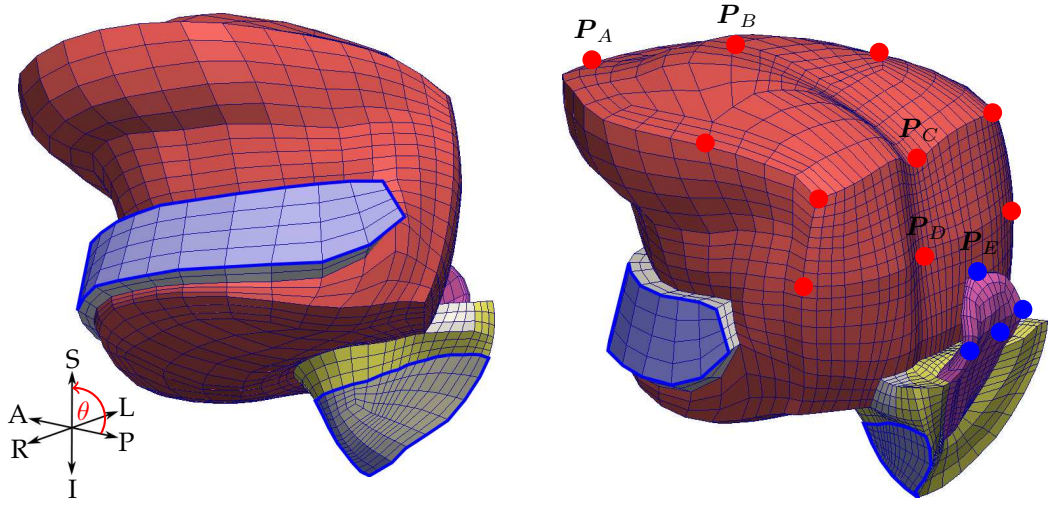

(a) Front isometric view

(b) Rear isometric view

Figure 8.11: Discretised model model of tongue and surrounding soft tissues. Part of the mandible and hyoid are shown in grey, the tongue in pink, the epiglottal cartilage in magenta and adipose tissue in yellow. The blue-shaded regions highlight nodes that have essential boundary conditions and remain at all times stationary. The position of active control points for neural model are marked with the red spheres.

The exposed surface of the tongue, epiglottis and the adipose tissue (highlighted in figure 8.12) are subject to the static pressure distribution of the surrounding air. The pressure applied to these surfaces is prescribed using either a spatially-correlated function, or data directly extracted from CFD models. Due to some simplifications present in the fluid model, there is direct special consideration for regions that have had anatomy removed and are artificially exposed to the influence of the air (i.e. regions of tongue where lateral sublingual glands should connect to the mandible, clearly visible in figure 8.3c).

Figure 8.13 presents an overview of the muscles and fibre directionality incorporated into the model of the tongue. In figure 8.13a, it can be seen that the GG was represented by three independently controlled functional units, namely the anterior, medial and posterior components, as discussed by Miyawaki et al. [183][5]

[5] They state that if such a decomposition exists, then it is not understood if we have voluntary control over the each individual component.

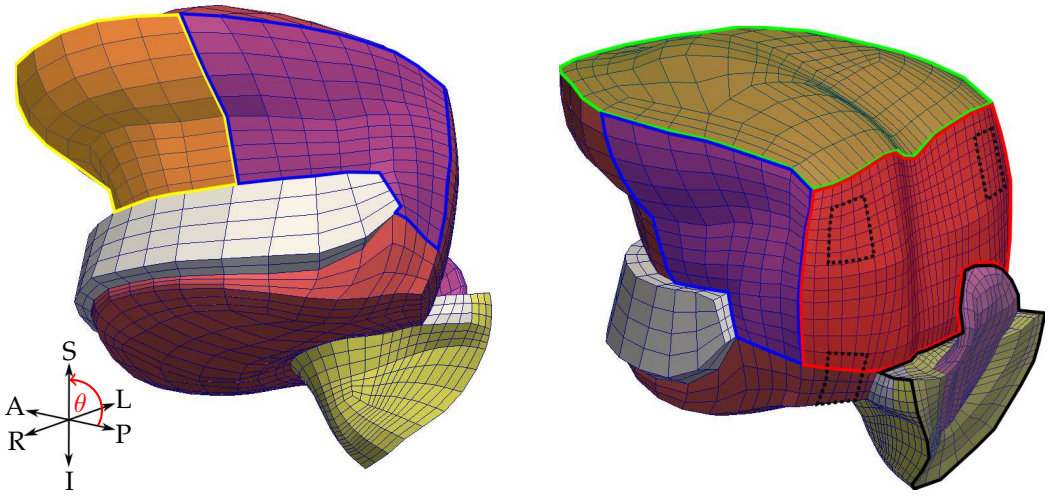

(a) Anterior lateral isometric view **(b)** Posterior lateral isometric view

Figure 8.12: Geometry of the soft tissue model highlighting the location of surfaces subject to Neumann boundary conditions. Element faces considered to constitute the anterior, left lateral, superior and anterior surfaces of the tongue are highlighted in yellow, blue, green and red respectively. Other tissues in the retroglossus exposed to airway pressures are indicated by a grey overlay. The surface interface $\Gamma_0^{t(u)}$ for external muscle groups are marked with dotted lines.

and used elsewhere Dang and Honda [50], Gérard et al. [85], Buchaillard et al. [29]. The activity of the GG has been shown to be somewhat heterogeneous [60], so this assumption along with that of the underlying fibre density will ensure that the local effective contractile activity is non-uniform. Due to the neurological (as opposed to physiological) nature of the division of the GG, it is not discussed in Davies [54] or other physiology literature.

8.6.1 Measurement points for neural control algorithm

Ten control points[6] were selected to form a coarse net defining the superior and posterior surfaces of the tongue. The points, depicted in figure 8.11, were at the apex of the tongue, on the superior surface of the tongue (both at the intersection of the posterior and superior surface and half-way between the posterior surface and apex), and half-way up the posterior surface of the tongue. The points were monitored on the midsagittal line, as well as lateral to the midplane. Control points located on the epiglottis, with weighting values $w_p = 0$, were used to monitor the displacement without influencing the neural algorithm.

8.6.2 Body forces

All tissues experience a body force due to their mass. The direction of the gravitational load depends on alignment of the body, namely whether the person is in an upright stance, laying supine or in some other

[6] The location of the chosen measurement points was a design decision, with the dispersed net of points assumed to ensure that the movement of the entire tongue body would be considered and controlled. Should corroboratory experimental data be available, it would be sensible to position a control point upon the corresponding position of the sensor. The concepts presented by Wang et al. [301] are relevant for the improvement of their location for both simulation and experimental purposes. Further discussion of the selection of the control points is presented in appendix G.2.

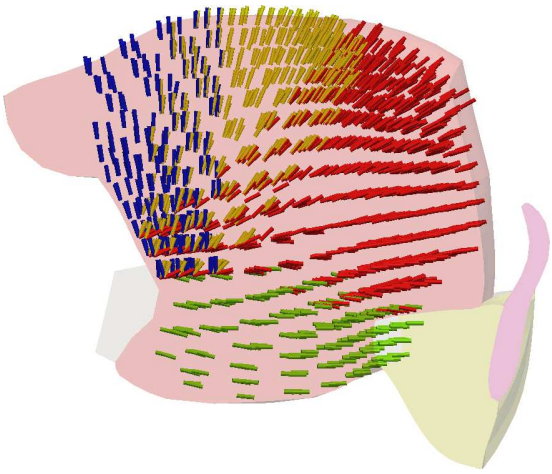

(a) GGa (blue), GGm (yellow) and GGp (red); GH (green)

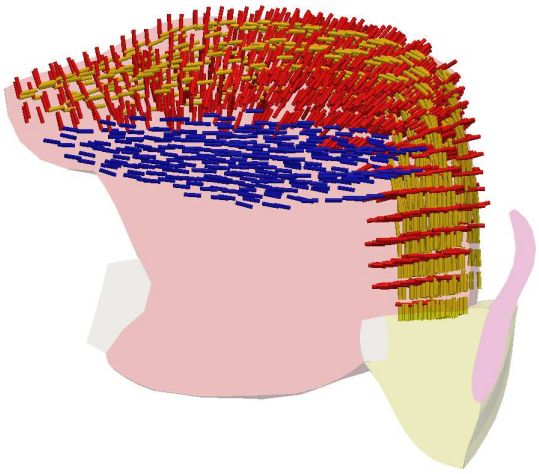

(b) IL (blue) and SL (yellow); VT (red)

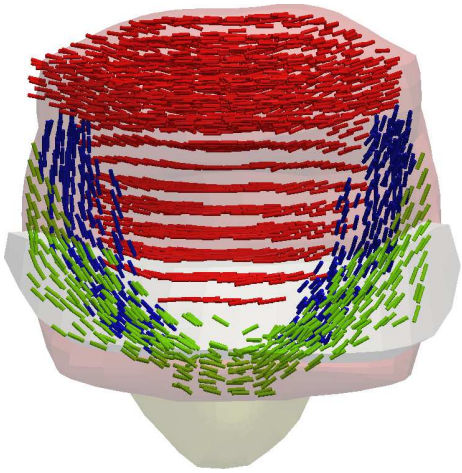

(c) HG (blue); MH (green); TV (red)

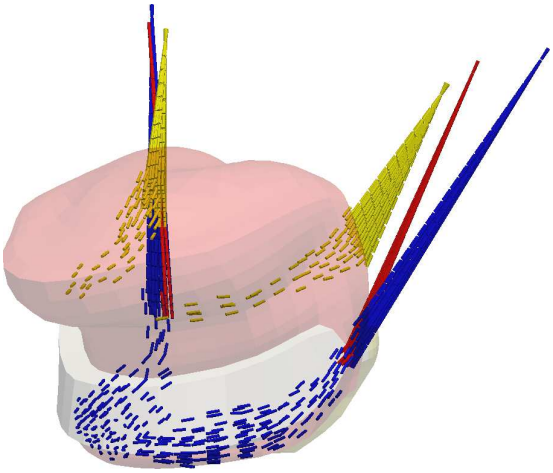

(d) DG (blue); SG (yellow); SH (red)

Figure 8.13: Geometric description of the tongue musculature. Each cylinder within the tongue body represents the average directionality of eight fibres embedded within a computational cell. Overall, 13 neurologically-distinct muscle groups are represented, with 5 of them having two components divided laterally on the midsagittal plane. The portion of the PG inserted into the tongue posterior was ignored.

configuration. In general, we express the gravitational force vector (with units m/s^2) in the form

$$\boldsymbol{g}\left(\theta,t\right)=9.81\;c_g\left(t\right)\hat{\boldsymbol{g}}\left(\theta\right) \tag{8.6}$$

where c_g is a function of the time and θ represents the angle of incline[7] measured from the horizontal position. With reference to the axes accompanying figure 8.11, the gravitational vector $\hat{\boldsymbol{g}}\left(\theta\right)$ is aligned in the posterior direction when $\theta=0^\circ$ and in the inferior direction when $\theta=90^\circ$. Special cases were used to represent lying in the prone or lateral positions.

[7] Under normal circumstances, pillow height is responsible for the variation of the head's position while sleeping on one's back.

8.6.3 Airway loading distribution

On that region of the natural boundary $\Gamma_0^{t(X)}$ that is exposed to the airway, a pressure load generated due to expansion and contraction of the lungs is applied. The surface traction, multiplicatively decomposed into temporal and spatially dependent components, is defined as

$$\boldsymbol{t}\left(\boldsymbol{X},t\right)=p_{\text{nom}}\,c_p\left(t\right)h_p\left(\boldsymbol{X}\right)\hat{\boldsymbol{n}}\quad , \tag{8.7}$$

where p_{nom} is the nominal value for the applied pressure. The spatial function h_p is defined such that the nominal pressure and the epiglottal pressure, often referred to in the literature and assumed to be measured at $\boldsymbol{P}_E$, coincide. The form of c_p and h_p are presented below.

8.6.3.1 Temporal description for quasi-static conditions

The dimensionless temporal domain is decomposed into two parts. In the first half of the domain, gravitational loading occurs without the presence of airway pressure while in the second, the gravitational load remains constant and the pressure load is linearly increased. The gravitational and pressure force constants are in these instances defined by

$$c_g:=\begin{cases}2t & \text{if}\quad t\in[0,0.5)\\ 1 & \text{if}\quad t\in[0.5,1]\end{cases}\quad,\quad c_p:=\begin{cases}0 & \text{if}\quad t\in[0,0.5)\\ 2t-1 & \text{if}\quad t\in[0.5,1]\end{cases}\quad. \tag{8.8}$$

8.6.3.2 Temporal description of loads for dynamic conditions

In the instance of dynamic loading, a gravitational preload is still applied. However the periodic pressure load, now a true function of time, is given by

$$c_p:=a\left(\sin\pi t^*\right)^e\quad,\quad t^*=b\frac{(t-c)\mod w}{w}\quad, \tag{8.9}$$

where w gives the oscillation period and the exponent $e=1.75$, is applied over a finite time domain.

Manipulations of equation 8.9 through the time-dependent functions a,b,c result in functions that mimic a representative sample of pressure data, limited to the inhalation potion of the breathing cycles, obtained from [165, 261, 221]. Similar representations of the temporal nature of inlet conditions have been used in CFD models (see [266, fig. 3 and 4],[328, fig. 2], [319, fig. 2F],[296, fig. 1]). As the modular arithmetic results in a positive value for the sinusoidal function, the piecewise step function a accounts for the pressure sign change between inhalation and exhalation and allows for rest-periods between cycles to be introduced. The function c provides a phase-shift for the sinusoidal function, and b allows for the possibility to alter the rate of change of pressure in various parts of the breathing cycle. This general form of temporal function provides a smooth transition (zero first-derivative) between inhalation and exhalation. In figure 8.14, three examples of temporal loading patterns generated with equation 8.9 as a template are illustrated.

8.6.3.3 Spatial description of airway-induced loading

Using the spatial function in equation 8.7, first-approximations of the pressure profile for nasal and oral breathing are described. It is assumed that during nasal breathing, the pressure field in the oral cavity is

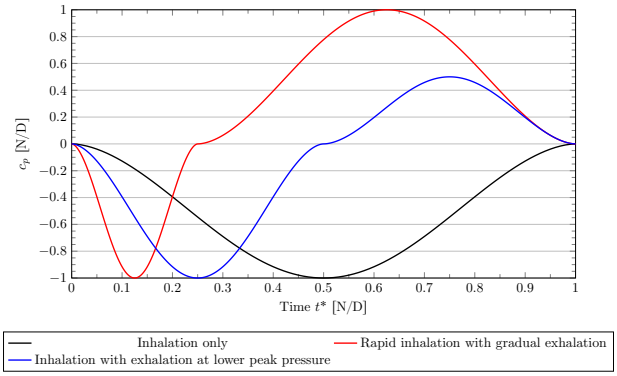

Figure 8.14: Temporal curves for c_p representing different breathing patterns.

constant, resulting in no fluid motion within it. However, pressure losses are still incurred in the nasal passage (inhalation) or trachea and glottis (expiration), and the average pressure is non-atmospheric. In this case, the spatial function is simply

$$h_p := 1 \quad . \tag{8.10}$$

In the case of oral breathing, the mouth is open and fluid moves over the surface of the tongue in the narrow gap between it and the oral cavity extents. Defining two points in the geometry, namely $\boldsymbol{P}_A$ and $\boldsymbol{P}_E$ shown in figure 8.12, we approximate the pressure difference in this gap as

$$h_p := \begin{cases} 0 & \text{if} \quad \boldsymbol{X}_2 > \boldsymbol{P}_2^A \\ 1 & \text{if} \quad \boldsymbol{X}_2 < \boldsymbol{P}_2^E \\ \left|\boldsymbol{X}_2 - \boldsymbol{P}_2^A\right| / \left|\boldsymbol{P}_2^E - \boldsymbol{P}_2^A\right| & \text{otherwise} \quad . \end{cases} \tag{8.11}$$

A linear variation of the pressure field in the anteroposterior direction is assumed and that the pressure gradient in the transverse direction is zero.

A third scenario to consider is that of nasal breathing with open mouth. In this situation, the tongue is pressed against the palate to form a seal, but the mouth can open to equalise the pressure in the oral cavity. The pressure in the oral cavity is thus atmospheric, while the posterior of the tongue is exposed to the pressure of the retropharynx. The function

$$h_p := \begin{cases} 0 & \text{if} \quad \boldsymbol{X}_2 > \boldsymbol{P}_2^C \\ 1 & \text{if} \quad \boldsymbol{X}_2 < \quad \text{otherwise} \end{cases} \tag{8.12}$$

approximates this pressure field.

To demonstrate the overall result of the pressure function (equation 8.7), consider figure 8.15 which shows the measured area-averaged pressure over a patch on the anterior, superior and posterior surfaces of the tongue for a single inhalation for both breathing mechanisms. For all spatial profiles h_p, the epiglottal pressure $p_{\text{epi}} = p\left(\boldsymbol{P}_E\right) = -p_{\text{nom}}$. For this single inhalation, the specified negative airway pressure changes in a sinusoidal profile with time. When inhalation occurs through the nose, the pressure field is constant. However, when oral inhalation is simulated, there exists a pressure difference between the anterior and posterior surfaces of the tongue. The anterior region of the tongue, being furthest forward in the mouth and open to the atmosphere, experiences the highest pressure. The pressure decreases towards the rear of the oral cavity

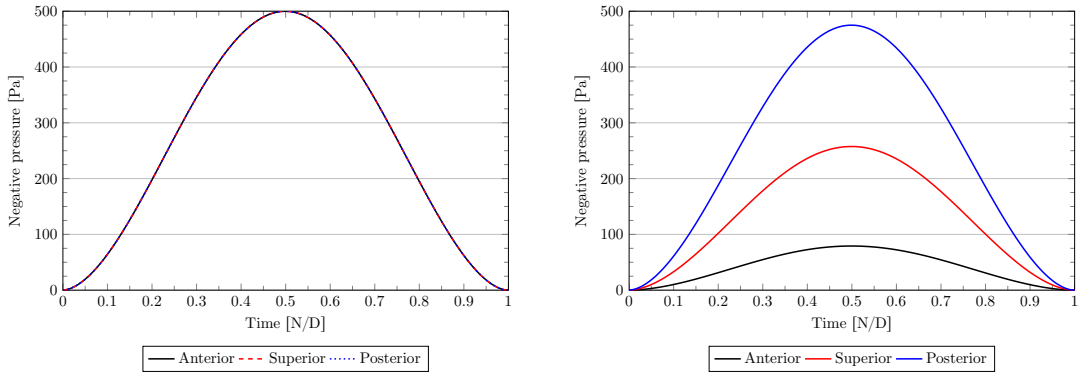

(a) Nasal breathing **(b)** Oral breathing

Figure 8.15: Computed area-weighted average pressure on various regions of the tongue surface during inhalation. In these cases $p_{\text{nom}} = 500\text{Pa}$.

where the posterior surface of the tongue, exposed to the retroglossal space, experiences low pressure. The superior and lateral surfaces of the tongue, which extend in the transverse plane, experience an intermediate average pressure of nearly half of that of the posterior surface.

8.7 Existing CFD studies of the upper airway

The study of airflow and the development of flow structures in the HUA is a very complex field of study in its own right. The spectrum of work performed in the area of upper airway fluid mechanics includes the study of flow structures, sleep disorders, aerosol deposition and lung mechanics, to name a few. The description of a representative geometry, be it idealised or patient-specific, the mathematical equations governing fluid flow and their associated boundary conditions, and mechanisms to capture the flow structures that influence the flow-field all remain difficult issues to overcome. A recent review by Pollard et al. [223] provides an excellent summary of the challenges involved in this area, as well as the state of experimental and computational research. Here, a brief overview of some of the relevant work in this field, and in particular that pertaining to the research of OSA, is provided. One of the key conclusions to be made from this review is that the methodologies used in each work was dramatically different, with no definitive choice in respect of any model construction or simulation being made. This was due to the nature of each study, its desired outcome and the technologies available at the time at which the work was conducted. Ultimately, it appears that best judgment stemming from the insights of previously performed work had to be exercised to produce a functional model for this work.

The flow structures present in the airway depend greatly on the geometry and breathing mechanism. The fluid-dynamics pertaining to oral breathing and air flow in the mouth and pharynx was presented in [12, 46, 195, 196], while involvement of the complex nasal cavities during nasal breathing was detailed in [139, 147, 156, 188, 305, 307, 325]. Mention of the flow developed in the pharynx due to nasal respiration was described in [217, 242].

Investigations into the nature and possible causes of OSA under the conditions of nasal inhalation were conducted by [132, 267, 319, 266, 298, 300] using models that included both the nasal and pharyngeal geometries. Simplified models, consisting of simply the pharynx, were utilised by [252, 161, 177] to conduct similar stud-

ies. Pre-surgical analysis and post-operative outcomes of OSA were evaluated by [119, 255] using models of the pharynx. More complex models were constructed by [67, 128, 299] to determine the effect of surgical procedures on airway fluid-dynamics during nasal breathing. Treatment of the OSA condition with oral devices was studied during oral [56] and nasal [327, 285] respiration. Fluid-structure interaction models were developed to determine the motion of the passive soft palate [41, 328], the consequences of surgery on airway and tissue dynamics [300] and study geometric influences on the presentation of OSA [111, 266].

Although the finite volume method (FVM) is the overwhelmingly popular choice in this area for solving the Navier-Stokes equations, the Lattice-Boltzmann method (LBM) has also been used successfully [12] in this regard. The studies considered here primarily consist steady state simulations, although a few time-dependent simulations [266, 328, 325] have been conducted. Lee et al. [147] demonstrated that, for the most part, qualitatively similar results could be obtained for steady state simulations that match the pressure conditions at a given instant in an unsteady simulation. Some of the work considers only idealised geometries (e.g. [12]), while realistic geometries, extracted using CT imaging or MRI, have also been considered. Collins et al. [46] determined that idealised geometries that included sharp edges produced inadequate results when compared to a realistic representation of the same geometry.

As in many other fields of application, large eddy simulation (LES), detached eddy simulation (DES) and direct numerical simulation (DNS), which are very computationally expensive, provide the best mechanism to resolve turbulent structures in the airways. Since these structures have a large influence on the pressure profile that develops in the oropharynx, adequate approximation of the effect of their presence is necessary. Work performed to compare the effect of choice of turbulence model in either nasal or oropharyngeal simulations include that of [252, 262, 12, 177, 132]. Collectively, these studies have demonstrated certain deficiencies with regard to RANS models predicting flow structures in the upper airway. However, it has been demonstrated that the k-ω model [188], in particular the low-Reynold's number (Re) shear-stress transport (SST) variant [177, 326], which has been developed specifically for transitional flow, produces reasonable results.

Meshing techniques are biased towards the use of fully unstructured meshes, primarily due to the complexity of the airway physiology. Saksono et al. [242] discussed the possibilities of using semi-automated mechanisms of producing high-quality airway geometries. Grid convergence studies performed by Jayaraju et al. [131] showed that velocity and pressure field convergence on the midsagittal plane could be obtained in a model of the glottis with 550000 cells. Wen et al. [307] demonstrated that 950000 cells provided a compromise between computational expense and accuracy in a nasal cavity model.

The extent of the geometry differs greatly between each model, as the focus of interest varies between studies. Nasal models may include an inlet extension [128], although some are truncated at the vestibules [139] or represent the facial geometry and far-field atmospheric conditions [328]. Similarly, many models that represent the oral cavity include an extension to the atmosphere [12]. Pharyngeal models may be truncated in the vicinity of the choanae or velopharynx [217]. Inlet boundaries have been defined using a velocity profile [195], prescribed pressure [266] or volume flow rate [305]. The position of the downstream boundary differs between models; it may be found in the upper pharynx [266], at the position of the larynx [300], in the lower trachea before the tracheal bifurcation [195] or distally after a number of bifurcations [242]. Boundary conditions have been implemented in a variety of manners, and in many cases are limited by the description of the geometry at the inlet and outlet. Choices for outlet boundaries include defining the pressure [242], velocity profile [328] or using an outflow [307] condition. Although techniques exist to simulate the presence of multiple bronchial branches in the lungs [296, 297, 169], a consideration which impacts greatly on the upstream pressure field, the majority of work surveyed truncates the airway well upstream of the lungs . In most cases,

walls have been considered as zero-slip boundaries.

8.8 Construction of the fluid model

In construction of the airway, the interior boundaries of the solid model define the anatomical boundary of the fluid domain in the regions of the oral cavity and pharynx. Additional anatomical features not represented in the solid model were considered in the construction of the fluid model. Figure 8.16 provides an overview of the fluid domain created from the geometry shown previously in figure 8.7. The sublingual and submandibular glands were ignored in the construction of the solid model but were integrated in a crude manner by preventing fluid flow into this anatomical region. The constriction of the larynx, the trachea and first branch of the main bronchi were also modelled, as the downstream flow field influences the upstream pressure field of the oropharynx.

(a) Midsagittal view **(b)** Transverse view

Figure 8.16: Geometric reconstruction of the fluid domain.

Due to the complex structure of the nasal passages and the difficulty in accurately extracting the passages from the photographic data, a coarse representation of their anatomy was produced. The approximate structure and dimension of the nasal passages were extracted from the imaging data through the reconstruction of a skeleton framework. Using the technique demonstrated by Zhang et al. [325], a greatly simplified representation of the the nasal canal that could be easily meshed and which was hypothesised to produce representative results was constructed. The gross anatomy of the nasal passages, including the position of the nasal vestibules, the width and height of the passage adjacent to the nasal septum, and the opening and length of the superior and inferior meatuses, was retained. However, the curvature of the anatomy was not captured. The simplified geometry of channels of the nose are illustrated in figure 8.17.

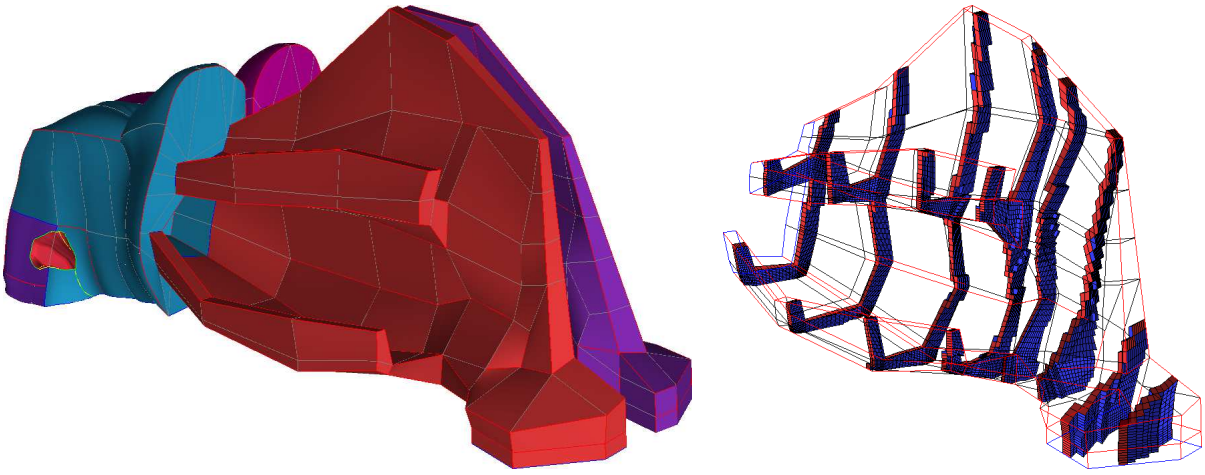

(a) Isometric view of surfaces used to approximate nasal passages and nasopharynx

(b) Coronal view of right nasal passage with discretisation highlighted

Figure 8.17: Geometric reconstruction of the nasal passages involved the creation of a simplified model for the geometrically intricate nasal passages.

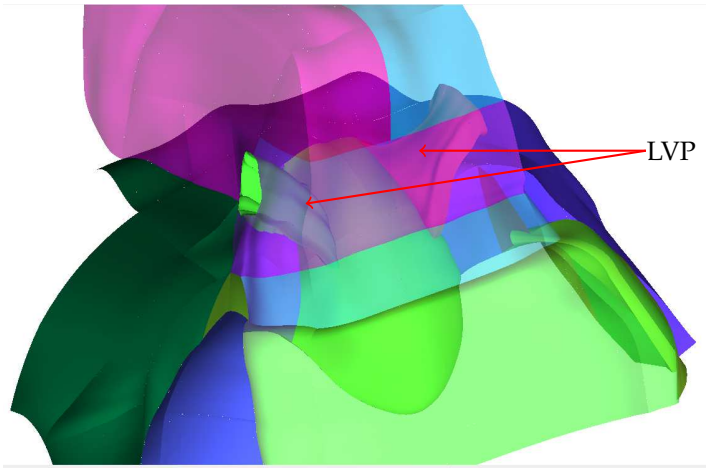

Figure 8.18: The external muscles of the soft palate, which obstruct airflow in the nasopharynx, were captured during reconstruction.

The extrinsic muscles of the soft palate, specifically the LVP, insert into the uvula and cause a flow obstruction for the air moving though the nasopharynx. As shown in figure 8.18, it was included as a boundary in the fluid model as it was felt that it may play a significant role in the channelling of the flow over the uvula.

In figure 8.19, a comparison is made between the nasopharynx, oropharynx and hypopharynx geometry extracted from the VHP dataset and one obtained directly by experimental methods. The overall fluid geometry embraced all of the core anatomical features that affect the fluid flow. However, due to the difficulties of using the photographic dataset and the uncertainties associated with the positioning of some of the tissues, the model of the pharynx had a CSA that appears to be on the upper limit of-, and in some regions exceeding, that measured and presented in the literature[8]. Specifically, the lateral dimension of the oropharynx appears visually larger in figure 8.19b when compared to figure 8.19a; however, it is comparable to other geometries in the literature (see [196, fig. 6]) and of the same scale of the posterior section of the tongue.

[8] This point is discussed in appendix E.2.

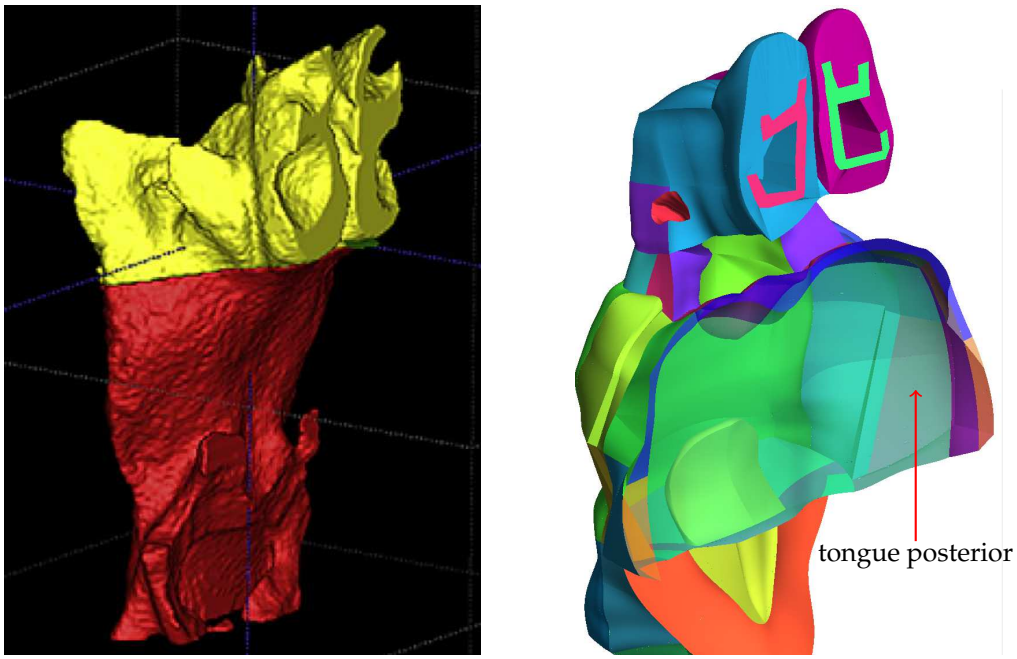

(a) Reconstructed pharynx from a cone-beam CT scan

(b) Pharyngeal region of model created in ICEMCFD©

Figure 8.19: The geometry reconstruction of the oropharynx resulted in a model that does not compare well with experimental data. From a visual inspection between figure 8.19a and the geometry shown in figure 8.19b, it is observed that the lateral dimension of the oropharynx has to be large to accommodate the width of the tongue. Figure 8.19a sourced from Grauer et al. [93].

As can be seen in figure 8.16, the airway was subdivided into a number of regions and different discretisation techniques were employed in each region according to its geometry. The nasal passages, oral cavity and lower trachea contained a fully structured mesh, while the oropharynx, nasopharynx, hypopharynx and upper trachea were meshed using an unstructured technique resulting in a tetrahedral mesh. This process resulted in the generation of discontinuous meshes, which were made conformal through the use of a mesh-merge technique. This produced a hybrid mesh with 5-noded prism elements at the interfaces of the structured and unstructured meshes. The prism and tetrahedral elements were subsequently converted into polyhedral elements in the CFD solver in order to reduce the element count and significantly increase the overall quality of the mesh.

8.8.1 Fluid boundary conditions

The boundary conditions used in conjunction with the fluid model were subject to a number of assumptions and simplifications. Depending on the type of breathing being modelled, the inlets either are exposed to atmospheric pressures or blocked off using a wall boundary condition (BC). As inhalation is to be simulated, a pressure inlet BC with 0Pa gauge pressure was utilised. Ideally, the atmosphere should be modelled as a reservoir, but this provides complexity in producing a flexible model that can simulate both oral and nasal inhalation and exhalation. A velocity BC was prescribed at the bronchi which allowed for the specification of the volumetric flow rate. Simple inlet and outlet extensions provide some allowance for flow development and reduce the effect that the imposition of constraints on the flow at the boundary has on the upstream flow.

All soft and hard tissues are considered completely rigid and are prescribed a zero-slip wall condition.

8.8.2 Anthropomorphic measurements of airway geometry

An account of the CSA of the airway is presented in figure 8.20, together with reviews of similar data derived from the published literature as an aid for comparison. Measurements of the model, only possible after the complete meshed model was produced, are graphically presented in figures 8.20b to 8.20d, with the planes on which the measurements were taken depicted in figure 8.20a.

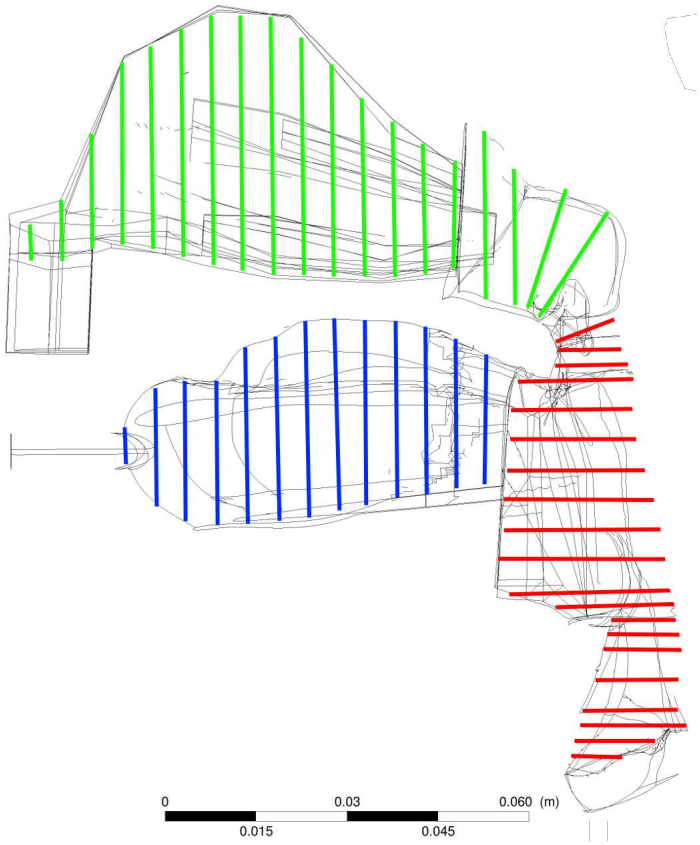

(a) Coronal measurement planes for nasal (green), buccal (blue) and pharyngeal (red) regions

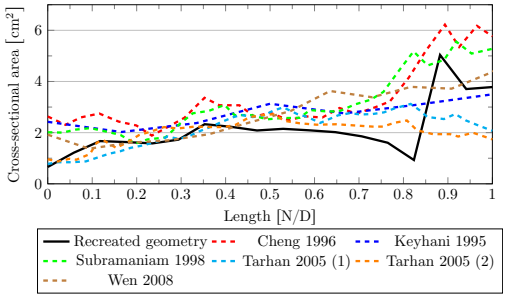

(b) Nasal passages and nasopharynx

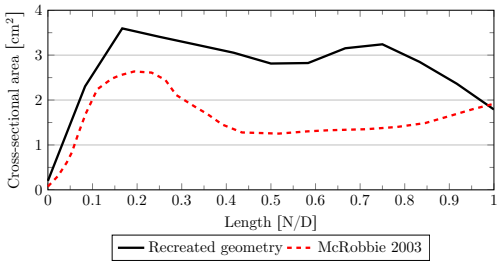

(c) Oral cavity.

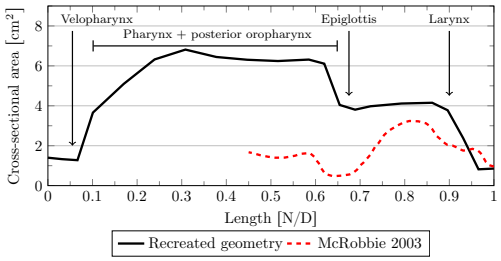

(d) Pharynx

Figure 8.20: Measurement of the CSA of the reconstructed HUA. The data extracted from the literature was manipulated to such that the marked features of each dataset aligned. In the data from McRobbie et al. [175] presented in figure 8.20c, no anatomical markers were present and the data scale was thus assumed. Liu et al. [156] further depict the plausible range of anthropomorphic measurements for the nasal cavity geometry.

As demonstrated in figure 8.20b, the reconstructed and simplified structure of the nasal passages resulted in a model that was representative of the CSA data presented in the literature [273, 307, 265, 40, 139]. Along the length of the nasal passage, the change in CSA mimics that captured through experimental methods on a variety of subjects. It is noted that the nasal passage narrows towards the opening of the nasopharynx, a feature not observed in prior published data. However, compared to a sample of 60 measurements conducted by Liu

et al. [156], the nasal passage CSA remains within the bounds observed using experimental techniques. The comparison shown in figure 8.20c illustrates that the oral cavity has a CSA profile almost clear of anatomical landmarks, consistent with that experimentally measured by McRobbie et al. [175]. It should be noted that the overall posture of the tongue in the oral cavity is significantly different in these two cases, and the inclusion of air space on the lateral and posterior aspects of the tongue result in an increased CSA of this geometry. In figure 8.20d, it is clear that the positioning of the tongue, oropharyngeal walls and other soft tissues does not make for an accurate representation of the pharyngeal region of the HUA. Although the measured region of the oropharynx does extend marginally into the oral cavity (as seen in figure 8.20a), the CSA of the airway from the velopharynx to the larynx appears significantly greater than that presented in the literature. The profile provided by McRobbie et al. [175] suggests that the airway that is represented in this geometry is greatly exaggerated in terms of the flow area, but the profile for the change in CSA is likely to be accurate.

As highlighted in table 8.1, the CSA of the velopharynx is near the upper value provided for a mild OSA patient by Ryan et al. [239], while the maximum measured CSA in the pharynx again greatly exceeds the value of 402mm^2 for healthy subjects determined experimentally by Avrahami and Englender [6] . The primary contributing factors to this inaccuracy are the protrusion of the tongue, resulting in an excessive anteroposterior dimension and the inaccurate representation of the oropharyngeal walls manifesting as an excessive lateral measurement.

Table 8.1: Measurement comparison between airway model and Ryan et al. [239] highlights some of the short-comings of the geometric model that has been developed.

Region	Reconstructed model	Ryan1999		
		ave	min	max
Cross-sectional area (mm^2)				
Velopharynx	139.94	96	43	281
Oropharynx	681.46	103	39	235
Hypopharynx	610.9	67	12	237
Anteroposterior diameter (mm)				
Velopharynx	3.48	7.8	4.7	19.9
Oropharynx	11.89	9.6	4.2	15.1
Hypopharynx	7.89	9.4	3	12.5
Lateral diameter (mm)				
Velopharynx	20.89	14.5	7.4	28.1
Oropharynx	41.78	17.4	11.9	22.2
Hypopharynx	49.1	11.6	5.3	24.3

Furthermore, a brief survey of the literature containing airway measurements of OSA sufferers [198, 6, 7, 239] illustrates that the geometry is not at all representative of such an individual. In these cases, the CSA of the oropharynx is a fraction[9] of that listed above. Importantly, the minimal anteroposterior diameter in the oropharynx (measured between the tongue and retropharyngeal wall) is within the range cited by Ryan et al. [239]. The anteroposterior distance between $\boldsymbol{P}_C$ on the tongue and the retropharyngeal wall is approximately

[9] The measurements differ greatly in each case and for each site of measurement, but in the typical lowest measurement (severe OSA) for the oropharynx CSA is on the order of $10 - 50\text{mm}^2$ (location of measurement planes unlisted in literature).

17mm. Along this line of measurement, the gap between the tongue and inferior surface of the uvula (which has a thickness of approximately 5.5mm) is 3.5mm.

8.9 Critique of the author's constructed models

Each individual has a distinctive anatomy and thus the anthropomorphic features presented in this model, although not exactly mirroring those seen in the standard medical and scientific literature, are not invalidated as a consequence.

A full discussion with regard to the construction of each of the author's models is presented in appendix E. However, at this juncture an overview is considered warranted. There are numerous factors that influenced the observed differences between measurements taken from the reconstructed geometry and experimental data. The use of photographic images made distinguishing different tissue groups difficult. Some modifications were made to reverse soft tissue deformation of the tongue by the surrounding anatomy. Further simplifications and modifications to the geometry and incorporated tissue types were necessary to assist in the design of a high-quality computational domain for use within the developed framework. Difficulties in determining the position of the oropharyngeal walls introduced potential error in the reconstructed fluid geometry. The difference in conditions experienced during *in vivo* data extraction presented in the literature and the VHP dataset could account for a significant portion of the measurement error; for example, McRobbie et al. [175] conducted measurements on a live subject, resting in a supine position during free breathing, while the VHP dataset is of a cadaver. With regard to the reconstructed geometry, the forward posture of the tongue increases the volume of the oropharyngeal space and may also cause the anterior displacement of other soft tissues, such as the epiglottis, similar to that observed was the use of MADs thereby reducing the potential for pharyngeal collapse.

Overall it is concluded that this airway model is not representative of a subject with OSA. Due to the complexities in the production of the model, the lack of truly representative experimentally derived data, and that the focus of the work is the solid model, no alterations were made to produce a fluid model with a more representative CSA. However, as is shown in chapters 12 and 13, this fluid model could still be used to provide insight into the differences between various conditions under which respiration takes place, and a tool to validate assumed loading conditions for the solid model.

9. MOVEMENT OF THE PASSIVE TONGUE

This chapter reflects some initial studies that were performed to demonstrate the functioning of numerous aspects of the developed model. A study of the motion of the passive tongue under the influence of gravitational and hypothetical airway forces was conducted in order to understand the influence of the displacement field on the underlying musculature of the tongue.

9.1 Pre-strain and prestress condition

The initial configuration is defined to be one which, when under the influence of gravity with the loading corresponding to a person standing in the upright position, results in the configuration defined by the reference configuration. Since the cadaver was orientated in an upright position when the images were taken, a known and simply described loading force acted on the body during imaging. It is hypothesised that the application of a body force could undo the deformation such that, when gravitational forces are reapplied, the configuration extracted from the imaging data is reattained.

As a first approximation to the zero strain configuration, a spatially constant body force with a magnitude proportional to that of gravity was applied in a direction opposite to the natural gravitational direction. The magnitude of the body force was chosen to be 1.2 times that of gravity and applied at an angle of 5° in the direction posterior to the axis aligned superiorly, thereby adding a component of the applied force in the supine direction.

Figures 9.1 to 9.4 are provided facilitate the description of the process of capturing the zero strain configuration. At time $t = 0$, the initial and reference configurations coincide. The pre-strain body force is then applied to deform the body to the configuration chosen to be the initial configuration. As shown in figure 9.1, this deformation results in a non-trivial stress and strain state. The inverse of deformation gradient $\boldsymbol{F}^{\mathrm{RI}}$ and fibre stretch λ^{RI} are then computed and recorded at each calculation point. The new zero strain state, following from equations 3.25 and 3.27, appears as in figure 9.2 together with the non-zero displacement. Ideally, application of the gravitational body force in the upright orientation (that assumed to be applied to the cadaver during cryogenic freezing) will result in the state depicted in figure 9.3. Here the displacement field is zero and the body and fibre strains are non-negligible.

In practise, the resulting equilibrium position does not coincide with the reference configuration. However, as figure 9.4a demonstrates, the difference between the two is minimal. The majority of the body remains

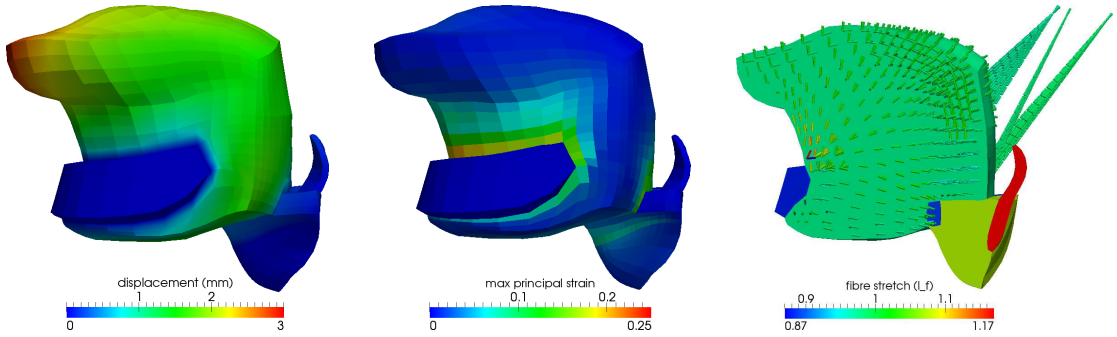

(a) Displacement **(b)** Cell average maximum principal strain **(c)** Fibre stretch (λ_f)

Figure 9.1: Zero strain configuration (pre-snapshot). Point-wise maximum principal strains of up to 0.45 were computed within the tongue in the vicinity of the mandible.

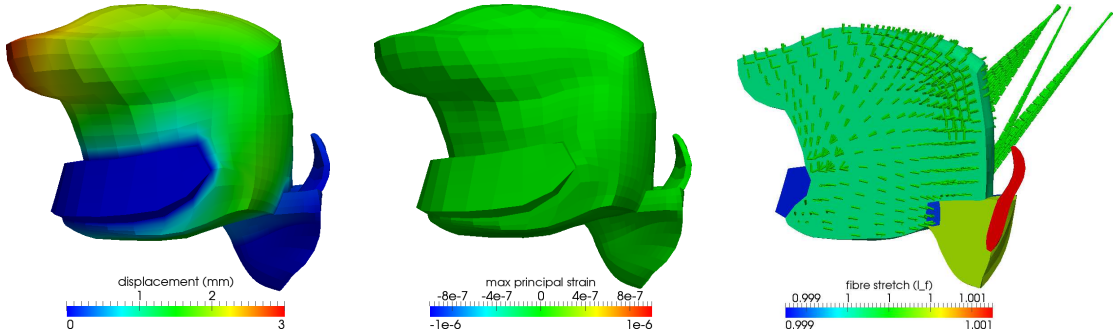

(a) Displacement **(b)** Cell average maximum principal strain **(c)** Fibre stretch (λ_f)

Figure 9.2: Zero strain configuration (post-snapshot).

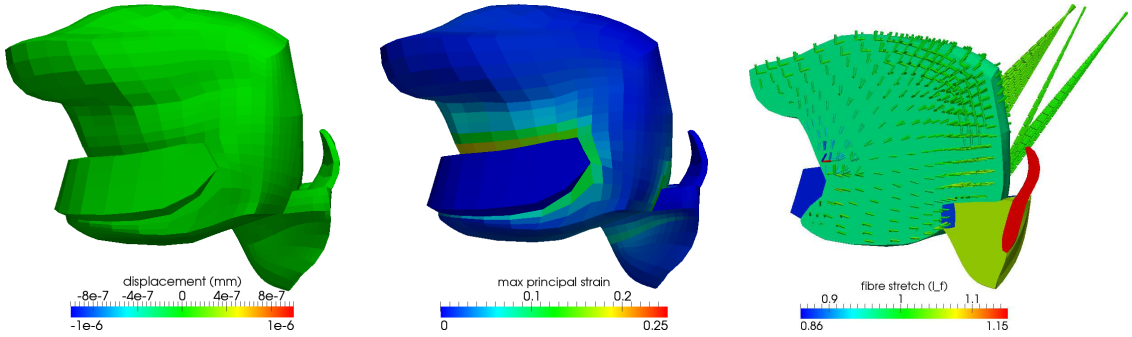

(a) Displacement **(b)** Cell average maximum principal strain **(c)** Fibre stretch (λ_f)

Figure 9.3: Zero displacement configuration (post-snapshot). Point-wise maximum principal strains of up to 0.34 were computed within the tongue in the vicinity of the mandible.

$0.2 - 0.4$mm away from the reference position while the maximum displacement error is approximately 0.6mm in the region of insertion of the SG. The small final displacement is present primarily as a result of the non-linearity of the material behaviour. Although not ideal, this is a sufficiently accurate approximation for the zero strain configuration for the purpose of this work. The large strains and muscle stretches respectively

illustrated in figure 9.4b and figure 9.4c demonstrate the importance of incorporating pre-loading into biological models of the HUA, as the material stiffness in this regime is significantly greater than in a zero strain state. It is observed that specific regions of the body, specifically near the attachment points of the tongue to both the mandible and hyoid bone, experience significant strain. Further, the strain field throughout muscle groups is non-uniform, with some regions of muscles being placed in tension and others experiencing compressive strain. It is noted that the strain field remained qualitatively similar to the ideal result, but is reduced in magnitude. This can be attributed to the sensitivity of the computational domain near the fixed mandible to displacement and the method used to post-process the result. Under more complex circumstances, there is a need to solve for the zero strain configuration iteratively [84].

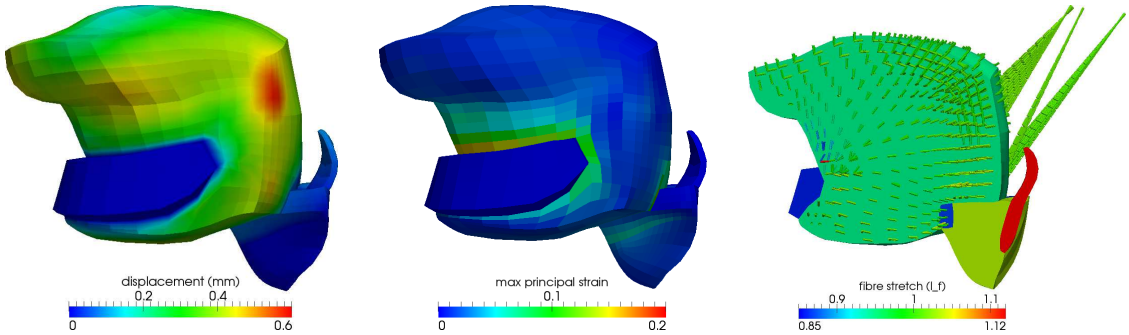

(a) Displacement

(b) Cell average maximum principal strain

(c) Fibre stretch (λ_f)

Figure 9.4: Application of upright gravitational body force from zero strain configuration. Point-wise maximum principal strains of up to 0.26 were computed within the tongue in the vicinity of the mandible. Vertically-aligned muscle fibres in the region of the mandible are seen to experience non-trivial shortening.

9.2 Mesh dependence study

A basic mesh-dependence study was performed to determine the appropriate element density required for the production of satisfactory model results. As low-order elements are utilised, either a large number of elements or strategic distribution of elements are required to ensure that displacement convergence is attained. Furthermore, the mesh distribution within muscular parts determines the degree of accuracy to which the underlying musculature is resolved. Three variations of the same model, depicted in figure 9.5, were developed based on the same underlying discretisation structure (ICEMCFD© blocking strategy) and evaluated in two independent tests to determine their relative performance. Since the focus of this study is on the movement of the tongue, the majority of the elements are located within this body and are concentrated in expected regions of large strains. The element counts in each part of the anatomy is documented in table 9.1. In each analysis, the results of the model with the highest element count were used as a basis from which to measure the performance of the other models.

Table 9.2 summarises the comparison between models under gravitational and pressure loading. In this case, the muscles remain in a purely passive state. It is observed in both scenarios that the performance of the *coarse* grid is similar to that of the most refined grid, with displacement errors of under 7% (corresponding to an accuracy of less than 1mm) attained at the measurement points. The recorded VWA fibre stretch for the GGp

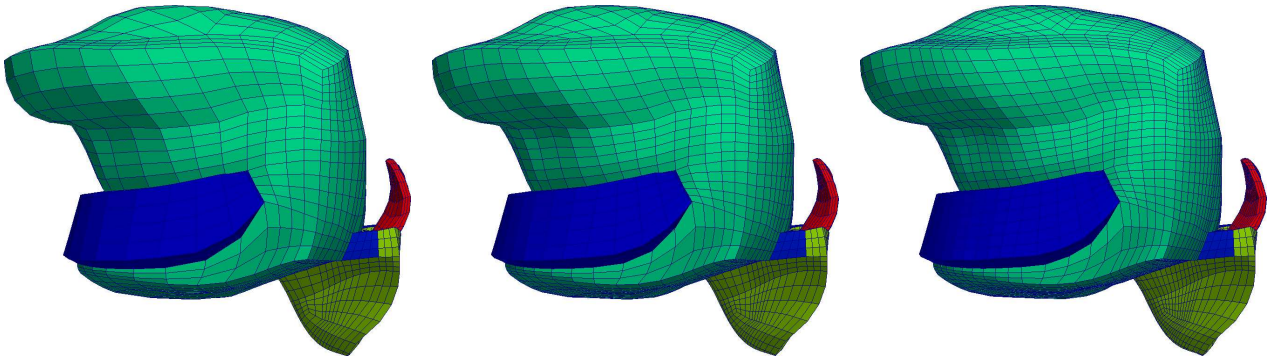

(a) Coarse grid **(b)** Medium grid **(c)** Fine grid

Figure 9.5: Illustration of levels of mesh refinement used in the grid dependence study. Due to the use of a structured grid, a complex blocking strategy had to be used to ensure that an even distribution of elements of similar size was obtained.

Table 9.1: Element count per part for refined meshes. In each model, the number of elements in the tongue were increased roughly by a factor of two.

Mesh density	Mandible	Hyoid	Tongue	Adipose	Epiglottis	**Total**	**Ratio (total)**
Coarse	128	156	4526	2332	522	7664	1
Medium	220	288	9078	4188	774	14548	1.90
Fine	360	360	18196	6620	1200	26736	3.49

Table 9.2: Relative error of total displacement for passive tongue under gravitational and pressure load. The points of measurement are given in figure 8.11b, with $\boldsymbol{P}_A$ corresponding to the least constrained region of the tongue and $\boldsymbol{P}_C$ a point of significance in evaluating the position of the tongue for models of OSA. The error measure was calculated as $E = \left|\boldsymbol{P}_i - \boldsymbol{P}_i^{\text{FINE}}\right| \Big/ \left|\boldsymbol{P}_i^{\text{FINE}}\right|$ and $\bar{\bar{\lambda}}_{\text{f}}$ given by equation 7.26.

Mesh density	Relative	Gravity			Gravity and pressure		
	CPU time	$\boldsymbol{P}_A$	$\boldsymbol{P}_C$	GGp $\bar{\bar{\lambda}}_{\text{f}}$	$\boldsymbol{P}_A$	$\boldsymbol{P}_C$	GGp $\bar{\bar{\lambda}}_{\text{f}}$
Coarse	0.21	-6.77%	-5.35%	0.10%	-6.55%	-5.21%	0.10%
Medium	0.45	-3.90%	-2.96%	0.06%	-3.80%	-2.93%	0.06%

is very consistent for each case, indicating that the strain field and fibre distribution are adequately matched in all cases.

In the second part of the study, contraction of a specified muscle was performed after gravitational loading in the upright orientation. In the first test, the GG (all three muscle subgroups) was activated and the second test involved activation of the SL. Table 9.3 shows that the coarse grid again performs well, providing sub millimetre precision for the recorded points. It should be noted that, in the case of SL activation, $\boldsymbol{P}_C$ undergoes very small displacements which results in a large relative error when compared to the other cases. The VWA fibre strain for the posterior portion of the GG is again very consistent between tests.

Due to the reasonably low displacement error margin between the coarse and benchmark model, and that result trends rather than absolute measures are of interest, the coarsest model was considered satisfactory for

Table 9.3: Grid refinement and the relative displacement error for the active tongue. Contraction of GG and SL occur from the upright configuration.

Mesh density	Gravity and GG activation				Gravity and SL activation			
	Rel. CPU time	$\boldsymbol{P}_A$	$\boldsymbol{P}_C$	GGp $\bar{\bar{\lambda}}_f$	Rel. CPU time	$\boldsymbol{P}_A$	$\boldsymbol{P}_C$	GGp $\bar{\bar{\lambda}}_f$
Coarse	0.22	5.23%	7.32%	0.02%	0.21	-7.79%	82.18%	0.28%
Medium	0.46	1.57%	2.55%	0.05%	0.44	-6.40%	19.97%	0.01%

use. The major benefit of this model was the computational time saved by using a model with less elements.

9.3 Resistance of the passive tongue to motion due to gravitational and pressure forces

An investigation was performed to determine the effect of the orientation of gravity as well as pressure loading on the passive tongue. Although the end result of the gravitational loading is intuitive, the role of the tongue histology in affecting the motion is undetermined. From this study, preliminary insight into the dynamics of the gross and histological anatomy in circumstances that cause maximum deflection of the tongue body was attained. Furthermore, analysis of the bulk stretch of each muscle group under various scenarios provide clarification as to which muscles may be most active to reduce the displacement due to loading. The loading parameters for the fully quasi-static problem under the conditions of oral inspiration are collectively presented in section 8.6.3.1.

9.3.1 Oral inhalation

The final displaced configuration of the tongue experiencing -500Pa pressure loading under different gravitational loading conditions is shown in figure 9.6. With no applied load, the tongue remains in a neutral position when gravity is orientated in the upright direction; while the supine orientation causes the tongue to move in a posterior direction. In both cases, the influence of pressure ensures that the tongue is drawn backwards towards the posterior region of the oral cavity. As it moves backward, the top of the tongue lifts. It is noted that in all cases, due to both prestressing and loading, the spatial variation of local fibre stretch is substantial with some regions of the GG in compression and others in tension. The fibres in the vicinity of the mandible, the GG origin, experience large stretches as tissue near the fixed mandible deforms greatly.

In figure 9.7, a quantification of the displacement of the tip and rear of the tongue due to the individual loading components is presented. Regardless of the problem non-linearities (material, geometric and loading), the displacement of the measured points scaled linearly with the applied loads. A steadily reclining orientation to the supine results in the displacement of the tongue tip and rear posteriorly, with a steady increase in the displacement magnitude. Reducing the airway pressure has a similar effect on the tongue displacement. At the maximum applied load of -1000Pa, the rear of the tongue moves posteriorly by 11mm, exceeding that observed in the upright orientation by 7mm. Lying in a prone position has the effect of drawing the tongue out of the oral cavity. Upon application of airway pressure in this orientation, at maximal load the pressure force only marginally overcomes the gravitational force to shift the tongue slightly back. At maxi-

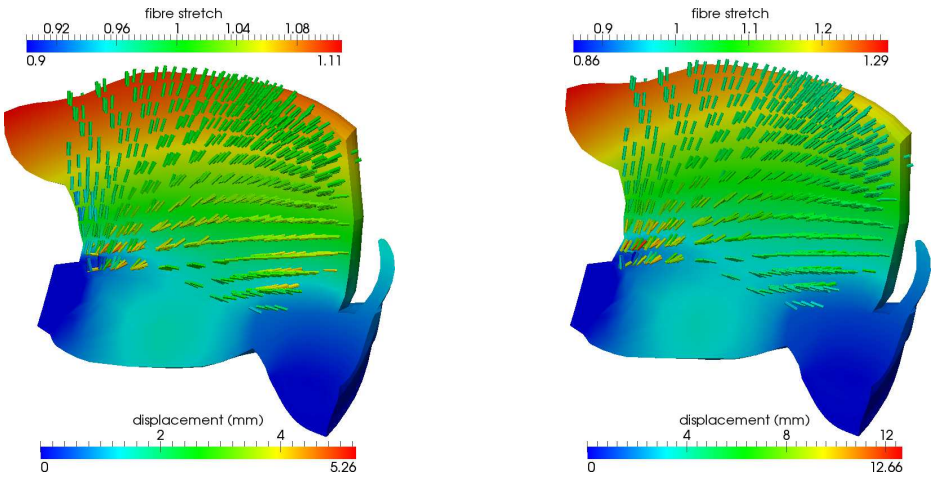

(a) Upright orientation **(b)** Supine orientation

Figure 9.6: Passive tongue under the influence of gravity and pressure loading (oral breathing). The nominal value for the pressure load is $p_{\text{nom}} = 500\text{Pa}$. The figures present information for both the displacement and GG fibre stretch.

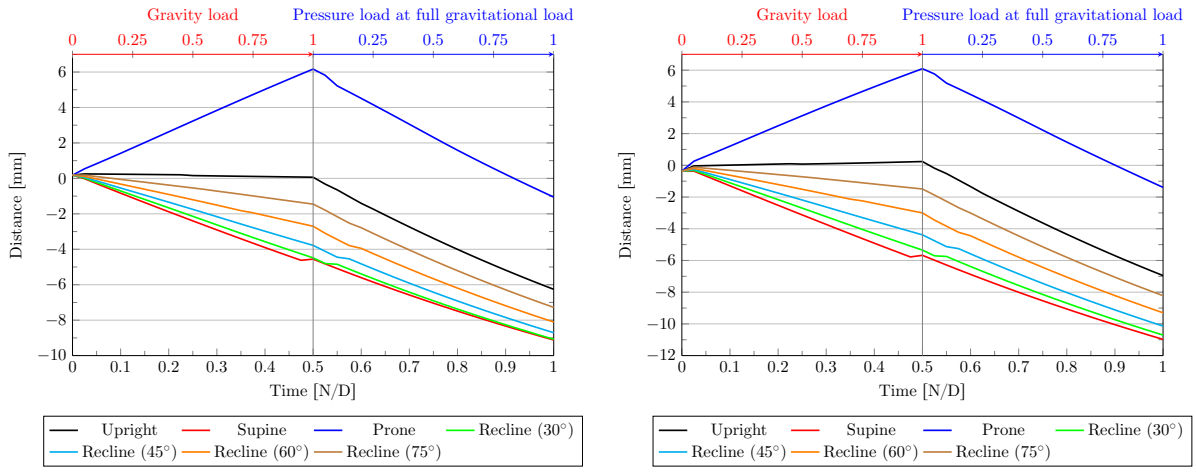

(a) Point $\boldsymbol{P}_C$ at the posterior of the tongue **(b)** Point $\boldsymbol{P}_A$ at the anterior of the tongue

Figure 9.7: Anterior displacement of the passive tongue due to gravitational and pressure loading (oral breathing). The nominal pressure applied at $t = 1\text{s}$ is $p_{\text{nom}} = 1000\text{Pa}$.

mal reclination, approximately half of the displacement of both points of measurement could be attributed to the gravitational forces. The lift experienced at the tip and rear of the tongue was 5.3mm and 4.7mm respectively. At maximal pressure with the same gravitational orientation, the these values were augmented by a further 5.3mm and 4.6mm respectively. Furthermore, subject to a gravitational load representing a lateral orientation, it was observed that the displacement history of the measured points in the posterior direction was very similar to that of the upright orientation.

In figure 9.8, the measure of overall muscle stretch (equation 7.26) is shown following increasing gravitational and pressure load. It is interesting to note that, independent of all the non-linearities present, there appears to be a linear dependence of measured average fibre-stretch for each muscle group on the load for the described cases.

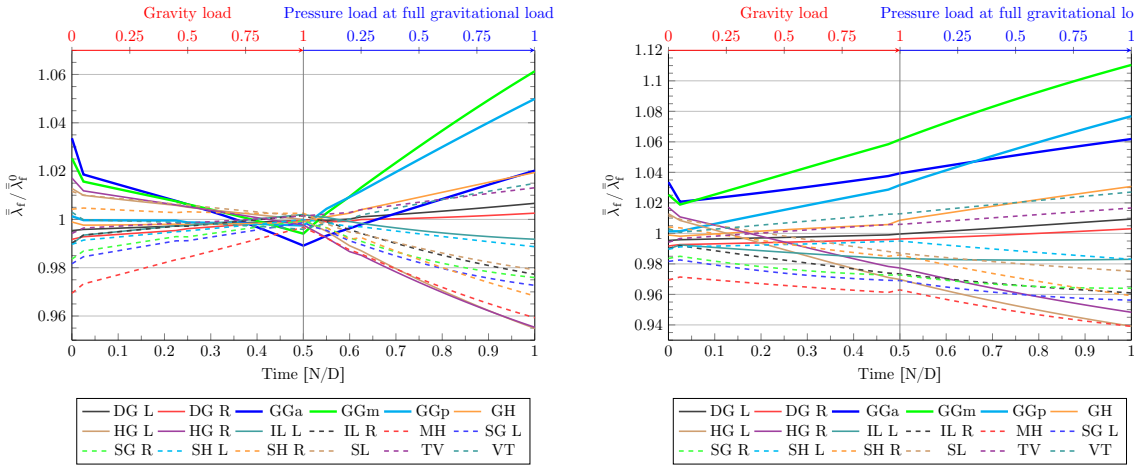

(a) Upright orientation

(b) Supine orientation

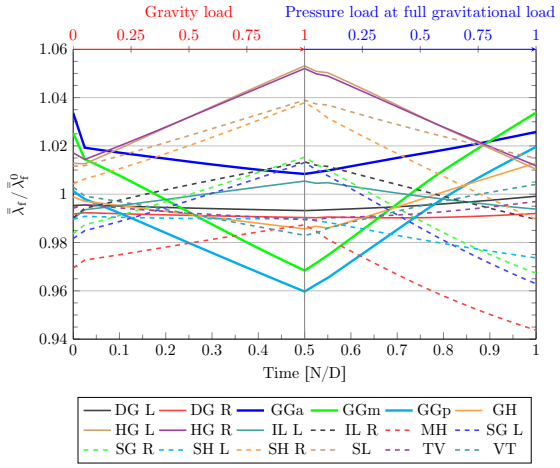

(c) Prone orientation

Figure 9.8: VWA fibre stretch ratio $\frac{\bar{\bar{\lambda}}_f}{\bar{\bar{\lambda}}_f^0}$ for muscles in the tongue under the influence of gravitational and pressure forces (oral breathing). The value $\bar{\bar{\lambda}}_f^0$ is the fibre stretch measured in the pre-strained reference (zero-displacement) configuration. At $t = 0$s, the body is in the initial (pre-strained) configuration. As this value is calculated with the exactly prescribed zero-displacement, there exists a small computational error between this value and the upright configuration which is assumed to, but doesn't quite, match the zero-displacement configuration.

From these figures it is apparent that both the gravitational orientation and pressure load have a significant influence on the stretch of the various muscle groups. In the upright position, gravitational loading reverses the stretch due to preloading and they attain a neutral strain state. For the most part in the supine case, muscles in tension under the influence of gravity remain thus when the pressure load is increased. In particular, the components of the GG are generally in compression in the upright stance, while in the supine configuration they are in tension. In both cases, application of a pressure load results in a significant increase in average stretch of the GG muscles, while the effect on other muscle groups is of a lesser magnitude. In the prone state, the GGm and GGp become compressed, but a large pressure load places them in a state of tension. For this loading configuration, a reversal of stain state is observed in the majority of muscle groups. By comparison to the other muscle groups, the effect of gravitational and pressure loading on the GGm and

GGp is the most significant as these muscles are often the most tensile-strained constituent muscles of the tongue.

Focusing on the posterior and middle components of the GG, figure 9.9 illustrates the relationship between the angle of recline, magnitude of pressure loading and the stretch-state of these muscles. Excluding the prone state, changing the angle of incline alters the degree of tension in which both of the muscles are placed after gravity loading. There is a linear relationship between the magnitude of the gravitational load and the muscle stretch. A similar relationship exists between the magnitude of the pressure load and the fibre strain; the gradient $\frac{\Delta\bar{\bar{\lambda}}_f}{\Delta p}$ remains nearly constant across all gravitational orientations and through the pressure loading step.

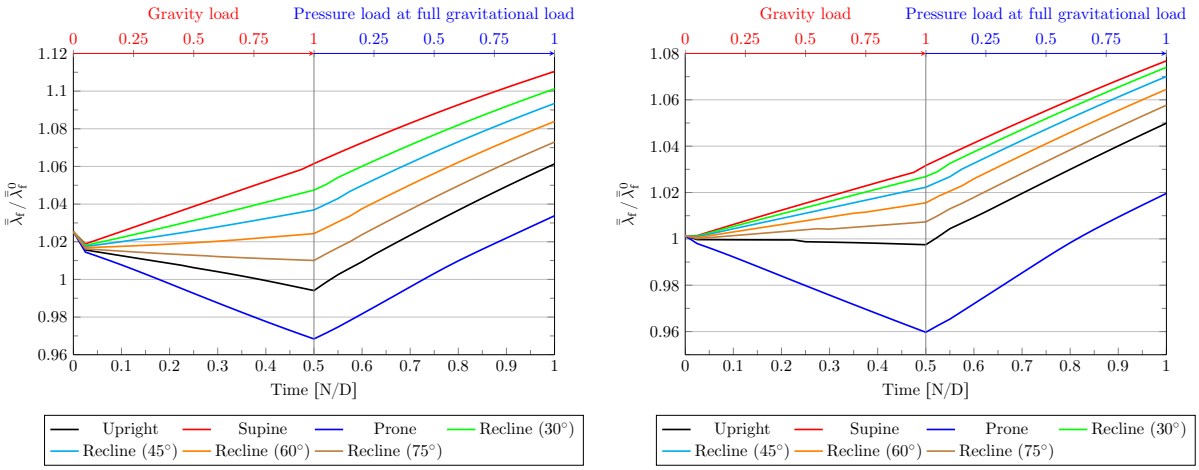

(a) GGm **(b)** GGp

Figure 9.9: VWA fibre stretch ratio $\frac{\bar{\bar{\lambda}}_f}{\bar{\bar{\lambda}}_f^0}$ for two of the component muscle of the passive GG under the influence of varying gravitational and pressure forces (oral breathing).

9.3.2 Nasal inhalation

In stark contrast to the results presented for oral breathing, the following results for the state of nasal inhalation demonstrate that the dominant load is that due to gravity. Figure 9.10 depicts the displacement of the tongue tip and rear in the anteroposterior direction. It shows that after gravitational loading, the spatially constant pressure load produces little further movement in the tongue, even at large negative airway pressures. Although the surface area at the rear of the tongue is larger than at the front, a marginal anterior deflection due to pressure loading is noted. This can be attributed to the lifting of the tongue due to the out-of-balance pressure load acting on the superior surface of the tongue. The result of the nearly balanced anteroposterior loading is that the maximum pressure induced anterior displacement, measured at the tongue tip for the supine case, is only 0.7mm. The rear of the tongue experiences an anterior motion of 0.25mm, but lifts by 1.75mm.

Although the overall posterior deflection of the tongue remains minor through the pressure loading steps, the values measured for fibre stretch changes significantly. Compression of the MH further indicates that

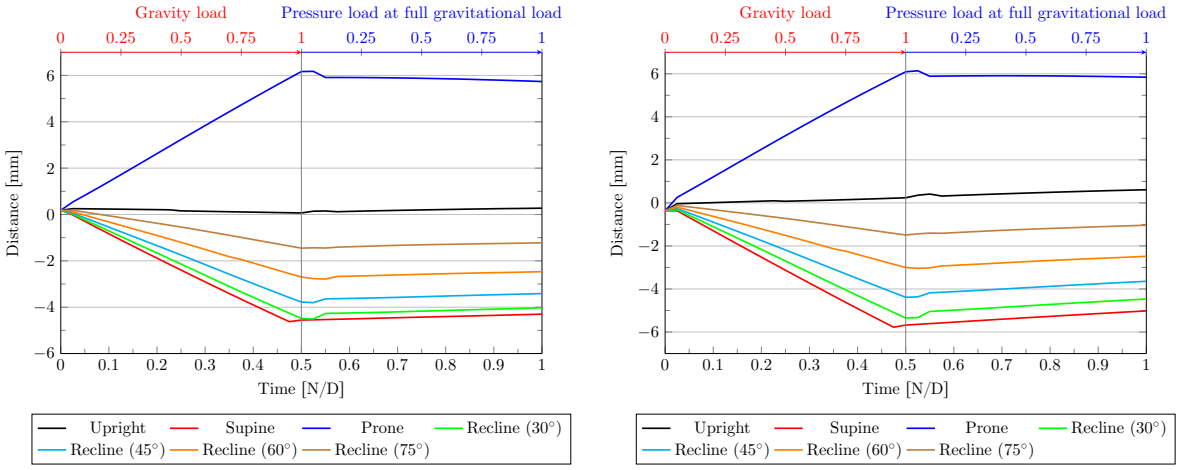

(a) Point $\boldsymbol{P}_C$ at the posterior of the tongue

(b) Point $\boldsymbol{P}_A$ at the anterior of the tongue

Figure 9.10: Anterior displacement of the passive tongue due to gravitational and pressure loading (nasal breathing). The nominal pressure value was $p_{\text{nom}} = 1000\text{Pa}$.

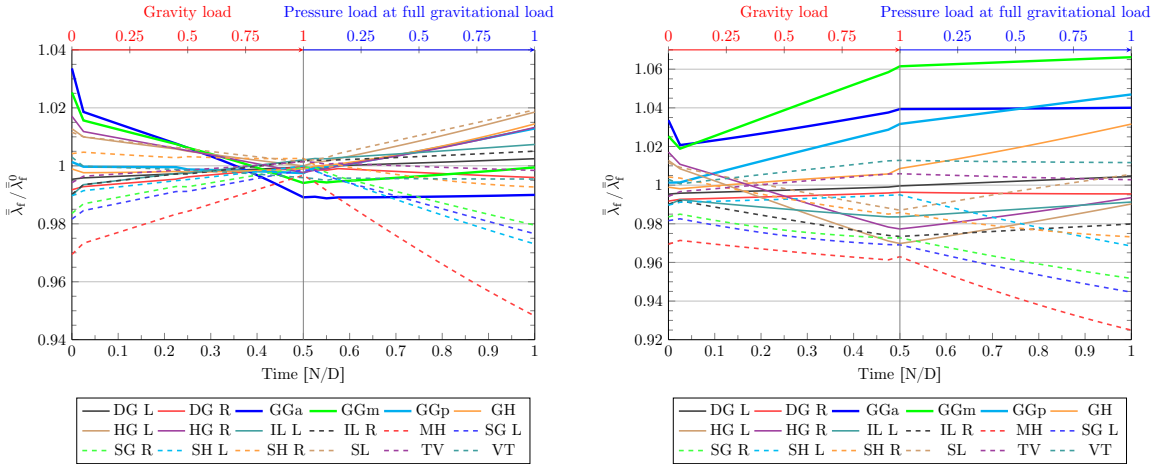

(a) Upright orientation

(b) Supine orientation

Figure 9.11: VWA fibre stretch ratio $\dfrac{\bar{\bar{\lambda}}_f}{\bar{\bar{\lambda}}_f^0}$ for muscles in the passive tongue under the influence of gravitational and pressure forces (nasal breathing).

the tongue is being raised in the oral cavity due to the airway pressure. Notably, the values obtained for the larger components of the GG muscles remain constant through pressure loading.

9.4 Summary and discussion of results

The results presented here indicate that the gravitational loading, the magnitude of the pressure load and the method of inhalation have a significant effect on the deformation of the passive tongue. Not only does the tongue tend to displace posteriorly under increased loading and reclination, thereby reducing the volume of the retroglossal space, but it tends to lift, threatening to block the oral cavity. Furthermore, it has been demonstrated that the measure of average fibre stretch $\bar{\bar{\lambda}}_f$ can be a good indicator for the overall tensile or

compressive state of the muscle. The average strain state experienced by each muscle differs considerably with the loading conditions applied to the tongue. A visual demonstration of the strain state of the GG given in figure 9.6, coupled with the presented measures extracted during various loading conditions give credence to the idea of using this as a filter (equation 7.24) for the GA search space.

10. TONGUE RESPONSE TO PRESCRIBED MUSCLE ACTIVATION

Up to this point, the model has remained entirely passive, with no muscle contraction performed to produce motion. This section documents the deformation caused by contraction in specific muscles in two distinct scenarios. Firstly, a demonstration and analysis of the effect of contracting individual muscle groups in isolation will be presented. Next follows a discussion of the efficacy of the components of the GG in preventing posterior motion of the tongue. Note that in the following scenarios, the muscle activation constant α was prescribed and the conditions remained completely quasi-static. Furthermore, unless stated, the gravitational orientation is set in the upright position.

10.1 Deflection due to individual muscle activation

The role of the muscles of the HUA is well understood and is extensively documented in medical literature. This section documents the observations made when invoking deformation through the control of individual muscle groups in the tongue. These observations provide a validation that the spatial description of the muscle groups and the associated contractile model produce a functional tongue model that exhibits physiologically realistic behaviour. Additionally, investigating the response of an individual muscle undergoing contraction provides insight into the role each muscle plays during complex operations when multiple muscles act simultaneously. A complete visual showcase of the response of the upper airway tissues during contraction of each muscle is presented in appendix F. These results may be compared to the descriptions of their actions given in the medical literature and documented in section 2.2.

Contraction of the GG, constituted of three distinct and separately controlled fibre groups, causes the tongue to be drawn towards the mandible where it has its origin. In each three subsets, lateral extension of the tongue due to its compression in the sagittal plane was observed. However, due to the relative symmetry of the geometry and the line of action of the muscles, minimal axial twisting is observed during muscle contraction. The GGp primarily draws the posterior portion of tongue anteriorly. As a result, the hyoid and epiglottis are displaced forward as well and the anterior region of the tongue is moved forward and inferiorly. The posterior region of the tongue surface is elevated due to the incompressibility of the tissue.

It was observed that the FEM mesh just superior to the mandible undergoes extreme and unrealistic deformation in contraction of this muscle. This computational artifact is the result of two factors. Firstly, the

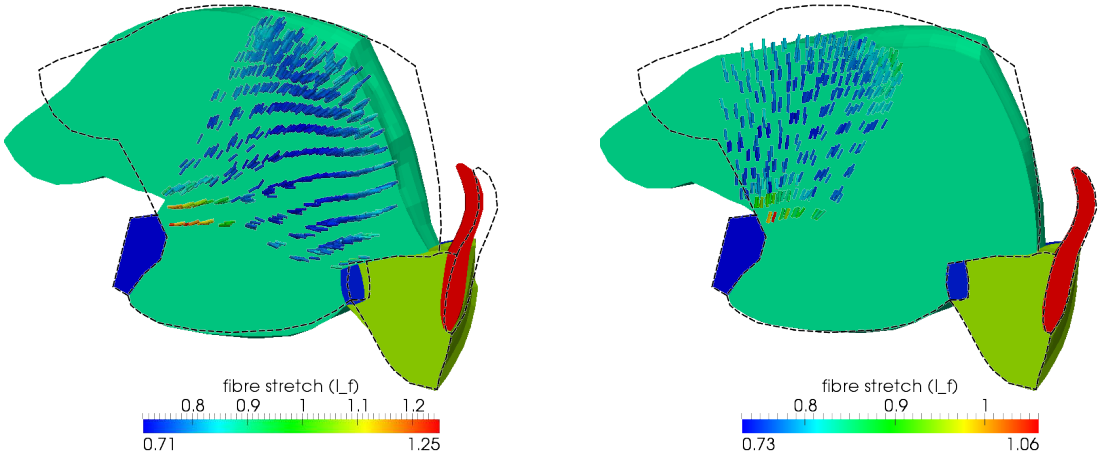

(a) GGp (FFMR 5%)

(b) GGm (FFMR 5%)

Figure 10.1: Isolated muscle activation of components of the GG. The reference position of the tissues is indicated by the dashed silhouette.

orientation of the GGp fibres in this region is such that, under contraction, the tissue deforms freely in this location with no point of fixture. Secondly, the constraint of the stiff mandible allows little flexibility here. To minimise this effect, further mesh refinement in this vicinity or the use of a higher-order FE approximation should be considered. As with the GGp, the GGm also draws the posterior tongue forward. However, the mechanics of motion differs in that the the posterior portion of the superior surface of the tongue nearest the uvula is moved inferiorly towards the point of fixation. The rear of the tongue is drawn forward with its upper surface. Consequently, the tongue tip undergoes a large deflection anteriorly. A comparison of figure 10.1a to figure 10.1b suggests that the GGp is more effective than the GGm at moving the rear surface of the tongue anteriorly. The anterior region of the tongue's superior surface moves inferiorly upon activation of the GGa. The deformation is localised, and the rear section of tongue remains largely unaffected in terms of spatial orientation. The tongue tip displaces also inferiorly and exhibits little movement in the coronal plane. A similar lack of transverse deformation occurs upon contraction of the other constituent muscles of the GG.

Activation of the SL results in the tongue tip curling backwards and upwards towards the soft palate as shown in figure 10.2a. Considerable lateral deformation, due to incompressibility effects, are also observed. The location of the epiglottal fat pad has a significant role in facilitating the functionality of this muscle which runs from the tip to the root of superficial regions of the tongue. Due to its location and orientation, the SL utilises the epiglottal fat pad to provide elastic resistance during contraction. Due to its incompressibility and the proximity of the thyroid cartilage to the tongue-fat-pad interface, the adipose tissue undergoes little deformation on SL contraction and the efficiency of the muscle contraction thus is maximised. High contraction strengths produce deformation magnitudes that may result in contact between the tongue and the hard palate.

The two IL muscles move the tip of the tongue inferiorly and in a posterior direction. Figure 10.2b demonstrates that they retract the tongue tip and increases the curvature of the tongue's superior surface. The lower parts of the bulk of the soft tissue also undergo little deformation. Collectively, the SL and IL appear to control the vertical motion of the tip of the tongue. Their contraction is also able to move the tip posteriorly, but cannot directly cause the tip to move anteriorly.

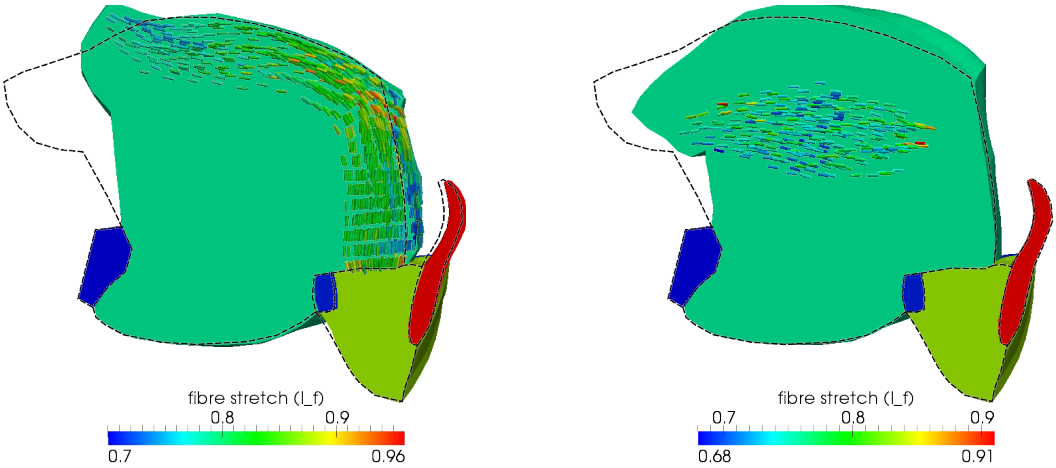

(a) SL (FFMR 5%) **(b)** IL (FFMR 5%)

Figure 10.2: Isolated muscle activation of primary muscles for use in controlling the vertical position of the tongue tip.

As the VT contracts, the upper surface of the blade of the tongue flattens and displaces laterally. Furthermore, the superior and posterior surfaces move inferiorly and anteriorly respectively as the alignment of the fibres pulls these surfaces in towards the bulk of the tongue tissue. A measurable deflection of the epiglottis is also evident.

The TV, which has fibres aligned in the transverse plane, serves to contract the tongue blade laterally, thereby causing the tip to deflect anteriorly. Tissue incompressibility dictates that the superior surface bulges towards the palate and the posterior surface towards the retropharynx. As this muscle is located only near the surface of the tongue, the main body of the tongue near the mandible remains in a low-stress state. As shown in figure 10.3a, as a result of the shortening of the tongue surface, the blade tends to curl downwards towards the mandible. However, it has less influence on this motion than the VT.

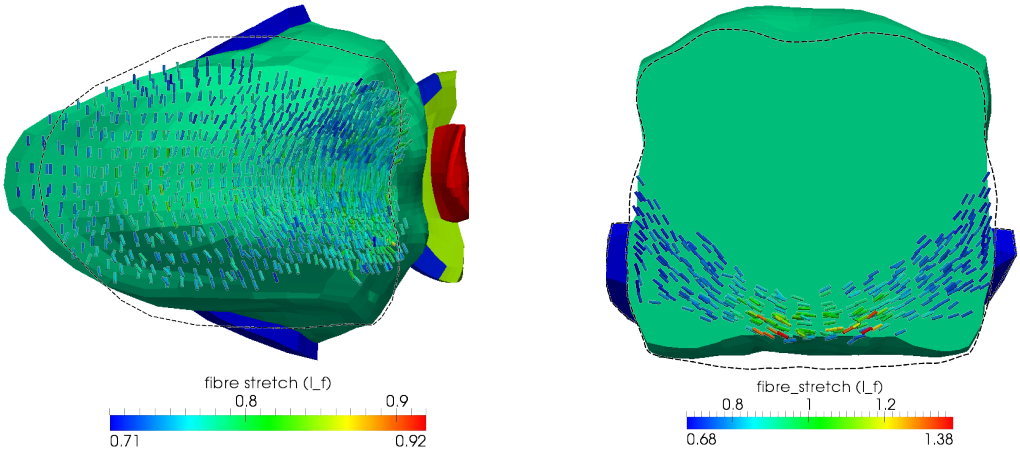

(a) TV (FFMR 5%), transverse view **(b)** MH (FFMR 5%), coronal view

Figure 10.3: Isolated muscle activation of muscles with action in the coronal and axial planes.

Shortening of the MH, which is located at the root of the tongue body, has action in the coronal plane and lifts

the tongue towards the palate. Figure 10.3b demonstrates that the highly curved muscle which originates at the mandible flattens out as it is pulled taut, leading to a pronounced vertical displacement of the hyoid bone. The epiglottis is moved posteriorly as the lower regions of the epiglottal fat-pad move anteriorly.

Upon activation of the HG, the rear of the tongue is drawn towards the hyoid, its point of origin. This results in the tongue blade rocking backwards and the tip displacing superiorly. The lateral edges of the upper surface move inferiorly and towards the midplane, while the tissue on the sagittal plane is displaced in the opposite direction. The action of this muscle appears to oppose that of the MH.

The SG, which is modelled as having a portion both internal and external to the tongue body, is shown to displace the tongue posteriorly and superiorly. Figure 10.4 demonstrates that the external muscle model successfully reproduces the action of the muscle external to the tongue body. The portion that is inserted into the tongue is aligned with the IL which, upon contraction, causes the tongue tip to retract and displace inferiorly. Due to the the muscle origin being more distant from the sagittal plane than the insertion, some lateral deflection is observed. However, this may be due to the assumption of a linear line-of-action in the portion of the muscle external to the bulk as opposed to the nonlinear complex geometry of the physical muscle.

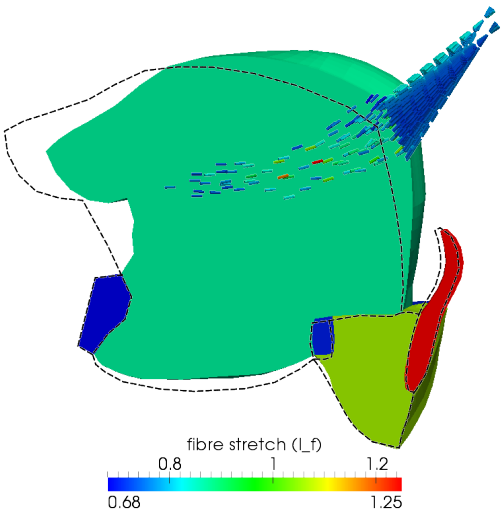

Figure 10.4: Isolated muscle activation of the internal and external components that comprise the SG (FFMR 25%). Due to the small CSA of the applied traction region on the posterior tongue surface, considerable muscle activation was required to attain a significant deformation.

Two other muscles in the tongue were modelled similarly. The DG, which constitutes a portion of the floor of the mouth, raises it upon shortening and draws the hyoid towards the anterior region of the mandible. The SH, which terminates at the hyoid, uses the mandible as a pivot to lift the rear of the tongue. As a consequence, the tongue tip is moved inferiorly.

The GH also influences the position of the hyoid. Its activation results in the hyoid bone being pulled anteriorly towards mandible, causing the epiglottis to move forward. The root of the tongue bulges due to the shortening of the muscle and the incompressibility of the tissue. The adipose tissue in which the epiglottis is embedded is attached to the hyoid and moves by the contraction of the GH. Significant movement of the lower-rear region of the tongue is also observed. As the GH is only present in the lower extremities of the tongue, the bulk of the tongue is unaffected by its contraction.

An additional observation that can be made is that contraction of almost all muscle groups significantly affects the position of the tip of the tongue; and, for this reason, controlling the motion of this anatomical point would be challenging. When in (an unstable) equilibrium, a perturbation in the contraction strength of any of numerous muscle groups could easily result in a considerable deflection of the tongue tip.

Observations suggest that, although the global average behaviour of the contracting muscle was to shorten, the dynamics of each representative fibre element differed considerably according to their location in the tongue. It has been noted that, on occasion, an element of the contracting muscle was computed to actually undergo extension. An example of this can be seen in the root of the GG in figures 10.1a and 10.1b. This contradictory result can be attributed to numerical error associated with using a coarse grid and a low-order FE with the enforcement of the incompressibility constraint. There is an inability of the mesh to deform in such a way as to correctly capture the dynamics of the muscle in these locations.

10.2 Simultaneous contraction of several muscle groups

Some of movements of the tongue are not possible without the simultaneous contraction of multiple muscles. A careful balance of the contractile force generated by each muscle is required in order to achieve a desired movement. To this end, several further experiments involving the simultaneous contraction of multiple muscle groups were performed in order to better understand the role of various muscles in the movement of the HUA soft tissues. These tests also served to evaluate further the stability of the numerical algorithms as the material non-linearities become increasingly complex. The interactions between the fibres become more pronounced and competition developed for extension between adjacent overlapping active muscular structures. With no rate-dependence, superlinear convergence rates were continually attained for these more complex scenarios.

Shortening of all three components of the GG causes the tongue to be deformed in the direction of the lower mandible, with the deformation in the transverse plane especially noticeable in the anterior region of the blade as well as at the root of the tongue. The deformation appears consistent with that of their individual contributions previously presented. As the force is distributed evenly throughout the bulk, in a sagittal section the tongue appears to retain its natural curvature. As shown previously, a relatively low FFMR is required to produce a large deflection of the tongue. Observed in figure 10.5 is that, due to their combined activation, the contractile effort required by the active components to produce a deflection of the order of that depicted in figure 10.1 is halved[1].

The act of protruding the tongue from the mouth is a complex task as there is no single muscle group that has a line of action in this direction. It is evident that the both the VT and TV result in partial anterior movements of the blade, with the former primarily compressing the blade ventrally along the superior surface and the latter shortening the blade laterally. Their combined contraction, due to the incompressibility of the matrix tissue, results in the anterior extension of the blade. However, due to the blade curvature, inferior motion occurs. To counter this, contraction of the SL pulls the tip level, but also results in slight opposition to the anterior movement. Figure 10.6 demonstrates an example of precise specification of the magnitude of the contractile force and that the resulting motion can be such that the tongue tip remains near level in order to prevent contact with the lower teeth.

[1] This demonstrates that the synergistic action of both large and small muscle groups may result in more efficient movements being produced. However, time-dependent studies must be performed to validate this claim.

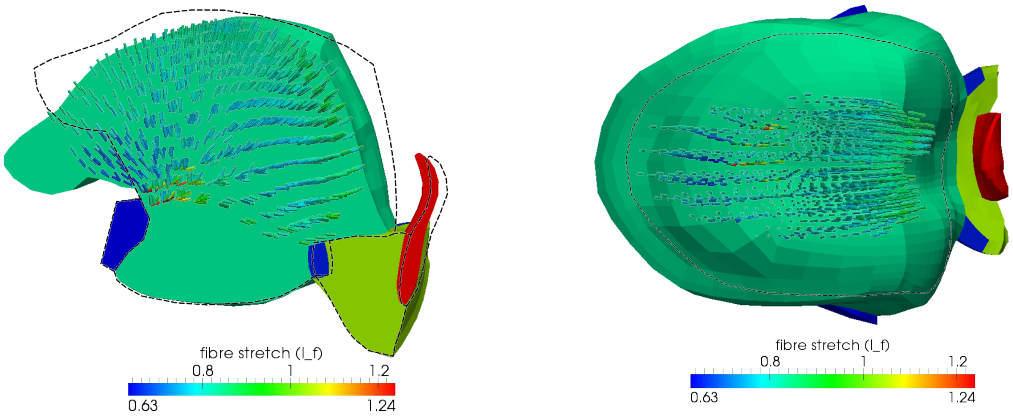

(a) Midsagittal view **(b)** Transverse view

Figure 10.5: Simultaneous muscle activation of all components of the GG, namely the GGa, GGm and GGp (FFMR are all 2.5%).

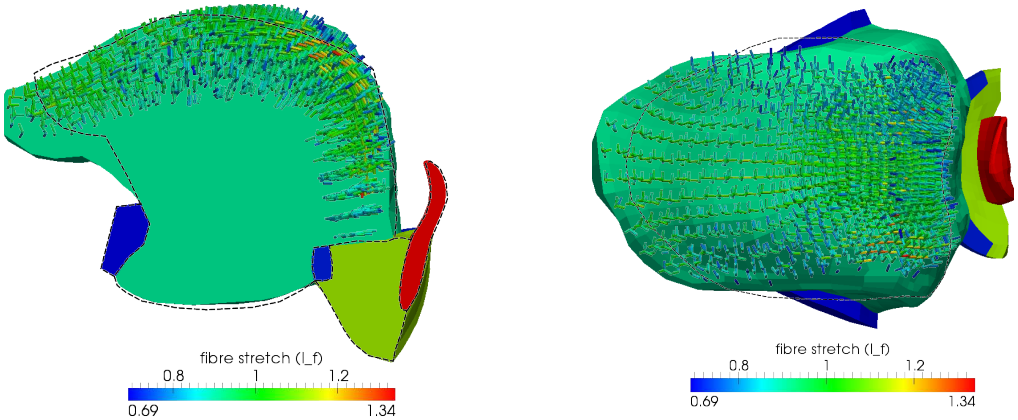

(a) Midsagittal view **(b)** Transverse view

Figure 10.6: Simultaneous muscle activation of the SL, TV and VT (FFMR are 7.5%, 7.5% and 5% respectively).

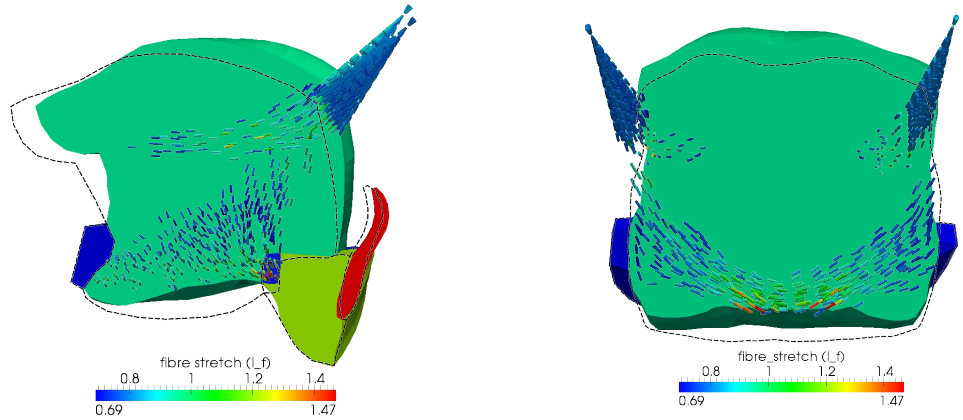

(a) Midsagittal view **(b)** Coronal view

Figure 10.7: Simultaneous muscle activation of the MH and SG (FFMR are 5% and 12.5% respectively).

Although the SG pulls the tongue towards the soft palate, its angle of insertion into the tongue is such that, as depicted in figure 10.4, it is unable to produce sufficient upwards force to lift the tongue. Shown in figure 10.7 is that the MH, located on the oral floor, is of assistance as the FFMR prescribed to the SG is halved to produce a similar amount of posterior displacement while producing a greater component of vertical motion. This is important in performing articulation and swallowing when the oral cavity must be sealed from the nasopharynx.

10.3 Quantification of isolation of muscle action during contraction

The histology and dynamics of the tongue is such that the contraction of an individual muscle group will alter the length of the other muscles. For a two-dimensional model, Sanguineti et al. [245] determined that contraction of muscle groups result in independent motions of the tongue. For a three-dimensional model however it is observed that, depending on the orientation and location of the other muscles with respect to the activated muscle, the contraction may result in regions of the surrounding muscles to be placed in tension or compression. In some cases, a muscle appears to contract in isolation of all other groups, resulting in a negligible change in length to the other muscles. This interaction is important from a control perspective, as the complex interaction of the muscles determines which are most effective at producing a prescribed motion. Analysis of this interaction also indicates which groups are antagonists of one another and thus highlight those that might be used to reverse the action of an other.

In order to demonstrate the (degree of) isolation of each muscle group, further analysis of data presented in section 10.1 was performed. The volume-average fibre stretch of each group was recorded after gravitational loading and monitored during the contraction phase. After the prescribed contraction, were a passive muscle to have undergone a stretch change of $\pm$ 5% then the contraction of the specified muscle was deemed to have a significant effect on the overall length of the passive muscle.

Fibre stretch data is tabulated in table 10.1, from which the extent to which the contraction of a muscle group remains isolated can be inferred. For example, it is clear that contraction of the DG, GH, MH, SG and SH have little effect on the surrounding muscle groups, while the constituent muscles of the GG, SL, TV and VT have a great influence over the lengths of 4 or more other muscle groups. The two main reasons for these contrasting results are the resulting deformation of the tongue and the orientation and location of the passive muscle with respect to the active one.

The diagonal values in table 10.1 indicate that the average compressive strain for the active muscle at the specified contraction strength is between 10% and 25%. Due to the compliance of the matrix, not much contractile force is needed to produce large deformation in these muscles. The colouring of the heat map depicts a certain symmetry across the diagonal. For some pairs of muscles, contraction of one results in shortening of the other; an example of such a pair being the GGm and VT. Muscle pairs that act antagonistically are noticeable when contraction of the one causes tension to appear in the other, and *vice versa*. This occurs in cases such as for the TV and VT or the TV and SL which may produce in excess of 10% average tensile strain in one another.

It should be noted that the values presented here provide a representative value of stretch for the entire muscle and do not reflect the extent to which the deformation is localised to a region of the muscle. The antagonistic effect of these muscles may be local in nature as the degree to which the muscle groups overlap

Table 10.1: Heat map of fibre stretch ratio $\frac{\bar{\bar{\lambda}}_f}{\bar{\bar{\lambda}}_f^0}$ resulting from the contraction of individual muscles at 5% FFMR. The relative shortening of the active muscle is indicated on the diagonal. Muscles placed in tension are highlighted in red, while blue highlights indicate that the muscle is in a compressive state.

Affected muscles	Active muscle												
	DG	GGa	GGm	GGp	GH	HG	IL	MH	SG	SH	SL	TV	VT
DG	0.88	1.002	1.003	1.007	0.994	1.006	1.003	1.006	1.003	1.01	1.006	0.998	0.99
GGa	0.99	0.766	0.85	0.972	0.998	1.003	1.055	0.992	0.984	0.98	1.1	1.025	0.842
GGm	0.996	0.904	0.774	0.899	0.995	1.032	1.069	1.008	1.022	0.986	1.05	1.057	0.855
GGp	0.998	0.979	0.948	0.761	0.97	1.046	0.975	1.032	1.002	0.993	1.009	1.035	0.914
GH	0.992	1.003	1	0.966	0.847	0.995	1	1.034	1	1.005	1.021	0.993	0.979
HG	1.005	1.006	1.038	1.074	0.997	0.763	1.03	0.995	1.007	1.001	0.979	1.044	1.055
IL	1.002	1.032	1.063	1.005	1	1.023	0.746	1.013	0.974	1	0.96	1.036	1.065
MH	1.004	0.995	1.006	1.036	1.011	0.987	1.01	0.81	0.989	0.987	1.016	0.993	0.984
SG	0.989	0.995	1.021	1.019	1	1.022	0.973	0.99	0.86	0.99	1.027	1.018	0.996
SH	0.942	0.996	1.013	0.995	1.018	1.015	0.998	0.983	0.985	0.902	1.018	0.99	1.009
SL	1.012	1.041	1.049	1.037	1.014	0.987	0.976	1.02	1.01	1.007	0.805	1.101	1.087
TV	0.998	1.017	1.036	1.04	1.001	1.031	1.022	1.002	1.01	0.999	1.064	0.765	1.125
VT	0.99	0.951	0.931	0.929	0.987	1.012	1.022	0.989	0.989	0.996	1.058	1.106	0.758

may be relatively small. For example, the VT and GG muscles are aligned and overlap in the superficial regions of the the tongue. The result of this alignment is that contraction of the VT induces a shortening of the GGa, GGm and GGp, but the VT would not play a significant role in shortening of the GG at the root of the tongue. This phenomenon, contrasted against the relatively isolated contraction of the GH, is demonstrated in figure 10.8. Additionally, since the SL and TV are locally orthogonal to the VT, the incompressibility of the tissue results in stretching of these two muscles. Shortening of the GH affects the length of the floor of the

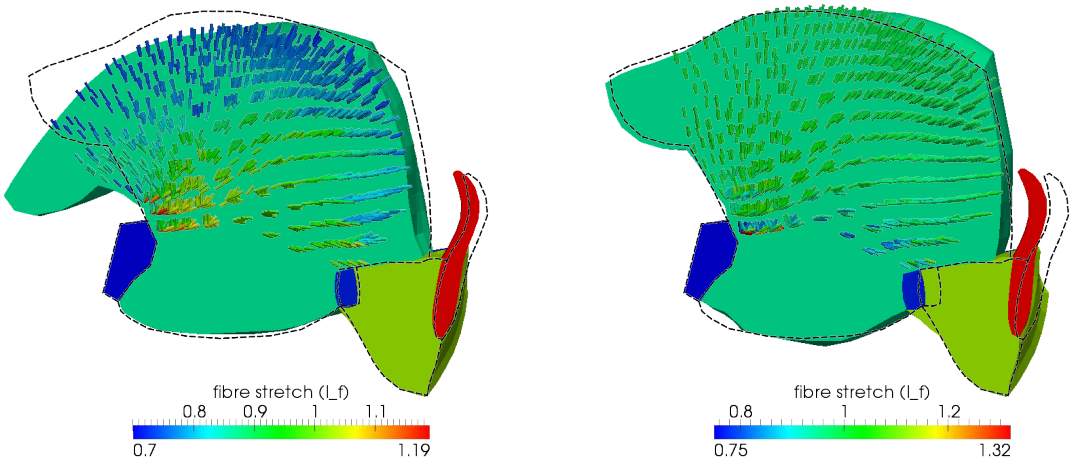

(a) VT (FFMR 5%) **(b)** GH (FFMR 5%)

Figure 10.8: Isolated muscle activation and its effect on the fibre stretch in the GG.

tongue complex, while the rest of the tongue remains largely undisplaced. Although the inferior portion of the GGp is adjacent to- and aligned with- the GH, according to its representative average it is shortened only marginally during contraction of the GH. It is also interesting to note that, due its low internal volume fibre

fraction, the SG does not cause a significant shortening of the IL with which it is aligned in the tongue bulk.

Given that the performance of each region of muscle is deformation- and rate- dependent, the interaction between the muscles has great consequences on the local dynamics of muscle contraction. From the data presented in table 10.1, it can be said that this interaction should not be ignored when determining the ideal set of active muscles for the purpose of developing a position-control algorithm for the tongue.

Further investigation of the relationship between the prescribed FFMR and the average fibre stretch revealed that, although the prescribed FFMR increased linearly in pseudo-time, the induced change in muscle length evolves in a nonlinear but asymptotic manner. It is observed that the stiffening effect of the tissue due to both the matrix and the extended fibre PEs resulted in a reduction in a rate of muscle length change. This phenomenon is illustrated for the GG in figure 10.9. Although not demonstrated, this relationship must be dependent on the orientation, loading and deformation preceding the muscle contraction.

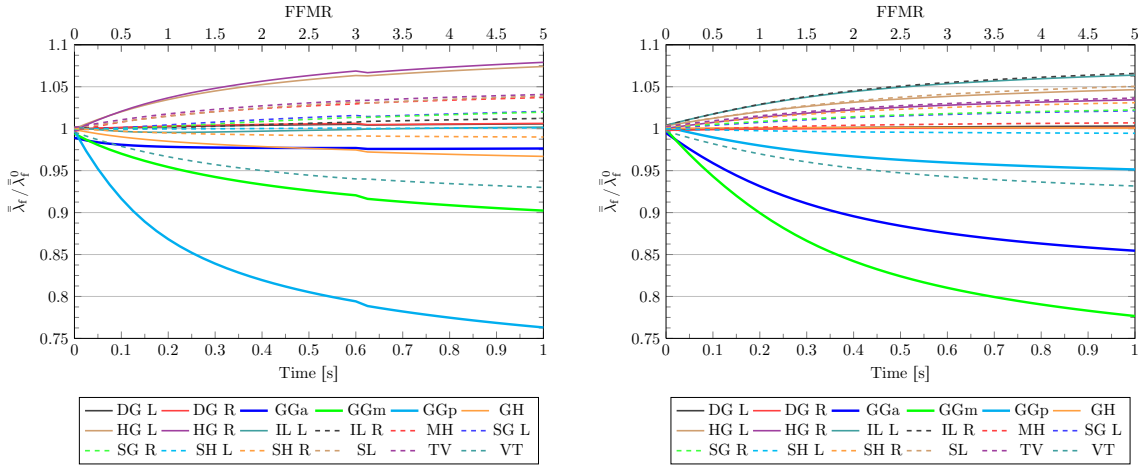

(a) GGp **(b)** GGm

Figure 10.9: VWA fibre stretch ratios of muscles during contraction of the GG components when in the upright orientation.

Figure 9.11 has suggested that the GG extends under gravitational and pressure loading and may therefore be required to contract to reduce deformation. Should the GGm and GGp be the primary muscles predicted for use as airway dilators, the data presented in figure 10.9 and table 10.1 suggests that some activation of the HG, IL, SL and TV may be necessary to prevent their extension due to the action of the GG. However, it has been demonstrated that the local effects of muscle contraction as well as external loading are complex and on occasion difficult to predict. Conceivably contraction of these muscles could induce further length changes in other muscle groups and therefore require an even more complex activation pattern to oppose the deformation.

The concepts presented here and in section 9.3 form the basis of and motivation for the muscle control algorithm presented in section 7.3.1. A full assessment of the performance of the algorithm is presented in chapter 11.

10.4 GG activation under loading

Since the GG is the main muscle of the tongue affecting airway patency, it is expected to have a significant level of activity during breathing. As demonstrated in section 10.1, two components of the GG appear effective in opposing posterior deflection of the tongue. However, the strength of muscle contraction required to prevent posterior movement of the tongue into the retroglossal space under full gravitational and pressure loading remains unknown. Assuming quasi-static conditions, this figure was quantified using a basic, manually controlled model representing the maintenance of airway patency under load. In each case, oral inhalation was simulated.

The data shown in figure 10.10 describes the level of muscle activity of the component muscle of the GG required to move point $\boldsymbol{P}_C$ to a position of zero displacement in the anteroposterior direction under various gravitational and pressure loading conditions. Since the exact position is never attained, the increases in activation level were kept small enough to prevent significant positional overshoot. The data between the steps when $\boldsymbol{P}_C$ was behind and in front of its reference position was interpolated to extract the estimated FFMR for zero displacement. The angle cosine gives the component of the gravitational force in the posterior direction. Please note that no other muscles were active in this study, and thus the overall shape and posture of the tongue after the desired goal position was attained was not considered.

The results indicate that the GGp is more effective reducing protrusion of the tongue into the retroglossal space than the GGm. It is observed that the FFMR required for the GGp to maintain the tongue's forward position is up to 60% less than GGm for the same loading conditions. This is because the GGp has a directionality and location that is better suited to drawing the rear of the tongue forward than the GGm, as can be noted when comparing figure 10.1a to figure 10.1b.

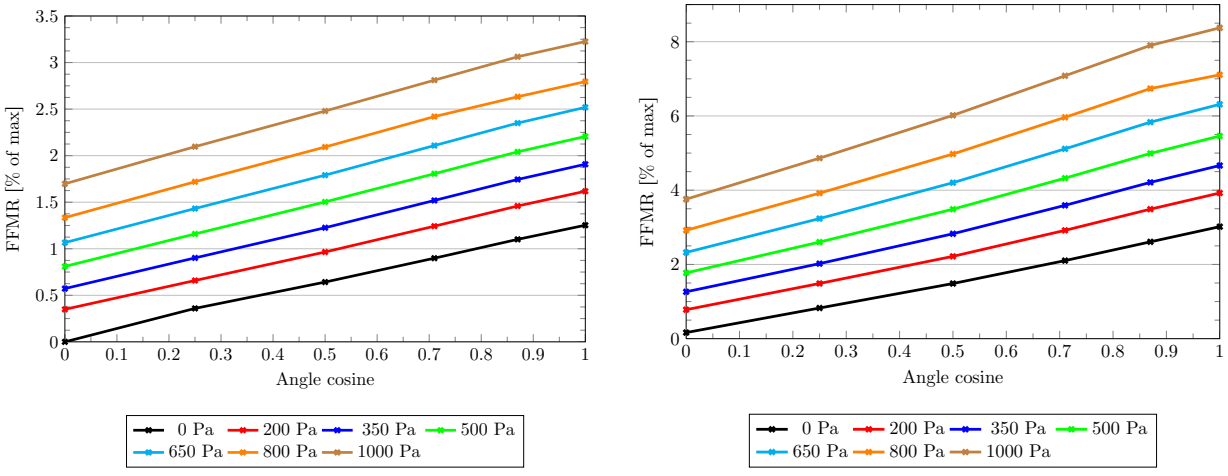

(a) GGp dependence on angle of incline

(b) GGm dependence on angle of incline

Figure 10.10: Quasi-static GG contraction under gravitational and pressure loading. The recorded values indicate the FFMR magnitude required to reduce the anteroposterior deflection of $\boldsymbol{P}_C$ to zero for a given nominal pressure. The angle cosine takes values of 0 and 1 when simulating the upright and supine orientations respectively.

It was also observed that, under no airway load, an increase in the degree of recline required a corresponding increase in activation to counter gravity-induced movement of the tongue. Similarly, as the negative pressure

increases at zero inclination, the FFMR required to prevent motion increases. Figure 9.7 indicated that under most scenarios, excluding the most extreme pressure loading cases, the gravitational loading of the prone orientation results in anterior deflection of the tongue, thus requiring no contribution from the GG to regulate this component of motion. For this reason, further evaluation of the prone orientation was not performed.

From the collected data, it is evident that there exists a linear relationship between required FFMR and angle of incline for a fixed pressure. Replotting the data with the pressure as the dependent variable (not shown) indicated that there is also a linear relationship between required FFMR and applied pressure for a fixed inclination angle. These relationships largely coincide with the measured data presented in [111, fig. 4] for the conscious condition where the relationship between the EMG amplitude and nominal pressure for an awake subject is approximately linear. A family of curves that fits this data is described by an equation of the form

$$\text{FFMR} = c\,p + m_1\,(1 + m_2\,p)\,\gamma \quad , \tag{10.1}$$

where p is the negative epiglottal pressure in Pa, c is a constant dictating the FFMR value in the upright orientation, m_1 is the nominal gradient, m_2 is a gradient pressure correction factor, and $\gamma = \cos\theta$ the angle cosine with θ being the angle of incline measured from the supine position. Table 10.2 provides the coefficients for equation 10.1 that fits the data shown infigure 10.10.

Table 10.2: Curve fitting for GG contraction for $\boldsymbol{P}_C$ anteroposterior reference position re-acquisition[a]

Muscle	Parameter			
	Coefficient	c	m_1	m_2
	Scale	10^{-5}	10^{-2}	10^{-4}
GGm		1.68	1.23	2.65
GGp		2.6	2.81	6.71

[a] Optimal values for the parameters were obtained using a least-squares fit and solved for using a nonlinear solver that utilised evolutionary algorithms [318]. For both sets of data, the fitted curves have a coefficient of determination $R^2 > 0.99$.

From these results the preliminary conclusion is that the GGp functions as the primary airway dilator component of the GG as it provides a more efficient mechanism for reducing the movement of the tongue into the retroglossus than the GGm. However, as the GGm has a greater influence on the motion of the superior surface of the tongue over which a non-trivial pressure field exists during breathing, it is anticipated that it plays a crucial role in position control of tongue during respiration.

The results presented here will be used again to validate the results predicted by the neural model in a later discussion. In reality, numerous muscles are simultaneously activated to control tongue orientation. It is assumed that the performance dictated by figure 10.10 represents the least efficient method for attaining position control as there exists an overlap in functionality of numerous muscles groups and, due to the CE length dependence, the muscles become less effective when strongly contracted.

10.5 Summary and discussion of results

It has been demonstrated that the muscle model, combined with the geometric representation and internal and external micro-histological description of the tongue's constituent muscles, produces realistic deformations of the tongue. The required activation level to produce large deformations is, in most instances, small for the chosen muscle parameters. However, it is also noted that most muscle groups readily influence the tongue tip position, thus making it difficult to attain stability under complex contraction conditions. The effect of isolated muscle contraction on the strain state of the other muscles has been quantified at a predefined FFMR, thereby highlighting possible antagonistic muscle groups. From this data, it can be speculated which muscles might be used in conjunction with the primary dilators to counter airway loads. Furthermore, this illustrates the purpose of implementation of the muscle stretch-based filter implemented within the neural model. Finally, a simple analytical model of contraction of the GG components was developed to describe a plausible, but inefficient, mechanism for counteracting gravitational and airway loading. The required contractile response, which was linear with respect to the orientation angle and nominal pressure, showed that the GGp was most efficient at controlling the anteroposterior position of the tongue's rear surface.

Further discussion

As a consequence of the complex geometry of the tongue, numerical difficulties in the global nonlinear solving algorithm exist and its convergence rate was superlinear. The reason for the loss of quadratic convergence can be attributed to the complex macroscopic and histological geometries, the interaction of the muscles and sensitivity of their constitutive equations to perturbations. Wilhelms-Tricarico [311] suggests that higher-order elements are more suitable for complex biological geometries in order to minimise numerical instabilities.

11. CHARACTERISTIC RESULTS, PERFORMANCE ANALYSIS AND PARAMETRIC STUDY USING NEURAL MODEL

The neural model, demonstrated to work under geometrically simple scenarios, was incorporated into the representative model of the tongue. The effectiveness and general response characteristics of the model is first demonstrated and discussed. Subsequently a comprehensive parametric study was performed to determine which environmental and material parameters affect the response of the tongue musculature during breathing. The influence of modifying loading, algorithmic and modelling parameters were tested individually and ultimately used to understand how to best configure the model for later application.

The baseline conditions for the parametric study, from which a single condition or parameter was altered for each set of simulations, were that:

1. A fully time-dependent model, for which $f_{\mathrm{c}}^{\mathrm{V}}$ is considered, was used. A fixed time-step size of 15ms was chosen such that 500 time-steps were evaluated per simulation.
2. The gravitational orientation was that simulating the supine configuration.
3. The spatial loading description for the airway represents that approximating mouth breathing, as given by equation 8.11.
4. In the breathing cycle, three successive inhalations (no exhalation) with a period of 2.5s are simulated.
5. The nominal pressure magnitude was set at $p_{\mathrm{nom}} = 500$Pa.
6. The fibre volume fraction for the tongue musculature was set at $\phi_{\mathrm{f}} = 0.7$.
7. For the activation parameters, $\tau_R = \tau_F = 150$ms.
8. The neural model was utilised to renew the active muscle set at every second time-step.

9. The control points used for the neural model are those shown in figure 8.11 and had a uniform weight of $w_p = 1$ for points on the tongue.

10. Work rate minimisation, the secondary objective function, was not incorporated.

The supine orientation was chosen because it produces the greatest displacements when the muscles are fully passive and was expected to accentuate the role that airway dilator muscles may play. Furthermore, due to the modelled breathing pattern, the peak epiglottal pressure is described by $p_{\text{epi}}^{\text{min}} = -p_{\text{nom}}$. With the chosen conditions, the minimum epiglottal pressure is in the range of that specified by Van Hirtum et al. [283, 284], Shome et al. [252] and just exceeds the threshold pressure for the loss of GG reflexive mechanisms [111].

The three characteristic phases used to perform the simulations were as follows:

1. Prestressing was performed and the average fibre stretches, referenced by the neural model, were recorded.

2. Full gravity loading was applied using several load-steps.

3. The neural model was utilised while a time-dependent pressure load was applied. Since the muscle activation required at $t = 0$s to attain the zero displacement position under gravitational load was unknown, zero initial muscle activation was assumed.

The results reported in this chapter illustrate the trends in muscle response under altered simulation conditions. The main focus is on the response of the GG as its role is considered to be most significant in the prevention of the OSA condition. We expand on the role of the other muscles when an optimised model is produced. To this end, significant results will be numerically evaluated and quantified for practical use in chapter 13.

11.1 Position maintenance and muscle activation characteristics

To demonstrate the efficacy of the neural model in controlling the configuration of the upper airway tissues, the position of several points on the tongue and epiglottis were monitored for both the active and fully passive models. Figure 11.1, which indicates their displacement from the goal position, allows a comparison to be made between the two cases, and the performance of the control model to be quantified. As expected, large displacements, which are consistent with those observed for the time-independent case, were present in the passive tongue. Its pattern of the movement mimicked the applied load. In this figure, it is clear that the active model successfully reduced the overall displacement of the control points. At zero-load conditions, all points are within 1.5mm of their goal position and at maximal load the displacement of these points is significantly reduced. An advantageous side-effect of the control of the tongue was that the motion of the epiglottis was decreased considerably.

From this data, a few preliminary observations can be made. Firstly, at each control point the exact goal position was not achievable. Secondly, a consistent and stable displacement could not be attained but overall it can be said that position control is maintained as the pressure varied. As the air-induced load increased, it became more difficult to remain close to the goal configuration. However, this result may be physiologically

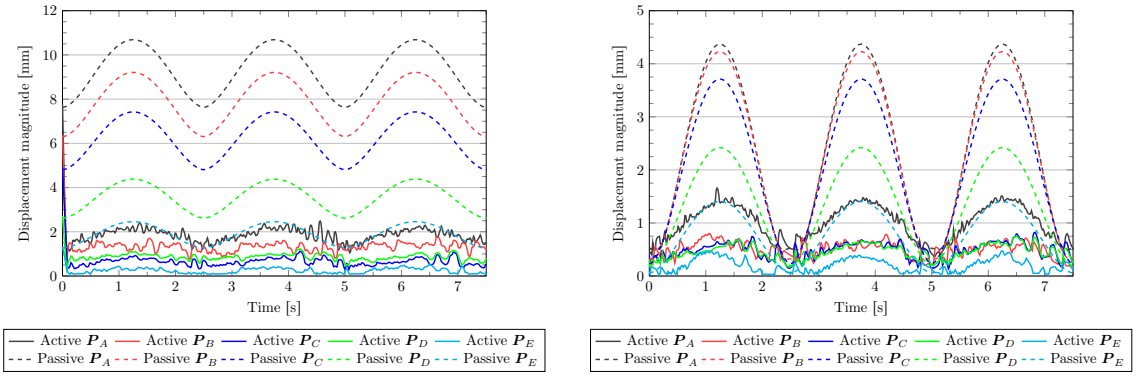

(a) Supine orientation

(b) Upright orientation

Figure 11.1: Effectiveness of neural control model in reducing and minimising displacement of control points on the tongue under the influence of gravitational and pressure loading. In the first few milliseconds, while the pressure load is minimal the GA aims to reverse the deformation that occurs under gravity pre-loading. Although the ability for position control in the upright configuration is demonstrated here, further results depicted in this section refer only to the supine orientation.

realistic, as a displacement of the order of 2mm has been measured by Cheng et al. [38] at the tongue posterior (approximately corresponding to $\boldsymbol{P}_C$) during regular breathing.

The analysis shown in table 11.1 further highlights the performance of the control model. Not only is the mean position of the control points closer to their goal, but the amplitude of displacement under load is significantly reduced. The poor displacement result at the tongue tip may be a consequence of having only a single control point at the apex. However, in order to further assess the root causes for the difficulties in position attainment and maintenance, the model behaviour in terms of muscle activation and lengths must first be presented.

Table 11.1: Relative performance of the neural control model in minimising motion of the tongue. The first 0.25s of data are disregarded as, up to this point, the GA is in the process of actively reversing deformation due to the full gravitational load and increasing pressure load.

Mean values			
Point	Passive	Active	Reduction
	mm	mm	%
$\boldsymbol{P}_A$	9.32	1.86	80.07
$\boldsymbol{P}_B$	7.91	1.32	83.34
$\boldsymbol{P}_C$	6.25	0.65	89.63
$\boldsymbol{P}_D$	3.59	0.86	75.94
$\boldsymbol{P}_E$	1.93	0.25	87.26

Peak-to-peak amplitude			
Point	Passive	Active	Reduction
	mm	mm	%
$\boldsymbol{P}_A$	3.06	1.43	53.27
$\boldsymbol{P}_B$	2.90	1.02	64.86
$\boldsymbol{P}_C$	2.61	0.82	68.67
$\boldsymbol{P}_D$	1.76	0.76	57.05
$\boldsymbol{P}_E$	1.18	0.45	62.10

The muscle activation level α, derived from the activation history for each muscle and the current input signal u is shown in figure 11.2a. A complex sequence of neural firings results in an overall increased activation level for the majority of muscles as the airway pressure decreases. With the *a priori* value of T_0^s chosen such that where possible $0.3 \leqslant \alpha^{\max} \leqslant 0.75$ for each muscle group, the muscles have sufficient resources

to respond to the displacement-causing stimuli[1]. The associated FFMR, depicted figure 11.2b, demonstrates that the primary muscles used to oppose the motion are the GGm and GGp, the airway dilators. Their response is synchronised with pressure load, indicating that they activate as a direct response to the load. This correlates well with the trends shown in [165, 261, 221]. It was observed that, in the supine orientation, these components of the GG are required to produce 1.75% of their maximum contractile force to oppose the 500Pa nominal pressure. This indicates that, for the large GG, not much effort is required to prevent the tongue from prolapsing into the airway.

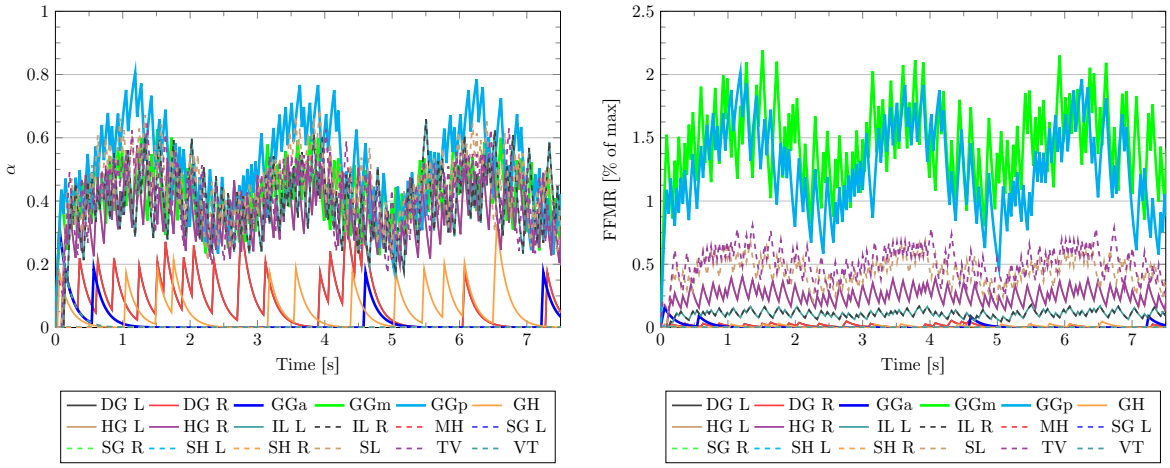

(a) Activation level α

(b) FFMR

Figure 11.2: Neural control response for each muscle of the tongue. The predicted neural signal u at each time-step results in an adjustment of the activation level (figure 11.2a) based on the activation history of the muscle. This value is then translated into the FFMR shown in figure 11.2b using equation 7.4. Within the first half-period $0 \leqslant t \leqslant 1.25$s, the muscle activity increased to a physiologically representative state to oppose all loading.

At peak pressure, these muscles produce approximately four times greater contractile force than next greatest contributors, the TV and SL. The role of these secondary contributors are, respectively, to reduce the lateral and inferior motions induced by GG contraction, as well as lift the tongue apex. The HG also plays a role in reducing lift at the rear of the tongue. Although their activation appears to be affected by the applied pressure, due to their low FFMR the role of the the other muscles in terms of overall posture control is minimal. Unexpectedly, included in the latter group is the GGa which was predicted to remain largely inactive throughout the simulation. Overall, these results suggest that collectively the muscles of the tongue are easily able to oppose the forces generated during oral inspiration.

From table 10.1, it had been predicted that a large active reduction in length of the GGm would result in significant lengthening of the HG, TV, MH and SL; while shortening of the GGp leads to an increase in the average stretch of the IL, SL and TV. Further it was hypothesised that contraction of these (antagonistic) muscles would assist is returning the tongue to its original configuration. It is observed in figure 11.2b that, with the exception of the MH, these muscles are the next most strongly contracting muscles. However, their level of activity cannot be inferred from table 10.1.

[1] These general guidelines for a suitable range for α were determined by trial-and-error. If the activation level is too low or high, the response plateaus thereby preventing a rapid response by the muscle group. This response was demonstrated visually in figure 2.15.

Due to the discrete nature of the time stepping and the fixture of activation parameters, the predicted FFMR appears to oscillate around what may be considered the ideal value. Using both a 5-point moving average and a 14-coefficient B-spline function[2], this mean value can be ascertained and visualised. Figure 11.3 illustrates that both filtering methods indicate similar results. Given the smoothness of the loading condition, it was decided that the B-spline smoothing technique produced the most probable candidate and thus was utilised extensively in further evaluations of similar data. Averaging the data over numerous cycles further increases the accuracy of the mean value approximation.

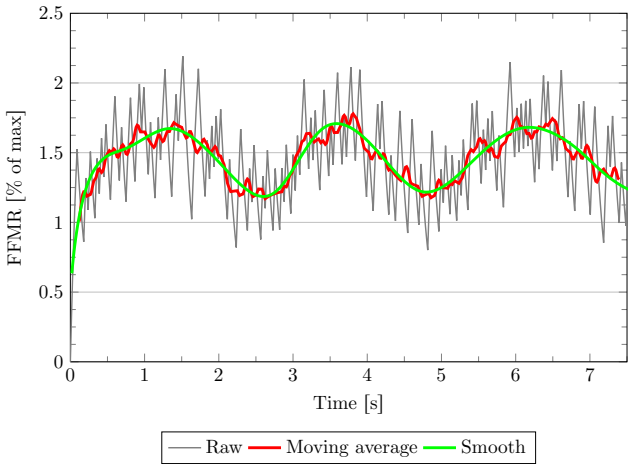

Figure 11.3: Smoothing of the resulting FFMR by use of a moving average and B-spline curve. The number of coefficients used in the spline determines its smoothness and sensitivity to the solution oscillations.

With respect to the lengths of the muscle after contraction, figure 11.4 demonstrates that using the chosen measurement technique, all muscles are in an overall contractile state when maintaining posture control. The GGm and GGp, the two main contributors of the control mechanism that are always tested by the GA regardless of their length, are in a contractile state. The length of the GGm remains constant while that of the GGp changes with the applied load. The other muscle groups, of which their length determines their active candidature status within the GA, remain near their threshold value for active candidacy. It is plausible that the GA deselects some of these muscles prematurely, forcibly deactivating them for a duration of time thereby incorrectly reducing their FFMR. However, given the overall magnitude of their contribution presented in figure 11.2b, the error introduced by this was considered negligible.

Now that the muscle activation and average length data has been shown, a decomposition of the displacement history (figure 11.1) for four of the control points is made in figure 11.5 to provide insight into the performance deficits of the model. The differences in the lateral motion of the front and rear of the tongue shown in figure 11.5a indicates that some twisting is present in the coronal plane. The lack of symmetry in the model and therefore loading, coupled with the assumed symmetry in contractile states of muscles with a left and right constituents, account for this observation. In figure 11.5b it is shown that the tongue tip retains a large component of movement in the posterior direction. From figure 11.2b, it was observed that the TV has a significant FFMR while the VT contracts less vigorously. Given the requirement for tongue protrusion demonstrated in section 10.2, it can be concluded that the strength of contraction of the VT is less than ideal.

[2] Increasing the number of coefficients in the spline polynomial caused this curve to start displaying some of the high-frequency oscillations that we wish to smooth out. Reducing the coefficient resulted in over-damping of the solution.

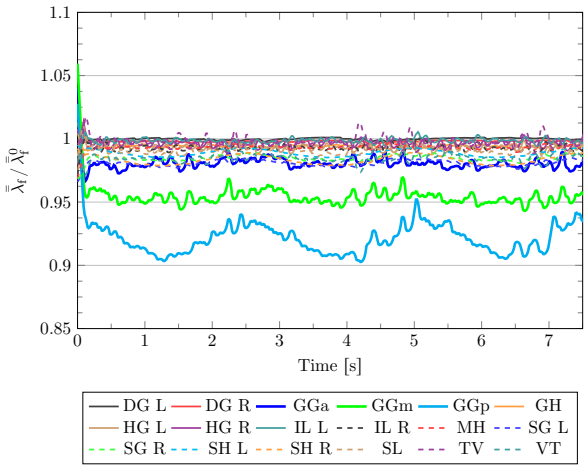

Figure 11.4: The VWA fibre stretch history for all tongue muscles under control of the neural model. This demonstrates that, according to this measure, all muscles are kept in an overall state of compression.

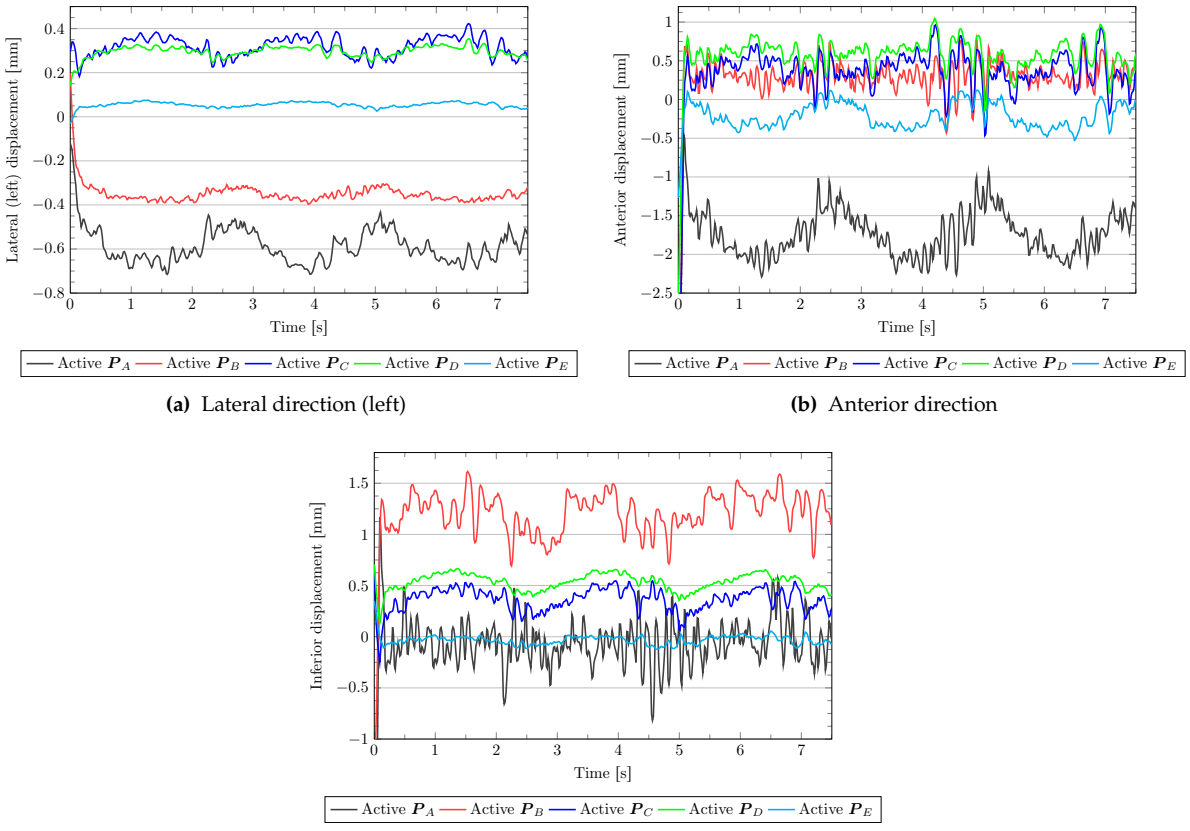

(a) Lateral direction (left)

(b) Anterior direction

(c) Inferior direction

Figure 11.5: Upon decomposition of the of the control point displacement history, it is observed that the tongue tip moves most in the posterior direction while the centre of the upper surface is displaced superiorly. The rear of the tongue undergoes sub-millimetre movement in both of these directions. The lack of symmetry of the model resulted in lateral movement of the tongue.

The interplay between the muscle groups does however successfully maintain the vertical position of the tongue tip. The middle of the superior surface, denoted as $\boldsymbol{P}_B$, experiences a superior displacement of be-

tween $1 - 1.5$mm. Greatly influenced by both the GGm and GGp, a balance must be reached between the position of this point as well as $\boldsymbol{P}_C$ and $\boldsymbol{P}_D$ (and the additional control points not illustrated). Each of these control points moves only slightly in the anteroposterior direction. Additional contraction of either of these muscles must result in a overall unacceptably large perturbation of the control points concentrated on and near the rear surface of the tongue.

The resulting oscillations of both the displacement and FFMR around their perceived ideal value are quite large. However, it should be emphasised that no optimisation of the control and input parameters has been made at this point.

11.2 Environmental influences

In demonstrating the characteristics of the neural model, it has already been shown that alteration of the physical conditions governing the loading on the upper airway soft tissues results in variable behaviour in the tongue muscles. It is sensible to suspect that these muscles will react differently due to a variation of the applied pressure field and gravitational orientation. In this section, it is demonstrated how these parameters, as well as variation of the breathing cycle itself, influence the response of the tongue.

11.2.1 Gravitational orientation

Sleep posture, and the consequent body forces acting on tissues, have been shown to produce large deformation in the passive tongue. Depicted in figure 11.6 is the predicted response of the GG to resist this motion during inhalation for a number of orientations.

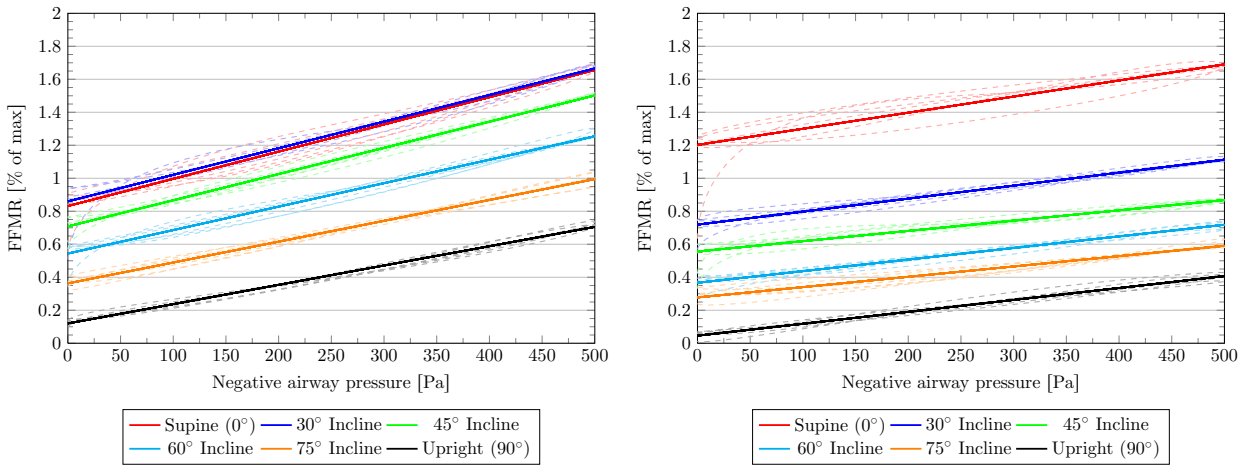

(a) GGp **(b)** GGm

Figure 11.6: Muscle response due to orientation of gravitational force (oral inhalation). The solid lines represent linear regression functions plotted against the smoothed data, shown as dashed lines. The contractile response of both muscles appears linear with respect to the epiglottal pressure. The smoothed result does not reflect that the predicted muscle activation for the upright gravitational configuration tends to zero when the pressure is removed.

Increasing the angle of incline effectively reduces the magnitude of the gravitational force vector in the direction that would cause the tongue to fall back into the retroglossal space. The response of both muscle groups is significantly affected by posture. Several important characteristics pertaining to the role of these muscles is revealed in this data. Firstly, the overall trend for both muscle groups is that the required contractile strength increases as the orientation changes from the upright to supine configuration; however, this response is nonlinear with respect to the angle of incline. Additionally, the minimal activation level present at zero-load increases. This indicates that a firmer tone must be maintained by both muscles to prevent the tongue from falling into the oral cavity at a greater recline. The peak-to-peak amplitude remains constant for both muscles in all cases, suggesting that this portion of the response is not affected by gravity.

The stark difference visible in response of the two muscles in the presented data is due to the combined influence of the gravitational orientation and distribution of pressure load. It has already been demonstrated that both the GGp and GGm have significant control over the position of the posterior and superior surfaces of the tongue in the sagittal plane. The GGp activates to resist the negative airway pressure from drawing the tongue posteriorly towards the pharynx, while the GGm primarily prevents the tongue lifting due to the pressure. As the posture moves towards the supine, the body force vector aligns better with the GGp. Similar to that illustrated in figure 9.6, the moment generated around the fixture point of the mandible due to body forces is such that increasing contraction of the GGm is required to prevent the superior region of the tongue from displacing backwards in the oral cavity. This in turn results in less force being generated by the GGp in order to oppose the gravitational force and describes the distinct change in response of both muscles between the supine and 30° incline orientation. The peak value for the upright case is less than the trough value for the supine orientation. This infers that, in terms of required contractile effort, sitting upright is the equivalent to an increase in epiglottal pressure of in excess of 500Pa. Increasing the inclination angle by 60° reduces the gravity vector by half in the posterior direction and results in halving the necessary contraction force generated in the GGp.

The GGm is more sensitive to an increase in incline, in that an increase in orientation angle at a small θ significantly reduced the required contraction level of this muscle. Furthermore, the GGm response is more greatly affected by contraction of the surrounding muscle groups than the GGp. The response of these other muscles remains minor in all instances. The most prominent auxiliary muscles in the supine configuration are the TV, SL and HG which have an FFMR range of $0.3 - 0.65\%$, $0.32 - 0.57\%$ and $0.18 - 0.31\%$ respectively, while in the upright orientation the SL and TV were both predicted to contract at between $0 - 0.27\%$ of their maximum strength.

With reference to figure 10.10, the results given here are well within the limits defined in section 10.4. The synergistic activation of multiple muscles clearly results in a reduction in the contractile force required to be generated by the dilators. This demonstrates the importance of muscle coordination within the tongue during breathing as the measured efficiency of the dilatory action of the GG is much greater when coactivation of several muscle groups is present. Furthermore, this confirms that the neural control model is quite effective at coordinating muscle activation in an effective manner.

A brief investigation involving laterally aligned gravitational forces, indicative of a subject lying on their side, was conducted. For these cases, symmetry of the muscle activation between split groups such as the IL was removed. It was observed that a response similar to the upright configuration was obtained and an asymmetrical activation of the split muscle groups was obtained. This was likely due to the lack of a posterior component of gravity. The activation response of these muscles remained insignificant in comparison to the GG components in figure 11.6; and increasing the size of the active muscle set significantly increased

computational cost. These cases were not concentrated on further in the study. However, this result remains important to note as it is inferred that rotation of the head in the transverse plane does not affect the response of the airway dilators.

11.2.2 Pressure distribution

It is hypothesised that significant differences in pressure distribution in the oral cavity can arise depending on the orifice though which inhalation takes place. In oral breathing, it is assumed that the pressure reduces significantly along the length of the tongue due to the proximity of the tongue to the hard palate and the low CSA of the buccal region of the oral cavity. In contrast, during nasal inhalation, pressure loss is most significant in the nasal passages and the it remains largely constant in the oral cavity. A third scenario to be considered is that when the nose is utilised for breathing but the mouth remains open.

A fair first-approximation to oral breathing is to presume that the pressure loss along the length of the tongue is linear. Additionally, the pressure distribution on the posterior of the surface is assumed to remain constant as the CSA of the pharynx is larger than the oral cavity. In the case of nasal breathing, the hypothesis of no fluid flow in the oral cavity infers that there exists no spatial pressure gradient over this anatomy. However, the pressure is non-zero as losses occur in the nasal passages. In the mixed third case, the oral cavity, open to the atmosphere, experiences zero gauge pressure while the posterior surface of the tongue, in the presence of the pharynx, experiences a negative airway pressure.

Figure 11.7 demonstrates that a marked difference in the response of the airway dilators exists between these three scenarios.

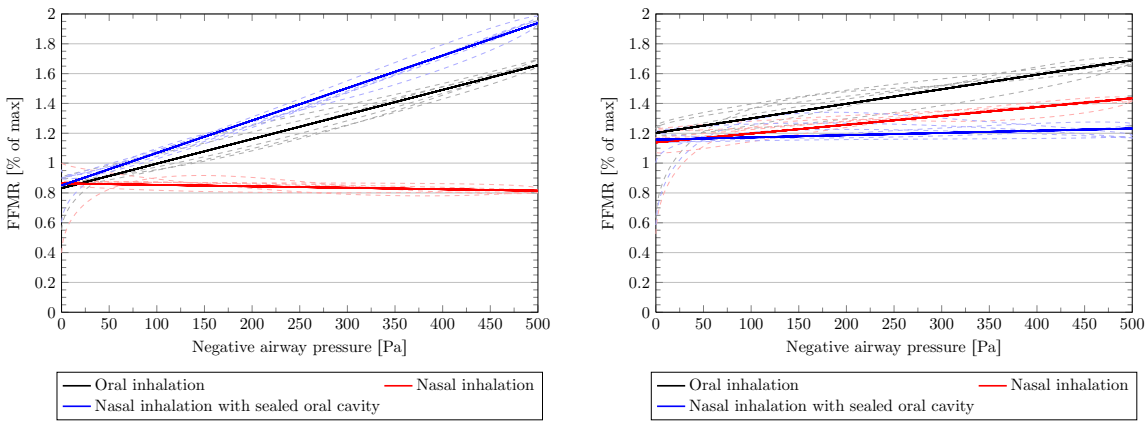

(a) GGp **(b)** GGm

Figure 11.7: Muscle response for differing spatial distributions of pressure load (supine orientation). The response remains linearly dependent on the applied pressure , but is qualitatively different in each loading case.

The case of oral breathing, which has been previously presented, demonstrates activity of both the GGm and GGp in resisting motion of the upper and posterior surfaces of the tongue. A spatially constant pressure distribution results in a completely different response in these muscles. The difference in curvature on the front and rear surfaces of the tongue is not sufficient to result in a anteroposterior force requiring the input of the GGp to resist; it however continues to contract in resistance to the gravitational load. This force is very

large in the third scenario, requiring greater contraction of the GGp than in the case of oral breathing.

For the case of nasal inhalation, the load on the upper surface of the tongue remains unbalanced. However, the generated moment with a normal perpendicular to the sagittal plane is lessened by the lack of the anteroposterior force that would otherwise assist in lowering the tongue posterior and raising its tip. This combined effect results in the GGm having a lesser oscillatory FFMR response in this case than observed for oral inhalation. Completely eliminating the pressure load on the tongue surface, as is done in the third scenario, reduces the GGms contraction response to the pressure almost entirely and the remaining contraction purely resists gravitational forces. This is as the upper surface undergoes little superior motion due to the posteriorly applied load.

11.2.3 Pressure loading magnitude

The airway pressure, affected by the CSA of the airway, influences the volume flow rate through the open orifice. When deeper breaths are taken or an apnoeic event occurs, a decrease in the upper airway pressure is induced. Figure 11.8 illustrates the predicted response of the GG at a range of applied pressures. Note that changing p_{nom} induces a change in both loading magnitude and loading rate. Rate effects in the muscle response therefore may play a role in the results observed in figure 11.8.

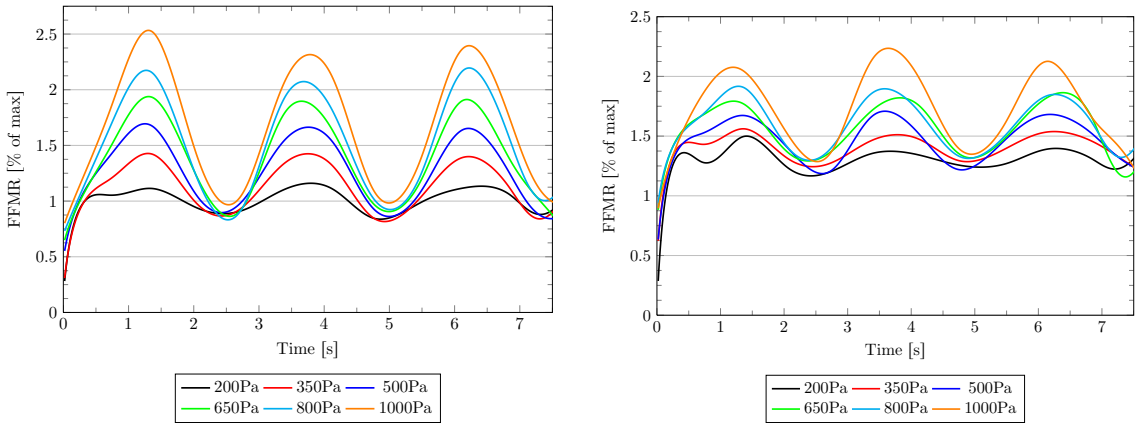

(a) GGp **(b)** GGm

Figure 11.8: Muscle response due to change of pressure load (oral inhalation).

In both of the results shown, the trends in the response appeared to correspond very closely to the applied load. It was observed that a near-linear increase in GGp FFMR could be predicted as the airway pressure dropped, and in all cases the zero-load FFMR was comparable. The response at low nominal pressures is flat, with a trend of an increasing peak pressure as the nominal pressure value increased. This corresponded well with the notion that the GGp acts as the main airway dilator.

The response of the GGm was consistent with the GGp in that there is an overall increase in muscle contraction as the applied load increases. However, the response is more erratic again due to the influence of the surrounding secondary muscles. Furthermore, due to the gravitational load, the overlap of functionality between these two muscles contributed further to this effect. Overall, the result for the GGm required further refinement before a definitive quantification of the response could be made.

As seen previously for the supine case, the next most influential muscles in all of these scenarios were the SL and TV. The predicted FFMR for these and all other muscles scaled linearly with the nominal pressure.

11.2.4 Temporal load pattern

Deviations from the "normal" breathing pattern during exertion (such as in exercise or an apnoeic event) may take several forms. Changes to the loading pattern could be elicited as part of this process. The temporal dependence of the function describing the loading was modified to assess the dependence of muscle response on the loading pattern. This was performed by increasing or decreasing the loading rate in various stages of the inhalation cycle. Figure 11.9 depicts the four loading cases evaluated. In the one case, a rest period was introduced to determine whether the GA would hold the muscle response steady once the load had been removed.

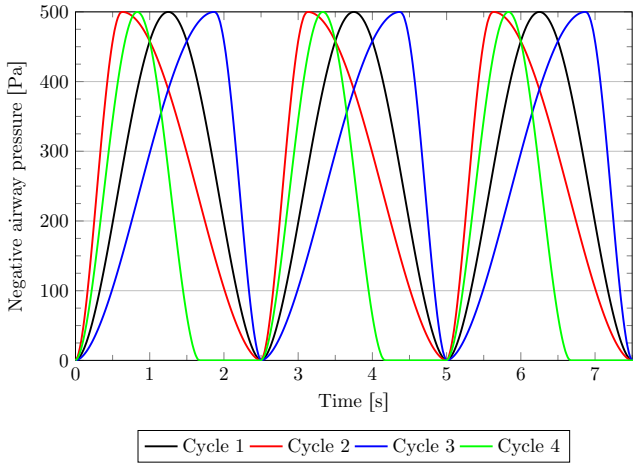

Figure 11.9: Temporally dependent nominal pressure value describing different inhalation pressure loads. Cycle 1 is the loading pattern used in previous examples. Cycles 2 and 3 increase the rate of the load change as the start and end of the inhalation process respectively. Cycle 4 includes a resting period at the end of inhalation.

The result reinforces the perception that the muscle activation pattern is a direct response to the applied load. For the medial and posterior GG, the activation level appears proportional to the epiglottal pressure. The response of the GG constituents, shown in figure 11.10, closely follows the temporal description of the loading pattern in all cases. As first observed in section 11.2.3, the GGp activation pattern matches the loading curve more accurately than the GGm.

For both the GGp and GGm, the maximum amplitudes remain very similar in all cases. However, the minimum values seen at the end of each loading cycle are slightly inconsistent. This could be a post-processing artifact. For all muscles, it was observed that during the rest period introduced in the fourth loading case, the FFMR remains largely consistent with that expected. Overall, the change in loading rate incurred by changing the loading pattern did not appear to significantly alter the characteristics of the response of the muscles of the tongue.

The link already established between the nominal load and the muscle FFMR infers that more rapid changes in the activation level are required to counter the changing load. Clearly a very different activation history

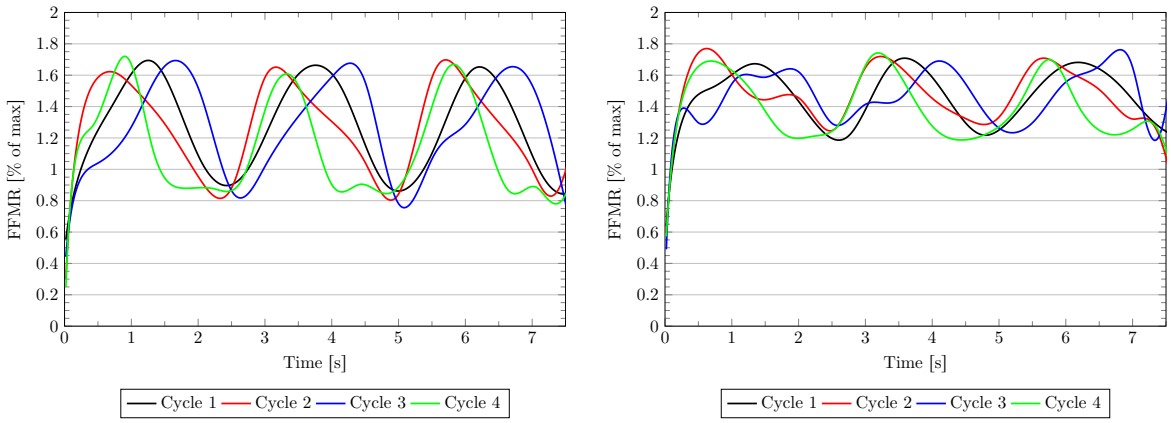

(a) GGp **(b)** GGm

Figure 11.10: Muscle response due to change in rate of change of pressure load by means of altering the temporal shape of the inhalation cycle.

is necessary for each breathing cycle in order to impose position control of the tongue under temporally different pressure loads.

11.2.5 Breathing cycle period

Proceeding from section 11.2.4, the time period over which an inhalation cycle was performed was systematically reduced from a value of 2.5s, representing a slow relaxed breath, to 0.25s, a sharp gasp that may be utilised during an apnoeic event. As a result, a more direct assessment of load-rate dependence is performed. The time-step size was reduced to maintain 500 steps per simulation.

It was observed in figure 11.11 that there exists a strong dependence of the tongue response on the duration over which a breathing cycle occurs. It was noted that as the cycle period decreased, the strength of contraction of the GG at peak pressure increased. This can be directly explained by the increased rate of contraction required to overcome the more rapidly applied load. The force-velocity relationship depicted in figure 6.6 describes the corresponding decrease in effectiveness of the muscle as the rate of shortening of the CE increases. During the loading phase, the velocity of contraction must increase to oppose the force, leading to higher FFMR values being recorded during this part of the cycle and at peak pressure. At higher frequencies during loading and unloading the muscle response is similar for all cases as the value for f_c^V is maximised and constant at a relatively low extension rate and thus the strength of contraction effectively becomes a function of the CE length. Particularly for the GGp, it appears that the zero-load FFMR is reduced with increasing load frequency.

Overall, the response of the GGp appears predictable and directly related to the epiglottal pressure, while the GGm again has a slightly erratic response. However, the stark contrast in the responses between the shortest and longest loading frequencies indicates that, for the latter muscle group, the trends remain similar to those observed for the GGp.

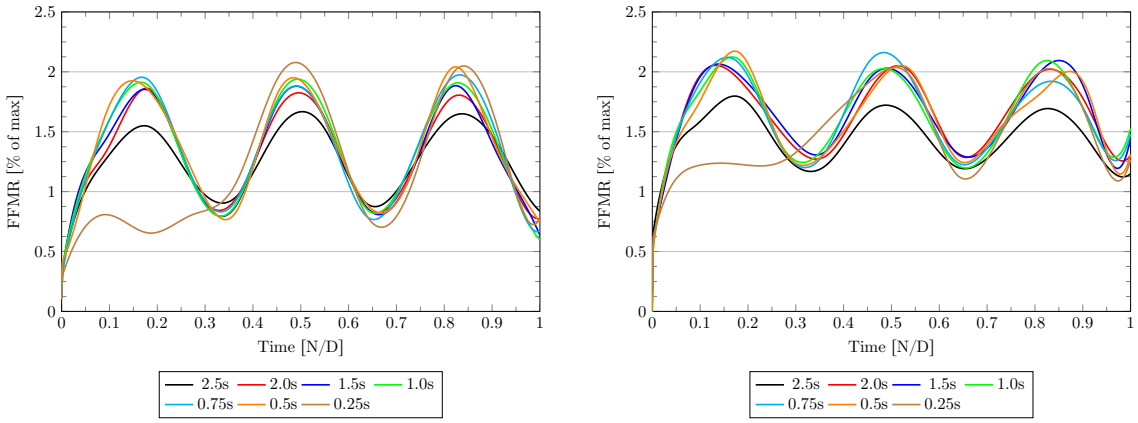

(a) GGp **(b)** GGm

Figure 11.11: Muscle response due to change in rate of change of pressure load by means of altering the inhalation cycle period. The time scale has been non-dimensionalised for ease of comparison between results. The poor result during the first cycle of the 0.25s test demonstrates that the activation parameters needed to be adjusted to increase the agility of the tongue to respond to both the gravitational load and the sudden increase in pressure load.

11.3 Physiological parameters

The primary physiologically linked parameter thought to influence the functioning of the tongue is the fibre volume fraction ϕ_{f}. This is related to the proportion of interstitial and adipose present in the tissue. Parameters related to the muscle model include the activation rate parameters τ_R, τ_F and the contractile force scaling constant T_0^s. A discussion on the influence of the first two parameters is presented below.

11.3.1 Muscle fibre volume fraction

The determination of the role of fibre volume fraction in muscle response is important when considering conditions that affect the ratio between muscle fibre and matrix. Pathologies causing an accumulation of adipose tissue, such as in obesity or loss of muscle bulk as in muscular degenerative diseases, influence this ratio.

Due to the complex spatial description of the muscles and the difficulties in determining their spatial volume fraction, a simplistic view of the local fibre/matrix decomposition has been adopted. In terms of describing the force generating properties of each local muscle fibre, the volume fraction occupied by the fibre (described by equation 5.2) acts as a force scaling factor (see equation 5.6c) and it is thus reasonable to assume that a linear change in the global fibre volume ascribed to the muscular tissue would elicit a proportional response. Figure 11.12 illustrates that this is indeed the case. The predicted peak-to-peak FFMR remains within 5% of a linear response for the GGp, while the GGm response is at worst within a margin of 9% of the linear response. Given a situation in which the local volume fraction does not change uniformly in space, this result would not necessarily be as predictable.

Considering the linear relationship between body BMI and the fat content of the tongue shown in table 6.3, this data indicates that the neural control mechanism for the tongue must be significantly affected as the body

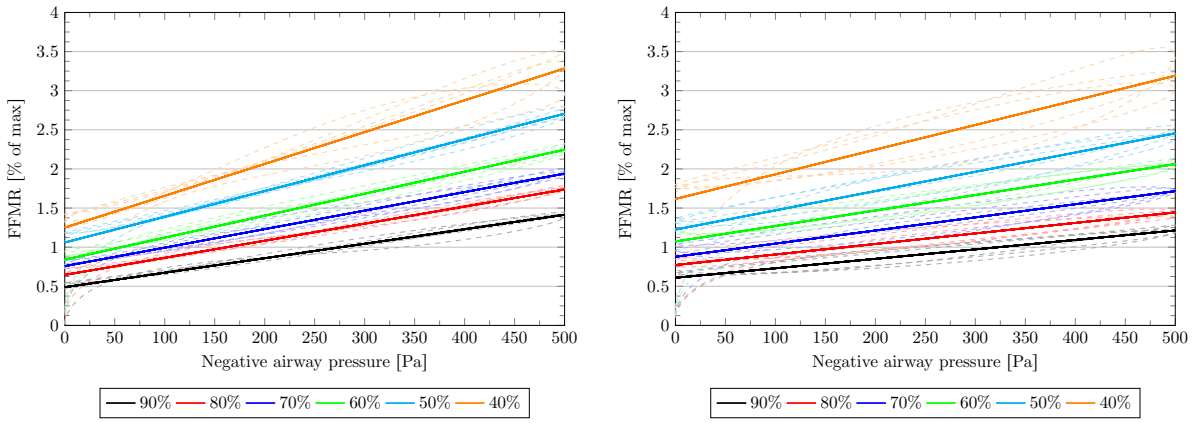

(a) GGp **(b)** GGm

Figure 11.12: Muscle response due to change the ratio between fibre and matrix volume fractions in the tongue. The muscle activity required to oppose the applied force is directly proportional to volume occupied in the tongue by the muscle fibres.

fat content changes. The resulting increase in posterior-tongue adipose tissue content from 30% to 60% as the BMI increases from 25 to 55 requires the GGp to contract on average 98% more intensely at resting state in the supine position and 89% when the epiglottal pressure is 500Pa. The corresponding increase in contraction intensity for the GGm are 110% and 127% respectively at rest and under load.

11.3.2 Rise and decay parameters

The rise and decay parameters τ_R, τ_F determine the rate at which the activation level changes due to the applied neural signal. The change in contraction strength between discrete time-steps, and thus the gradation of the control response, is directly associated with this parameter. As these parameters are nominated *a priori*, a balance must be struck between the necessity for agility and smoothness of the muscle response for the given scenario being simulated.

Figure 11.13a demonstrates that for the given loading pattern, a wide choice of activation rate parameters result in the same trend for the position control of the tongue. It was observed that, with increasing values for the parameters, the changes in displacement solution between time-steps became less erratic. This is related to the change in contraction strength between time-steps, illustrated for the GGm in figure 11.13b. When the muscles are made highly responsive, oscillations around the optimal FFMR value are large in magnitude. This over-sensitivity leads to rapid changes in position and ultimately difficulties in finely adjusting the tongue posture.

The choice of more suitable activation parameters reduces oscillations of the FFMR value around the mean trend. This will ultimately lead to more accurate and reproducible results, and significantly reduce uncertainty in the analysis of the trends in the contraction patterns for each muscle group. Using the splined result for each individual case as a baseline, a quantification of the magnitude of the oscillations around the trend was performed to determine the increase in accuracy gained through more careful selection of the parameters. Table 11.2 indicates that up to a 60% reduction in magnitude of the oscillations is achievable through careful selection of the muscle activation parameters.

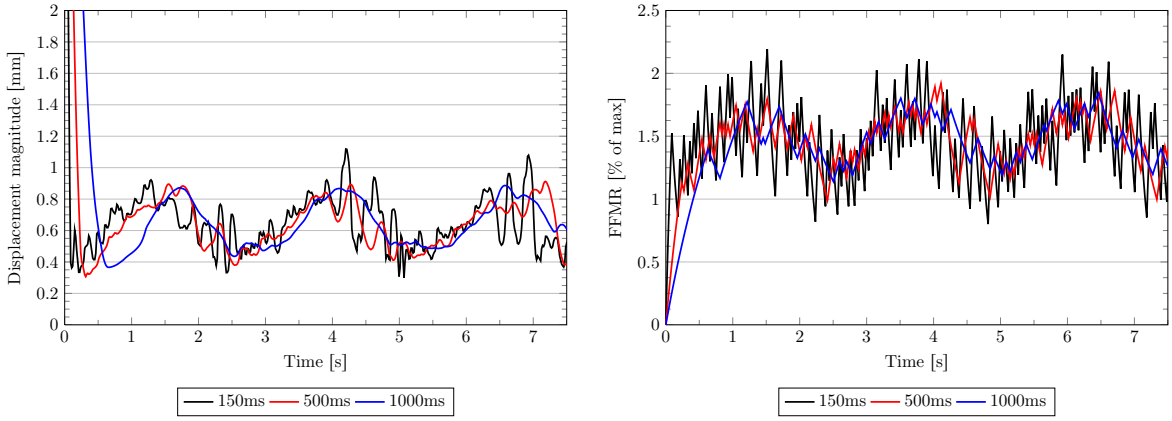

(a) Total displacement of $\boldsymbol{P}_C$

(b) GGm FFMR

Figure 11.13: Behaviour of the neural model due to the change in muscle activation parameters. Altering the responsiveness of the tongue muscles affects the accuracy of the unfiltered prediction for the tongue response.

Table 11.2: Root mean squared error (RMSE) between raw FFMR data and B-spline result trends for each simulation. The tabulated value, expressed as a percentage, relates the magnitude of the error associated with the raw data relative to the splined results averaged out between all of the five simulations, i.e. RMSE $= \sqrt{\frac{1}{n}\sum^{n}(x_n - \bar{x})^2}$. The values leading up to the first peak of the loading were discarded as the rate at which the muscles respond to the sudden gravitational and pressure loading leads to different and incomparable behaviour in this regime.

Muscle	**Activation parameters** τ_R, τ_F				
	150ms	250ms	500ms	750ms	1000ms
GGm	22.53	17.66	11.65	8.77	7.70
GGp	18.08	14.31	9.00	6.77	5.33

11.4 Summary and discussion of results

Collectively between the results shown in sections 11.2.1 and 11.2.2, it has been demonstrated that the GGp takes the role of the primary airway dilator, counteracting the anteroposterior pressure gradient developed in the oropharynx. The GGm primarily resists lifting forces acting on the superior surface of the tongue. However, the two muscle components have overlapping functionality and thus collectively act to resist forces causing motion during inhalation. This validates the initial observations made regarding the function of the GG components in section 10.4.

Application of the non-optimised neural model has demonstrated that the predicted pressure-activation relationship, appears qualitatively similar to that shown in the literature [111, 3] and that the influence of environmental and physical parameters on this response appears, in some cases, predictable. It has been shown that the head and neck posture [205, 122, 269, 15, 8, 18] has a major influence on the contractile effort of the GG required to maintain the spatial position of the tongue. The relationship between the epiglottal pressure and GG activation has also been shown to be highly sensitive to the pressure distribution on the

tongue, and it was demonstrated that the load simulating oral inhalation leads to greater force generation requirements by the GG. This indicates that any mechanism, such as increased nasal resistance or obstruction [238, 294, 227, 236, 75, 174, 250], leading to the preferential use of the mouth during inspiration may result in the retroglossal movement of the tongue if neurological weaknesses in the functioning of the GG exists. Furthermore, the response of both muscles are significantly affected by magnitude and the proportion of tongue body occupied by muscle fibres, indicating a link to the tissue deposits synonymous with obesity [125, 173, 191, 33, 8].

Further discussion

Although some difficulties and inconsistencies exist, it has been demonstrated that, generally, this model is useful in predicting trends in the response of the constituent muscle groups of the tongue subjected to external influences. The robustness of the neural model is, for example, illustrated in section 11.2.4. The result shown here is somewhat independent of choice of τ_R and τ_F, parameters that have not yet been optimised, demonstrating that the methodology can produce reliable predictions over a wide range of loading parameters. Numerous mechanisms for increasing the accuracy of the model are presented and will be collectively employed from this point on. These will assist in minimising the error associated with the post-processing mechanism (smoothing the results), essentially due to the oscillatory nature of the response from the neural model. Further factors that were evaluated for the purpose of model optimisation are presented in appendix G.

The mixture of fast- and slow-twitch fibres present in the tongue allows for it to move with high precision and through a large range of speeds. It has been shown that the use of more physiologically consistent values for the rise and decay parameters results in a very sensitive model, demonstrating that the tongue has the ability to react to stimuli that are applied far more rapidly than those applied in this work. Considering their role in the neural model, it functions optimally when they are no longer interpreted as physiologically derived values and rather as optimisation parameters that are bounded by physiological constants. From these results, it was determined that a satisfactory choice for τ_R, τ_F, leading to good responsiveness with minimal solution overshoot, could be made with

$$\tau_R = \tau_F = \frac{1}{10}\frac{1}{\beta}\omega \tag{11.1}$$

where ω is the loading cycle period and $\beta \in \{0.5, 1\}$ set according to whether a full cycle of inhalation and exhalation was simulated ($\beta = 1$ in this case) or whether half of the breathing cycle was considered, as has been done up to now.

It has been demonstrated that there are many factors that influence the outcome of each simulation. What is apparent, although not specifically discussed, is the predictably replicable nature of the results. Although the GA employed in the neural model is non-deterministic, the evaluated population size was small and non-optimal model parameters were utilised, the model was successfully able to follow the applied load and produce a sufficiently adequate and physiologically reasonable result. Given a fixed set of parameters, the model will reproduce the muscle response with a fair and comparable degree of precision. Furthermore, given the non-optimal parameters, the GA nevertheless is able to predict quantitatively sensible trends in results. This provides confidence that the model is robust enough to cope with and produce sufficiently accurate results under complex loading conditions.

12. CFD STUDY DETAILING UPPER AIRWAY PRESSURE DISTRIBUTION

A basic CFD model was designed to gain insight under various conditions into the pressure distribution on the tissues lining the airway. There are many factors that might affect the pressure profile of the airway, all of which change with both time and the associated response of the airway muscles. These include the geometry of the airway, the instantaneous flow rate and the breathing pattern. As the problem is very complex, it was studied under simplified and restricted conditions, namely assuming a static geometry and steady state flow.

A physiologically plausible model was developed to understand the fundamental flow characteristics and compute airway pressure distributions in a healthy individual during light and moderate-to-heavy breathing. The primary purposes of this model is to determine the likely state and phase of breathing that leads to low epiglottal pressures and unfavourable pressure distributions on the tongue. By simulating breathing through the nose and mouth, the effect that these had on the airway pressure profile was deduced. The pressure data from these models was exported to the tissue model to evaluate the tissue movement under passive conditions, as well as the muscle response required to resist movement and potential airway collapse.

In the interest of brevity, this chapter will focus solely on the pressure distribution in the airway and on the tongue. The details of the simulation procedure, discussion on the flow characteristics, and validation by means of a comparison to the literature is presented in appendix H.

12.1 General pressure profiles

The general pressure profiles developed during oral and nasal breathing are presented. The differences between inspiration and expiration are discussed for each case.

12.1.1 Nasal and oral inspiration

During nasal inspiration there is a significant pressure drop through the nasal passages (approximately $50-60\%$ static pressure loss at all measured flow rates). Figure 12.1a depicts the static pressure field developed during normal breathing. Note that in the region of the velopharynx (the region between nasopharynx and pharynx that is bounded by the uvula), a flow restriction that acts as a converging nozzle is present.

There is only a slight pressure drop across the velopharynx (not discernible in the image) and no significant pressure recovery once flow enters the pharynx. The pharyngeal pressure does not change appreciably along its length; however, a large pressure loss occurs across the laryngeal constriction at the junction between the pharynx and trachea. A significant feature of the pressure field is that the pressure in the oral cavity appears constant, resulting in little fluid motion in this region. Although the pressure is less than atmospheric, this is still physiologically accurate assuming the lips are closed and preventing an ingress of air through the mouth. If the oral cavity were to be sealed off by the posterior portion of tongue pressing against palate (as does happen during normal nasal breathing with one's mouth open), then the pressure in the oral cavity would be atmospheric and only the posterior surface of the tongue experiences the negative airway pressure.

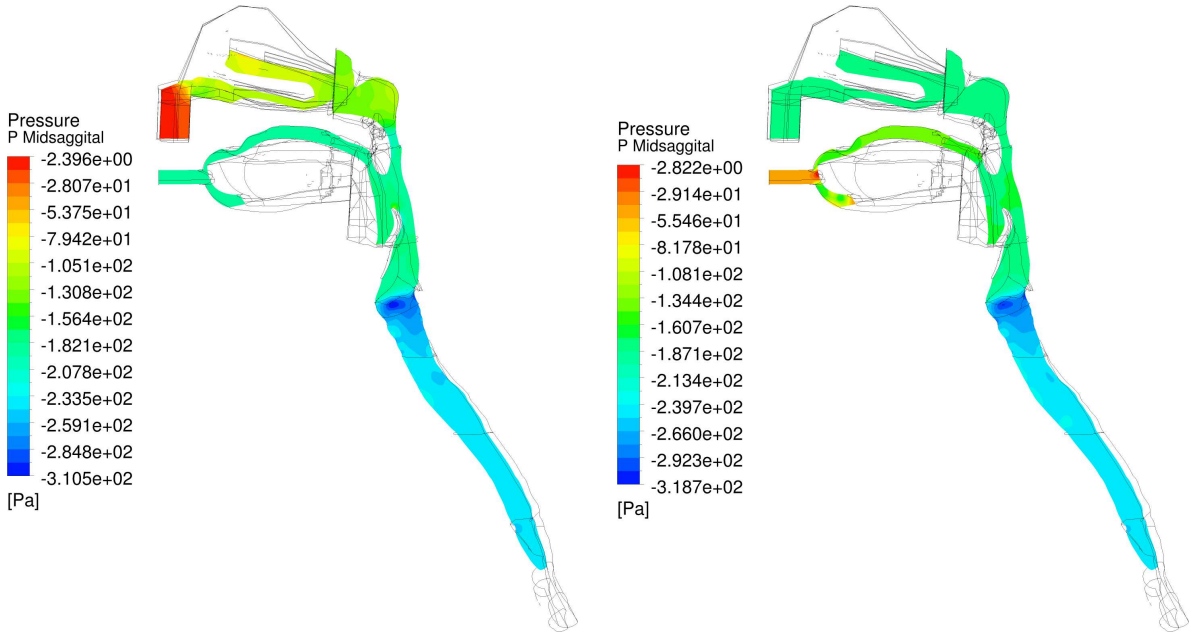

(a) Nasal inspiration **(b)** Oral inspiration

Figure 12.1: Static pressure on the midsagittal plane during inspiration at 60L/min.

Illustrated in figure 12.1b for the case of normal oral inspiration, a high pressure loss at the external opening to the oral cavity exists due to impingement of flow by tongue. This phenomenon is not necessarily consistent with normal physiology and bodily functioning where the tongue drops inferiorly to allow air to flow over its upper surface[1]. Also potentially inconsistent with reality is the flow around the sides of the tongue. This flow feature is present because the teeth (which usually form a lateral barrier to flow movement) were removed from the geometry due to their contact with the tongue. The lifted position of the tongue further exacerbated the issue.

The average static pressure drop between the atmospheric boundary and the rear of the tongue was 59% of the total value at the stipulated flow rate, with a range of $53 - 63\%$ for the tested flow rates. The static pressure was, again, nearly constant along length of pharynx, although lateral movement of air from the oral cavity into the pharynx resulted in secondary effects due to the formation of turbulent vortices. Similar to the previous case, the nasopharyngeal region experienced the same pressure as the velopharynx. This may be physiologically inaccurate as such a negative pressure in the nasal passage would cause air to flow into the nasal passage through the nasal vestibule. This scenario can be obviated by opening the mouth sufficiently

[1] Jayaraju et al. [131] demonstrates the physiologically correct position of the tongue during inhalation.

and depressing the tongue, minimising pressure drop through oral cavity into the pharynx and making this the preferential pathway for the air.

Comparing the two cases, it is clear that the pressure profile in nasopharynx and oropharynx varies significantly depending on whether nasal breathing or oral breathing takes place. In both cases there was a large pressure drop across laryngeal constriction. For the cases illustrated here, the total pressure drop between the atmosphere and the bronchus appears roughly similar for a constant flow rate. The preliminary results presented in chapter 11 suggest that these base cases did not result in pharyngeal pressures low enough initiate appreciably large deflections of the active tongue. The measured epiglottal pressure, approximately -180Pa, was significantly larger than that necessary to institute large deformations of the tongue or precipitate a loss of dilator reflexes.

Figure 12.2 illustrates the pressure distribution on the tongue surface. Distinct differences between oral and nasal breathing are evident from these results.

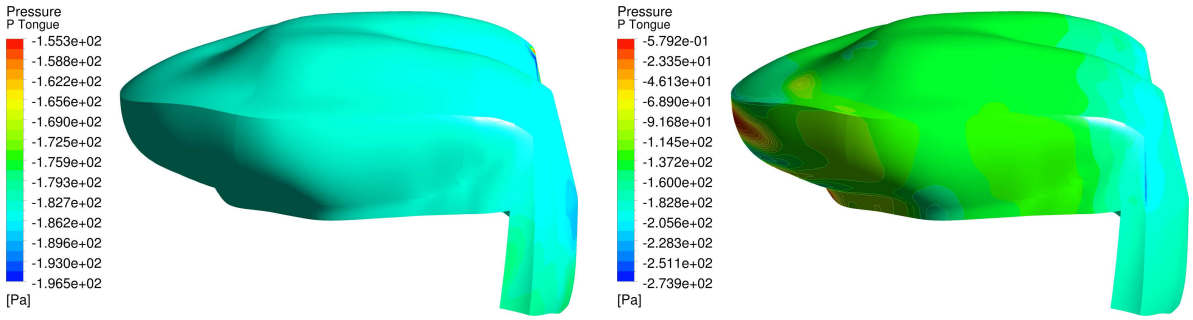

(a) Nasal inhalation **(b)** Oral inhalation

Figure 12.2: Air-pressure distribution on the tongue surface for inspiration at 60L/min.

In the case of nasal breathing, the pressure distribution on the surface of the tongue remained nearly constant as hypothesised in the simplified FEM case study of the tongue. As there was little difference in pressure between the anterior and posterior surfaces, it could be expected that the anteroposterior pressure force generated on the tongue was minimal. Oral breathing resulted in a significant pressure drop across the length of the tongue, which was synonymous with the hypothesised case of a linear pressure profile. It could be expected that this pressure distribution would draw the tongue posteriorly into the oropharynx. Comparison between this case and that of nasal breathing provided an insight into why OSA is prevalent in instances of mouth breathing.

12.1.2 Nasal and oral expiration

To highlight the differences between expiration and inspiration, a scenario similar to that presented in section 12.1.1 is produced with the velocity at the tracheal boundary now altered such that this boundary represents an inlet and the oral or nasal features an outlet. Expiration is thus simulated at a constant flow rate of 60L/min.

The midsagittal pressure fields attained during expiration are shown in figure 12.3. A notable feature of nasal exhalation is that the pressure field in buccal cavity, like during inspiration, has a largely constant distribution. A pressure gradient between the superior and inferior surfaces of the soft palate was observed.

Significant pressure losses occurred at the laryngeal constriction and in the region of the velopharynx. A local high pressure region was observed at the tip of the uvula due to the stagnation point present as the flow divides between moving into the oral and nasal cavities.

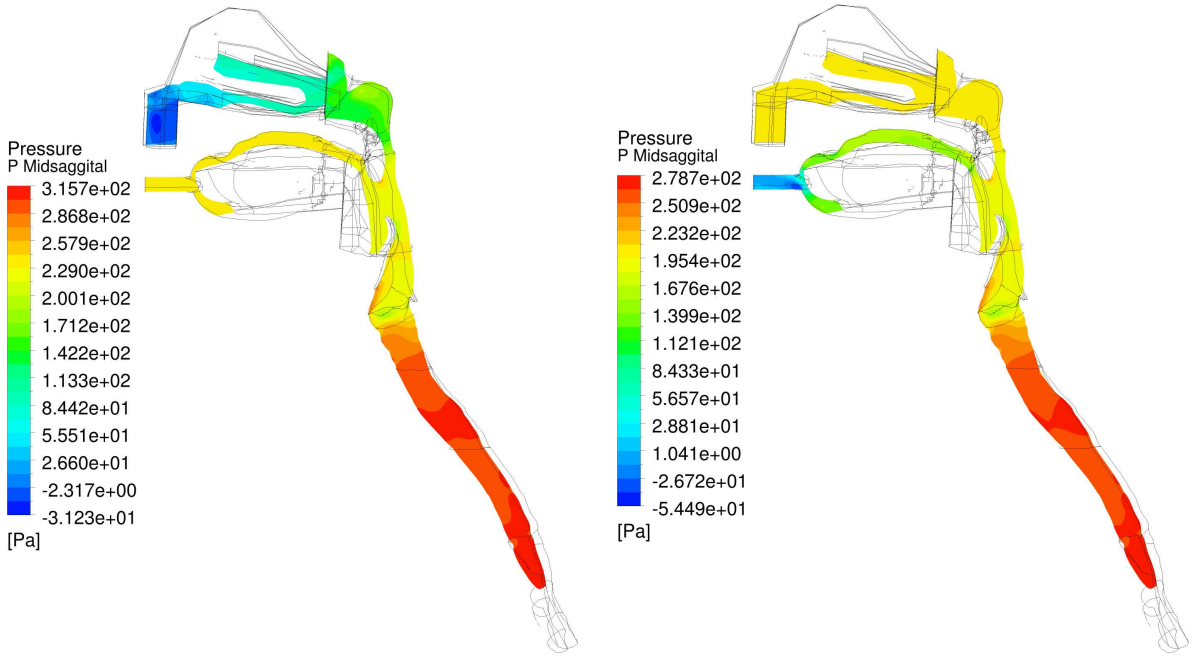

(a) Nasal expiration **(b)** Oral expiration

Figure 12.3: Static pressure on the midsagittal plane during expiration at 60L/min.

In the regions inferior to the hypopharynx the pressure distribution developed during oral expiration, illustrated in figure 12.3b, was remarkably similar to that on nasal exhalation. However, a large pressure difference existed between the pharynx and mouth. Similar to the previous case, the uvula tip experienced high pressures due to flow stagnation at this point.

The pressure distribution on the tongue during expiration are depicted in figure 12.4. From these images, distinct differences between oral and nasal breathing were evident. The tongue was exposed to a constant positive pressure during nasal expiration and a pressure gradient in the anteroposterior direction when oral expiration occurs. Figure 12.4b suggests that a suitable first-approximation to the latter scenario would be a linear gradient with the posterior region exposed to a high pressure and the anterior a low pressure. In both cases the entire tongue surface experiences a pressure greater than atmospheric pressure. This would result the development of a resultant force acting to move the tongue anteriorly in the buccal cavity.

12.2 Airway pressure drop due to flow rate change

A spectrum of flow rates was evaluated to determine its influence on the pressure distribution and loss in the pharynx. The volumetric flow rates chosen ranged from those representative of very light breathing (5L/min), through the average flow rate during moderate or natural breathing (60L/min), to an estimate of the peak flow rate during gasping (180L/min), which conceivably would be the result a loss of pharyngeal patency.

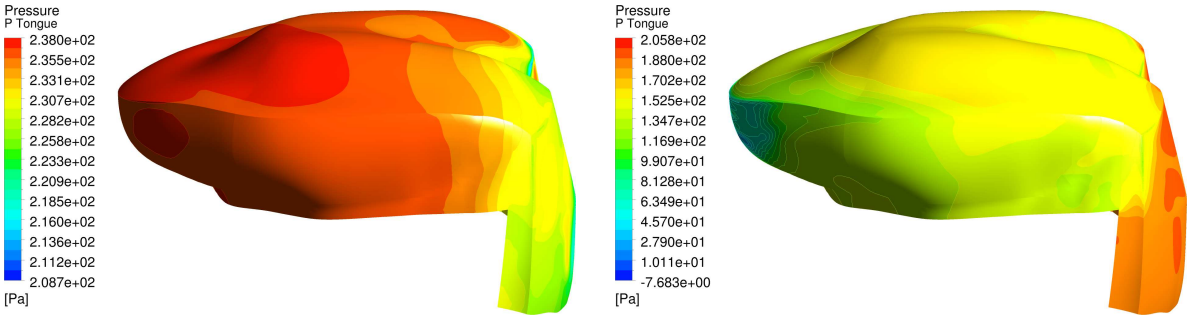

(a) Tongue: Nasal expiration

(b) Tongue: Oral expiration

Figure 12.4: Air-pressure distribution on the tongue surface during expiration at 60L/min.

Tables 12.1 and 12.2 present the volume-weighted average pressure distribution measured at various sections of the airway along the path which the fluid flows through during inspiration. Firstly, an examination of nasal inhalation is performed. The magnitude of the pressure loss or recovery increases almost quadratically as the flow rate increases. Pressure recovery was observed in most instances in the upper pharynx and the trachea, although it was marginal in comparison to the pressure magnitude due to previously experienced losses. Although the pharyngeal pressure at 60L/min appears too marginal for the loss of reflexive mechanisms in the GG, at 120L/min the negative pharyngeal pressure is in excess of 500Pa which could precipitate such an event.

Table 12.1: Pressure loss in HUA at differing flow rates during nasal inhalation. The value describes the average pressure loss between the upstream and downstream measurement surfaces. The measured pressure losses in the nasal passage compared favourably with the literature (see [307, fig. 5]). The highlighted entries represent regions that are in the pharynx.

Flow rate (L/min)		5	15	30	60	90	120	150	180
Upstream	**Downstream**	**Static pressure loss (Pa)**							
Vestibules	Anterior nasopharynx	2.4	11.3	35.1	116.5	240.2	406.5	618.8	889.4
Anterior nasopharynx	Upper velopharynx	0.6	4.5	16.8	64.4	142.9	248.6	385.1	549.0
Upper velopharynx	Upper pharynx	0.1	0.1	-0.9	-6.3	-15.9	-31.7	-58.0	-80.0
Upper pharynx	Upper hypopharynx	-0.1	-0.3	-1.7	-11.1	-25.9	-36.0	-50.0	-74.0
Upper hypopharynx	Upper larynx	0.3	3.1	11.8	46.8	108.4	187.4	301.0	434.0
Upper larynx	Upper trachea	0.6	4.4	16.2	49.8	107.2	173.7	227.0	325.0
Upper trachea	Lower trachea	-0.1	-2.0	-8.4	-33.5	-75.0	-130.2	-216.0	-277.0
Inlet	Outlet	4.1	21.8	71.1	139.9	492.6	835.11	1230.0	1821.4

An evaluation of the flow rate effect on pressure-losses during oral breathing demonstrates that the losses in the oral cavity can be large enough to create a change in the response of the airway and tongue dilator muscles. During normal oral breathing, the losses in the buccal cavity reduce the epiglottal static pressure; however, only at flow rates upwards of 120L/min the pharyngeal pressure reduces to below the suggested critical value of -450Pa [111]. There is no pressure recovery in the pharynx during oral inhalation. Due to similarities in the flow-field, the pressure drop in the sections inferior to the epiglottis are quantitatively similar for both the cases of oral and nasal inhalation.

Table 12.2: Pressure loss in HUA at differing flow rates during oral inhalation. The value describes the average pressure loss between the upstream and downstream measurement surfaces. At low to moderate flow rates, the total pressure loss between inlet and outlet at various flow rates is of the same order of magnitude as that measured in an idealised geometry [196]. The highlighted entries represent regions that are in the pharynx.

Flow rate (L/min)		5	15	30	60	90	120	150	180
Upstream	**Downstream**	**Static pressure loss (Pa)**							
Mouth	Posterior oral cavity	1.5	9.1	30.2	107.6	223.6	382.6	580.0	829.6
Posterior oral cavity	Upper hypopharynx	0.4	1.9	5.3	15.4	30.4	44.0	52.5	77.0
Upper hypopharynx	Upper larynx	0.4	3.2	11.9	48.1	104.8	189.9	298.0	455.0
Upper larynx	Upper trachea	0.6	4.6	15.7	51.4	99.2	189.7	299.0	349.0
Upper trachea	Lower trachea	-0.1	-1.6	-8.9	-33.6	-74.2	-145.3	-247.0	-317.0
Inlet	Outlet	3.1	18.6	59.8	122.1	413.1	710.7	1034.5	1472.3

12.3 Summary and discussion of results

The model of the airway was evaluated under steady state conditions, testing numerous breathing behaviours and validating the reduced-complexity representation of the nasal passages. Correlation of flow phenomena and measured pressure drops within certain regions of the anatomy and those data presented in the literature demonstrates that the model is sufficiently accurate for the aims of this work.

In summary, oral inhalation leads to an anteroposterior pressure gradient across the length of the tongue that may lead to its movement into the retroglossal space. The assumed simple load distribution for oral breathing described in section 8.6.3.3 appears to be qualitatively representative of that shown in figures 12.2b and 12.4b. Nasal breathing with a closed mouth results in a near constant distribution of pressure on the surface of the tongue, qualifying the load distribution assumption made and likely resulting in little movement due to air-induced force. Exhalation develops positive pressures throughout the airway which, due to its geometry, may lead either to minimal or anterior movement of the tongue in the cases of nasal and oral breathing respectively.

An increase of flow rate during oral inhalation leads to a greater pressure gradient between the anterior and posterior surface of the tongue. Nasal inhalation at high flow rates generated high pressure losses in the nasal passages; this is unsurprising as a near constant pressure field on the tongue surface was always predicted.

Collectively, these results indicate that oral inhalation creates a scenario most likely to produce posterior motion of the tongue. It was observed that the threshold epiglottal pressure required for the loss of GG reflexes during sleep could be achieved at moderate-to-high flow rates during inspiration through either the nose or mouth.

13. MUSCLE RESPONSE TO SIMULATED BREATHING AND CONDITIONS OF PHARYNGEAL COLLAPSE USING STATIC AND DYNAMIC LOADING

In the previous chapters, various aspects of the muscle and neural model development with respect to the tongue were highlighted. Data that demonstrated which factors are most significant determinants of the active response of the constituent muscles of the tongue was presented. Points pertaining to the optimisation of the model parameters were also discussed, although an optimised model had not yet been utilised. Using this data, an optimal set of control parameters were chosen and from this point on the model is considered optimised in all respects to a level that are currently is feasible. Furthermore, a fluid model was produced to capture more realistic pressure data and qualitatively compare the observed pressure distributions to those assumed in earlier simulations of the tongue.

This chapter is devoted to utilising the optimised tongue model to achieve three goals. Firstly, it will be determined whether a quasi-static model can be representative of the dynamic phenomenon that is OSA, caused by complex fluid-structure interaction. This will be useful as then computationally inexpensive means of evaluating these problems may be made possible. In doing so, validation of the simplified, assumed pressure distributions for the dynamic cases will be performed by evaluating the muscle response. In summary, the two simulation mechanisms will validate different aspects of one another.

Secondly, with the dynamic model optimised in terms of control parameters, aspects of the functioning of the GG will be analysed in more detail. A determination of the spatially-dependent force-generation characteristics will be made factoring in the influence of the surrounding muscles. Such information may be useful in understanding the consequences of surgical procedures, such as implants or the removal of tissues due to the formation of tumours or necrosis.

Finally, once validated models have been produced, we will present analytical models which replicate the response predicted by the neural model. These will be formed in such a way that the effect of the environmental influences will be clear. This will allow the simulation of deficiencies in the response of the tongue musculature, thereby reproducing a number of scenarios that may lead to an OSA event. Both the simulated

response of the GG and the magnitude of the predicted retroglossal movement will be documented for two cases; one that represents the threshold of the onset of an OSA-type event and one that simulates a complete loss of airway patency.

13.1 Quantification of muscle response with static loading derived from CFD models

In chapter 12, simulation of nasal and oral inhalation was performed under steady state conditions at numerous volume flow rates. The pressure distributions obtained from these models were extracted and applied directly to the model presented in chapter 11. Due to the steady nature of the fluid model, a similar approach was observed in conducting these simulations. A quasi-static approach, the conditions of which were previously detailed in section 8.6.3.1, was adopted and time represented an evolution parameter for the neural activation. It was assumed that, over numerous pseudo-time-steps, the neural model would evolve the set of activation parameters to the optimum value, balancing the energetic characteristics and spatial control. However, no further optimisation of the model (swapping from one best suited for dynamic simulations) was considered. In all, 250 evolution steps were used in each simulation, with the average neural stimulus for the last 150 taken as the values shown in the following illustrations.

First it was thought prudent to evaluate the pressure loads on the tongue as predicted by the fluid simulations and compare them with those initially used in chapter 11. Figure 13.1 depicts the pressure load, averaged over the anterior, superior and posterior surfaces of the tongue, for inhalation from two orifices under increasing volume-flow rate[1]. Qualitative comparison between this data and figure 8.15, the equivalent measurement for the assumed distributions simulating both cases, can be made to determine discrepancies between the two cases.

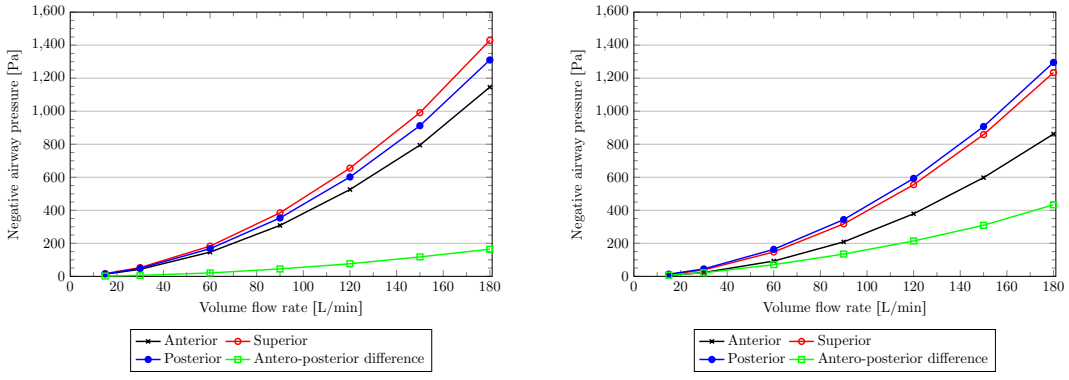

(a) Nasal inhalation **(b)** Oral inhalation

Figure 13.1: Area weighted average air-pressure (derived from CFD analysis) applied to the tongue surface.

In both cases, the average pressure generated on all surfaces increases quadratically with increasing inlet velocity. During nasal breathing, an anteroposterior pressure gradient is developed and the average pressure on the superior and posterior surfaces are nearly identical. This is dissimilar to that which was previously proposed, where zero anteroposterior pressure gradient was assumed. However, oral inhalation leads to the

[1] The reader is referred back to figure 12.2 for a visual comparison between the pressure conditions developed during oral and nasal inhalation.

development of a far more substantial pressure gradient; at high flow rates, the gradient is $2-3$ times that of nasal inhalation and it becomes more substantial at lower flow rates. Interestingly, the posterior surface experiences similar pressures in both cases[2] and the superior surface is exposed to a greater lifting force during nasal inhalation.

The load distribution generated during oral inhalation is predicted to produce displacements of the passive tongue qualitatively comparable to that of the assumed load in the dynamic case. Comparing figure 13.2 to figure 9.7, it is observed that the displacement history at $\boldsymbol{P}_C$ as the epiglottal pressure decreases is linear in both cases.

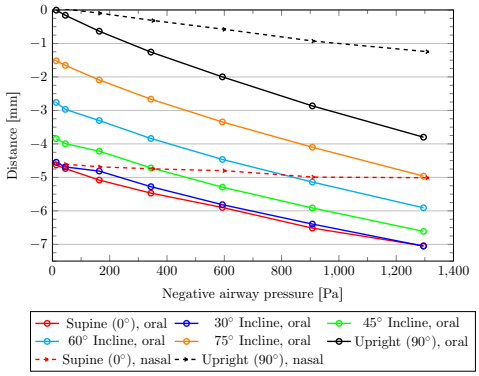

Figure 13.2: Anterior displacement of point $\boldsymbol{P}_C$ on passive tongue due to pressure loading.

However, the resulting displacements from the CFD derived loads are significantly lower (on the order of 3mm at 1000Pa for the upright case, corresponding to 100% of the pressure-induced displacement) as the anteroposterior pressure gradient is far less than that in the idealised case. The effect of passive stiffening resulting from fibre stretch due to gravitational loading can be observed during nasal inhalation. The more upright the posture and greater the negative pressure, the more significant the load-induced displacement is; whilst in the supine position, minimal anterior movement occurs as the epiglottal pressure drops.

Evaluating this resistance against loads using the neural model results a qualitatively similar prediction to that shown in section 11.2.2 for the dynamic case. Figure 13.3 illustrates the difference in GG response for the two postural extremes. Qualitatively, the response is similar in that the muscle activity appears to be increasing proportionally with a decrease in epiglottal pressure. The amount of contractile effort required by the GGp depends on the anteroposterior pressure gradient, while the GGm has a similar response for both breathing mechanisms as the pressure developed on the superior surface of the tongue is similar.

Orientation remains a significant factor in determining amount of muscle activity required to resist motion. The gradient of the muscle response with changing pressure appears to be the same for both the upright and supine postures. For the supine case, the predicted response appears to oscillate severely around an ideal line of response. This larger error at higher FFMR values can be attributed to a larger T_0^s being employed, resulting in greater oscillations around the solution during the evolution process, thus increasing uncertainty in the result. Furthermore, the GA appears more sensitive to the choice of energy-minimisation parameter in the static case than for the dynamic one; further evaluation of a more appropriate choice for the weighting factors is necessary.

[2] The average pressure distributions between the CFD-derived data and the approximated configurations have a great similarity. A determination and comparison of the centre-of-pressure of each surface and computation of the generated force is required to come to a more conclusive determination on the accuracy of the simplified representation of the pressure load. This task has, however, not been performed.

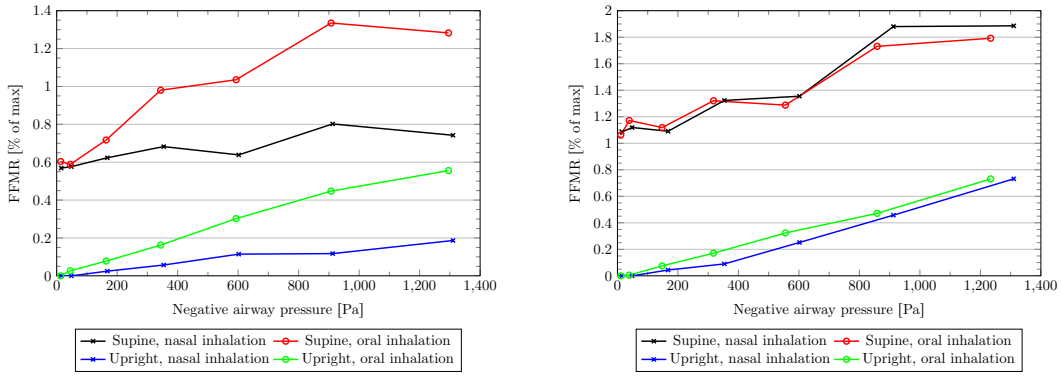

(a) GGp **(b)** GGm

Figure 13.3: Response of the GG to the quasi-statically applied gravitational and pressure load. It has already been established that the muscle response is proportional to the angle of incline, therefore only the limits are depicted in this figure.

Compared to the dynamic case with the approximated pressure distribution, the zero-pressure crossing-points are similar. The GGp also demonstrates similar characteristics when comparing the response under conditions of oral and nasal inhalation. However, the difference in pressure distribution, coupled with rate-effects and the use of the unoptimised model result in significant discrepancies in the magnitudes of the predicted GGp FFMR. The response of the GGm during oral inhalation compared very well between the dynamic and static cases, but that of nasal inhalation differed significantly in that a greater contraction has been predicted in the static scenario. It should be noted that the results shown in section 11.2.2 do not incorporate any energy minimisation requirement, and are thus overestimates of that which would be obtained with comparable energetic qualities. This would further influence the outcome of the neural model, as the effective use of smaller muscles would be preferred over large ones. This may explain the prediction that the GGm would be more active than the GGp during nasal inhalation, as it is less voluminous than the GGp and serves a duel role in position maintenance.

13.1.1 Analytical model of static muscle response for oral inhalation

Performing a similar analysis for oral inhalation under different postures, a collection of data representing the likely response of the GG constituents was obtained. Figure 13.4 depicts the results of this study. Inspired by the response shown in [111] and following from the linear function presented in equation 10.1, regression lines that were a linear function of the epiglottal pressure, were fitted to predict the response of each muscle group. The predicted activity was approximated[3] by the set of curves given by

$$\mathrm{FFMR}\,(p,\gamma) := \underbrace{\left(c_0 + c_1\gamma + c_2\gamma^2\right)}_{\text{Gravity shift}} + \underbrace{\left(m_0 + m_1\gamma\right)p}_{\text{Pressure response}} \tag{13.1}$$

which accounted for their nonlinear dependence on gravitational orientation with no airway-induced load. Furthermore, as the response was observed to stiffen marginally with decreasing inclination angle, it was coupled with the angle cosine. The coefficients for each muscle, determined with the use of evolutionary algorithms [318], are given in table 13.1.

[3] The coefficient of determination for the GGp and GGm predictions were $R^2 = 0.92$ and $R^2 = 0.96$ respectively.

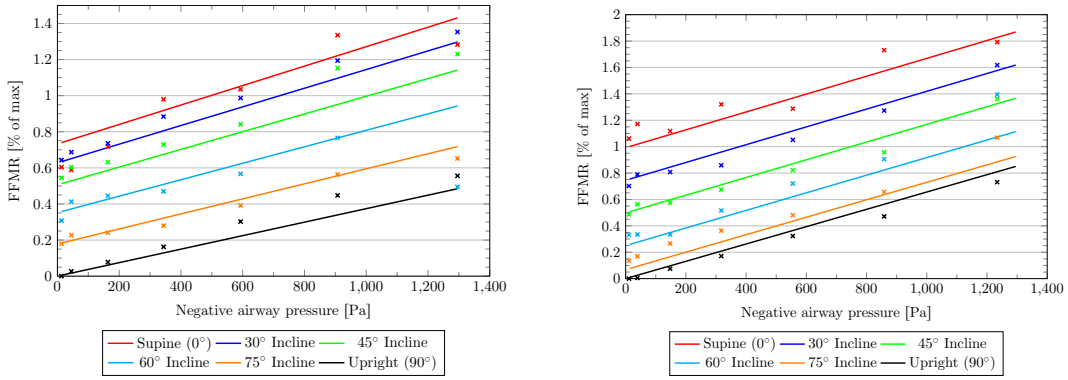

(a) GGp **(b)** GGm

Figure 13.4: Response of the GG to the quasi-statically applied pressure load under differing postures. The overall trend is a linear increase in contractile activity as the epiglottal pressure decreases. However, the accuracy of the predicted response is less than desired.

Table 13.1: Analytical model of tongue muscle control during quasi-static oral respiration: Coefficients for FFMR.

		Gravity factor			Pressure response	
Muscle	Coefficient	c_0	c_1	c_2	m_0	m_1
	Scale	10^{-3}	10^{-3}	10^{-6}	10^{-6}	10^{-6}
GGm		0.096	9.83	0.175	6.56	0.206
GGp		6.73	0.634	-32.99	3.74	1.65

Overall, these trends are qualitatively similar to that described by Huang et al. [111], which assumed a linear dependence between the airway pressure and GG activation. This demonstrates that the neural model has merit as a valid mechanism of producing and extracting the trends of muscle response under loading scenarios. The results presented here later will be used as a basis for comparison for further models developed from the dynamic simulations using the neural model.

13.2 Quantification of muscle response during time-dependent, idealised loading

In order to fully quantify the tongue response during breathing, oral inspiration was simulated when in different postures. This case has already been shown to provide the largest anteroposterior pressure gradient, thereby resulting in the most dynamic response. The loading cycle was governed by the spatial and temporal functions given in equations 8.9 and 8.11. 3.5 full inhalation and exhalation cycles (resulting in 3 full cycles of viable data, discarding the lead-in data obtained in the first cycle) were represented. A nominal airway pressure of 500Pa was chosen, resulting in a peak-to-peak epiglottal pressure difference of 1000Pa. Four different loading rates were tested as the period T of each cycle was reduced in even steps from 2.5s to 1s. The split between the optimisation function weights was chosen as $\{0.7, 0.3\}$, the former applied to the displacement function.

Due to the optimisation of all model parameters, the predicted response of the muscles is less oscillatory than presented previously. This is demonstrated when comparing an example of the new results shown in figure 13.5 to those given in figure 11.2. As the exhalation process has also been simulated, the GG deactivation in this regime is also captured.

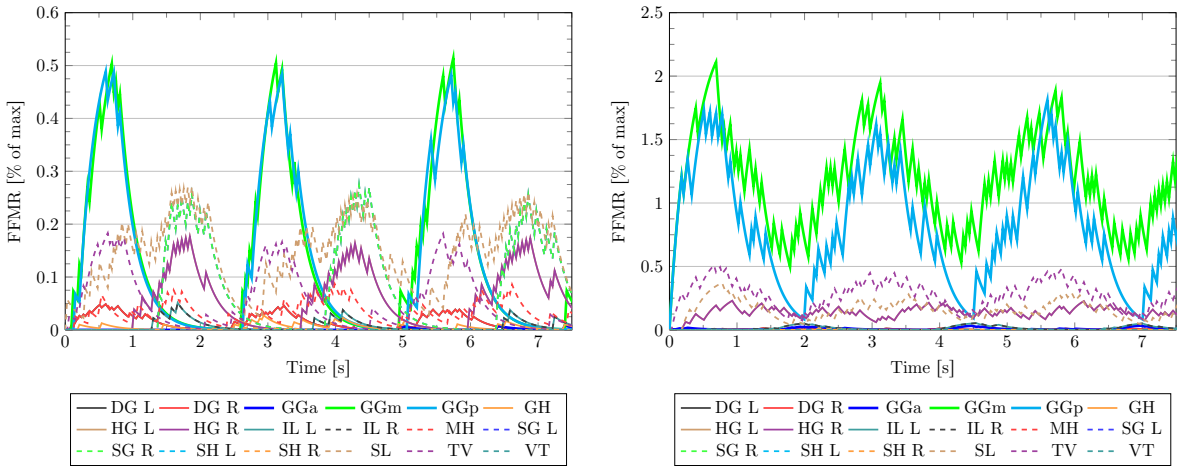

(a) Upright orientation

(b) Supine orientation

Figure 13.5: An example of the predicted muscle response to changing gravitational orientation and airway pressure during oral respiration using the optimised neural model.

In the upright position, all constituent parts of the GG fully deactivate during exhalation and other muscles regulate its position. The TV is utilised to prevent lateral extension due to the contraction of the GG constituents. Contraction of the SL and SG, with peak FFMR values of the same order of magnitude as that of the GG, are required to prevent depression and anterior motion of the tongue. It is observed that activation of the SL occurs first as the negative airway pressure is reduced, and subsequently increases again during exhalation. The HG is also used to depress the rear of the tongue during exhalation, opposing the lifting effect of the SG. Other muscles, such as the MH, DG, IL and GH are predicted to provide minor roles in controlling the tongue in this gravitational configuration.

However, at reclined configurations many of these muscles are not required as the gravitational forces pulling the tongue anteriorly are not overcome. In the supine configuration, the GGp nearly completely deactivates during exhalation, while the GGm remains active. As previously discussed, the GGm is clearly used to moderate tongue position and resist gravitational forces that try to raise the tongue towards the palate at high angles of reclination, while the GGp is more directly correlated to the epiglottal pressure. The TV, SL and HG contract when the airway pressure reduces but relax during exhalation. The other muscle groups produce negligible contraction during both inhalation and exhalation, with peaks of the IL and GGa observed at maximal exhalation pressures and are orders of magnitude less than the peak GGm response.

In both cases, the effect of the decay parameter τ_F is prevalent with the deactivation rate of the muscles as the breathing state changes limited by this value. Furthermore, work-minimisation has reduced the peak FFMR value attained for the GGp by 20% when compared to that shown in figure 11.2b. However, the average response remains consistent with the data depicted in figure 11.6.

Figure 13.6 depicts the spatially non-homogeneous f_c values for fibres distributed throughout the GG at peak negative airway pressure for two gravitational orientations. It is observed that the regions of the GG

that contract most effectively and produce the greatest fibre tension are at the root near the mandible and in the region of the tongue surface. This is due to the f_c^L relationship and that the fibres in these regions experience a lower reduction in fibre length as the muscle contracts, thus working near optimally in terms of their length relationship. In the former case, this is due to the constraint imposed by the mandible, while the latter is due local deformation caused by contraction of other muscles such as the TV.

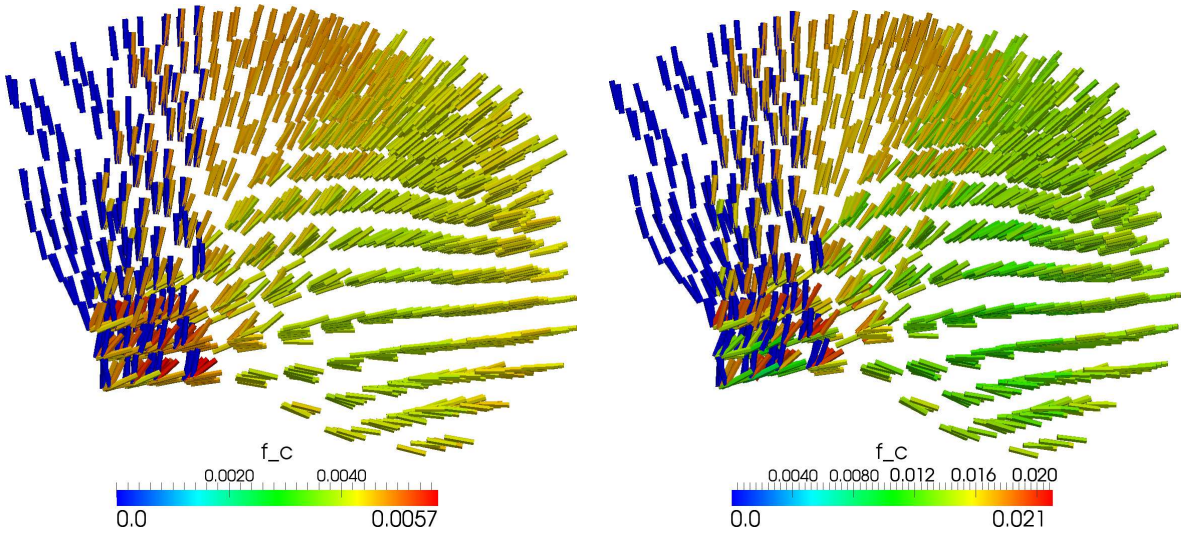

(a) Upright orientation **(b)** Supine orientation

Figure 13.6: Non-uniform local fibre contractile function values (equation 6.11) shown for the GG (sagittal view) at $p_{\text{epi}} = -500$Pa. Independent of gravitational orientation, muscle fibres at the central portions of the GGm and GGp are less effective force generators than those located at the tongue surface or near the mandible. The GGa has a relatively low activity in comparison to the GGm and GGp.

However, as shown in figure 13.7, it is the core of GG in which the greatest contractile stresses are generated. Even though figure 13.6 suggests that the contractile elements function more effectively near the surface of the tongue, the volume fraction of fibres is lower here than in the central region. The constraint of the mandible results in the generation of large hydrostatic stresses at root of GG. Overall, the stresses generated at peak inhalation pressure in the supine orientation are approximately triple in magnitude than those generated in the upright position at peak negative airway pressure, and the contractile stresses produced in the GG double.

As depicted in figure 13.8, the result of the greater contractile stresses is that the central volume of the tongue experiences the greatest principal strains. The tissue in the central region of the GGp experiences up to 25% strain due to the action of the GGp, while the tissue near the tongue surface tends to deflect with little resulting strain. The large strains measured at the mandible and hyoid-tongue interface are due to a combination of the restriction of movement in this region and computational error resulting from the coarse approximation of the solution in this region.

For the sake of completeness, figure 13.9 is presented to illustrate the muscle response under the approximated loading conditions that represent nasal respiration in the supine position. When compared to figure 13.5b, it is clear that the pressure loads are such that the muscle input necessary to balance them is much less than that for oral respiration. These results are consistent with those detailed in section 11.2.2 and those

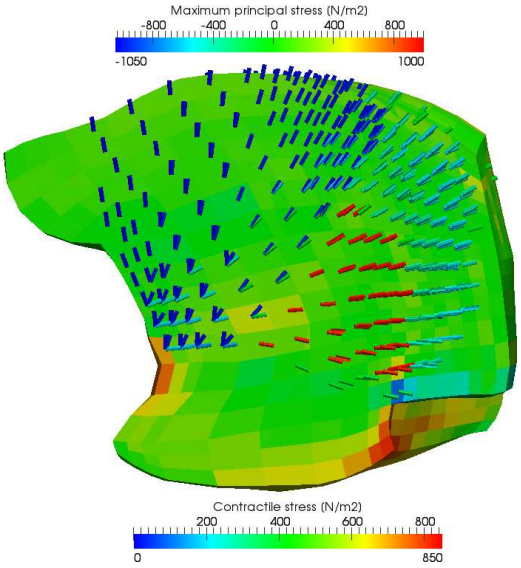

(a) Upright orientation, $p_{\text{epi}} = 0\text{Pa}$

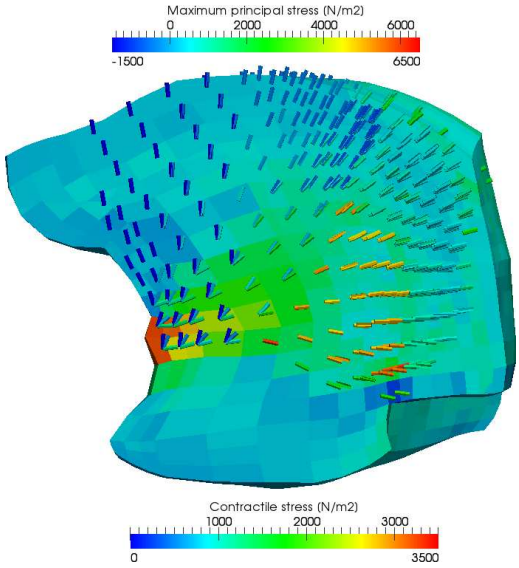

(b) Upright orientation, $p_{\text{epi}} = -500\text{Pa}$

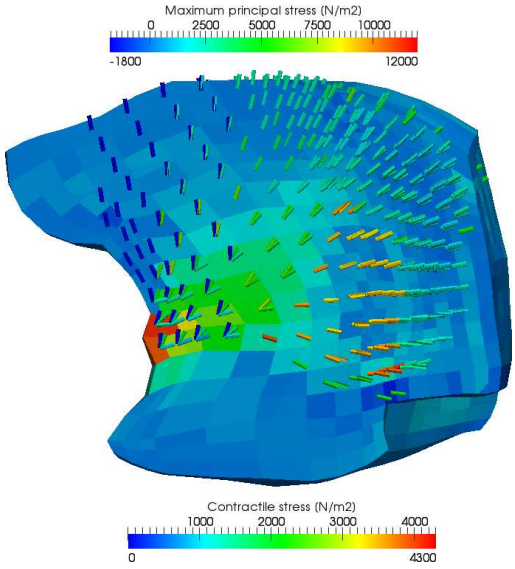

(c) Supine orientation, $p_{\text{epi}} = 0\text{Pa}$

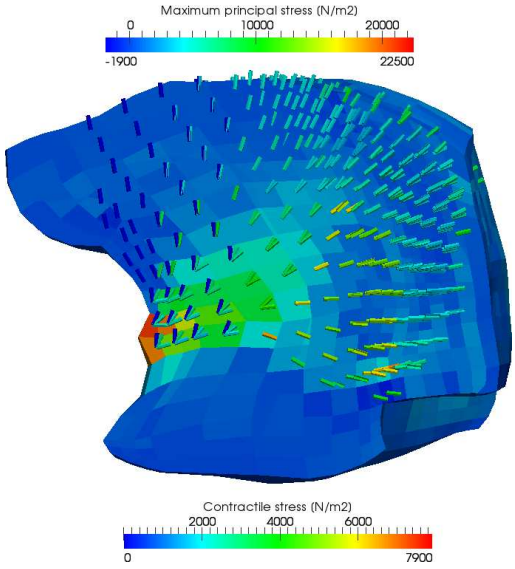

(d) Supine orientation, $p_{\text{epi}} = -500\text{Pa}$

Figure 13.7: Element-average maximum principal stress depicted on the midsagittal plane of the tongue. Stresses are induced in the tongue due to gravitational and pressure forces (oral inhalation), as well as muscle activation. They are concentrated at the the mandible where movement of the muscle tissue is most restricted, as well as in the central volume where the contractile stresses generated by the GG is greatest.

observed in figure 13.3. However, in the upright case (not shown), both the gravitational and pressure forces are very low in magnitude and therefore the muscles require negligible activation for position control. This differs to the response for the pressure distribution obtained from CFD analysis, which exhibited a measurable response in the GGm and GGp.

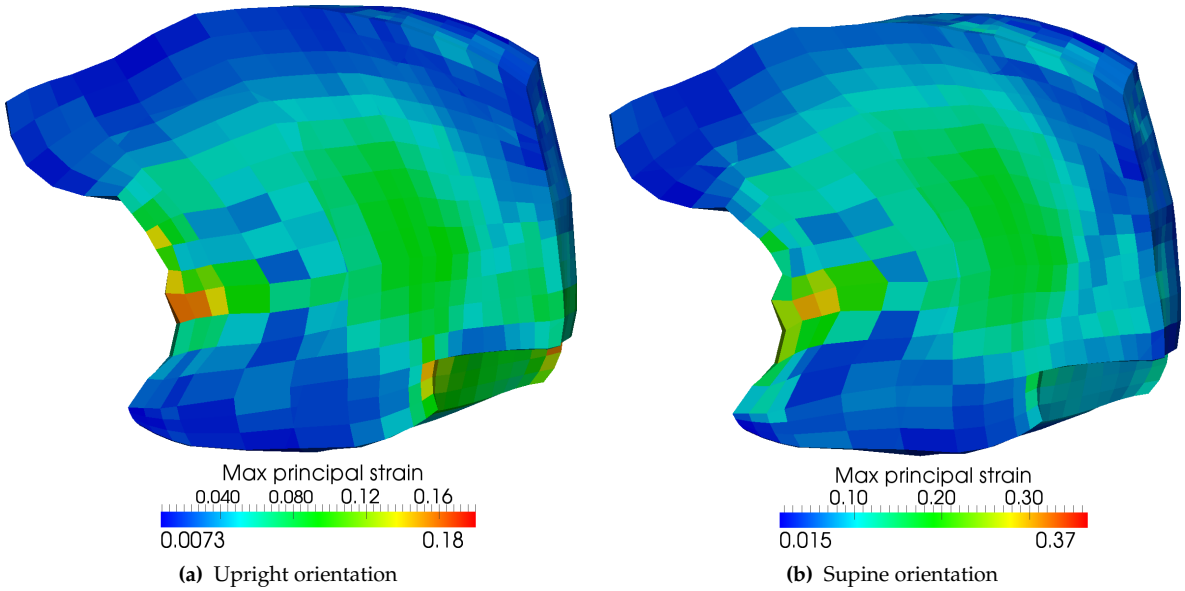

(a) Upright orientation **(b)** Supine orientation

Figure 13.8: Element-average maximum principal strain depicted on the midsagittal plane of the tongue at $p_{\text{epi}} = -500\text{Pa}$. Strains are greatest in the central volume of the tongue where the compliant tissue deforms readily due to the generation of large contractile forces in the GG.

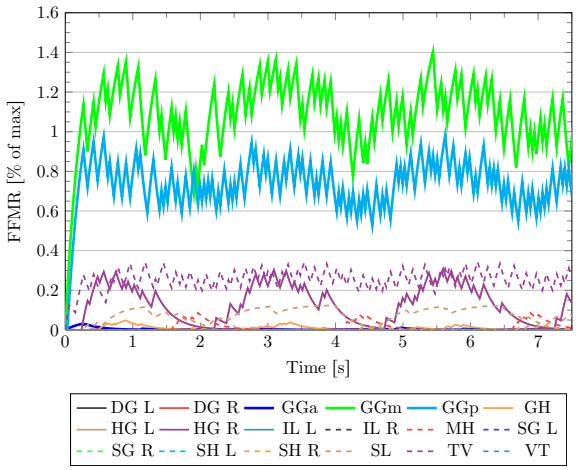

Figure 13.9: Predicted muscle response to changing airway pressure during nasal respiration in the supine orientation using optimised neural model.

13.2.1 Analytical model of dynamic muscle response

For each muscle M, we present an approximate analytical model of the muscle response which incorporates the environmental influences that have been shown to significantly influence their behaviour. To achieve this, a trial function FFMR* is defined for the physical parameters present at time t. The resulting FFMR value is chosen to remain within physical limits

$$\begin{aligned} \text{FFMR} &= \max\left[0, \text{FFMR}^*\right] \quad \text{with} \\ \text{FFMR}^*\left(p, \dot{p}, \gamma, T\right) &:= \varepsilon_{MR}\left[\text{FFMR}_{\text{ave}}\left(p, \gamma, T\right) + \text{FFMR}_{\text{hyst}}\left(\dot{p}, \gamma, T\right)\right] \quad . \end{aligned} \tag{13.2}$$

It is assumed that the response can be decomposed into a rate-independent mean component and a hysteresis component that incorporates the rate-effects of loading. The former term would represent the limiting value if the time taken to attain the specified epiglottal pressure was infinitely long. The parameter ε_{MR} was introduced as a mechanism to modify the ideal response, allowing the simulation of reduced muscle activation during the sleep state.

To motivate the description of these two functions, consider figure 13.10 which presents data for the GGm captured in one load cycle for two different gravitational configurations.

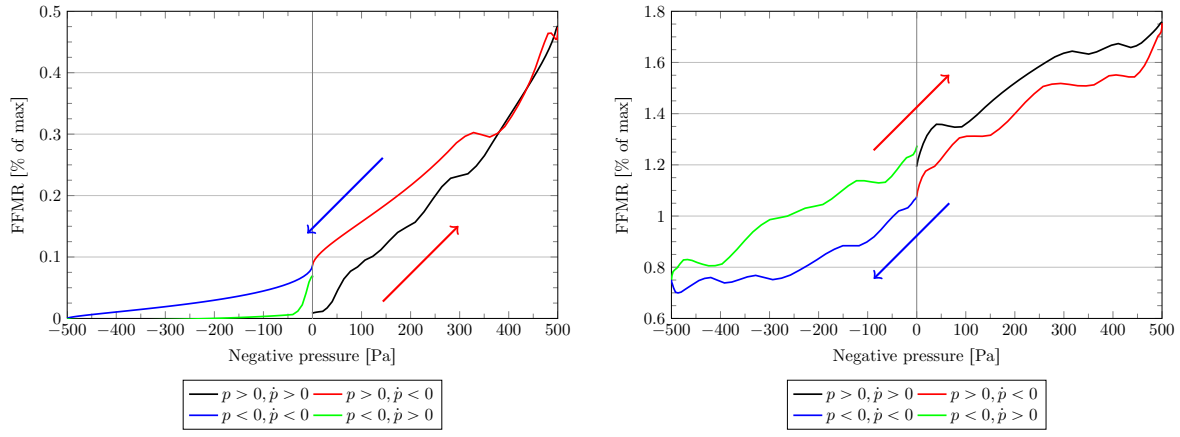

(a) Upright orientation

(b) Supine orientation

Figure 13.10: Raw FFMR data extracted for a single breathing cycle for the GGm. The response has been decomposed into the four distinct components of the breathing cycle, where the pressure and pressure-rates change signs. The arrows indicate the path of changing contraction intensity during inhalation (red) and exhalation (blue).

From the figures (and results not presented here), we observe the following:

- The muscle response is nonlinear with respect to pressure; however, a component of this nonlinearity may be due to rate-effects. A consideration of additional results leads to the conclusion that the response is also nonlinear with respect to inclination angle.
- There exists a different response during inhalation and exhalation. This is further affected by the gravitational orientation.
- The response exhibits a hysteresis effect during loading and unloading. In some muscles, this hysteresis is significant (for example, the peak difference in FFMR at a specified pressure was measured at 22% of the response range in figure 13.10b).
- In general, the cyclic behaviour of the hysteresis response is clockwise, with the measured FFMR greater when the negative pressure rate is positive (i.e. epiglottal pressure is decreasing) than when it is negative. This is due to the force-velocity relationship of active muscular tissue: During muscle relaxation (experienced when $\dot{p} < 0$ for the GG), the contractile element extends while the opposite occurs during active contraction. For a fixed CE length and α, the f_c^V relationship dictates that the generated contractile force is significantly greater during elongation than contraction. Therefore, the FFMR can be reduced during relaxation, with the result that the muscle generates the same overall contractile force

as required during a period of active contraction. The change in directionality observed in figure 13.10a may be non-physical and attributed to the choice of τ_F. This is supported by the observation that the GG activation does not decrease to zero when the load is removed.

The contraction-relaxation effect on the force-velocity relationship captured in the Hill-model is depicted for the GG in figure 13.11. Here it is observed that the fibres that are undergoing extension have a higher f_c^V value than those actively contracting. In this state, the muscle is a more efficient force-generator due to various physiological reasons discussed in section 2.5.2.3. Therefore, the required level of activation (or, in this case, the FFMR) to overcome a set load is less during muscle relaxation (i.e. when the load is decreasing).

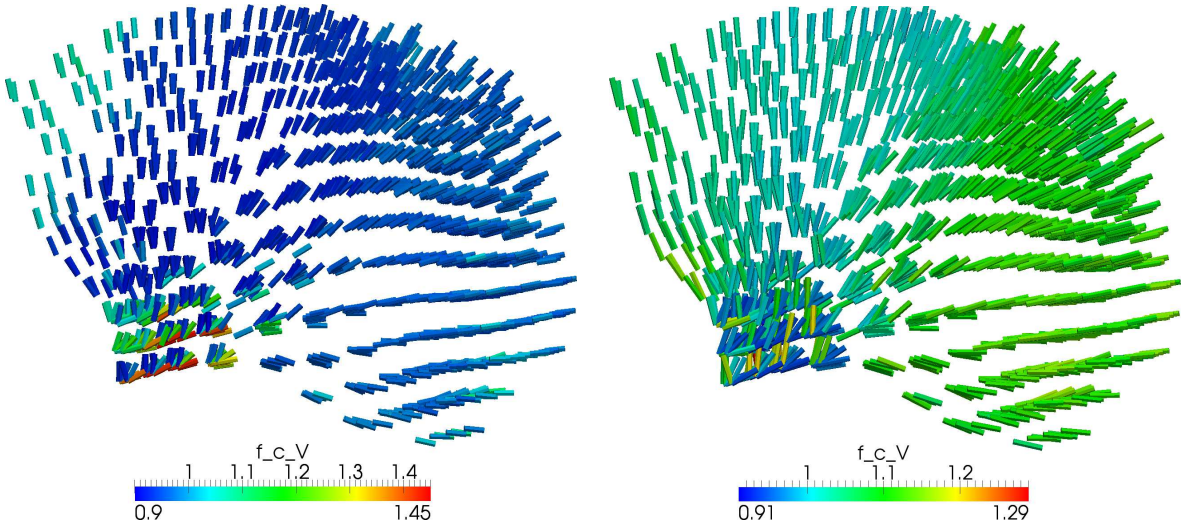

(a) GG is contracting when the negative airway pressure is increasing ($\dot{p} > 0$).

(b) GG is relaxing when the negative airway pressure is decreasing ($\dot{p} < 0$).

Figure 13.11: Force-velocity function values (equation 6.13) in the Hill-element of fibres of the GG during inhalation and exhalation. The airway pressure is fixed at at $p_{\text{epi}} = -250\text{Pa}$ in both cases, but the pressure rates differ in sign.

Following from the linear functions presented in equations 10.1 and 13.1, we define a polynomial function to describe the relationship between the mean response of each muscle group and the negative epiglottal pressure p as

$$\text{FFMR}_{\text{ave}}\left(p,\gamma,T\right) := \underbrace{\left(c_0 + c_1\gamma + c_2\gamma^{p_0}\right)}_{\text{Gravity shift}} + \underbrace{\left(m_0 + m_1 p + m_2\gamma + m_3\gamma p + m_4\gamma T^{-1}\right)p}_{\text{Average value}} \quad . \tag{13.3}$$

This function is applied separately to the positive and negative pressure regimes, with different coefficients determined for each region of the applied pressure spectrum. The first set of terms shift the zero-pressure FFMR value according to the angle of incline. The second set of terms defines the gradient of the $p-\text{FFMR}$ relationship. In contrast to equation 10.1, this term is quadratic in p and linear in γ. The necessity for higher-order pressure terms can be inferred by observing in figure 13.10 that the gradient of the response is not equal at $p = \{p_{\text{min}}, 0, p_{\text{max}}\}$, where the effects of change in pressure rates have been negated. Furthermore, the stiffness of the response is heavily influenced by the reclination angle[4]. A slight overall stiffening in the

[4] Overall, only three parameters define the response in the upright position when $\gamma = 0$. The other parameters are used to modify this curve to produce the desired response in other gravitational configurations.

average response for various cycle periods T was observed and accounted for[5].

To supplement equation 13.3, a model to capture the rate-induced hysteresis has been produced. As a function of the angle of incline and rate-of-change of negative epiglottal pressure, equation 13.4 is used to produce a perturbation from the rate-independent response that is noticeable in figure 13.10b. As there is no hysteresis demonstrated in quasi-static cases, the function vanishes when the pressure-rate is zero. In turn, this forces the magnitude of the perturbation at $p = \{p_{\text{min}}, 0, p_{\text{max}}\}$ to be zero, as these are stationary points in the assumed pressure loading path[6]. The function, defined by

$$\text{FFMR}_{\text{hyst}}\left(\dot{p}, \gamma, T\right) := \underbrace{\left(b_0 + b_1\gamma + b_2\gamma^2\right)}_{\text{Gravity factor}} \underbrace{\left(n_0 + n_1\dot{p} + n_2\gamma + n_3\gamma\dot{p}\right) T^{0.75}\dot{p}}_{\text{Hysteresis}} \tag{13.4}$$

is quadratic in pressure-rate and cubic with respect to the angle cosine. The terms in the first bracket are primarily utilised to change the direction of the hysteresis from clockwise to anti-clockwise dependent under specific gravitation orientations. The second term produces the majority of the perturbation, observed to be greatest in the supine orientation and at high pressure-rates. The magnitude of the hysteresis also appeared to be greater at lower cycle frequencies. As with the pressure-dependent function, this function also has two separate sets of coefficients valid for the two pressure regimes are determined. It is assumed that with a decrease in the FFMR-pressure gradient, there exists a proportionate reduction in the response hysteresis.

With reference to the discussion in section 2.6, there are two different mechanisms leading to muscle atonia during sleep, and their method of incorporation into the model is accounted for in the following paragraphs. Firstly we define the general factor used to reduce the muscle activity as

$$\varepsilon_{MR} = 1 - \frac{R}{100} \tag{13.5}$$

where R represents a percentage reduction in the muscle response to the pressure load. This deactivation function, chosen *a priori* to simulate in particular the response of the airway dilators during sleep or the onset of OSA [308, 231], assumes that the muscles of the tongue no longer continue to respond ideally to the gravitational nor pressure forces. This definition is aligned with the sleep response described in [111, fig. 4], where both the zero and non-zero muscle activities are less than those used when awake. According to [111, 113, 73], a reduction in tonic and phasic muscle activity in the range of 15%-30% has been measured during sleep.

The second mechanism captured is that the maximum rate-independent FFMR may be limited for certain muscles. This is described through the prescription of the additional constraint

$$\text{FFMR}_{\text{ave}} = \min\left[\text{FFMR}_{\text{ave}}\left(p\right), \text{FFMR}_{\text{ave}}\left(p_{\text{thr}}\right)\right] \quad . \tag{13.6}$$

This effectively restricts the degree of muscle contraction developed at low airway pressures, which mimics to the response depicted by [111], with the baseline threshold negative epiglottal pressure chosen as $p_{\text{thr}} = 450\text{Pa}$. Beyond this threshold, these muscles are assumed no longer to respond to the falling airway pressure (and thus produces a loss of reflexive response) and, in order to ensure a smooth contractile response, only rate-based effects will result in a change in their FFMR.

5 Although derived from a measurable quantity, this term cannot be further motivated as the frequency of the load cycle (if it is at all periodic) cannot be known *a priori*.

6 Using t*, the fraction of the cycle period that has elapsed, it is possible to artificially incorporate zero-pressure hysteresis into the model. This, however, voids the assertion that all significant contributors to the response should relate to physical parameters and that quasi-static loading should result in the average value being obtained.

Tables 13.2 and 13.3 list the coefficients determined for the most significant muscle groups that were active during simulations. Evolutionary algorithms [318] were utilised to solve for the coefficients of the GGm, GGp and TV using only data obtained for nominal inhalation pressures of 500Pa. The resulting predictive functions reproduce the behaviour to a moderate-to-high degree of accuracy[7]. These coefficients have also been validated by checking their functionality outside the tested range of p and $\dot{p}$, with physically plausible results still obtained at $p_{\text{nom}} = 1000$Pa and double the pressure-rate serving as verification that the analytical model with the fitted parameters functions sufficiently well for a spectrum of loading conditions. Figure 13.12 demonstrates the overall accuracy of the analytical model in capturing the gross and rate-dependent behaviour of the response of the most active GG components.

Table 13.2: Analytical model of tongue muscle control during transient oral respiration: Coefficients for FFMR_{ave}.

		Gravity shift				Average value				
Muscle	Coefficient	c_0	c_1	c_2	p_0	m_0	m_1	m_2	m_3	m_4
	Scale	10^{-3}	10^{-3}	10^{-3}	1	10^{-6}	10^{-9}	10^{-6}	10^{-9}	10^{-6}
GGm	$p \geqslant 0$	0.5	5	6.5	4.25	5.5	5	5.5	-6	2
	$p < 0$					2.5	1.5	12	4	-2
GGp	$p \geqslant 0$	0.5	9.5	-2	2	6	5	13	-10.5	2
	$p < 0$					3	1.5	16	8	-2
TV	$p \geqslant 0$	0.3	4	-1.4	2	2	1.25	2	-3	1.5
	$p < 0$					1.25	0.5	3.25	1.75	0.001
SL	$p \geqslant 0$	1	1.1	-0.35	2	-0.01	-0.25	1.5	-0.25	0.5
	$p < 0$					-2.3	0.2	4	0	0.25
HG	$p \geqslant 0$	0.3	-0.1	1.2	12	-0.6	0	0.55	0	0
	$p < 0$					-2.5	0	2.5	0	0
MH	$p \geqslant 0$	0.4	1.85	-2.5	3	-0.35	0	-0.35	0	0
	$p < 0$					-0.25	0	-0.25	0	0
SG	$p \geqslant 0$	0.3	-0.2	-0.15	2	-0.6	0	0.6	0	0
	$p < 0$					-4	0	4.5	0	0

However. it was determined that the model requires additional coefficients to fully realise the response of the SL, HG, MH and SG. The manually determined coefficients presented for these muscles represents only an approximation that captures their gross response. Furthermore, the zero-pressure hysteresis for the SL was large enough to diminish the accuracy of the model significantly, but no physically motivated terms can be introduced to the model to account for this. In most instances, the magnitude of their contraction is significantly lower than that produced by the GG constituents so it is assumed the error in the model will not produce significant deviations from the scenarios from which coefficients were determined.

Figures 13.13 to 13.15 present the response for each of the specified muscle groups for a range of inclinations and a cycle period of 2.5s. With reference to the experimental works of Remmers et al. [231], Malhotra et al.

[7] In this instance, the statistical significance of the analytical model was analysed through the calculation of the coefficient of determination. Observation in the data trends, coupled with the computation of the statistical significance of the analytical models, truly motivated the requirement to capture the hysteresis effects, as the average value model alone produced sub-standard results on its own for certain muscle groups. The addition of $\text{FFMR}_{\text{hyst}}$ increased the minimum coefficient of determination from $R^2 = 0.89$ to $R^2 = 0.94$ for the GGm, $R^2 = 0.90$ to $R^2 = 0.94$ for the GGp. An average value of $R^2 = 0.94$ was obtained for the TV and a poor $R^2 = 0.68$ for the SL for which the result trends are not resolved in full.

Table 13.3: Analytical model of tongue muscle control during transient oral respiration: Coefficients for $FFMR_{hyst}$.

		Gravity factor			Hysteresis			
Muscle	Coefficient	b_0	b_1	b_2	n_0	n_1	n_2	n_3
	Scale	1	1	1	10^{-9}	10^{-12}	10^{-9}	10^{-12}
GGm	$p \geqslant 0$	-1	5.33	-3.33	125	10	150	25
	$p < 0$				125	-10	125	-25
GGp	$p \geqslant 0$	-1	5.33	-3.33	125	10	150	25
	$p < 0$				125	-10	125	-25
SL	$p \geqslant 0$	1	0	0	-150	7.5	75	2.5
	$p < 0$				-75	-1	-25	-2.5

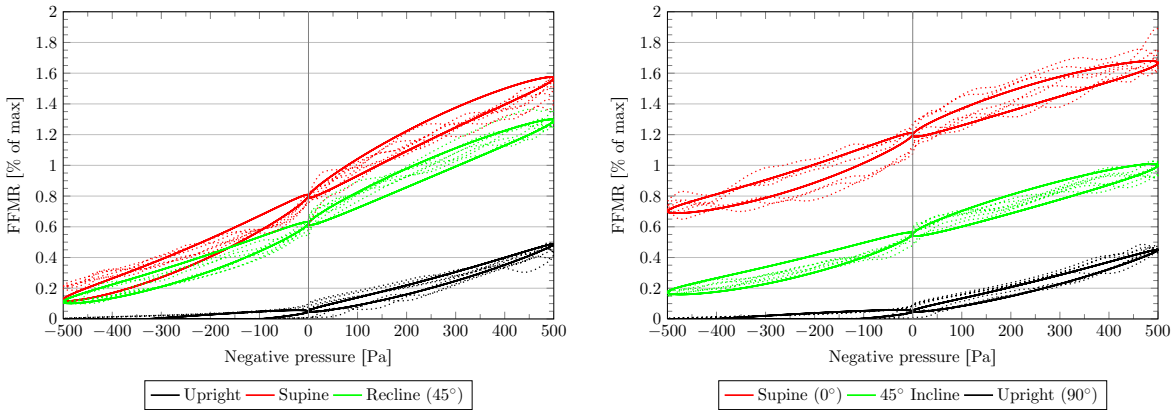

(a) GGp **(b)** GGm

Figure 13.12: Validation of transient analytical model accuracy for the GG. Overlaid on a weighted average of raw and smoothed FFMR datasets extracted from the neural model is the solid lines which indicate the response predicted by the analytical model. It is important to note that the directionality of the hysteresis, not shown in this picture, is also successfully captured by the model.

[167] and Akahoshi et al. [3] (an extract of which is shown in figure 2.17), and the model of Huang et al. [111] depicted in figure 2.18, the neural and analytical models capture the response of the GG very well, with the trends indicated by both sources being mimicked in the response illustrated in figure 13.13. The most obvious correlation between this data and that obtained experimentally is that the activity of the GGm and the GGp increases significantly as the airway pressure drops. Furthermore, the zero-pressure activity in the supine state is non-zero in the experimental and this computationally derived data. The clockwise hysteresis observed in the predicted response of the neural model at negative airway pressures has been observed in the experimental analysis of Akahoshi et al. [3] (and is most prevalent shown in [3, fig. 5b]) and [231, fig. 8]. Furthermore, this data and the wakeful-state model used by Huang et al. [111] depict a reduction in the gradient of the response at greater negative airway pressures. This trend has also been captured in the model at high angles of reclination, which corresponds to the conditions under which the data was collected by Akahoshi et al. [3].

The poor correlation between the magnitude of the FFMR values and EMG values presented in the literature

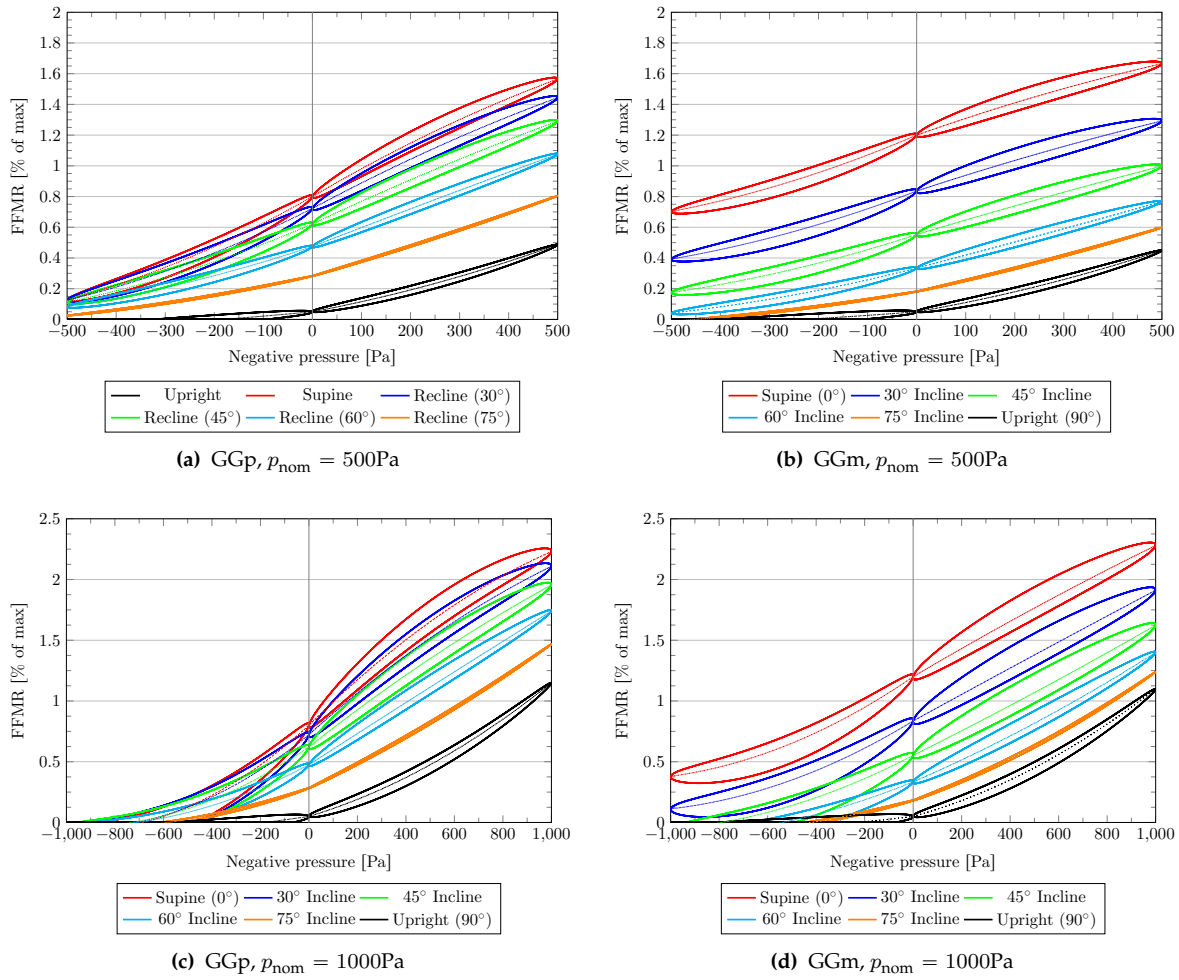

(a) GGp, $p_{\text{nom}} = 500$Pa **(b)** GGm, $p_{\text{nom}} = 500$Pa

(c) GGp, $p_{\text{nom}} = 1000$Pa **(d)** GGm, $p_{\text{nom}} = 1000$Pa

Figure 13.13: Response of the GG constituents as predicted by the analytical model for oral breathing. The thick solid lines indicate the overall response, while the rate-independent value produced from equation 13.3 is drawn as a thin line. Note that at an inclination of 75°, the hysteresis contribution is practically zero. This was also observed in the data obtained in the simulations and is near the inclination at which the response loop changes from clockwise to anti-clockwise.

[165, 261, 221] can be attributed to the choice of material parameters for the muscle model (specifically $T_0^{\max}$, but also variations of material constitution amongst individuals), the modelled physical conditions and the interpretation of the EMG scale itself. However, that the trends have been captured extends confidence that the model approximates the function of the GG for the case of oral breathing.

From a comparison between figure 13.14a and figure 13.13c it is deduced that the TV and GGp activity are closely linked. Although the GGm and GGp both result in lateral expansion of the tongue, the TV has a larger proportion of its volume distributed in regions of the GGp than the GGm and is therefore better suited to oppose the motion caused by the GGp than the GGm. Negligible hysteresis was predicted by the neural model, and thus was not accounted in the analytical model.

The response of the SL varied greatly with the environmental conditions. As illustrated in figure 13.14, the gravitational orientation dictated whether this muscle is most critical during inhalation or exhalation. Considering the extreme cases, it can be determined why the SL is needed to prevent the deflection of the

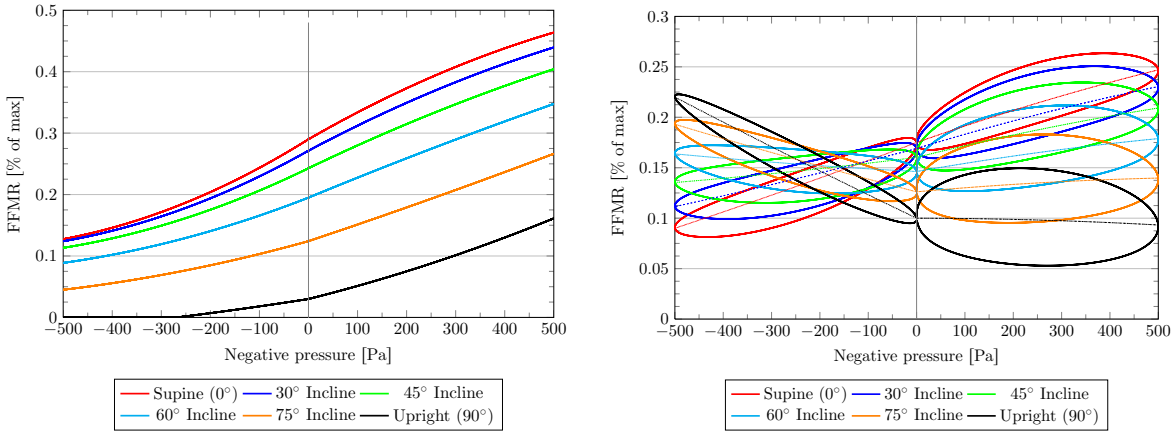

(a) TV **(b)** SL

Figure 13.14: Response of the TV and SL, both located near the superior surface of the tongue, as predicted by the analytical model for oral breathing.

tongue tip towards the mandible. The SL is most active during inhalation in the supine condition as then the GG contracts strongly. However, in the upright condition it is required to contract during exhalation when the loading forces act to produce a similar effect. The zero-pressure hysteresis associated with the SL was very large and not accounted for, leading to the poor correlation mentioned in footnote 7 on page 205.

Figure 13.15 illustrates the activity in the HG, MH and SG. The general trend for these muscles is that they are required to produce a greater contractile force during exhalation than inhalation. When a positive pressure is produced in the airway, the load is such that the tongue is pushed anteriorly. The SG is used to prevent this, but also leads to a resulting upwards force on the rear surface of the tongue. The action of the HG is therefore necessary to prevent lifting of the tongue posterior. The MH further assists in moderating the amount of lift on the tongue body. A further point to note is that the response of the HG and MH has a more complex relationship with the gravitational orientation than observed in other muscles. The MH shows most activity at 60° above the horizontal, while the HG demonstrates a very different response below 45°. This could be attributed to the energy-minimisation requirement (see section 7.3.2) and the interaction between these muscles and other muscle groups not detailed here.

With regard to the frequency of inspiration, figure 13.16 illustrates the stiffening of the GG response as the period of the breathing cycle is reduced. The phenomenon appears relatively minor, but capturing its effect for all postures improved the statistical accuracy of the model considerably.

13.3 Dynamic vs quasi-static analysis: The role of load history and the rate-dependence of muscular tissue

It has been demonstrated that it is possible to gain insight into the functioning and response of the tongue using two techniques, both of which have certain advantages and disadvantages in terms of simplicity and computational expense. A choice must now be made as to which methodology will be utilised to simulate the state of sleep. To do so, a comparison between results attained by the two methods is first made and an analysis of the conclusions that can be drawn from them is presented.

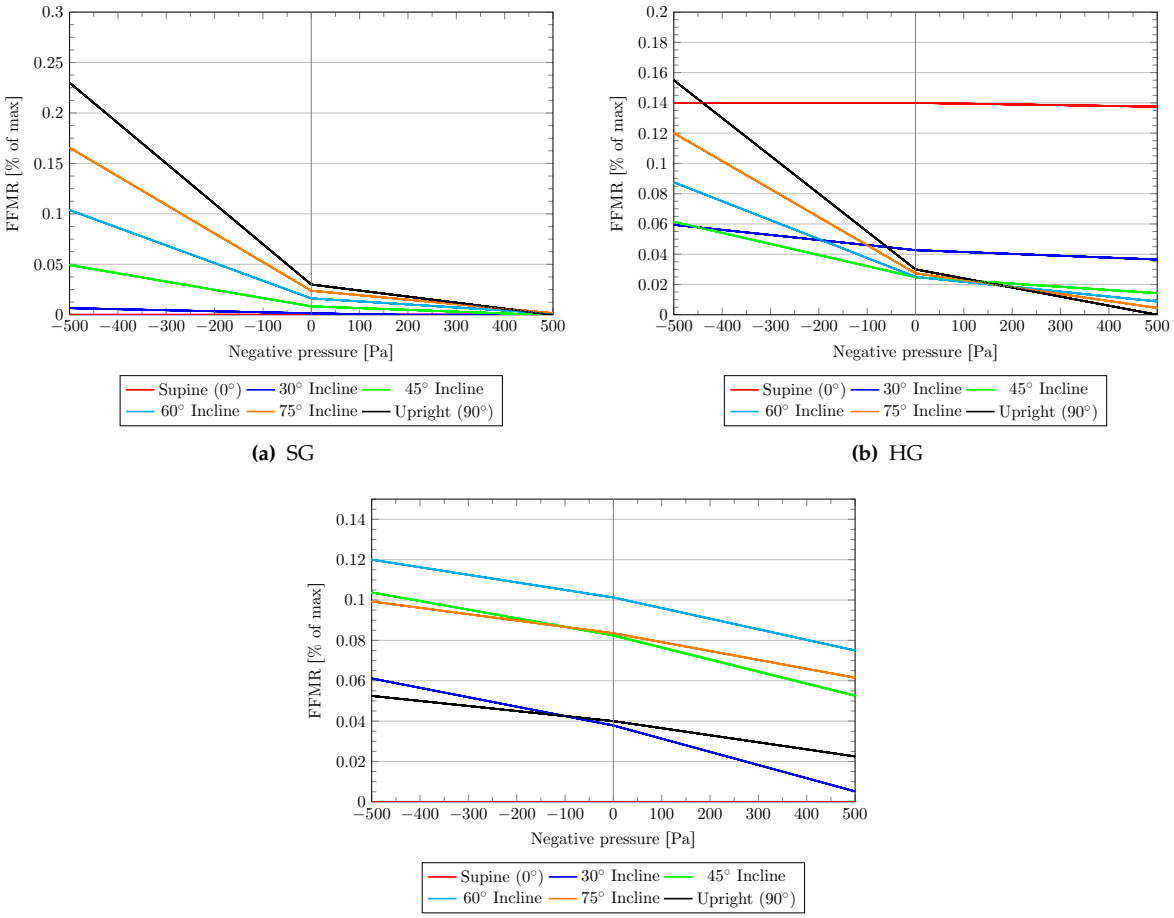

(a) SG

(b) HG

(c) MH

Figure 13.15: Response of the SG, HG and MH as predicted by the analytical model for oral breathing.

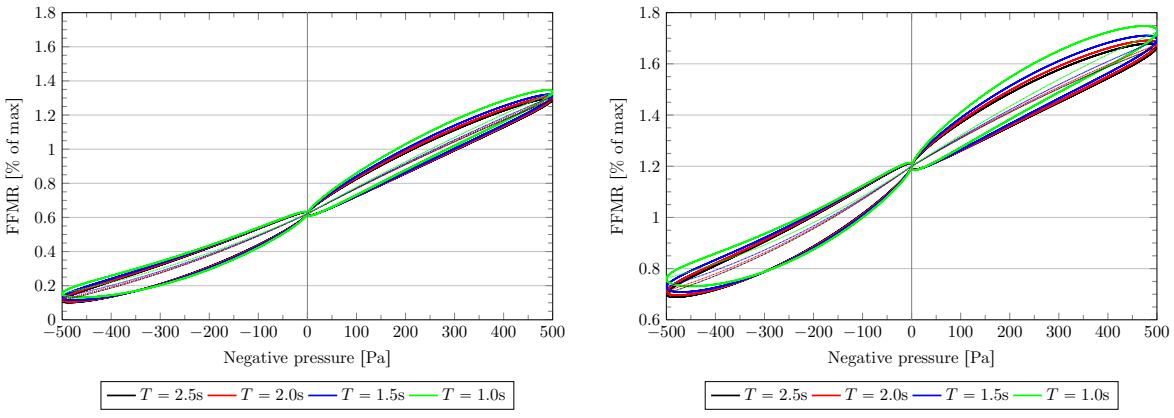

(a) GGp

(b) GGm

Figure 13.16: Change in activity of the GG in the supine orientation due to reduced breathing cycle period.

Firstly, a reminder of the fundamental differences in the simulation philosophies: the time-dependent load has been a simplified and assumed field, while the static-load is determined from the final pressure field extracted from the CFD data. The muscle and neural models, both of which have been developed for dynamic situations, have been applied directly to the quasi-static case with only the removal of the rate-dependent

response of the muscle. To arrive at a decision, the collective effect of the boundary conditions and control algorithm result must be considered.

In section 13.1 and section 13.2, it has been shown that the neural model produces comparable results between the two methodologies. This is a surprising result, given the significantly different passive tongue movement due to the ideal and CFD derived pressure fields. With respect to the functioning of the GGp and GGm in particular, both of which have been demonstrated to be directly affected by posture and play the role of airway dilators, comparison between figure 13.4 and figure 13.13 indicate that qualitatively and quantitatively similar trends are produced. This suggests that the approximated loading distribution used in the dynamic cases is sufficiently accurate to represent mouth and nasal inhalation. It also demonstrates that the neural and muscle models can be used successfully in static analysis.

As was noted in section 13.1, the overall accuracy of the control algorithm (in its current form) is less than desirable while the performance for the dynamic case is adequate. The alternate methodology, with the current representation of the pressure distributions present in the airway, results in an over-prediction of the retroglossal displacement in the passive state. However, the dynamic scenario may provide additional insights in terms of the displacement and muscle contraction histories resulting from the temporally-variable load. The dynamic methodology, using approximate descriptions of the loading conditions, therefore will be utilised in section 13.4 to simulate one possible scenario leading to a loss of upper airway patency.

13.4 Induced retroglossal movement due to idealised dynamic loading during sleep

The analytical model presented in section 13.2.1 has been demonstrated to reproduce a response similar to that predicted by the neurological control model. Through manipulation of this response, it is now possible to predict the outcome of changing both anatomical and environmental conditions in conjunction with a sub-optimal muscle reaction. This allows the simulation of conditions that may lead to sleep disorders. Possible scenarios that could be investigated include

Neurological response: A reduction in the ability of muscles to resist air and gravitational loads. These may be caused by a slow adaptation of activity to rapidly changing environmental conditions, or an innate or developing neuromuscular disability.

Pathophysiological: An increase in adipose tissue content in the muscle requires an adaptation of the muscle response as the material parameters change over time. Suppressed muscle learning may result in insufficient contractile force, namely that required for the "learned" composition of the tongue, being utilised.

To simulate these conditions, a similar problem configuration to that used before was utilised. Using the temporally-dependent model, three full cycles of oral breathing were reproduced. Each cycle of inhalation and exhalation was considered to be 2.5s in length, and the nominal pressure for the period of exhalation was initially fixed at $p_{\text{nom}} = 500$Pa. Other specific changes to each scenario is listed where appropriate.

By modulating the value of ε_{MR} (equation 13.5), simulated depression of tongue muscle response to surrounding air-pressure during sleep can be produced. Furthermore, enforcing the relationship given in equation 13.6 ensures a further limitation of muscle activity at epiglottal pressures of lower than -450Pa. We

restrict the usage of these modifications to the airway dilators, and assume that all other muscles function optimally[8].

In the following results, the anteroposterior position of the rear of the tongue, namely the y-component of the displacement of $\boldsymbol{P}_C$, are measured relative to the solution determined with the optimised response (figures 13.13 to 13.15) as the baseline. This was done as the displacement solution obtained the analytical model as a control mechanism, like that when directly using the GA controlled neural model, is small but non-trivial.

13.4.1 Posture and the depression of genioglossal response to airway pressure

Assuming the worst-case scenario in terms of response depression ε_{MR} which may arise during sleep, figure 13.17 gives an indication to the greatly altered genioglossal response for nominal inhalation pressures near and well over the threshold pressure stated in [111]. Increasing the maximum negative airway pressure from 500Pa to 1000Pa for a fixed inhalation period results in an increase in the amount of hysteresis induced in the muscle response. More pertinent is the activity at pressures lower than the threshold pressure. Although the rate-effects result in a differing response during periods of pressure increase and decrease, the slope of the average response at a set pressure below the threshold value is now zero. Comparison with figure 13.13 demonstrates that the dilators have been severely compromised and that muscle activation is substantially less than that required to sustain position control under airway loads. Furthermore, the zero-pressure response is also reduced, suggesting that movement of the tongue under gravitational loads may be expected.

The two loading cases presented here are interpreted in the following manner: In the first, setting $p_{\text{nom}} = 500$Pa for the inhalation cycle in conjunction with a non-trivial value of ε_{MR} simulates destimulation of components of the GG without sufficient movement to result in a total loss of airway patency. The second scenario, where $p_{\text{nom}} = 1000$Pa for the inhalation cycle, reduced activation is assumed to lead to a partial or total blockage of the retroglossal space or contribute to a loss of patency in the lower pharynx (leading to very low pressures). This could be related to the increased adipose deposits in, or movement of, the retroglossal and pharyngeal tissues, resulting in a decreased normal pharyngeal CSA.

The anteroposterior position of the rear of the tongue which changes due to partial deactivation of the genioglossus is shown in figures 13.18 and 13.19. For the two pressure cases, the result of sub-optimal response of the GGp and GGm, and the GGp alone are evaluated. The latter case was tested as the GGp has been previously shown to be primarily responsible for the control of the anteroposterior position of $\boldsymbol{P}_C$.

The first case to be evaluated is that when the maximal negative airway pressure approaches and only slightly exceeds the threshold pressure. As shown in figure 13.18, a change in posture and lowering of the airway pressure resulted in a rearward movement of the tongue. Significant motion solely due to the influence of body forces is predicted in the supine orientation, especially when both GG components are understimulated. In all cases, loss of the effective functioning of both the GGm and GGp results in much larger motions than the GGp alone. In the supine case, at maximal applied pressure an extra 1mm rearward movement can be attributed to the loss of control of the GGm.

A decreasing angle of incline resulted in greater displacements due to the increased posterior component of

[8] Up to this point, no mention of sleep-induced atonia in the other muscles of the tongue had been found in the literature.

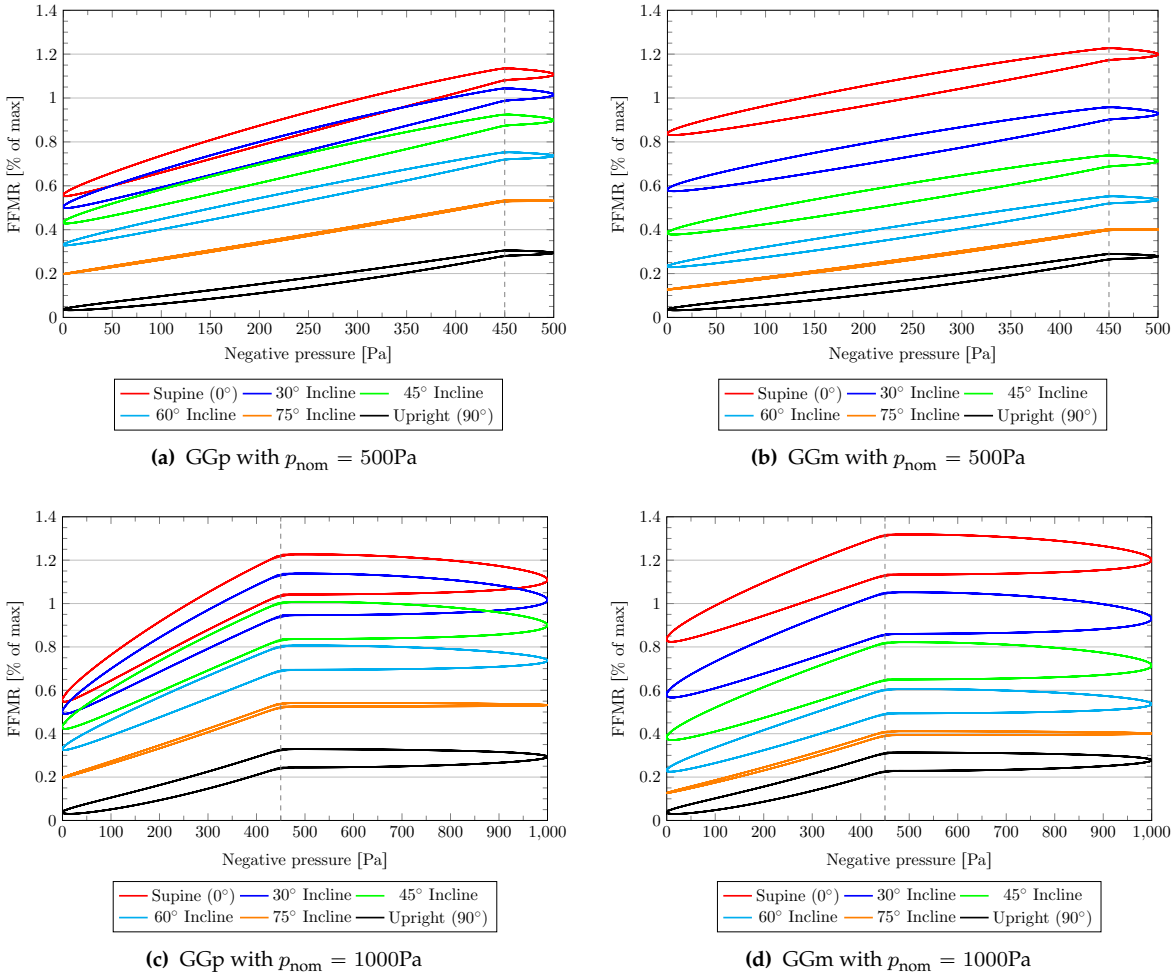

(a) GGp with $p_{\text{nom}} = 500$Pa

(b) GGm with $p_{\text{nom}} = 500$Pa

(c) GGp with $p_{\text{nom}} = 1000$Pa

(d) GGm with $p_{\text{nom}} = 1000$Pa

Figure 13.17: FFMR for muscles experiencing atonia and loss of reflexive action of the lowing air-pressure In each case, 30% atonia (deactivation) is achieved by setting $R = 30$ in equation 13.5. The threshold pressure, prescribed as $p_{\text{thr}} = 450$Pa, for limitation of the average muscle response is marked by a dashed line. Comparison of figure 13.17a with figure 13.17c, and figure 13.17b with figure 13.17d, reveals the pressure-rate effects on the prescribed FFMR.

gravitational loading. However, the average gradient of the pressure-displacement curve is greater in magnitude for the upright case than of the supine case. This was due to increased muscle tone and the resulting tissue stiffening that occurs as increased gravitational resistance is required. There exists a noticeable change in displacement gradient for high inclinations once threshold pressure has been exceeded. Conceptually, this may be sufficient enough to induce a marked change in the airway pressure profile and result in a loss a patency.

A number of secondary phenomena also can be noted. Due to the general reduction in tonic activity, the zero-load displacement increases as the orientation moves towards the supine. The displacement hysteresis occurs in clockwise manner indicating that during relaxation movement of the tongue (particularly posterior displacement) increases. This effect is marginal in the supine case, but becomes more significant as the inclination angle increases. Furthermore, for the case of only having GGp atonia, a convergence of displacement histories of $\boldsymbol{P}_C$ occurs at inclinations less than $60°$.

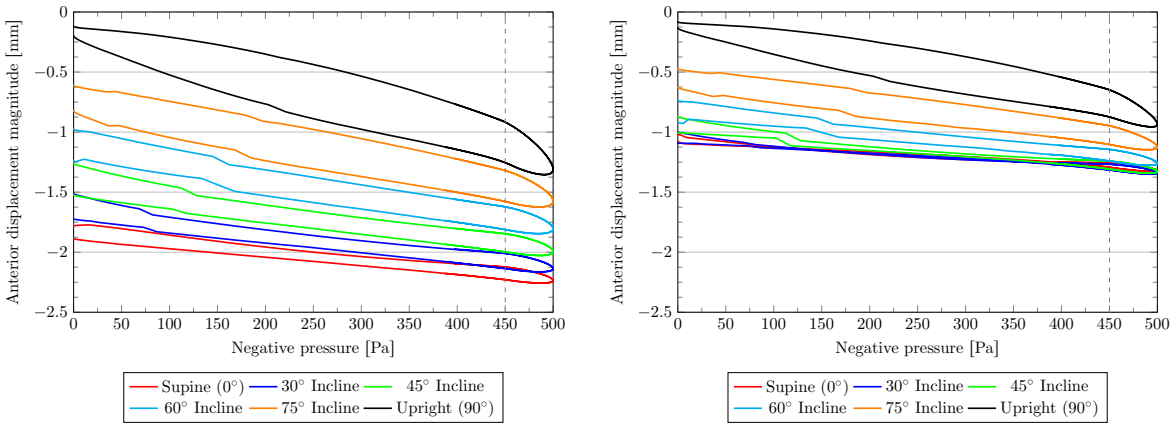

(a) GGp and GGm

(b) GGp only

Figure 13.18: Anterior displacement of point $\boldsymbol{P}_C$ during partial deactivation of GG with changing posture. Minimum epiglottal pressure produced with $p_{\text{nom}} = 500$Pa, while a pressure threshold $p_{\text{thr}} = 450$Pa and 30% atonia ($R = 30$) are assumed. The slight step in the displacement curves at higher pressures is due to the changing number of Uzawa iterations used to enforce incompressibility.

Once the threshold pressure is exceeded, large motions (between $2-3$ times that predicted for a lower nominal pressure) are predicted at maximal load. Figure 13.19 indicates that the predicted tongue movement is dramatically altered by the posture and an increased pressure loading. There exists a significant reduction in position control and resistance to the effects of increased airway loads once threshold pressure is crossed. In all cases, the pressure-displacement slope is altered significantly after this point. The overall result of this motion would be a significant reduction in pharyngeal CSA[9]. Loss of governance of the GGp alone results in a similar behaviour of the tongue, although again the displacements are smaller overall.

Counter-intuitively, increasing the inclination does not necessarily result in an increase in airway patency. Tissue is far more compliant in upright position due to decreased muscle tone, thereby leading to greater displacements under pressure load. Due to the lessened tone, the resulting displacement at maximal load is greater in the upright position than the supine orientation.

The movement recorded during the transition from inhalation to exhalation and *vice versa* is significantly different. Hysteresis effects are large, and natural recovery of airway patency is weakened by the viscoelastic behaviour of the tissue. Interestingly, this leads to the maximum displacement of the tongue occurring at an epiglottal pressure slightly greater than the minimum pressure. Rate-effects persist as the zero-pressure point is reached. There also exists a convergent point at 850Pa where the load-based displacement is identical during the period of pressure drop.

13.4.2 Modulation of pressure threshold governing loss of reflexive muscle response during sleep

The pressure at which a loss of reflexive mechanisms occur is certainly gender specific [111], but also has a wide spectrum of other aetiologies. One can speculate that various factors, such as neurological disorders and

[9] Recall from section 8.8.2 that the anteroposterior diameter of the pharynx is approximately 17mm.

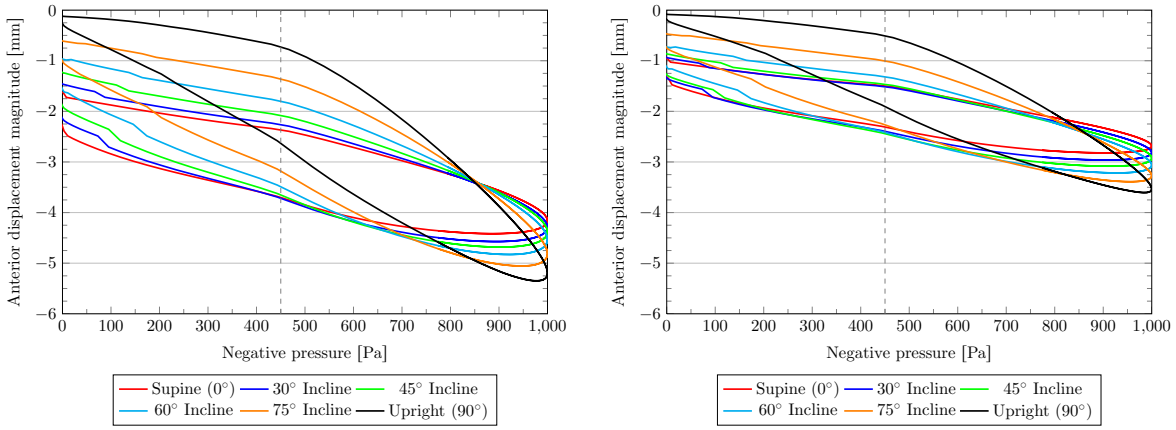

(a) GGp and GGm **(b)** GGp only

Figure 13.19: Anterior displacement of point $\boldsymbol{P}_C$ during partial deactivation of GG with changing posture. Minimum epiglottal pressure produced with $p_{\text{nom}} = 1000\text{Pa}$, while a pressure threshold $p_{\text{thr}} = 450\text{Pa}$ and 30% atonia ($R = 30$) are assumed. The difference in displacement magnitude between the intersection points of a vertical line with the displacement history quantifies the *displacement hysteresis* in the loading cycle at a set pressure.

changing physiology, could contribute to an increase of this threshold value in comparison to that measured in healthy individuals.

In the following scenarios, the baseline value of p_{thr} is increased, with the expected result being that the resistance to movement is also increased. The resulting muscle activity for the primary airway dilators is shown in figure 13.20. As expected, the response of the GG components below $p_{\text{epi}} = -450\text{Pa}$ is identical in all cases, but as the threshold pressure is exceeded the muscle activity levels out. The result is that between the threshold and peak pressure, the amount of contractile force generated within these muscles is severely reduced as the threshold pressure is increased.

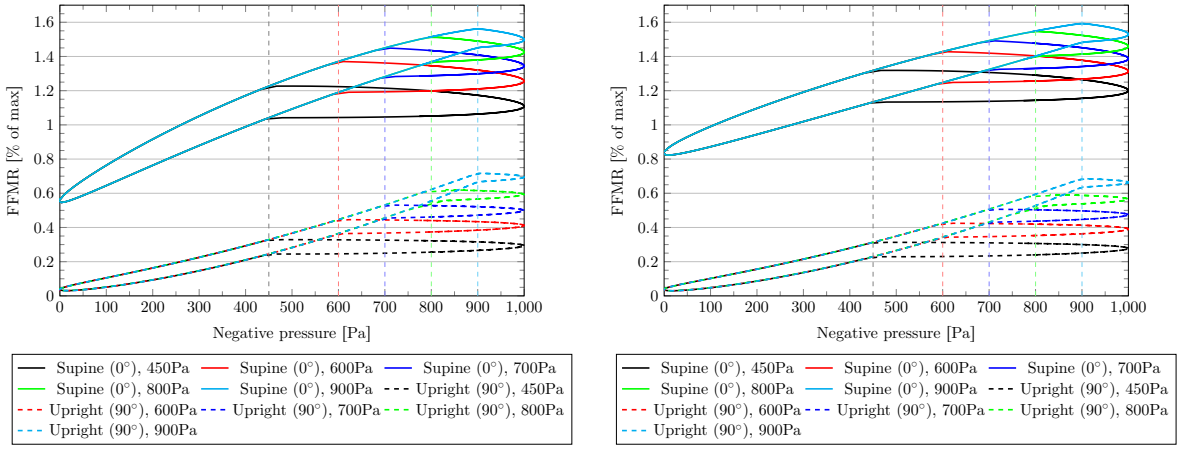

(a) GGp **(b)** GGm

Figure 13.20: FFMR for partially deactivated muscles at varying values for the pressure modulation threshold p_{thr}. Minimum epiglottal pressure produced with $p_{\text{nom}} = 1000\text{Pa}$, while 30% atonia ($R = 30$) is assumed.

As a percentage of the FFMR produced at peak pressure in the wakeful state, this mechanism of muscle deactivation is far more severe when the body is situated in the upright posture than the supine one. Table 13.4 demonstrates that, in the worst-case, a loss of up to 75% of dilator activity may be induced during sleep in the upright posture, while the equivalent case may limited to 50% when the body is in the supine orientation.

Table 13.4: The influence of sleep reflex loss pressure threshold on GG contraction strength. Tabulated is the difference of GG FFMR at peak pressure with respect to that produced during the awake state.

(a) GGp

p_{thr}	**Upright**	**Supine**
450Pa	-74.4%	-50.4%
600Pa	-64.1%	-43.8%
700Pa	-56.5%	-39.8%
800Pa	-48.3%	-36.2%
900Pa	-39.4%	-32.9%

(b) GGm

p_{thr}	**Upright**	**Supine**
450Pa	-74.6%	-47.4%
600Pa	-64.4%	-42.5%
700Pa	-56.7%	-39.3%
800Pa	-48.5%	-36.1%
900Pa	-39.5%	-33.0%

For the upright case it is this effect, coupled with the overall minimal muscle tone used to regulate the tongue position, that results in a large anterior deflection of the tongue once the pressure threshold has been exceeded. Figures 13.21a and 13.21b indicate that in the period of pressure decrease, up to 4.5mm anterior deflection may occur when both dilatory components of the GG are affected. When the GGp alone experiences atonia, the maximal displacement magnitude post-threshold is reduced to 3mm. In each case, the maximal anterior displacement and magnitude of the displacement hysteresis measured during pressure drop and rise is proportional to the threshold pressure. The latter point can be explained by the fact that position recovery during the period of pressure normalisation is severely affected by threshold pressure through both viscoelastic effects and the reduced peak level muscle activity. In summary, the higher the pressure threshold, the greater the length of time for which the tongue experiences large retroglossal deflection.

However, in contrast to this, for the supine posture the effect that the pressure threshold has on the displacement is significantly reduced due to the overall increased muscle tone. The zero-load displacement is greater than that of the upright case as the tonic muscle activity is reduced during the sleep state. As was observed for the upright case, an increase in the pressure threshold does result in a greater anterior deflection of the tongue, and this is exacerbated by the reduction of activity of the GGm in addition to the GGp. This motion is limited to only 2mm after the pressure dropped below the threshold value in the worst case, and when only the GGp experiences atonia this value is only 1.25mm. For p_{thr} between 700Pa and 900Pa, the displacement histories were quite similar in this orientation when compared to that of previous case where measurable differences are visible.

13.4.3 Degree of muscle atonia during sleep

Evaluation of the effect of general atonia of the tongue muscles during inspiration was conducted by altering the value of R in equation 13.5 with p_{thr} remaining at the baseline value. It is indicated in figure 13.22 that the retroglossal movement of the tongue is most significantly influenced as the angle of recline increases.

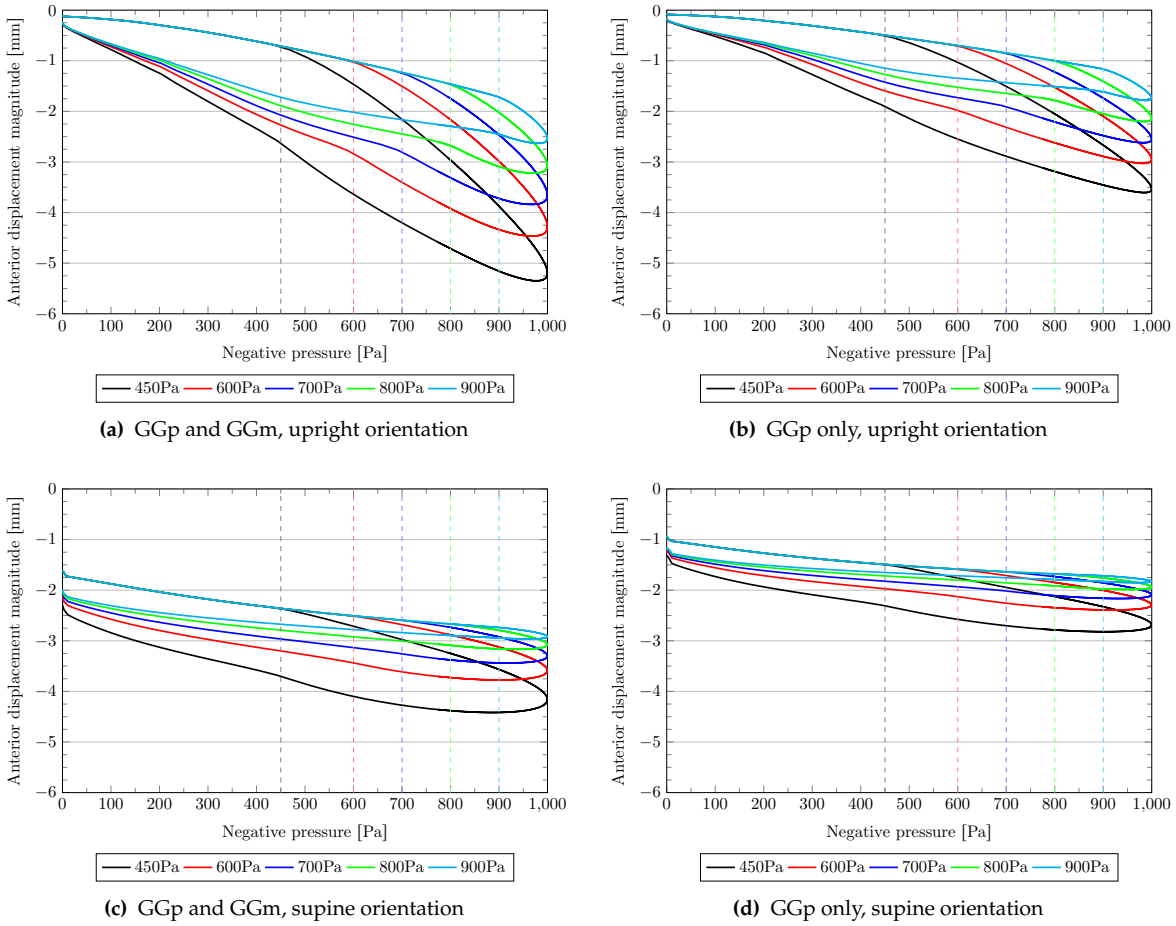

(a) GGp and GGm, upright orientation

(b) GGp only, upright orientation

(c) GGp and GGm, supine orientation

(d) GGp only, supine orientation

Figure 13.21: Anterior displacement of point $\boldsymbol{P}_C$ during partial deactivation of GG due to a changing pressure threshold p_{thr} value. Minimum epiglottal pressure produced with $p_{\text{nom}} = 1000$Pa, while 30% atonia ($R = 30$) is assumed.

In the upright posture, the difference in anteroposterior movement at peak pressure between the extreme cases was 0.75mm when both the GGp and GGm experienced a reduction in muscle activity, while a difference of 0.5mm was measured when the GGp alone functioned suboptimally. It was also observed that throughout the inhalation cycle the anterior motion increased marginally as the value of R increased. This was primarily due to the loss of reflexive mechanisms, but is also partially attributed to the viscoelastic behaviour of the muscles. Regardless of the degree of atonia present in the muscles, once the pressure threshold is exceeded during inhalation, the tongue's position remains severely compromised for the rest of the inhalation cycle.

When there is no air-induced load and the orientation is changed to that of the supine posture, the increased atonia compromises the tongue's ability to resist gravitational forces. When both components of the GG are affected, the zero-load displacement at the start of the inhalation increases by a margin of 1.5mm, while in the second case 0.75mm of initial movement can be attributed to this factor. This leads to a marked difference in the pressure-displacement history and a greatly increased difference in the zero-to-maximum pressure displacement value: 2.25mm and 1.5mm for the two- and one- GG component destimulation cases respectively.

By comparing these two sets of results, eliminating the gravitational effects and ignoring the loss of reflexive muscle tone, it can be concluded that, regardless of orientation, less than 1mm of additional retroglossal

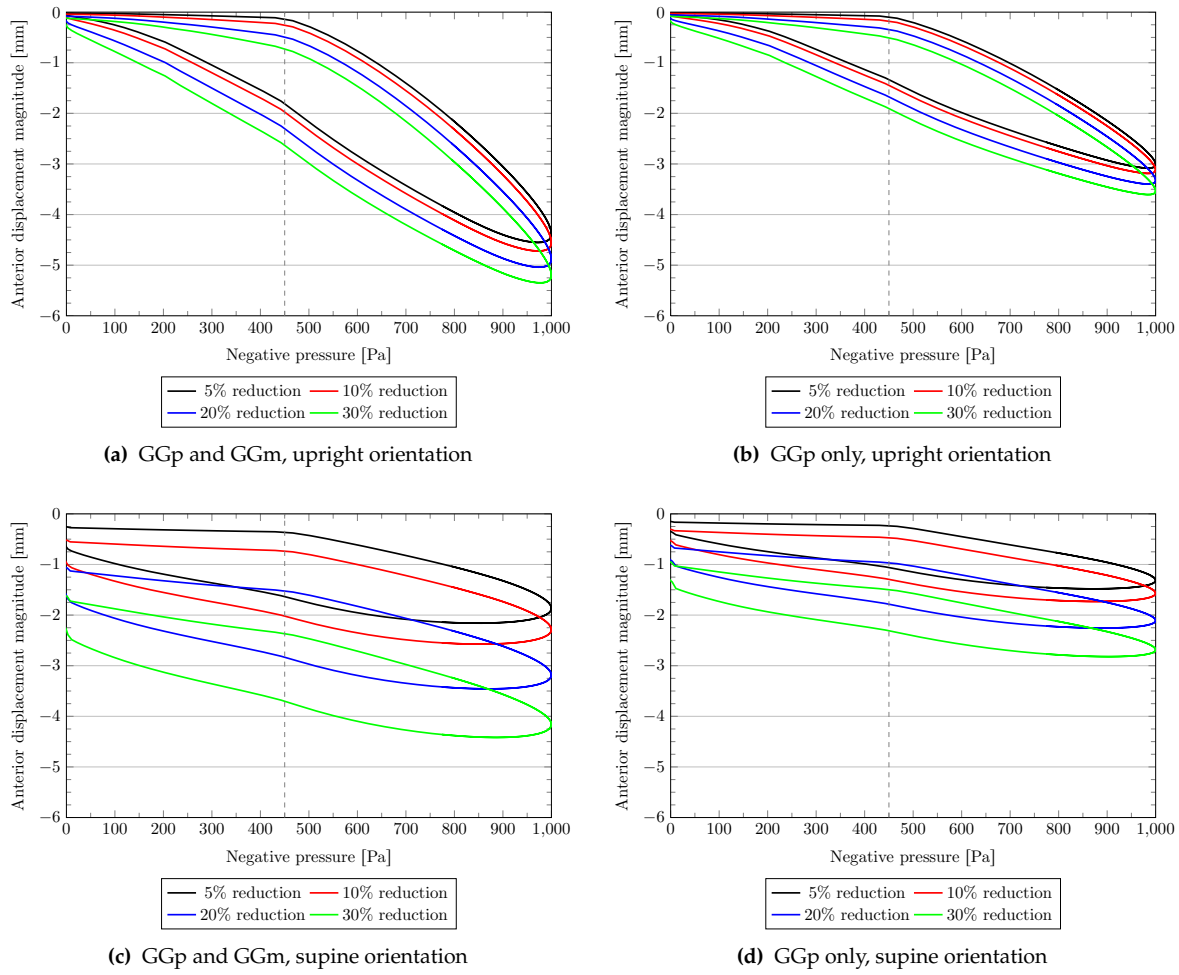

(a) GGp and GGm, upright orientation

(b) GGp only, upright orientation

(c) GGp and GGm, supine orientation

(d) GGp only, supine orientation

Figure 13.22: Anterior displacement of point $\boldsymbol{P}_C$ during partial deactivation of GG due to a variation of the degree of muscle atonia. Minimum epiglottal pressure produced with $p_{\text{nom}} = 1000\text{Pa}$, while a threshold pressure $p_{\text{thr}} = 450\text{Pa}$ is assumed.

movement is generated due to the presence of an airway load on the tongue when in a state of reduced muscle tone. Overall, it can be stated that the loss of muscle tone may certainly lead to increased movement of the tongue as the angle of incline is reduced.

13.4.4 Delay in muscle response during sleep

Simulation of a neurological deficiency leading to a delayed response of all muscles to an external loading stimulus can be achieved by altering the pressure value used in equation 13.2. In practice, this means that a epiglottal pressure $p = p\,(t)$ is applied to the tongue surface, while $p = p\,(t - \Delta t)$ is registered and responded to by the tongue muscles. As it is assumed that such a situation may only arise during sleep, the delayed response also was coupled with a partial deactivation of the dilator muscles.

Figure 13.23 shows the resulting muscle response as a function of the epiglottal pressure with a sinusoidal temporal loading pattern. It is quite apparent that even a small delay, of the order of tens of milliseconds, drastically changes the recorded stimulation history of the dilators. Due to the temporal offset, the portion of the FFMR curve associated with pressure drop is shifted right with respect to the non-delayed curve, while

that recorded during a pressure increase is shifted left. The result of this is that for the supine posture each set of response curves has a clockwise looped shape for the supine orientation with the cross-over point shifting right as the delay increases. A similar phenomenon may also be seen in the work of Akahoshi et al. [3] shown previously in figure 2.17, although it appears from this data only very small neural delays may be appropriate. As the upright posture normally results in an anti-clockwise activation hysteresis curve, a neural signal delay tends to widen the loop further.

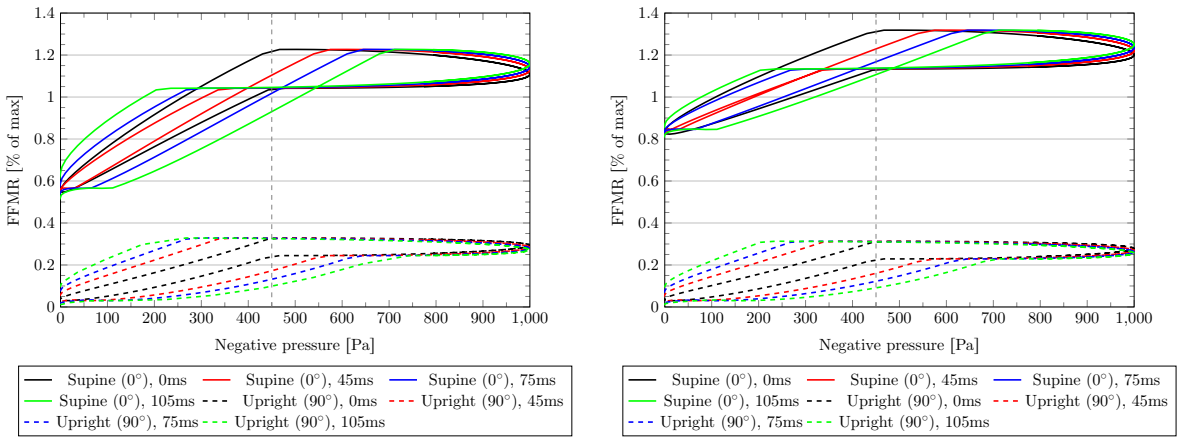

(a) GGp **(b)** GGm

Figure 13.23: FFMR for partially deactivated GG muscles with a preset delay in the activation with respect to the applied airway pressure load. Minimum epiglottal pressure produced with $p_{\text{nom}} = 1000$Pa, while a threshold pressure $p_{\text{thr}} = 450$Pa and 30% atonia ($R = 30$) are assumed.

As is shown in figure 13.24, the effect that the offset response of the dilators to the applied load has a situation varied effect on the retroglossal displacement history of the tongue rear surface. The presence of an activation delay leads to a significantly altered displacement history, particularly at high airway pressures, with the result that displacement is increased when the pressure-rate is negative. When both components of the GG experience a delayed neural response, as well as the destimulation associated with sleep, the maximal resulting rearwards tongue motion appears no larger when the neural delay is large than when there is no delay at all. However, when only the GGp FFMR is limited at the threshold pressure, the addition of a neural delay results in a measurably larger posterior deflection. The magnitude of the displacement remains less than in the case where the functioning of both muscles are compromised.

In the supine orientation, a cross-over point in the displacement-pressure loop is noted when long delays are present. This signifies that the typical behaviour of less movement during the pressure drop than during pressure increase is reversed. This is attributed to an increased contraction of the GG as it neurologically registers lower pressures than those actually experienced by the tongue, which in turn causes a larger contractile force to be applied thereby partially offsetting the atonia that is present. Conversely, at the inception of the inspiratory pressure drop the dilators are still responding to the expiratory pressures and thus the tongue experiences a greater no-load deflection than in the previous case-studies that have been presented.

If the head posture remains upright, the maximal anteroposterior displacement value occurs at minimum airway pressure while in the supine posture occurs at a higher pressure. In the supine case, the trend is that the magnitude of the motion produced as the pressure drops is increased due to the increased lag in response of the GG. For delays in excess of 105ms, the FFMR history no longer appears physiologically plausible.

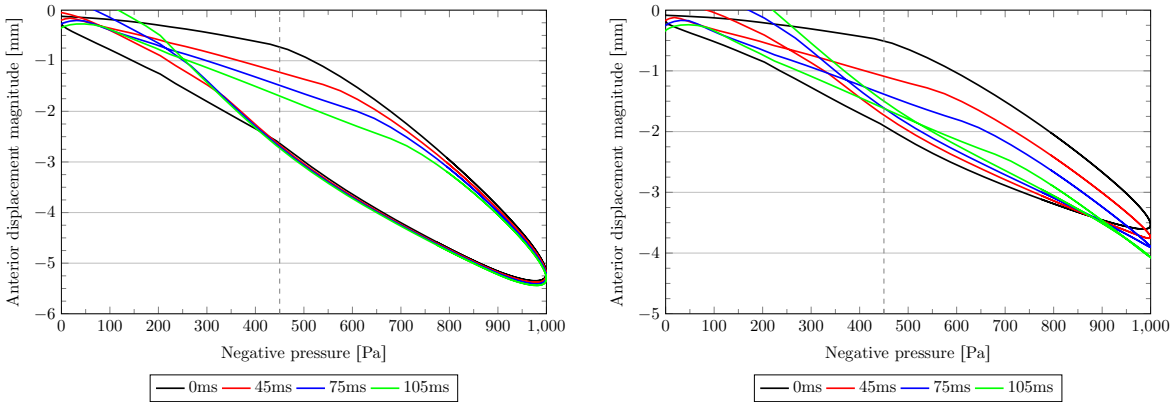

(a) Deactivation of GGp and GGm, upright orientation

(b) Deactivation of GGp only, upright orientation

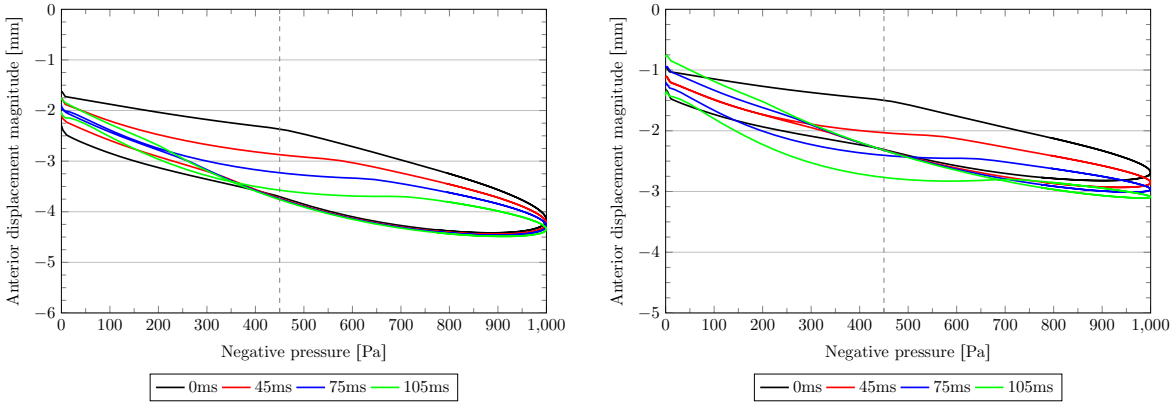

(c) Deactivation of GGp and GGm, supine orientation

(d) Deactivation of GGp only, supine orientation

Figure 13.24: Anterior displacement of point $\boldsymbol{P}_C$ during partial deactivation of GG with delayed neural response of all muscles. Minimum epiglottal pressure produced with $p_{\text{nom}} = 1000$Pa, while a threshold pressure $p_{\text{thr}} = 450$Pa and 30% atonia ($R = 30$) are assumed.

In these cases, the maximal posterior movement occurs at significantly higher pressures than the minimal epiglottal pressure and results in larger displacements than recorded in figures 13.24c and 13.24d.

13.4.5 Increase of non-muscular tissue mass in tongue

Using the analytical control model, it is feasible to simulate soft tissue accumulation in the interstitial space of the tongue musculature with no subsequent adaption by motor learning. This is achieved by keeping the coefficients listed in tables 13.2 and 13.3, valid for $\phi_{\text{f}} = 0.7$, constant and changing the fibre volume fraction applied to the physiology. As previously described, this material parameter is specified constant throughout the tongue and all muscles are affected in terms of the contractile stress that they generate locally. As some performance degradation is expected in the awake and sleep states, both are evaluated and discussed below.

13.4.5.1 Wakeful state

As was demonstrated in section 11.3.1, the genioglossal activity required to control tongue movement under both gravitational and pressure loading increases as the fibre volume fraction is reduced. Therefore even

in the wakeful state when the dilators are most responsive, large retroglossal movement of the tongue is possible if the increased volume of interstitial tissue is not accounted for.

Figure 13.25a illustrates that, on average, for every 10% by volume of adipose tissue increase, a displacement of 1mm per 1kPa can be expected when orientated in an upright position. In the supine posture, the performance is further affected by gravitational influences. Again, the overall stiffening of the muscular tissue results in a general resistance to airway loading but the deflection due to gravitational loading alone is approximately 0.75mm per 10% volume increase of interstitial tissue. However, it was observed that the resistance to a drop in epiglottal pressure decreases considerably as ϕ_f decreases. Rate-effects only appear to become significant if the difference between the neurologically-apparent and physiological values for the ϕ_f differ greatly.

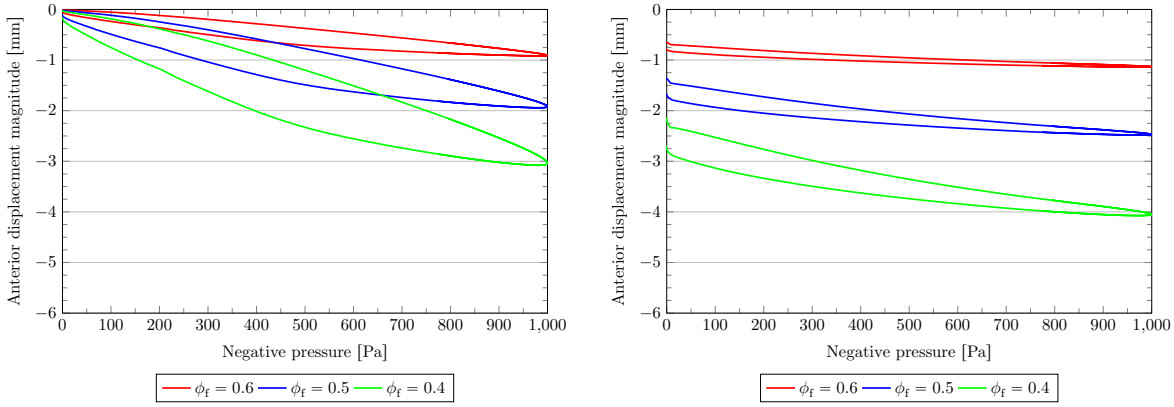

(a) Upright orientation

(b) Supine orientation

Figure 13.25: Anterior displacement of point $\boldsymbol{P}_C$ during wakeful state inhalation due to reduced fibre volume fraction with GG response prescribed for $\phi_f = 0.7$.

13.4.5.2 Sleep state

The addition of reduced contractile force due to soft tissue build-up, in conjunction with the performance degradation of the GGp and GGm associated with the sleep state, leads to very large rearward movement when the supine posture is maintained. As can be seen in figure 13.26b, at no load the retroglossal displacement is doubled when the value of ϕ_f is decreased from 0.7 to 0.4. At very low pressures up to a further 1.5mm anterior motion can be attributed in the extreme case to the mismatch between muscle stimulation and interstitial tissue volume.

In contrast, having the head in the upright position leads to far lesser deviation due to soft tissue build-up alone. At the pressure threshold, for the most extreme case an additional 0.75mm of movement may be induced while at the minimum airway pressure this value is 1.25mm.

13.5 Summary and discussion of results

Using the knowledge accumulated in producing the parametric study, the parameter-optimised neural model was used to perform two studies. The first was conducted under quasi-static conditions and using the pres-

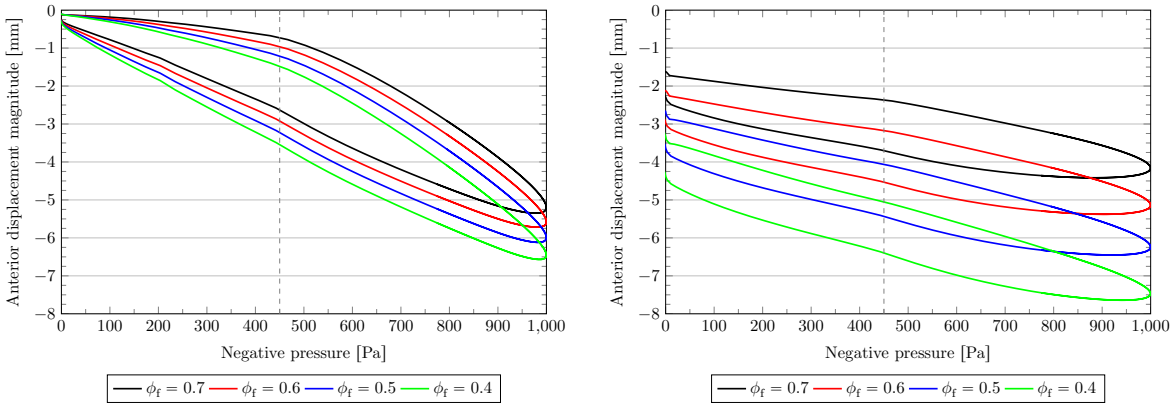

(a) Upright orientation

(b) Supine orientation

Figure 13.26: Anterior displacement of point $\boldsymbol{P}_C$ during sleep state inhalation due to reduced fibre volume fraction with GG response prescribed for $\phi_f = 0.7$. Minimum epiglottal pressure produced with $p_{nom} = 1000$Pa, while a threshold pressure $p_{thr} = 450$Pa and 30% atonia ($R = 30$) are assumed.

sure fields generated from the CFD analysis of the HUA. Loading of the passive tongue demonstrated that the displacement trends resulting from the assumed and CFD pressure distributions were similar. However, the assumed distribution resulted in an over-prediction of the air-induced movement at a set epiglottal pressure. Application of the neural model allowed the resolution of the FFMR required by the GG to resist movement during the wakeful state. The trends in the predicted response were qualitatively similar to those observed in the temporally-dependent parametric studies. From this, an analytical model, linear in terms of the epiglottal pressure, was produced and confirmed to be of a similar nature to that described in the literature. However, the accuracy of the data extracted from the neural model was declared questionable. Ultimately, it was decided that understanding the transient behaviour of the tongue was important and could lead to a deeper understanding of the tongue's functioning than static simulations could achieve.

The second study involved the application of the neural model to scenarios in which a temporally-dependent pressure distribution, incorporating phases of both inhalation and exhalation, was utilised. Due to the complexity and computational expense of the task, the spatial description of the load was approximated with the knowledge of the general magnitude of the difference in the results under passive conditions. The effectiveness of the optimised neural model was reexamined under these conditions, and it was demonstrated that good results, consistent with those observed during the parametric study, were obtained. A deeper evaluation of the macro- and microscopic functioning of the airway dilators under differing loading conditions was performed.

Using data extracted from 24 independent simulations with a variation in angle of recline and duration of the breathing cycle, a nine parameter analytical model predicting the approximate response of seven muscle groups was produced. More specifically, the determined coefficients approximate the optimal activation of the tongue muscles during the wakeful condition and within a pressure regime consistent with a patent airway. The model primarily links posture and the epiglottal pressure and its rate of change to the muscle response. Furthermore, this model accounted for hysteresis effects and incorporated additional parameters which could simulate the muscle atonia present during sleep. It was validated by comparing the response predicted at negative pressures, exceeding that for which the parameters were extracted, to those generated by the neural model under the same conditions.

The sophisticated analytical model was used to simulate the tongue's behaviour assuming a variety of conditions and pathologies, with an emphasis on functioning during the sleep-state. Posture, the fraction of tongue non-muscular tissue, the quantity of muscle atonia, the reflex mechanism critical pressure threshold and neurological signal delay all were evaluated and their influence on retroglossal tongue movement due to airway pressure was quantified. In these scenarios, it was assumed that some loss of airway patency had occurred, thus lowering the minimal epiglottal pressure.

From the results presented in section 13.4, it is evident that the normal loss of tone in the GG associated with sleep leads to several millimetres of retroglossal movement. This motion is amplified when both the GGp and GGm are affected, as opposed to the GGp (the main dilator) alone. Displacement hysteresis was also observed during the breathing cycle, indicating the significance of the viscoelastic nature of active muscular tissue. During normal sleep with no airway occlusion, gravitational influences dominate and posterior motion of the tongue is greatest in the supine posture. Atonia in both the GGp and GGm lead to in excess of 1.5mm posterior movement at atmospheric epiglottal pressure in this orientation. Under load, the maximal displacement condition was still that of the most reclined posture, but the pressure-induced displacement was greatest for the upright posture. The effect of many pathologies on the response to airway loading in a collapsed airway are more noticeable in the upright or lateral[10] posture when the muscle tone, and therefore pre-load stiffness of the muscular tissue required to overcome gravitational forces, is lowest. Although this appears contrary to the literature (see [268, 269]), it primarily suggests that the no-load response of the tongue at the initiation of inhalation is a critical factor in the determination as to whether a loss of patency of the upper airway will occur in a given breathing cycle.

In the upright posture, the cessation of reflexive actions is the primary mechanism that leads to large displacements, even at low levels of sleep-induced atonia. However, for the supine orientation it is general GG atonia resulting in a loss of resistance to gravitational forces that remains the dominant contributor to anteroposterior tongue movement unless the threshold pressure is very high. For a prescribed air-pressure load pattern, a delay in the reflexive action of the dilators leads to no increase in the maximal displacement of the tongue posterior but did result in an increase in movement at higher pressures during the initial stages of inspiration. This may again lead to a pathogenic scenario due to the low-load movement of the tongue. Lastly, it was observed that a decrease in the volume occupied by the muscle fibres with no corresponding change in the muscular activity during sleep leads to very large deformations in both the upright and supine orientations.

Related to the cephalometric measurements of this geometry mentioned in section 8.8.2, the motion resulting from individual sleep-related phenomena evaluated here, without accounting for the movement of the pharyngeal constrictors, reduce the anteroposterior diameter of this upper pharynx geometry by up to 30% during high-resistance oral inhalation with a $\phi_{\mathrm{f}} = 0.7$. However, it is reasonable to assume the cumulative displacement due to the compounding effect of multiple pathologies will be greater than this. The natural limiting case for this geometry and a $\phi_{\mathrm{f}} = 0.7$ is the supine orientation with the maximal oral pressure load applied to the passive tongue. This leads to a 9.1mm of posterior movement of its rear surface. This limit is nearly reached when introducing a large ϕ_{f} and dilator response mismatch, with up to 45% reduction in the

[10] The reader is reminded of the supplementary study discussed in section 11.2.1, in which it was stated that the tongue muscle response when in lateral postures is qualitatively similar to that with the body assuming the upright posture. Assuming that the two component non-dilatory muscles lateral to the midsagittal plane keep the tongue out of contact with the palate, teeth and other buccal tissues, then it can be inferred that lying on one's side may be detrimental due to decreased tone of the GG. However, the act of performing lateral control of the tongue position results in increased stiffness of certain regions of tissue and may partially negate this effect.

anteroposterior diameter achieved during sleep.

Given the spectrum of measurements presented in the literature (see table 8.1), it is noted that for many subjects the pathology-induced displacements[11] predicted during sleep could result in a near complete filling of the upper pharyngeal space by the tongue. In the worst cases, the lack of resistance to the gravitational forces alone could induce such a behaviour. This reinforces the importance of sleep posture described in the literature, but also demonstrates that any of the pathologies investigated here, or the exacerbation thereof, may play a significant role in the induction of an apnoeic event.

[11] The reader should also be reminded of the points made in the comparison drawn in section 13.3, where it was inferred that, due to the simulation methodology employed, the large displacements measured due to airway load in section 13.4 may be significantly exaggerated. That said, the retroglossal displacements predicted to occur during sleep and for the varying pathologies are sizable in comparison to the anteroposterior cephalometric measurements for OSA patients listed in table 8.1.

14. CONCLUSIONS

Imaging data has been used to construct a physiologically realistic model of the human tongue and surrounding tissues. Micro-histological data was also extracted and used to describe the tongue musculature. Simultaneously, the geometry of the surrounding airway including the nasal passages, buccal cavity, pharynx and trachea was reconstructed. CAD software was utilised to translate the extracted imaging data into meshed models for use in FEA and CFD analysis. A customised quasi-incompressible finite-strain elastic solver, based on well established and robust numerical methods, was developed using an open-source FE library. A muscle model, linking the micro- and macro-scale geometries, was introduced to describe the transverse isotropic behaviour of both passive and active muscular tissue. A method of simplifying complex geometries produced by capturing some of the extrinsic muscles of the tongue was developed.

A number of small studies were conducted to better understand the functioning of the tongue and ultimately assist in the derivation and motivation of mechanisms incorporated into a neuromuscular control algorithm. Initially, simple scenarios were evaluated to establish the response of the passive tongue as a whole and together with its underlying histology to gravitational and airway loading. The motion produced through the isolated contraction of individual tongue muscles was then tested and determined to be consistent with that described in both the human anatomical and computational literature. The importance of muscle coactivation was shown by demonstrating the complex movements only possible through the coordinated contraction of several muscle groups. The change in length of each muscle induced by the contraction of other muscles was then measured, and the minimal activation of the GG required to resist posterior movement of the tongue due to airway and gravitational loading was computed.

An open-source GA library was coupled to the FE solver for the purpose of providing an automated method of muscle control in response to *a priori* unknown stimuli. Control of the spatial position and energetic properties of the active tongue was established through the use of a multi-objective optimisation function. The steps related to the development of the control algorithm, as well as its basic functioning, were shown in detail. Numerous methods were employed to minimise the number of expensive state evaluations required by the non-deterministic GA. However, it was demonstrated that the model was robust and provided good spatial control and repeatable trends for the active muscle set under various scenarios. The results also appeared consistent with data presented in the cited literature.

A wide parametric study was conducted to optimise the functioning of the neural control model and establish the parameters most critical to the general functioning of the tongue under complex loading situations. It was demonstrated that the neural model captured the dilatory action of the GG and the role that several

physiological and environmental factors play in its response to loads. Importantly, it was demonstrated that the GG, as well as the other muscles of the tongue, are more than capable of producing sufficient contractile force to overcome airway loading, even during periods of very heavy respiration.

A CFD model was developed and validated by demonstrating that the flow-field and pressure losses in various regions of the anatomy were consistent with data and studies described in the literature. Analysis of the airflow in the HUA was used to corroborate the initial pressure distribution assumed to develop under conditions of nasal and oral inspiration and expiration. It was shown that the pressure field developed during oral inspiration leads to the greatest anteroposterior pressure gradient on the tongue surface, and that an increase in the air flow rate increases the pressure losses in the buccal cavity.

The now optimised neural model was subsequently applied to the tongue when loaded using the pressure distribution extracted from the CFD study. A comparison was made between the passive behaviour of the tongue and a response for the airway dilators, qualitatively similar to that determined during the transient parametric study, was established. However, it was decided that the quasi-static behaviour of the neural model was sub-optimal, and that further exploration on the response of the tongue under transient conditions would be most enlightening in terms of understanding the precipitators of SDB.

Using the information and understanding gained from the previous studies, a wide-scale set of simulations was performed and data extracted from the neural model was used to produce an analytical model describing the awake response of several muscle groups during breathing to variable environmental influences. The resulting model was derived from, and consistent with, previous iterations developed under more simple conditions. It fitted the extracted trends accurately and captured the hysteresis effects developed due to the viscoelastic nature of active muscular tissue. Later, parameters were introduced to invoke the sleep-state response of the airway dilators observed during polysomnography.

Applied to several pathogenic scenarios, the model was used to highlight the importance of the no-load response of the tongue in resisting gravitational forces and preventing the initial movement that may lead to SDB, such as OSA. Additionally, it was shown that the degradation of dilator response, by atonia or the loss of reflexive mechanisms, may lead to large retroglossal movement of the tongue which for some patients could result in complete occlusion of the retropharynx. Since these phenomena are normal during sleep, the degree to which they affect the retroglossal movement was methodically quantified. A delay of the order of tens of milliseconds in the response of the dilators to the airway load was shown to lead to abnormal behaviour in the tongue especially at the onset of inhalation. The potential degradation in the performance of the dilators, both during wakefulness and sleep, due to increased deposition of non-muscular tissue in the tongue was also quantified. Comparing these results with experimental studies documented in the literature, it was concluded that the tissue deformation present at the inception of airway pressure drop was particularly important in terms of the precipitation of airway collapse. All of the factors listed above have been demonstrated to have an influence in this regard.

15. RECOMMENDATIONS

There are a number of areas in which the models developed for the purpose of this work can be improved. These include the

Geometry: It would be ideal to find a dataset more suitable for the study of OSA and other SDB syndromes, namely one derived from a patient confirmed as having been inflicted with the disorder. Such a dataset should also ensure the tongue is in a more natural position. A more accurate description of the spatial distribution of tongue muscle volume fractions should be attained and and incorporated into this data. Extension of the solid geometry to incorporate other soft tissue structures of the HUA, such as that presented in appendix I.1, would assist in gaining a deeper understanding of the interaction between the tongue and soft palate during breathing.

Materials : More experimental work needs to be performed to come to a definitive conclusion on the material parameters of the passive tongue. This should distinguish the effects of sample age and extraction site on the measured properties. If measured *in vivo*, additional consideration of the residual muscle tone should be made. A frequency analysis, similar to that conducted in appendix I.2, could be correlated against experimental measurements of resonance in the buccal region to assist in the validation of the model. The material models should be expanded to include effects of viscoelasticity or viscoplasticity to capture the hysteresis effects observed in passive muscular tissue. The importance of muscle fatigue should be determined and incorporated into the muscle model if necessary.

FE model: Inertial effects should be added to the FE model so that an extension of application into the field of linguistics, where large accelerations and velocities are present, can be made. The incorporation of rigid body dynamics would make the simulation of hard tissues, such as bone and cartilage, more simple and enhance the functioning of the soft tissue solver. Contact between the tongue, teeth and palate, which greatly influences tongue movement and the airflow developed during breathing, should be accounted for. The use of higher-order elements would further increase the accuracy of the FE solution. Using adaptive mesh refinement or hp-refinement would add further accuracy and help compensate for the mesh count disadvantages incurred when using structured mesh.

Neural model: It would be ideal to devise a predictive control mechanism to emulate better the true nature of proprioception and muscle control. The implementation of a learning algorithm, such as neural networks, for use as a muscle control mechanism would work well for this purpose. To assist with the computational expense of these algorithms, the use of a surrogate model, such as one based on

the coarsest level of a multi-grid approach, should be investigated. It should be determined whether a better method of describing the change in muscle activation, from a neurological perspective, could be developed. This model, used to link the neural signal to the muscle activation level, should have a better physiological basis for its parameters than that used in this work.

Boundary values for the pressure field: A substantial improvement regarding the description of pressure BCs on the solid model is possible. Ideally, a transient coupled FSI model should be developed to capture the effect of the deformation of the pressure field developed in the airway and *vice versa*. This would greatly reduce the complex load assumptions needed for the solid model, and counter the circular argument (regarding airway resistance developed from complex flow in a deformable domain) which is needed to motivate the pressure field applied to the model. It is felt that accounting for the changes in CSA associated with deformation of the upper airway tissues may produce different results.

Analytical model of muscle response: This portion of the model can be further refined by correlating the coefficients to more realistic breathing cycle and loading patterns. This may require the addition of extra terms to fit the new data. Computation of the response of the other tongue muscles to the epiglottal pressure may also be useful for further studies.

Tongue models have been explored in considerable detail for a number of purposes (see section 8.2). Although tailored for the application of researching SDB, the HUA tissue model can be applied to further fields of research, including

Movement analysis: As demonstrated in appendix I.3, path-line following can be incorporated into the neural control model. This allows for the analysis of dynamic tongue movement, such as that achieved by some of the control algorithms presented in the literature.

Linguistics Following on from the above point, the use of the neural model would allow the determination of muscle synergisms involved in the performance of dynamic motions during speech.

Surgery and tumours: Understanding the effect of the development of tumours in the tongue and surrounding tissues, and the impact of their surgical removal, has been presented in the literature. Changes in the material parameters (stiffening mimicking the presence of a tumour) and geometry (tumour excision) can be used to simulate these conditions prior to physical intervention. Subsequent application of the neural control model can allow the determination of the degree to which motion is lost, and whether the muscles can be retrained to recover lost mobility.

REFERENCES

[1] S. Abd-el Malek. Observations on the morphology of the human tongue. *Journal of Anatomy*, 73:201–210, 1939.

[2] A. M. R. Agur and A. F. Dalley. *Grant's Atlas of Anatomy*. Lippincott Williams & Wilkins, Maryland, USA, 11th edition, 2005. ISBN 9780781742566.

[3] T. Akahoshi, D. P. White, J. K. Edwards, J. Beauregard, and S. A. Shea. Phasic mechanoreceptor stimuli can induce phasic activation of upper airway muscles in humans. *The Journal of Physiology*, 531.3:677–691, 2001. doi: 10.1111/j.1469-7793.2001.0677h.x.

[4] Ansys Inc. ANSYS ICEM CFD, 2010. URL `http://www.ansys.com/Products/Other+Products/ANSYS+ICEM+CFD`. Accessed July 2013.

[5] F. Armero. On the locking and stability of finite elements in finite deformation plane strain problems. *Computers & Structures*, 75:261–290, 2000. doi: 10.1016/S0045-7949(99)00136-4.

[6] E. Avrahami and M. Englender. Relation between CT axial cross-sectional area of the oropharynx and obstructive sleep apnea syndrome in adults. *American Journal of Neuroradiology*, 16:135–140, 1995.

[7] E. Avrahami, A. Solomonovich, and M. Englender. Axial CT measurements of the cross-sectional area of the oropharynx in adults with obstructive sleep apnea syndrome. *American Journal of Neuroradiology*, 17:1107–1111, 1996.

[8] I. Ayappa and D. M. Rapoport. The upper airway in sleep: physiology of the pharynx. *Sleep Medicine Reviews*, 7:9–33, 2003. doi: 10.1053/smrv.2002.0238.

[9] F. Baaijens, C. Bouten, and N. Driessen. Modeling collagen remodeling. *Journal of Biomechanics*, 43:166–175, 2010. doi: 10.1016/j.jbiomech.2009.09.022.

[10] E. F. Bailey. Activities of human genioglossus motor units. *Respiratory Physiology & Neurobiology*, 179:14–22, 2011. doi: 10.1016/j.resp.2011.04.018.

[11] T. A. Baker. *A biomechanical model of the human tongue for understanding speech production and other lingual behaviors*. PhD thesis, University of Arizona, 2008.

[12] C. G. Ball, M. Uffin, and A. Pollard. Mean flow structures inside the human upper airway. *Flow, Turbulence and Combustion*, 81:155–188, 2008. doi: 10.1007/s10494-007-9113-3.

[13] W. Bangerth, R. Hartmann, and G. Kanschat. deal.II — A general-purpose object-oriented finite element library. *ACM Transactions on Mathematical Software*, 33, 2007. doi: 10.1145/1268776.1268779.

[14] W. Bangerth, R. Hartmann, and G. Kanschat. `deal.II` *Differential Equations Analysis Library, Technical Reference*, 2007. URL `http://www.dealii.org`.

[15] J. M. Battagel, A. Johal, A-M. Smith, and B. Kotecha. Postural variation in oropharyngeal dimensions in subjects with sleep disordered breathing: a cephalometric study. *European Journal of Orthodontics*, 24:263–276, 2002. doi: 10.1093/ejo/24.3.263.

[16] N. A. Bernshteĭn. *The Coordination and Regulation of Movements*. Pergamon Press, 1st edition, 1967.

[17] D. A. Berry, J. B. Moon, and D. P. Kuehn. A finite element model of the soft palate. *The Cleft Palate–Craniofacial Journal*, 36:217–223, 1999. doi: 10.1597/1545-1569(1999)036<0217:AFEMOT>2.3.CO;2.

[18] R. B. Berry, D. P. White, J. Roper, G. Pillar, R. B. Fogel, M. Stanchina, and A. Malhotra. Awake negative pressure reflex response of the genioglossus in OSA patients and normal subjects. *Journal of Applied Physiology*, 94:1875–1882, 2003. doi: 10.1152/japplphysiol.00324.2002.

[19] D. P. Bertsekas. *Constrained Optimisation and Lagrange Multiplier Methods*. Athena Scientific, Massachusetts, USA, 1984. ISBN 1-886529-04-3.

[20] L. J. Bhargava, M. G. Pandy, and F. G. Anderson. A phenomenological model for estimating metabolic energy consumption in muscle contraction. *Journal of Biomechanics*, 37:81–88, 2004. doi: 10.1016/S0021-9290(03)00239-2.

[21] M. J. Birch and P. D. Srodon. Biomechanical properties of the human soft palate. *The Cleft Palate–Craniofacial Journal*, 46:268–274, 2009. doi: 10.1597/08-012.1.

[22] E. Bizzi, N. Hogan, F. A. Mussa-Ivaldi, and S. Giszter. *Movement Control*, chapter 1: Does the nervous system use equilibrium-point control to guide single and multiple joint movements?, pages 1–11. Cambridge University Press, New York, USA, 1994. ISBN 9780521456074.

[23] S. S. Blemker and S. L. Delp. Rectus femoris and vastus intermedius fiber excursions predicted by three-dimensional muscle models. *Journal of Biomechanics*, 39:1383–1391, 2006. doi: 10.1016/j.jbiomech.2005.04.012.

[24] S. S. Blemker, P. M. Pinsky, and S. L. Delp. A 3D model of muscle reveals the causes of nonuniform strains in the biceps brachii. *Journal of Biomechanics*, 38:657–665, 2005. doi: 10.1016/j.jbiomech.2004.04.009.

[25] M. B. Blumen, A. P. de La Sota, M. A. Quera-Salva, B. Frachet, F. Chabolle, and F. Lofaso. Tongue mechanical characteristics and genioglossus muscle EMG in obstructive sleep apnoea patients. *Respiratory Physiology & Neurobiology*, 140:155–164, 2004. doi: 10.1016/j.resp.2003.12.001.

[26] J. Bonet and R. Wood. *Nonlinear Continuum Mechanics for Finite Element Analysis*. Cambridge University Press, New York, USA, 1997. ISBN 0-521-57272-X.

[27] S. Buchaillard, P. Perrier, and Y. Payan. A 3D biomechanical vocal tract model to study speech production control: How to take into account the gravity?

[28] S. Buchaillard, M. Brix, P. Perrier, and Y. Payan. Simulations of the consequences of tongue surgery on tongue mobility: implications for speech production in post-surgery conditions. *The International Journal of Medical Robotics and Computer Assisted Surgery*, 3:252–261, 2007. doi: 10.1002/rcs.142.

[29] S. Buchaillard, P. Perrier, and Y. Payan. A biomechanical model of cardinal vowel production: Muscle activations and the impact of gravity on tongue positioning. *Acoustical Society of America*, 126:2033–2051, 2009. doi: 10.1121/1.3204306.

[30] N. J. Buchner, B. M. Sanner, J. Borgel, and L. C. Rump. Continuous positive airway pressure treatment of mild to moderate obstructive sleep apnea reduces cardiovascular risk. *American Journal of Respiratory and Critical Care Medicine*, 176:1274–1280, 2007. doi: 10.1164/rccm.200611-1588OC.

[31] B. F. BuSha, R. J. Strobel, and S. J. England. The length–force relationship of the human genioglossus in patients with obstructive sleep apnea. *Respiratory Physiology & Neurobiology*, 130:161–168, 2002. doi: 10.1016/S0034-5687(01)00340-1.

[32] M. Butt, G. Dwivedi, O. Khair, and G. Y. H. Lip. Obstructive sleep apnea and cardiovascular disease. *International Journal of Cardiology*, 139:7–16, 2010. doi: 10.1016/j.ijcard.2009.05.021.

[33] M. Carrera, F. Barbé, J. Sauleda, M. Tomás, C. Gómez, C. Santos, and A. G. N. Agustí. Effects of obesity upon genioglossus structure and function in obstructive sleep apnoea. *European Respiratory Journal*, 23:425–429, 2004. doi: 10.1183/09031936.04.00099404.

[34] D. R. Carter and M. Wong. Modelling cartilage mechanobiology. *Philosophical Transactions of the Royal Society B: Biological Sciences*, 358:1461–1471, 2003. doi: 10.1098/rstb.2003.1346.

[35] E. Cavallaro, J. Rosen, J. C. Perry, S. Burns, and B. Hannaford. Hill-based model as a myoprocessor for a neural controlled powered exoskeleton arm-parameters optimization. In *Robotics and Automation, 2005. ICRA 2005. Proceedings of the 2005 IEEE International Conference on*, pages 4525–4530, Barcelona, Spain, April 2005. IEEE. doi: 10.1109/ROBOT.2005.1570815.

[36] J. B. Chapman and C. L. Gibbs. An energetic model of muscle contraction. *Biophysical Journal*, 12:227–236, 1972. doi: 10.1016/S0006-3495(72)86082-X.

[37] A. Chawla, S. Mukherjee, and B. Karthikeyan. Characterization of human passive muscles for impact loads using genetic algorithm and inverse finite element methods. *Biomechanics and modeling in mechanobiology*, 8:67–76, 2009. doi: 10.1007/s10237-008-0121-6.

[38] S. Cheng, J. E. Butler, S. C. Gandevia, and L. E. Bilston. Movement of the tongue during normal breathing in awake healthy humans. *The Journal of Physiology*, 586:4283–4294, 2008. doi: 10.1113/jphysiol.2008.156430.

[39] S. Cheng, S. C. Gandevia, M. Green, R. Sinkus, and L. E. Bilston. Viscoelastic properties of the tongue and soft palate using MR elastography. *Journal of Biomechanics*, 44:450–454, 2011. doi: 10.1016/j.jbiomech.2010.09.027.

[40] Y. S. Cheng, H. C. Yeh, R. A. Guilmette, Q. S. Simpson, K. H. Cheng, and D. L. Swift. Nasal deposition of ultrafine particles in human volunteers and its relationship to airway geometry. *Aerosol Science and Technology*, 25:274–291, 1996. doi: 10.1080/02786829608965396.

[41] F. Chouly, A. Van-Hirtum, P-Y. Lagrée, X. Pelorson, and Y. Payan. Reproduction of hypopnea phenomenon using a physical and numerical model. In *6th International Symposium on Computer Methods in Biomechanics and Biomechanical Engineering*, Madrid, Spain, 2004. ISBN 978-0954967000.

[42] F. Chouly, A. Van Hirtum, P-Y. Lagrée, J-R. Paoli, X. Pelorson, and Y. Payan. Simulation of the retroglossal fluid-structure interaction during obstructive sleep apnea. In *Third International Symposium, ISBMS 2006*, pages 48–57, Zurich, Switzerland, 10–11 July 2006. doi: 10.1007/11790273_6.

[43] G. T. Clark. Mandibular advancement devices and sleep disordered breathing. *Sleep Medicine Reviews*, 2:163–174, 1998. doi: 10.1016/S1087-0792(98)90019-3.

[44] R. H. Clayton, O. Bernus, E. M. Cherry, H. Dierckx, F. H. Fenton, L. Mirabella, A. V. Panfilov, F. B. Sachse, G. Seemann, and H. Zhang. Models of cardiac tissue electrophysiology: Progress, challenges and open questions. *Progress in Biophysics and Molecular Biology*, 104:22–48, 2011. doi: 10.1016/j.pbiomolbio.2010.05.008.

[45] G. K. Cole, A. J. van den Bogert, W. Herzog, and K. G. M. Gerritsen. Modelling of force production in skeletal muscle undergoing stretch. *Journal of Biomechanics*, 29:1091–1104, 1996. doi: 10.1016/0021-9290(96)00005-X.

[46] T. P. Collins, G. R. Tabor, and P. G. Young. A computational fluid dynamics study of inspiratory flow in orotracheal geometries. *Medical & Biological Engineering & Computing*, 45:829–836, 2007. doi: 10.1007/s11517-007-0238-2.

[47] K. Comley and N. Fleck. The mechanical response of porcine adipose tissue. *Journal of Biomechanical Engineering*, 2010. (submitted).

[48] R. Cooke, H. White, and E. Pate. A model of the release of myosin heads from actin in rapidly contracting muscle fibers. *Biophysical Journal*, 66:778–788, 1994. doi: 10.1016/S0006-3495(94)80854-9.

[49] F. Dalmasso and R. Prota. Snoring: analysis, measurement, clinical implications and applications. *European Respiratory Journal*, 9:146–159, 1996. doi: 10.1183/09031936.96.09010146.

[50] J. Dang and K. Honda. A physiological articulatory model for simulating speech production process. *Acoustical Science and Technology*, 22:415–425, 2001. doi: 10.1250/ast.22.415.

[51] J. Dang and K. Honda. Construction and control of a physiological articulatory model. *Acoustical Society of America*, 115:853–870, 2004. doi: 10.1121/1.1639325.

[52] D. d'Aulignac, J. A. C. Martins, E. B. Pires, T. Mascarenhas, and R. M. Natal Jorge. A shell finite element model of the pelvic floor muscles. *Computer Methods in Biomechanics and Biomedical Engineering*, 8:339–347, 2005. doi: 10.1080/10255840500405378.

[53] T. M. Davidson. Sleep medicine for surgeons. *The Laryngoscope*, 118:915–931, 2008. doi: 10.1097/MLG.0b013e3181670fc4.

[54] D.V. Davies, editor. *Gray's Anatomy*. Longmans, Green & Co Ltd., London, United Kingdom, 34th edition, 1967. ISBN 9780443010118.

[55] T. A. Davis. Algorithm 832: UMFPACK V4.3 — an unsymmetric-pattern multifrontal method. *ACM Transactions on Mathematical Software*, 30:196–199, 2004. doi: 10.1145/992200.992206.

[56] J. W. De Backer, O. M. Vanderveken, W. G. Vos, A. Devolder, S .L. Verhulst, J. A. Verbraecken, P. M. Parizel, M. J. Braem, P.H. Van de Heyning, and W. A. De Backer. Functional imaging using computational fluid dynamics to predict treatment success of mandibular advancement devices in sleep-disordered breathing. *Journal of Biomechanics*, 40:3708–3714, 2007. doi: 10.1016/j.jbiomech.2007.06.022.

[57] S. L. Delp, F. C. Anderson, A. S. Arnold, P. Loan, A. Habib, C. T. John, E. Guendelman, and D. G. Thelen. OpenSim: Open-source software to create and analyze dynamic simulations of movement. *IEEE Transactions on Biomedical Engineering*, 54:1940–1950, 2007. doi: 10.1109/TBME.2007.901024.

[58] N. J. B. Driessen, C. V. C. Bouten, and F. P. T. Baaijens. A structural constitutive model for collagenous cardiovascular tissues incorporating the angular fiber distribution. *Journal of Biomechanical Engineering*, 127:494–503, 2005. doi: 10.1115/1.1894373.

[59] A. Düster, S. Hartmann, and E. Rank. p-FEM applied to finite isotropic hyperelastic bodies. *Computer Methods in Applied Mechanics and Engineering*, 192:5147–5166, 2003. doi: 10.1016/j.cma.2003.07.003.

[60] P. R. Eastwood, G. T. Allison, K. L. Shepherd, I. Szollosi, and D. Hillman. Heterogeneous activity of the human genioglossus muscle assessed by multiple bipolar fine-wire electrodes. *Journal of Applied Physiology*, 94:1849–1858, 2003. doi: 10.1152/japplphysiol.01017.2002.

[61] H. Edelsbrunner and E. P. Mücke. Simulation of simplicity: A technique to cope with degenerate cases in geometric algorithms. *ACM Transactions on Graphics*, 9:66–104, 1990. doi: 10.1145/77635.77639.

[62] A. E. Ehret, M. Bol, and M. Itskov. A continuum constitutive model for the active behaviour of skeletal muscle. *Journal of the Mechanics and Physics of Solids*, 59:625–636, 2011. doi: 10.1016/j.jmps.2010.12.008.

[63] T. Elguedj, Y. Bazilevs, V.M. Calo, and T.J.R. Hughes. $\bar{B}$ and $\bar{F}$ projection methods for nearly incompressible linear and nonlinear elasticity and plasticity using higher-order NURBS elements. *Computer Methods in Applied Mechanics and Engineering*, 197:2732–2762, 2008. doi: 10.1016/j.cma.2008.01.012.

[64] M. Epstein and W. Herzog. Aspects of skeletal muscle modelling. *Philosophical Transactions of the Royal Society B: Biological Sciences*, 358:1445–1452, 2003. doi: 10.1098/rstb.2003.1344.

[65] A. Erdemir, M. L. Viveiros, J. S. Ulbrecht, and P. R. Cavanagh. An inverse finite-element model of heel-pad indentation. *Journal of Biomechanics*, 39:1279–1286, 2006. doi: 10.1016/j.jbiomech.2005.03.007.

[66] M. Esler and N. Eikelis. Is obstructive sleep apnea the cause of sympathetic nervous activation in human obesity? *Journal of Applied Physiology*, 100:11–12, 2006. doi: 10.1152/japplphysiol.01294.2005.

[67] Y. Fan, L. K. Cheung, M. M. Chong, H. D. Chua, K. W. Chow, and C. H. Liu. Computational fluid dynamics analysis on the upper airways of obstructive sleep apnea using patient – specific models. *IAENG International Journal of Computer Science*, 38:401–408, 2011.

[68] Q. Fang, S. Fujita, X. Lu, and J. Dang. A model-based investigation of activations of the tongue muscles in vowel production. *Acoustical Science and Technology*, 30:277–287, 2009. doi: 10.1250/ast.30.277.

[69] M. S. Farvid, T. W. Ng, D. C. Chan, P. H. Barrett, and G. F. Watts. Association of adiponectin and resistin with adipose tissue compartments, insulin resistance and dyslipidaemia. *Diabetes, Obesity and Metabolism*, 7:406–413, 2005. doi: 10.1111/j.1463-1326.2004.00410.x.

[70] S. Federico and T. C. Gasser. Nonlinear elasticity of biological tissues with statistical fibre orientation. *Journal of the Royal Society Interface*, 7:955–966, 2010. doi: 10.1098/rsif.2009.0502.

[71] A. G. Feldman and M. L. Latash. Testing hypotheses and the advancement of science: recent attempts to falsify the equilibrium point hypothesis. *Experimental Brain Research*, 161:91–103, 2005. doi: 10.1007/s00221-004-2049-0.

[72] S. Fels, J. E. Lloyd, K. van den Doel, F. Vogt, I. Stavness, and E. Vatikiotis-Bateson. Developing physically-based, dynamic vocal tract models using ArtiSynth. In *Proceedings of the 7th International Seminar on Speech Production (ISSP '06)*, pages 59–66, Ubatuba, Brazil, 13–15 December 2006. ISBN 9788599598023.

[73] R. B. Fogel, A. Malhotra, and D. P. White. Pathophysiology of obstructive sleep apnoea/hypopnoea syndrome. *Thorax*, 59:159–163, 2004. doi: 10.1136/thx.2003.015859.

[74] S. I. Fox. *Human Physiology*. McGraw-Hill, Massachusetts, USA, 9th edition, 2006. ISBN 978-0072852936.

[75] M. Friedman, H. Tanyeri, J. W. Lim, R. Landsberg, K. Vaidyanathan, and D. Caldarelli. Effect of improved nasal breathing on obstructive sleep apnea. *Otolaryngology – Head and Neck Surgery*, 122:71–74, 2000. doi: 10.1016/S0194-5998(00)70147-1.

[76] U. Frohberg, R. J. Naples, and D. L. Jones. Cephalometric comparison of characteristics in chronically snoring patients with and without sleep apnea syndrome. *Oral Surgery, Oral Medicine, Oral Pathology, Oral Radiology and Endodontics*, 80:28–33, 1995. doi: 10.1016/S1079-2104(95)80012-3.

[77] S. Fujita, J. Dang, N. Suzuki, and K. Honda. A computational tongue model and its clinical application. *Oral Science International*, 4:97–109, 2007. doi: 10.1016/S1348-8643(07)80004-8.

[78] Y. C. Fung. *Biomechanics: Mechanical Properties of Living Tissues*. Springer-Verlag, New York, USA, 2nd edition, 1993. ISBN 0-387-97947-6.

[79] E. Gabriel, G. E. Fagg, G. Bosilca, T. Angskun, J. J. Dongarra, J. M. Squyres, V. Sahay, P. Kambadur, B. Barrett, A. Lumsdaine, R. H. Castain, D. J. Daniel, R. L. Graham, and T. S. Woodall. Open MPI: Goals, concept, and design of a next generation MPI implementation. In *Recent Advances in Parallel Virtual Machine and Message Passing Interface*, pages 97–104. Springer, 2004. doi: 10.1007/978-3-540-30218-6_19.

[80] T. A. Gaige, T. Benner, R. Wang, V. J. Wedeen, and R. J. Gilbert. Three dimensional myoarchitecture of the human tongue determined in vivo by diffusion tensor imaging with tractography. *Journal of Magnetic Resonance Imaging*, 26:654–661, 2007. doi: 10.1002/jmri.21022.

[81] M. Galassi, J. Davies, J. Theiler, B. Gough, G. Jungman, P. Alken, M. Booth, and F. Rossi. *GNU Scientific Library Reference Manual*. Network Theory Ltd, Bristol, UK, 3rd edition, 2010.

[82] T. C. Gasser and G. A. Holzapfel. A rate-independent elastoplastic constitutive model for biological fiber-reinforced composites at finite strains: continuum basis, algorithmic formulation and finite element implementation. *Computational Mechanics*, 29:340–360, 2002. doi: 10.1007/s00466-002-0347-6.

[83] M. W. Gee, C. M. Siefert, J. J. Hu, R. S. Tuminaro, and M. G. Sala. ML 5.0 smoothed aggregation user's guide. Technical Report SAND2006-2649, Sandia National Laboratories, 2006.

[84] M. W. Gee, C. Förster, and W. A. Wall. A computational strategy for prestressing patient-specific biomechanical problems under finite deformation. *International Journal for Numerical Methods in Engineering*, 26:52–72, 2010. doi: 10.1002/cnm.1236.

[85] J-M. Gérard, R. Wilhelms-Tricarico, P. Perrier, and Y. Payan. A 3D dynamical biomechanical tongue model to study speech motor control. *Recent Research Developments in Biomechanics*, 1:49–63, 2003.

[86] J-M. Gérard, J. Ohayon, V. Luboz, P. Perrier, and Y. Payan. Non-linear elastic properties of the lingual and facial tissues assessed by indentation technique: Application to the biomechanics of speech production. *Medical Engineering & Physics*, 27:884–892, 2005. doi: 10.1016/j.medengphy.2005.08.001.

[87] J-M. Gérard, P. Perrier, and Y. Payan. *Speech Production: Models, Phonetic Processes, and Techniques*, chapter 6: 3d biomechanical tongue modeling to study speech production, pages 85–102. Psychology Press, 1st edition, 2006. ISBN 978-1841694375.

[88] D. E. Goldberg. *Genetic algorithms in search, optimization and machine learning*. Addison-Wesley Longman Publishing Co., Inc., Massachusetts, USA, 1st edition, 1989. ISSN 978-0201157673.

[89] D. E. Goldberg and M. Rudnick. Genetic algorithms and the variance of fitness. *Complex Systems*, 5:265–278, 1991.

[90] A. M. Gordon, A. F. Huxley, and F. J. Julian. Tension development in highly stretched vertebrate muscle fibres. *The Journal of Physiology*, 184:143–169, 1966.

[91] A. M. Gordon, A. F. Huxley, and F. J. Julian. The variation in isometric tension with sarcomere length in vertebrate muscle fibres. *The Journal of Physiology*, 184:170–192, 1966.

[92] G. L. Gottlieb. Rejecting the equilibrium-point hypothesis. *Motor Control*, 2:10–12, 1998.

[93] D. Grauer, L. S. H. Cevidanes, M. A. Styner, J. L. Ackerman, and W. R. Proffit. Pharyngeal airway volume and shape from cone-beam computed tomography: Relationship to facial morphology. *American Journal of Orthodontics and Dentofacial Orthopedics*, 136:805–814, 2009. doi: 10.1016/j.ajodo.2008.01.020.

[94] J. P. Grover, D. T. Corr, H. Toumi, D. M. Manthei, A. L. Oza, R. Vanderby, and T. M. Best. The effect of stretch rate and activation state on skeletal muscle force in the anatomical range. *Clinical Biomechanics*, 22:360–368, 2007. doi: 10.1016/j.clinbiomech.2006.10.009.

[95] M. Hagopian. Contraction bands at short sarcomere length in chick muscle. *Journal of Cell Biology*, 47:790–796, 1970.

[96] E. P. P. M. Hamans, E. A. Van Marck, W. A. De Backer, W. Creten, and P. H. Van de Heyning. Morphometric analysis of the uvula in patients with sleep-related breathing disorders. *European Archives of Oto-Rhino-Laryngology*, 257:232–236, 2000. ISSN 0937-4477. doi: 10.1007/s004050050229.

[97] R. Hartl. A global convergence proof for a class of genetic algorithms. Technical report, Institut für Ökonometrie & Operations Research, Technische Universität Wien, 1990.

[98] R. L. Haupt and S. E. Haupt. *Practical Genetic Algorithms*. John Wiley & Sons Inc., New Jersey, USA, 2nd edition, 2004. ISBN 0-471-45565-2.

[99] M. A. Heroux. AztecOO user guide. Technical Report SAND2004-3796, Sandia National Laboratories, 2007.

[100] M. A. Heroux, R. A. Bartlett, V. E. Howle, R. J Hoekstra, J. J. Hu, T. G. Kolda, R. B. Lehoucq, K. R. Long, R. P. Pawlowski, E. T. Phipps, A. G. Salinger, H. K. Thornquist, R. S. Tuminaro, J. M. Willenbring, A. Williams, and K. S. Stanley. An overview of the Trilinos project. *ACM Transactions on Mathematical Software*, 31:397–423, 2005. doi: 10.1145/1089014.1089021.

[101] W. Herzog and R. Ait-Haddou. Considerations on muscle contraction. *Journal of Electromyography and Kinesiology*, 12:425–433, 2002. doi: 10.1016/S1050-6411(02)00036-6.

[102] W. Herzog and P. Binding. Effects of replacing 2-joint muscles with energetically equivalent 1-joint muscles on cost-function values of non-linear optimization approaches. *Human Movement Science*, 13:569–586, 1994. doi: 10.1016/0167-9457(94)90006-X.

[103] A. V. Hill. The heat of shortening and the dynamic constants of muscle. *Proceedings of the Royal Society of London, Series B*, 126:136–195, 1938. doi: 10.1098/rspb.1938.0050.

[104] A. V. Hill. The mechanics of active muscle. *Proceedings of the Royal Society of London. Series B.*, 141:104–117, 1953. doi: 10.1098/rspb.1953.0027.

[105] M. R. Hinder and T. E. Milner. The case for an internal dynamics model versus equilibrium point control in human movement. *The Journal of Physiology*, 549:953–963, 2003. doi: 10.1113/jphysiol.2002.033845.

[106] G. A. Holzapfel. *Nonlinear solid mechanics*. John Wiley & Sons Ltd., West Sussex, England, 2007. ISBN 0 471 82304 X.

[107] G. A. Holzapfel, T. C. Gasser, and R. W. Ogden. A new constitutive framework for arterial wall mechanics and a comparative study of material models. *Journal of Elasticity*, 61:1–48, 2000. doi: 10.1023/A:1010835316564.

[108] K. Honda. Organisation of tongue articulation for vowels. *Journal of Phonetics*, 24:39–52, 1996. doi: 10.1006/jpho.1996.0004.

[109] L. Hu, X. Xu, Y. Gong, X. Fan, L. Wang, J. Zhang, and Y. Zeng. Percutaneous biphasic electrical stimulation for treatment of obstructive sleep apnea syndrome. *IEEE Transactions on Biomedical Engineering*, 55:181–187, 2008. doi: 10.1109/TBME.2007.897836.

[110] L. Huang, S. J. Quinn, P. D. Ellis, and J. E. Williams. Biomechanics of snoring. *Endeavour*, 19:96–100, 1995. doi: 10.1016/0160-9327(95)97493-R.

[111] Y. Huang, A. Malhotra, and D. P. White. Computational simulation of human upper airway collapse using a pressure-/state-dependent model of genioglossal muscle contraction under laminar flow conditions. *Journal of Applied Physiology*, 99:1138–1148, 2005. doi: 10.1152/japplphysiol.00668.2004.

[112] Y. Huang, D. P. White, and A. Malhotra. The impact of anatomic manipulations on pharyngeal collapse: Results from a computational model of the normal human upper airway. *Chest Journal*, 128:1324–1330, 2005. doi: 10.1378/chest.128.3.1324.

[113] Y. Huang, D. P. White, and A. Malhotra. Use of computational modeling to predict responses to upper airway surgery in obstructive sleep apnea. *The Laryngoscope*, 117:648–653, 2007. doi: 10.1097/MLG.0b013e318030ca55.

[114] T. J. Hughes. *The Finite Element Method: Linear Static and Dynamic Finite Element Analysis*. Dover Publications Inc., New York, USA, 2000. ISBN 978-0486411811.

[115] I. A. Humbert, S. B. Reeder, E. J. Porcaro, S. A. Kays, J. H. Brittain, and J. Robbins. Simultaneous estimation of tongue volume and fat fraction using IDEAL-FSE. *Journal of Magnetic Resonance Imaging*, 28:504–508, 2008. doi: 10.1002/jmri.21431.

[116] J. D. Humphrey and F. C. P. Yin. On constitutive relations and finite deformations of passive cardiac tissue: I. A pseudostrain-energy function. *Journal of Biomechanical Engineering*, 109:298–304, 1987. doi: 10.1115/1.3138684.

[117] J. D. Humphrey, R. K. Strumpf, and F. C. P. Yin. Determination of a constitutive relation for passive myocardium: I. A new functional form. *Journal of Biomechanical Engineering*, 112:333–339, 1990. doi: 10.1115/1.2891193.

[118] A. F. Huxley. Review lecture: Muscular contraction. *The Journal of Physiology*, 243:1–43, 1974.

[119] J. Huynh, K. B. Kim, and M. McQuilling. Pharyngeal airflow analysis in obstructive sleep apnea patients pre- and post-maxillomandibular advancement surgery. *Journal of Fluids Engineering*, 131:091101–1–091101–10, 2009. doi: 10.1115/1.3192137.

[120] B. S. Ibrahim, M. S. Huq, M. O. Tokhi, S. C. Gharooni, R. Jailani, and Z. Hussain. Identification of active properties of knee joint using GA optimization. *World Academy of Science, Engineering and Technology*, 55:441–446, 2009.

[121] B. S. Ibrahim, M. O. Tokhi, S. C. Gharooni, and M. S. Huq. Development of fuzzy muscle contraction and activation model using multi-objective optimisation. In *Systems Conference, 2010 4th Annual IEEE*, 2010. doi: 10.1109/SYSTEMS.2010.5482462.

[122] T. Ingman, T. Nieminen, and K. Hurmerinta. Cephalometric comparison of pharyngeal changes in subjects with upper airway resistance syndrome or obstructive sleep apnoea in upright and supine positions. *European Journal of Orthodontics*, 26:321–326, 2004. doi: 10.1093/ejo/26.3.321.

[123] *Intel(R) Threading Building Blocks: Reference Manual*. Intel Corporation, 2011. URL `http://software.intel.com/sites/products/documentation/hpc/tbb/referencev3.pdf`. Document no. 315415-015US. Accessed June 2013.

[124] I. Ionescu, T. Conway, A. Schonning, M. Almutairi, and D. W. Nicholson. Solid modeling and static finite element analysis of the human tibia. In *2003 Summer Bioengineering Conference*, Key Biscayne, Florida, USA, 25-29 June 2003.

[125] S. Isono, J. E. Remmers, A. Tanaka, Y. Sho, J. Sato, and T. Nishino. Anatomy of pharynx in patients with obstructive sleep apnea and in normal subjects. *Journal of Applied Physiology*, 82:1319–1326, 1997.

[126] S. Isono, A. Tanaka, and T. Nishino. Effects of tongue electrical stimulation on pharyngeal mechanics in anaesthetized patients with obstructive sleep apnoea. *European Respiratory Journal*, 14:1258–1265, 1999.

[127] S. Isono, A. Tanaka, and T. Nishino. Dynamic interaction between the tongue and soft palate during obstructive apnea in anesthetized patients with sleep-disordered breathing. *Journal of Applied Physiology*, 95:2257–2264, 2003. doi: 10.1152/japplphysiol.00402.2003.

[128] Y. Ito, G. C. Cheng, A. M. Shih, R. P. Koomullil, B. K. Soni, S. Sittitavornwong, and P. D. Waite. Patient-specific geometry modeling and mesh generation for simulating obstructive sleep apnea syndrome cases by maxillomandibular advancement. *Mathematics and Computers in Simulation*, 81:1876–1891, 2011. doi: 10.1016/j.matcom.2011.02.006.

[129] S. Jaric and M.L. Latash. The equilibrium-point hypothesis is still doing fine. *Human Movement Science*, 19:933–938, 2000. doi: 10.1016/S0167-9457(01)00041-0.

[130] A. Javili and P. Steinmann. A finite element framework for continua with boundary energies. Part II: The three-dimensional case. *Computer Methods in Applied Mechanics and Engineering*, 199:755–765, 2010. doi: 10.1016/j.cma.2009.11.003.

[131] S. T. Jayaraju, M. Brouns, S. Verbanck, and C. Lacor. Fluid flow and particle deposition analysis in a realistic extrathoracic airway model using unstructured grids. *Journal of Aerosol Science*, 38:494–508, 2007. doi: 10.1016/j.jaerosci.2007.03.003.

[132] S-J. Jeong, W-S. Kim, and S-J. Sung. Numerical investigation on the flow characteristics and aerodynamic force of the upper airway of patient with obstructive sleep apnea using computational fluid dynamics. *Medical Engineering & Physics*, 29:637–651, 2007. doi: 10.1016/j.medengphy.2006.08.017.

[133] T. Johansson, P. Meier, and R. Blickhan. A finite-element model for the mechanical analysis of skeletal muscles. *Journal of Theoretical Biology*, 206:131–149, 2000. doi: 10.1006/jtbi.2000.2109.

[134] N. T. Johnson and J. Chinn. Uvulopalatopharyngoplasty and inferior sagittal mandibular osteotomy with genioglossus advancement for treatment of obstructive sleep apnea. *Chest Journal*, 105:278–283, 1994. doi: 10.1378/chest.105.1.278.

[135] Y. Kajee, J-P. V. Pelteret, and B. D. Reddy. The biomechanics of the human tongue. *International Journal for Numerical Methods in Biomedical Engineering*, 29:492–514, 2013. doi: 10.1002/cnm.2531.

[136] G. Karypis and V. Kumar. MeTis: Unstructured graph partitioning and sparse matrix ordering system, version 4.0, 2009. URL `http://glaros.dtc.umn.edu/gkhome/views/metis`. Accessed July 2013.

[137] E. S. Katz and D. P. White. Genioglossus activity during sleep in normal control subjects and children with obstructive sleep apnea. *American Journal of Respiratory and Critical Care Medicine*, 170:553–560, 2004. doi: 10.1164/rccm.200403-262OC.

[138] E. S. Katz, C. L. Marcus, and D. P. White. Influence of airway pressure on genioglossus activity during sleep in normal children. *American Journal of Respiratory and Critical Care Medicine*, 173:902–909, 2006. doi: 10.1164/rccm.200509-1450OC.

[139] K. Keyhani, P. W. Scherer, and M. M. Mozeli. Numerical simulation of airflow in the human nasal cavity. *Journal of Biomechanical Engineering*, 117:429–441, 1995. doi: 10.1115/1.2794204.

[140] A. S. Khalil, B. E. Bouma, and M. R. Kaazempur Mofrad. A combined FEM/genetic algorithm for vascular soft tissue elasticity estimation. *Cardiovascular Engineering*, 6:93–102, 2006. doi: 10.1007/s10558-006-9013-5.

[141] J. A. Kieser, M. G. Farland, H. Jack, M. Farella, Y. Wang, and O. Röhrle. The role of oral soft tissues in swallowing function: what can tongue pressure tell us? *Australian Dental Journal*, Accepted, 2013. doi: 10.1111/adj.12103.

[142] W. Kim and M. Voss. Multicore desktop programming with Intel Threading Building Blocks. *IEEE Software*, 28: 23–31, 2011. doi: 10.1109/MS.2011.12.

[143] M. Kojic, S. Mijailovic, and N. Zdravkovic. Modelling of muscle behaviour by the finite element method using Hill's three-element model. *International Journal for Numerical Methods in Engineering*, 43:941–953, 1998. doi: 10.1002/(SICI)1097-0207(19981115)43:5<941::AID-NME435>3.0.CO;2-3.

[144] D. P. Kuehn and J. C. Kahane. Histologic study of the normal human adult soft palate. *The Cleft Palate–Craniofacial Journal*, 27:26–35, 1990. doi: 10.1597/1545-1569(1990)027<0026:HSOTNH>2.3.CO;2.

[145] K. Lange. *Optimization*. Springer-Verlag, New York, USA, 2004. ISBN 0-387-20332-X.

[146] W. R. Ledoux and J. J. Blevins. The compressive material properties of the plantar soft tissue. *Journal of Biomechanics*, 40:2975–2981, 2007. doi: 10.1016/j.jbiomech.2007.02.009.

[147] J-H. Lee, Y. Na, S-K. Kim, and S-K. Chung. Unsteady flow characteristics through a human nasal airway. *Respiratory Physiology & Neurobiology*, 172:136–146, 2010. doi: 10.1016/j.resp.2010.05.010.

[148] I. Lekšan, M. Marcikić, V. Nikolić, R. Radić, and R. Selthofer. Morphological classification and sexual dimorphism of hyoid bone: New approach. *Collegium Antropologicum*, 29:237–242, 2005.

[149] R. R. Lemos, M. Epstein, W. Herzog, and B. Wyvill. A framework for structured modeling of skeletal muscle. *Computer Methods in Biomechanics and Biomedical Engineering*, 7:305–317, 2004. doi: 10.1080/10255840412331317398.

[150] H. Li and Q. Zhang. Multiobjective optimization problems with complicated pareto sets, MOEA/D and NSGA-II. *IEEE Transactions on Evolutionary Computation*, 13:284–302, 2009. doi: 10.1109/TEVC.2008.925798.

[151] J. Li, X. Y. Luo, and Z. B. Kuang. A nonlinear anisotropic model for porcine aortic heart valves. *Journal of Biomechanics*, 34:1279–1289, 2001. doi: 10.1016/S0021-9290(01)00092-6.

[152] L. P. Li, J. Soulhat, M. D. Buschmann, and A. Shirazi-Adl. Nonlinear analysis of cartilage in unconfined ramp compression using a fibril reinforced poroelastic model. *Clinical Biomechanics*, 14:673–682, 1999. doi: 10.1016/S0268-0033(99)00013-3.

[153] A. Y. Liang. Simulation of tongue muscle deformation. Master's thesis, Massachusetts Institute of Technology, 2008.

[154] R. L. Lieber. *Skeletal Muscle Structure, Function and Plasticity: The Physiological Basis of Rehabilitation*. Lippincott, Williams and Wilkins, Maryland, USA, 2nd edition, 2002. ISBN 9780781730617.

[155] R. L. Lieber, E. Runesson, F. Einarsson, and J. Fridén. Inferior mechanical properties of spastic muscle bundles due to hypertrophic but compromised extracellular matrix material. *Muscle & Nerve*, 28:464–471, 2003. doi: 10.1002/mus.10446.

[156] Y. Liu, M. R. Johnson, E. A. Matida, S. Kherani, and J. Marsan. Creation of a standardized geometry of the human nasal cavity. *Journal of Applied Physiology*, 106:784–795, 2009. doi: 10.1152/japplphysiol.90376.2008.

[157] Z. S. Liu, X. Y. Luo, H. P. Lee, and C. Lu. Snoring source identification and snoring noise prediction. *Journal of Biomechanics*, 40:861–870, 2007. doi: 10.1016/j.jbiomech.2006.03.022.

[158] D. G. Lloyd and T. F. Besier. An EMG-driven musculoskeletal model to estimate muscle forces and knee joint moments in vivo. *Journal of Biomechanics*, 36:765–776, 2003. doi: 10.1016/S0021-9290(03)00010-1.

[159] J. E. Lloyd, I. Stavness, and S. Fels. ArtiSynth: a fast interactive biomechanical modeling toolkit combining multibody and finite element simulation. *Soft Tissue Biomechanical Modeling for Computer Assisted Surgery*, 11:355–394, 2012. doi: 10.1007/8415_2012_126.

[160] Y. T. Lu, H. X. Zhu, S. Richmond, and J. Middleton. Numerical modelling of the fibre–matrix interaction in biaxial loading for hyperelastic soft tissue models. *International Journal for Numerical Methods in Biomedical Engineering*, 28:401–411, 2012. doi: 10.1002/cnm.1455.

[161] A. D. Lucey, A. J. C. King, G. A. Tetlow, J. Wang, J. J. Armstrong, M. S. Leigh, A. Paduch, J. H. Walsh, D. D. Sampson, P. R. Eastwood, and D. R. Hillman. Measurement, reconstruction, and flow-field computation of the human pharynx with application to sleep apnea. *IEEE Transactions on Biomedical Engineering*, 57:2535–2548, 2010. doi: 10.1109/TBME.2010.2052808.

[162] M. Madani. Surgical treatment of snoring and mild obstructive sleep apnea. *Oral & Maxillofacial Surgery Clinics of North America*, 14:333–350, 2002. doi: 10.1016/S1042-3699(02)00028-6.

[163] G.T. Malcom, A. K. Bhattacharyya, M. Velez-Duran, M. A. Guzman, M. C. Oalmann, and J. P. Strong. Fatty acid composition of adipose tissue in humans: differences between subcutaneous sites. *American Journal of Clinical Nutrition*, 50:288–291, 1989.

[164] A. Malhotra and D. P. White. Obstructive sleep apnoea. *The Lancet*, 360:237–245, 2002. doi: 10.1016/S0140-6736(02)11967-2.

[165] A. Malhotra, G. Pillar, R. B. Fogel, J. Beauregard, J. K. Edwards, D. I. Slamowitz, S. A. Shea, and D. P. White. Genioglossal but not palatal muscle activity relates closely to pharyngeal pressure. *American Journal of Respiratory and Critical Care Medicine*, 162:1058–1062, 2000. doi: 10.1164/ajrccm.162.3.9912067.

[166] A. Malhotra, Y. Huang, R. B. Fogel, G. Pillar, J. K. Edwards, R. Kikinis, S. H. Loring, and D. P. White. The male predisposition to pharyngeal collapse: Importance of airway length. *American Journal of Respiratory and Critical Care Medicine*, 166:1388–1395, 2002. doi: 10.1164/rccm.2112072.

[167] A. Malhotra, G. Pillar, R. B. Fogel, J. K. Edwards, N. Ayas, T. Akahoshi, D. Hess, and D. P. White. Pharyngeal pressure and flow effects on genioglossus activation in normal subjects. *American Journal of Respiratory and Critical Care Medicine*, 165:71–77, 2002. doi: 10.1164/ajrccm.165.1.2011065.

[168] A. Malhotra, S. Bertisch, and A. Wellman. Complex sleep apnea: It isn't really a disease. *Journal of Clinical Sleep Medicine*, 4:406–408, 2008.

[169] M. Malvé, S. Chandra, J. L. López-Villalobos, E. A. Finol, A. Ginel, and M. Doblaré. CFD analysis of the human airways under impedance- based boundary conditions: application to healthy, diseased and stented trachea. *Computer Methods in Biomechanics and Biomedical Engineering*, 16:198–216, 2013. doi: 10.1080/10255842.2011.615743.

[170] J. A. C. Martins, E. B. Pires, R. Salvado, and P. B. Dinis. A numerical model of passive and active behaviour of skeletal muscles. *Computer Methods in Applied Mechanics and Engineering*, 151:419–433, 1998. doi: 10.1016/S0045-7825(97)00162-X.

[171] J. A. C. Martins, M. P. M. Pato, and E. B. Pires. A finite element model of skeletal muscles. *Virtual and Physical Prototyping*, 1:159–170, 2006. doi: 10.1080/17452750601040626.

[172] Materialise NV. Mimics: Medical image segmentation for engineering on anatomy, December 2010. URL `http://biomedical.materialise.com/mimics`. Accessed July 2013.

[173] P. Mayer, J-L. Pépin, G. Bettega, D. Veale, G. Ferretti, C. Deschaux, and P. Lévy. Relationship between body mass index, age and upper airway measurements in snorers and sleep apnoea patients. *European Respiratory Journal*, 9:1801–1809, 1996. doi: 10.1183/09031936.96.09091801.

[174] W. T. McNicholas. The nose and OSA: variable nasal obstruction may be more important in pathophysiology than fixed obstruction. *European Respiratory Journal*, 32:3–8, 2008. doi: 10.1183/09031936.00050208.

[175] D. W. McRobbie, S. Pritchard, and R. A. Quest. Studies of the human oropharyngeal airspaces using magnetic resonance imaging. I. Validation of a three-dimensional MRI method for producing ex vivo virtual and physical casts of the oropharyngeal airways during inspiration. *Journal of Aerosol Medicine*, 16:401–415, 2003. doi: 10.1089/089426803772455668.

[176] C. Miehe. Aspects of the formulation and finite strain element inplementation of large strain isotropic elasticity. *International Journal for Numerical Methods in Engineering*, 37:1981–2004, 1994. doi: 10.1002/nme.1620371202.

[177] M. Mihaescu, S. Murugappan, M. Kalra, S. Khosla, and E. Gutmark. Large Eddy Simulation and Reynolds-Averaged Navier–Stokes modeling of flow in a realistic pharyngeal airway model: An investigation of obstructive sleep apnea. *Journal of Biomechanics*, 41:2279–2288, 2008. doi: 10.1016/j.jbiomech.2008.04.013.

[178] S. M. Mijailovich, J. J. Fredberg, and J. P. Butler. On the theory of muscle contraction: Filament extensibility and the development of isometric force and stiffness. *Biophysical Journal*, 71:1475–1484, 1996. doi: 10.1016/S0006-3495(96)79348-7.

[179] J. L. Miller, K. L. Watkin, and M. F. Chen. Muscle, adipose, and connective tissue variations in intrinsic musculature of the adult human tongue. *Journal of Speech, Language, and Hearing Research*, 45:51–65, 2002. doi: 10.1044/1092-4388(2002/004).

[180] J. E. Miller-Young, N. A. Duncan, and G. Baroud. Material properties of the human calcaneal fat pad in compression: experiment and theory. *Journal of Biomechanics*, 35:1523–1531, 2002. doi: 10.1016/S0021-9290(02)00090-8.

[181] R. P. Millman, C. L. Rosenberg, C. C. Carlisle, N. R. Kramer, D. M. Kahn, and A. E. Bonitati. The efficacy of oral appliances in the treatment of persistent sleep apnea after uvulopalatopharyngoplasty. *Chest Journal*, 113:992–996, 1998. doi: 10.1378/chest.113.4.992.

[182] M. Mitchell. *An Introduction to Genetic Algorithms*. MIT Press, Massachusetts, USA, 1st edition, 1999. ISBN 0−262−13316−4.

[183] K. Miyawaki, H. Hirose, T. Ushijima, and M. Sawashima. A preliminary report on the electromyographic study of the activity of lingual muscles. *Annual Bulletin Research Institute of Logopedics and Phoniatrics*, 9:91–106, 1975.

[184] J. J. Moré and D. J. Thuente. Line search algorithms with guaranteed sufficient decrease. *ACM Transactions on Mathematical Software*, 20:286–307, 1994. doi: 10.1145/192115.192132.

[185] M. E. Mortley. *The Development and Disorders of Speech in Childhood*. Churchhill Livingstone, Edinburgh, Scotland, 2nd edition, 1972. ISBN 9780443008955.

[186] D. J. Murray-Smith. The inverse simulation approach: a focused review of methods and applications. *Mathematics and Computers in Simulation*, 53:239–247, 2000. doi: 10.1016/S0378-4754(00)00210-X.

[187] S. Murtada, Kroon M., and G. A. Holzapfel. Modeling the dispersion effects of contractile fibers in smooth muscles. *Journal of the Mechanics and Physics of Solids*, 58:2065–2082, 2010. doi: 10.1016/j.jmps.2010.09.003.

[188] G. Mylavarapu, S. Murugappan, M. Mihaescu, M. Kalra, S. Khosla, and E. Gutmark. Validation of computational fluid dynamics methodology used for human upper airway flow simulations. *Journal of Biomechanics*, 42:1553–1559, 2009. doi: 10.1016/j.jbiomech.2009.03.035.

[189] J. C. Nagtegaal, D. M. Parks, and J. R. Rice. On numerically accurate finite element solutions in the fully plastic range. *Computer Methods in Applied Mechanics and Engineering*, 4:153–177, 1974. doi: 10.1016/0045-7825(74)90032-2.

[190] V. J. Napadow, Q. Chen, V. J. Wedeen, and R. J. Gilbert. Intramural mechanics of the human tongue in association with physiological deformations. *Journal of Biomechanics*, 32:1–12, 1999. doi: 10.1016/S0021-9290(98)00109-2.

[191] N. Nashi, S. Kang, G. C. Barkdull, J. Lucas, and T. M. Davidson. Lingual fat at autopsy. *The Laryngoscope*, 117: 1467–1473, 2007. doi: 10.1097/MLG.0b013e318068b566.

[192] R. R. Neptune, C. P. McGowan, and S. A. Kautz. Forward dynamics simulations provide insight into muscle mechanical work during human locomotion. *Exercise and Sport Sciences Reviews*, 37:203–210, 2009. doi: 10.1097/JES.0b013e3181b7ea29.

[193] N. Nethercote and J. Seward. Valgrind: A framework for heavyweight dynamic binary instrumentation. In *Proceedings of the ACM SIGPLAN International Conference on Object-Oriented Programming, Systems, Languages and Applications*, pages 89–100, San Diego, California, USA, June 2007. doi: 10.1145/1250734.1250746.

[194] P. Ngatchou, A. Zarei, and M. A. El-Sharkawi. Pareto multi objective optimization. In *Proceedings of the 13th International Conference on Intelligent Systems Application to Power Systems, 2005.*, pages 84–91, Arlington, Virginia, USA, 6-10 November 2005. IEEE. doi: 10.1109/ISAP.2005.1599245.

[195] P. Nithiarasu, C. B. Liu, and N. Massarotti. Laminar and turbulent flow calculations through a model human upper airway using unstructured meshes. *Communications in Numerical Methods in Engineering*, 23:1057–1069, 2007. doi: 10.1002/cnm.939.

[196] P. Nithiarasu, O. Hassan, K. Morgan, N. P. Weatherill, C. Fielder, H. Whittet, P. Ebden, and K. R. Lewis. Steady flow through a realistic human upper airway geometry. *International Journal for Numerical Methods in Fluids*, 57:631–651, 2008. doi: 10.1002/fld.1805.

[197] G. M. Odegard, T. L. Haut Donahue, D. A. Morrow, and K. R. Kaufman. Constitutive modeling of skeletal muscle tissue with an explicit strain-energy function. *Journal of Biomechanical Engineering*, 130:061017–1–061017–9, 2008. doi: 10.1115/1.3002766.

[198] T. Ogawa, R. Enciso, W. H. Shintaku, and G. T. Clark. Evaluation of cross-section airway configuration of obstructive sleep apnea. *Oral Surgery, Oral Medicine, Oral Pathology, Oral Radiology and Endodontology*, 103:102–108, 2007. doi: 10.1016/j.tripleo.2006.06.008.

[199] A. Oliven, N. Tov, L. Geitini, U. Steinfeld, R. Oliven, A. R. Schwartz, and M. Odeh. Effect of genioglossus contraction on pharyngeal lumen and airflow in sleep apnoea patients. *European Respiratory Journal*, 30:748–758, 2007. doi: 10.1183/09031936.00131106.

[200] T. Ono, A. A. Lowe, K. A. Ferguson, E-K. Pae, and J. A. Fleetham. The effect of the tongue retaining device on awake genioglossus muscle activity in patients with obstructive sleep apnea. *American Journal of Orthodontics and Dentofacial Orthopedics*, 110:28–35, 1996. doi: 10.1016/S0889-5406(96)70084-7.

[201] C. W. J. Oomens, M. Maenhout, C. H. van Oijen, M. R. Drost, and F. P. Baaijens. Finite element modelling of contracting skeletal muscle. *Philosophical Transactions of the Royal Society B: Biological Sciences*, 358:1453–1460, 2003. doi: 10.1098/rstb.2003.1345.

[202] J. E. Osborne, E. Z. Osman, P. D. Hill, B. V. Lee, and C. Sparkes. A new acoustic method of differentiating palatal from non–palatal snoring. *Clinical Otolaryngology*, 24:130–133, 1999. doi: 10.1046/j.1365-2273.1999.00229.x.

[203] D. J Ostry and A. G. Feldman. A critical evaluation of the force control hypothesis in motor control. *Experimental Brain Research*, 153:275–288, 2003. doi: 10.1007/s00221-003-1624-0.

[204] E. Otten. Inverse and forward dynamics: models of multi-body systems. *Philosophical Transactions of the Royal Society B: Biological Sciences*, 358:1493–1500, 2003. doi: 10.1098/rstb.2003.1354.

[205] M. M. Ōzbek, K. Miyamoto, A. A. Lowe, and J. A. Fleetham. Natural head posture, upper airway morphology and obstructive sleep apnoea severity in adults. *European Journal of Orthodontics*, 20:133–143, 1998. doi: 10.1093/ejo/20.2.133.

[206] E-K. Pae, A. A. Lowe, and J. A. Fleetham. A role of pharyngeal length in obstructive sleep apnea patients. *American Journalof Orthodontics and Dentofacial Orthopedics*, 111:12–17, 1997. doi: 10.1016/S0889-5406(97)70296-8.

[207] M. G. Pandy. Computer modelling and simulation of human movement. *Annual Review of Biomedical Engineering*, 3:245–273, 2001. doi: 10.1146/annurev.bioeng.3.1.245.

[208] M. G. Pandy, F. E. Zajac, E. Sim, and W. S. Levine. An optimal control model for maximum-height human jumping. *Journal of Biomechanics*, 23:1185–1198, 1990. doi: 10.1016/0021-9290(90)90376-E.

[209] S. Pearce and P. Saunders. Obstructive sleep apnoea can directly cause death. *Thorax*, 58:369, 2003. doi: 10.1136/thorax.58.4.369.

[210] J-P. V. Pelteret and A. McBride. `deal.II` step-44 tutorial: Three-field formulation for non-linear solid mechanics, 2010. URL `http://www.dealii.org/developer/doxygen/deal.II/step_44.html`. Accessed July 2013.

[211] J-P. V. Pelteret and B. D. Reddy. Computation model of tissues in the human upper airway, August 2010. Poster presented in Respiratory Mechanics Track, 6th World Congress of Biomechanics (WCB 2010), Singapore.

[212] J-P. V. Pelteret and B. D. Reddy. Computational model of soft tissues in the human upper airway. *International Journal for Numerical Methods in Biomedical Engineering*, 28:111–132, 2012. doi: 10.1002/cnm.1487.

[213] J-P. V. Pelteret and B. D. Reddy. Development of a computational biomechanical model of the human upper–airway soft–tissues towards simulating obstructive sleep apnea. *Clinical Anatomy*, 2013. doi: 10.1002/ca.22313. Accepted.

[214] P. Perrier, D. J. Ostry, and R. Laboissière. The equilibrium point hypothesis and its application to speech motor control. *Journal of Speech and Hearing Research*, 39:365–378, 1996.

[215] P. Perrier, Y. Payan, M. Zandipour, and J. Perkell. Influences of tongue biomechanics on speech movements during the production of velar stop consonants: A modeling study. *Journal of the Acoustical Society of America*, 114:1582–1599, 2003. doi: 10.1121/1.1587737.

[216] P. Perrier, Y. Payan, S. Buchaillard, M. A. Nazari, and M. Chabanas. Biomechanical models to study speech. *Faits de Langues*, 37:155–171, 2011.

[217] S. C. Persak, S. Sin, J. M. McDonough, R. Arens, and D. M. Wootton. Noninvasive estimation of pharyngeal airway resistance and compliance in children based on volume-gated dynamic MRI and computational fluid dynamics. *Journal of Applied Physiology*, 111:1819–1827, 2011. doi: 10.1152/japplphysiol.01230.2010.

[218] C. S. Peskin. *Mathematical Aspects of Heart Physiology*. Courant Institute of Mathematical Sciences, New York, USA, 1975.

[219] D.R. Peterson and J.D. Bronzino, editors. *Biomechanics: Principles and Applications*. CRC Press, Florida, USA, 2008. ISBN 978-0-8493-8534-6.

[220] D. Pevernagie, R. M. Aarts, and M. De Meyer. The acoustics of snoring. *Sleep Medicine Reviews*, 14:131–144, 2010. doi: 10.1016/j.smrv.2009.06.002.

[221] R. Pierce, D. White, A. Malhotra, J.K. Edwards, D. Kleverlaan, L. Palmer, and J. Trinder. Upper airway collapsibility, dilator muscle activation and resistance in sleep apnoea. *European Respiratory Journal*, 30:345–353, 2007. doi: 10.1183/09031936.00063406.

[222] J. Planas, G. V. Guinea, and M. Elices. Constitutive model for fiber-reinforced materials with deformable matrices. *Physical Review E - Statistical, Nonlinear and Soft Matter Physics*, 76:041903, 2007. doi: 10.1103/PhysRevE.76.041903.

[223] A. Pollard, M. Uddin, A. M. Shinneeb, and C. G. Ball. Recent advances and key challenges in investigations of the flow inside human oro-pharyngeal-laryngeal airway. *International Journal of Computational Fluid Dynamics*, 26:363–381, 2012. doi: 10.1080/10618562.2012.668616.

[224] W.H. Press, S.A. Teukolsky, W.T. Vetterling, and B.P. Flannery. *Numerical Recipies: The Art of Scientific Computing*. Cambridge University Press, New York, USA, 3rd edition, 2007. ISBN 978-0521880688.

[225] B. I. Prilutsky and V. M. Zatsiorsky. Optimization-based models of muscle coordination. *Exercise and Sport Sciences Reviews*, 30:32–38, 2002.

[226] S. S. Rao. *Mechanical Vibrations*. Pearson Prentice Hall, Singapore, 4th edition, 2004. ISBN 9780130489876.

[227] M. Rappai, N. Collop, S. Kemp, and R. deShazo. The nose and sleep-disordered breathing: What we know and what we do not know. *Chest Journal*, 124:2309–2323, 2003. doi: 10.1378/chest.124.6.2309.

[228] D. E. Rassier, W. Herzog, J. Wakeling, and D. A. Syme. Stretch-induced, steady-state force enhancement in single skeletal muscle fibers exceeds the isometric force at optimum fiber length. *Journal of Biomechanics*, 36:1309–1316, 2003. doi: 10.1016/S0021-9290(03)00155-6.

[229] S. Reese, P. Wriggers, and B. D. Reddy. A new locking-free brick element technique for large deformation problems in elasticity. *Computers and Structures*, 75:291–304, 2000. doi: 10.1016/S0045-7949(99)00137-6.

[230] D. T. Reilly and A. H. Burstein. The mechanical properties of cortical bone. *The Journal of Bone and Joint Surgery*, 56:1001–1022, 1974.

[231] J. E. Remmers, W. J. de Groot, E. K. Sauerland, and A. M. Anch. Pathogenesis of upper airway occlusion during sleep. *Journal of Applied Physiology: respiratory, environmental and exercise physiology*, 44:931–938, 1978.

[232] M. A. F. Rodrigues, D. F. Gillies, and P. Charters. Realistic deformable models for simulating the tongue during laryngoscopy. In *MIAR01: Proceedings of the International Workshop on Medical Imaging and Augmented Reality*, pages 125–130, Shatin, Hong Kong, 10–12 June 2001. doi: 10.1109/MIAR.2001.930274.

[233] M. L. Roemhildt, K. M. Coughlin, G. D. Peura, B. C. Fleming, and B. D. Beynnon. Material properties of articular cartilage in the rabbit tibial plateau. *Journal of Biomechanics*, 39:2331–2337, 2006. doi: 10.1016/j.jbiomech.2005.07.017.

[234] O. Röhrle. Simulating the electro-mechanical behavior of skeletal muscles. *Computing in Science & Engineering*, 12: 48–58, 2010.

[235] O. Röhrle and A. J. Pullan. Three-dimensional finite element modelling of muscle forces during mastication. *Journal of Biomechanics*, 40:3363–3372, 2007. doi: 10.1016/j.jbiomech.2007.05.011.

[236] P. Rombaux, G. Liistro, M. Hamoir, B. Bertrand, G. Aubert, T. Verse, and D. Rodenstein. Nasal obstruction and its impact on sleep-related breathing disorders. *Rhinology*, 43:242–250, 2005.

[237] G. Rudolph. Convergence analysis of canonical genetic algorithms. *IEEE Transactions on Neural Networks*, 5:96–101, 1994. doi: 10.1109/72.265964.

[238] C. M. Ryan and T. D. Bradley. Pathogenesis of obstructive sleep apnea. *Journal of Applied Physiology*, 99:2440–2450, 2005. doi: 10.1152/japplphysiol.00772.2005.

[239] C.F. Ryan, L. L. Love, D. Peat, J. A. Fleetham, and A. A. Lowe. Mandibular advancement oral appliance therapy for obstructive sleep apnoea: effect on awake calibre of the velopharynx. *Thorax*, 54:972–977, 1999. doi: 10.1136/thx.54.11.972.

[240] M. S. Sacks and W. Sun. Multiaxial mechanical behavior of biological materials. *Annual Review of Biomedical Engineering*, 5:251–284, 2003. doi: 10.1146/annurev.bioeng.5.011303.120714.

[241] H. Saigusa, K. Yamashita, K. Tanuma, M. Saigusa, and S. Niimi. Morphological studies for retrusive movement of the human adult tongue. *Clinical Anatomy*, 17:93–98, 2004. doi: 10.1002/ca.10156.

[242] P. H. Saksono, P. Nithiarasu, I. Sazonov, and S. Y. Yeo. Computational flow studies in a subject-specific human upper airway using a one-equation turbulence model. Influence of the nasal cavity. *International Journal for Numerical Methods in Engineering*, 87:96–114, 2011. doi: 10.1002/nme.2986.

[243] I. Sanders and L. Mu. A three-dimensional atlas of human tongue muscles. *The Anatomical Record*, 296:1102–1114, 2013. doi: 10.1002/ar.22711.

[244] V. Sanguineti, R. Laboissière, and Y. Payan. A control model of human tongue movements in speech. *Biological Cybernetics*, 77:11–22, 1997. doi: 10.1007/s004220050362.

[245] V. Sanguineti, R. Laboissière, and D. J. Ostry. A dynamic biomechanical model for neural control of speech production. *Journal of the Acoustical Society of America*, 103:1615–1627, 1998. doi: 10.1121/1.421296.

[246] C. Sansour. On the physical assumptions underlying the volumetric-isochoric split and the case of anisotropy. *European Journal of Mechanics – A/Solids*, 27:28–39, 2008. doi: 10.1016/j.euromechsol.2007.04.001.

[247] E. K. Sauerland and R. M. Harper. The human tongue during sleep: Electromyographic activity of the genioglossus muscle. *Experimental Neurology*, 51:160–170, 1976. doi: 10.1016/0014-4886(76)90061-3.

[248] R. J. Schwab, M. Pasirstein, R. Pierson, A. Mackley, R. Hachadoorian, R. Arens, G. Maislin, and A. I. Pack. Identification of upper airway anatomic risk factors for obstructive sleep apnea with volumetric magnetic resonance imaging. *American Journal of Respiratory and Critical Care Medicine*, 168:522–530, 2003. doi: 10.1164/rccm.200208-866OC.

[249] Y. Segal, A. Malhotra, and G. Pillar. Upper airway length may be associated with the severity of obstructive sleep apnea syndrome. *Sleep and Breathing*, 12:311–316, 2008. doi: 10.1007/s11325-008-0191-9.

[250] F. Sériès, S. St. Pierre, and G. Carrier. Effects of surgical correction of nasal obstruction in the treatment of obstructive sleep apnea. *American Review of Respiratory Disease*, 146:1261–1265, 1992. doi: 10.1164/ajrccm/146.5_Pt_1.1261.

[251] B. Sharafi and S. S. Blemker. A micromechanical model of skeletal muscle to explore the effects of fiber and fascicle geometry. *Journal of Biomechanics*, 43:3207–3213, 2010. doi: 10.1016/j.jbiomech.2010.07.020.

[252] B. Shome, L. P. Wang, M. H. Santare, A. K. Prasad, A. Z. Szeri, and D. Roberts. Modelling of airflow in the pharynx with application to sleep apnea. *Journal of Biomechanical Engineering*, 120:416–422, 1998. doi: 10.1115/1.2798009.

[253] J. C. Simo and R. L. Taylor. Quasi-incompressible finite elasticity in principal stretches. Continuum basis and numerical algorithms. *Computer Methods in Applied Mechanics and Engineering*, 85:273–310, 1991. doi: 10.1016/0045-7825(91)90100-K.

[254] J. C. Simo, R. L. Taylor, and K. S. Pister. Variational and projection methods for the volume constraint in finite deformation elasto-plasticity. *Computer Methods in Applied Mechanics and Engineering*, 51:177–208, 1985. doi: 10.1016/0045-7825(85)90033-7.

[255] S. Sittitavornwong, P. D. Waite, A. M. Shih, R. Koomullil, Y. Ito, G. C. Cheng, and D. Wang. Evaluation of obstructive sleep apnea syndrome by computational fluid dynamics. *Seminars in Orthodontics*, 15:105–131, 2009. doi: 10.1053/j.sodo.2009.01.005.

[256] A. J. Sokoloff. Activity of tongue muscles during respiration: it takes a village? *Journal of Applied Physiology*, 96:438–439, 2004. doi: 10.1152/japplphysiol.01079.2003.

[257] V. Spitzer, M. J. Ackerman, A. L. Scherzinger, and D. Whitlock. The visible human male: A technical report. *Journal of the American Medical Informatics Association*, 3:118–130, 1996. doi: 10.1136/jamia.1996.96236280.

[258] L. A. Spyrou and N. Aravas. Muscle and tendon tissues: Constitutive modeling and computational issues. *Journal of Applied Mechanics*, 78:041015–1–041015–10, 2011. doi: 10.1115/1.4003741.

[259] P. Stål, S. Marklund, L. E. Thornell, R. De Paul, and P. O. Eriksson. Fibre composition of human intrinsic tongue muscles. *Cells Tissues Organs*, 173:147–161, 2003. doi: 10.1159/000069470.

[260] J. Stålhand, A. Klarbring, and M. Karlsson. Towards in vivo aorta material identification and stress estimation. *Biomechanics and modelling in mechanobiology*, 2:169–186, 2004. doi: 10.1007/s10237-003-0038-z.

[261] M. L. Stanchina, A. Malhotra, R. B. Fogel, N. Ayas, J. K. Edwards, K. Schory, and D. P. White. Genioglossus muscle responsiveness to chemical and mechanical stimuli during non–rapid eye movement sleep. *American Journal of Respiratory and Critical Care Medicine*, 165:945–949, 2002. doi: 10.1164/ajrccm.165.7.2108076.

[262] K. W. Stapleton, E. Guentsch, M. K. Hoskinson, and W. H. Finlay. On the suitability of $k-\epsilon$ turbulence modeling for aerosol deposition in the mouth and throat: a comparison with experiment. *Journal of Aerosol Science*, 31:739–749, 2000. doi: 10.1016/S0021-8502(99)00547-9.

[263] I. Stavness, J. E. Lloyd, Y. Payan, and S. Fels. Coupled hard-soft tissue simulation with contact and constraints applied to jaw-tongue-hyoid dynamics. *International Journal for Numerical Methods in Biomedical Engineering*, 27:367–390, 2011. doi: 10.1002/cnm.1423.

[264] I. K. Stavness. *Byte Your Tongue: A Computational Model of Human Mandibular-Lingual Biomechanics for Biomedical Applications*. PhD thesis, University of British Columbia, 2011.

[265] R. P. Subramaniam, R. B. Richardson, K. T. Morgan, J. S. Kimbell, and R. A. Guilmette. Computational fluid dynamics simulations of inspiratory airflow in the human nose and nasopharynx. *Inhalation Toxicology*, 10:91–120, 1998. doi: 10.1080/089583798197772.

[266] X. Sun, C. Yu, Y. Wang, and Y. Liu. Numerical simulation of soft palate movement and airflow in human upper airway by fluid-structure interaction method. *Acta Mechanica Sinica*, 23:359–367, 2007. doi: 10.1007/s10409-007-0083-4.

[267] S-J. Sung, S-J. Jeong, Y-S. Yu, C-J. Hwang, and E-K. Pae. Customized three-dimensional computational fluid dynamics simulation of the upper airway of obstructive sleep apnea. *The Angle Orthodontist*, 76:791–799, 2006. doi: 10.2319/071305-231.

[268] I. Szollosi, T. Roebuck, B. Thompson, and M. T. Naughton. Lateral sleeping position reduces severity of central sleep apnea/cheyne–stokes respiration. *Sleep*, 29:1045–1051, 2006.

[269] Y. Tagaito, S. Isono, A. Tanaka, T. Ishikawa, and T. Nishino. Sitting posture decreases collapsibility of the passive pharynx in anesthetized paralyzed patients with obstructive sleep apnea. *Anesthesiology*, 113:812–818, 2010. doi: 10.1097/ALN.0b013e3181f1b834.

[270] M. Tagaya, S. Nakata, F. Yasuma, A. Noda, N. Hamajima, N. Katayama, H. Otake, M. Teranishi, and T. Nakashima. Morphological features of elderly patients with obstructive sleep apnoea syndrome: a prospective controlled, comparative cohort study. *Clinical Otolaryngology*, 36:139–146, 2011. doi: 10.1111/j.1749-4486.2011.02296.x.

[271] H. Takemoto. Morphological analyses of the human tongue musculature for three-dimensional modeling. *Journal of Speech, Language, and Hearing Research*, 44:95–107, 2001. doi: 10.1044/1092-4388(2001/009).

[272] C. Y. Tang, G. Zhang, and C. P. Tsui. A 3D skeletal muscle model coupled with active contraction of muscle fibres and hyperelastic behaviour. *Journal of Biomechanics*, 42:865–872, 2009. doi: 10.1016/j.jbiomech.2009.01.021.

[273] E. Tarhan, M. Coskun, O. Cakmak, H. Celik, and M. Cankurtaran. Acoustic rhinometry in humans: accuracy of nasal passage area estimates, and ability to quantify paranasal sinus volume and ostium size. *Journal of Applied Physiology*, 99:616–623, 2005. doi: 10.1152/japplphysiol.00106.2005.

[274] H. E. D. J. ter Keurs, T. Iwazumi, and G. H. Pollack. The sarcomere length-tension relation in skeletal muscle. *Journal of General Physiology*, 72:565–592, 1978. doi: 10.1085/jgp.72.4.565.

[275] J. Teran, E. Sifakis, S. Blemker, V. Ng-Thow-Hing, C. Lau, and R. Fedkiw. Creating and simulating skeletal muscle from the visible human data set. *IEEE Transactions on Visualization and Computer Graphics*, 11:317–328, 2005. doi: 10.1109/TVCG.2005.42.

[276] R. J. Thomas, J. E. Mietus, C-K. Peng, G. Gilmartin, R. W. Daly, A. L. Goldberger, and D. J. Gottlieb. Differentiating obstructive from central and complex sleep apnea using an automated electrocardiogram-based method. *Sleep*, 30:1756–1769, 2007.

[277] L. H. Ting. Dimensional reduction in sensorimotor systems: a framework for understanding muscle coordination of posture. *Progress in Brain Research*, 165:299–321, 2007. doi: 10.1016/S0079-6123(06)65019-X.

[278] L. H. Ting and J. L. McKay. Neuromechanics of muscle synergies for posture and movement. *Current Opinion in Neurobiology*, 17:622–628, 2007. doi: 10.1016/j.conb.2008.01.002.

[279] U.S. National Library of Medicine. The Visible Human Project ®, August 2009. URL `http://www.nlm.nih.gov/research/visible/visible_human.html`. Accessed July 2013.

[280] A. J. van den Bogert, K. G. M. Gerritsen, and G. K. Cole. Human muscle modelling from a user's perspective. *Journal of Electromyography and Kinesiology*, 8:119–124, 1998. doi: 10.1016/S1050-6411(97)00028-X.

[281] K. van den Doel, F. Vogt, R. E. English, and S. Fels. Towards articulatory speech synthesis with a dynamic 3D finite element tongue model. 2006.

[282] C. A. Van Ee, A. L. Chasse, and B. S. Myers. Quantifying skeletal muscle properties in cadaveric test specimens: Effects of mechanical loading, postmortem time, and freezer storage. *Journal of Biomechanical Engineering*, 122:9–14, 2000. doi: 10.1115/1.429621.

[283] A. Van Hirtum, F. Chouly, A. Teule, Y. Payan, and X. Pelorson. In-vitro study of pharyngeal pressure losses at the origin of obstructive sleep apnea. In *Engineering in Medicine and Biology Society, 2003. Proceedings of the 25th Annual International Conference of the IEEE*, volume 1, Cancun, Mexico, September 17–21 2004. doi: 10.1109/IEMBS.2003.1279665.

[284] A. Van Hirtum, X. Pelorson, and P. Y. Lagrée. In vitro validation of some flow assumptions for the prediction of the pressure distribution during obstructive sleep apnoea. *Medical & Biological Engineering & Computing*, 43:162–171, 2005. doi: 10.1007/BF02345139.

[285] C. Van Holsbeke, J. De Backer, W. Vos, P. Verdonck, P. Van Ransbeeck, T. Claessens, M. Braem, O. Vanderveken, and W. De Backer. Anatomical and functional changes in the upper airways of sleep apnea patients due to mandibular repositioning: A large scale study. *Journal of Biomechanics*, 44:442–449, 2011. doi: 10.1016/j.jbiomech.2010.09.026.

[286] M. Van Loocke, C. G. Lyons, and C. K. Simms. A validated model of passive muscle in compression. *Journal of Biomechanics*, 39:2999–3009, 2006. doi: 10.1016/j.jbiomech.2005.10.016.

[287] M. Van Loocke, C. G. Lyons, and C. Simms. *Topics in Bio-Mechanical Engineering*, chapter VIII: The three-dimensional mechanical properties of skeletal muscle: experiments and modelling, pages 216–234. Trinity Centre for Bio-Engineering, Dublin, Ireland, 2007. ISBN 0-9548583-0-1.

[288] M. Van Loocke, C. G. Lyons, and C. K. Simms. Viscoelastic properties of passive skeletal muscle in compression: Stress-relaxation behaviour and constitutive modelling. *Journal of Biomechanics*, 41:1555–1566, 2008. doi: 10.1016/j.jbiomech.2008.02.007.

[289] M. Van Loocke, C. K. Simms, and C. G. Lyons. Viscoelastic properties of passive skeletal muscle in compression – cyclic behaviour. *Journal of Biomechanics*, 42:1038–1048, 2009. doi: 10.1016/j.jbiomech.2009.02.022.

[290] C. H. G. A. van Oijen. *Mechanics and design of fiber-reinforced vascular prostheses*. PhD thesis, Technische Universiteit Eindhoven, 2003. Eindhoven, Netherlands.

[291] M. Veldi, V. Vasar, T. Hion, M. Kull, and A. Vain. Ageing, soft-palate tone and sleep-related breathing disorders. *Clinical Physiology*, 21:358–364, 2001. doi: 10.1046/j.1365-2281.2001.00339.x.

[292] F. Vogt. *Towards an Interactive Framework for Upper Airway Modeling*. PhD thesis, University of British Columbia, 2009.

[293] F. Vogt, J. E. Lloyd, S. Buchaillard, P. Perrier, M. Chabanas, Y. Payan, and S. S. Fels. Efficient 3D finite element modeling of a muscle-activated tongue. In *Third International Symposium, ISBMS 2006*, pages 19–28, Zurich, Switzerland, July 10–11 2006. Springer. doi: 10.1007/11790273_3. ISBN 978-3540360094.

[294] P. D. Waite. Obstructive sleep apnea: A review of the pathophysiology and surgical management. *Oral Surgery, Oral Medicine, Oral Pathology, Oral Radiology and Endodontology*, 85:352–361, 1998. doi: 10.1016/S1079-2104(98)90056-7.

[295] Matthew Wall. GAlib: A C++ library of genetic algorithm components, July 2010. URL `http://lancet.mit.edu/ga/`. Version 2.4.7. Accessed July 2013.

[296] W. A. Wall and T. Rabczuk. Fluid–structure interaction in lower airways of CT-based lung geometries. *International Journal for Numerical Methods in Fluids*, 57:653–675, 2008. doi: 10.1002/fld.1763.

[297] W. A. Wall, L. Wiechert, A. Comerford, and S. Rausch. Towards a comprehensive computational model for the respiratory system. *International Journal for Numerical Methods in Biomedical Engineering*, 26:807–827, 2010. doi: 10.1002/cnm.1378.

[298] J. Wang, G. A. Tetlow, and A. D. Lucey. Flow-structure interaction in the upper airway: Motions of a cantilevered flexible plate in channel flow with flexible walls. In *16th Australasian Fluid Mechanics Conference*, pages 342–345, Gold Coast, Australia, 3–7 December 2007. School of Engineering, The University of Queensland. ISBN 978-1-864998-94-8.

[299] Y. Wang, Y. Lui, X. Sun, Z. Chen, and F. Gao. Evaluation of the upper airway in children with obstructive sleep apnea undergoing adenoidectomy using computational fluid dynamics. In *2nd International Conference on Biomedical Engineering and Informatics*, pages 1–4, Tianjin, China, 17–19 October 2009. doi: 10.1109/BMEI.2009.5305292. ISBN 978-1-4244-413-1.

[300] Y. Wang, J. Wang, Y. Liu, S. Yu, X. Sun, S. Li, S. Shen, and W. Zhao. Fluid–structure interaction modeling of upper airways before and after nasal surgery for obstructive sleep apnea. *International Journal for Numerical Methods in Biomedical Engineering*, 28:528–546, 2012. doi: 10.1002/cnm.1486.

[301] Y. K. Wang, M.P. Nash, A.J. Pullan, J.A. Kieser, and O. Röhrle. Model-based identification of motion sensor placement for tracking retraction and elongation of the tongue. *Biomechanics and Modeling in Mechanobiology*, 12:383–399, 2013. doi: 10.1007/s10237-012-0407-6.

[302] webanatomy.com. The visible human project, April 2012. URL `http://www.webanatomy.com/bobCSA/visible_human_project.asp`. Accessed July 2013.

[303] J. Weidendorfer. Kcachegrind, July 2012. URL `http://kcachegrind.sourceforge.net/html/Home.html`. Accessed July 2013.

[304] E. J. Weinberg and M. R. Kaazempur-Mofrad. A large-strain finite element formulation for biological tissues with application to mitral valve leaflet tissue mechanics. *Journal of Biomechanics*, 39:1557–1561, 2006. doi: 10.1016/j.jbiomech.2005.04.020.

[305] I. Weinhold and G. Mlynski. Numerical simulation of airflow in the human nose. *European Archives of Oto-Rhino-Laryngology and Head & Neck*, 261:452–455, 2004. doi: 10.1007/s00405-003-0675-y.

[306] J. A. Weiss, B. N. Maker, and S. Govindjee. Finite element implementation of incompressible, transversely isotropic hyperelasticity. *Computer Methods in Applied Mechanics and Engineering*, 135:107–128, 1996. doi: 10.1016/0045-7825(96)01035-3.

[307] J. Wen, K. Inthavong, J. Tu, and S. Wang. Numerical simulations for detailed airflow dynamics in a human nasal cavity. *Respiratory Physiology & Neurobiology*, 161:125–135, 2008. doi: 10.1016/j.resp.2008.01.012.

[308] D. P. White. The pathogenesis of obstructive sleep apnea: Advances in the past 100 years. *American Journal of Respiratory Cell and Molecular Biology*, 34:1–6, 2006. doi: 10.1165/rcmb.2005-0317OE.

[309] D. Whitley. A genetic algorithm tutorial. *Statistics and Computing*, 4:65–85, 1994. doi: 10.1007/BF00175354.

[310] R. Wilhelms-Tricarico. Geometric representation of a human tongue for computational biomechanical modelling. Retrieved on December 2008, accessed July 2013. URL `http://webpages.charter.net/reinerwt/JSHLRmanuscript.pdf`.

[311] R. Wilhelms-Tricarico. Physiological modeling of speech production: Methods for modeling soft-tissue articulators. *Journal of the Acoustical Society of America*, 97:3085–3098, 1995. doi: 10.1121/1.411871.

[312] W. O. Williams. Huxley's model of muscle contraction with compliance. *Journal of Elasticity*, 105:365–380, 2011. doi: 10.1007/s10659-011-9304-y.

[313] P. Wriggers. *Computational Contact Mechanics*. Springer-Verlag, Berlin, Germany, 2nd edition, 2006. ISBN 978-3-540-32608-3.

[314] P. Wriggers. *Nonlinear Finite Element Methods*. Springer-Verlag, Berlin, Germany, 2008. ISBN 978-3-540-71000-4.

[315] J. Z. Wu and W. Herzog. Modeling dynamic contraction of muscle using the cross-bridge theory. *Mathematical Biosciences*, 139:69–78, 1997. doi: 10.1016/S0025-5564(96)00115-0.

[316] J. Z. Wu and W. Herzog. Modelling concentric contraction of muscle using an improved cross-bridge model. *Journal of Biomechanics*, 32:837–848, 1999. doi: 10.1016/S0021-9290(99)00057-3.

[317] M. C. Wu, J. C. Han, O. Röhrle, W. Thorpe, and P. Nielsen. Using three-dimensional finite element models and principles of active muscle contraction to analyse the movement of the tongue. In *11th Australian International Conference on Speech Science & Technology*, pages 354–359, University of Auckland, New Zealand, 6–8 December 2006. Australasian Speech Science and Technology Association Inc. ISBN 0 9581946 2 9.

[318] X. F. Xie. NLPSolver, 2012. URL `http://wiki.openoffice.org/wiki/NLPSolver`. Accessed July 2013.

[319] C. Xu, S. H. Sin, J. M. McDonough, J. K. Udupa, A. Guez, R. Arens, and D. M. Wootton. Computational fluid dynamics modeling of the upper airway of children with obstructive sleep apnea syndrome in steady flow. *Journal of Biomechanics*, 39:2043–2054, 2006. doi: 10.1016/j.jbiomech.2005.06.021.

[320] C. Xu, M. J. Brennick, L. Dougherty, and D. M. Wootton. Modeling upper airway collapse by a finite element model with regional tissue properties. *Medical Engineering & Physics*, 31:1343–1348, 2009. doi: 10.1016/j.medengphy.2009.08.006.

[321] M. S. Yeoman, B. D. Reddy, H. C. Bowles, P. Zilla, D. Bezuidenhout, and T. Franz. The use of finite element methods and genetic algorithms in search of an optimal fabric reinforced porous graft system. *Annals of Biomedical Engineering*, 37:2266–2287, 2009. doi: 10.1007/s10439-009-9771-5.

[322] C. A. Yucesoy, B. H. F. J. M. Koopman, P. A. Huijing, and H. J. Grootenboer. Three-dimensional finite element modeling of skeletal muscle using a two-domain approach: linked fiber-matrix mesh model. *Journal of Biomechanics*, 35:1253–1262, 2002. doi: 10.1016/S0021-9290(02)00069-6.

[323] G. I. Zahalak. Non-axial muscle stress and stiffness. *Journal of theoretical biology*, 182:59–84, 1996. doi: 10.1006/jtbi.1996.0143.

[324] G. I. Zahalak and S-P. Ma. Muscle activation and contraction: Constitutive relations based directly on cross-bridge kinetics. *Journal of Biomechanical Engineering*, 112:52–62, 1990. doi: 10.1115/1.2891126.

[325] J. Zhang, Y. Lui, X. Sun, S. Yu, and C. Yu. Computational fluid dynamics simulations of respiratory airflow in human nasal cavity and its characteristic dimension study. *Acta Mechanica Sinica*, 24:223–228, 2008. doi: 10.1007/s10409-008-0148-z.

[326] Z. Zhang, C. Kleinstreuer, and C. S. Kim. Micro-particle transport and deposition in a human oral airway model. *Journal of Aerosol Science*, 33:1635–1652, 2002. doi: 10.1016/S0021-8502(02)00122-2.

[327] M. Zhao, T. Barber, P. Cistulli, K. Sutherland, and G. Rosengarten. Computational fluid dynamic study of upper airway flow to predict the success of oral appliances in treating sleep apnea. In *17th Australasian Fluid Mechanics Conference*, pages 579–582, Auckland, New Zealand, 5–9 December 2010. ISBN 978-1-61782-913-0.

[328] J. H. Zhu, H. P. Lee, K. M. Lim, S. J. Lee, L. S. L. Teo, and D. Y. Wang. Passive movement of human soft palate during respiration: A simulation of 3D fluid/structure interaction. *Journal of Biomechanics*, 45:1992–2000, 2012. doi: 10.1016/j.jbiomech.2012.04.027.

[329] M. A. Zulliger, A. Rachev, and N. Stergiopulos. A constitutive formulation of arterial mechanics including vascular smooth muscle tone. *American Journal of Physiology - Heart and Circulatory Physiology*, 287:H1335–H1343, 2004. doi: 10.1152/ajpheart.00094.2004.

APPENDICES

A. CONTINUUM MECHANICS

A.1 Zero strain condition

Considering the new definitions of total displacement, deformation gradient, and line element stretch and direction provided in equations 3.24, 3.25, 3.28 and 3.30 (which also define the quantities in the current configuration), evaluation of the two modified deformation states is made below.

A.1.1 Initial (zero strain) configuration

When the body takes the configuration which is classified to be the zero strain configuration, the displacement $\boldsymbol{u}^{\mathrm{CR}} = \boldsymbol{x}^{\mathrm{I}} - \boldsymbol{X}$ is possibly non-zero. In this configuration, the deformation gradient $\boldsymbol{F}^{\mathrm{CR}} = \boldsymbol{F}^{\mathrm{IR}}$, and therefore

$$\boldsymbol{F}^{\mathrm{CI}} = \boldsymbol{F}^{\mathrm{IR}}\boldsymbol{F}^{\mathrm{RI}} = \boldsymbol{F}^{\mathrm{IR}}\left(\boldsymbol{F}^{\mathrm{IR}}\right)^{-1} = \boldsymbol{I} \quad , \tag{A.1}$$

from which all strain measures will have a magnitude of unity. When this configuration is attained, the measure $\boldsymbol{F}^{\mathrm{RI}}$ is recorded and used to determine the total deformation gradient as defined in equation 3.25 from that point onwards. The corresponding stretch of a line element is

$$\lambda^{\mathrm{CI}} = \lambda^{\mathrm{I}} = |\boldsymbol{I}\boldsymbol{N}| = 1 \quad . \tag{A.2}$$

Noting that the original direction vectors for line elements are recorded in the reference configuration, their updated direction in the initial configuration is

$$\boldsymbol{n}^{\mathrm{I}} = \frac{\boldsymbol{F}^{\mathrm{IR}}\boldsymbol{N}}{|\boldsymbol{F}^{\mathrm{IR}}\boldsymbol{N}|} \quad . \tag{A.3}$$

A.1.2 Reference configuration

By definition, the displacement of the reference configuration is $\boldsymbol{u}^{\mathrm{CR}} = \boldsymbol{0}$. Assuming that a non-trivial initial configuration has been defined, the deformation gradient $\boldsymbol{F}^{\mathrm{CR}} = \boldsymbol{I}$ and it follows that

$$\boldsymbol{F}^{\mathrm{CI}} = \boldsymbol{I}\boldsymbol{F}^{\mathrm{RI}} = \boldsymbol{F}^{\mathrm{RI}} \quad , \tag{A.4}$$

which describes a pre-strained condition in this configuration. This is further demonstrated though the referential line element stretch magnitude

$$\lambda^{\mathrm{CI}} = \lambda_0 = |\boldsymbol{F}^{\mathrm{RI}}\boldsymbol{N}| \neq 1 \quad \text{if} \quad \boldsymbol{F}^{\mathrm{RI}} \neq \boldsymbol{I} \quad . \tag{A.5}$$

As the original line element direction vector is recorded in this configuration, it is expected that the (identity) deformation has no effect on this direction vector. This is precisely the result given by

$$\boldsymbol{N}_0 = \left.\frac{\boldsymbol{F}^{\mathrm{CR}}\boldsymbol{N}}{|\boldsymbol{F}^{\mathrm{CR}}\boldsymbol{N}|}\right|_{\boldsymbol{F}^{\mathrm{CR}}=\boldsymbol{I}} = \boldsymbol{N} \quad . \tag{A.6}$$

A.2 Tensor operations

Due to the simplicity arising with working in the stationary reference configuration, the derivation of derivatives of quantities with respect to referential deformation measures are provided below. Where useful, their spatial equivalents are derived as well.

A.2.1 Derivatives

A.2.1.1 Rank 2 tensors

The derivative of the invariants (equations 3.21a and 3.21b) with respect to the right Cauchy-Green deformation tensor are

$$\frac{\partial I_1^C}{\partial \boldsymbol{C}} = \boldsymbol{I} \tag{A.7}$$

$$\frac{\partial I_2^C}{\partial \boldsymbol{C}} = I_1^C\boldsymbol{I} - \boldsymbol{C} \quad , \tag{A.8}$$

while that of the volumetric Jacobian (related to equation 3.21c by equation 3.22) is

$$\frac{\partial J}{\partial \boldsymbol{C}} = \frac{1}{2}J\boldsymbol{C}^{-1} \quad . \tag{A.9}$$

This can be confirmed by comparing the time-rate $\dot{J} = \dfrac{\partial J}{\partial \boldsymbol{C}} : \dot{\boldsymbol{C}}$ with a manipulation the result given later in equation B.6. A quantity that often appears in later text is the term

$$\frac{\partial J^{-\frac{2}{3}}}{\partial \boldsymbol{C}} = \frac{\partial J^{-\frac{2}{3}}}{\partial J}\frac{\partial J}{\partial \boldsymbol{C}} = \left(-\frac{2}{3}J^{-\frac{5}{3}}\right)\left(\frac{1}{2}J\boldsymbol{C}^{-1}\right) = -\frac{1}{3}J^{-\frac{2}{3}}\boldsymbol{C}^{-1} \quad . \tag{A.10}$$

The derivative of stretch of a line element (a reference-frame invariant quantity) with respect to the right Cauchy-Green tensor is derived by from the definition of the magnitude of stretch given in equation 3.23a. Taking the derivatives of both sides with respect to $\boldsymbol{C}$,

$$2\lambda\frac{\partial \lambda}{\partial \boldsymbol{C}} = \boldsymbol{N}\otimes\boldsymbol{N} \quad \Rightarrow \quad \frac{\partial \lambda}{\partial \boldsymbol{C}} = \frac{1}{2\lambda}\boldsymbol{N}\otimes\boldsymbol{N} \quad . \tag{A.11}$$

The quantity $\boldsymbol{N}\otimes\boldsymbol{N}$ is sometimes referred to as the structure tensor.

A.2.1.2 Rank 4 tensors

The rank 4 tensor $\dfrac{\partial \boldsymbol{C}^{-1}}{\partial \boldsymbol{C}}$ is evaluated by the expression

$$\frac{\partial C^{-1}_{AB}}{\partial C_{CD}} = -C^{-1}_{AC}C^{-1}_{BD} = -\frac{1}{2}\left(C^{-1}_{AC}C^{-1}_{BD} + C^{-1}_{AD}C^{-1}_{BC}\right) \quad . \tag{A.12}$$

This can be derived in the following manner: Taking derivatives of both sides of the identity equation $\boldsymbol{I} = \boldsymbol{C}^{-1}\,\boldsymbol{C}$ produces

$$0 = \frac{\partial}{\partial C_{CD}}\delta_{AE} = \frac{\partial}{\partial C_{CD}}\left(C^{-1}_{AB}C_{BE}\right) = \frac{\partial C^{-1}_{AB}}{\partial C_{CD}}C_{BE} + C^{-1}_{AB}\delta_{BC}\delta_{DE} \quad .$$

Multiplying by a factor of $\boldsymbol{C}^{-1}$, the final result

$$0 = \left(\frac{\partial C^{-1}_{AB}}{\partial C_{CD}}C_{BE} + C^{-1}_{AC}\delta_{DE}\right)C^{-1}_{EF} = \frac{\partial C^{-1}_{AF}}{\partial C_{CD}} + C^{-1}_{AC}C^{-1}_{DF}$$

is obtained, which upon rearrangement leads to equation A.12.

Using equation A.10, the derivative of the isochoric right Cauchy-Green deformation tensor with respect to its non-isochoric counterpart

$$\begin{aligned}\frac{\partial \bar{\boldsymbol{C}}}{\partial \boldsymbol{C}} &= \frac{\partial}{\partial \boldsymbol{C}}\left(J^{-\frac{2}{3}}\boldsymbol{C}\right) = \boldsymbol{C}\otimes\frac{\partial J^{-\frac{2}{3}}}{\partial \boldsymbol{C}} + J^{-\frac{2}{3}}\frac{\partial \boldsymbol{C}}{\partial \boldsymbol{C}} = \boldsymbol{C}\otimes\left[-\frac{1}{3}J^{-\frac{2}{3}}\boldsymbol{C}^{-1}\right] + J^{-\frac{2}{3}}\mathbb{I} \\ &= J^{-\frac{2}{3}}\left(\mathbb{I} - \frac{1}{3}\boldsymbol{C}\otimes\boldsymbol{C}^{-1}\right) =: \widehat{\mathbb{P}}\end{aligned} \tag{A.13}$$

leads to the definition of the the referential deviator tensor $\widehat{\mathbb{P}}$.

A.2.2 Push-forward operations

This operation is defined by equation 3.37 for rank 2 tensors and equation 3.56 for rank 4 tensors.

A.2.2.1 Rank 2 tensors

Common rank 2 tensors that undergo push-forward operation in later calculations include that of the identity tensor

$$\boldsymbol{\chi}(\boldsymbol{I}) = \boldsymbol{b} \quad , \tag{A.14}$$

the right Cauchy-Green deformation tensor

$$\boldsymbol{\chi}(\boldsymbol{C}) = \boldsymbol{b}^2 \tag{A.15}$$

and its inverse

$$\boldsymbol{\chi}\left(\boldsymbol{C}^{-1}\right) = \boldsymbol{I} \quad . \tag{A.16}$$

The referential structure tensor can also be defined in a spatial setting by

$$\boldsymbol{\chi}(\boldsymbol{N}\otimes\boldsymbol{N}) = (\boldsymbol{F}\boldsymbol{N})\otimes(\boldsymbol{F}\boldsymbol{N}) = \lambda^2\boldsymbol{n}\otimes\boldsymbol{n} \quad . \tag{A.17}$$

A.2.2.2 Rank 4 tensors

In general, the transformation of a fourth-order tensor which produced by the dyadic-product of two second-order tensors can be described by the dyadic product of the transformation of the individual rank-2 tensors:

$$\boldsymbol{\chi}(\mathbf{G}\otimes\mathbf{H}) = \boldsymbol{\chi}(\mathbf{G})\otimes\boldsymbol{\chi}(\mathbf{H}) \quad . \tag{A.18}$$

Using equation A.18 in conjunction with equations A.14 to A.17, the following commonly used identities become self-evident:

$$\boldsymbol{\chi}(\boldsymbol{I}\otimes\boldsymbol{I}) = \boldsymbol{b}\otimes\boldsymbol{b} \tag{A.19}$$
$$\boldsymbol{\chi}(\boldsymbol{C}\otimes\boldsymbol{C}) = \boldsymbol{b}^2\otimes\boldsymbol{b}^2 \tag{A.20}$$
$$\boldsymbol{\chi}(\boldsymbol{C}\otimes\boldsymbol{I}) = \boldsymbol{b}^2\otimes\boldsymbol{b} \tag{A.21}$$
$$\boldsymbol{\chi}(\boldsymbol{I}\otimes\boldsymbol{C}) = \boldsymbol{b}\otimes\boldsymbol{b}^2 \tag{A.22}$$
$$\boldsymbol{\chi}\left(\boldsymbol{C}^{-1}\otimes\boldsymbol{C}^{-1}\right) = \boldsymbol{I}\otimes\boldsymbol{I} \tag{A.23}$$
$$\boldsymbol{\chi}(\boldsymbol{N}\otimes\boldsymbol{N}\otimes\boldsymbol{N}\otimes\boldsymbol{N}) = \lambda^4\,\boldsymbol{n}\otimes\boldsymbol{n}\otimes\boldsymbol{n}\otimes\boldsymbol{n} \tag{A.24}$$

Furthermore, the spatial transformation operation acting on the fourth order identity tensor results in

$$\boldsymbol{\chi}(\mathbb{I}) = \boldsymbol{b}\bar{\otimes}\boldsymbol{b} \tag{A.25}$$

where the operation $\bar{\otimes}$ has the definition provided in equation 3.57, and result given in equation A.12 is pushed forward by

$$\boldsymbol{\chi}\left(\frac{\partial\boldsymbol{C}^{-1}}{\partial\boldsymbol{C}}\right) = -\mathbb{I} \quad . \tag{A.26}$$

A.3 Volumetric-deviatoric split of SEF

Starting with the SEF described using referential quantities

$$\psi = \widehat{\psi}_{\text{vol}}(J) + \widehat{\psi}_{\text{iso}}\left(\bar{\boldsymbol{C}}, \bar{\lambda}_{\text{f}}\right) \quad , \tag{A.27}$$

application of equation 3.51 results in the additive decomposition of the second Piola-Kirchhoff stress

$$\boldsymbol{S} = \boldsymbol{S}_{\text{vol}}(J) + \boldsymbol{S}_{\text{iso}}\left(\bar{\boldsymbol{C}}, \bar{\lambda}_{\text{f}}\right) \quad . \tag{A.28}$$

The volumetric component of the stress can be computed with the assistance of equation A.9 as

$$\boldsymbol{S}_{\text{vol}} = 2\frac{\partial\widehat{\psi}_{\text{vol}}}{\partial J}\frac{\partial J}{\partial\boldsymbol{C}} = \widehat{\psi}'_{\text{vol}}J\boldsymbol{C}^{-1} \tag{A.29}$$

which upon the use of equation 3.37 results in equation 3.82a. Using equation A.13, the isochoric component of the second Piola-Kirchhoff stress is given by

$$\boldsymbol{S}_{\text{iso}} = 2\frac{\partial\widehat{\psi}_{\text{iso}}}{\partial\bar{\boldsymbol{C}}} : \frac{\partial\bar{\boldsymbol{C}}}{\partial\boldsymbol{C}} = \bar{\boldsymbol{S}} : \widehat{\mathbb{P}} = \widehat{\mathbb{P}} : \bar{\boldsymbol{S}} \tag{A.30}$$

where the symmetry of $\widehat{\mathbb{P}}$ is exploited and we define an auxiliary stress quantity

$$\bar{\boldsymbol{S}} = 2\frac{\partial \widehat{\psi}_{\text{iso}}}{\partial \boldsymbol{C}}\bigg|_{\boldsymbol{C}=\bar{\boldsymbol{C}}} \tag{A.31}$$

which is the referential counterpart to that given in equation 3.82c.

Noting that $\boldsymbol{S} : \boldsymbol{C} = \boldsymbol{\tau} : \boldsymbol{I}$, the push-forward of equation A.30 using equation 3.37 in conjunction with equations 3.75 and A.13 results in

$$\begin{aligned}
\tau^{\text{iso}}{}_{ab} &= F_{aA}S^{\text{iso}}{}_{AB}F_{bB} \\
&= F_{aA}\left[J^{-\frac{2}{3}}\left(\delta_{AC}\delta_{BD} - \frac{1}{3}C_{CD}C^{-1}_{AB}\right)\bar{S}_{CD}\right]F_{bB} \\
&= \left[\left(\left(J^{-\frac{1}{3}}F_{aA}\right)\delta_{AC}\delta_{BD}\left(J^{-\frac{1}{3}}F_{bB}\right) - \frac{1}{3}\left(J^{-\frac{2}{3}}C_{CD}\right)F_{aA}C^{-1}_{AB}F_{bB}\right)\bar{S}_{CD}\right] \\
&= \bar{F}_{aC}\bar{S}_{CD}\bar{F}_{bD} - \frac{1}{3}\bar{S}_{CD}\bar{C}_{CD}\delta_{ab} \\
&= \bar{\tau}_{ab} - \frac{1}{3}\bar{\tau}_{dd}\delta_{ab} \\
&= \left(\delta_{ac}\delta_{bd} - \frac{1}{3}\delta_{ab}\delta_{cd}\right)\bar{\tau}_{cd} \\
&= \mathbb{P}_{abcd}\bar{\tau}_{cd}
\end{aligned} \tag{A.32}$$

from which the definition of the spatial auxiliary stress equation 3.82c and deviatoric projection operator equation 3.84 are produced. The latter performs the operation to a rank 2 spatial tensor

$$\mathbb{P} : (\bullet) = (\bullet) - \frac{1}{3}\,\text{tr}\,(\bullet)\,\boldsymbol{I} \quad . \tag{A.33}$$

Following from equation A.28, the additive decomposition of the elastic tangent is

$$\mathbb{H} = \mathbb{H}_{\text{vol}} + \mathbb{H}_{\text{iso}} \tag{A.34}$$

with the volumetric contribution

$$\begin{aligned}
\mathbb{H}_{\text{vol}} &= 4\frac{\partial^2 \widehat{\psi}_{\text{vol}}}{\partial \boldsymbol{C}^2} = 2\frac{\partial \boldsymbol{S}_{\text{vol}}}{\partial \boldsymbol{C}} \\
&= 2\left(\widehat{\psi}''_{\text{vol}}\frac{\partial J}{\partial \boldsymbol{C}} \otimes J\boldsymbol{C}^{-1} + \widehat{\psi}'_{\text{vol}}\frac{\partial J}{\partial \boldsymbol{C}} \otimes \boldsymbol{C}^{-1} + \widehat{\psi}'_{\text{vol}}J\frac{\partial \boldsymbol{C}^{-1}}{\partial \boldsymbol{C}}\right) \\
&= J\left(\left(\widehat{\psi}'_{\text{vol}} + J\widehat{\psi}''_{\text{vol}}\right)\boldsymbol{C}^{-1} \otimes \boldsymbol{C}^{-1} + 2\widehat{\psi}'_{\text{vol}}\frac{\partial \boldsymbol{C}^{-1}}{\partial \boldsymbol{C}}\right)
\end{aligned} \tag{A.35}$$

derived making use of equations 3.55, A.9 and A.12. Equation 3.83a is subsequently computed using equations 3.56, A.23 and A.26.

The lengthy derivation of the isochoric tangent is summarised in the following lines. Using equation 3.55 in conjunction with equations A.13 and A.30, the isochoric component of the elastic modulii is given by

$$\begin{aligned}
\mathbb{H}_{\text{iso}} &= 2\frac{\partial \boldsymbol{S}_{\text{iso}}}{\partial \boldsymbol{C}} = 2\frac{\partial}{\partial \boldsymbol{C}}\left(\widehat{\mathbb{P}} : \bar{\boldsymbol{S}}\right) \\
&= 2\left[\frac{\partial \widehat{\mathbb{P}}}{\partial \boldsymbol{C}} : \bar{\boldsymbol{S}} + \widehat{\mathbb{P}} : \frac{\partial \bar{\boldsymbol{S}}}{\partial \bar{\boldsymbol{C}}} : \frac{\partial \bar{\boldsymbol{C}}}{\partial \boldsymbol{C}}\right] \\
&= 2\frac{\partial \widehat{\mathbb{P}}}{\partial \boldsymbol{C}} : \bar{\boldsymbol{S}} + \widehat{\mathbb{P}} : \bar{\mathbb{H}} : \widehat{\mathbb{P}} \quad .
\end{aligned} \tag{A.36}$$

From the definition of the referential deviatoric operator, the first term in equation A.36 can be expanded to the expression

$$2\frac{\partial\widehat{\mathbb{P}}}{\partial\boldsymbol{C}}:\bar{\boldsymbol{S}}=-\frac{2}{3}\left[\left(\boldsymbol{S}_{\text{iso}}\otimes\boldsymbol{C}^{-1}+\boldsymbol{C}^{-1}\otimes\boldsymbol{S}_{\text{iso}}\right)-\left(\bar{\boldsymbol{S}}:\bar{\boldsymbol{C}}\right)\left(\boldsymbol{C}^{-1}\bar{\otimes}\boldsymbol{C}^{-1}-\frac{1}{3}\boldsymbol{C}^{-1}\otimes\boldsymbol{C}^{-1}\right)\right] \tag{A.37}$$

Pushing this quantity forward into the current configuration results in the expression

$$J\mathbb{C}^{\text{iso}}{}_{abcd}=F_{aA}F_{bB}\left(2\frac{\partial\widehat{\mathbb{P}}_{ABEF}}{\partial C_{CD}}\bar{S}_{EF}+\widehat{\mathbb{P}}_{ABEF}\bar{\mathbb{H}}_{EFGH}\widehat{\mathbb{P}}_{GHCD}\right)F_{cC}F_{dD} \tag{A.38}$$

where, upon expansion, the first term simplifies to

$$F_{aA}F_{bB}2\frac{\partial\widehat{\mathbb{P}}_{ABEF}}{\partial C_{CD}}\bar{S}_{EF}F_{cC}F_{dD}=-\frac{2}{3}\left[\left(\tau^{\text{iso}}{}_{ab}\delta_{cd}+\delta_{ab}\tau^{\text{iso}}{}_{cd}\right)-\left(\bar{\tau}_{ee}\right)\mathbb{P}_{abcd}\right] \quad . \tag{A.39}$$

After some manipulation, the second term is simply

$$\begin{aligned}
&F_{aA}F_{bB}\widehat{\mathbb{P}}_{ABEF}\bar{\mathbb{H}}_{EFGH}\widehat{\mathbb{P}}_{GHCD}F_{cC}F_{dD}\\
&\quad=J^{\frac{2}{3}}\left(F_{aA}F_{bB}\widehat{\mathbb{P}}_{ABEF}F^{-1}_{Ee}F^{-1}_{Ff}\right)\left(\bar{F}_{eI}\bar{F}_{fJ}\bar{\mathbb{H}}_{IJKL}\bar{F}_{gK}\bar{F}_{hL}\right)J^{\frac{2}{3}}\left(F^{-1}_{Gg}F^{-1}_{Hh}\widehat{\mathbb{P}}_{GHCD}F_{cC}F_{dD}\right)\\
&\quad=\mathbb{P}_{abef}J\bar{\mathbb{C}}_{efgh}\mathbb{P}_{ghcd}
\end{aligned} \tag{A.40}$$

using equation 3.83c and the identity

$$F_{aA}F_{bB}\widehat{\mathbb{P}}_{ABEF}F^{-1}_{Eh}F^{-1}_{Fg}=J^{-\frac{2}{3}}\mathbb{P}_{abgh} \quad . \tag{A.41}$$

Insertion of equations A.39 and A.40 into equation A.38 leads to the result given in equation 3.83b.

A.4 Motion-dependent boundary conditions

A.4.1 Fictitious material layer

With reference to figure 3.5 and the definitions provided in section 3.7.1.1, the following paragraphs detail the linearisation of the displacement-dependent traction conditions (section 3.7.1.2) associated with the fictitious material layer.

Linearisation with respect to the displacement of the material thickness equation 3.92 leads to

$$\frac{\partial \mathrm{h}}{\partial u_j}=\frac{\partial}{\partial u_j}\left[\mathrm{h}_0-u_kN_k\right]=-\frac{\partial u_k}{\partial u_j}N_k=-N_j \tag{A.42}$$

while, using equation A.42, that of its inverse equation 3.92 results in

$$\frac{\partial \mathrm{h}^{-1}}{\partial u_j}=-\mathrm{h}^{-2}\frac{\partial \mathrm{h}}{\partial u_j}=\mathrm{h}^{-2}N_j \quad . \tag{A.43}$$

With the use of equations 3.92 and A.42, the derivative of the scalar normal strain equation 3.93 with respect to the displacement is

$$\frac{\partial\varepsilon}{\partial u_j}=\frac{\partial}{\partial u_j}\left[\ln\left(\frac{\mathrm{h}}{\mathrm{h}_0}\right)\right]=\left(\frac{\mathrm{h}}{\mathrm{h}_0}\right)^{-1}{\mathrm{h}_0}^{-1}\frac{\partial \mathrm{h}}{\partial u_j}=-\mathrm{h}^{-1}N_j \tag{A.44}$$

and that of the shear strain equation 3.94 is

$$\frac{\partial \gamma_\alpha}{\partial u_j} = \frac{\partial}{\partial u_j}\left[\frac{u_k e_k^{\mathrm{S}_\alpha}}{\mathrm{h}}\right] = \frac{\partial u_k}{\partial u_j} e_k^{\mathrm{S}_\alpha} \mathrm{h}^{-1} + u_k e_k^{\mathrm{S}_\alpha} \frac{\partial \mathrm{h}^{-1}}{\partial u_j} = \mathrm{h}^{-1} e_j^{\mathrm{S}_\alpha} + \left(u_k e_k^{\mathrm{S}_\alpha}\right) \mathrm{h}^{-2} N_j = \mathrm{h}^{-1}\left(e_j^{\mathrm{S}_\alpha} + \gamma N_j\right) \tag{A.45}$$

using equation A.43 and the definition of the shear strain itself.

Application of the product rule leads to the definition of the derivative of the normal traction magnitude equation 3.97 with respect to the normal strain

$$\frac{\partial \sigma_{\mathrm{N}}}{\partial \varepsilon} = \frac{\partial}{\partial \varepsilon}\left[E\left(\varepsilon\right)\varepsilon\right] = \frac{\partial E}{\partial \varepsilon}\varepsilon + E \tag{A.46}$$

and that of the shear traction magnitude equation 3.98 with respect to the shear strain is

$$\frac{\partial \sigma_{\mathrm{S}_\alpha}}{\partial \gamma_\alpha} = \frac{\partial}{\partial \gamma_\alpha}\left[-G\left(|\gamma_\alpha|\right)\gamma_\alpha\right] = -\left(\frac{\partial G}{\partial \gamma_\alpha}\gamma_\alpha + G\right) = -\left(\frac{\partial G}{\partial |\gamma_\alpha|}|\gamma_\alpha| + G\right) \quad . \tag{A.47}$$

The definition of the tangent matrix provided in equation 3.99 is derived from the linearisation of traction vector (equation 3.95)

$$\frac{\partial t_i}{\partial u_j}\Delta u_j = \left[\frac{\partial t_i^{\mathrm{N}}}{\partial u_j} + \sum_\alpha \frac{\partial t_i^{\mathrm{S}_\alpha}}{\partial u_j}\right]\Delta u_j \tag{A.48}$$

where upon application of equations A.44 and A.46 to the first term of equation A.48 leads to equation 3.100, the definition of the normal tangent

$$\frac{\partial t_i^{\mathrm{N}}}{\partial u_j} = \frac{\partial}{\partial u_j}\left[t^{\mathrm{N}} N_i\right] = \frac{\partial t^{\mathrm{N}}}{\partial \varepsilon}\frac{\partial \varepsilon}{\partial u_j} N_i \quad , \tag{A.49}$$

and use of equations A.45 and A.47 on the second term of equation A.48 results in equation 3.101a, the stiffness of the tangential component of the traction

$$\frac{\partial t_i^{\mathrm{S}_\alpha}}{\partial u_j} = \frac{\partial}{\partial u_j}\left[t_{\mathrm{S}_\alpha} e_i^{\mathrm{S}_\alpha}\right] = \frac{\partial t_{\mathrm{S}_\alpha}}{\partial \gamma}\frac{\partial \gamma}{\partial u_j} e_i^{\mathrm{S}_\alpha} \quad . \tag{A.50}$$

A.4.2 External fibres

Using trigonometric relations and the definitions provided in figure 3.6, the angle between the displacement vector and reference fibre vector determined from scalar product

$$\cos\left(\theta\right) = \frac{\boldsymbol{L}_{\mathrm{f}}^0 \cdot \boldsymbol{u}}{|\boldsymbol{L}_{\mathrm{f}}^0||\boldsymbol{u}|} = \frac{\boldsymbol{L}_{\mathrm{f}}^0 \cdot \boldsymbol{u}}{L_{\mathrm{f}}^0|\boldsymbol{u}|} \quad , \tag{A.51}$$

which leads to the definition of the fibre length in current configuration as determined from triangle cosine formula

$$L_{\mathrm{f}}{}^2 = L_{\mathrm{f}}^{0\,2} + u_k u_k - 2L_{\mathrm{f}\,k}^0 u_k \quad . \tag{A.52}$$

Taking derivatives of both sides of equation A.52 with respect to displacement, and noting the definition of the current fibre direction given in equation 3.104 results in

$$2L_{\mathrm{f}}\frac{dL_{\mathrm{f}}}{du_j} = 2u_k\frac{du_k}{du_j} - 2L_{\mathrm{f}\,k}^0\frac{du_k}{du_j} \quad \Rightarrow \quad \frac{dL_{\mathrm{f}}}{du_j} = \frac{1}{L_{\mathrm{f}}}\left(u_j - L_{\mathrm{f}\,j}^0\right) = -n_{\mathrm{f}j} \quad . \tag{A.53}$$

Furthermore, linearisation of the current fibre stretch (equation 3.105) is determined using equation A.53

$$\frac{d\lambda_\mathrm{f}}{du_i} = \frac{1}{L_\mathrm{f}^0}\frac{dL_\mathrm{f}}{du_i} = -\frac{1}{L_\mathrm{f}^0} n_{\mathrm{f}i} \tag{A.54}$$

while that of equation 3.104, the current fibre direction, is calculated with the use of equation A.53 and results in

$$\begin{aligned}
\frac{dn_{\mathrm{f}i}}{du_j} &= \frac{d}{L_\mathrm{f}}\left[\frac{1}{L_\mathrm{f}}\right]\frac{dL_\mathrm{f}}{du_j}\left(L^0_{\mathrm{f}\,i} - u_i\right) + \frac{1}{L_\mathrm{f}}\frac{d}{du_j}\left(L^0_{\mathrm{f}\,i} - u_i\right) \\
&= \left(-\frac{1}{{L_\mathrm{f}}^2}\right)\left(-n_{\mathrm{f}j}\right)\left(L^0_{\mathrm{f}\,i} - u_i\right) + \frac{1}{L_\mathrm{f}}\left(-\frac{du_i}{du_j}\right) \\
&= \frac{1}{L_\mathrm{f}}\left(n_{\mathrm{f}i}n_{\mathrm{f}j} - \delta_{ij}\right) \quad .
\end{aligned} \tag{A.55}$$

Finally, the linearisation of the traction, equation 3.106, is determined using the chain rule and equations 3.105 and A.53 to A.55 with the result that

$$\begin{aligned}
\frac{dt_{\mathrm{f}i}}{du_j} &= \phi_\mathrm{f}\left[\frac{d\lambda_\mathrm{f}}{du_j}T_\mathrm{f}n_{\mathrm{f}i} + \lambda_\mathrm{f}\frac{dT_\mathrm{f}}{du_j}n_{\mathrm{f}i} + \lambda_\mathrm{f}T_\mathrm{f}\frac{dn_{\mathrm{f}i}}{du_j}\right] \\
&= \phi_\mathrm{f}\left[\frac{d\lambda_\mathrm{f}}{du_j}\left(T_\mathrm{f} + \lambda_\mathrm{f}\frac{dT_\mathrm{f}}{d\lambda_\mathrm{f}}\right)n_{\mathrm{f}i} + \lambda_\mathrm{f}T_\mathrm{f}\frac{dn_{\mathrm{f}i}}{du_j}\right] \\
&= \frac{\phi_\mathrm{f}}{L_\mathrm{f}^0}\left[-\left(T_\mathrm{f} + \lambda_\mathrm{f}\frac{dT_\mathrm{f}}{d\lambda_\mathrm{f}}\right)n_{\mathrm{f}i}n_{\mathrm{f}j} + T_\mathrm{f}\left(n_{\mathrm{f}i}n_{\mathrm{f}j} - \delta_{ij}\right)\right] \quad ,
\end{aligned} \tag{A.56}$$

which lead to the definition provided in equation 3.107.

B. VARIATIONAL FORMULATIONS

B.1 Evaluation of deformation increments

For a general motion $\boldsymbol{\varphi}$, pressure p and dilatation θ, the virtual increments $\delta\boldsymbol{\varphi}, \delta p, \delta\theta$ are defined as

$$\boldsymbol{v} = \boldsymbol{\varphi} + \varepsilon\,\delta\boldsymbol{\varphi} \quad , \quad q = p + \varepsilon\,\delta p \quad , \quad \gamma = \theta + \varepsilon\,\delta\theta \tag{B.1}$$

with $\boldsymbol{v}, q, \gamma$ representing the total virtual displacement, pressure and dilatation and ε a perturbation.

From the above, the deformation gradient (equation 3.3) associated with the total virtual displacement is

$$\boldsymbol{F}(\boldsymbol{v}) = \boldsymbol{I} + \frac{\partial \boldsymbol{v}}{\partial \boldsymbol{X}} = \boldsymbol{I} + \frac{\partial(\boldsymbol{\varphi} + \varepsilon\delta\boldsymbol{\varphi})}{\partial \boldsymbol{X}} \quad . \tag{B.2}$$

Making use of the Frechét derivative defined in equation 4.4, the virtual deformation gradient associated with the virtual displacement increment $\delta\boldsymbol{\varphi}$ is

$$D_{\boldsymbol{\varphi}}\boldsymbol{F}(\boldsymbol{\varphi}) \cdot \delta\boldsymbol{\varphi} = \left.\frac{d\boldsymbol{F}(\boldsymbol{v})}{d\varepsilon}\right|_{\varepsilon=0} = \nabla_0\,\delta\boldsymbol{\varphi} = \nabla\,\delta\boldsymbol{\varphi}\,\boldsymbol{F} := \delta\boldsymbol{F} \quad , \tag{B.3}$$

which also implies that

$$\nabla\,\delta\boldsymbol{\varphi} = \delta\boldsymbol{F}\boldsymbol{F}^{-1} \quad . \tag{B.4}$$

Note that the result of the computations of the virtual increment $\delta(\bullet)$, linear increment $\Delta(\bullet)$ and time-rate $(\bullet)^{\dot{}}$ have the same form. For example, using a different interpretation of the definition prescribed to ε and the incremental operator, equation 3.10 can be inferred from equation B.4.

Using the chain rule and equation B.3, the virtual left Cauchy-Green deformation tensor (equation 3.14b) is

$$\delta\boldsymbol{b} := \delta\boldsymbol{F}\boldsymbol{F}^T + \boldsymbol{F}\delta\boldsymbol{F}^T = 2\left(\delta\boldsymbol{F}\boldsymbol{F}^T\right)^{\mathrm{S}} = 2\left(\nabla\,\delta\boldsymbol{\varphi}\,\boldsymbol{b}\right)^{\mathrm{S}} \tag{B.5}$$

using the symmetric operator $(\bullet)^{\mathrm{S}}$ defined in section 3.1.

Noting the identity $\nabla\cdot(\bullet) = \boldsymbol{I} : \nabla(\bullet) = \boldsymbol{I} : [\nabla(\bullet)]^{\mathrm{S}}$, the virtual increment of the volumetric Jacobian is

$$\delta J := J\boldsymbol{F}^{-T} : \delta\boldsymbol{F} = J\boldsymbol{I} : \nabla\,\delta\boldsymbol{\varphi} = J\,\mathrm{tr}\,(\nabla\,\delta\boldsymbol{\varphi}) = J\,\nabla\cdot\delta\boldsymbol{\varphi} \tag{B.6}$$

using equations 3.14a, A.9 and B.3 and the symmetry of $\boldsymbol{C}$.

With the assistance of equations B.3 and B.6 and noting the operation performed by the spatial deviator tensor (equation A.33) and its symmetric properties, the virtual isochoric deformation gradient (equation 3.74b) is determined to be

$$\delta\bar{\boldsymbol{F}} := J^{-\frac{1}{3}}\left(\delta\boldsymbol{F} - \frac{1}{3}\nabla\cdot\delta\boldsymbol{\varphi}\;\boldsymbol{F}\right) = J^{-\frac{1}{3}}\left(\nabla\,\delta\boldsymbol{\varphi} - \frac{1}{3}\,\mathrm{tr}\,\left(\nabla\,\delta\boldsymbol{\varphi}\right)\right)\boldsymbol{F} = \left(\mathbb{P} : \left(\nabla\,\delta\boldsymbol{\varphi}\right)^{\mathrm{S}}\right)\bar{\boldsymbol{F}} \quad . \tag{B.7}$$

Furthermore, the virtual isochoric left Cauchy-Green tensor (equation 3.76), calculated using equation B.7 and the same properties of the deviator tensor described above, is

$$\delta\bar{\boldsymbol{b}} := J^{-\frac{2}{3}}\left(\delta\boldsymbol{b} - \frac{2}{3}\nabla\cdot\delta\boldsymbol{\varphi}\;\boldsymbol{b}\right) = 2\left(\left(\nabla\,\delta\boldsymbol{\varphi}\right)^{\mathrm{S}} - \frac{1}{3}\left(\left(\nabla\,\delta\boldsymbol{\varphi}\right)^{\mathrm{S}} : \boldsymbol{I}\right)\right)\bar{\boldsymbol{b}} = 2\left(\mathbb{P} : \left(\nabla\,\delta\boldsymbol{\varphi}\right)^{\mathrm{S}}\right)\bar{\boldsymbol{b}} \tag{B.8}$$

B.2 Mixed three-field formulation

B.2.1 Residual formulation

The residual equation is for the three-field problem is developed by taking the first variation of equation 4.3a with respect to all independent fields using the Frechét derivative (equation 4.4). The result of this procedure is

$$\begin{aligned}\mathrm{R}\left(\delta\boldsymbol{\varphi}, \delta\theta, \delta p, \boldsymbol{\varphi}, \theta, \Lambda, p\right) &= D_{\boldsymbol{\varphi}}\Pi\cdot\delta\boldsymbol{\varphi} + D_p\Pi\cdot\delta p + D_\theta\Pi\cdot\delta\theta \\ &= \mathrm{R}^{\delta\boldsymbol{\varphi}}_{\mathrm{int}} + \mathrm{R}^{\delta\boldsymbol{\varphi}}_{\mathrm{ext}} + \mathrm{R}^{\delta p}_{\mathrm{int}} + \mathrm{R}^{\delta\theta}_{\mathrm{int}}\end{aligned} \tag{B.9}$$

with the expansion of the individual terms provided below.

Equation 4.5a, the internal residual contribution derived from the motion, results from

$$\begin{aligned}\mathrm{R}^{\delta\boldsymbol{\varphi}}_{\mathrm{int}} &= D_{\boldsymbol{\varphi}}\Pi_{\mathrm{int}}\cdot\delta\boldsymbol{\varphi} \\ &= \int_{\Omega_0}\left\{\frac{\partial\psi_{\mathrm{iso}}\left(\bar{\boldsymbol{b}}\right)}{\partial\bar{\boldsymbol{b}}} : \delta\bar{\boldsymbol{b}} + p\delta J\right\}\mathrm{d}\Omega_0 \\ &= \int_{\Omega_0}\left\{\frac{\partial\psi_{\mathrm{iso}}\left(\bar{\boldsymbol{b}}\right)}{\partial\bar{\boldsymbol{b}}} : 2\left(\mathbb{P} : \left(\nabla\,\delta\boldsymbol{\varphi}\right)^{\mathrm{S}}\right)\bar{\boldsymbol{b}} + pJ\left(\left(\nabla\,\delta\boldsymbol{\varphi}\right)^{\mathrm{S}} : \boldsymbol{I}\right)\right\}\mathrm{d}\Omega_0 \\ &= \int_{\Omega_0}\left\{2\frac{\partial\psi_{\mathrm{iso}}\left(\bar{\boldsymbol{b}}\right)}{\partial\bar{\boldsymbol{b}}}\bar{\boldsymbol{b}} : \mathbb{P} : \left(\nabla\,\delta\boldsymbol{\varphi}\right)^{\mathrm{S}} + pJ\boldsymbol{I} : \left(\nabla\,\delta\boldsymbol{\varphi}\right)^{\mathrm{S}}\right\}\mathrm{d}\Omega_0\end{aligned} \tag{B.10}$$

using equations 3.82b, A.33, B.6 and B.8 and the symmetry of $\boldsymbol{I}$, $\bar{\boldsymbol{b}}$ and $\mathbb{P}$, and noting that that the push forward of the auxiliary second Piola-Kirchhoff stress can be written as

$$\bar{\boldsymbol{\tau}} = \bar{\boldsymbol{F}}\bar{\boldsymbol{S}}\bar{\boldsymbol{F}}^T = \bar{\boldsymbol{F}}\,2\frac{\partial\widehat{\psi}_{\mathrm{iso}}\left(\boldsymbol{C}\right)}{\partial\boldsymbol{C}}\bigg|_{\boldsymbol{C}=\bar{\boldsymbol{C}}}\bar{\boldsymbol{F}}^T = \boldsymbol{F}\,2\frac{\partial\widehat{\psi}_{\mathrm{iso}}\left(\boldsymbol{C}\right)}{\partial\boldsymbol{C}}\boldsymbol{F}^T\bigg|_{\boldsymbol{F}=\bar{\boldsymbol{F}}} = 2\frac{\partial\psi_{\mathrm{iso}}\left(\boldsymbol{b}\right)}{\partial\boldsymbol{b}}\boldsymbol{b}\bigg|_{\boldsymbol{b}=\bar{\boldsymbol{b}}} = 2\frac{\partial\psi_{\mathrm{iso}}\left(\bar{\boldsymbol{b}}\right)}{\partial\bar{\boldsymbol{b}}}\bar{\boldsymbol{b}} \tag{B.11}$$

resulting in equation 3.82c. The first variation of the total external work is

$$\mathrm{R}^{\delta\boldsymbol{\varphi}}_{\mathrm{ext}} = D_{\boldsymbol{\varphi}}\Pi_{\mathrm{ext}}\cdot\delta\boldsymbol{\varphi} = -\int_{\Omega_0}\left\{\delta\boldsymbol{\varphi}\cdot\boldsymbol{b}\right\}\mathrm{d}\Omega_0 - \int_{\Gamma^{\mathrm{t}}_0}\left\{\delta\boldsymbol{\varphi}\cdot\boldsymbol{t}\left(\boldsymbol{\varphi}\right)\right\}\mathrm{d}\Gamma^{\mathrm{t}}_0 \tag{B.12}$$

which leads directly to equation 4.16c when the boundary decomposition described in section 3.7 taken into account. Variation of the constraint leading to the equality of volumetric Jacobian and dilatation (equation 4.2a) is

$$\mathrm{R}^{\delta p}_{\mathrm{int}} = D_p\Pi_{\mathrm{int}}\cdot\delta p = \frac{d}{d\varepsilon}\bigg|_{\varepsilon=0}\int_{\Omega_0}\left\{q\left(J-\theta\right)\right\}\mathrm{d}\Omega_0 \quad , \tag{B.13}$$

resulting in equation 4.5c, while that of the incompressibility condition (equation 4.2b)

$$\mathrm{R}_{\mathrm{int}}^{\delta\theta} = D_\theta \Pi_{\mathrm{int}} \cdot \delta\theta = \left. \frac{d}{d\varepsilon} \right|_{\varepsilon=0} \int_{\Omega_0} \left\{ \psi_{\mathrm{vol}}(\gamma) - (\Lambda - p)\,\gamma \right\} \mathrm{d}\Omega_0 \tag{B.14}$$

leads to equation 4.5d using the chain rule derived identity $\psi_{\mathrm{vol}}(\gamma) = \dfrac{\partial \psi_{\mathrm{vol}}(\theta)}{\partial \theta} \delta\theta$.

B.2.1.1 Domain of integration

Notice that in equation 4.5a the integral is over the reference domain and the integrand involves quantities defined in the current configuration. Using equations 3.41 and 3.46, this expression is shown to be equivalent to equation 3.72

$$\int_{\Omega_0} \nabla \delta\boldsymbol{\varphi} : \boldsymbol{\tau}\, \mathrm{d}\Omega_0 = \int_{\Omega_0} \nabla \delta\boldsymbol{\varphi} : J\boldsymbol{\sigma}\, \mathrm{d}\Omega_0 = \int_{\Omega} \nabla \delta\boldsymbol{\varphi} : \boldsymbol{\sigma}\, \mathrm{d}\Omega \quad . \tag{B.15}$$

Similarly, the tangent matrix integrals developed in appendix B.2.2 have the form

$$\int_{\Omega_0} \nabla \delta\boldsymbol{\varphi} : J\mathbb{C} : \nabla \Delta\boldsymbol{\varphi}\, \mathrm{d}\Omega_0 = \int_{\Omega} \nabla \delta\boldsymbol{\varphi} : \mathbb{C} : \nabla \Delta\boldsymbol{\varphi}\, \mathrm{d}\Omega \quad . \tag{B.16}$$

B.2.2 Linearisation

Linearisation of the residual equation (equation B.9) results in the tangent

$$\begin{aligned}
\mathrm{K}(\delta\boldsymbol{\varphi}, \delta\theta, \delta p, \Delta\boldsymbol{\varphi}, \Delta\theta, \Delta p, \boldsymbol{\varphi}, \theta, p) &= D^2_{\boldsymbol{\varphi}} \Pi \cdot \Delta\boldsymbol{\varphi} + D^2_p \Pi \cdot \Delta p + D^2_\theta \Pi \cdot \Delta\theta \\
&= \left(D_{\boldsymbol{\varphi}} \mathrm{R}_{\mathrm{int}}^{\delta\boldsymbol{\varphi}} \cdot \Delta\boldsymbol{\varphi} + D_{\boldsymbol{\varphi}} \mathrm{R}_{\mathrm{ext}}^{\delta\boldsymbol{\varphi}} \cdot \Delta\boldsymbol{\varphi} + D_p \mathrm{R}_{\mathrm{int}}^{\delta\boldsymbol{\varphi}} \cdot \Delta p \right) + \left(D_{\boldsymbol{\varphi}} \mathrm{R}_{\mathrm{int}}^{\delta p} \cdot \Delta\boldsymbol{\varphi} + D_\theta \mathrm{R}_{\mathrm{int}}^{\delta p} \cdot \Delta\theta \right) \\
&\quad + \left(D_p \mathrm{R}_{\mathrm{int}}^{\delta\theta} \cdot \Delta p + D_\theta \mathrm{R}_{\mathrm{int}}^{\delta\theta} \cdot \Delta\theta \right) \\
&= \mathrm{K}_{\mathrm{int}}^{\delta\boldsymbol{\varphi},\Delta\boldsymbol{\varphi}} + \mathrm{K}_{\mathrm{ext}}^{\delta\boldsymbol{\varphi},\Delta\boldsymbol{\varphi}} + \mathrm{K}_{\mathrm{int}}^{\delta\boldsymbol{\varphi},\Delta p} + \mathrm{K}_{\mathrm{int}}^{\delta p,\Delta\boldsymbol{\varphi}} + \mathrm{K}_{\mathrm{int}}^{\delta p,\Delta\theta} + \mathrm{K}_{\mathrm{int}}^{\delta\theta,\Delta p} + \mathrm{K}_{\mathrm{int}}^{\delta\theta,\Delta\theta} \quad .
\end{aligned} \tag{B.17}$$

Following Holzapfel et al. [107], the derivation of the first term of equation B.17 is completed using a rate-based description for the purpose of increased legibility. As the virtual displacement field is independent of the real displacement, its rate is

$$(\nabla(\delta\boldsymbol{\varphi}))^{\cdot} = \delta\boldsymbol{F}\dot{\boldsymbol{F}}^{-1} = -\delta\boldsymbol{F}\boldsymbol{F}^{-1}\boldsymbol{l} = -\nabla(\delta\boldsymbol{\varphi})\boldsymbol{l} \tag{B.18}$$

using the identity

$$\left(\boldsymbol{F}^{-1}\boldsymbol{F}\right)^{\cdot} = \dot{\boldsymbol{I}} = \boldsymbol{0} \quad \Rightarrow \quad \dot{\boldsymbol{F}}^{-1} = -\boldsymbol{F}^{-1}\dot{\boldsymbol{F}}\boldsymbol{F}^{-1} \quad ,$$

which, by application of equation 3.10, also implies that

$$\boldsymbol{F}\dot{\boldsymbol{F}}^{-1} = -\boldsymbol{l} \quad . \tag{B.19}$$

The Lie time-derivative of the Kirchhoff stress, which provides the stress rate, is

$$\mathcal{L}(\boldsymbol{\tau}) = \dot{\boldsymbol{\tau}} - \boldsymbol{l}\boldsymbol{\tau} - \boldsymbol{\tau}\boldsymbol{l}^T \tag{B.20}$$

$$\equiv J\mathbb{C} : \boldsymbol{d} \quad , \tag{B.21}$$

the first part coming from the definition of the Lie time-derivative (total time derivative of contravariant tensors) with the use of equation B.19

$$\begin{aligned}\mathcal{L}(\boldsymbol{\tau}) := \frac{d\boldsymbol{\tau}}{dt} &= \boldsymbol{F}\left(\frac{D}{Dt}\left(\boldsymbol{F}^{-1}\boldsymbol{\tau}\boldsymbol{F}^{-T}\right)\right)\boldsymbol{F}^{T}\\ &= \boldsymbol{F}\left(\dot{\boldsymbol{F}}^{-1}\boldsymbol{\tau}\boldsymbol{F}^{-T} + \boldsymbol{F}^{-1}\dot{\boldsymbol{\tau}}\boldsymbol{F}^{-T} + \boldsymbol{F}^{-1}\boldsymbol{\tau}\dot{\boldsymbol{F}}^{-T}\right)\boldsymbol{F}^{T}\\ &= \boldsymbol{F}\dot{\boldsymbol{F}}^{-1}\boldsymbol{\tau}\boldsymbol{F}^{-T}\boldsymbol{F}^{T} + \boldsymbol{F}\boldsymbol{F}^{-1}\dot{\boldsymbol{\tau}}\boldsymbol{F}^{-T}\boldsymbol{F}^{T} + \boldsymbol{F}\boldsymbol{F}^{-1}\boldsymbol{\tau}\dot{\boldsymbol{F}}^{-T}\boldsymbol{F}^{T}\\ &= -\boldsymbol{l}\boldsymbol{\tau} + \dot{\boldsymbol{\tau}} - \boldsymbol{\tau}\boldsymbol{l}^{T}\end{aligned} \tag{B.22}$$

and the second from the equivalence of the form of the total time derivative and the linearisation of $\boldsymbol{\tau}$, that is

$$\Delta\boldsymbol{\tau} = \frac{\partial\boldsymbol{\tau}}{\partial\nabla(\Delta\boldsymbol{\varphi})} : \nabla(\Delta\boldsymbol{\varphi}) = J\mathbb{C} : \nabla(\Delta\boldsymbol{\varphi}) \quad \Rightarrow \quad \dot{\boldsymbol{\tau}} = J\mathbb{C} : \nabla(\dot{\boldsymbol{\varphi}}) \quad . \tag{B.23}$$

Equating and rearranging equations B.21 and B.22, the Kirchhoff stress rate can therefore be written as

$$\dot{\boldsymbol{\tau}} = J\mathbb{C} : \boldsymbol{d} + \boldsymbol{l}\boldsymbol{\tau} + \boldsymbol{\tau}\boldsymbol{l}^{T} \quad . \tag{B.24}$$

Expressed in terms of rates and through the application of equations B.18 and B.24, the linearisation of the integrand of equation 4.5a is thus

$$\begin{aligned}(\nabla(\delta\boldsymbol{\varphi}) : \boldsymbol{\tau})^{\cdot} &= (\nabla(\delta\boldsymbol{\varphi}))^{\cdot} : \boldsymbol{\tau} + \nabla(\delta\boldsymbol{\varphi}) : \dot{\boldsymbol{\tau}}\\ &= -\nabla(\delta\boldsymbol{\varphi}) : \boldsymbol{\tau}\boldsymbol{l}^{T} + \nabla(\delta\boldsymbol{\varphi}) : \left(J\mathbb{C} : \boldsymbol{d} + \boldsymbol{l}\boldsymbol{\tau} + \boldsymbol{\tau}\boldsymbol{l}^{T}\right)\\ &= \nabla(\delta\boldsymbol{\varphi}) : (J\mathbb{C} : \boldsymbol{d} + \boldsymbol{l}\boldsymbol{\tau})\end{aligned} \tag{B.25}$$

where $\boldsymbol{\tau} = \boldsymbol{\tau}_{\text{iso}} + pJ\boldsymbol{I}$ and the total displacement tangent $J\mathbb{C} = J\mathbb{C}_{\text{iso}} + pJ(\boldsymbol{I}\otimes\boldsymbol{I} - 2\mathbb{I})$. The contribution to the incremental problem for the motion-dependent portion of the residual equation therefore appears in the form

$$\begin{aligned}\mathrm{K}_{\text{int}}^{\delta\boldsymbol{\varphi},\Delta\boldsymbol{\varphi}} = &\int_{\Omega_0}\left\{\nabla(\delta\boldsymbol{\varphi}) : [J\mathbb{C}_{\text{iso}} + pJ(\boldsymbol{I}\otimes\boldsymbol{I} - 2\mathbb{I})] : \nabla(\Delta\boldsymbol{\varphi})\right\}\mathrm{d}\Omega_0\\ &+ \int_{\Omega_0}\left\{\nabla(\delta\boldsymbol{\varphi}) : \nabla(\Delta\boldsymbol{\varphi})\,[\boldsymbol{\tau}_{\text{iso}} + pJ\boldsymbol{I}]\right\}\mathrm{d}\Omega_0 \quad ,\end{aligned} \tag{B.26}$$

and that for the motion-dependent portion of the external energy equation is

$$\mathrm{K}_{\text{ext}}^{\delta\boldsymbol{\varphi},\Delta\boldsymbol{\varphi}} = -\int_{\Gamma_0^{\mathrm{t}(u)}}\left\{\delta\boldsymbol{\varphi}\cdot\frac{\partial\boldsymbol{t}(\boldsymbol{u})}{\partial\boldsymbol{\varphi}}\Delta\boldsymbol{\varphi}\right\}\mathrm{d}\Gamma_0^{\mathrm{t}(u)} \tag{B.27}$$

which is equivalent to equation 4.17e. The other linearisation terms following from the three-field formulation, that is when Λ is not treated as field-variable, are simply

$$\mathrm{K}_{\text{int}}^{\delta\boldsymbol{\varphi},\Delta p} = \int_{\Omega_0}\left\{\nabla(\delta\boldsymbol{\varphi}) : \Delta pJ\boldsymbol{I}\right\}\mathrm{d}\Omega_0 = \int_{\Omega_0}\left\{J\nabla\cdot(\delta\boldsymbol{\varphi})\Delta p\right\}\mathrm{d}\Omega_0 \tag{B.28}$$

$$\mathrm{K}_{\text{int}}^{\delta p,\Delta\boldsymbol{\varphi}} = \int_{\Omega_0}\left\{\delta pJ\boldsymbol{I} : \nabla\Delta\boldsymbol{\varphi}\right\}\mathrm{d}\Omega_0 = \int_{\Omega_0}\left\{\delta pJ\nabla\cdot\Delta\boldsymbol{\varphi}\right\}\mathrm{d}\Omega_0 \tag{B.29}$$

$$\mathrm{K}_{\text{int}}^{\delta p,\Delta\theta} = -\int_{\Omega_0}\left\{\delta p\Delta\theta\right\}\mathrm{d}\Omega_0 \tag{B.30}$$

$$\mathrm{K}_{\text{int}}^{\delta\theta,\Delta p} = -\int_{\Omega_0}\left\{\delta\theta\Delta p\right\}\mathrm{d}\Omega_0 \tag{B.31}$$

$$\mathrm{K}_{\text{int}}^{\delta\theta,\Delta\theta} = \int_{\Omega_0}\left\{\delta\theta\psi''_{\text{vol}}(\theta)\,\Delta\theta\right\}\mathrm{d}\Omega_0 \tag{B.32}$$

using equation B.6 and noting that $\Delta\psi_{\text{vol}}(\theta) = \dfrac{\partial\psi_{\text{vol}}(\theta)}{\partial\theta}\Delta\theta$.

B.3 Mean dilatation Q1-P0 element

As the name suggests, the mean dilatation Q1-P0-P0 element assumes that the dilatation and pressure quantities are piecewise constant and discontinuous. Due to this property, these terms can be filtered out on an element level resulting in a displacement-only formulation.

On a per-element basis, the weak-form of equation 4.2a can be modified such that

$$\int_{\Omega_0^e} \theta^e \, \mathrm{d}\Omega_0^e = \int_{\Omega_0^e} J \, \mathrm{d}\Omega_0^e \quad \Rightarrow \quad \theta^e \int_{\Omega_0^e} \mathrm{d}\Omega_0^e = \int_{\Omega_0^e} J \, \mathrm{d}\Omega_0^e \tag{B.33}$$

resulting in equation 4.14, along with the associated equations 4.12 and 4.13, by application of equation 3.46. Variation and linearisation of equation B.33 using equation B.6 leads to

$$\delta\theta^e = \frac{1}{V^e} \int_{\Omega_0^e} \delta J \, \mathrm{d}\Omega_0^e = \frac{1}{V^e} \int_{\Omega_0^e} J \left(\nabla \left(\delta\boldsymbol{\varphi} \right) : \boldsymbol{I} \right) \, \mathrm{d}\Omega_0^e \tag{B.34}$$

$$\Delta\theta^e = \frac{1}{V^e} \int_{\Omega_0^e} J \left(\nabla \left(\Delta\boldsymbol{\varphi} \right) : \boldsymbol{I} \right) \, \mathrm{d}\Omega_0^e \quad . \tag{B.35}$$

From equation 4.5d, the element-wise pressure is determined to be

$$\begin{aligned} \int_{\Omega_0^e} p^e \, \mathrm{d}\Omega_0^e = p^e \int_{\Omega_0^e} \mathrm{d}\Omega_0^e = \int_{\Omega_0^e} \left\{ \psi'_{\mathrm{vol}} \left(\theta \right) + \Lambda \right\} \mathrm{d}\Omega_0^e \\ \Rightarrow \quad p^e = \frac{1}{V^e} \int_{\Omega_0^e} \left\{ \psi'_{\mathrm{vol}} \left(\theta \right) + \Lambda \right\} \mathrm{d}\Omega_0^e \end{aligned} \tag{B.36}$$

which leads to equation 4.15 when it is assumed that Λ is constant on an element. Using equation B.34, the resulting variation and linearisation of equation B.36 is

$$\delta p^e = \psi''_{\mathrm{vol}} \left(\theta^e \right) \delta\theta^e = \psi''_{\mathrm{vol}} \left(\theta^e \right) \frac{1}{V^e} \int_{\Omega_0^e} J \left(\nabla \left(\delta\boldsymbol{\varphi} \right) : \boldsymbol{I} \right) \, \mathrm{d}\Omega_0^e \tag{B.37}$$

$$\Delta p^e = \Delta \left(\psi'_{\mathrm{vol}} \left(\theta^e \right) + \Lambda \right) = \psi''_{\mathrm{vol}} \left(\theta^e \right) \Delta\theta^e = \psi''_{\mathrm{vol}} \left(\theta^e \right) \frac{1}{V^e} \int_{\Omega_0^e} J \left(\nabla \left(\Delta\boldsymbol{\varphi} \right) : \boldsymbol{I} \right) \, \mathrm{d}\Omega_0^e \quad . \tag{B.38}$$

The reduced displacement residual formulation, attained by substitution of equation B.34, equation B.37 into equation B.9, is

$$\begin{aligned} \mathrm{R}^{\mathrm{int}} \left(\delta\boldsymbol{\varphi}, \boldsymbol{\varphi}, \theta, p \right) = & \int_{\Omega_0} \left\{ \nabla \left(\delta\boldsymbol{\varphi} \right) : \left[\boldsymbol{\tau}_{\mathrm{iso}} \left(\bar{\boldsymbol{b}}, \bar{\lambda}_{\mathrm{f}} \right) + pJ\boldsymbol{I} \right] \right\} \mathrm{d}\Omega_0 \\ & + \int_{\Omega_0} \left\{ \psi''_{\mathrm{vol}} \left(\theta^e \right) \frac{1}{V^e} \int_{\Omega_0^e} J \left(\nabla \left(\delta\boldsymbol{\varphi} \right) : \boldsymbol{I} \right) \, \mathrm{d}\Omega_0^e \left(J - \theta \right) \right\} \mathrm{d}\Omega_0 \\ & + \int_{\Omega_0} \left\{ \frac{1}{V^e} \int_{\Omega_0^e} J \left(\nabla \left(\delta\boldsymbol{\varphi} \right) : \boldsymbol{I} \right) \, \mathrm{d}\Omega_0^e \left(\left[\psi'_{\mathrm{vol}} \left(\theta \right) + \Lambda \right] - p \right) \right\} \mathrm{d}\Omega_0 \\ = & \int_{\Omega_0} \left\{ \nabla \left(\delta\boldsymbol{\varphi} \right) : \left[\boldsymbol{\tau}_{\mathrm{iso}} \left(\bar{\boldsymbol{b}}, \bar{\lambda}_{\mathrm{f}} \right) + p^e J\boldsymbol{I} \right] \right\} \mathrm{d}\Omega_0 \\ & + \sum_{e=1}^{n_{\mathrm{el}}} \psi''_{\mathrm{vol}} \left(\theta^e \right) \frac{1}{V^e} \int_{\Omega_0^e} J \left(\nabla \left(\delta\boldsymbol{\varphi} \right) : \boldsymbol{I} \right) \, \mathrm{d}\Omega_0^e \int_{\Omega_0^e} \left\{ J - \theta^e \right\} \mathrm{d}\Omega_0^e \\ & + \sum_{e=1}^{n_{\mathrm{el}}} \frac{1}{V^e} \int_{\Omega_0^e} J \left(\nabla \left(\delta\boldsymbol{\varphi} \right) : \boldsymbol{I} \right) \, \mathrm{d}\Omega_0^e \int_{\Omega_0^e} \left\{ \left[\psi'_{\mathrm{vol}} \left(\theta^e \right) + \Lambda^e \right] - p^e \right\} \mathrm{d}\Omega_0^e \end{aligned} \quad . \tag{B.39}$$

By using the element-wise definitions of θ, p listed in equations 4.14 and 4.15, this further reduces to the form given in equation 4.16b.

Using the discontinuity of the fields, their constant value over the element and applying equation B.34, equation B.37, equation B.35, equation B.38 to equations B.28 to B.32 as required in equation B.17, the expression

$$
\begin{aligned}
&\int_{\Omega_0} \left\{ \nabla(\delta\boldsymbol{\varphi}) : J\boldsymbol{I}\Delta p \right\} \mathrm{d}\Omega_0 + \int_{\Omega_0} \left\{ \delta p J\boldsymbol{I} : \nabla(\Delta\boldsymbol{\varphi}) \right\} \mathrm{d}\Omega_0 \\
&\quad - \int_{\Omega_0} \left\{ \delta\theta\ \Delta p \right\} \mathrm{d}\Omega_0 - \int_{\Omega_0} \left\{ \delta p\ \Delta\theta \right\} \mathrm{d}\Omega_0 + \int_{\Omega_0} \left\{ \delta\theta\ \psi''_{\mathrm{vol}}(\theta)\,\Delta\theta \right\} \mathrm{d}\Omega_0 \\
&= \sum_{\mathrm{e}=1}^{\mathrm{n_{el}}} \left[\int_{\Omega_0^{\mathrm{e}}} \left\{ \nabla(\delta\boldsymbol{\varphi}) : J\boldsymbol{I}\Delta p^{\mathrm{e}} \right\} \mathrm{d}\Omega_0^{\mathrm{e}} + \int_{\Omega_0^{\mathrm{e}}} \left\{ \delta p^{\mathrm{e}} J\boldsymbol{I} : \nabla(\Delta\boldsymbol{\varphi}) \right\} \mathrm{d}\Omega_0^{\mathrm{e}} \right. \\
&\quad \left. - \int_{\Omega_0^{\mathrm{e}}} \left\{ \delta\theta^{\mathrm{e}}\ \Delta p^{\mathrm{e}} \right\} \mathrm{d}\Omega_0^{\mathrm{e}} - \int_{\Omega_0^{\mathrm{e}}} \left\{ \delta p^{\mathrm{e}}\ \Delta\theta^{\mathrm{e}} \right\} \mathrm{d}\Omega_0^{\mathrm{e}} + \int_{\Omega_0^{\mathrm{e}}} \left\{ \delta\theta^{\mathrm{e}}\ \psi''_{\mathrm{vol}}(\theta^{\mathrm{e}})\,\Delta\theta^{\mathrm{e}} \right\} \mathrm{d}\Omega_0^{\mathrm{e}} \right] \\
&= \sum_{\mathrm{e}=1}^{\mathrm{n_{el}}} \left[\int_{\Omega_0^{\mathrm{e}}} \nabla(\delta\boldsymbol{\varphi}) : J\boldsymbol{I}\ \mathrm{d}\Omega_0^{\mathrm{e}}\ \psi''_{\mathrm{vol}}(\theta^{\mathrm{e}})\ \frac{1}{\mathrm{V^e}} \int_{\Omega_0^{\mathrm{e}}} J\left(\nabla(\Delta\boldsymbol{\varphi}) : \boldsymbol{I}\right)\ \mathrm{d}\Omega_0^{\mathrm{e}} \right. \\
&\quad + \psi''_{\mathrm{vol}}(\theta^{\mathrm{e}})\ \frac{1}{\mathrm{V^e}} \int_{\Omega_0^{\mathrm{e}}} J\left(\nabla(\delta\boldsymbol{\varphi}) : \boldsymbol{I}\right)\ \mathrm{d}\Omega_0^{\mathrm{e}} \int_{\Omega_0^{\mathrm{e}}} J\boldsymbol{I} : \nabla(\Delta\boldsymbol{\varphi})\ \mathrm{d}\Omega_0^{\mathrm{e}} \\
&\quad - \frac{1}{\mathrm{V^e}} \int_{\Omega_0^{\mathrm{e}}} J\left(\nabla(\delta\boldsymbol{\varphi}) : \boldsymbol{I}\right)\ \mathrm{d}\Omega_0^{\mathrm{e}} \int_{\Omega_0^{\mathrm{e}}} \mathrm{d}\Omega_0^{\mathrm{e}}\ \psi''_{\mathrm{vol}}(\theta^{\mathrm{e}})\ \frac{1}{\mathrm{V^e}} \int_{\Omega_0^{\mathrm{e}}} J\left(\nabla(\Delta\boldsymbol{\varphi}) : \boldsymbol{I}\right)\ \mathrm{d}\Omega_0^{\mathrm{e}} \\
&\quad - \psi''_{\mathrm{vol}}(\theta^{\mathrm{e}})\ \frac{1}{\mathrm{V^e}} \int_{\Omega_0^{\mathrm{e}}} J\left(\nabla(\delta\boldsymbol{\varphi}) : \boldsymbol{I}\right)\ \mathrm{d}\Omega_0^{\mathrm{e}} \int_{\Omega_0^{\mathrm{e}}} \mathrm{d}\Omega_0^{\mathrm{e}}\ \frac{1}{\mathrm{V^e}} \int_{\Omega_0^{\mathrm{e}}} J\left(\nabla(\Delta\boldsymbol{\varphi}) : \boldsymbol{I}\right)\ \mathrm{d}\Omega_0^{\mathrm{e}} \\
&\quad \left. + \frac{1}{\mathrm{V^e}} \int_{\Omega_0^{\mathrm{e}}} J\left(\nabla(\delta\boldsymbol{\varphi}) : \boldsymbol{I}\right)\ \mathrm{d}\Omega_0^{\mathrm{e}} \int_{\Omega_0^{\mathrm{e}}} \psi''_{\mathrm{vol}}(\theta^{\mathrm{e}})\ \mathrm{d}\Omega_0^{\mathrm{e}}\ \frac{1}{\mathrm{V^e}} \int_{\Omega_0^{\mathrm{e}}} J\left(\nabla(\Delta\boldsymbol{\varphi}) : \boldsymbol{I}\right)\ \mathrm{d}\Omega_0^{\mathrm{e}} \right] \\
&= \sum_{\mathrm{e}=1}^{\mathrm{n_{el}}} \left[\frac{1}{\mathrm{V^e}} \int_{\Omega_0^{\mathrm{e}}} J\left(\nabla(\delta\boldsymbol{\varphi}) : \boldsymbol{I}\right)\ \mathrm{d}\Omega_0^{\mathrm{e}} \right] \left[\psi''_{\mathrm{vol}}(\theta^{\mathrm{e}})\,\mathrm{V^e} \right] \left[\frac{1}{\mathrm{V^e}} \int_{\Omega_0^{\mathrm{e}}} J\left(\nabla(\Delta\boldsymbol{\varphi}) : \boldsymbol{I}\right)\ \mathrm{d}\Omega_0^{\mathrm{e}} \right]
\end{aligned}
\tag{B.40}
$$

is resolved. Applying equation B.40 to the internal contributions of equation B.17, the final form of the reduced stiffness formulation derived from the internal energy is

$$
\mathrm{K^{int}}(\delta\boldsymbol{\varphi}, \Delta\boldsymbol{\varphi}, \boldsymbol{\varphi}) = \mathrm{K_{vol}} + \mathrm{K_{mat}} + \mathrm{K_{geo}} \tag{B.41}
$$

with the definitions of these terms provided in equations 4.17b to 4.17d.

C. MATERIAL MODELS

C.1 Constitutive relations for general fibrous hyperelastic materials

Beginning with the definition of the material SEF

$$\psi = \widehat{\psi}_J\left(J\right) + \widehat{\psi}_{\mathrm{M}}\left(\boldsymbol{C}\right) + \sum_{\mathrm{f}} \widehat{\psi}_{\mathrm{f}}\left(\lambda_{\mathrm{f}}\right) = \psi_J\left(J\right) + \psi_{\mathrm{M}}\left(\boldsymbol{b}\right) + \sum_{\mathrm{f}} \psi_{\mathrm{f}}\left(\lambda_{\mathrm{f}}\right) \quad , \tag{C.1}$$

a precursor to equation 5.1b, the derivation of the stress and tangent tensors for the volumetric component (equations 5.4a and 5.5a) follows the same approach adopted in the determination of equations 3.82a and 3.83a.

Energetic contributions from the bulk, ψ_{M}, are assumed to be a function of the tensor invariants. Using equation 3.51, applying the chain rule and the derivatives noted in equations A.7 and A.8, the second Piola-Kirchhoff stress is

$$\boldsymbol{S}_M = 2\frac{\partial \widehat{\psi}_{\mathrm{M}}}{\partial \boldsymbol{C}} = 2\left(\frac{\partial \widehat{\psi}_{\mathrm{M}}}{\partial I_1^C}\frac{\partial I_1^C}{\partial \boldsymbol{C}} + \frac{\partial \widehat{\psi}_{\mathrm{M}}}{\partial I_2^C}\frac{\partial I_2^C}{\partial \boldsymbol{C}}\right) = 2\left(\left(\frac{\partial \widehat{\psi}_{\mathrm{M}}}{\partial I_1^C} + I_1^C\frac{\partial \widehat{\psi}_{\mathrm{M}}}{\partial I_2^C}\right)\boldsymbol{I} - \frac{\partial \widehat{\psi}_{\mathrm{M}}}{\partial I_2^C}\boldsymbol{C}\right) \quad , \tag{C.2}$$

which can be transformed to the spatial Kirchhoff stress tensor using equation 3.37, the result of which is

$$\boldsymbol{\tau}_M = 2\left(\left(\frac{\partial \psi_{\mathrm{M}}}{\partial I_1^b} + I_1^b\frac{\partial \psi_{\mathrm{M}}}{\partial I_2^b}\right)\boldsymbol{I} - \frac{\partial \psi_{\mathrm{M}}}{\partial I_2^b}\boldsymbol{b}\right)\boldsymbol{b} = 2\frac{\partial \psi_{\mathrm{M}}}{\partial \boldsymbol{b}}\boldsymbol{b} \tag{C.3}$$

and equivalent to that provided in equation 5.4b. The tangent associated with equation C.2 is expanded to

$$\mathbb{H}_M = 4\frac{\partial^2 \widehat{\psi}_{\mathrm{M}}}{\partial \boldsymbol{C}^2} = 2\frac{\partial \boldsymbol{S}_M}{\partial \boldsymbol{C}} = 4\left(\frac{\partial}{\partial \boldsymbol{C}}\left(\frac{\partial \widehat{\psi}_{\mathrm{M}}}{\partial I_1^C}\boldsymbol{I}\right) + \frac{\partial}{\partial \boldsymbol{C}}\left(I_1^C\frac{\partial \widehat{\psi}_{\mathrm{M}}}{\partial I_2^C}\boldsymbol{I}\right) + \frac{\partial}{\partial \boldsymbol{C}}\left(-\frac{\partial \widehat{\psi}_{\mathrm{M}}}{\partial I_2^C}\boldsymbol{C}\right)\right) \tag{C.4}$$

where the derivative quantities are given by

$$\begin{aligned}\frac{\partial}{\partial \boldsymbol{C}}\left(\frac{\partial \widehat{\psi}_{\mathrm{M}}}{\partial I_1^C}\boldsymbol{I}\right) &= \boldsymbol{I}\otimes\left(\frac{\partial^2 \widehat{\psi}_{\mathrm{M}}}{\partial {I_1^C}^2}\frac{\partial I_1^C}{\partial \boldsymbol{C}} + \frac{\partial^2 \widehat{\psi}_{\mathrm{M}}}{\partial I_2^C \partial I_1^C}\frac{\partial I_2^C}{\partial \boldsymbol{C}}\right) \\ &= \left(\frac{\partial^2 \widehat{\psi}_{\mathrm{M}}}{\partial {I_1^C}^2} + \frac{\partial^2 \widehat{\psi}_{\mathrm{M}}}{\partial I_2^C \partial I_1^C}I_1^C\right)\boldsymbol{I}\otimes\boldsymbol{I} - \left(\frac{\partial^2 \widehat{\psi}_{\mathrm{M}}}{\partial I_2^C \partial I_1^C}\right)\boldsymbol{I}\otimes\boldsymbol{C}\end{aligned} \tag{C.5}$$

$$\begin{aligned}\frac{\partial}{\partial \boldsymbol{C}}\left(I_1^C\frac{\partial \widehat{\psi}_{\mathrm{M}}}{\partial I_2^C}\boldsymbol{I}\right) &= \boldsymbol{I}\otimes\left(\frac{\partial I_1^C}{\partial \boldsymbol{C}}\frac{\partial \widehat{\psi}_{\mathrm{M}}}{\partial I_2^C} + I_1^C\left(\frac{\partial^2 \widehat{\psi}_{\mathrm{M}}}{\partial I_1^C \partial I_2^C}\frac{\partial I_1^C}{\partial \boldsymbol{C}} + \frac{\partial^2 \widehat{\psi}_{\mathrm{M}}}{\partial {I_2^C}^2}\frac{\partial I_2^C}{\partial \boldsymbol{C}}\right)\right) \\ &= \left(\frac{\partial \widehat{\psi}_{\mathrm{M}}}{\partial I_2^C} + \frac{\partial^2 \widehat{\psi}_{\mathrm{M}}}{\partial I_1^C \partial I_2^C}I_1^C + \frac{\partial^2 \widehat{\psi}_{\mathrm{M}}}{\partial {I_2^C}^2}{I_1^C}^2\right)\boldsymbol{I}\otimes\boldsymbol{I} - \left(\frac{\partial^2 \widehat{\psi}_{\mathrm{M}}}{\partial {I_2^C}^2}I_1^C\right)\boldsymbol{I}\otimes\boldsymbol{C}\end{aligned} \tag{C.6}$$

$$-\frac{\partial}{\partial \boldsymbol{C}}\left(\frac{\partial \widehat{\psi}_{\mathrm{M}}}{\partial I_2^C}\boldsymbol{C}\right) = -\left(\boldsymbol{C}\otimes\left(\frac{\partial^2\widehat{\psi}_{\mathrm{M}}}{\partial I_1^C\partial I_2^C}\frac{\partial I_1^C}{\partial \boldsymbol{C}}+\frac{\partial^2\widehat{\psi}_{\mathrm{M}}}{\partial {I_2^C}^2}\frac{\partial I_2^C}{\partial \boldsymbol{C}}\right)+\frac{\partial\widehat{\psi}_{\mathrm{M}}}{\partial I_2^C}\frac{\partial \boldsymbol{C}}{\partial \boldsymbol{C}}\right)$$
$$= -\left(\frac{\partial^2\widehat{\psi}_{\mathrm{M}}}{\partial I_1^C\partial I_2^C}+\frac{\partial^2\widehat{\psi}_{\mathrm{M}}}{\partial {I_2^C}^2}I_1^C\right)\boldsymbol{C}\otimes\boldsymbol{I}+\left(\frac{\partial^2\widehat{\psi}_{\mathrm{M}}}{\partial {I_2^C}^2}\right)\boldsymbol{C}\otimes\boldsymbol{C}-\left(\frac{\partial\widehat{\psi}_{\mathrm{M}}}{\partial I_2^C}\right)\mathbb{I} \tag{C.7}$$

which, on substitution into equation C.4, produces the final result

$$\mathbb{H}_M = 4\left[\left(\frac{\partial^2\widehat{\psi}_{\mathrm{M}}}{\partial {I_1^C}^2}+2\frac{\partial^2\widehat{\psi}_{\mathrm{M}}}{\partial I_2^C\partial I_1^C}I_1^C+\frac{\partial^2\widehat{\psi}_{\mathrm{M}}}{\partial {I_2^C}^2}{I_1^C}^2+\frac{\partial\widehat{\psi}_{\mathrm{M}}}{\partial I_2^C}\right)\boldsymbol{I}\otimes\boldsymbol{I}\right.$$
$$\left.-\left(\frac{\partial^2\widehat{\psi}_{\mathrm{M}}}{\partial I_2^C\partial I_1^C}+\frac{\partial^2\widehat{\psi}_{\mathrm{M}}}{\partial {I_2^C}^2}I_1^C\right)(\boldsymbol{I}\otimes\boldsymbol{C}+\boldsymbol{C}\otimes\boldsymbol{I})+\left(\frac{\partial^2\widehat{\psi}_{\mathrm{M}}}{\partial {I_2^C}^2}\right)\boldsymbol{C}\otimes\boldsymbol{C}-\left(\frac{\partial\widehat{\psi}_{\mathrm{M}}}{\partial I_2^C}\right)\mathbb{I}\right) \quad . \tag{C.8}$$

The spatial transformation of equation C.8 using equations 3.56, A.19 to A.21 and A.25 returns the result given in equation 5.5b.

With the use of equation A.11, the second Piola-Kirchhoff stress derived from the internal fibre contributions

$$\boldsymbol{S}_f = 2\frac{\partial\widehat{\psi}_{\mathrm{f}}}{\partial \boldsymbol{C}} = 2\frac{\partial\widehat{\psi}_{\mathrm{f}}}{\partial\lambda_{\mathrm{f}}}\frac{\partial\lambda_{\mathrm{f}}}{\partial \boldsymbol{C}} = \widehat{\psi}'_{\mathrm{f}}{\lambda_{\mathrm{f}}}^{-1}\boldsymbol{N}_{\mathrm{f}}\otimes\boldsymbol{N}_{\mathrm{f}} \tag{C.9}$$

which leads to equation 5.4c using equations 3.37 and A.17 The fibre tangent is then

$$\mathbb{H}_f = 4\frac{\partial^2\widehat{\psi}_{\mathrm{f}}}{\partial {\boldsymbol{C}}^2} = 2\frac{\partial \boldsymbol{S}_f}{\partial \boldsymbol{C}} = 2\boldsymbol{N}\otimes\boldsymbol{N}\otimes\left(\frac{\partial\widehat{\psi}'_{\mathrm{f}}}{\partial\lambda_{\mathrm{f}}}{\lambda_{\mathrm{f}}}^{-1}+\widehat{\psi}'_{\mathrm{f}}\frac{\partial{\lambda_{\mathrm{f}}}^{-1}}{\partial\lambda_{\mathrm{f}}}\right)\frac{\partial\lambda_{\mathrm{f}}}{\partial \boldsymbol{C}}$$
$$= \left(\widehat{\psi}''_{\mathrm{f}}-\widehat{\psi}'_{\mathrm{f}}{\lambda_{\mathrm{f}}}^{-1}\right){\lambda_{\mathrm{f}}}^{-2}\boldsymbol{N}\otimes\boldsymbol{N}\otimes\boldsymbol{N}\otimes\boldsymbol{N} \tag{C.10}$$

from which its spatial counterpart given in equation 5.5c is produced through the use of equations 3.56 and A.24.

C.2 Total work done by active contraction of muscles within a continuum

Starting from the continuum definition of rate of work expended on a body in quasi-static deformation as defined by equation 3.45, the insertion of the relations given by equation 5.6a along with the use of equation 3.41 results in

$$\dot{W} = \int_{\Omega}(-p\boldsymbol{I}+\boldsymbol{\sigma}_{\mathrm{M}}+\textstyle\sum_{\mathrm{f}}\phi_{\mathrm{f}}\boldsymbol{\sigma}_{\mathrm{f}}) : \boldsymbol{l}\,\mathrm{d}\Omega \tag{C.11}$$

which is equivalent to

$$\dot{W} = \dot{W}^{\mathrm{vol}}+\dot{W}^{\mathrm{iso}} = \dot{W}^{\mathrm{vol}}+\dot{W}^{\mathrm{M}}+\sum_{\mathrm{f}}\dot{W}^{\mathrm{f}} \quad .$$

From this, one can determine the total work rate of a specific muscle by noting that

$$\dot{W}_{\mathrm{f}} = \int_{\Omega^{\mathrm{f}}}\phi_{\mathrm{f}}\boldsymbol{\sigma}_{\mathrm{f}} : \boldsymbol{l}\,\mathrm{d}\Omega^{\mathrm{f}} = \int_{\Omega_0^{\mathrm{f}}}\phi_{\mathrm{f}}\boldsymbol{\tau}_{\mathrm{f}} : \boldsymbol{l}\,\mathrm{d}\Omega_0^{\mathrm{f}} \tag{C.12}$$

which includes contributions from the PE, SE and CE. After decomposing the fibre Kirchhoff stress into magnitude and directional components, further manipulation of equation C.12 using equations 3.10, 3.20,

6.6, 7.15 and 7.16 produces

$$\begin{aligned}\dot{W}_{\mathrm{f}} &= \int_{\Omega_0^{\mathrm{f}}} \phi_{\mathrm{f}} T_{\mathrm{f}} \lambda_{\mathrm{f}} \boldsymbol{n}_{\mathrm{f}} \otimes \boldsymbol{n}_{\mathrm{f}} : \boldsymbol{l} \, \mathrm{d}\Omega_0^{\mathrm{f}} \\ &= \int_{\Omega_0^{\mathrm{f}}} \phi_{\mathrm{f}} T_{\mathrm{f}} \lambda_{\mathrm{f}} \left(\boldsymbol{n}_{\mathrm{f}} \cdot \dot{\boldsymbol{F}} \boldsymbol{F}^{-1} \boldsymbol{n}_{\mathrm{f}} \right) \, \mathrm{d}\Omega_0^{\mathrm{f}} \\ &= \int_{\Omega_0^{\mathrm{f}}} \phi_{\mathrm{f}} T_{\mathrm{f}} \left(\dot{\lambda}_{\mathrm{f}} \boldsymbol{n}_{\mathrm{f}} \cdot \boldsymbol{n}_{\mathrm{f}} + \lambda_{\mathrm{f}} \boldsymbol{n}_{\mathrm{f}} \cdot \dot{\boldsymbol{n}}_{\mathrm{f}} \right) \, \mathrm{d}\Omega_0^{\mathrm{f}} \end{aligned} \tag{C.13}$$

and results in equation 7.14. Next, the use of the Hill-model relationships given in equations 6.3 and 6.4 and stretch and stretch-rate relationship described in equations 6.7b and 7.17 to decompose equation C.13 into the PE, SE and CE components

$$\begin{aligned}\dot{W}_{\mathrm{f}} &= \int_{\Omega_0^{\mathrm{f}}} \phi_{\mathrm{f}} T_{\mathrm{p}} \dot{\lambda}_{\mathrm{f}} \, \mathrm{d}\Omega_0^{\mathrm{f}} + \int_{\Omega_0^{\mathrm{f}}} \phi_{\mathrm{f}} T_{\mathrm{c}} \dot{\lambda}_{\mathrm{f}} \, \mathrm{d}\Omega_0^{\mathrm{f}} \\ &= \int_{\Omega_0^{\mathrm{f}}} \phi_{\mathrm{f}} T_{\mathrm{p}} \dot{\lambda}_{\mathrm{f}} \, \mathrm{d}\Omega_0^{\mathrm{f}} + \int_{\Omega_0^{\mathrm{f}}} \phi_{\mathrm{f}} T_{\mathrm{c}} \left(\dot{\lambda}_{\mathrm{s}} \lambda_{\mathrm{c}} + \lambda_{\mathrm{s}} \dot{\lambda}_{\mathrm{c}} \right) \, \mathrm{d}\Omega_0^{\mathrm{f}} \\ &= \int_{\Omega_0^{\mathrm{f}}} \phi_{\mathrm{f}} T_{\mathrm{p}} \dot{\lambda}_{\mathrm{f}} \, \mathrm{d}\Omega_0^{\mathrm{f}} + \int_{\Omega_0^{\mathrm{f}}} \phi_{\mathrm{f}} T_{\mathrm{c}} \lambda_{\mathrm{f}} \left(\dot{\lambda}_{\mathrm{s}} {\lambda_{\mathrm{s}}}^{-1} + \dot{\lambda}_{\mathrm{c}} {\lambda_{\mathrm{c}}}^{-1} \right) \, \mathrm{d}\Omega_0^{\mathrm{f}} \end{aligned} \tag{C.14}$$

from which the final result given in equation 7.18 is resolved.

D. VALIDATION STUDIES

D.1 Finite-strain incompressible elasticity

A study verifying the FEM implementation of the incompressible finite-strain elasticity was performed. The tests described below demonstrate the accuracy of implementation under compressive and shear loading.

D.1.1 Indentation test

The indentation test presented by Reese et al. [229] and elaborated on by Elguedj et al. [63] demonstrated the effectiveness of the quasi-incompressible formulation under severe compressive loading. A cubic block with an edge length of 1mm represents a quarter of the entire domain. Planar constraints on -X,-Y,-Z surfaces account for the symmetry of the problem. The +X,+Y surfaces are traction free while the +Z surface is constrained in X,Y directions. A vertical load is applied on a 0.5mm^2 patch on +Z surface, aligned against the X-Z and Y-Z planes. The load, which is applied in the reference configuration, has a value of $-\frac{p}{p_0}$, with the nominal load $p_0 = 4$MPa. The cube, which is considered near-incompressible, is composed of a Neo-Hookean material with material parameters $\mu = 80.19$GPa and $\nu = 0.499$. The maximum dilatation error allowed was 1×10^{-4}.

Figure D.1a depicts the displacement solution after 10 load steps at which the maximum load had been applied. The convergence of the solution under h-refinement is illustrated in figure D.1b. The results compared very well with the literature.

D.1.2 Cook's membrane

The Cook cantilever problem is used by Armero [5] to test the properties of FEM formulations under shear loading and their resistance to volumetric locking. A non-regular beam is fully constrained on one side and has a total vertical load of 100kN on the opposite face. The beam is in plane-strain and is thus constrained through its thickness. The upper and lower surfaces remain traction free. The cantilever is composed of a near-incompressible Neo-Hookean material with material properties $\mu = 80.1938$GPa and $\nu = 0.499$. Incompressibility was considered to be obtained when the dilatation error was reduced to 1×10^{-5}.

Five load steps were used to obtain the displacement solution shown in figure D.2a. Comparing the results given in figure D.2b to those found in the literature, the mixed formulation with regular (non-skewed)

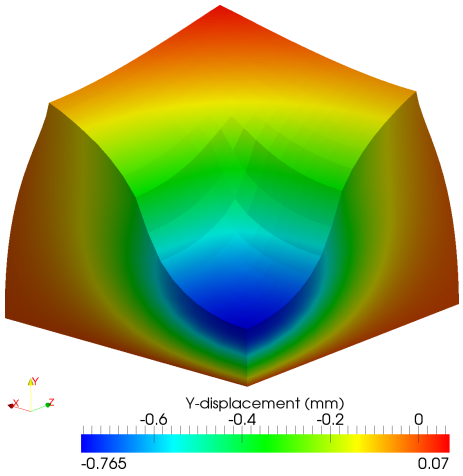

(a) Compression of the block for $\frac{p}{p_0} = 100$ (16 elements per side).

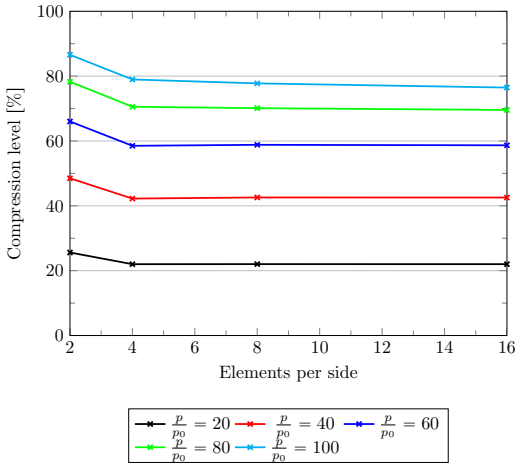

(b) Convergence of centre compression level for various values of $\frac{p}{p_0}$.

Figure D.1: Indentation of a quasi-incompressible isotropic hyperelastic material

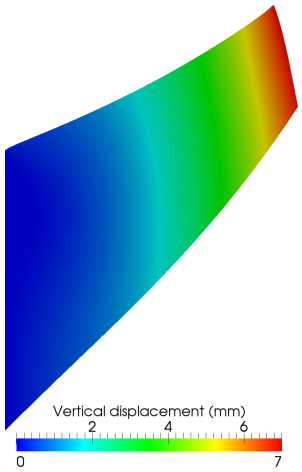

(a) Vertical displacement

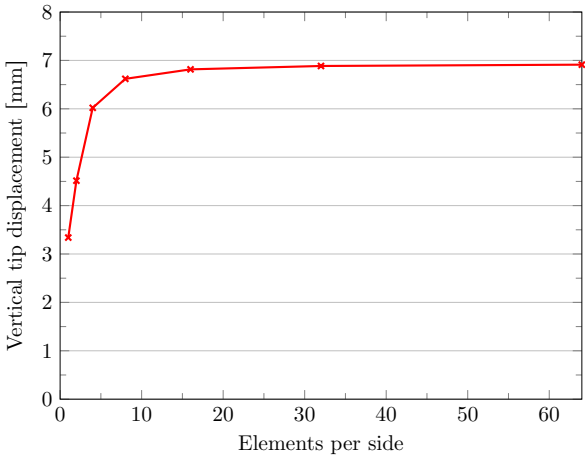

(b) Convergence of vertical tip displacement

Figure D.2: Cook membrane with total vertical load of 100kN.

discretisation demonstrated similar results for convergence to those given for the Q1-P0 formulation. Comparable results were also obtained when evaluating the effect of mesh skewness as was performed by Armero [5].

D.2 External/fictitious material model

To demonstrate the external tissue model, consider a $1 \times 2 \times 1\text{mm}^3$ volume composed of two dissimilar materials, namely muscle matrix (without fibres) and adipose tissue. The volume is made to undergo shear deformation by imposing a displacement constraint on both surfaces. The adipose tissue was fixed on the upper surface, while the lower surface of the muscle had a prescribed lateral displacement and was fixed in the other two directions. All other surfaces are considered traction-free. Both materials are of equal volume, and have identical FEM meshes consisting of 64 identical elements. In the case where the fictitious material

is considered, the adipose volume is removed and the interface surface treated with the traction condition described by equations 3.97 and 3.98 in conjunction with the constitutive model given in section 5.4.3.1. The fixed surface for the fictional material is set in the same position as that of the preceding case.

Comparison between the two results generated using equivalent boundary conditions is presented in figure D.3. It is demonstrated in figure D.3a that qualitatively similar solutions are produced using both methods. Since the muscle tissue is more compliant than the adipose, it undergoes a larger deformation. The leading edge of the muscle is raised, while the trailing edge drops. Similar configuration of the traction-free surfaces of the muscle body were also observed.

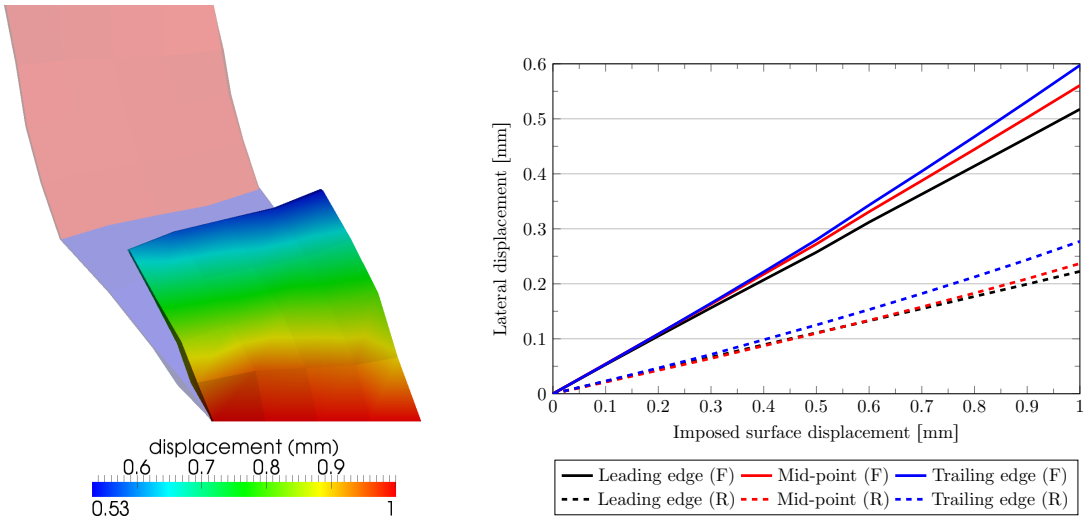

(a) Displaced solution

(b) Lateral displacement of muscle-adipose interface

Figure D.3: Displacement of the interface between different tissue types. In figure D.3a, the silhouette of the displaced solution for the two-material model is also depicted. The adipose tissue is coloured red and fixed at the upper surface, while blue represents the muscle tissue volume which undergoes translation of its lower surface. The dotted lines in figure D.3b denote values measured when two material volumes exist.

However, as is clear from both figure D.3a and figure D.3b, the fictitious material case is conservative in terms of the production of traction forces. The displacement of the material interface was significantly larger when the presence of the adipose tissue was directly simulated, but the overall displacement trends are similar. The performance difference is due to the conservancy of the shear component of the material model and the lack of volumetric effects which form a constraint on the motion of the adipose tissue in the former case.

D.3 Passive tissue model

Validation of the constitutive models for passive skeletal muscle is presented. Some aspects regarding the chosen material parameters are discussed and some initial observations on the reinforcing properties of the muscle fibres, as well as the effect of fibre volume fraction, are made.

D.3.1 Muscle matrix of the tongue

A comprehensive survey of models of the tongue and other relevant skeletal muscle models has been conducted in order to characterise an accurate constitutive model for the passive tongue. Table D.1 provides an account of the reported small strain Young's modulus of passive tongue tissue used in various models and from experimental analysis of skeletal muscle tissue.

Table D.1: Literature survey of muscle small strain Young's modulus (human tongue unless otherwise noted).

Source	Value (kPa)	Source	Value (kPa)
Gérard et al. [86]	1.1[a]	Vogt et al. [293]	10.1[a]
Van Loocke et al. [286]	1[b], 3.5[c]	Van Ee et al. [282]	11[d]
Cheng et al. [39]	2.67[e]	Perrier et al. [215]	12.25
Huang et al. [111]	6	Gérard et al. [85]	15
Buchaillard et al. [28], [29]	6.2	Dang and Honda [51]	20
Sanguineti et al. [245]	6.2	Fujita et al. [77]	30
Sanguineti et al. [244]	10		

[a] Computationally derived value
[b] Fresh porcine / ovine skeletal muscle. Approximate value derived from reported data
[c] Aged porcine / ovine skeletal muscle. Approximate value derived from reported data
[d] Freshly post-mortem rabbit tibialis
[e] Calculated from a shear modulus value assuming $\nu = 0.5$.

In order to evaluate the various matrix models found in the literature that describe passive tongue muscle tissue, a number of the models were implemented and evaluated with the uniaxial-stress test described in footnote 4 on page 65. The resulting stress-strain curves (both maximum principal values) are shown in figure D.4a and the approximate modulus of elasticity associated with the materials is given in figure D.4b.

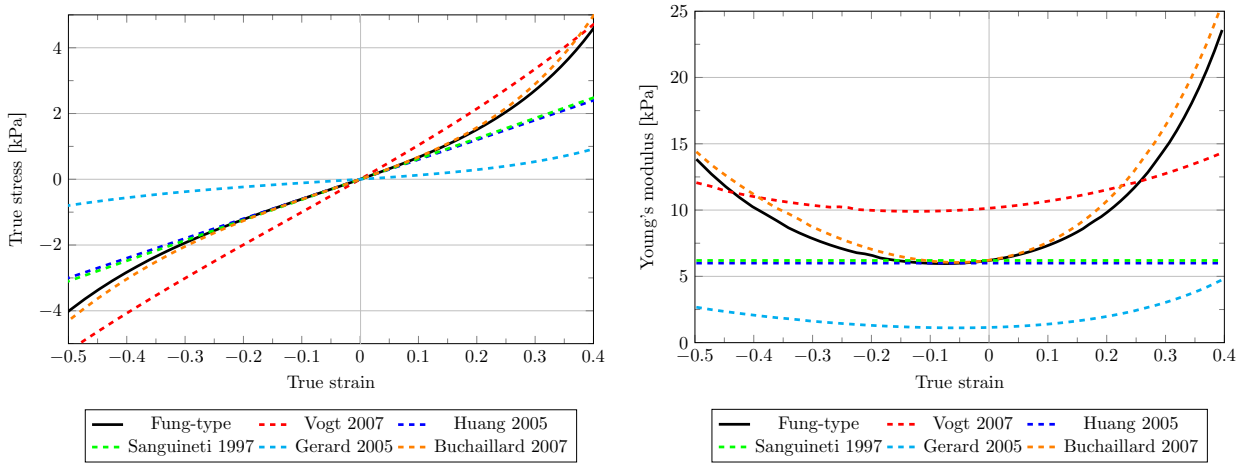

(a) True stress vs true strain

(b) Young's modulus vs true strain

Figure D.4: Comparison between the muscle matrix model and other models for the tongue in the literature [293, 111, 244, 86, 28]. The result for the matrix model used in this work is shown in black.

From both table D.1 and the before-mentioned figures, there appears to be a large variation in the constitutive relationships used to describe the passive tongue. Not only does the account of the zero strain Young's

modulus vary significantly, but the nature of the material nonlinearity and the degree to which it stiffens with increased strain varies as well[1]. The result is an order-of-magnitude discrepancy of large-strain stiffness for the tested models. It should be noted that although the model of Gérard et al. [86] shown in figure D.4, derived from indentation tests of a human tongue, it was the most compliant model and shows little similarity to the rest of the cited literature. However, it appears to be consistent with the experimental analysis conducted by Van Loocke et al. [286] for freshly harvested tissue, as seen in figure D.5. Similar results for fresh tissue were also observed by Buchaillard et al. [29]. This is due to Gérard et al. [86] assuming zero muscle activation for the fresh tissue whereas models with a stiffness modulus in the range of 6kPa assume that some residual muscle activation is present [29]. The effect of the sample freshness on the results obtained in experimental analysis is discussed by Van Ee et al. [282] and Van Loocke et al. [286]. Furthermore, it has been observed in tests performed by Van Ee et al. [282] and Van Loocke et al. [288] that strain-rate and the effects of cyclic loading are factors that should be considered.

Ultimately, material parameters for the muscle matrix were chosen such that the small strain stiffness was 6.2kPa, which aligned with a number of the models in literature. The notion that this figure includes the effect a minimal degree of muscle activation is taken into account in the development of the neural model presented in chapter 7. The rate of increase of stiffness at small strains was set to mimic that of the Yeoh material model of Buchaillard et al. [28], which resulted in the models correlating well at large strains. The resulting stiffness modulus at $+0.4$ strain was 23.78kPa and at -0.5 strain was 13.84kPa.

D.3.2 Passive component of muscle fibre

In addition to providing a valid range of parameters for the matrix model, the experimental data in Van Loocke et al. [286] was used as an initial benchmark against which the parameters chosen for the PE were validated. Figure D.5 demonstrates that the increase in stiffness shown when a transverse fibre family is added is in the range of that observed in the fresh and aged tissue. The transverse fibres are placed in tension as the uniaxially displaced tissue is compressed, while axially orientated fibres are loaded in compression and have no effect on the tissue stiffness. The resulting stiffness curve demonstrates that the small strain stiffness is comparable to that of aged tissue. However, at large strains the reinforcing effect of the PE, which is superimposed on that of the muscle matrix, is similar to that seen in fresh tissue samples.

Further comparison can be made to the combined experimental results of Gordon et al. [91] and ter Keurs et al. [274] that outlined the nature of the PE. In figure D.6, the combined effect of the PE and the length-dependent part of the CE are plotted as a function of fibre stretch. This result represents iso-velocity elongation of a muscle fibre at maximum activation, and is presented as a fraction of the peak isometric force. The chosen parameters for the PE make this element more compliant than that presented by ter Keurs et al. [274], but the overall effect of a highly increased material stiffness at high strains is attained.

D.3.3 Fibre volume fraction

From equation 5.6c, it is ascertained that the stress generated within the muscle fibre components is directly proportional to their volume fraction. In appendix D.3.2 the parameters chosen for PE, as listed in table 6.4, were selected and validated for the volume fraction value specified for the tongue in section 6.5.1.

[1] This large variation in experimental data has been noted by Van Loocke et al. [286].

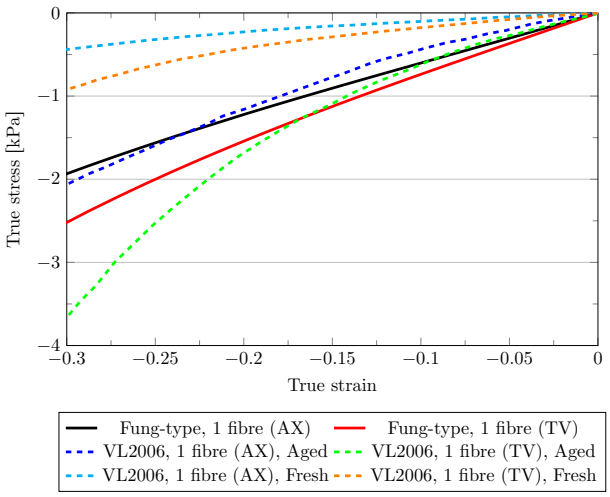

Figure D.5: Comparison between fresh and aged experimental compression data from [286] and the muscle model. Legend: AX – axial alignment of fibre with deformation; TV – transverse alignment of fibre with deformation.

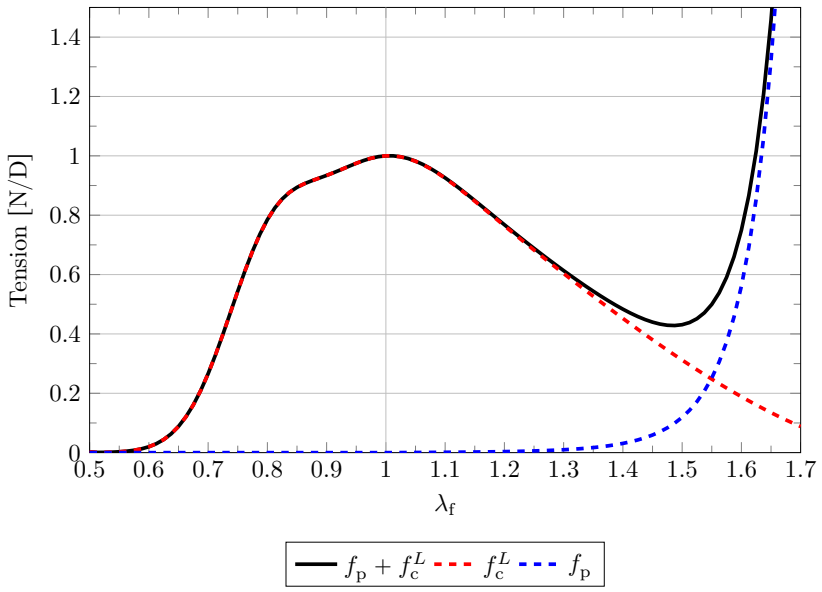

Figure D.6: Combined response of active and passive components of muscular tissue, namely $f_p + f_c^L$. Comparison of the described functions with data from ter Keurs et al. [274] for the passive tissue response, combined with active muscle response described in Herzog and Ait-Haddou [101] and Gordon et al. [91], demonstrates that the overall response of the tissue is correct. The response of the PE used here is slightly less stiff than that described by ter Keurs et al. [274].

Figure D.7 demonstrates that both the stress and stiffness properties of passive tissue are, as expected, linearly dependent on the fibre volume fraction and that the correct configuration of the PE parameters is paramount to the accuracy of the model. It is observed in figure D.7b that the variation in tensile stiffness of the muscular tissue relative to that of the muscle matrix (7.26kPa at $+0.1$ strain) due to the effect of fibre volume fraction is significant at even very low-strains. The stiffness of the PE increases exponentially in comparison to the underlying tissue matrix.

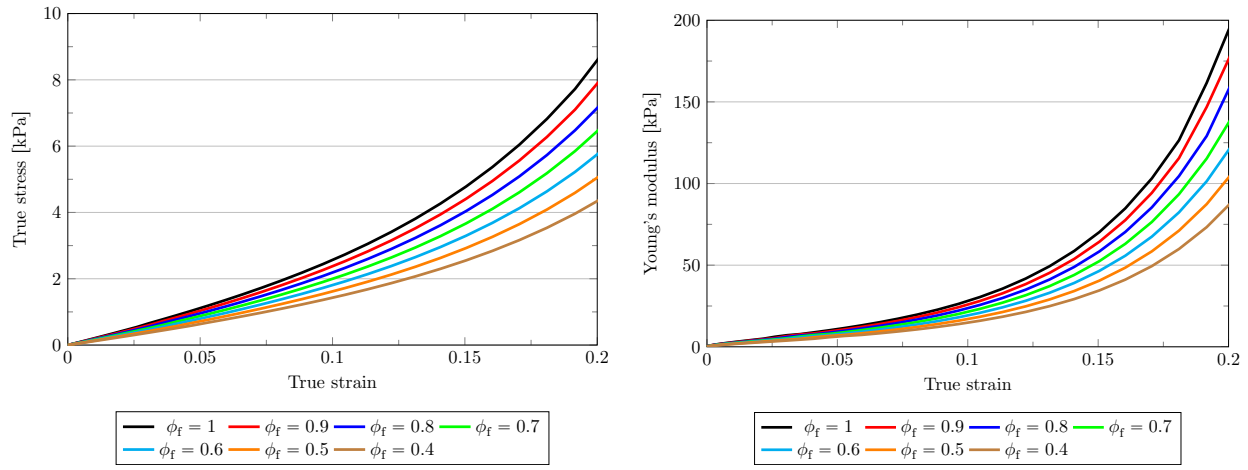

(a) True stress vs true strain

(b) Young's modulus vs true strain

Figure D.7: The change in stress response and stiffness properties of passive fibrous tissue resulting from modification of the fibre volume fraction.

D.3.4 Number and orientation of reinforcing fibres

In the tongue, numerous fibre families meet and interact throughout its volume. The number of muscle groups present at each point and their orientation with respect to one another alter the passive properties of the tissue. Figure D.8 illustrates the effect of the number of fibre families and orientation on the tensile and compressive stress-strain behaviour of muscle tissue.

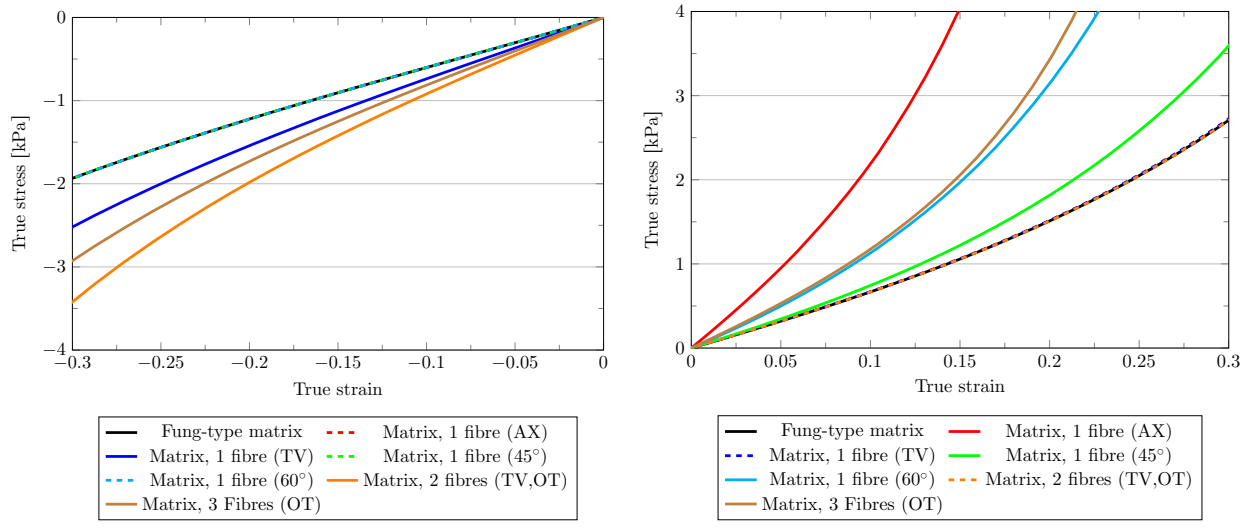

(a) Compression

(b) Tension

Figure D.8: Passive tissue stiffening due to fibre reinforcement. Axially-aligned fibres produce a large stiffening effect in tension, but no passive resistance during compression. Transversely aligned and off-axis fibres add some stiffness during compression as they are placed in tension during the deformation. Legend: AX – axial alignment of fibre with deformation; TV – transverse alignment of fibre with deformation; OT – fibres are orthogonal. The angle given is that of the fibre with respect to transverse plane.

For the case of compression shown in figure D.8a, the addition of fibres in the transverse direction results in reinforcement of the material while fibres aligned in the axial direction do not affect the material stiffness. Due to the nature of the deformation during compression, it was observed that orientating fibres at up to 60° to the axial direction resulted in negligible reinforcement. The addition of a single fibre family in the transverse plane has the effect of stiffening the tissue, but because the reinforcement is in the direction of only one of the transverse axes, the tissue remains compliant. Adding an extra transverse fibre family orthogonal to the first results in the stiffest tissue measured in compression. When an axial fibre is added, the tissue becomes more compliant but remains stiffer in comparison to when only one transverse fibre was present. The latter two scenarios demonstrate that the volume fraction for each family is reduced as the overall fibre volume fraction remains constant regardless of the number of muscle groups present.

Under tension, the incorporation of fibres off the transverse plane results in stiffening of the tissue. It is clear that the closer the alignment of the fibres to the direction of deformation, the greater the resistance to motion due to the stiffness of the PE. By comparing the cases having only 1 fibre group and 3 orthogonal fibre groups, the former being aligned with the deformation and the latter having one fibre family aligned with the deformation, the effect of the fibre volume fraction can again be observed. The volume fraction occupied by the axial fibre in the latter case is $\frac{1}{3}$ of that of the former case, reducing the effective stiffness of the tissue in the axial direction. As the PE offers no resistance in compression, the cases where only fibres transverse to the direction of motion exist result in the same material stiffness of that of having just the matrix present.

In summary, it is evident that the alignment of the fibres with respect to the load affects the degree to which the PE is loaded. Under certain loading configurations, the fibre volume fraction may not play a significant role in the effective stiffness of the tissue. According to figure D.8b, tensile uniaxial loading of tissue with a single fibre family at 45° with a $\phi_\mathrm{f} = 0.7$ results in little added stiffness due to the PE at strains of up to $+0.15$. The result of this is that the volume fraction has a more significant effect in altering the effective stiffness of tissue in scenarios in which the tensile principal direction of deformation is aligned with the fibre direction.

D.4 Active tissue model

The implementation of the model for internal fibres is compared to examples presented by Martins et al. [171]. The slight differences between the results shown below and the benchmark results can be attributed to differences in the implementation of the muscle models.

D.4.1 Internal fibres

A $10 \times 5 \times 1$mm geometry discretised into 1mm^3 cells was used to reproduce half of the grid used by Martins et al. [171]. Muscle fibres were aligned in the direction of longest grid edge. The symmetry of the model in the fibre direction was accounted for, thus replicating the square grid used in the benchmark. The plane-strain response was ensured by enforcing zero displacement in the third direction. The muscle matrix parameters were altered to be consistent with the used by Martins et al. [171] ($b = 23.46, c = 379.52$Pa). The activation parameters were set to $T_0^s = 1, \tau_R = 20\text{ms}, \tau_R = 200\text{ms}$. The time-step size used in the first example is $\Delta t = 50$ms, while the second required a smaller step size of $\Delta t = 20$ms.

Isometric contraction of the muscle group demonstrates that the activation function is correctly evaluated and

that the fibre constitutive model produces correct results. In this example, no displacement of any boundaries is allowed. In figure D.9a, it was observed that the rise and fall of the activation level is exponentially increasing and decaying. The temporal history of the total axial stress, depicted in figure D.9, has a similar shape to the neural history.

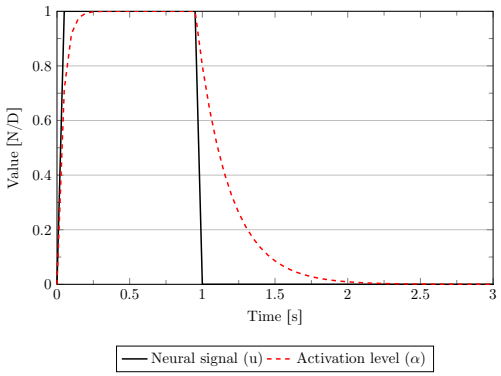

(a) Neural signal and consequent muscle activation level for the single muscle fibre family

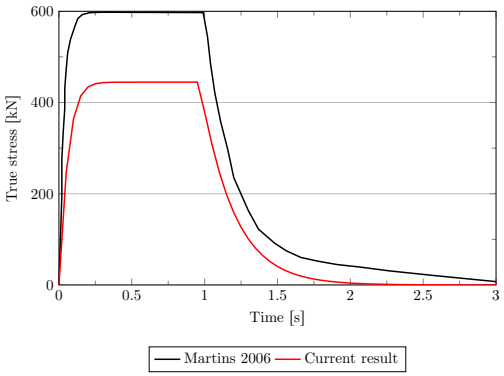

(b) True stress generated in the tissue due to active contraction

Figure D.9: Replication of the isometric contraction test described by Martins et al. [171]. The result in black was produced using an implementation of the exact muscle relationships used by Martins et al. [171] and correlates well with that which they documented.

Isotonic contraction, where the generated contractile force in a muscle is sufficient to overcome an applied traction, is demonstrated in the same geometry. One of the 5mm sides is planarly constrained, while a axial stress is applied, in the reference configuration to the opposite surface. The stress is linearly increased to its maximal value of 4805.26Pa over the first second, and is maintained for an additional 2.5s. At $t = 1$s, a neural stimulus is provided to the muscle and maintained for a duration of 1s, after which the stimulus is removed. The stimulus and resulting activation histories are illustrated in figure D.10a and the axial stress and strain shown in figure D.10c.

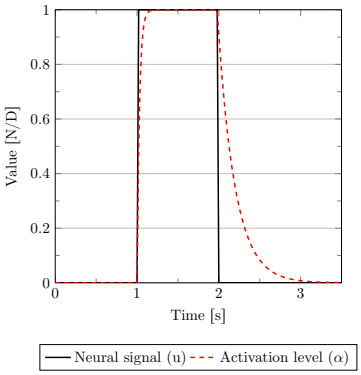

(a) Neural signal and consequent muscle activation level for the single muscle fibre family

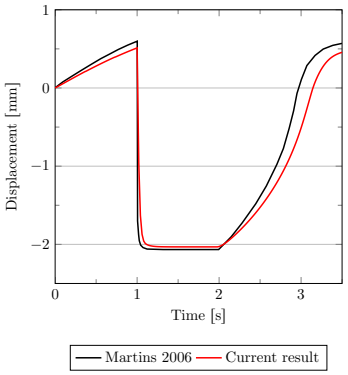

(b) End-point displacement in the axial direction

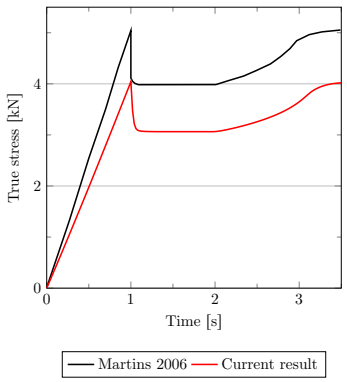

(c) True stress generated in the tissue due to active contraction

Figure D.10: Replication of the isotonic contraction test described by Martins et al. [171].

Both of the problems outlined above match the benchmark results shown in the literature and demonstrate

that the muscle model functions as expected[2]. The inconsistency in the stress-time results are primarily due to the differences in the materials models, as both the length and velocity relationships of muscle tissue, as well as the account of fibre volume-fraction, differs between the two approaches.

[2] An interesting catastrophic instability was observed for this problem, namely that the slightest perturbation of the solution in the Newton-Raphson algorithm caused solution divergence. This highlighted an unforeseen difficulty when using this model in geometrically regular grids and a regular arrangement of embedded fibres. Ultimately, this problem required the employment of a direct solver to ensure a very high precision linear step.

E. CRITIQUE OF THE CONSTRUCTED MODELS

In order to critically evaluate the accuracy of the model as a whole, a summary of the anatomical inconsistencies and nuances observed in portion of the VHP dataset pertaining to this research is presented. Where aspects of the underlying physiology extracted from the images are ignored or modified, a full account of these modifications and a motivation for the changes is given.

E.1 Anatomical inconsistencies of the VHP dataset

The most disadvantageous aspect of the dataset is that the tongue is in an unnatural position, clearly illustrated in figure 8.4. Not only does the tongue rest forward in the mouth, but it is clamped between the teeth on its blade and the sides, causing the tip of the tongue to protrude forward to the lips. The frenulum and underside of tongue blade are also in contact with the mandible and portions of the superior surface of the tongue are in contact with the hard palate. These points needed to be corrected in order for a functional model to the produced, as the position of the tongue is inconsistent with that observed *in vivo* while breathing naturally.

Upon extraction of the thyroid cartilage, it was discovered that only one of the processes to which the oropharyngeal constrictors attach was present.

E.2 Accuracy of geometry reconstruction

When considering the accuracy of the geometric reconstruction, four elements need be addressed. They are:

1. Constraints inherent in imaging, modelling and simulation software.
2. The process used for reconstructing the tissue structures from imaging data.
3. The process of developing the fluid domain from the solid model.
4. Fundamental problems with the data source.

E.2.1 Software constraints

The complex nature of the HUA together with limitations in the software required that the model be separated into several files to reduce the overall number of masks used to segment the data. A similar limitation was met when extracting the muscle fibre data. The reconstructed dataset could as a result not be viewed in its entirety during construction, hindering the detection of errors early in the reconstruction process.

An additional pertinent point is that the FE software was restricted to hexahedral elements, so that detail in certain parts of the model had to be removed. Furthermore connectivity constraints forced some regions to have an unnecessarily fine mesh. Finally, since only linear elements can be read in by the software, the description of tissue boundaries was relatively coarse in places.

E.2.2 Modelling tissue structures

The following section outlines the geometric differences between the voxel data extracted from the images and the three-dimensional model that was recreated from the data. Since the solid and fluid models are distinct but interlinked, the details for the solid model, which is the focus of the work, is presented first with the additional points that pertain only to the fluid model introduced afterwards.

As the underlying histological data for the tongue is linked to its configuration with in the imaging data, the extent to which alterations could be made to the solid geometry were limited. Some muscles that are not expected to have an impact its movement, such as the PG and infrahyoid muscles, were ignored entirely. The teeth, which constrained the tongue, were removed leading to the presence of small gap the tongue and hard palate, as well as the the mandible. Deformation in the apex and blade of tongue caused by the clamping of the teeth on the tongue was removed. The anterior sublingual gland and frenulum in-between the tongue and the mandible was ignored in order to prevent initial contact between the tongue and the mandible, as well as to reduce the degree of constraint present on the anterior surface of the tongue. The lateral sublingual glands have been represented as soft tissue within the tongue body but their connectivity between the tongue and mandible is not maintained, again to relax the constraint placed on the tongue. Since it is expected that these tissues are relatively compliant, their removal in order to simplify the model was thought to be valid.

The hyoid was reshaped so that it was less tapered at its posterior margin and its lesser horn removed, facilitating the construction of a high-quality mesh for this part of the model. The anatomy between the epiglottis, thyroid cartilage and hyoid bone was treated as though entirely composed of adipose tissue. Although the epiglottis is known to rest on a fat pad, there exist several bursae and other tissues in this region as well. The ligaments in the region of the hyoid and thyroid, as well as the thyroid and hyoepiglottic membranes, were also ignored. Although these thin collagenous structures, when in tension, serve to constrain the motion of parts of the anatomy, their influence on the gross movement of the tongue was considered to be insignificant enough to warrant their current representation[1].

Furthermore, the surface of the hard palate was displaced marginally so as to introduce a gap between it and the tongue thereby removing in the initial contact between these two entities. The thyroid process was added to the right hand side of thyroid cartilage and the laryngeal prominence was removed.

[1] The influence of these parts could be included using a boundary energy model, such as that described by Javili and Steinmann [130].

Due to their thin structure, the presence of image artifacts and the perspective of the dataset, the pharyngeal constrictors were difficult to discern in the axial and reconstructed images. However, it did appear that regions of the airway were collapsed, which is a distinct possibility as no muscle activity is present to ensure airway patency. Based on the anatomical literature, a structure representing the constrictors was reconstructed, but indications are that this may call for revision. This is discussed in more detail in appendix E.2.4 below. The apparent inner wall of the collapsed oropharynx is contrasted in figure E.1 against that of the reconstructed geometry. Since various muscle groups, such as the SG penetrate the oropharyngeal walls, these regions of penetration were ignored, patched up and considered to be a part of the pharyngeal constrictors.

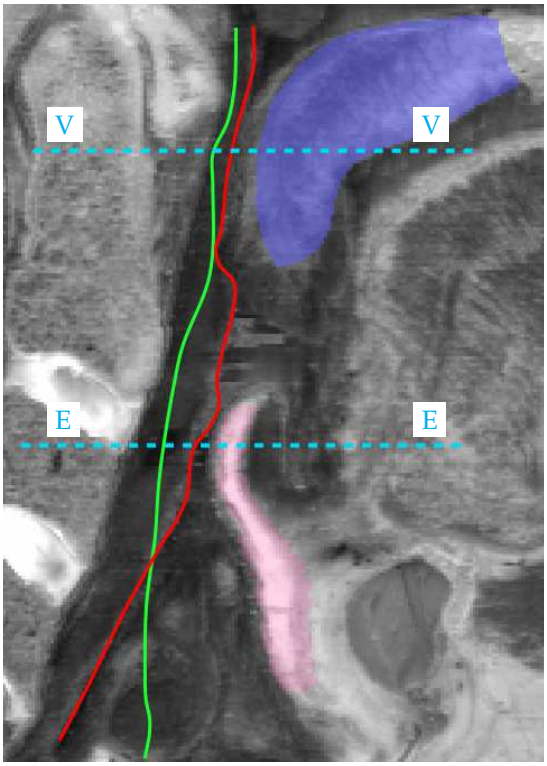

(a) Midsagittal view of the pharynx

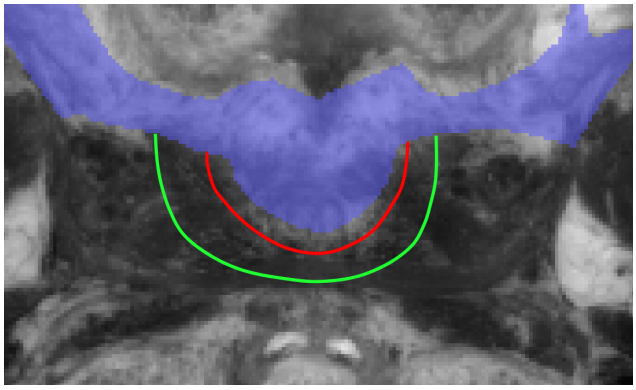

(b) Axial view of the velopharynx (plane V-V)

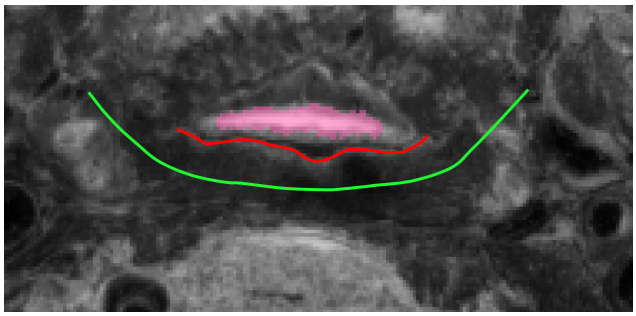

(c) Axial view of the epiglottal region (plane E-E)

Figure E.1: View in Mimics© of the inner wall of the oropharyngeal constrictors, with the position of the epiglottis (pink) and soft palate (blue). The apparent true position of the inner wall (red) along with final (green) reconstructed geometries indicated. The degree to which the reconstruction could be made to accurately represent the oropharyngeal constrictors was constrained by the length of time required to produce each geometry and, ultimately, mesh requirements.

E.2.3 Developing the fluid domain

The solid model was used as a basis for the fluid model, and the changes in the solid geometry therefore reflect directly on the construction of the fluid model. However, further deviations from the extracted imaging data was required to produce an adequate model. A slight alteration of the cheeks, which now serve as the enclosing boundary for the air in the oral cavity, was performed to remove contact between them and the tongue. The region lateral and anterior to the tongue where the sublingual glands are present was removed from the free-stream, thereby reducing the flow area in the oral cavity. Due to their complexity and the difficulty in extracting accurate details from the imaging data, the nasal passage was simplified substantially

using the method presented in Zhang et al. [325], and the sinuses totally ignored. Although the presence of external muscles in region nasopharynx was accounted for, it is likely that the complex geometry in this region hasn't been fully represented. Furthermore, the effect that the muscles emanating from the tongue body have on the impingement of flow has not been considered.

E.2.4 Data source problems

Many of the inaccuracies in the construct of the fluid model can be attributed to source of the data, specifically that a solid model or description of the fluid boundaries was required before the volume of dataset that makes up the airway could be inferred. Ideally, accurate MRI or CT data should have been be used to directly extract the description of the airway instead of the inverse method employed in this work. However, because of the low-resolution of the associated MRI or CT data, this information was not explored. Consequently the methodology used to construct the fluid model and its associated simplifications resulted in a several unrealistic features appearing in the model.

As is shown in section 8.8.2, several issues pertaining to the airway CSA exist. The transverse profile of the air gap in the oral cavity is incorrect when in a state of inhalation. This is due to the blockage of the oral cavity by the tongue, restricting the flow area over the superior surface of the tongue. Additionally, because the teeth were removed, the area though which fluid would move in the lateral regions of the mouth is excessive. Due to the coarse representation of the nasal passage geometry and the position of the pharyngeal walls, the CSA of the nasal passage does not truly match the anatomical literature as well as would be hoped. The CSA of the lower nasopharynx and the velopharynx appears quite large. The lateral distance between uvula and nasopharynx as reconstructed appears larger than usually illustrated in literature; for example, see [2, p771].

F. Isolated activation of individual tongue muscles

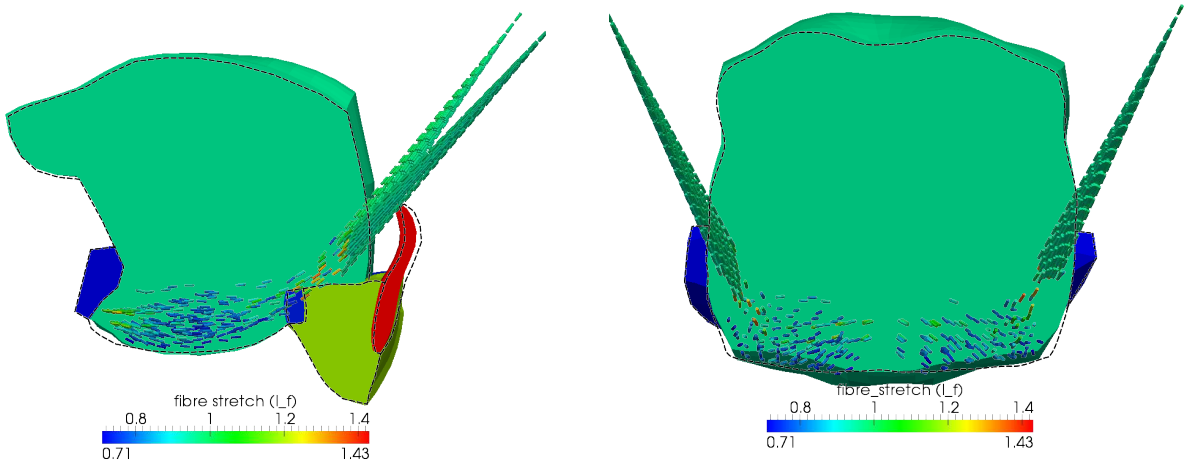

(a) Midsagittal view

(b) Coronal view

Figure F.1: Isolated contraction of the GGa (FFMR 5%)

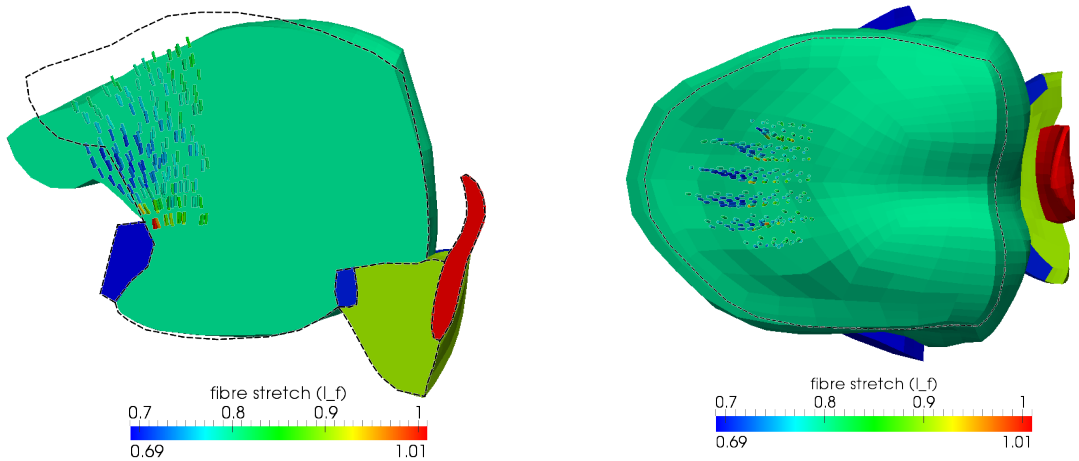

(a) Midsagittal view

(b) Transverse view

Figure F.2: Isolated contraction of the GGa (FFMR 5%)

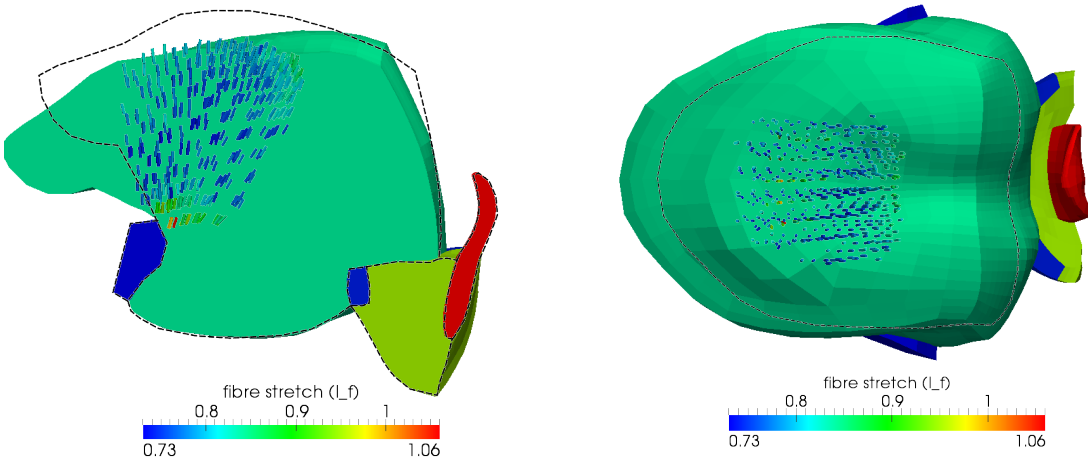

(a) Midsagittal view **(b)** Transverse view

Figure F.3: Isolated contraction of the GGm (FFMR 5%)

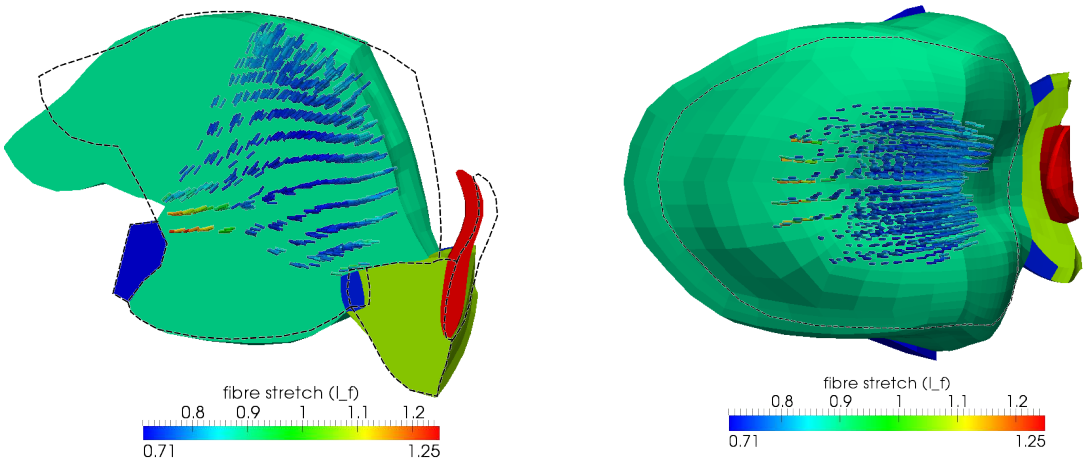

(a) Midsagittal view **(b)** Transverse view

Figure F.4: Isolated contraction of the GGp (FFMR 5%)

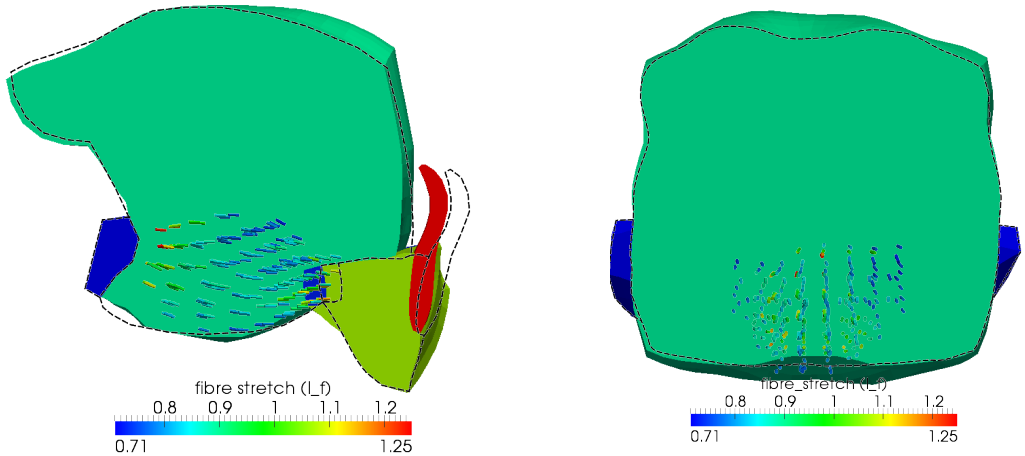

(a) Midsagittal view **(b)** Coronal view

Figure F.5: Isolated contraction of the GH (FFMR 5%)

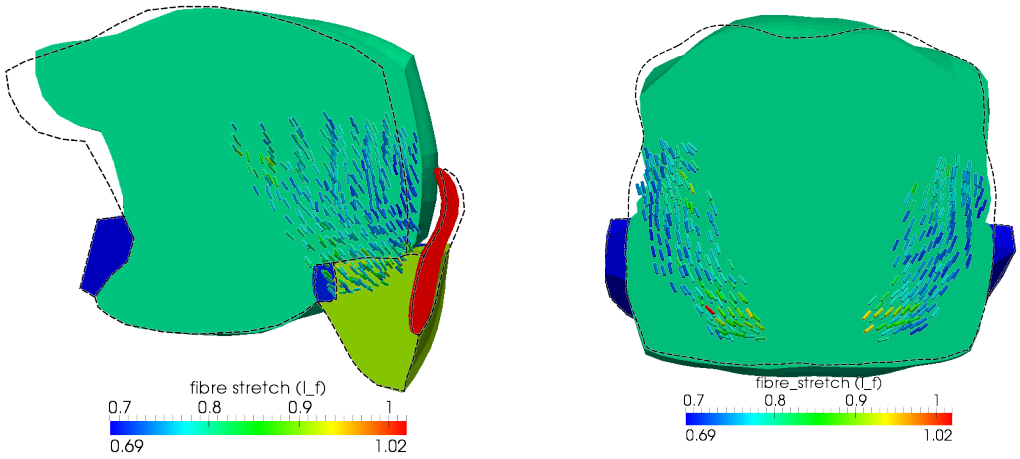

(a) Midsagittal view **(b)** Coronal view

Figure F.6: Isolated contraction of the HG (FFMR 5%)

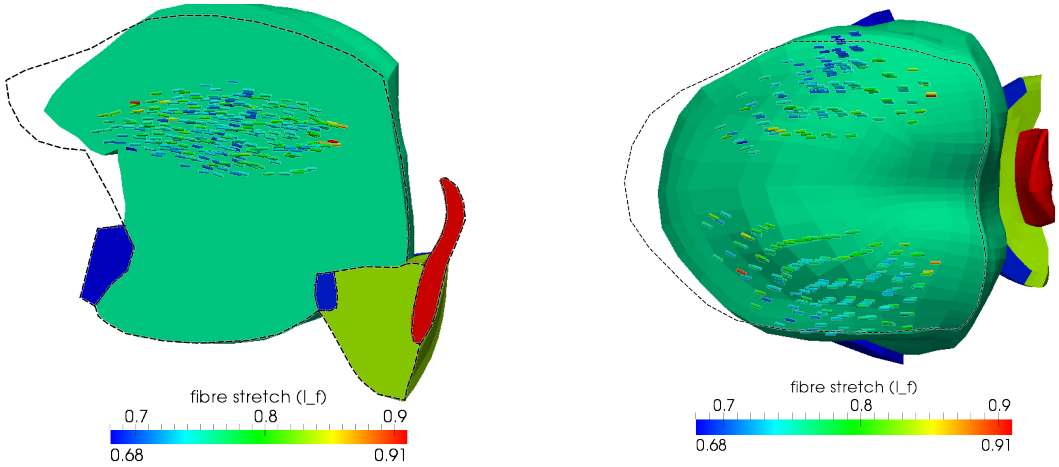

(a) Midsagittal view **(b)** Transverse view

Figure F.7: Isolated contraction of the IL (FFMR 5%)

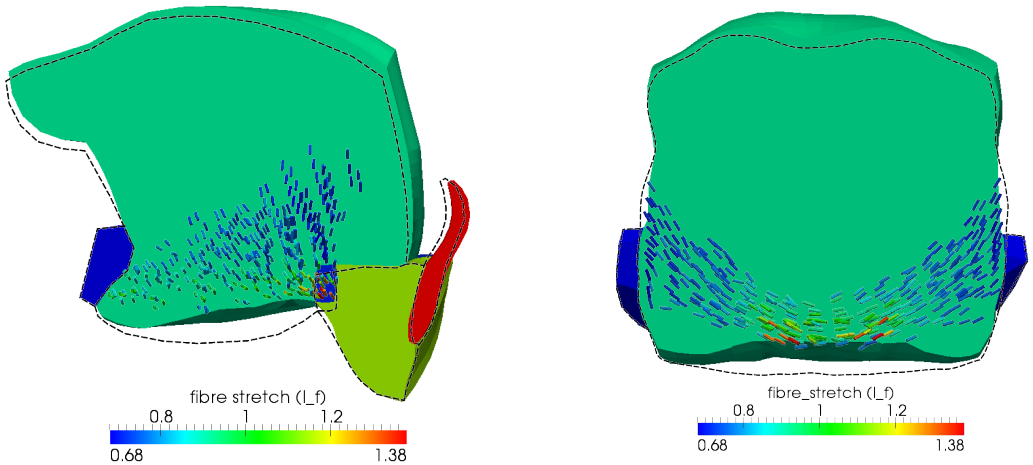

(a) Midsagittal view **(b)** Coronal view

Figure F.8: Isolated contraction of the MH (FFMR 5%)

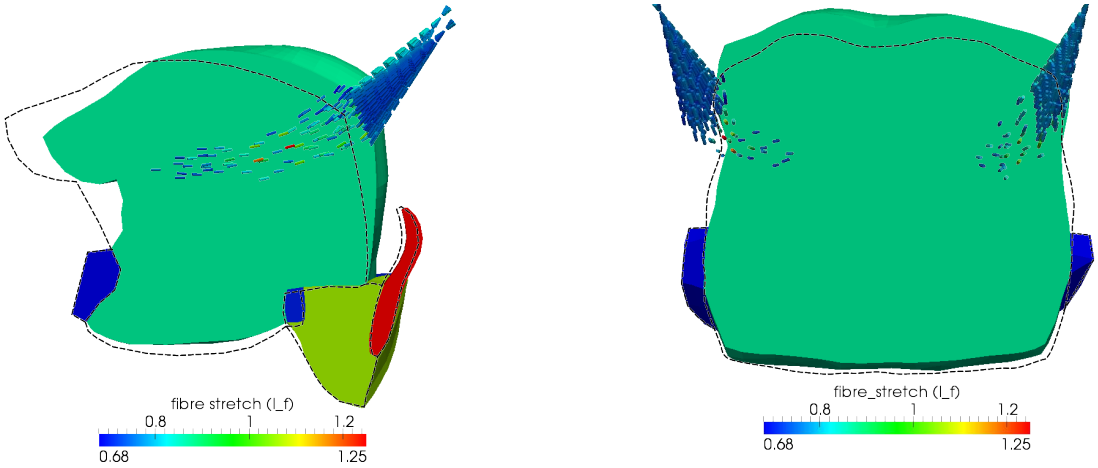

(a) Midsagittal view **(b)** Coronal view

Figure F.9: Isolated contraction of the SG (FFMR 25%)

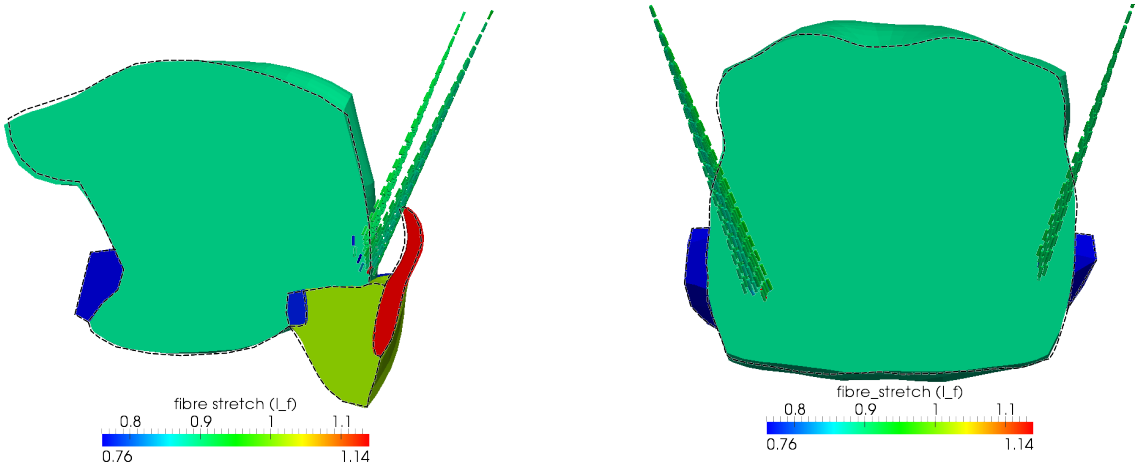

(a) Midsagittal view **(b)** Coronal view

Figure F.10: Isolated contraction of the SH (FFMR 5%)

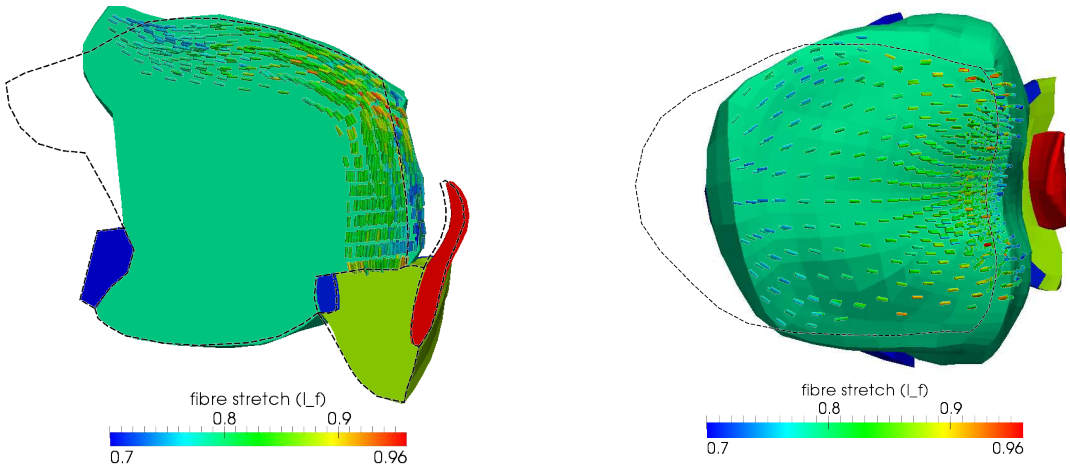

(a) Midsagittal view **(b)** Transverse view

Figure F.11: Isolated contraction of the SL (FFMR 5%)

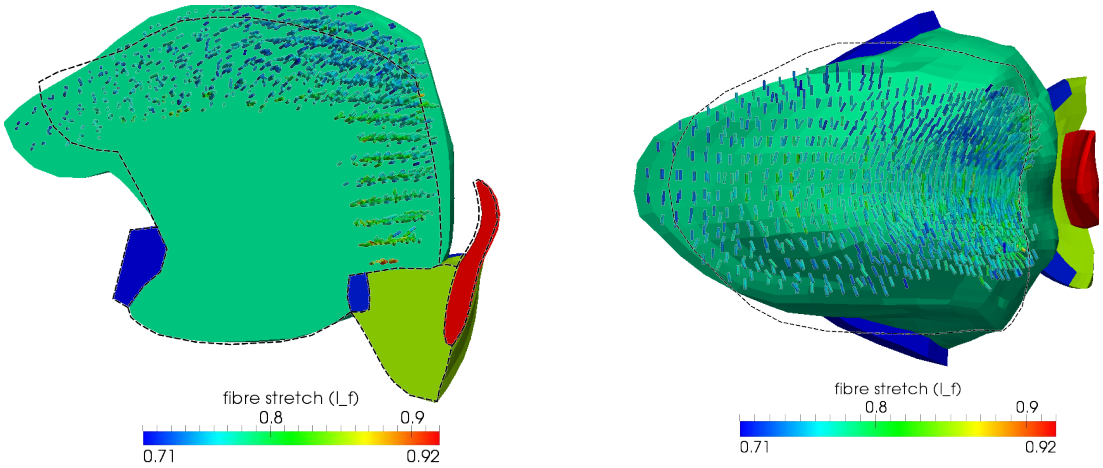

(a) Midsagittal view **(b)** Transverse view

Figure F.12: Isolated contraction of the TV (FFMR 5%)

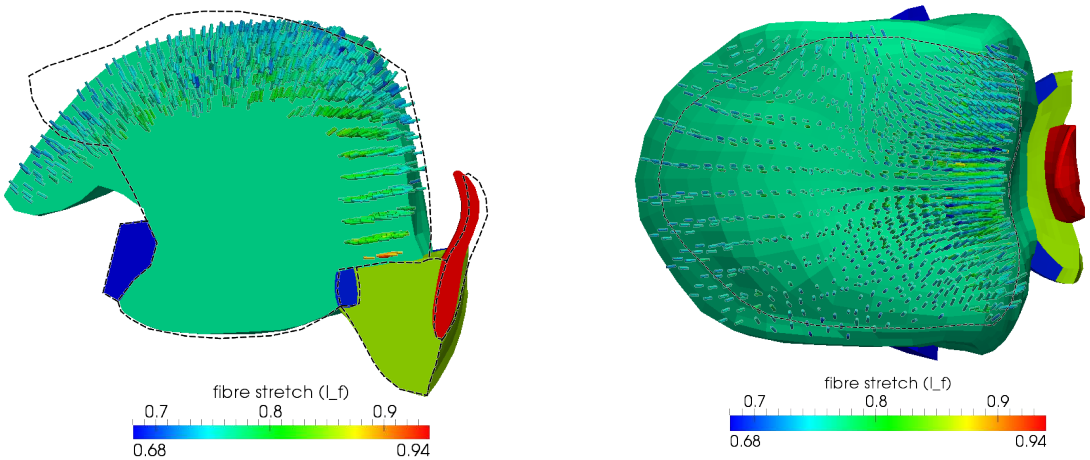

(a) Midsagittal view **(b)** Transverse view

Figure F.13: Isolated contraction of the VT (FFMR 5%)

G. PARAMETRIC STUDY OF NEURAL MODEL

The neural control model has a number of physical and non-physical parameters associated with it. These include variables utilised to reduce computational cost and some which affect the interpretation of the cost-benefit to contracting specified muscle groups. Below, a discussion on how these parameters influence the accuracy of the result is presented. These results were applied in the development of a more accurate model for later use.

Not demonstrated is the effect of the evaluation rate, that is the number of time-steps between those at which the neural model is utilised to produce a new active muscle set. In a previous iteration of the model, it was determined that, for the given time-step size, using the same active set for a single additional time-step reduced the computational time (naturally, by a factor of 2) without a proportional loss in accuracy of the result. Similarly, the time discretisation, itself not immediately associated with the neural model, was chosen to ensure that accurate results were maintained under all scenarios to be tested.

G.1 Muscle selection factor

Introduced in section 7.4.3, the value used to filter out unlikely candidates for muscle activation, c_L, has a great influence on the duration of each simulation. The bounding values for c_L were chosen to provide a balance between computational efficiency and the overall solution results. It was determined that a greater likelihood for inaccuracies in the calculation of $\bar{\bar{\lambda}}_{\mathrm{f}}$ exist as the gravitational orientation moves towards the upright position, hence the need for a lower value of c_L in this regime.

In terms of the effectiveness of this method, a typical reduction of the order of 50% of the simulation time was achieved when utilising equation 7.24 in conjunction with equation 7.25 versus having no filter (i.e. $c_L = 0$) on the active muscle set. Considering the base problem used thus far, the average number of evaluations required for each occasion the neural model reconfigured the muscle state was reduced from 62 when $c_L = 0$ to 26 for $c_L = 0.995$.

Comparison of figures 11.1a, 11.2b and G.1 indicates that, qualitatively, the response of the muscles with and without filtering was very similar. The intensity of the contraction in each muscle group remained consistent between both simulations, although it was noted that the HG was predicted to have a slightly

greater contractile force when no filtering is used, suggesting that it is prematurely forced to be inactive by the algorithm. However, the overall quality of the position control is effectively identical between the two cases. In this single case, the GGp is noted to contract with slightly greater intensely at the time of peak pressure due to the increased contraction of the HG. Nevertheless the overall trends in terms of magnitude of contraction for the GG constituents remain similar.

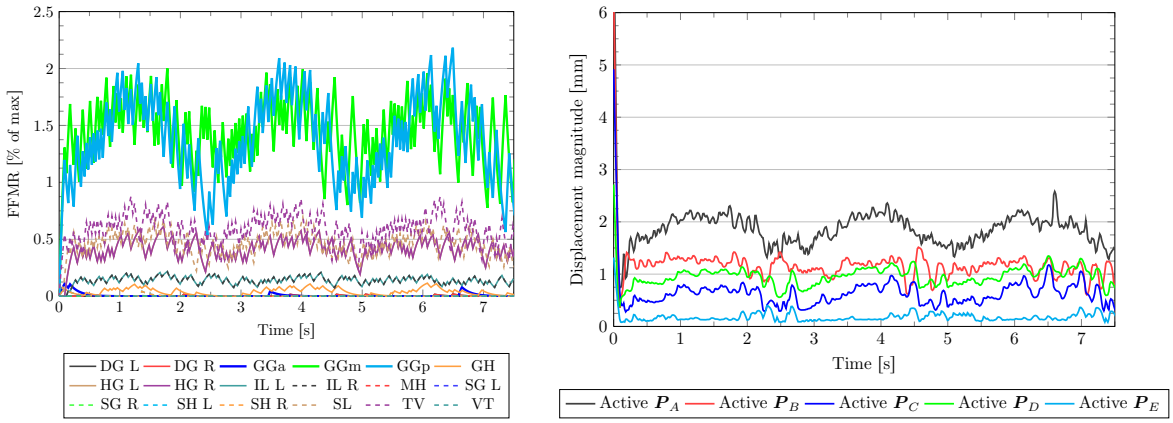

(a) Intensity of muscle contraction

(b) Measurement point displacement

Figure G.1: The response of the model using the described filtering technique was very similar to that obtained when no filtering of the active muscle set occurred.

The trade-off between simulation time and loss of accuracy in terms of positional and muscular control caused by introducing equation 7.25 appears worthwhile. The recruitment of additional muscles does slightly affect the predicted activation patterns of the airway dilators, but this effect is small and will likely be further diminished when energy-conservation is included as an optimisation parameter in the neural model.

G.2 Number of control points

A secondary fine net for the control points was evaluated to determine whether more control points should be utilised in further studies. The coarse distribution, shown previously in figure 8.11, was used as a base to which supplementary points were added. Figure G.2 depicts the finer distribution of the control points on the upper and rear surfaces of the tongue. 10 points were positioned on the upper surface, 7 were placed on the rear and 5 on the transitioning edge between the two surfaces. The position of these points remained regular in order to prevent the GA from favouring any point on the tongue.

From the data shown in Table G.1, it can be deduced that including additional control points decreases the effectiveness of the neural model in maintaining the position of the control points on the midsagittal plane. For all but $\boldsymbol{P}_D$, an increase in the mean displacement was recorded. With the contraction of each muscle group affecting a large region of the tongue, perturbations in the contraction of some muscles now have a greater influence on the result. Consideration of the additional points reduced the effectiveness of the control model as it was required to make a compromise in the position of more points with no control point being more important than another.

From the results, it is clear that an increase in number of control points does not necessarily produce more optimal control of the tongue. It can be concluded that the number of control points used should be minimised,

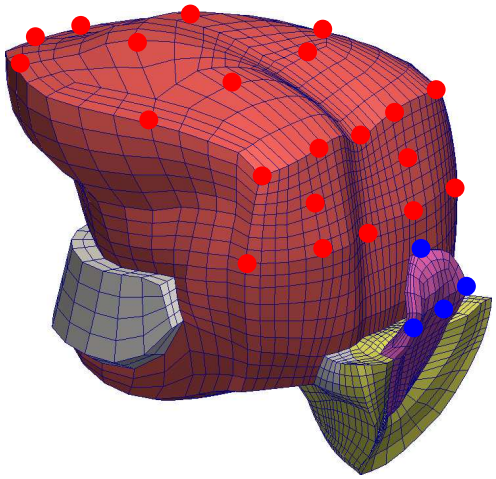

Figure G.2: The position of all of the control points in the fine net.

Table G.1: The effect that altering the control point distribution has on the mean displacement measured on the midsagittal plane. The mean displacement, in mm, was computed from displacement data recorded at the prescribed control points over the course of the simulation. The listed measurement points were common between the two tested distributions.

Control point	Distribution	
	Coarse	Fine
$\boldsymbol{P}_A$	1.86	2.24
$\boldsymbol{P}_B$	1.31	1.59
$\boldsymbol{P}_C$	0.65	0.71
$\boldsymbol{P}_D$	0.87	0.74

but chosen with care. They should still be distributed in such a manner as to ensure that the overall configuration of the tongue body remains physiologically realistic while the points that are important to control should be explicitly evaluated and considered by the model.

G.3 Weighting values of control points

The weights assigned to each control point provide the facility to prescribe their significance on the solution of the GA. Increasing the value from unity is the artificial equivalent to clustering them in a region of geometry. As the position of the tongue tip, $\boldsymbol{P}_A$, has been found to be most difficult to control due to its flexibility, the weight at this point was increased from 1 to 3. The weight at $\boldsymbol{P}_C$ was also altered to the same value as to prevent the GA from focusing excessively on the control of $\boldsymbol{P}_A$ and to maintain a good result at this position.

Table G.2 provides a summary of the influence of the described weights on the mean displacement solution at the various control points on the midsagittal plane. As desired, the result of increasing weight at $\boldsymbol{P}_A$ is that the mean displacement at this position was reduced by 32%. The associated modification of the weight at the tongue posterior, $\boldsymbol{P}_C$, produced a 21% improvement in result. There was however a reduction in the ability to maintain the position of the upper mid-surface of the tongue, denoted by $\boldsymbol{P}_B$, with the mean displacement increasing by 14%.

Table G.2: The mean displacement, in mm, at control points on the midsagittal plane due to the influence of changing the weighting values at $\boldsymbol{P}_A$ and $\boldsymbol{P}_C$.

Control point	Weight w_p		
	1	2	3
$\boldsymbol{P}_A$	1.86	1.41	1.27
$\boldsymbol{P}_B$	1.31	1.36	1.5
$\boldsymbol{P}_C$	0.65	0.55	0.51
$\boldsymbol{P}_D$	0.87	0.81	0.75

From this data, it was concluded that the combined increase in the weights at $\boldsymbol{P}_A$ and $\boldsymbol{P}_C$ to a value of 3 was an effective measure at improving the functioning of the optimisation algorithm.

G.4 Energy minimisation parameters

Finally, to introduce the requirement of work rate minimisation, the objective weights are altered from the trivial combination $\{1, 0\}$. From this we will determine optimal parameters and as well as their influence on the displacement result. As we expect the displacement result to decrease in quality, it must be ensured that the resultant oscillations of the tongue surface remained within physiologically realistic bounds.

In figure G.3, the sequentially increasing importance of the work rate has little effect on the position control of the tongue until a critical threshold is exceeded. At this point, the displacement control in the first loading cycle is not obtained. However, at later loading cycles the displacement solution is significantly better and remains within reasonable limits. An increase in the movement of the rear of the tongue is detected, although again it remains within realistic limits.

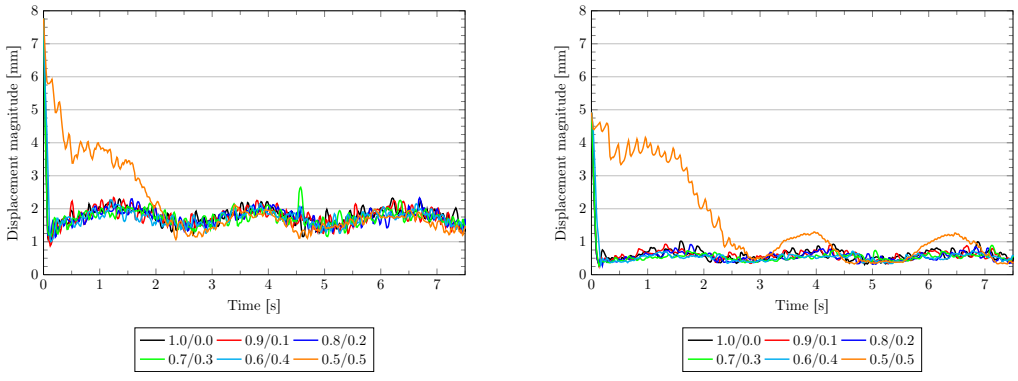

(a) $\boldsymbol{P}_A$ **(b)** $\boldsymbol{P}_C$

Figure G.3: Position control of control points on the tongue surface under a change in objective function weights. Extreme differences are only observed when the weighting value on the energetic objective functions was increased to 0.5.

However, evaluation of the response of the GG demonstrates that the solution obtained for the weights $\{0.5, 0.5\}$ is very much inconsistent with the other results. As can be seen in figure G.4, bias towards energy conservation leads to a steady but plausible reduction of the muscle activity for all tested cases except one. For

the former scenarios, the peak FFMR is reduced in the GGp, while the GGm attained a lower zero-pressure FFMR. In the problem case, the FFMR of both of these muscles increased to a certain value at $t = 3$s which remained roughly constant thereafter. This indicates two things, the first being that the response on the GG, which is known to be linked to the epiglottal pressure, is no longer physiologically consistent. Secondly, and more interestingly, although the FFMR result is non-realistic, the displacement solution after $t = 3$s remained reasonably good, indicating that other muscle groups must be working collectively to oppose the applied load.

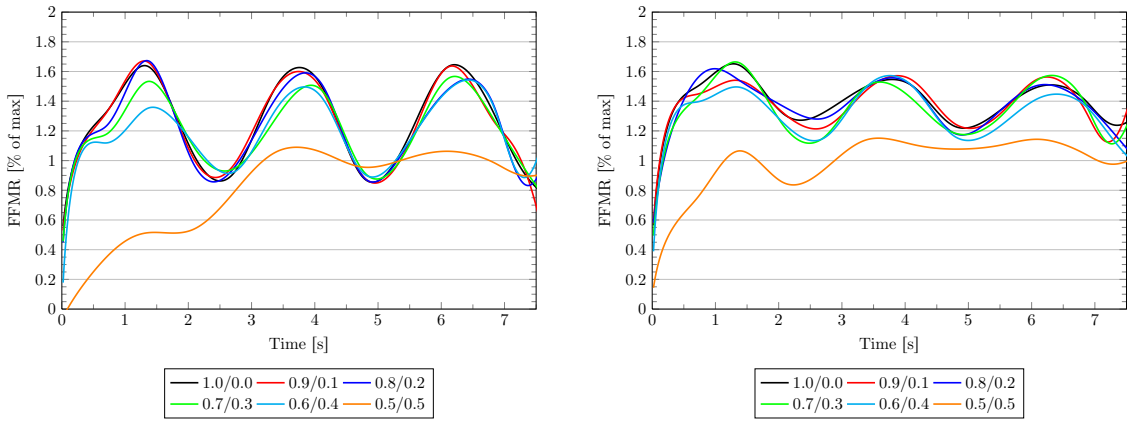

(a) GGp **(b)** GGm

Figure G.4: Muscle response due to a change in objective function weights. The response of the GG further indicates that the threshold for reasonable results lies with a work rate weighting factor of between $0.4 - 0.5$.

Taking a slightly conservative stance on the results, we consider the weight factors $\{0.7, 0.3\}$, respectively for displacement and energy functions, to be ideal for use for the tongue model. This choice remains within the bounds that produce physiologically realistic and repeatable results, while allowing some buffer for unforeseen influences. This introduces flexibility that may be required when evaluating scenarios not evaluated in this part of the parametric study. To further justify this choice, a brief discussion on the statistical characteristics of the heuristic model is presented below.

Figure G.5 demonstrates that, with this choice of weighting parameters, the displacement score range of the tested population is balanced, while many of the tested solutions can be characterised as energy-efficient muscle configurations. This results in an overall score solution that is Gaussian and uni-modal, with a wide standard deviation.

The maintenance of bias towards low-scoring solutions is demonstrated in figure G.6. 85% of the solutions chosen as the best choice for each time-step had a displacement solution with a score of less than 0.25. Utilising this data in conjunction with that shown in figure G.5, it can be concluded that although fewer very high-quality solutions were evaluated, the results remain near optimal for the chosen objective weights.

It appears that, for this model, the wide standard deviation of the overall tested population is a necessity to ensure that an adequate displacement solution is obtained on average. As seen in figure G.7, increasing the weight of the energy function reduces the standard deviation of the overall population score, indicating that solutions with good displacement characteristics are tested less frequently. This is a logical development as the GA will tend to converge on a solution that utilises less muscle action and thus focus more evaluations on solutions with these characteristics.

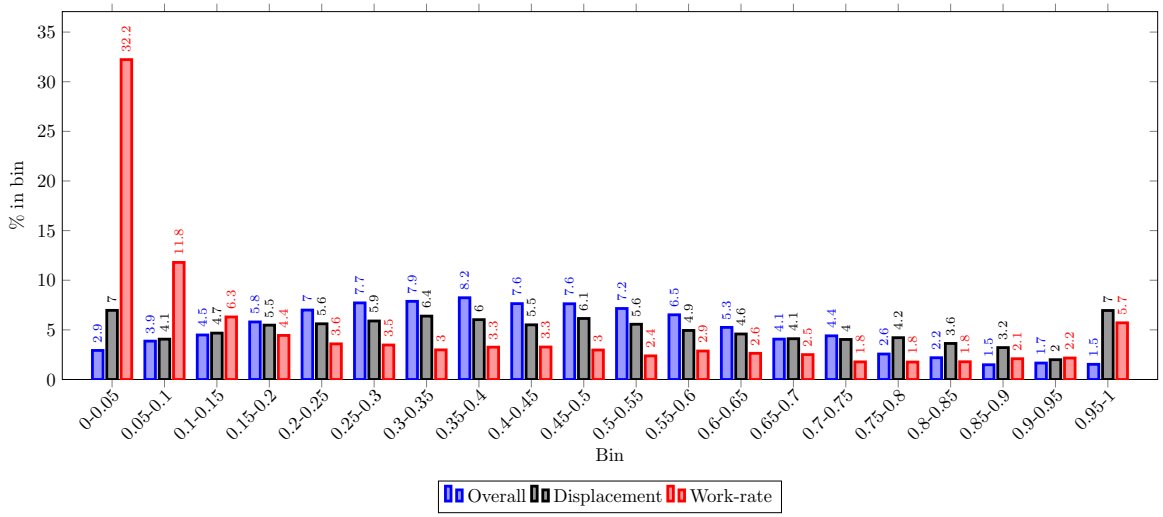

Figure G.5: Histogram of scores of the evaluated population accumulated over the entire duration of a simulation. Weights for the displacement and work rate objective functions were 0.7 and 0.3 respectively. Although the distribution of the displacement scores is relatively even across all bins, the linear combination the objective functions results in normal distribution with a large standard deviation.

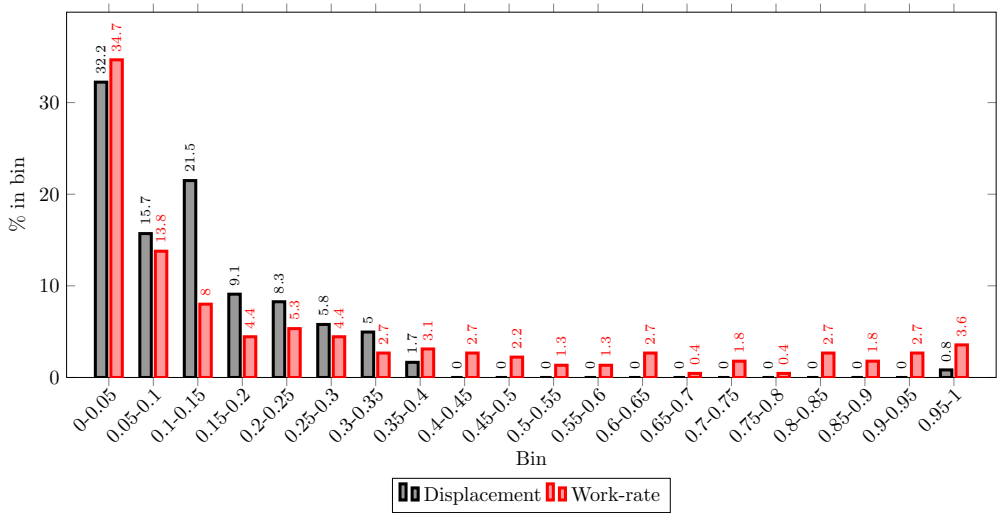

Figure G.6: Histogram of scores of the best genome accumulated over the entire duration of a simulation. Weights for the displacement and work rate objective functions were 0.7 and 0.3 respectively. The chosen best-solutions generally represent globally excellent results in comparison to the test population distribution given in figure G.5.

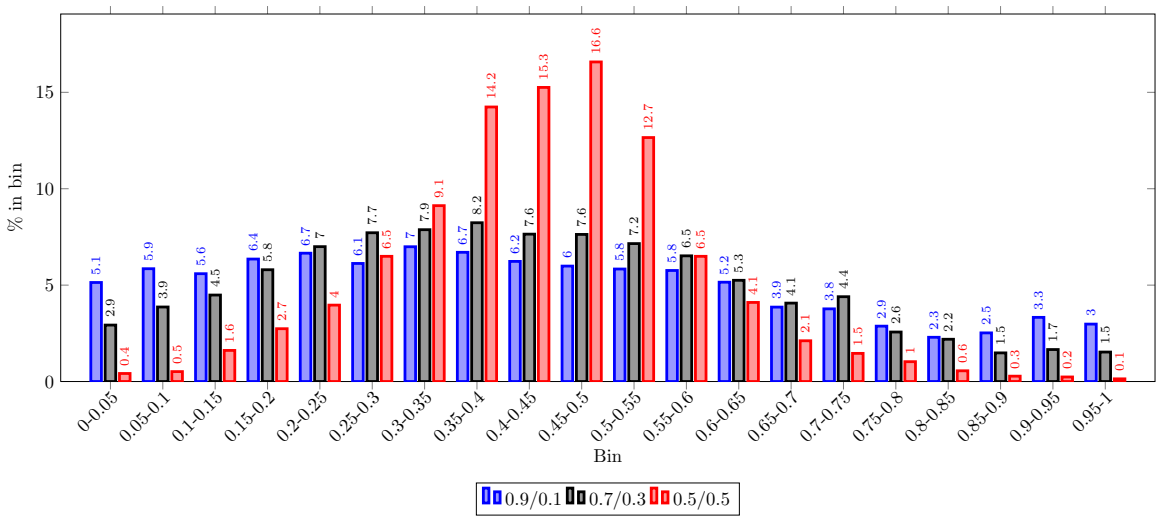

Figure G.7: Histogram comparing the scores of the evaluated population accumulated over the entire duration of a simulation for different objective weights. Increasing the bias towards work rate minimisation decreases the standard deviation of solution scores.

H. CFD STUDY OF UPPER AIRWAY FLOW

H.1 Simulation configuration

The CFD simulations were conducted using the commercial software FLUENT©. The full steady state Navier-Stokes equations were solved using the FVM. Due to the mixed flow conditions expected at the varying range of volume flow rates, a turbulence model that is capable of correctly representing flow in the laminar, transitional and fully turbulent flow regimes was required. As the computational expense of LES, DES and DNS turbulence models was too great, a RANS model was deemed ideal to approximate the turbulent effects on the flow field. In particular, the k-ω SST model, incorporating low Re corrections, was selected as it has been shown to give a solution close to that obtained when using LES [177]. It provides a reasonable solution to transitional and fully turbulent flow while also accommodating fully laminar flow[1].

Higher order solution schemes were utilised to ensure solution accuracy. The Semi-Implicit Method for Pressure-Linked Equations (consistent) (SIMPLEC) algorithm was used for pressure-velocity coupling. The pressure and momentum fields were solved using the Pressure Staggering Option (PRESTO!) and Monotone Upstream-Centered Schemes for Conservation Laws (MUSCL) algorithms respectively. The Quadratic Upstream Interpolation for Convective Kinetics (QUICK) algorithm was used to solve all turbulence equations.

The final model of the fluid domain was comprised of 1.25 million hexahedral and polyhedral cells, with 50% of the them located in the pharynx, 26% in the oral cavity, 10% in the trachea and the rest distributed in the nasal passages[2]. A no-slip condition was applied to all walls, which were considered rigid and stationary. The boundary conditions at the inlets and outlets varied slightly according to the nature of the breathing and the part of the breathing cycle being simulated. At the outlet, namely a section of the trachea, a prescribed velocity condition was used to induce a specified volume flow rate through the domain. The mass-flow between each branch of the bronchus was split according to the CSA of the boundary surface. The region of the airway open to the atmosphere was represented as a pressure boundary condition. Depending on

[1] Validation studies confirmed that simulations within the laminar flow regime conducted with and without the k-ω SST turbulence model enabled produced similar results.

[2] A brief validation study determined that this cell count and distribution resulted in sufficiently accurate results. Three meshes were evaluated, the other two comprised a total of 0.53 million and 0.78 million cells respectively. Both nasal and oral inspiration were simulated at 5L/min and 60L/min using each mesh. Using the finest grid as the benchmark result, at a low flow rate the difference in predicted pressure drop between the inlet and outlet was, in the worst-case, 2% and the difference in the maximal velocity within the domain was 3%. At a high flow rate, the worst-case relative difference in pressure and velocity measurements increased to 3.5% and 3.5% respectively. As the results between coarse and fine grids matched both quantitatively and qualitatively, it was determined that the chosen grid was sufficiently fine for the use in this work.

whether nasal or mouth breathing was modelled, the appropriate boundary condition was changed to a wall BC to ensure that fluid only flowed through those boundaries that matched the breathing type being simulated[3].

H.2 General flow characteristics

The general flow characteristics of oral and nasal breathing are presented. The differences between inspiration and expiration are discussed for each case. This information supplements the discussion in section 12.1.

H.2.1 Nasal and oral inspiration

The velocity profile shown in figure H.1a illustrates the high velocity regions in the vestibules (nose opening) and larynx. Jetting over the posterior surface of the uvula due to the flow constriction is visible. This phenomenon is more pronounced at high flow rates and matches the observations reported in the literature [56, 67, 147, 195]. The retroglottal jet is not strongly developed in this scenario but has been resolved fully in other studies [56].

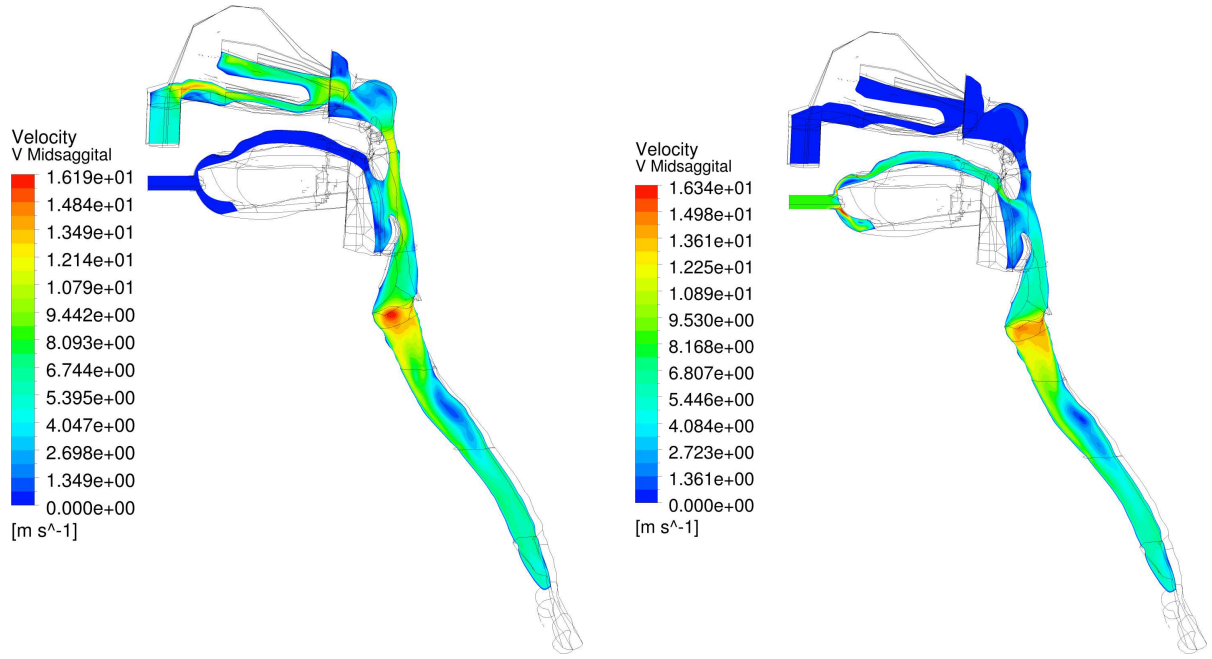

(a) Nasal inspiration

(b) Oral inspiration

Figure H.1: Magnitude of velocity on the midsagittal plane during inspiration at 60L/min.

Figure H.2 depicts velocity contours on coronal sections through the nasopharynx. It was observed that the majority of the fluid mass moves through the medial part of the septum. Towards the posterior third of the nasal passages, air moves into the superior metus and to a lesser extent the inferior metus as the height of the septum is reduced; a flow feature that has also described by Zhang et al. [325]. Upon entering the choanae, the fluid exiting the narrow nasal passages interacts with the surrounding stagnant air and the flow stream

[3] The drawback to this approach is that the static pressure on the blocked inlet wall will be non-atmospheric, which is a non-realistic approximation.

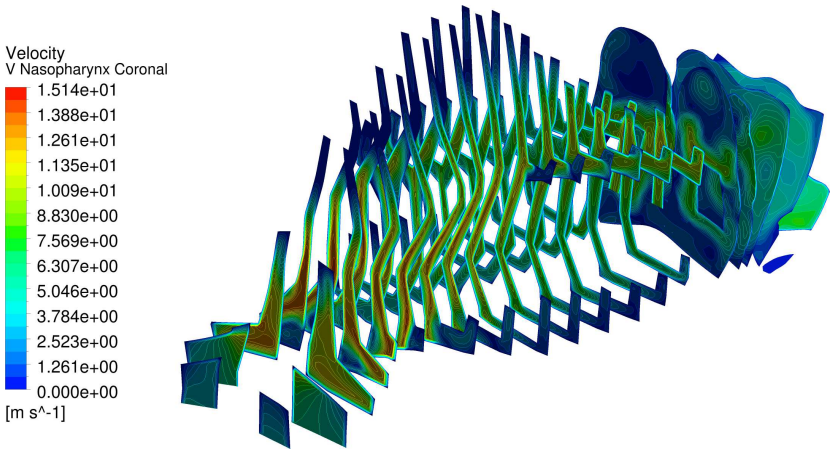

Figure H.2: Coronal sections of the nasopharynx showing fluid velocity during nasal inspiration at $60\mathrm{L/min}$.

becomes more diffusive as it moves towards the velopharynx. Overall, the velocity and pressure profiles in the nasal cavity were qualitatively comparable to the steady simulations shown in [325, 147].

The midsagittal velocity profile for oral inspiration, shown in figure H.1b, was qualitatively similar in low and high flow rate cases. As the tongue blocked the entrance to the mouth, the air moved over its upper surface as well as around its sides. In these images, this was partially illustrated by the stagnation of the air at the tongue tip and the downwards flow from this point. Weak flow jetting was visible between the inferior surface of the uvula and the tongue. The uvula assisted in deflecting the air past the epiglottis and down the pharynx. At lower flow rates, the jet was directed partially onto the epiglottis. At higher flow rates, the jet appeared less well directed due to the secondary effects and the interaction of this jet with the lateral flow moving around the sides of the tongue. The air moving past the uvula remained attached by the Coanda effect and was directed over the epiglottis, a phenomenon also reported in the literature [131].

The flow profile though the buccal cavity is presented in figure H.3. It was very apparent in this image that a large quantity of the air moving through the mouth is channelled along the sides of the tongue. As previously mentioned, this is not necessarily an accurate representation of the normal physiology in humans, but may approximate a condition where the tongue has lifted and deflected back in the mouth. The gap between the tongue and the hard palate was very narrow, while the gap between the sides of the tongue and the inner walls of the cheeks was much wider. This resulted in the latter being the preferred flow path. As large quantities of air moved around the side of the tongue, it was deflected laterally inwards towards the pharynx centreline by the palatopharyneus (PP). The air originating from the superior and lateral surfaces of the tongue then mixed in the pharynx.

Flow acceleration at the larynx was clearly visible for both cases in figure H.1. Inferior to the larynx, a recirculation zone appeared in the trachea. This flow structure was also noted in the literature [196] and is explained by the laryngeal jet that is developed (as shown in [131]). The flow structure in trachea, at a set flow rate, appears independent of orifice of inhalation.

Full-field streamlines (not shown) indicated that, for the case of nasal inspiration, the flow path is very similar at high and low flow rates. The secondary flow pattern of the pharyngeal vortex, as depicted in the literature and shown in figure H.4a, was visible in these cases. Two recirculation loops, lateral to the main flow channel and constrained by the pharyngeal walls, were present during nasal breathing. These vortices were generated

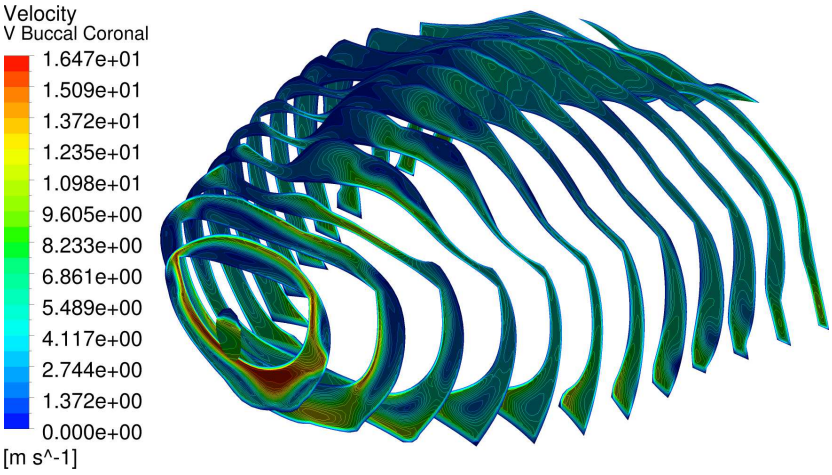

Figure H.3: Coronal sections of the buccal cavity showing fluid velocity during oral inspiration at 60L/min.

by the shear stresses set up by the channel of air moving down the pharynx acting on the stagnant air in the lateral cavities of the pharynx. Additional vortices were present between the tongue and epiglottis. All of these turbulent structures were quite weak and therefore did not produce a significant effect on the pressure field. It was observed that the laryngeal jet was stronger at high flow rates than low flow rates.

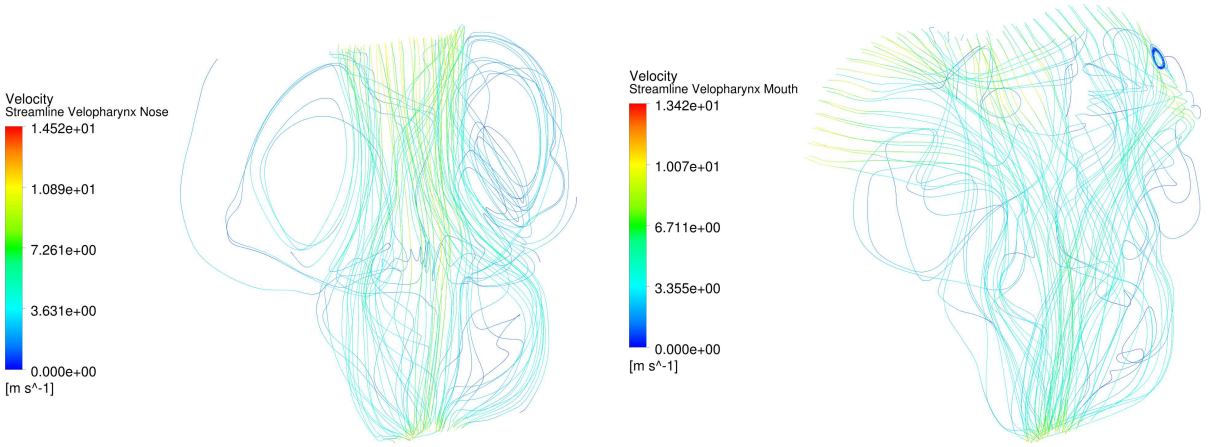

(a) Nasal inhalation

(b) Oral inhalation

Figure H.4: Streamlines of airflow in the pharynx for inspiration at 60L/min.

During oral inspiration, flow around the sides of tongue, clearly seen in figure H.4b, had higher momentum at a higher flow rate and thus resisted changes in direction as it moved into the open passage of the oropharynx. The flow therefore entered the pharynx more directly, while at a low flow rate the air moved around the region of the lateral sublingual glands. However, the turbulence and mixing in the oropharynx was stronger at higher flow rates. Two large vortices were again present in the pharynx, but their location and cause differed considerably in comparison to nasal breathing. The vortices were generated in the wake of the tongue, as the flow moved over the top and sides of it. These turbulent phenomena produced little effect on the low pressure zone that had developed in this region due to losses in the buccal cavity. It is clear from this image that there was quite a lot of transverse movement of air, which had a significant impact on the development of the flow field in the pharynx.

H.2.2 Nasal and oral expiration

The midsagittal flow profile for nasal exhalation is shown in figure H.5a. Apart from a small contribution from flow directed into the oral cavity due to attachment to the epiglottis, the fluid was near stationary in the oral cavity. Fluid flowing from the velopharynx was jetted into the nasopharynx due to the constriction present there. The flow detached from surface of the uvula and was directed towards the superior meatus of the nasal cavity.

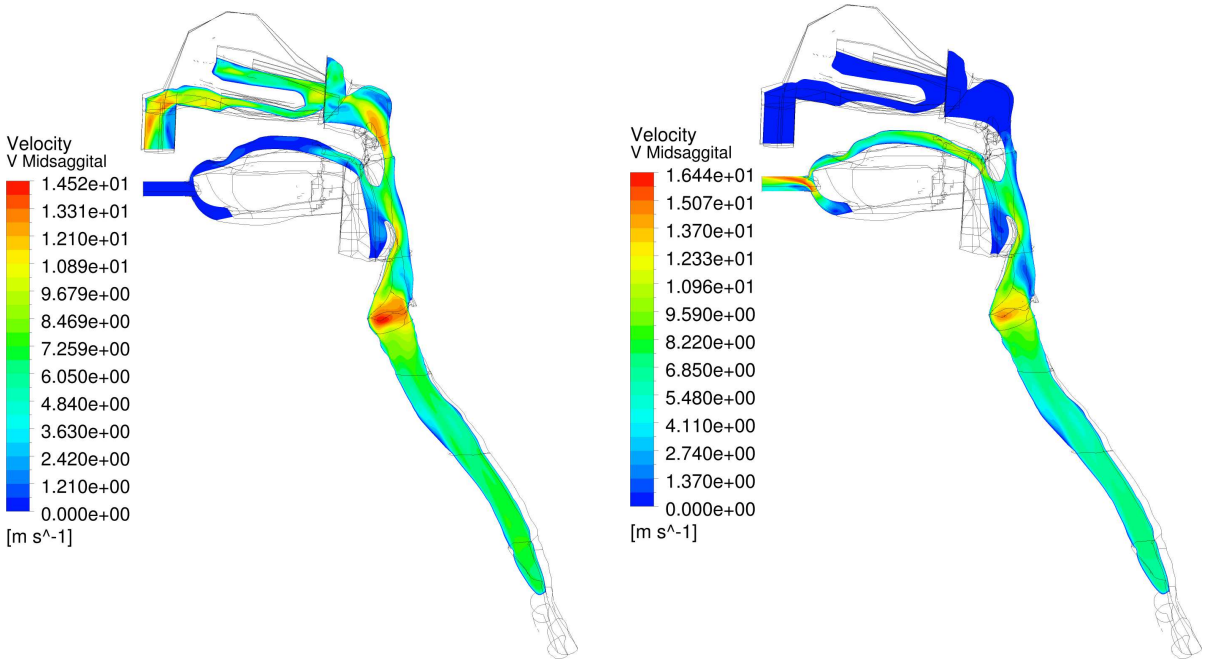

(a) Nasal expiration **(b)** Oral expiration

Figure H.5: Magnitude of velocity on the midsagittal plane during expiration at 60L/min.

Figure H.5b demonstrates that during oral expiration the flow was attached to the epiglottis and directed towards the oral cavity due to the curvature of the epiglottis. However, some fluid was forced into the velopharynx and recirculated in this region. From the nature of the velocity field at the outlet, it was evident that a significant proportion of the fluid mass moved laterally around the tongue body and not over its upper surface. This physiological inaccuracy has been previously discussed in terms of its effect on the nature of inhalation simulated in this work.

H.3 Pressure distribution on the soft palate

Figure H.6 illustrates the pressure distribution on the soft palate. When simulating inspiration though the nose, the soft palate experienced a decreasing pressure profile in the posterior direction over its upper surface while the pressure on the surfaces bounding the oropharynx were near constant. As the superior surface remained a high pressure region, and from a sagittal viewpoint the upper surface has a strong curvature, it was predicted that the air-induced resultant force would move the uvula in the superior direction. However, due to the complex geometry and pressure distribution, this could only be confirmed through further studies using FEA. The pressure drop expected due to the velopharyngeal jet was not large enough to be captured.

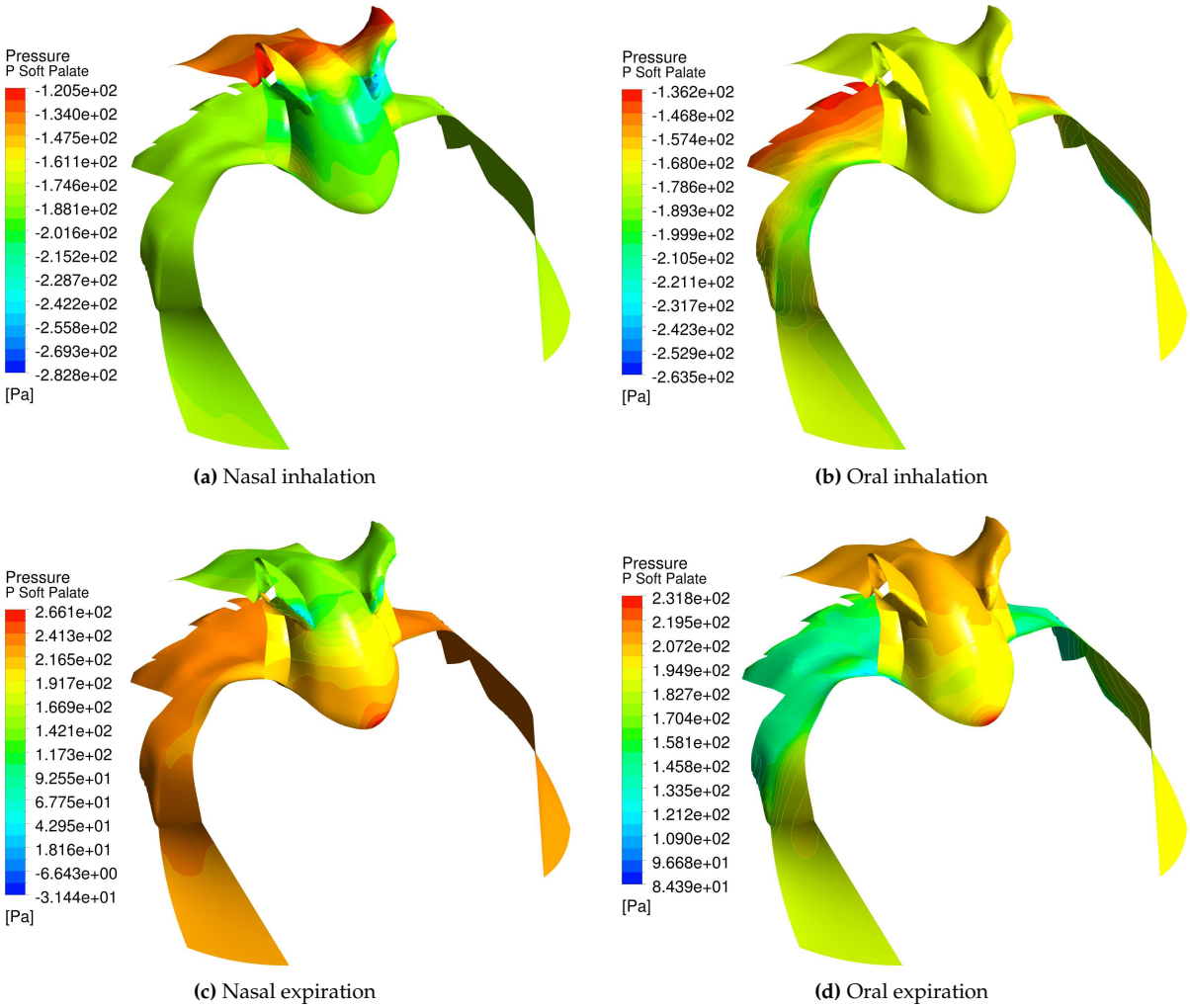

(a) Nasal inhalation

(b) Oral inhalation

(c) Nasal expiration

(d) Oral expiration

Figure H.6: Air-pressure distribution on the soft palate for breathing at 60L/min.

During oral inspiration, the posterior pressure drop was continuous along the oropharyngeal surfaces of the soft palate. Static pressure was recovered in the velopharynx and the posterior surface of the uvula and superior surfaces of the soft palate were exposed to a constant pressure. With the posterior oropharyngeal parts of the soft palate being a low pressure region, the resulting force acting on the pliable regions of the soft palate might have been expected to move the uvula towards the tongue. However, the complex pressure profile on the inferior soft palate made this scenario somewhat more difficult to predict as the anterior of the oropharyngeal soft palate remained a high pressure zone.

The soft palate experiences vastly different pressure distributions for expiration with the two breathing mechanisms. During nasal expiration, the lateral and inferior surfaces in the oropharynx experience a high pressure, while the pressure drop across the velopharynx results in a low pressure region on the superior surface. A significant pressure gradient was observed across the length of the uvula. In contrast, the inferior and lateral surfaces of the uvula are at low static pressure relative to the superior surface during oral expiration. In both cases, the high pressure region at the uvula tip was clearly visible.

Further discussion

The data collected during the CFD study also demonstrated that during high flow rate inhalation the pharyngeal walls are subject to very low pressures due to losses in the buccal cavity or nasal passages. Without stiffening of the pharyngeal constrictors, this may lead to movement of these tissues which would further exacerbate any loss of patency caused by the position of the tongue alone. The pressure distribution on the soft palate is complex and requires further examination in order to predict its motion due to the airway load. An initial study of the movement of the soft palate is presented in appendix I.2, and demonstrates that inhalation through either the nose or mouth tends to displace the uvula forward towards the tongue. This is counter-intuitive for the case of nasal inhalation, and merits further examination preferably using time-dependent FSI analysis. For oral inspiration, this may result in further losses of airway patency and lower epiglottal pressures.

I. FURTHER OPPORTUNITIES FOR RESEARCH

I.1 Complete soft and hard tissue model of HUA

Following on from the discussion in section 8.5, figure I.1a shows the full reconstruction of the tissue of the HUA from the volumetric dataset. Both soft and hard tissues within the region of interest, and which define the extents of the fluid model, are represented. The full micro-histology of the tongue, soft palate and oropharynx is described. The overall goal of creating such a model was to simulate the full deformation of the soft tissues under airway loading conditions, using both FSI and simplified airway pressure models.

To this end, a frictionless surface-to-surface contact model described by Wriggers [313], accompanied by a custom contact detection model, was implemented to cater for the expected contact between the tongue and the soft and hard palate, as well as the lateral tissues under conditions of large deformation. Figure I.2 illustrates the results of a benchmark example, demonstrating the effectiveness of the implemented contact model. Furthermore, the neural model was extended to allow for the simultaneous computation of optimum muscle activation patterns in isolated and non-interacting muscle groups. Subject to the hypothesis that the muscles keeping each tissue group stationary in space resulting in no contact between them, the motion of the tongue, palate and oropharynx remain largely independent. Ultimately, the computational cost of using the full HUA geometry was too large for use within the current computational framework, and focus was placed on the use of models of reduced complexity.

I.2 Soft palate model

A model of the soft palate is illustrated in figure I.1b. The model includes the pliable region of the palate that attaches to the posterior surface of the hard palate, as well as the portion of muscular tissue that forms the palatoglossal arch. Visible is a complex of muscular fibres that exist in the glandular soft tissue of the soft palate, prominent amongst which is the musculus uvulae (UV) which moves the tip of the uvula and the palatopharyneus (PP) that extends through the palatoglossal arch. The external muscles of the levator veli palatini (LVP) and tensor veli palatini (TVP) are shown, as are their origins.

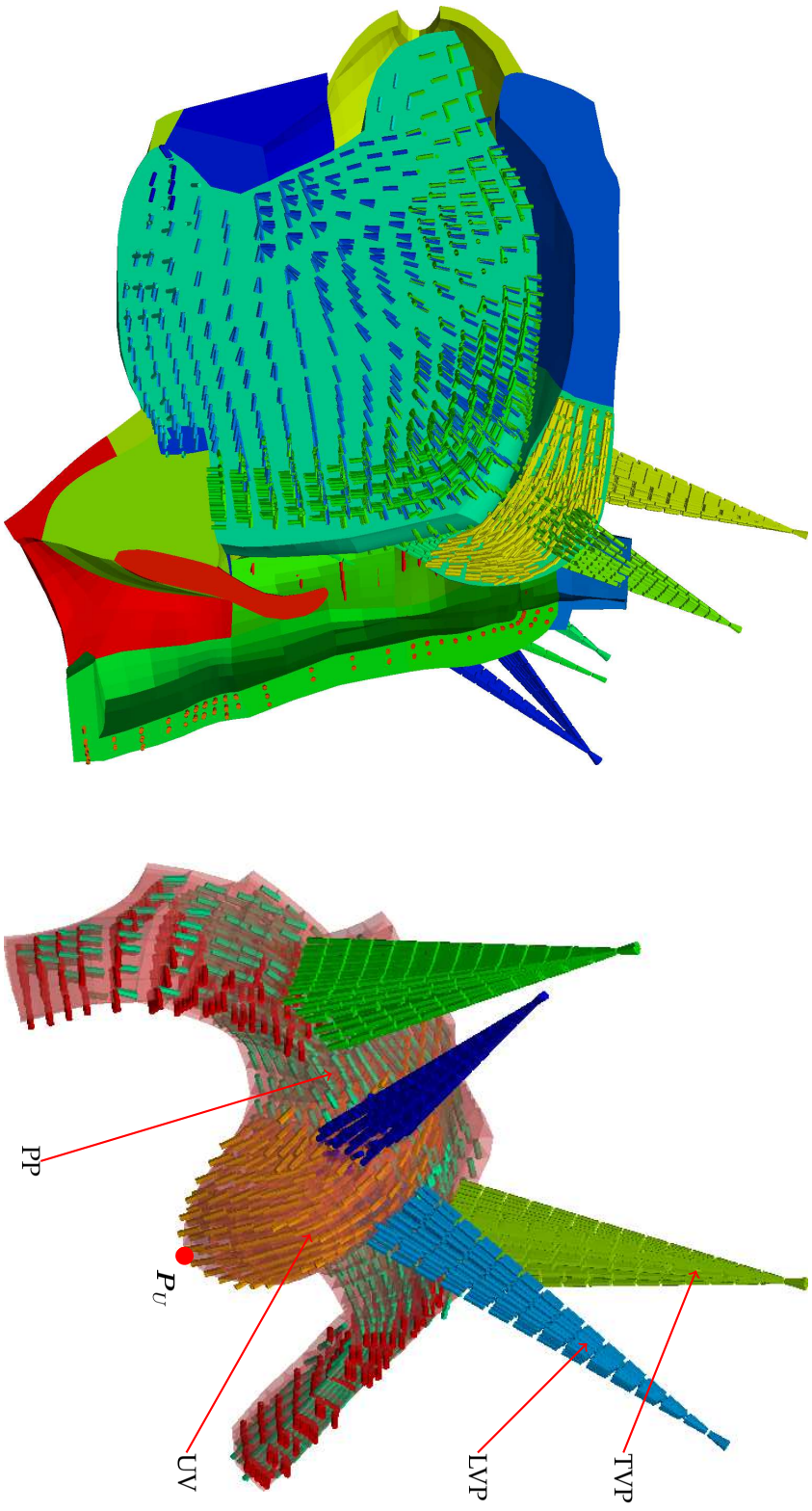

(a) Complete upper airway soft and hard tissue model

(b) Soft palate (posterior isometric view)

Figure I.1: Details of full HUA tissue model

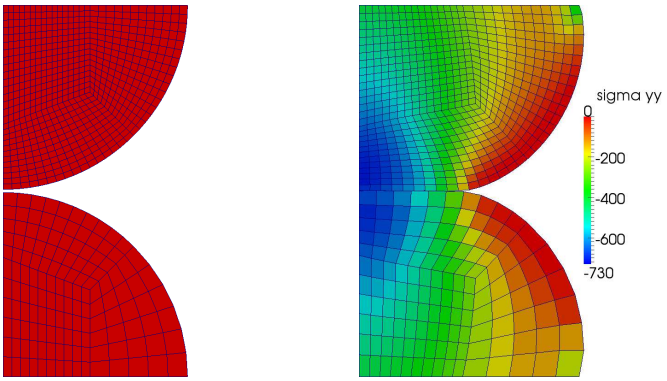

(a) Initial position

(b) Displaced solution with vertical stress distribution

Figure I.2: Surface-to-surface contact of two hard discs

Numerous models, of varying complexity, simulating the uvula and soft palate are represented in the literature [143, 17, 41, 266, 298, 300, 328], as is histological data extracted from experiments [144, 21, 112, 39]. In figure I.1b, the tissue of the soft palate is represented by a mixture of adipose and muscular tissue such that the small strain stiffness modulus of the material is comparable to the (wide) range presented within the literature (approximately 7200Pa). From the data presented in Hamans et al. [96], which presents with a volume fraction of interstitial and connective tissue in the uvula, it was assumed that the volume fraction of muscular fibres in the soft palate was $\phi_f = 0.15$. To pre-strain the tissue, the applied body force was 1.075 times that of gravity in the vertical direction.

Zero-displacement constraints were applied to surfaces that exist on the interface between the hard and soft palates, as well as to the inferior surface of the palatoglossal arch where the PP inserts into the floor of the oropharynx. The presence of adipose and other tissues surrounding the oropharynx and lateral portions of the soft palate are crudely approximated using traction BCs. This tissue adjacent to the palatopharyngeal and lateral pharyngeal constrictor muscles represents the buffer between these muscle and the external muscles of the tongue amongst other anatomical features. In actuality, these tissues would be separated by facial layers that would allow them to slide over one another (tangential motion), but normal motion would be presented due to the contact pressure present between the two parts. However, this reality cannot be accounted for in this stylised model. The interior surfaces of the model exposed to the air existing in the oropharynx, along with the uvula and a portion of the superior surface, experience forces due to air present in the velopharynx and nasopharynx.

Modal analysis was conducted using an implementation of the inverse iteration (power) method [226] to validate the chosen boundary conditions and material characteristics. Figure I.3 shows the first two modes computed for the problem. The captured harmonics appear physiologically plausible as the PP which lines the oropharynx is highly constrained while the palate roof is free to move. A combination of the FE mass lumping method, compliant passive material parameters and the prescribed BCs likely lead to an underprediction of the primary frequency of vibration. The second to fifth harmonics ($14.7 - 21.8$Hz) were within the lower range excited during palatal snoring [202, 157, 220] but well below the spectrum of other frequencies active during snoring. Gravitational orientation was not seen to change the vibration characteristics of the passive soft palate ($\pm$1Hz).

The effect of gravitational and pressure loading on the movement of the passive soft palate was examined

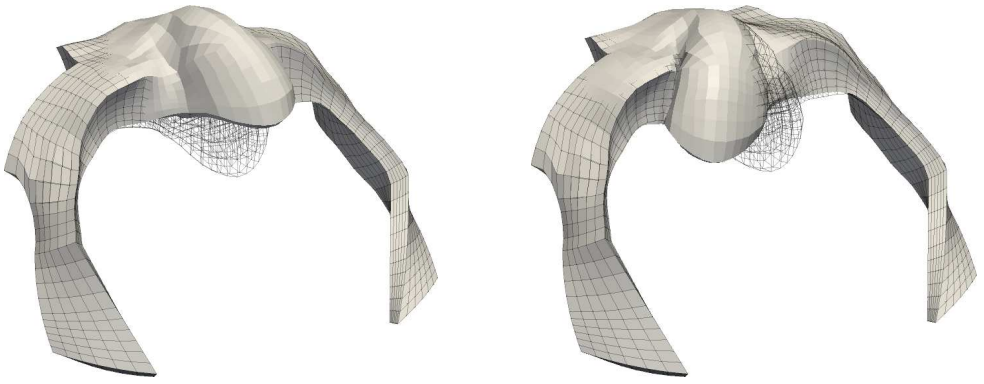

(a) Primary mode: Sagittal planar oscillation (7.1Hz)

(b) Secondary mode: Axial planar oscillation (14.7Hz)

Figure I.3: Harmonics of the soft palate under (upright) gravitational load.

in brief. The pressure distribution extracted from CFD simulations for the inhalation condition were applied to the surface of the soft palate exposed to the airway. Figure I.4 shows the result of this analysis. It was observed that, under no airway loading, the passive palate undergoes very large deflections in the posterior and superior directions when gravity is orientated in the supine direction. This is illustrated visually in figure I.5 for the supine position. Interestingly, the uvula is displaced in the same direction when in the prone orientation. This is due to the location of its centre-of-mass, which is inferior to the palatal arch. Compared to the supine orientation, the magnitude of these zero-pressure movements decreases considerably as the orientation moves towards upright. Overall, the measured displacements are significantly larger than that predicted by Sun et al. [266] (0.004mm) but were of the order of those given by Wang et al. [298] (maximum of 6.7mm).

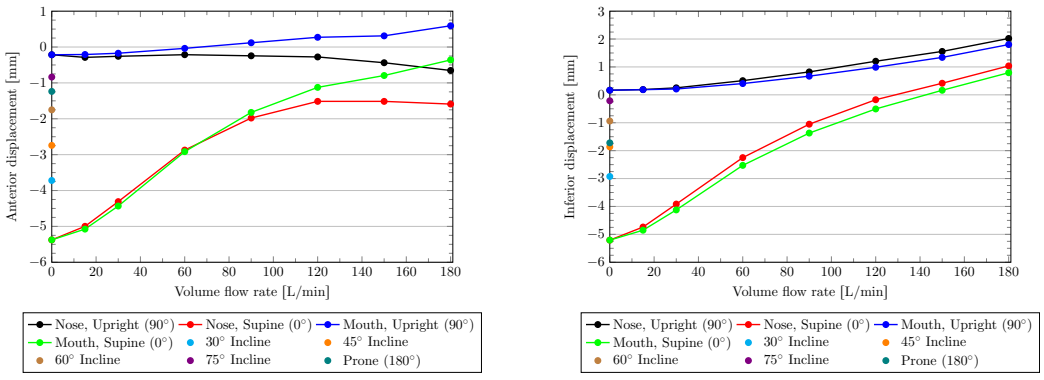

(a) Anterior displacement

(b) Inferior displacement

Figure I.4: Displacement of the uvula apex due to gravitation and pressure loading

Upon inhalation through either the nose or mouth, the general trend was for the uvula to displace anteriorly and inferiorly. This contradicted the initial prediction made in section 12.1.1, that nasal inspiration would result in the uvula displacing superiorly and posteriorly. Fascinatingly, the lack of tissue pre-strain in the upright orientation leads to differing anteroposterior motion when inhalation is through different orifices. Overall, the movement was largest at high flow rates and when gravity acted in the supine direction. Since static CFD simulations were used to generate the pressure field and did not take into account the initial large deformations of the palate, these results appear questionable and represent first approximations only. At inspiration through the nose, it is expected that the reduction in CSA of the velopharynx associated with

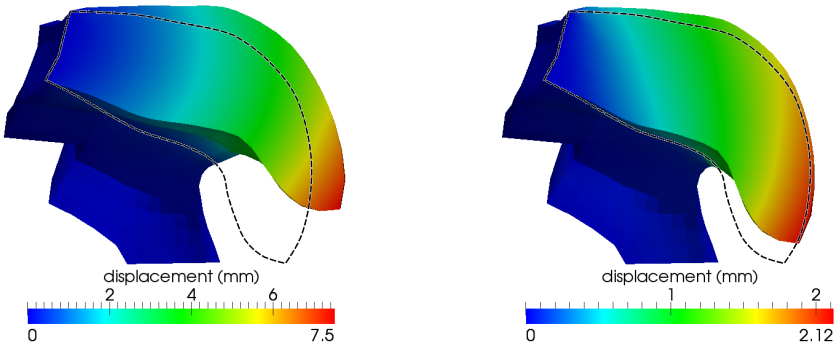

(a) Supine orientation **(b)** Prone orientation

Figure I.5: Displacement on midsagittal plane of soft palate due to gravitational loading.

the posterior movement of the uvula when in the supine orientation would have a significant effect on the pressure distribution over the soft palate.

Figure I.6 shows the displacement of the uvula after the pressure distribution extracted at a fixed flow rate for various breathing scenarios was applied. Comparison with the equivalent no-load case shown in figure I.5a visually demonstrates the forward movement of the uvula predicted during inspiration. However, the very large displacements predicted during the exhalation phase illustrate the need for a more precise material parameters to be developed for use in the model. Providing a more accurate distribution and volume fraction of muscle fibres and adjusting their general tone would result in uvula and palatal stiffening. This would resist such large movements and also increase the primary frequency of vibration.

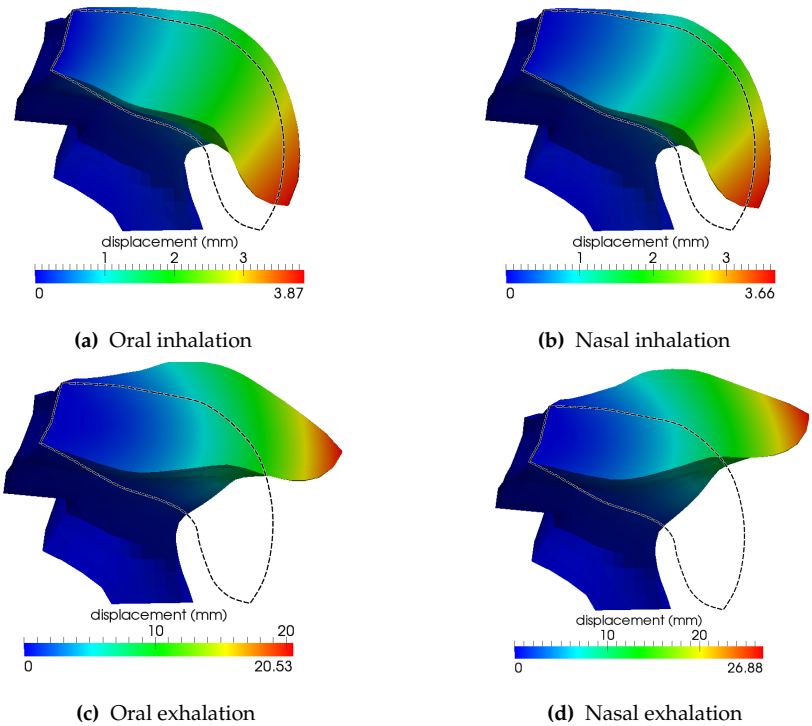

(a) Oral inhalation **(b)** Nasal inhalation

(c) Oral exhalation **(d)** Nasal exhalation

Figure I.6: Displacement on midsagittal plane of soft palate due to gravitational (supine orientation) and pressure (60L/min) loading.

I.3 Neural model

In an extension of the example given in section 7.5.1, the question as to whether the neural model could track a temporally changing goal position was explored. Under no pressure loading, the goal point $\overset{\star}{\boldsymbol{P}}$ was moved in a prescribed manner and the GA was tasked with finding the combination of neural signals that kept the free-corner of the block $\boldsymbol{P}$ nearest $\overset{\star}{\boldsymbol{P}}$ (with no energetic considerations). Figure I.5 shows the relative position of $\boldsymbol{P}$ to $\overset{\star}{\boldsymbol{P}}$ as the goal point moved along different trajectories. It is evident that the model was able to keep distance between the goal and actual positions of the block corner low at all times when the movement of the goal changes smoothly in time. However, introducing a sudden direction change demonstrated a shortcoming of the activation model used resulting in the appearance of a reflexive delay. It can be seen that, given the set of activation parameters, the recovery time taken to reattain the goal position is of the order of 0.1s. This further motivates the desirability of enhancing the model linking the neurological signal to the muscle activation.

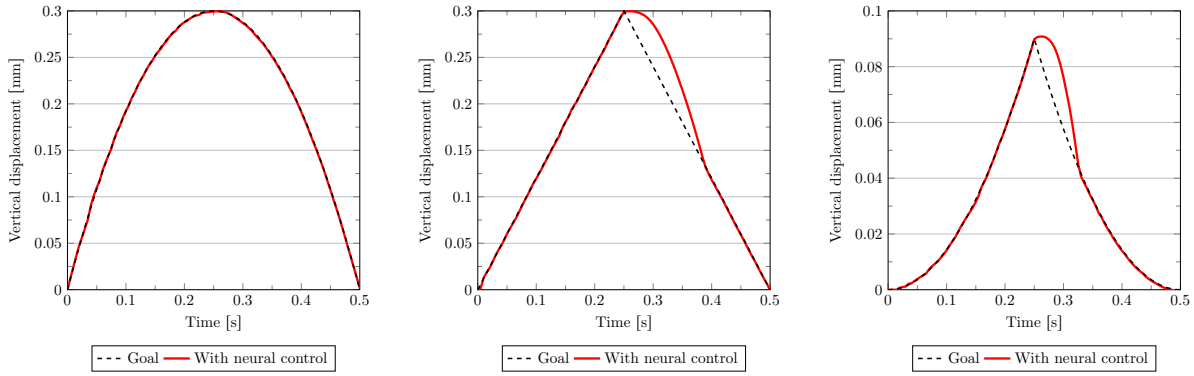

(a) Parabolic **(b)** Linear **(c)** Inverse parabolic with

Figure I.7: Displacement on midsagittal plane of soft palate due to gravitational loading.